issn 0424-7116
**An open-access journal by the German Quaternary Association**
Editor-in-chief: Christopher Lüthgens

# E&G

## Quaternary Science Journal

Eiszeitalter und Gegenwart

Volume 68
No. 1 & 2
2019

**An open-access journal of the German Quaternary Association**

Copernicus Publications
The Innovative Open Access Publisher

# E&G Quaternary Science Journal

An open-access journal of the German Quaternary Association

E&G Quaternary Science Journal (EGQSJ) is an interdisciplinary open-access journal, which publishes peer-reviewed articles and express reports, as well as thesis abstracts related to Quaternary geology, paleo-environments, paleo-ecology, soil science, paleo-climatology, geomorphology, geochronology, archaeology, geoarchaeology, and now also encompassing methodological advances and aspects of the societal relevance of Quaternary research. EGQSJ is a non-profit, community-based effort: It is run by Quaternary scientists, financed by Quaternary scientists, and supporting Quaternary scientists, because any revenue generated is only used to support publications in the journal.

Copernicus Publications
The Innovative Open Access Publisher

Copernicus Publications
Bahnhofsallee 1e
37081 Göttingen
Germany

Phone: +49 551 90 03 39 0
Fax: +49 551 90 03 39 70

**publications@copernicus.org**
**https://publications.copernicus.org**

Printed in Germany.
Schaltungsdienst Lange o.H.G.

ISSN 0424-7116

Published by Copernicus GmbH (Copernicus Publications) on behalf of the German Quaternary Association (DEUQUA).

E&G Quaternary Science Journal
An open-access journal of the German Quaternary Association
https://www.eg-quaternary-science-journal.net/

E&G
Quaternary Science Journal
An open-access journal of the German Quaternary Association
https://www.eg-quaternary-science-journal.net/

E&G Quaternary Science Journal
An open-access journal of the German Quaternary Association
https://www.eg-quaternary-science-journal.net/

## Advisory board



Copernicus Publications
The Innovative Open Access Publisher

Editorial Support

Natascha Töpfer
editorial@copernicus.org

Publication Production

Sarah Schneemann
production@copernicus.org

E&G Quaternary Sci. J., 68, 243–244, 2020
https://doi.org/10.5194/egqsj-68-243-2020


Open Access E&G Quaternary Science Journal

Editorial

# Editorial: *E&G Quaternary Science Journal* – a community-based open-access journal

**Christopher Lüthgens[1], Daniela Sauer[2], Michael Zech[3], Becky Briant[4], Eleanor Brown[5], Elisabeth Dietze[6], Markus Fuchs[7], Nicole Klasen[8], Sven Lukas[9], Jan-Hendrik May[10], Julia Meister[11], Tony Reimann[12], Gilles Rixhon[13], Zsófia Ruszkiczay-Rüdiger[14], Bernhard Salcher[15], Tobias Sprafke[16], Ingmar Unkel[17], Hans von Suchodoletz[18], and Christian Zeeden[19]**

[1]Institute of Applied Geology, University of Natural Resources and Life Sciences, Vienna, Vienna, Austria
[2]Physical Geography, Institute of Geography, University of Göttingen, Göttingen, Germany
[3]Heisenberg Chair of Physical Geography with Focus on Paleoenvironmental Research, Institute of Geography, Technical University of Dresden, Dresden, Germany
[4]Department of Geography, Birkbeck, University of London, London, UK
[5]Chief Scientist Directorate, Natural England, Worcestershire, UK
[6]Polar Terrestrial Environmental Systems Group, Helmholtz Centre for Polar and Marine Research, Alfred Wegener Institute, Research Unit Potsdam, Potsdam, Germany
[7]Physical Geography, Department of Geography, Justus Liebig University Giessen, Giessen, Germany
[8]Institute of Geography, Faculty of Mathematics and Natural Science, University of Cologne, Cologne, Germany
[9]Department of Geology, University of Lund, Lund, Sweden
[10]School of Geography, University of Melbourne, Carlton, Australia
[11]Chair of Geography I – Physical Geography, Institute of Geography and Geology, University of Würzburg, Würzburg, Germany
[12]Netherlands Centre for Luminescence dating, Soil Geography and Landscape group, Wageningen University, Wageningen, the Netherlands
[13]Laboratoire LIVE, Ecole Nationale du Génie de l'Eau et de l'Environnement Strasbourg, Université de Strasbourg, Strasbourg, France
[14]Institute for Geological and Geochemical Research, Research Centre for Astronomy and Earth Sciences, Hungarian Academy of Sciences (MTA), Budapest, Hungary
[15]Quaternary Geology, Department of Geography and Geology, Salzburg University, Salzburg, Austria
[16]Institute of Geography, Faculty of Science, University of Bern, Bern, Switzerland
[17]Environmental History and Environmental Archives, Institute for Ecosystem Research, Kiel University, Kiel, Germany
[18]Chair of Landscape Ecology, Institute of Geography, Technical University of Dresden, Dresden, Germany
[19]Section 5 – Rock Physics & Borehole Geophysics, Leibniz Institute for Applied Geophysics, LIAG, Hanover, Germany

**Correspondence:** Christopher Lüthgens (christopher.luethgens@boku.ac.at)

**Relevant dates:** Published: 16 January 2020

**How to cite:** Lüthgens, C., Sauer, D., Zech, M., Briant, B., Brown, E., Dietze, E., Fuchs, M., Klasen, N., Lukas, S., May, J.-H., Meister, J., Reimann, T., Rixhon, G., Ruszkiczay-Rüdiger, Z., Salcher, B., Sprafke, T., Unkel, I., von Suchodoletz, H., and Zeeden, C.: Editorial: *E&G Quaternary Science Journal* – a community-based open-access journal, E&G Quaternary Sci. J., 68, 243–244, https://doi.org/10.5194/egqsj-68-243-2020, 2020.

*E&G Quaternary Science Journal* (*EGQSJ*) was established under the name *Eiszeitalter & Gegenwart* (i.e. “ice age and present” in German) in 1951 and has since then covered the broad range of Quaternary research. By linking insights from the past (i.e. the ice age) with the present, our publications provide an interdisciplinary understanding and knowledge that becomes even more important in the context of the current challenges of global climate change. Unrestricted access to such knowledge is key, and consequently the year 2019 marked the 10th anniversary of *EGQSJ* as a gold open-access journal. During this last decade, the scientific publishing sector has undergone a number of significant transformations. These include the final shift from analogue to digital formats and the concentration of publications under the terms of a few large scientific publishing houses, offering exclusive paywall protected access to the published scientific work. The most recent transformation is the shift towards open-access publication. This trend has recently been enforced (and supported by extra funding) through changes in the regulations of a number of European and national science funders (e.g. German Science Foundation, DFG; Austrian Science Fund, FWF; European Research Council, ERC), who explicitly demand publication of the results from funded research projects as open access. In this respect, *EGQSJ* has not only stood the test of time, but has been at the leading edge of this development.

In contrast to the large majority of geoscientific and Quaternary-related journals, *EGQSJ* has always been, and will always stay, a non-profit, community-based effort: it is run by Quaternary scientists, financed by Quaternary scientists, and supports Quaternary scientists, because any revenue generated is only used to support publications in the journal. In close cooperation with Copernicus Publications, the journal offers an up-to-date publishing infrastructure guaranteeing high-quality, open-access, peer-reviewed publications adhering to all quality standards and publication ethics. Not least because of that, *EGQSJ* is a member of the Committee on Publication Ethics (COPE) and was awarded the DAOJ (Directory of Open Access Journals) seal in 2018, recognizing the journal’s exceptionally high level of publishing standards and best practice. All content of *EGQSJ* is distributed under the Creative Commons Attribution 4.0 International License (CC BY 4.0). Thus, the journal provides free immediate access to and unrestricted reuse of all types of original works by any user. Of course, authors do retain copyright. Apart from assigning each publication with a digital object identifier (DOI), articles and bibliographic metadata are also distributed to scientific databases and indices, long-term preservation is guaranteed by external archives, and article alert service is offered. *EGQSJ* is listed in the Zoological Record within the Web of Science, and the aim is to establish *EGQSJ* as a fully indexed journal in the Science Citation Index Expanded (SCIE). However, our primary aim is to establish *EGQSJ* as a leading platform for the publication of high-quality, open-access Quaternary-related papers.

We, the new editorial board established in January 2019, fully support the course of the journal and aim to even push *EGQSJ* to new levels. *EGQSJ*’s 2019 publication record must be regarded as an excellent start in this respect, comprising the highest number of papers compared to the last eight volumes, including full research papers but also express reports dealing with innovative aspects of Quaternary research. All papers of course adhere to the exceptionally high quality standards of *EGQSJ*. In 2019, two teams of guest editors strongly supported the editorial team, which led to the publication of two special issues introduced in separate editorials in this volume. Overall, the published papers cover the whole range of subject areas of the journal, including Quaternary geology, paleo-environments, paleo-ecology, soil science, paleo-climatology, geomorphology, geochronology, archaeology, geoarchaeology, and now also encompassing methodological advances and aspects of the societal relevance of Quaternary research. Beyond that, thesis abstracts have become an essential part of *EGQSJ*, reflecting the effort in supporting in particular young researchers in making their high-quality work visible and accessible to a broader audience. To guarantee fair access to thesis abstracts, the Quaternary scientific community, as represented by the host institution of *EGQSJ*, the German Quaternary Association (DEUQUA), always covers the article processing charges (APCs) for the publication of thesis abstracts. This is in line with the journal’s general guidance, to put scientific quality first and not let money be a limiting factor in open-access publication of high-quality research. However, all authors who have third-party funding available to cover the APCs themselves can thereby actively support the journal, and with it the Quaternary scientific community.

Please take your chance to join us in shaping the future of the journal by considering *EGQSJ* as a reputable, worthwhile alternative for publication of scientific papers, innovative express reports, and thesis abstracts dealing with Quaternary research. Submit now at https://www.eg-quaternary-science-journal.net/.

**Financial support.** The article processing charge was funded by the Quaternary scientific community, as represented by the host institution of EGQSJ, the German Quaternary Association (DEUQUA).

E&G Quaternary Sci. J., 68, 237–240, 2020
https://doi.org/10.5194/egqsj-68-237-2020


Open Access E&G Quaternary Science Journal

Preface

# Preface: Special Issue "Geoarchaeology and past human–environment interactions"

**Hans von Suchodoletz[1,2], Stefanie Berg[3], Eileen Eckmeier[4], Lukas Werther[5], and Christoph Zielhofer[2]**

[1]Institute of Geography, University of Technology Dresden, Helmholtzstrasse 10, 01069 Dresden, Germany
[2]Institute of Geography, University of Leipzig, Johannisallee 19, 04103 Leipzig, Germany
[3]Bavarian State Department of Cultural Heritage, Hofgraben 4, 80539 Munich, Germany
[4]Chair of Physical Geography and Land Management Systems, Ludwig Maximilian University Munich, Luisenstrasse 37, 80333 Munich, Germany
[5]Institute of Prehistory, Early History and Archaeology of the Middle Ages, Eberhard Karls University of Tübingen, Schloss Hohentübingen, 72070 Tübingen, Germany

**Correspondence:** Hans von Suchodoletz (hans.von_suchodoletz@tu-dresden.de)

**Relevant dates:** Published: 9 January 2020

**How to cite:** von Suchodoletz, H., Berg, S., Eckmeier, E., Werther, L., and Zielhofer, C.: Preface: Special Issue "Geoarchaeology and past human–environment interactions", E&G Quaternary Sci. J., 68, 237–240, https://doi.org/10.5194/egqsj-68-237-2020, 2020.

## 1 Geoarchaeology: emerging fields and current challenges

Geoarchaeology incorporates various research areas at the interface between geosciences and archaeology. The discipline had already evolved during the 19th century when concepts of geology and stratigraphy were applied to archaeological contexts, but the use of the term geoarchaeology, and its recognition as an independent discipline, only started in the 1970s and 1980s (Cannell, 2012). However, several definitions of geoarchaeology have been proposed and discussed during the last years, depending on the scientific background of the authors (e.g., Butzer, 1982; Leach, 1992; Rapp and Hill, 1998; Benedetti et al., 2011; Engel and Brückner, 2014). Focusing on the equal role of both sciences, we follow the definition of Tinapp (2013) and define geoarchaeology as the application of geoscientific concepts in archaeology, and also of archaeological concepts in geosciences, to investigate the interactions between humans and geoecosystems during different periods. Geoarchaeology is an approach rather than a technique, so any technique or method can be included as it addresses the understanding of past human activities in a landscape and their environmental context (Cannell, 2012).

Given that humans always lived in landscapes and ecosystems and that those landscapes and ecosystems have been influenced by humans since the beginning of human activity, integrative investigations using a geoarchaeological approach are a mandatory precondition to obtain a comprehensive understanding of past human–environmental interactions. Furthermore, given its regional- to local-scale approach in documenting the often long and intricate history of human–environmental interactions, geoarchaeology is well suited for anthroposphere research that looks at regional landscape changes linked with human activity rather than at global phenomena (Kluiving and Hamel, 2016). The discipline strongly evolved during the last years, and different methods such as micromorphology, palynology, geochemistry, isotopic studies, geographical information systems and geophysics were integrated, leading to very multidisciplinary approaches in which the discontinuities and limitations of one proxy can be overcome by the evaluation of another (Ghilardi and Desruelles, 2009; Cannell, 2012; Engel and Brückner, 2014; Zielhofer et al., 2018; Schneider et al., 2019). Furthermore, geoarchaeology was even established as a subject at different universities (Tinapp, 2013).

However, comprehensive and systematic multidisciplinary geoarchaeological research often remains limited to well-funded scientific research and larger commercial projects, although it contributes to a better understanding of complex human–environment interactions and could improve the sampling strategies (Cannell, 2012). In Germany, for example, most excavations are advance archaeological excavations in the context of construction works that are carried out by state departments of archaeology either on their own or by authorized private excavation companies in agreement with the authorities. The comprehensive and systematic application of geoarchaeological approaches is now slowly being realized at archaeological excavations, which also holds true for its use in the context of other applied archaeological questions such as creating databases for monument preservation (Gerlach et al., 2012; Tinapp, 2013; Beilharz and Krausse, 2015; Nadler, 2019). In addition to the development and integration of innovative methods and the further development of existing geoarchaeological concepts, the application of comprehensive and systematic geoarchaeological approaches in the daily practice of archaeological excavations and monument conservation is therefore a current challenge that must be addressed in the coming years in order to prevent further research gaps and an irreversible loss of potential knowledge.

## 2 The contributions of this volume

This Special Issue includes studies that were presented at the 15th annual meeting of the German Working Group for Geoarchaeology (Deutscher Arbeitskreis für Geoarchäologie) that was held during May 2018 at the main seat of the Bavarian State Department for Cultural Heritage in Munich. The working group was founded in 2004 and annually unites around 100 geoscientists and archaeologists from different German-speaking universities and research institutions as well as colleagues from state departments of archaeology, private excavation companies and geoarchaeological freelancers. Besides presenting and discussing current geoarchaeological research projects and the integration of new methods into geoarchaeological contexts, one goal of these meetings is to connect geoscientific and archaeological scientists from universities, research institutions and the daily archaeological practice in order to also distribute geoarchaeological approaches within the latter field. According to the broad-ranging interdisciplinary audience of the meeting, the seven articles in this Special Issue report about current geoarchaeological research projects, the application of innovative methods and approaches in geoarchaeological contexts, and issues related to the daily practice of monument management, mirroring the broad range of current developments and challenges in geoarchaeology.

The study of Hensel et al. (2019) was carried out by scientists at the University of Cologne in the framework of the DFG-funded CRC806 project "Our way to Europe". The authors investigated the recent relations between hydrological systems and the distribution of Palaeolithic sites and obsidian raw material outcrops in southwestern Ethiopia by combining geomorphological–hydrological analyses with field surveys and GIS mapping. Doing so, the authors aimed to transfer these recent interrelations into the past to better understand the factors that influenced prehistoric human settlement activity. Although – due to intensive current morphodynamics – a simple transfer of the recent situation into the past seems rather complicated, this study demonstrates an innovative way to deal with geoarchaeological questions such as former raw material availability at larger regional scales.

The study of Miera et al. (2019) was carried out by scientists at the University of Tübingen in the framework of the DFG-funded CRC1070 project "Resource Cultures" and aims to decipher the Neolithic settlement dynamics in several landscapes of southwestern Germany. The authors combined existing archaeological and new archaeopedological data from colluvial deposits. The latter were dated using radiocarbon and luminescence methods and are regarded as indicators of former settlement activity. This study presents an innovative geoarchaeological approach to complement generally incomplete archaeological datasets of former settlement activity, allowing researchers to derive better-based conclusions about the former settlement dynamics.

The study of Tolksdorf et al. (2019) reports about the results of the EU-funded bilateral German–Czech research project "ArchaeoMontan – Mittelalterlicher Bergbau in Sachsen und Böhmen" and was carried out under the leadership of the Archaeological Heritage Office in Saxony. The authors used palaeobotanical and geochemical methods as well as radiocarbon and potsherd dating to reconstruct the Medieval settlement and mining history as well as desertion processes in a small catchment in the Saxon Ore Mountains of eastern Germany. This study is a good example for how geoarchaeological investigations can complement patchy archaeological and historical datasets, leading to a better understanding of historical processes that are not documented elsewhere.

The study of Engel et al. (2020) reports the results of a joint German–Qatari study that was carried out in the southern Qatari peninsula and was led by scientists from the University of Cologne. The authors investigated the current geomorphic setting and palaeoenvironmental changes recorded in karstic depressions that were centers of prehistoric settlement activity at least since the Neolithic period, focusing on the former availability of water resources. By integrating geomorphic mapping, geophysical prospection, sediment coring, sediment analyses and luminescence dating and relating their results with the location of archaeological sites, the authors aim to contribute to building up a palaeoenvironmental framework of prehistoric settlement.

The study of Reichel et al. (2019) was carried out by scientists from the University of Applied Sciences Berlin. It addresses soil erosion at archaeological sites that on the one hand affects the site through destruction processes and on the other hand builds up a record of former agricultural activity in the form of colluvial layers. The authors investigated Late Holocene colluvia in combination with the position of an adjacent lake shoreline next to an archaeological site in eastern Germany by using sedimentological–pedological analyses, tachymetric mapping and archaeological dating of archaeological finds, photogrammetric methods and GIS. The study demonstrates that this combination of methods allows for a more precise stratigraphical classification of archaeological finds in geoarchaeological trenches, leading to a better chronological classification of colluvial layers.

The study of Teegen et al. (2019) is mostly based on field courses for students that were carried out under the supervision of scientists from the Ludwig Maximilian University in Munich. The authors report about archaeological prospections of a Celtic to Roman site in western Germany using a combination of field and geophysical surveys, lidar scans, aerial photographs, and GIS analyses that resulted in kernel density maps of bricks and ceramics. The authors demonstrate that such an integrated methodological approach leads to a significant gain in knowledge about the location of former houses, the way of their destruction and former waste management.

The study of Vogt and Kretschmer (2019) exemplifies the use of a geoarchaeological approach for cultural heritage management. It emerged from the archaeological practice of the Archaeological Heritage Office in Saxony and the State Office for Cultural Heritage Management Baden-Württemberg. The authors address the conflicts between archaeology and agriculture linked with soil erosion and the drainage of wetlands that endanger archaeological sites in intensively used agrarian landscapes. To locate archaeological sites that are affected by soil erosion, the authors use a geoarchaeological approach that includes aerial photographs, soil mapping and soil coring. The use of this knowledge, by incorporating the interests of landowners and farmers, allows researchers to develop individual conservation and protection strategies for endangered archaeological sites.

## References

Beilharz, D. and Krausse, D.: Archäologische Denkmale in land- und forstwirtschaftlich genutzten Gebieten, edited by: Landesamt für Denkmalpflege im Regierungspräsidium Stuttgart, Archäologie – Landwirtschaft – Forstwirtschaft: Wege zur integrativen Nutzung von Bodendenkmalen in der Kulturlandschaft, 8–19, 2015.

Benedetti, M. M., Cordova, C. E., and Beach, T.: Soils, sediments and geoarchaeology: Introduction, Catena, 85, 83–86, 2011.

Butzer, K. W.: Archaeology as human ecology: method and theory for a contextual approach, Cambridge University Press, Cambridge, 1982.

Cannell, R. J. S.: On the definition and practice of geoarchaeology, Primitive Tider, 14, 1–15, 2012.

Engel, M. and Brückner, H.: Late Quaternary environments and societies: progress in geoarchaeology, Z. Geomorphol., 58, 1–6, 2014.

Engel, M., Rückmann, S., Drechsler, P., Brill, D., Opitz, S., Fassbinder, J. W., Pint, A., Peis, K., Wolf, D., Gerber, C., Pfeiffer, K., Eichmann, R., and Brückner, H.: Sediment-filled karst depressions and riyad – key archaeological environments of south Qatar, E&G Quaternary Sci. J., 68, 215–236, https://doi.org/10.5194/egqsj-68-215-2020, 2020.

Gerlach, R., Fischer, P., Eckmeier, E., and Hilgers, A.: Buried dark soil horizons and archaeological features in the Neolithic settlement region of the Lower Rhine area, NW Germany: Formation, geochemistry and chronostratigraphy, Quatern. Int., 265, 191–204, 2012.

Ghilardi, M. and Desruelles, S.: Geoarchaeology: where human, social and earth science meet with technology, SAPIENS, 2.2, 2, 2009.

Hensel, E. A., Bödeker, O., Bubenzer, O., and Vogelsang, R.: Combining geomorphological–hydrological analyses and the location of settlement and raw material sites – a case study on understanding prehistoric human settlement activity in the southwestern Ethiopian Highlands, E&G Quaternary Sci. J., 68, 201–213, https://doi.org/10.5194/egqsj-68-201-2019, 2019.

Kluiving, S. J. and Hamel, A.: How can archaeology help us unravel the Anthropocene? RCC Perspectives 5: Molding the Planet: Human niche construction at work, 55–62, 2016.

Leach, E. K.: On the definition of geoarchaeology, Geoarchaeology, 7, 405–417, 1992.

Miera, J. J., Henkner, J., Schmidt, K., Fuchs, M., Scholten, T., Kühn, P., and Knopf, T.: Neolithic settlement dynamics derived from archaeological data and colluvial deposits between the Baar region and the adjacent low mountain ranges, southwest Germany, E&G Quaternary Sci. J., 68, 75–93, https://doi.org/10.5194/egqsj-68-75-2019, 2019.

Nadler, M.: Befunde zum Paläorelief im denkmalpflegerischen Alltag: Archäologie in der 3. (und 4.) Dimension, Beiträge zur Archäologie in Mittelfranken 9, 13–52, 2019.

Rapp, G. and Hill, C. L.: Geoarchaeology – The Earth-Science Approach to Archaeological Interpretation, New Haven and London, 1998.

Reichel, J., Heisig, S. F., Schenk, T., and Schatz, T.: Archaeological dating of colluvial and lacustrine deposits in a GIS environment investigating the multi-period site Gortz 1 on Oberer Beetzsee, Brandenburg, E&G Quaternary Sci. J., 68, 107–117, https://doi.org/10.5194/egqsj-68-107-2019, 2019.

Schneider, S., Seeliger, M., and Pint, A.: Multi-proxy geoarchaeology: Editorial, Quatern. Int., 511, 1–5, 2019.

Teegen, W.-R., Cordie, R., Over, P., Mägdefessel, S., Retzlaff, R., and Stoffels, J.: Archaeological prospections in the Roman vicus Belginum (Rhineland-Palatinate, Germany), E&G Quaternary Sci. J., 68, 5–11, https://doi.org/10.5194/egqsj-68-5-2019, 2019.

Tinapp, C.: Geoarchäologie – Beispiele interdisziplinärer Zusammenarbeit aus Sachsen, in: Dokumentation und Innovation bei der Erfassung von Kulturgütern II, edited by: Faulstich, E. I., Schriften des BfK 5, available at: https://www.b-f-k.de/webpub03/content/index.html (last access: 2 January 2020), 2013.

Tolksdorf, J. F., Schubert, M., Schröder, F., Petr, L., Herbig, C., Kočár, P., Bertuch, M., and Hemker, C.: Fortification, mining, and charcoal production: landscape history at the abandoned medieval settlement of Hohenwalde at the Faule Pfütze (Saxony, Eastern Ore Mountains), E&G Quaternary Sci. J., 67, 73–84, https://doi.org/10.5194/egqsj-67-73-2019, 2019.

Vogt, R., and Kretschmer, I.: Archaeology and agriculture: conflicts and solutions, E&G Quaternary Sci. J., 68, 47–51, https://doi.org/10.5194/egqsj-68-47-2019, 2019.

Zielhofer, C., Rabbel, W., Wunderlich, T., Vött, A., and Berg, S.: Integrated geophysical and (geo)archaeological explorations in wetlands, Quatern. Int., 473, 1–2, 2018.

E&G Quaternary Sci. J., 68, 241–242, 2020
https://doi.org/10.5194/egqsj-68-241-2020


Open Access E&G Quaternary Science Journal

Preface

# Preface: Introduction to the special issue "Connecting disciplines – Quaternary archives and geomorphological processes in a changing environment (proceedings of the Central European Conference on Geomorphology and Quaternary Sciences)"

**Johanna Lomax, Thomas Kolb, and Markus Fuchs**

Department of Geography, Justus Liebig University Giessen, Senckenbergstr. 1, 35390 Giessen, Germany

**Correspondence:** Johanna Lomax (johanna.lomax@geogr.uni-giessen.de)

**Relevant dates:** Published: 16 January 2020

**How to cite:** Lomax, J., Kolb, T., and Fuchs, M.: Preface: Introduction to the special issue "Connecting disciplines – Quaternary archives and geomorphological processes in a changing environment (proceedings of the Central European Conference on Geomorphology and Quaternary Sciences)", E&G Quaternary Sci. J., 68, 241–242, https://doi.org/10.5194/egqsj-68-241-2020, 2020.

This special issue contains five scientific papers, which were presented at the "Central European Conference on Geomorphology and Quaternary Sciences", held in Giessen (Germany) in September 2018. The conference was organized by the German Association on Geomorphology (AKG – Deutscher Arbeitskreis für Geomorphologie) and the German Quaternary Association (DEUQUA – Deutsche Quartärvereinigung) and was hosted by the Department of Geography at the Justus Liebig University Giessen.

The aim of the conference was to bring together the closely related fields of geomorphology and Quaternary sciences under the guiding theme "Connecting Disciplines". The necessity of connecting the two disciplines arises from the fact that Quaternary deposits, accumulated thousands or hundred thousands of years ago, can only be understood if the geomorphological processes forming these deposits are known. Vice versa, today's geomorphological processes are often a reorganization of Quaternary (or older) sediments. Therefore, the Quaternary history of deposits and landforms needs to be considered when studying recent morphodynamics. Further sessions of the conference concentrated on geoarchaeology and on recent methodological advances.

Over 260 scientists from 19 different countries participated in the meeting, presenting cutting-edge research from both disciplines as keynote lectures, talks and posters. Student prizes for best oral presentations were awarded to Stefanie Tofelde (Potsdam) for her talk on "Effects of deep-seated versus shallow hillslope processes on cosmogenic $^{10}$Be concentrations in fluvial sand and gravel" and to Anna Schoch (Bonn) for her talk on "Outsize fan evolution – internal structure and influence on the upper Rhone Valley, Switzerland". Two prizes for best poster presentations were handed over to Sebastian Kreutzer (Bordeaux) for his poster on "The Mousterian Loess Sequence La Combette (France): Chronological Evidence of Rapid Environmental Changes in the MIS 4/3 Transition" and to Janek Walk (Aachen) for his poster on "The Guanillos fan complex – implications for the morphogenesis of Atacama's coastal alluvial fans".

Following the guiding theme of the conference, this special issue assembles papers from geomorphology, Quaternary sciences and geoarchaeology. Von Scheffer et al. (2019) reconstruct palaeoenvironmental change and human impact recorded in the Kleinwalser Valley (northern Central Alps, Austria), using X-ray fluorescence (XRF), pollen analysis,

Published by Copernicus Publications on behalf of the Deutsche Quartärvereinigung (DEUQUA) e.V.

and radiocarbon chronologies. They identify the first anthropogenic impact at around 5700 to 6300 BP, large-scale deforestation during the mid to late Bronze Age, and the arrival of the Walser people after around 1300 CE. Tinapp et al. (2019) investigate sediments from the lower Pleiße river in Saxony (Germany) using archaeological finds, plant remains, micromorphological and geochemical analysis and radiocarbon dating. They detect a prominent mid-Holocene black clay horizon, underlain by a sedge peat of Boreal and Preboreal age, as well as Weichselian sands. From 400 BCE onwards, overbank fines dominate, testifying land clearance activities, which intensified further during the Middle Ages. Marr et al. (2019) present $^{10}$Be surface exposure ages of bedrock and boulder samples from southern Norway. These ages indicate an onset of deglaciation of the Scandinavian ice sheet at around 13 ka in southwestern Norway. The paper of Schellmann et al. (2019) focusses on electron spin resonance (ESR) dating of small gastropod shells in order to establish a chronology of Pleistocene gravel terraces from valleys in the Bavarian Alpine Foreland. Their results match the stratigraphy very well and agree well with luminescence ages where available, showing the high potential of ESR dating for constraining the age of Pleistocene fluvial deposits. Dietze and Dietze (2019) use end-member modelling analysis (EMMA) of grain size distributions in order to decipher grain size populations and infer sedimentary histories. They provide R protocols for a robust EMMA and present tests of their model on a synthetic data set of natural sediment types such as loess, dunes and floodplain deposits.

## References


Dietze, E. and Dietze, M.: Grain-size distribution unmixing using the R package EMMAgeo, E&G Quaternary Sci. J., 68, 29–46, https://doi.org/10.5194/egqsj-68-29-2019, 2019.

Marr, P., Winkler, S., Binnie, S. A., and Löffler, J.: $^{10}$Be-based exploration of the timing of deglaciation in two selected areas of southern Norway, E&G Quaternary Sci. J., 68, 165–176, https://doi.org/10.5194/egqsj-68-165-2019, 2019.

Schellmann, G., Schielein, P., Rähle, W., and Burow, C.: The formation of Middle and Upper Pleistocene terraces (Übergangsterrassen and Hochterrassen) in the Bavarian Alpine Foreland – new numeric dating results (ESR, OSL, 14C) and gastropod fauna analysis, E&G Quaternary Sci. J., 68, 141–164, https://doi.org/10.5194/egqsj-68-141-2019, 2019.

Tinapp, C., Heinrich, S., Herbig, C., Schneider, B., Stäuble, H., Miera, J., and von Suchodoletz, H.: Holocene floodplain evolution in a central European loess landscape – geoarchaeological investigations of the lower Pleiße valley in NW Saxony, E&G Quaternary Sci. J., 68, 95–105, https://doi.org/10.5194/egqsj-68-95-2019, 2019.

von Scheffer, C., Lange, A., De Vleeschouwer, F., Schrautzer, J., and Unkel, I.: 6200 years of human activities and environmental change in the northern central Alps, E&G Quaternary Sci. J., 68, 13–28, https://doi.org/10.5194/egqsj-68-13-2019, 2019.

E&G Quaternary Sci. J., 68, 1–4, 2019
https://doi.org/10.5194/egqsj-68-1-2019


Open Access E&G Quaternary Science Journal

Thesis abstract

# Quaternary fluvial environments in NE Morocco inferred from geochronological and sedimentological investigations

**Melanie Bartz**

Institute of Geography, University of Cologne, Cologne, Germany

**Correspondence:** Melanie Bartz (m.bartz@uni-koeln.de)

**Relevant dates:** Published: 25 January 2019

**How to cite:** Bartz, M.: Quaternary fluvial environments in NE Morocco inferred from geochronological and sedimentological investigations, E&G Quaternary Sci. J., 68, 1–4, https://doi.org/10.5194/egqsj-68-1-2019, 2019.

*Supervisors*: Helmut Brückner, Olaf Bubenzer and Gilles Rixhon
*Dissertation online*:
https://kups.ub.uni-koeln.de/7993/

The investigation of fluvial archives in NE Morocco is of high interest for unravelling palaeoenvironmental changes linked to Quaternary climate fluctuations, long-term tectonic activity and/or human influence in NW Africa. The prehistoric site of Ifri n'Ammar is situated in NE Morocco (Fig. 1) and represents a key location for deciphering the history of anatomically modern humans (AMHs) in northern Africa because it reveals Middle and Late Palaeolithic occupation phases since $\sim 170$ ka (Moser, 2003; Nami and Moser, 2010, Richter et al., 2010; Klasen et al., 2018; Fig. 2). This study uses two fluvial systems of different nature – the ephemeral stream Wadi Selloum and the perennial Moulouya River (Fig. 1) – in order to reconstruct the varying environmental conditions for the last $\sim 170$ kyr, the time when AMH started to disperse into the region.

Both fluvial systems provide valuable insights into the geomorphic evolution of the region. It could be demonstrated that both responded to different environmental triggers: the small catchment of the Wadi Selloum ($\sim 290\,\mathrm{km}^2$) is highly affected by the sensitive ecosystem of the Mediterranean region. This ephemeral stream is characterised by a discontinuous and heterogeneous sediment record (Fig. 1a) caused by short-term climatic shifts and human influence (Bartz et al., 2015, 2017). In contrast, the terrace record of the lower Moulouya was considerably affected by tectonic processes related to the collision between the African and Eurasian plates. A W–E-striking thrust fault, associated with N–S compressive shortening in this region, could be identified; it strongly deformed the late Neogene sedimentary sequence of the lowermost basin drained by the Moulouya (Fig. 1) (Rixhon et al., 2017). While long-lasting aggradation led to the formation of composite fill terraces several tens of metres thick in the footwall reach (Triffa plain; Fig. 1b), a terrace staircase with at least three distinct terrace levels characterises the hanging wall reach (Ouled Mansour plateau; Fig. 1c). Tectonic activity appears thus to be the main driver for the evolution of the lower Moulouya terraces (Rixhon et al., 2017; Bartz et al., 2018).

Establishing chronostratigraphies of river sedimentary sequences always remains challenging. However, fluvial deposits of the Wadi Selloum could be well dated via optically stimulated luminescence (OSL) of quartz and post-infrared infrared stimulated luminescence of K feldspar. Although an independent age control was not possible, inter-method comparisons with thermoluminescence (TL) dating of a pottery shard (Bartz et al., 2015) and OSL and post-infrared infrared dating of two samples from the same sedimentary unit (Bartz et al., 2017) allowed the establishment of robust chronologies of the ephemeral stream deposits. The ages range between

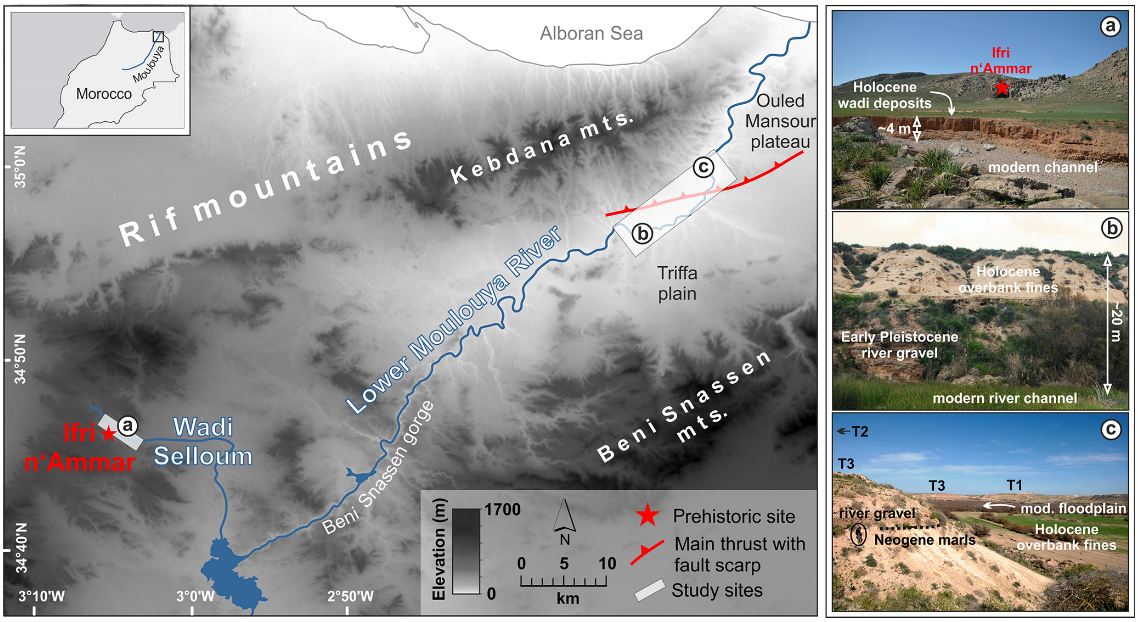


**Figure 1.** Relief map (based on ASTER Global DEM) of the lower Moulouya catchment including the two study areas (greyish rectangles) of the Wadi Selloum and the ∼ 20 km long investigated river reach of the Moulouya River. The red star denotes the prehistoric site of Ifri n'Ammar. **(a–c)** Images of the study areas. **(a)** Ephemeral stream Wadi Selloum in the direct vicinity of Ifri n'Ammar with up to 5 m high Holocene overbank fines (view towards the SE). **(b)** Footwall reach of the thrust zone showing stacked fluvial terraces of the Moulouya with Early Pleistocene gravel deposits and Holocene overbank fines (view towards N). **(c)** Hanging wall reach characterised by a well-preserved staircase of up to three Pleistocene Moulouya terraces above Holocene overbank fines and the modern floodplain. A clear unconformity (dashed line) between Neogene marls and Pleistocene river gravel is illustrated. Person for scale (ellipse) (view towards the NE).

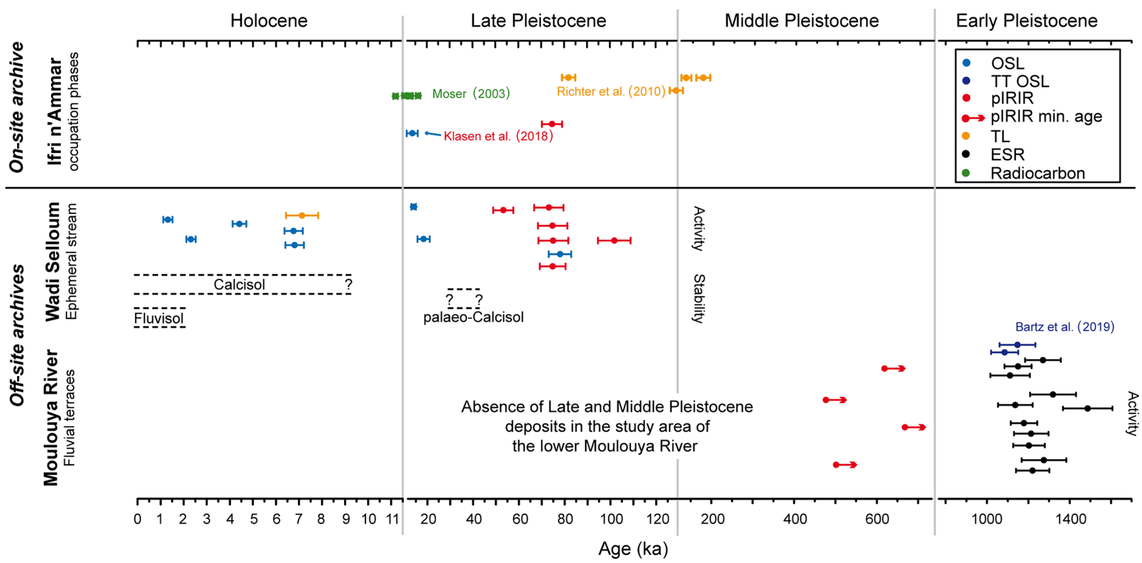


**Figure 2.** Chronological correlation between the on-site archive (occupation phases of the rock shelter Ifri n'Ammar) and the off-site archives (ephemeral stream deposits of Wadi Selloum and fluvial terrace deposits of the lower Moulouya). Chronological data of the two fluvial systems are based on optically stimulated luminescence (OSL), thermoluminescence (TL) (see Bartz et al., 2015), thermally transferred OSL (TT OSL) (see Bartz et al., 2019), post-infrared infrared stimulated luminescence and electron spin resonance (ESR) dating (see Bartz et al., 2017, 2018). From these results, phases of morphodynamic activity and stability can be deduced. The chronological framework of the prehistoric site of Ifri n'Ammar is based on radiocarbon (Moser, 2003) and luminescence dating (Richter et al., 2010; Klasen et al., 2018).

$102 \pm 8$ and $1.3 \pm 0.2$ kyr; they highlight the discontinuous fluvial deposition between MIS 5c and the Holocene (Fig. 2).

Due to the expected Early to Middle Pleistocene age of the fluvial terraces of the lower Moulouya it was challenging to establish luminescence chronologies. Quartz and K feldspar luminescence signals of the studied deposits had reached saturation, suggesting fluvial deposition at least as early as the Middle Pleistocene (Bartz et al., 2018; Fig. 2). However, electron spin resonance (ESR) dating offered a useful alternative way to gain further chronological information. Based on the multiple-centre approach in fluvial environments (Duval et al., 2015), aluminium (Al) and titanium (Ti) centres were measured in quartz; this was cross-checked with palaeomagnetic analyses (Bartz et al., 2018). Thus, a robust geochronological framework was established for the fluvial terraces, with numerical ages dating back to the Early Pleistocene and ranging between $\sim 1.5$ and $\sim 1.1$ Ma (Bartz et al., 2018) (Fig. 2). Recently, Bartz et al. (2019) additionally applied thermally transferred (TT) OSL on the same strata. The single-grain TT OSL results matched well with the newly established ESR chronology and proved the lower Quaternary (Calabrian) age of the fluvial terraces (Bartz et al., 2018, 2019).

Bearing in mind that chronostratigraphies of the ephemeral stream deposits and of the pre-Holocene Moulouya fluvial terraces do not yet exist, the application of different trapped charge dating techniques in combination with palaeomagnetic research served as a valuable tool to obtain chronological information about the deposition in the different fluvial systems.

In addition to using numerical and relative dating techniques, sedimentological, geochemical, mineralogical and micromorphological analyses have been carried out to distinguish periods of enhanced flooding–aggradation from periods of relative stability favourable for pedogenesis. The Wadi Selloum gives information about morphodynamic phases in the time of the settling of AMH (Fig. 2): periods of enhanced aggradation occurred around $\sim 100$, $\sim 75$ and $\sim 55$ ka, after the Last Glacial Maximum, and during the Holocene, whilst sedimentation ended after $\sim 1.3$ ka. Pedogenesis may be used as an environmental indicator for more humid climate conditions during MIS 3 (palaeo-Calcisol), the early Holocene (Calcisol) and the late Holocene (Fluvisol) (Fig. 2).

Although palaeoenvironmental implications should be taken with caution due to the discontinuity of the ephemeral stream system, it appears that more humid and warmer climate conditions may have favoured human settling in this area. This study thus provides the first insights into the palaeoenvironmental changes around the prehistoric site of Ifri n'Ammar during the last glacial–interglacial cycle. In contrast, the absence of Middle and Late Pleistocene deposits in the sedimentary record (Fig. 2) of the lower Moulouya seems to rule out climate as the main driver for long-term fluvial evolution in that region at least during the lower Quaternary. However, it provides valuable information on the regional tectonic history in NE Morocco (Bartz et al., 2018).

**Data availability.** The data are not deposited in data repositories, but are published in the articles Bartz et al. (2015), (2017), (2018) and (2019).

**Acknowledgements.** This research is affiliated with the CRC 806 "Our way to Europe", which is funded by the German Research Foundation (DFG; grant no. SFB 806/2). The support from the "Institut National des Sciences de l'Archéologie et du Patrimoine du Maroc" (INSAP), especially Abdeslam Mikdad at Rabat, and by the "Commission for Archaeology of Non-European Cultures" (KAAK), especially Josef Eiwanger, of the German Archaeological Institute (DAI) is gratefully acknowledged. Furthermore, my sincere thanks go to Mathieu Duval (Griffith University, Australia, and CENIEH, Spain), without whose support this research could not have been successfully completed.

## References

Bartz, M., Klasen, N., Zander, A., Brill, D., Rixhon, G., Seeliger, M., Eiwanger, J., Weniger, G.-C., Mikdad, A., and Brückner, H.: Luminescence dating of ephemeral stream deposits around the Palaeolithic site of Ifri n'Ammar (Morocco), Quat. Geochronol., 30, 460–465, https://doi.org/10.1016/j.quageo.2015.02.012, 2015.

Bartz, M., Rixhon, G., Kehl, M., El Ouahabi, M., Klasen, N., Brill, D., Weniger, G.-C., Mikdad, A., and Brückner, H.: Unravelling fluvial deposition and pedogenesis in ephemeral stream deposits in the vicinity of the prehistoric rock shelter of Ifri n'Ammar (NE Morocco) during the last 100 ka, Catena, 152, 115–134, https://doi.org/10.1016/j.catena.2016.12.007, 2017.

Bartz, M., Rixhon, G., Duval, M., King, G. E., Álvarez Posada, C., Parés, J. M., and Brückner, H.: Successful combination of electron spin resonance, luminescence and palaeomagnetic dating methods allows reconstruction of the Pleistocene evolution of the lower Moulouya river (NE Morocco), Quaternary Sci. Rev., 185, 153–171, https://doi.org/10.1016/j.quascirev.2017.11.008, 2018.

Bartz, M., Arnold, L. J., Demuro, M., Duval, M., King, G. E., Rixhon, G., Álvarez Posada, C., Parés, J. M., and Brückner, H.: Single-grain TT-OSL dating results confirm an Early Pleistocene age for the lower Moulouya River deposits (NE Morocco), Quaternary Geochronol., 49, 138–145, https://doi.org/10.1016/j.quageo.2018.04.007, 2019.

Duval, M., Sancho, C., Calle, M., Guilarte, V., and Penna-Monné, J. L.: On the interest of using the multiple centre approach in ESR dating of optically bleached quartz grains: Some examples from the Early Pleistocene terraces of the Alcanadre River (Ebro basin, Spain), Quaternary Geochronol., 29, 58–69, 2015.

Klasen, N., Kehl, M., Mikdad, A., Brückner, H., and Weniger, G.-C.: Chronology and formation processes of the Middle to Upper Palaeolithic deposits of Ifri n'Ammar using multi-method luminescence dating and micromorphology, Quatern. Int., 485, 89–102, 2018.

Moser, J.: La grotte d'Ifri n'Ammar. Tome 1. L'Ibéromaurusien. AVA-Forschungen Band 8, Kommission für Allgemeine und Vergleichende Archäologie des Deutschen Archäologischen Instituts, Köln, 2003.

Nami, M. and Moser, J.: La grotte d'Ifri n'Ammar, Le Paléolithique moyen, Forschungen zur Archäologie Außereuropäischer Kulturen, 9, Reichert Verlag, Wiesbaden, 2010.

Richter, D., Moser, J., Nami, M., Eiwanger, J., and Mikdad, A.: New chronometric data from Ifri n'Ammar (Morocco) and the chronostratigraphy of the Middle Palaeolithic in the Western Maghreb, J. Hum. Evol., 59, 672–679, 2010.

Rixhon, G., Bartz, M., El Ouahabi, M., Szemkus, N., and Brückner, H.: Contrasting terrace systems of the lower Moulouya river as indicator of crustal deformation in NE Morocco, J. Afr. Earth Sci., 126, 45–57, 2017.

E&G Quaternary Sci. J., 68, 5–11, 2019
https://doi.org/10.5194/egqsj-68-5-2019


Open Access E&G Quaternary Science Journal

Express report

# Archaeological prospections in the Roman vicus Belginum (Rhineland-Palatinate, Germany)

**Wolf-Rüdiger Teegen[1,2], Rosemarie Cordie[3,4], Philomena Over[1], Simon Mägdefessel[1], Rebecca Retzlaff[5], and Johannes Stoffels[5]**

[1]Institut für Vor- und Frühgeschichtliche Archäologie und Provinzialrömische Archäologie, Ludwig-Maximilians-Universität, Munich, 80539, Germany
[2]ArchaeoBioCenter, Ludwig-Maximilians-Universität, Munich, 80539, Germany
[3]Klassische Archäologie, Universität Trier, Trier, 54286, Germany
[4]Archäologiepark Belginum, Morbach-Wederath, 54497, Germany
[5]Umweltfernerkundung und Geoinformatik, Universität Trier, Trier, 54286, Germany

**Correspondence:** Wolf-Rüdiger Teegen (w.teegen@lmu.de)

**Relevant dates:** Received: 31 January 2019 – Accepted: 21 March 2019 – Published: 11 April 2019

**How to cite:** Teegen, W.-R., Cordie, R., Over, P., Mägdefessel, S., Retzlaff, R., and Stoffels, J.: Archaeological prospections in the Roman vicus Belginum (Rhineland-Palatinate, Germany), E&G Quaternary Sci. J., 68, 5–11, https://doi.org/10.5194/egqsj-68-5-2019, 2019.

**Abstract:** The Roman vicus Belginum and the associated Celtic–Roman cemetery have been the subject of systematic archaeological research since 1954. Since 2004, archaeological prospections have been carried out in and around Belginum. Participants included students from the universities of Leipzig, Trier, and Munich as part of study-accompanying field work.

This paper deals with the prospections of 2004 and 2016, when nearly 2 ha of land south of the federal road B327 (Hunsrückhöhenstraße) were surveyed. The study area is located on a NW-to-SE-running hillside. All non-local objects present on the surface were collected and three-dimensionally recorded. Previously in 2013, the area was geomagnetically prospected by Posselt & Zickgraf (Marburg). Both surveys revealed a hitherto unknown extent of the vicus about 200 m to the southwest. The findings date back to the late first to third centuries common era.

All finds (ceramic, bricks, roof slate, glass, and metal) were recorded and analysed in a QGIS and ArcGIS environment together with lidar scans, the geomagnetic data, and other geographical information. The overall distributions of bricks and pottery were studied in detail. The distribution of bricks is in particular connected to the individual plots, while the pottery is mainly concentrated in the backyards. Regarding surveys in other Roman vici, the brick distribution could be a helpful indicator to identify plots, when no geophysical information is available.

**Kurzfassung:** Der römische *vicus Belginum* und das zugehörige keltisch-römische Gräberfeld sind seit 1954 Gegenstand systematischer archäologischer Forschungen. Seit 2004 werden archäologische Prospektionen in und um Belginum durchgeführt. Beteiligt waren Studierende der Universitäten Leipzig, Trier und München im Rahmen von Lehrveranstaltungen.

Diese Veröffentlichung stellt die Ergebnisse der Prospektionen von 2004 und 2016 vor. Prospektiert wurden etwa 2 ha Fläche südlich der Hunsrückhöhenstraße B327. Das begangene Areal liegt auf einem von NW zu SO verlaufenden Hang. Sämtliche auf der Geländeoberfläche beobachteten nicht-lokalen Gegenstände wurden dreidimensional eingemessen und eingesammelt. Bereits 2013 war das Gebiet von der Firma Posselt & Zickgraf (Marburg) geomagnetisch prospektiert worden. Beide Surveys ergaben eine bis dahin unbekannte Ausdehnung des Vicus um 200 m nach Westen. Die datierbaren Funde, überwiegend Keramik, gehören in den Zeitraum zwischen dem späten 1. Jh. und dem 3. Jh. n. Chr.

Sämtliche Funde (Keramik, Ziegel, Dachschiefer, Glas und Metall) wurden in einer Lehrveranstaltung aufgenommen. Die Daten wurden in einer QGIS- und ArcGIS-Umgebung zusammen mit Lidar-Scans, den geomagnetischen Daten und anderen geographischen Informationen analysiert. Die Gesamtverteilungen der Ziegel und Keramik wurden detailliert untersucht. Vor allem die Verteilung der Ziegelfunde folgt den einzelnen, auf dem Magnetometerplot erkennbaren Parzellen. Die Keramik ist dagegen überwiegend im Hinterhofbereich konzentriert. Bei zukünftigen Prospektionen in anderen römischen *vici* kann die Verteilung der Ziegelfunde ein wichtiges Hilfsmittel zur Identifizierung von Grundstücksparzellen darstellen, wenn keine geophysikalischen Daten vorliegen.

## 1 Introduction

Wederath-Belginum (Gde. Morbach, Kr. Bernkastel-Wittlich; localization: Fig. 1, insert) is one of the remarkable rural archaeological sites in Rhineland-Palatinate, Germany. The archaeological ensemble consists of a Celtic and Roman cemetery, the Roman vicus Belginum with at least three sanctuaries and an early Roman military camp (Fig. 1). The ancient name of the vicus is known from a Roman inscription (. . . *vicani belginates*. . . ) and from the well-known *Tabula Peutingeriana* (Haffner, 1989, inside back cover).

Belginum was located at the intersection of the ancient west–east road, linking the capitals of the Roman provinces Gallia Belgica and Germania Superior, Trier-Augusta Treverorum and Mainz-Mogontiacum, and the north–south route connecting the rivers Moselle and Nahe (Haffner, 1989).

The site Wederath-Belginum has been the subject of systematic archaeological research since 1954 (overview in Haffner, 1989, and Cordie, 2007). The burial ground has been comprehensively published in six volumes so far (details and references in Cordie, 2007).

Excavations in the settlement area itself were carried out in 1969–1973 and 2000–2014. The excavations showed that strip houses were present at the Belginum. They are typical for the Roman northwest provinces. The plots are about 10 m wide and up to 80 m long. A (stone) cellar is located near to the street and the building begins above the cellar. A porticus is set in front of the house. The house with half-timbered construction extends about 20–25 m into the rear part of the property (Cordie et al., 2013). Such a plot organization can also be seen on the images of the new geomagnetic prospections (see Figs. 2–3).

## 2 Material and methods

### 2.1 Prospection and data

Since 2004, prospections of various types have been carried out at the Belginum site in the framework of course-related university training with the aim to gain knowledge of the Iron Age settlement (Lukas et al., 2012), the Roman land use, and the extent of the vicus. Students participating came from the universities of Leipzig (UL), Trier (UT), and Munich (LMU). Within Belginum's surroundings (Fig. 1), several *villae rusticae* and at least one settlement of pre-Roman Iron Age could be identified as reported by Teegen et al. (2014, with further references).

#### 2.1.1 Prospection 2004

Already in late autumn of 2004, an approximately 50 m wide and 200 m long strip of ground had been prospected by UL students and staff, along the road to Hintzerath (EV2004,167) (Fig. 1 No. 1). A large number of finds were discovered in 1670 spots. The Roman pottery and the glass finds generally date back to the first to third centuries common era. The find distributions were analysed in a LMU bachelor thesis by Mägdefessel (2018) using the geographic information system QGIS (QGIS Development Team, 2018).

#### 2.1.2 Geomagnetic prospection 2013

In advance of the construction work for the federal road B50neu, large areas south of the federal road B327 (Hunsrückhöhenstraße) were geomagnetically prospected in 2013 by the company Posselt & Zickgraf (Marburg) (see below Figs. 2–3). Surprisingly, it turned out that the vicus extends about 200 m further to the west.

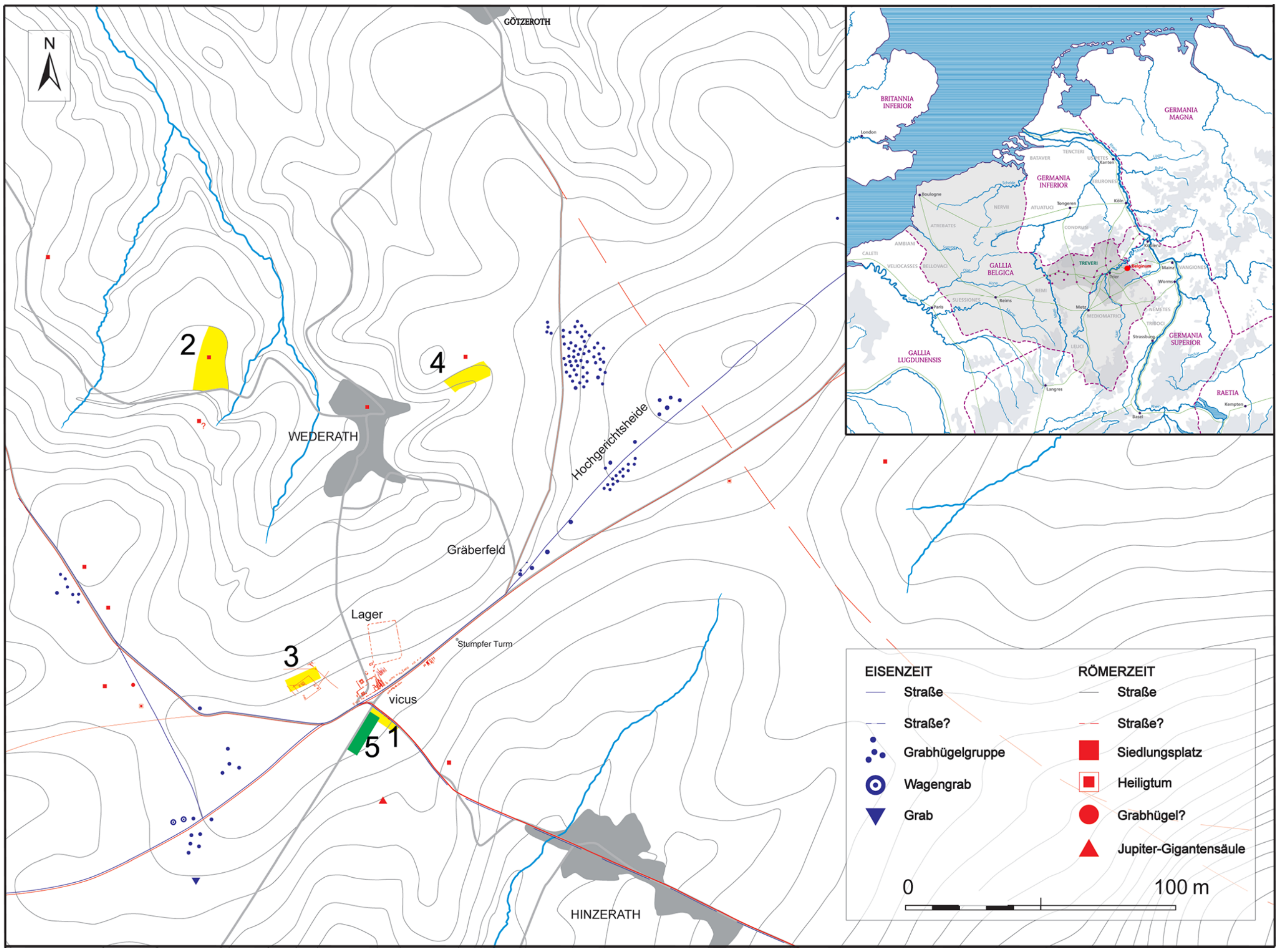


**Figure 1.** The archaeological site Wederath-Belginum during the Iron Age (Eisenzeit) and the Roman times (Römerzeit). Localization of archaeological features, and the survey areas from 2004 to 2008 (1–4, yellow) and 2016 (5, green). Archaeological features are as follows. Vicus: Roman vicus; Lager: Roman military camp; Gräberfeld: Celtic and Roman cemetery; "StumpferTurm": medieval tower. Legend is as follows. Straße: road; Grabhügelgruppe: group of tumuli; Wagengrab: wagon burial; Grab: burial; Siedlungsstelle: *villa rustica*; Heiligtum: sanctuary; Jupiter-Gigantensäule: column of Jupiter and the Giants (map: Marco Schrickel, Jan König, Wolf-Rüdiger Teegen). The insert shows a localization of the site Belginum (red) in the Roman province Gallia Belgica (map: Archaeological Park Belginum).

### 2.1.3 Prospection 2016

In October 2016, a joint field exercise for 10–15 students of (geo-)archaeology and geo-informatics organized by UT and LMU was carried out in the vicinity of Belginum in an agricultural field of approximately 1 ha in size located at the southern side of the federal road B327 within the parish Hundheim (Fig. 1 No. 5) (EV2016,205).

During the first couple of days, the students surveyed the field on a 1 m density grid. All non-local finds (pottery, bricks, glass, metal, etc.) were deposited into plastic bags together with a unique identification code. These were then three-dimensionally sited by means of a total station (Leica) and a differential Global Navigation Satellite System (GNSS) (TopconPositioning Systems, Inc.). As collected fragments in 2016 were abundant, the finds of the site's western part were sampled at 5 m × 5 m quadrants. All together 2856 find locations were sampled containing a total of 9979 finds.

The aim of this prospection was to gather information about dating and material culture in this newly discovered western part of the settlement.

## 2.2 Data integration and analysis in GIS

The archaeological finds were inventoried and classified into the general material groups pottery, bricks, roof slate, glass, and metal during another course at LMU. They were later recorded in an Excel spread sheet. In the consecutive GIS exercise in 2017, these tables were integrated into an ArcGIS geodatabase, which required reorganization of the standard archaeological table structure into an appropriate geodata format. The prospection areas of 2004 and 2016 partly overlap at the north-northeastern region south of the federal

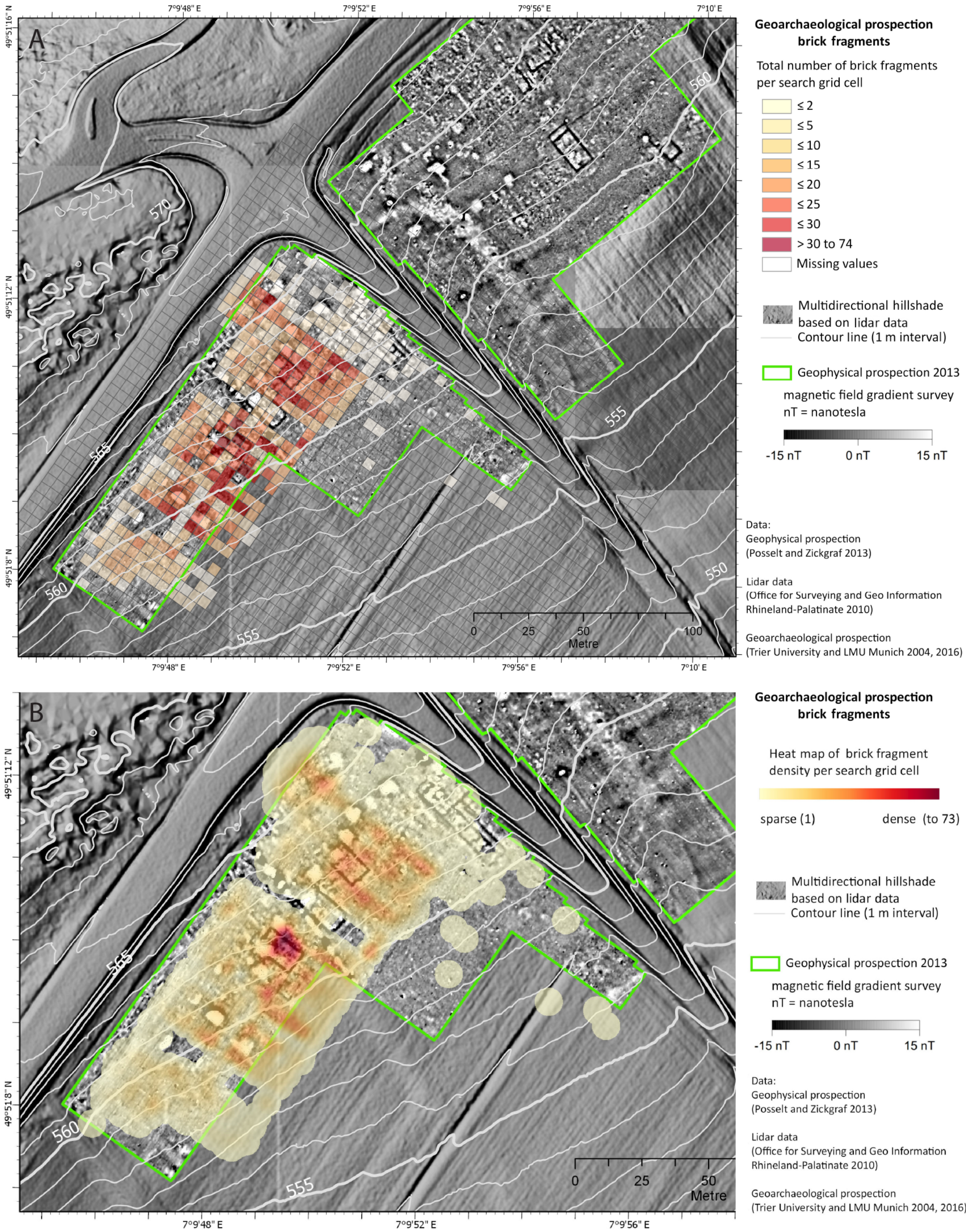


**Figure 2.** Wederath-Belginum, archaeological survey 2004, 2016. **(a)** Total number of brick fragments (1 to 74) per search grid cell (5 m × 5 m) in the western part of the vicus (GIS map: Johannes Stoffels). **(b)** Close-up of the heat map of brick fragments (1 to 74) per search grid cell (5 m × 5 m) in the western part of the vicus (GIS map: Johannes Stoffels).


**Figure 3.** Wederath-Belginum, archaeological survey 2004, 2016. **(a)** Total number of pottery fragments (1 to 52) per search grid cell (5 m × 5 m) in the western part of the vicus (GIS map: Johannes Stoffels). **(b)** Close-up of the heat map of pottery fragments (1 to 52) per search grid cell (5 m × 5 m) in the western part of the vicus (GIS map: Johannes Stoffels).

road Hunsrückhöhenstraße B327 (see Fig. 1 No. 1 and 5). The 3-D position data were projected to ETRS89/UTM32N and archaeological attribute data were merged with the point data for further find density analysis following Allen (2016), exemplary for pottery and bricks. In concordance to the sampling, a regular fishnet of 5 m cells was generated and oriented to follow the study site orientation (SW–NE) as a base for density mapping by summarizing finds for each respective cell (Figs. 2a–3a). Finds were further described by kernel density maps (heat maps) visualizing the number of bricks or pottery fragments for a search grid cell of 5 m × 5 m (Figs. 2b–3b) (Silverman, 1986). Furthermore, the geomagnetic prospection, Rhineland-Palatinate's lidar scans, and topographic raster maps were available. From the lidar elevation data, a multidirectional hillshade raster and contour lines were derived at 5 m elevation intervals. The aim was (a) to explore the data and (b) to map and analyse the occurrence of material groups, which were also further analysed in a bachelor thesis at LMU (Over, 2018) using QGIS.

## 3 Results and interpretation

The classification and inventory of the finds during a course in winter 2016/17 at LMU revealed a dating in a time span from the late first to the third centuries common era. This is consistent with the results of the 2004 prospection (see above). During another course in winter 2018/19 at LMU, handmade pottery of the late Latène or early Roman period (second half of the first century before common era) was discovered. This is the first indication for a late Latène (late pre-Roman) to early Roman settlement at Belginum itself.

The data collected in the above-mentioned bachelor theses (Over, 2018; Mägdefessel, 2018) were summarized in the overall mapping using ArcGIS (see Figs. 2–3).

The geomagnetic prospection from 2013 (Posselt & Zickgraf) revealed several cellars and some houses south of the B327 (see Figs. 2–3). The width of the houses is mostly equal to the plot widths. There is, however, sometimes a small distance between the houses, as the excavations in the last decades have shown (Cordie, 2007). Every house has a quadrangular or rectangular cellar in its front part. The width of the cellars is sometimes equal to the house or plot widths. In general, the cellars are smaller.

The number of fragments per search grid cell and the kernel density map of the bricks (Figs. 2–3) show a clear relation to the single plots. The bricks are distributed from the cellars to the probable house extents up to the backyard area. This means a distance of 30 to 40 m. The finds concentrate in the longitudinal axis of the plots. There is a decreasing intensity of finds to the lateral periphery of the plots. The same distribution may be observed for the adjacent plots. We can, therefore, assume that the distribution of bricks mirrors the houses on the single plots. This is quite an important result for further archaeological prospections on Roman sites, where no geophysical information is available. Here, a reconstruction of the plots would be possible, using the density distributions of bricks.

Focussing on the density or heat maps of bricks within the houses (see Fig. 2), we can see a strong concentration of bricks within the houses. This is probably due to the fact that after leaving the houses at some point the roof truss collapsed inwards (see Bentz, 2013, p. 78). As a result, the roof tiles fell into the interior of the house. This is a quite different mechanism compared to earthquakes, where walls generally collapse to the outside (Stiros, 1995, p. 729, Fig. 4).

From the excavations of the years 1969–1973 and 2000–2014 in the vicus Belginum, we know that the place was not subject to a fire disaster, but had been abandoned. The descriptions of the ruins of the vicus in the early 19th century show that at that time some of the houses towered right up to the first floor (Merten in Cordie, 2007). In the middle and second half of the 19th century, stone and bricks were robbed for modern road and house construction and thus completed the destruction of the vicus. Today, not a single upright wall is present. However, part of the vicus must have already been demolished in late antiquity. The new *burgus*, discovered during rescue excavations in 2015, clearly shows the walls were constructed with secondary building materials.

The distribution of the ceramic sherds shows a different pattern (Fig. 3). Here, the finds are concentrated in the rear part of some houses and in the backyard area. The major concentration of pottery is present in the rear part and in the backyard of three houses in the northern part of the survey area (Fig. 3). From an archaeological perspective, this distribution makes sense. When a Roman strip house is excavated, the major quantity of (storing) vessels, glass, and other household items will be discovered in the backyard. Here, the waste pits are usually localized. The waste pits were partly destroyed due to agricultural work in the last 2 centuries, and their contents came to light. The plowing activity might shift ceramics and other finds downhill by about $\geq 5$ m.

## 4 Prospect

This work has shown that curricular practical course prospections bring further insights into settlement archeology. This can be achieved with systematic field surveys, geophysical surveys, lidar scans, and aerial photographs obtained by plane, drone, or fixed-wing unmanned aerial vehicle.

The use of various archaeological and geophysical prospection methods and the following GIS analyses brought a significant gain in knowledge for the site Belginum regarding size and type of development – without excavation.

**Data availability.** For the next years, there is an ongoing project regarding the spatial distribution of pre-Roman and Roman findings in the vicus Belginum. This will result in some theses at LMU and UT. Furthermore, due to illegal activities of non-authorized detec-

torists, find co-ordinates will not be published. They will be, however, stored in due course in the find archive of the Rheinisches Landesmuseum Trier.

**Author contributions.** RC and WRT organized the archaeological prospection, funding, and the identification of the findings. RR and WRT were responsible for on-site data catchment. JS and RR organized the GIS course and GIS analysis. JS, RR, SM, and PO analysed GIS data. WRT and RC interpreted GIS data. WRT and RR wrote the paper with contributions from all co-authors.

**Competing interests.** The authors declare that they have no conflict of interest.

**Special issue statement.** This article is part of the special issues "Geoarchaeology and past human–environment interactions". It is not associated with a conference.

**Acknowledgements.** The work has been carried out using ESRI ArcGIS and QGIS. Special thanks go to the students eagerly collecting fragments despite sometimes harsh weather conditions. Lidar and topographic map raster data (Basis-DLM) have kindly been provided by Rhineland-Palatinate's surveying office Vermessungs- und Katasterverwaltung (topicality), 2014, 2015. The Archaeological Heritage of Rhineland-Palatinate at Trier (GDKE) kindly gave the necessary permissions. The group of students from Munich was gratefully supported by LMU and the local archaeological association (Förderverein Archäologiepark Belginum e.V.). For correcting the English in a previous version of the paper, we are grateful to Anneli O'Neill (LMU Munich). All remaining errors are, of course, our own.

## References

Allen, D. W.: GIS Tutorial 2: Spatial Analysis Workbook (GIS Tutorials), 4th edn., ESRI Press, Redlands, USA, 2016.

Bentz, M.: Das Handwerkerviertel von Selinunt. Die Töpferwerkstatt in der Insula S 16/17-E, Vorbericht zu den Kampagnen 2010–2012, Röm. Mitteil., 119, 69–98, 2013.

Cordie, R. (Ed.): 50 Jahre Ausgrabungen und Forschungen, Schriften des Archäologieparks Belginum 5, Philipp von Zabern, Mainz, Germany, 2007.

Cordie, R., König, J., and Teegen, W.-R.: Der vicus von Belginum. Zum Stand seiner Erforschung, in: Neue Forschungen zu zivilen Kleinsiedlungen (vici) in den römischen Nordwest-Provinzen, edited by: Heising, A., Akten der Tagung Lahr, 21–23 October 2010, Verlag Dr. Rudolf Habelt, Bonn, Germany, 101–118, 2013.

Haffner, A. (Ed.): Gräber – Spiegel des Lebens, Schriftenreihe des Rheinischen Landesmuseums Trier 1, Philipp von Zabern, Mainz, Germany, 1989.

Lukas, D., Teegen, W.-R., Cordie, R., Schrickel, M., König, J., and Fleischer, F.: Auf der Suche nach den Kelten – Systematische Prospektionen im Umkreis von Belginum, in: Die Eisenzeit zwischen Champagne und Rheintal, edited by: Schönfelder, M. and Sievers, S., 34. Internationales Kolloquium der Association Française pourl'Étude de l'âge du Fer, 13–16 May 2010, Aschaffenburg, Römisch-Germanisches Zentralmuseum, Mainz, 263–290, 2012.

Mägdefessel, S.: Eine GIS-gestützte Untersuchung von Prospektionsfunden aus Wederath-Belginum (Kampagne 2004), BA thesis, Ludwig-Maximilians-University Munich, Germany, 41 pp., 2018.

Over, P. M.: Zur Dokumentation, Visualisierung und Analyse von Prospektionsfunden aus Wederath-Belginum, BA thesis, Ludwig-Maximilians-University Munich, Germany, 116 pp., 2018.

QGIS Development Team: QGIS Geographic Information System. Open Source Geospatial Foundation Project, available at: http://qgis.osgeo.org, last access: 17 December 2018.

Silverman, B. W.: Density estimation for statistics and data analysis, Chapman and Hall, New York, USA, 1986.

Stiros, S. C.: Archaeological evidence of antiseismic constructions in antiquity, Annali di Geofisica, 38, 725–736, 1995.

Teegen, W.-R., Lukas, D., and Cordie, R.: Untersuchungen zur eisenzeitlichen Besiedlung von Wederath/*Belginum*, Archaeol. Mosellana, 9, 215–235, 2014.

E&G Quaternary Sci. J., 68, 13–28, 2019
https://doi.org/10.5194/egqsj-68-13-2019


Open Access E&G Quaternary Science Journal

Research article

# 6200 years of human activities and environmental change in the northern central Alps

**Clemens von Scheffer[1,2], Annika Lange[1], François De Vleeschouwer[2,3], Joachim Schrautzer[1], and Ingmar Unkel[1]**

[1]Institute for Ecosystem Research, Christian-Albrechts University, Olshausenstraße 75, 24118 Kiel, Germany
[2]EcoLab/Campus Ensat, Toulouse INP, Avenue de l'Agrobiopole, 31326 Castanet-Tolosan, France
[3]Instituto Franco-Argentino para el Estudio del Clima y sus Impactos (UMI IFAECI/CNRS-CONICET-UBA) Dpto. de Ciencias de la Atmosfera y los Oceanos, FCEN, Universidad de Buenos Aires Intendente Guiraldes 2160, Ciudad Universitaria (C1428EGA) Ciudad Autónoma de Buenos Aires, Argentina

**Correspondence:** Clemens von Scheffer (cscheffer@ecology.uni-kiel.de)

**Relevant dates:** Received: 19 December 2018 – Revised: 18 March 2019 – Accepted: 3 April 2019 – Published: 8 May 2019

**How to cite:** von Scheffer, C., Lange, A., De Vleeschouwer, F., Schrautzer, J., and Unkel, I.: 6200 years of human activities and environmental change in the northern central Alps, E&G Quaternary Sci. J., 68, 13–28, https://doi.org/10.5194/egqsj-68-13-2019, 2019.

**Abstract:** In this study, we combine erosion and anthropogenic proxies (Ti, Pb) from calibrated portable XRF with pollen and radiocarbon chronologies in peat from mires of the Kleinwalser Valley (Kleinwalsertal, Vorarlberg, Austria) to reconstruct palaeoenvironmental change and human impact in the northern central Alps. Favoured by a wetter climate, two analysed mires formed 6200 years ago in a densely forested valley. Landscape opening suggests that the first anthropogenic impact emerged around 5700 to 5300 cal BP. Contemporaneously, lead enrichment factors (Pb EFs) indicate metallurgical activities, predating the earliest archaeological evidence in the region. Pollen and erosion proxies show that large-scale deforestation and land use by agro-pastoralists took place from the mid- to late Bronze Age (3500 to 2800 cal BP). This period was directly followed by a prominent peak in Pb EF, pointing to metallurgical activities again. After 200 cal CE, a rising human impact was interrupted by climatic deteriorations in the first half of the 6th century CE, probably linked to the Late Antique Little Ice Age. The use of the characteristic Pb EF pattern of modern pollution as a time marker allows us to draw conclusions about the last centuries. These saw the influence of the Walser people, arriving in the valley after 1300 cal CE. Later, the beginning of tourism is reflected in increased erosion signals after 1950 cal CE. Our study demonstrates that prehistoric humans were intensively shaping the Kleinwalser Valley's landscape, well before the arrival of the Walser people. It also demonstrates the importance of palaeoenvironmental multiproxy studies to fill knowledge gaps where archaeological evidence is lacking.

**Kurzfassung:** In dieser Studie kombinieren wir Paläoproxies für Erosion und menschliche Aktivitäten (Ti, Pb) aus Messungen eines mobilen RFA- bzw. XRF-Analysators mit Pollen und Radiokohlenstoffdatierungen in Torfproben aus Mooren des Kleinwalsertals (Vorarlberg, Österreich). Auf diese Weise sollen der Wandel der Paläoumweltbedingungen sowie der Einfluss des Menschen auf die Landschaft der nördlichen Zentralalpen untersucht werden. Begünstigt durch feuchteres Klima, begann vor ca. 6200 Jahren im damals dicht bewaldeten Tal die Torfbildung in zwei der untersuchten Moore. Aulichtungen des Waldes deuten auf den ersten menschlichen Einfluss zwischen cal B.P. 5700 und 5300 hin. Gleichzeitig suggerieren Bleianreicherungen (Pb EF) metallurgische Aktivitäten, die weit vor jeglichen archäologischen Beweisen in der Region liegen. Pollen und Erosionsproxies bezeugen eine weitläufige Entwaldung und Landnutzung durch Landwirtschaft und Beweidung in der mittleren und späten Bronzezeit (3500 bis 2800 cal B.P.). Dieser Phase folgte ein vorläufiger Höchstwert des Pb EF zum Beginn der Eisenzeit, der erneut auf Bergbau oder Metallurgie in der näheren Umgebung hindeutet. Eine im cal A.D. 3. Jahrhundert einsetzende verstärkte Landnutzung wird im cal A.D. 6. Jahrhundert unvermittelt durch klimatisch ungünstigere Bedingungen unterbrochen, welche der sogenannten spätantiken kleinen Eiszeit zugeschrieben werden können. Unter Zuhilfenahme des charakteristischen Verlaufs der modernen Bleiemissionen als Zeitmarker, konnten die Analyseergebnisse der letzten Jahrhunderte eingeordnet werden. Diese waren von der Ansiedlung der Walser im cal A.D. 14. Jahrhundert geprägt. Nach cal A.D. 1950 zeigt sich außerdem der erstarkende Tourismus anhand höherer Erosionsspuren. Unsere Ergebnisse machen deutlich, dass die Landschaft des Kleinwalsertals schon weit vor Ankunft der Walser vom Menschen genutzt und verändert wurde. Unsere Studie betont zudem die Wichtigkeit der Anwendung unterschiedlicher Paläoproxies, insbesondere, wenn archäologische Anhaltspunkte zur Landnutzungsgeschichte fehlen.

## 1 Introduction

Humans have been recurringly present in Alpine environments since the last deglaciation (e.g. Cornelissen and Reitmaier, 2016). These harsh landscapes are heterogeneous and sensitive to climate (Barry, 2002), which requires specific human adaptation (Clegg et al., 1970). Half nomadic lifestyles or transhumance have been strategies to survive, and are still today the basis for seasonal livestock management practice in mountainous regions (e.g. Reitmaier et al., 2018). There is however no consensus on the human colonisation of European mountains during the Holocene. In the Alps, the onset of human impact is still not fully understood because occupation pulses were radiating from different regions and societies at different time periods (e.g. Bätzing, 2015; Carcaillet, 1998; Dietre et al., 2017; Oeggl and Nicolussi, 2009; Valese et al., 2014). It is therefore important to document human occupation and its impact on mountain environments to a certain level of detail, as each region or each valley reveals pieces of information on the complex spatial linkages between humans and environmental and climatic conditions.

Another challenge in reconstructing past human impacts in the Alps is the general scarcity of suitable palaeoenvironmental archives in high mountain areas. Archaeological records and historical sources cannot provide continuous information and may bias interpretations towards separate findings. These gaps are generally closed by environmental archives, such as trees, lakes, glaciers or mires, which potentially provide uninterrupted records of past environmental changes (anthropogenic or natural). However, except for pollen or dendrochronological studies, mountain mires are so far rarely used as environmental archives.

In this paper, we present a multiproxy study of the Kleinwalser Valley (Kleinwalsertal) in the Austrian northern central Alps, using small mountain mires as environmental archives. The valley is historically known for its human occupation, animal husbandry and forestry only since the Late Middle Ages (Fink and von Klenze, 1891; Wagner, 1950). Before that, the human impact on this valley is unclear. While Romans were present in the Alpine foreland (Mackensen, 1995; Weber, 1995), there are no records of their presence in the valley. Palaeovegetation information suggests prehistoric land use (Dieffenbach-Fries, 1981; Grosse-Brauckmann, 2002) but chronologies and data are limited. Other evidence points to early activities at archaeological sites in the valley (Bachnetzer, 2017; Gulisano, 1994, 1995; Leitner, 2003), which are located close to our study sites (Fig. 1). These spots may have acted as strategic points between Alpine foreland and the surrounding mountain ranges, leading prehistoric humans to cross and occupy the Kleinwalser Valley.

By combining geochemical and palynological data together with radiocarbon chronologies, we aim at better understanding the points in time and impacts of human occupation in the Kleinwalser Valley's landscape and beyond. We also aim at detecting early metallurgical activities, possibly where archaeological evidence is lacking. By looking into the past, using multiple proxies on chronologically constrained peat sequences from a key area, we provide new insights into the development and interaction of landscape, climate and humans from mid-Holocene to modern times in the northern central Alps.

## 2 Study sites

The Kleinwalser Valley belongs to the federal state of Vorarlberg in the north-western part of Austria (Fig. 1) and is located at the junction of the geological units of the Northern Calcareous Alps, Penninic flysch and Helvetic (Völk, 2001). The valley floor elevates around 1100 m a.s.l. and is surrounded by mountains ranging from 2000 to 2500 m a.s.l. Geologically speaking, the watershed is composed of calcareous as well as silicate rocks. During the late Pleistocene, the valley was glaciated (Völk, 2001) and several moraines are still present. Iron (Fe), lead (Pb), zinc (Zn) and copper (Cu) ores are present outside the valley. Within 20 km N-NE, iron had been exploited since 1471 CE in Sonthofen (Merbeler, 1995). Pb–Zn deposits are known to the NE at Himmelschrofen (Fig. 1) (von Gümbel, 1861) and in the Ostrach Valley since 1620 cal CE (Oblinger, 1996). To the south, Zn–Pb deposits exist at Zug, at St. Anton at Arlberg, and at St. Christoph at Arlberg and Cu can be found at Bartholomäberg (Weber, 1997) within 35 km off the lower Kleinwalser Valley.

A temperate climate in the Kleinwalser Valley is reflected by a mean annual temperature of 5.7 °C and 1863 mm of mean annual precipitation (HDÖ, 1994). In combination with impermeable sediments of glacial or postglacial lacustrine origin, these climate conditions foster the development of many mires in the valley (Schrautzer et al., 2019; El Balti et al., 2017; Völk, 2001).

The main study site, Hoefle Mire (HFL, GPS: 47°21′52.5″ N, 10°10′37.2″ E, Fig. 1), is at an elevation of 1020 m a.s.l. and in immediate proximity of the early Mesolithic archaeological site "Egg" (Bachnetzer, 2017) (Fig. 1a) on a small rise almost in the middle of the valley bottom. Its sheltered position between the rivers Breitach and Schwarzwasser protects it from both river erosion and direct sediment input from the mountainsides. Therefore, this mire is a suitable archive to record atmospheric signals, undisturbed by small-scale processes. The current vegetation consists of typical bog species such as *Sphagnum* spp., *Eriophorum vaginatum* and several species of the family *Ericaceae*. Glacial ground moraine material and localised lake clays form the underlying sediment (Zacher, 1990). Mowing and a drainage ditch, accompanied by a gravelled hiking road, affect the mire at present.

A second study site, the Ladstatt Mire (LAD, GPS: 47°21′28.1″ N, 10°09′26.9″ E), is situated at a distance of 1.7 km to the south-west of Hoefle Mire at 1140 m a.s.l., just at the foot of a forested slope (Küren Valley) to the Gottesacker plateau and downhill of the archaeological site "Schneiderkürenalpe" (Fig. 1b). This slope is characterised by almost no surface runoff. All precipitation disappears into the karstic underground (Goldscheider, 1998). LAD is comparable to HFL in terms of size and surface vegetation, although *Sphagnum* is more dominant. A road with ditches separates the mire from the valley's slope.

A third peat profile at "Halden-Hochalpe" (HHA, GPS: 47°20′18.3″ N, 10°03′49.2″ E) (Fig. 1) was only surveyed in 2017. The HHA mire developed on a sediment-filled glacial cirque form (de Graaff et al., 2003) at 1660 m a.s.l. The uppermost Subersach River meanders through the peatland, which allowed sampling of the bottom of the profile to date the onset of peat formation.

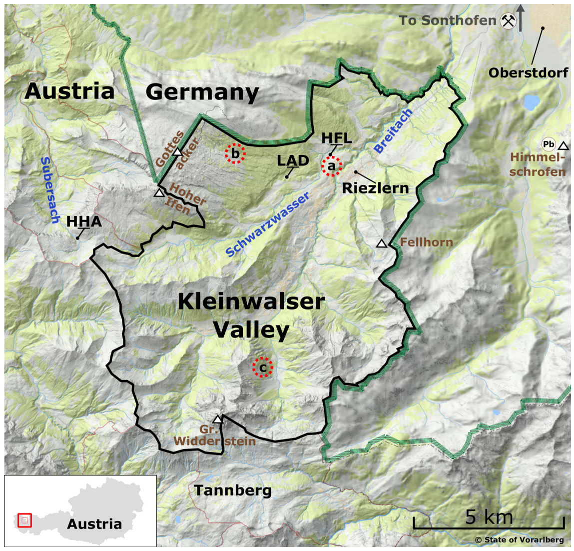


**Figure 1.** The Kleinwalser Valley and surrounding areas. Archaeological sites (red dotted circles): Egg **(a)**, Schneiderkürenalpe **(b)**, Neolithic flint mine **(c)**. Sampled mire sites: Hoefle Mire (HFL), Ladstatt Mire (LAD), Halden-Hochalpe (HHA). Mountains (white triangles). Modified from data source: state of Vorarlberg – http://data.vorarlberg.gv.at (last access: 6 October 2018).

## 3 Methods

### 3.1 Coring and sampling

Field sampling was performed in early August 2016 in the centre of HFL. A peat sequence of 240 cm was recovered in three parallel, overlapping cores (B, C, D) using a Russian peat corer with a chamber of 5 cm in diameter. Additionally, a 10 × 10 × 30 cm monolith of the topmost part was sampled with a serrated ceramic blade, to avoid compression in the fibrous living part of the acrotelm. Similarly, we recovered an 83 cm long sediment core and a 28 cm monolith at LAD. All cores and monoliths were wrapped into cling film, transferred to PVC half-tubes in closed plastic hoses and stored at 3 °C. At HHA, only a charred wood sample was collected for $^{14}C$ dating, just below the bottom peat layers.

After freezing the cores for 2 d at −18 °C, each of the sections was cut into 1 cm thick slices with a stainless-steel band saw. Subsamples of every slice were cut with ceramic knives, stored in ziplock bags and frozen again. Contamination was minimised following cutting protocols by De Vleeschouwer et al. (2010a) and Givelet et al. (2004). The dimensions of the subsamples dedicated to geochemistry were measured with a Vernier calliper. These were then freeze-dried and weighed to obtain dry bulk density. To cover the gap between the first two core sections in HFL, an overlapping part of core (C) was subsampled and fitted to the main core (B) by using dry bulk density and element concentration profiles.

### 3.2 Radiocarbon dating and chronology

*Sphagnum* stems and leaves were selected for radiocarbon dating from fresh samples in ultrapure water. When *Sphagnum* was absent (in deeper/more decomposed peat layers), other plant remains (*Eriophorum* spindles, seeds, *Ericaceae* leaves, wood) as well as bulk peat were selected and sent to Poznan AMS Radiocarbon Laboratory (Poland). The calibrated ages (Table 1) and age–depth models (Fig. 2) were produced in R, version 3.4.2 (R Core Team, 2017), by using the packages clam version 2.3.2 (Blaauw, 2010) and rbacon version 2.3.3 (Blaauw and Christen, 2011). Both packages work with the IntCal13 radiocarbon calibration curve (Reimer et al., 2013). Unless denoted otherwise, ages are given as calibrated before present (cal BP, i.e. years before 1950) for prehistoric times. For a more convenient comparison to historical sources, interpretations for the last 2000 years are made in cal CE. The classification of cultural periods was performed based on the study of Roepke and Krause (2013).

### 3.3 Pollen analysis

A volume of 2 mL was taken from 14 peat samples of cores HFL-B and HFL-C in the overlapping section and prepared for pollen analysis, following the method described by Moore et al. (1991). The material was pretreated in separate steps in 10 % HCl and 10 % KOH to get rid of carbonates and humic substances. Macro remains were removed with a 200 µm mesh. The sample was first cooked for 4 min in a 9 : 1 solution of acetic anhydride and concentrated sulfuric acid and centrifuged. Particles below 6 µm were removed with ultrasonic sieving. The absence of siliciclastic sediment layers in the analysed samples made the use of HF obsolete. Pollen were counted to a sum of 200 tree pollen (excluding *Corylus*). Fern spores without perine were counted as indeterminate pteridophytes. The counts were compiled with Tilia version 2.0.60 (Grimm, 2018).

### 3.4 Geochemistry

This study concentrated on calcium (Ca), lead (Pb) and titanium (Ti) for interpretation. While Ca can yield information on the trophic state of a mire, Ti can be used as an erosion or human impact proxy (Hölzer and Hölzer, 1998). Pb often originates from anthropogenic sources when it exceeds its natural background (e.g. Weiss et al., 1999). Using portable X-ray fluorescence spectrometry (pXRF) on peat samples in palaeoenvironmental research has rarely been done so far and is hence not well understood, despite some studies that were assessing its general potential (Kalnicky and Singhvi, 2001; Mejía-Piña et al., 2016; Shand and Wendler, 2014; Shuttleworth et al., 2014). Therefore, a regression analysis was conducted to evaluate and calibrate the semi-quantitative pXRF by several parallel quantitative measurements with inductively coupled plasma mass spectrometry (ICP-MS). In HFL-B and HFL-C, a total of 187 and 51 samples were selected for pXRF scanning and ICP-MS analyses, respectively. A total of 62 samples were selected from the LAD core for pXRF scanning. The samples were transferred into Falcon tubes together with eight glass beads (4 mm) and ground $3 \times 20$ s using a FastPrep-24® mixer at maximum speed.

Samples dedicated to pXRF were transferred into 12.5 mL polypropylene vials, closed with Fluxana TF-240-255 film and rubber band. All samples were measured using a Thermo Fisher Niton XL3t pXRF equipped with an Au anode and a 50 kV X-ray tube. The predefined "soil mode" was used with 180 s of measurement time each for the main and low filter, which is 60 s above the minimum duration recommended by Shuttleworth et al. (2014). Every sample was measured at least three times and shaken after each scan to control the reproducibility of measurements (precision). In addition to the Certified Reference Materials (CRM) used with ICP-MS (see below), BCR-060 (aquatic plants), IAEA-336 (lichen), IPE-176 (reed/*Phragmites*) and NIST-1575a (pine needles) were scanned. Table 2 shows the quality control of pXRF. Estimated standard sample deviations (SD) based on *n* repeated measurements remained mostly below or around 10 %. Only for Ti, did a higher SD of 18.8 % occur in NJV941. All three elements were above the certified concentrations.

Samples dedicated to ICP-MS were digested using $HNO_3$, HF and $H_20_2$ in a class 100 clean room following the protocol of Vanneste et al. (2015). Depending roughly on the dry bulk density of the peat sediment sample, the final aliquots were diluted to total factors between 2500 and 28 500. To verify the analytical quality, precision and accuracy of the ICP-MS results, the CRMs (GBW-07603 bush branches and leaves, NIST-1515 apple leaves, NIST-1547a peach leaves, NJV-941 *Carex*/sedge peat, NJV-942 *Sphagnum* peat) were digested and measured along with the samples. Procedural blanks were added to monitor possible contamination or systematic errors. Measurements were performed on an Agilent 7500 CE at Observatoire Midi-Pyrénées, Toulouse, France. The internal ICP-MS calibration with a multi-element standard was run every 10th sample. Measured concentrations were within 11 % of the certified values (Table 3). Only NJV941 deviated more than 10 % for Ca and Pb.

## 4 Results

### 4.1 Age–depth model

Median ages were extracted from the age–depth model for further interpretation. The accumulation rates for the model of each core were calculated as the median of 1000 estimates by rbacon for each depth. In the lowermost 60 cm of HFL, an accumulation of almost 0.9 mm $a^{-1}$ is observed (Fig. 2), while rates of 0.3 to 0.6 mm $a^{-1}$ prevailed up to 37 cm in depth. The following section of 12 cm was characterised by a very low accumulation of 0.2 to 0.1 mm $a^{-1}$ and comprised almost 900 years. In contrast, accumulation or growth

**Table 1.** List of radiocarbon samples including information about origin, depth, dated material, $^{14}C$ ages and calibrated ages within a 95 % confidence interval (probabilities < 1 % excluded).

| Lab. no. | Site | Depth (cm) | Material | $^{14}C$ age (BP) | Cal age (BP) | Comment |
|---|---|---|---|---|---|---|
| Poz-101727 | HFL | 21.3 | *Sphagnum* stems and leaves, few *Eriophorum* spindles | 127 ± 0.35 pMC | −32 to −29.9 (80.8 %)<br>−12.1 to −12 (4.2 %)<br>−9.7 to −9.4 (10 %) | |
| Poz-104865 | HFL | 29.9 | *Eriophorum* spindles, *Sphagnum* stems and leaves | 65 ± 30 | 31–138 (71.4 %)<br>222–257 (23.5 %) | 0.5 mg C |
| Poz-92252 | HFL | 36.0 | *Eriophorum* spindles | 1110 ± 30 | 939–959 (1.4 %)<br>951–1071 (93.5 %) | 0.7 mg C |
| Poz-101728 | HFL | 48.3 | *Sphagnum* stems and leaves, *Eriophorum* spindles | 1525 ± 30 | 1348–1424 (55.6 %)<br>1428–1444 (4.3 %)<br>1454–1522 (34.9 %) | |
| Poz-92255 | HFL | 80.0 | *Sphagnum* leaves | 2410 ± 30 | 2351–2496 (81.2 %)<br>2596–2612 (2.9 %)<br>2637–2684 (10.9 %) | |
| Poz-92251 | HFL | 120.3 | *Sphagnum* stem, *Eriophorum* remains | 3065 ± 35 | 3180–3200 (4.6 %)<br>3206–3363 (90.4 %) | |
| Poz-86728 | HFL | 152.0 | Bulk peat | 4105 ± 35 | 4453–4461 (1 %)<br>4521–4713 (70.5 %)<br>4753–4814 (22.7 %) | |
| Poz-96113 | HFL | 176.7 | Wood and *Eriophorum* remains, | 4710 ± 40 | 5322–5419 (46.4 %)<br>5439–5486 (20.8 %)<br>5507–5581 (27.6 %) | |
| Poz-92253 | HFL | 202.0 | Ligneous material, wood | 2730 ± 35 | 2759–2883 (93.5 %)<br>2911–2918 (1.5 %) | Excluded outlier, 0.2 mg C |
| Poz-86726 | HFL | 235.0 | Wood | 5330 ± 40 | 5996–6208 (93.9 %)<br>5254–6260 (1 %) | |
| Poz-86729 | HFL | 175.0 | Bulk peat | 4400 ± 35 | 4860–5054 (91 %)<br>5190–5256 (3.3 %) | Core D |
| Poz-95963 | HHA | ∼ 145.0 | Charred wood, tree age outer age ring, > 50 | 3195 ± 35 | 3357–3479 (94.8 %) | |
| Poz-99319 | LAD | 24.8 | *Sphagnum* stems and leaves | 127.74 ± 0.37 pMC | −32 to −29.3 (81.9 %)<br>−12.1 to −12 (5.8 %)<br>−9.7 to −9.4 (7.3) | 0.7 mg C |
| Poz-103202 | LAD | 31.2 | *Eriophorum* spindles | 40 ± 30 | −5 to 2 (6.9 %)<br>32–83 (52.1 %)<br>97–108 (3 %)<br>112–137 (13.8 %)<br>223–255 (19 %) | 0.8 mg C |
| Poz-99198 | LAD | 63.5 | *Eriophorum* spindles | 3185 ± 35 | 2253–3475 (95 %) | |
| Poz-86730 | LAD | 102.5 | Bulk peat | 5320 ± 40 | 5991–6210 (93.5 %)<br>6250–6262 (1.5 %) | |

**Table 2.** Repeated pXRF measurements ($n$) of Ca, Pb and Ti versus certified (Cert.) concentrations in organic Certified Reference Materials (CRM). Sample standard deviations (SDs) from certified values as a percentage.

| Element | Ca | | | | Pb | | | | Ti | | | |
|---|---|---|---|---|---|---|---|---|---|---|---|---|
| Value<br>Unit | Cert.<br>(mg kg$^{-1}$) | pXRF<br>(mg kg$^{-1}$) | SD<br>(%) | $n$ | Cert.<br>(mg kg$^{1}$) | pXRF<br>(mg kg$^{-1}$) | SD<br>(%) | $n$ | Cert.<br>(mg kg$^{1}$) | pXRF<br>(mg kg$^{-1}$) | SD<br>(%) | $n$ |
| BCR060 | – | 54 013 | 2.0 | 8 | 64 | 92.5 | 4.3 | 8 | – | 280.5 | 11.6 | 8 |
| GBW07603 | 16 800 | 42 761 | 0.4 | 5 | 47 | 73.7 | 3.0 | 5 | 95 | 214.4 | 4.1 | 5 |
| IAEA336 | – | 8262 | 5.2 | 4 | 4.9 | 6.2 | 10.1 | 4 | – | 219.6 | 6.0 | 4 |
| IPE176 | 4160 | 8736 | 6.1 | 5 | 8.24 | 13.4 | 8.7 | 5 | – | 1172.5 | 6.8 | 5 |
| NIST1515 | 15 260 | 44 634 | 1.9 | 3 | 0.47 | – | – | – | – | 15.9 | – | 1 |
| NIST1547a | 15 600 | 41 795 | 0.1 | 3 | 0.87 | – | – | – | – | 18.7 | 0.1 | 2 |
| NIST1575a | 2500 | 8882 | 0.3 | 3 | 0.167 | – | – | – | – | 15.3 | 12.4 | 2 |
| fNJV941 | 10 200 | 33 937 | 4.4 | 8 | 2.4 | 2.3 | 10.8 | 8 | – | 64.1 | 18.8 | 8 |
| NJV942 | 1200 | 4024 | 2.5 | 6 | 10.1 | 14.3 | 3.4 | 6 | – | 262.0 | 2.9 | 6 |

**Table 3.** Quality control of Ca, Ti and Pb. Measurements by ICP-MS of procedural blanks and in organic Certified Reference Materials (CRM). Total deviations (Dev.) from certified values as a percentage.

| | Ca | | | Ti | | | Pb | | |
|---|---|---|---|---|---|---|---|---|---|
| CRM/blank | Cert. | ICP-MS | Dev. | Cert. | ICP-MS | Dev. | Cert. | ICP-MS | Dev. |
| | (mg kg$^{-1}$) | (mg kg$^{-1}$) | (%) | (mg kg$^{-1}$) | (mg kg$^{-1}$) | (%) | (mg kg$^{-1}$) | (mg kg$^{-1}$) | (%) |
| Blank 1 | – | 0.03 | – | – | 0.000 | – | – | 0.000 | – |
| Blank 2 | – | 0.01 | – | – | 0.000 | – | – | 0.000 | – |
| Blank 3 | – | 0.01 | – | – | 0.000 | – | – | 0.000 | – |
| NIST1515 (a) | 15 250 | 14 216 | −6.8 | – | 13.3 | – | 0.47 | 0.44 | −5.7 |
| NIST1515 (b) | 15 250 | 13 900 | −8.8 | – | 12.4 | – | 0.47 | 0.49 | 3.7 |
| GBW07603 (a) | 16 800 | 16 143 | −3.9 | 95 | 92.1 | −3.0 | 47 | 47.32 | 0.7 |
| GBW07603 (b) | 16 800 | 16 696 | −0.6 | 95 | 90.2 | −5.1 | 47 | 48.60 | 3.4 |
| NJV941 (a) | 10 200 | 8766 | −14.1 | – | 34.5 | – | 2.4 | 2.09 | −13.1 |
| NJV941 (b) | 10 200 | 8743 | −14.3 | – | 33.6 | – | 2.4 | 2.11 | −11.9 |
| NJV941 (c) | 10 200 | 8689 | −14.8 | – | 27.1 | – | 2.4 | 2.10 | −12.6 |
| NJV942 (a) | 1200 | 1262 | 5.2 | – | 51.8 | – | 10.1 | 9.48 | −6.1 |
| NJV942 (b) | 1200 | 1232 | 2.7 | – | 115.2 | – | 10.1 | 9.13 | −9.6 |
| NJV942 (c) | 1200 | 1181 | −1.6 | – | 49.6 | – | 10.1 | 9.48 | −6.2 |
| NIST1547a | 15 600 | 14 652 | −6.1 | – | 24.1 | – | 0.87 | 0.86 | −1.1 |

rates of the topmost layers reached a maximum of more than 8 mm a$^{-1}$. The age–depth model of LAD (Fig. 2) had a net accumulation rate of only 0.15 mm a$^{-1}$. However, the model is less constrained than in HFL, with a modern age at 25 cm in depth and 3450 cal BP at 62 cm in depth. Especially in the uppermost 30 cm, peat growth took a development similar to HFL, with accumulation or growth rates reaching 9 mm a$^{-1}$.

## 4.2 Pollen profile

A detailed interpretation of the pollen record from HFL Mire (Fig. 3) is provided in the discussion below. We can, however, point out major changes in the pollen profile. The deepest part was strongly characterised by *Picea* pollen. A significant change is observed between 200 and 175 cm (5700 to 5300 cal BP) when deciduous forest pollen and herbs appeared. After tree pollen were dominating again at 140 cm (4000 cal BP), the sudden and strong signals of *Poaceae*, herbs and cultural plants illustrate a diversification in the spectrum between 125 and 115 cm (3450 to 3150 cal BP). The opposite trend started above, although the overall pattern did not return to a complete dominance of tree pollen. Only in the uppermost 37 cm (1000 cal CE), did *Poaceae*, herbs and cultural plants represent a larger proportion of the spectrum once again. In order to facilitate the interpretation of palynological data in the discussion, we have assembled pollen into six groups (Fig. 3): 1 – cultural and pastoral; 2 – open grassland; 3 – herbs and heather; 4 – forest border; 5 – swamp/wetland; 6 – ferns.

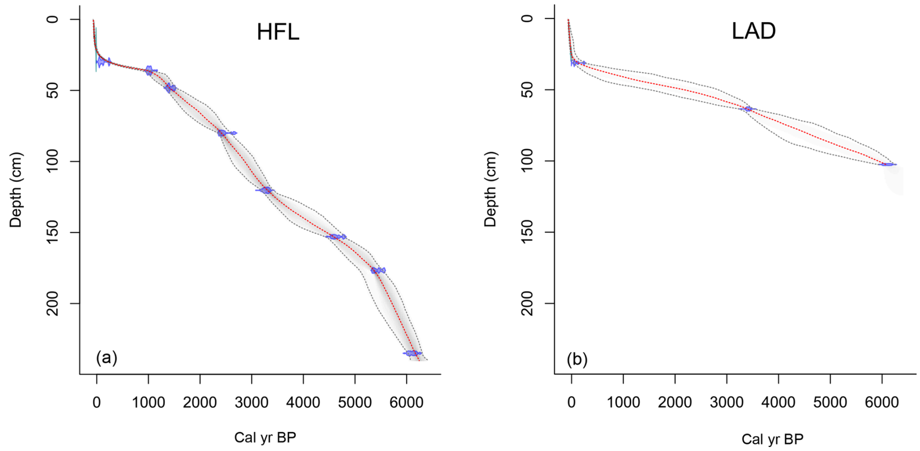


**Figure 2.** Age–depth models of Hoefle Mire **(a)** and Ladstatt Mire **(b)**. The median is plotted as a red dotted line amidst the confidence range of 95 % in grey.

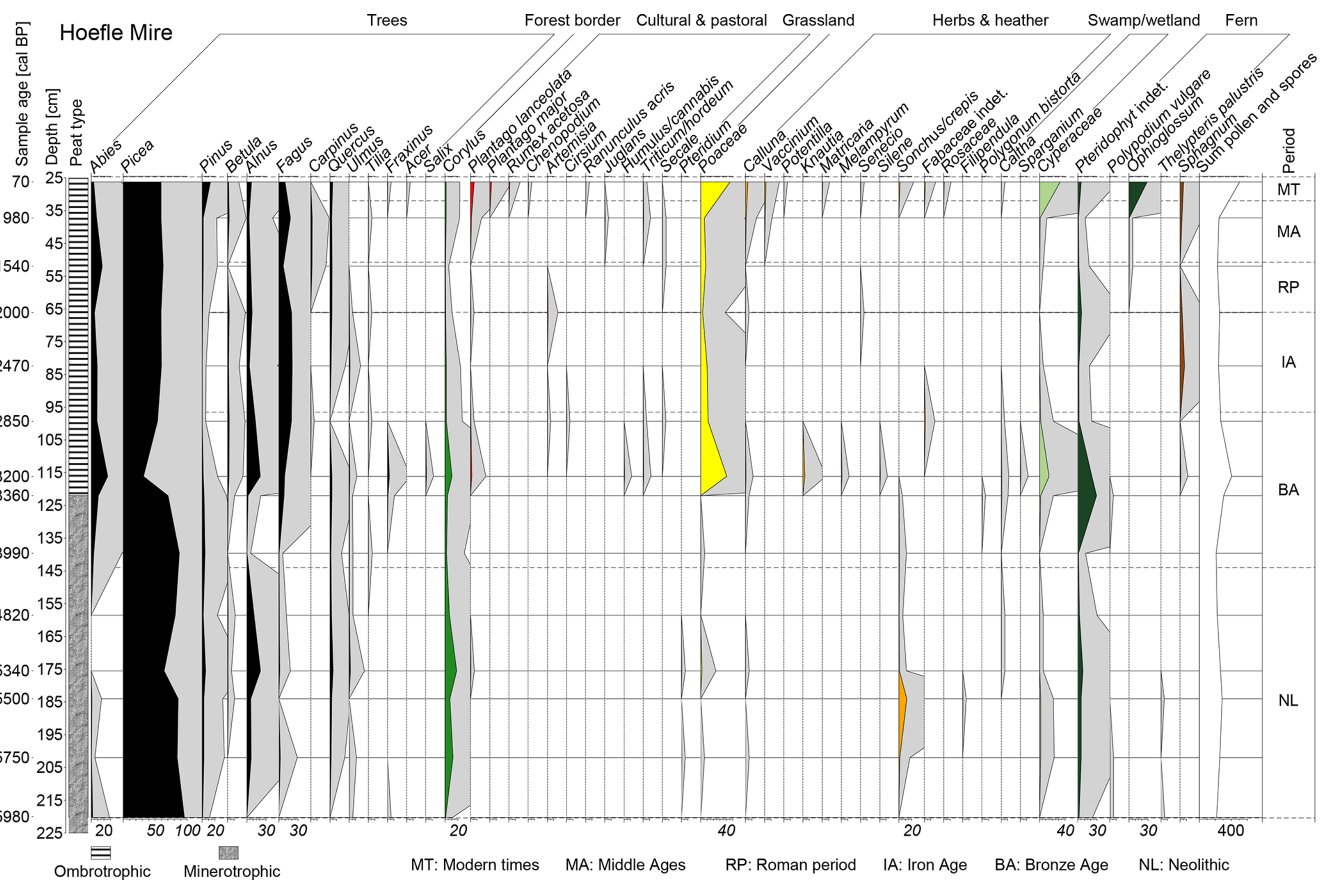


**Figure 3.** Pollen diagram of HFL Mire. Fully coloured profiles represent pollen percentages, shaded areas enhanced by factor 12. Black: trees; green: forest border (*Corylus*); yellow: open grassland (*Poaceae*); red: cultural and pastoral indicators; orange: herbs and heather; light green: swamp/wetland; dark green: fern; brown: *Sphagnum*; white: total spores and pollen. Vertical lines depict calibrated sample ages. Vertical dashed lines are boundaries of cultural periods.

### 4.3 Geochemistry

The quantitative and validated ICP-MS results of HFL were compared to the pXRF scans of the same sample, which allowed us to constrain our calibration. The regression analysis in the HFL peat samples showed high adjusted $R^2$ values or coefficient of determination ($R^2$), as a measure for the fit of the model ($R^2_{Ca} = 0.95$, $R^2_{Ti} = 0.97$, $R^2_{Pb} = 0.99$, Fig. 2). As the two deepest samples (240–230 cm) were composed of sediment and not peat, they plotted as outliers and were excluded. In the range of measured ICP-MS concentrations (Ca: 2000–14 000, Pb: 2–110 and Ti: 25–400 mg kg$^{-1}$), pXRF values were generally higher than the concentrations obtained by ICP-MS. Transfer functions were therefore calculated to calibrate the pXRF scans of all 187 samples (Fig. 4).

The element-specific overestimation of the pXRF output illustrates that this method cannot be used to quantify element concentrations in peat without a cross-calibration against quantitative methods. Specification and type of sample need to be considered during such a calibration. Shuttleworth et al. (2014) used a Niton XL3t with an Ag anode to evaluate the applicability of pXRF for Pb contents in peat. Their results suggested a linear relationship between pXRF and ICP-OES (optical emission spectrometry), which was confirmed in this study. However, their observed overestimation by pXRF was much lower and was attributed to an incomplete Pb extraction with aqua regia. As a complete digestion was performed in this study, the overestimation by pXRF for Pb cannot have a similar explanation. Additionally, the high content of light organic matter in peat should rather result in an underestimation of heavier elements in XRF analysis (Löwemark et al., 2011). Nevertheless, the regression analysis allowed us to generate quantitative results of Ca, Pb and Ti in both minerotrophic and ombrotrophic peat. The only exception was the measurement of mineral-rich bottom layer samples with a high element load, which plotted outside the linear regression.

The Pb enrichment factor (Pb EF) was calculated following (Weiss et al., 1999) using Ti as a conservative element, which is not affected by dissolution in acidic environments (Nesbitt and Markovics, 1997).

Here we used the background Pb/Ti ratio of the bottom sediment, measured by ICP-MS (0.0037), which is close to the generally used upper continental crust (UCC) value (0.004) from McLennan (2001). It is explained by the local geology consisting of limestone, marl and sandstone, resulting in a mixed weathering product.

$$\mathrm{Pb\,EF} = \frac{(\mathrm{Pb/Ti})_{\mathrm{sample}}}{(\mathrm{Pb/Ti})_{\mathrm{background}}}$$

Titanium originates from natural local erosion/sources and is therefore used as a human-impact proxy. Following Shotyk et al. (2002), we calculated a mineral accumulation rate (MAR) on the mires' surfaces in g m$^{-2}$ a$^{-1}$ with a Ti (UCC) of 0.41 %:

$$\mathrm{MAR} = 100/0.41 \times \mathrm{Ti} \times \delta \times \mathrm{pa},$$

where $\delta$ is the dry bulk density and pa is the peat accumulation rate.

The temporal variability of Ca, Pb EF and MAR shown in Fig. 5 is based on the calibrated pXRF concentrations, calibrated ages, densities and accumulation rates (tables in Supplement). Ca concentrations in HFL constantly declined towards the top. After a max. of 15 000 mg kg$^{-1}$ in the deepest peat layers (6000 cal BP), they fell permanently below 6000 mg kg$^{-1}$ after 122 cm (3250 cal BP). Above 62 cm (1950 cal BP) they decreased to a level below 3000 mg kg$^{-1}$.

The concentrations of Ti in HFL decreased from 1040 to around 50 mg kg$^{-1}$ in the deepest 12 cm of the core (6250 to 6000 cal BP) and remained low until an increasing trend started above 133 cm (3700 cal BP), which culminated at 122 cm (3250 cal BP) with over 385 mg kg$^{-1}$. Although higher than in the lower half of the profile, concentrations returned to values between 40 and 110 mg kg$^{-1}$ until an increasing trend, which was shortly interrupted around 48 cm (500 cal CE), started above 58 cm (200 cal CE). This trend turned after reaching 360 mg kg$^{-1}$ at 32 cm (1500 cal CE) and ultimately came to a halt at the surface.

Excluding the deepest samples of HFL, Pb was below the detection limit from 230 to 190 cm (6250 to 5600 cal BP) and did not exceed 9 mg kg$^{-1}$ until 98 cm in depth. From 97 to 91 cm (2800 to 2650 cal BP), concentrations rose to values around 25 mg kg$^{-1}$. From then on, Pb oscillated around 15 mg kg$^{-1}$ until it increased between 50 and 20 cm (500 to 1970 cal CE) to a maximum of 115 mg kg$^{-1}$. Thereafter, the profile sharply dropped to 6 mg kg$^{-1}$ within the next 7 cm and fell below the detection limit at the subsurface.

In the LAD core, Ti concentrations were above 1000 mg kg$^{-1}$ until 85 cm in depth (4900 cal BP) and briefly dropped to 200 mg kg$^{-1}$ at 78 cm (4800 cal BP). A peak, exceeding 1000 mg kg$^{-1}$, appeared at 61 cm (3200 cal BP), after which the profile stayed slightly below 600 mg kg$^{-1}$. The concentrations decreased from 34 cm to 20 cm in depth (1700–1982 CE) and continued to less than 30 mg kg$^{-1}$ at the surface.

## 5 Discussion

### 5.1 Mire formation

Peat formation in HFL and LAD began around 6200 cal BP. Pollen proportions suggest a *Picea* swamp in a densely forested valley at 6000 cal BP, fitting well to the findings of Dieffenbach-Fries (1981). For the same period, other studies reported a wetter and colder climate in the central Alps (Haas et al., 1998; Van der Knaap et al., 2004; Wurth et al., 2004). The fine clayey sediment of a glacial till followed by gyttja at the bottom of both HFL and LAD indicates standing water

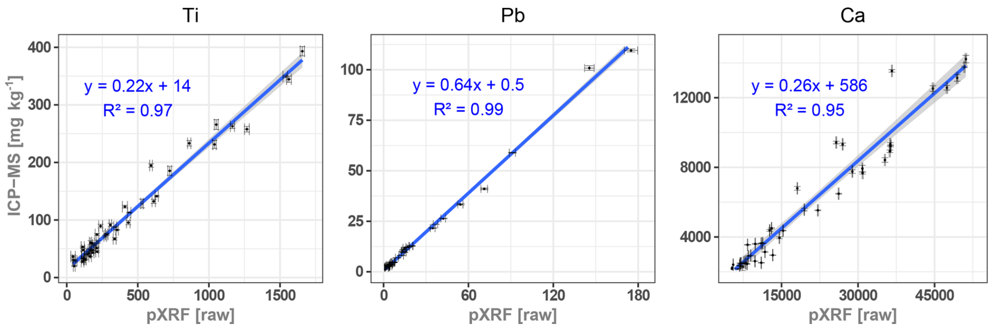


**Figure 4.** Cross-plots of measured concentrations of Ca, Ti and Pb with ICP-MS ($mg\,kg^{-1}$) versus measured values with pXRF (raw) for regression analyses.

conditions, which favoured peat formation. Land- or rock-slides in the watershed (Schmidt-Thomé, 1960; Völk, 2001) could have resulted from a wetter climate as well and may have reorganised the valley's hydrology, which is very complex (Goldscheider, 1998). This could have further promoted mire formation in certain places, as suggested by Grosse-Brauckmann (2002).

## 5.2 5800 to 3500 cal BP: early human occupation

Only very little archaeological evidence suggests early human occupation in the area (Bachnetzer, 2017; Leitner, 2003). Similarly, little palaeoecological evidence exists on early local land use. Regional studies showed evidence for fire practices (Clark et al., 1989) and crop cultivation around Lake Constance (Jacomet, 2009; Rösch, 1992) and at Oberstdorf, north of the valley (Fig. 1) (Dieffenbach-Fries, 1981). In HFL, increasing *Poaceae* pollen and the presence of *Plantago* as well as the emergence of *Corylus* suggest anthropogenic landscape opening around 5550 cal BP. This interpretation is further strengthened by a significantly elevated erosion signal (MAR) in HFL. Prehistoric fire practices in the valley can be inferred from the presence of *Pteridium* and *Calluna*. While not dendrochronologically dated, a charred tree trunk was pierced (horizontally) at parallel depth in the parallel HFL-D core (not analysed in detail). Although the cause of this fire (anthropogenic or natural) cannot be deciphered, it supports the other indicators in suggesting prehistoric patchy land clearances, possibly for livestock grazing.

Almost simultaneously to the observed pollen signals in HFL, the Pb EF rose significantly to 50 at 5450 cal BP and remained around an average value of 22 until 3500 cal BP. While this elevated Pb EF period falls in the minerotrophic part of the core, several authors showed that Pb, an immobile element, could carefully be used as an anthropogenic indicator in minerotrophic peat (e.g. Baron et al., 2005; Shotyk et al., 2001). Archaeological evidence shows that metal tools were circulating in the central Alps (e.g. Artioli et al., 2017). Metallurgy was dominated by Cu at that time, but Pb can be present as an impurity (Höppner et al., 2005; Lutz and

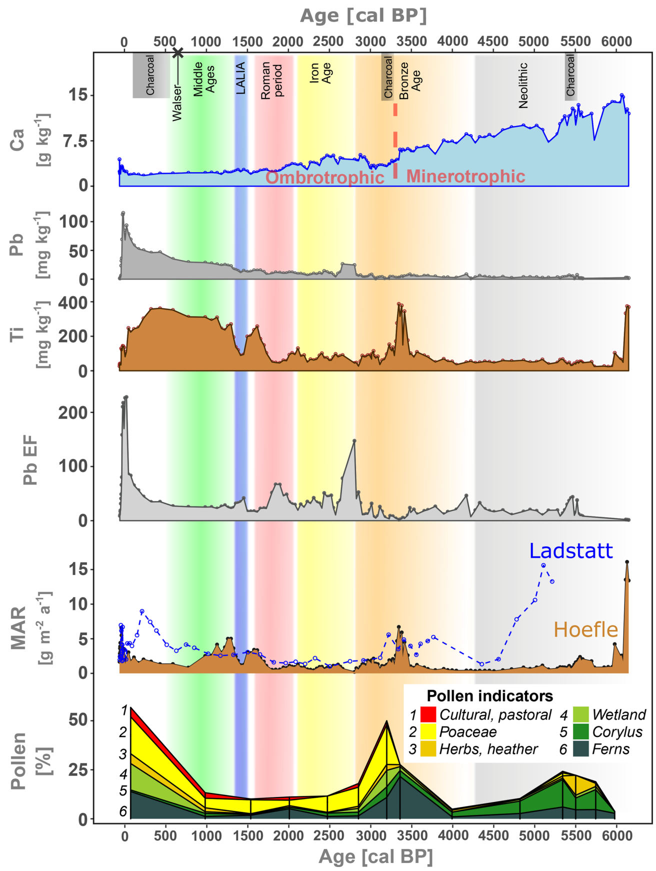


**Figure 5.** Chronological profile of Ca, Pb and Ti concentrations in HFL, Pb EF in HFL, and mineral accumulation rates ($g\,m^{-2}\,a^{-1}$) in HFL and LAD. Pollen groups as a percentage of total pollen (%) in HFL. Colours of shaded areas represent cultural periods in the northern central Alps: grey – Neolithic; orange – Bronze Age; yellow – Iron Age; red – Roman period; green – Middle Ages.

Pernicka, 2013). Despite the existence of different ore deposits in the region (see Sect. 2), archaeological evidence suggests that the closest and earliest copper mining emerged in the Lower Inn Valley in the early to mid-Bronze Age around 3600 cal BP (Breitenlechner et al., 2013; O'Brien, 2015; Tomedi et al., 2013). Our HFL record strongly suggests that metallurgical activities around the Kleinwalser Valley could have already taken place around 5500 cal BP, which would be almost 2000 years earlier. Our findings are, however, in agreement with other studies, which indicate that Alpine metallurgy started well before 5000 cal BP (Bartelheim et al., 2002; Frank and Pernicka, 2012; Höppner et al., 2005).

## 5.3 3500 to 2800 cal BP: Bronze Age

The start of this period saw the evolution from minerotrophic to ombrotrophic conditions in HFL, characterised by the occurrence of *Sphagnum* and a stabilisation of Ca values, which suggests an independence from bottom sediment influence. The landscape opened, as shown by the emergence of *Poaceae, Cyperaceae* and *Corylus*, while tree pollen sank below 50 %. Moreover *Calluna*, *Plantago*, cereals and other cultural indicators *(Triticum/Hordeum, Humulus/Cannabis)* support the interpretation of a landscape opening with human presence. A drastic MAR peak in HFL and LAD (Fig. 5) suggests that deforestation and openness strongly promoted soil and slope erosion between 3500 and 3200 cal BP. A bottom layer of partly charred wood debris at HHA was dated to 3360–3480 cal BP, which points to deforestation by fire and further supports land openness. Archaeological evidence from Schneiderkürenalpe (Fig. 1) also suggests pastoral activities in the valley (Leitner, 2003), which would have promoted soil erosion on the karstic western slopes. On the same slopes, a speleothem record from the Hölloch cave (Wurth et al., 2004) showed a contemporary negative $\delta^{13}C$ excursion, which could have been caused by an enhanced input of soil-derived carbon. Cultural pollen indicators and pastoral weeds were observed locally by Dieffenbach-Fries (1981), while Walde and Oeggl (2004) documented fire clearings in the Tannberg area (Fig. 1) between 3600 and 3300 cal BP. Several lake and mire records showed an increasing human impact on the central Alp's landscape during that period (Festi et al., 2014; Schmidl and Oeggl, 2005; Vorren et al., 1993; Wick and Tinner, 1997). Contemporaneously, settlement patterns changed after 3500 cal BP as a result of climatic deteriorations and new sites appeared at higher elevations in the central Alps (Della Casa, 2013). The same author saw technical and agricultural innovations as a driver of higher impact during the middle to late Bronze Age. In terms of climate, a trend to wetter and colder conditions began after approximately 3300 cal BP (Hormes et al., 2001; Ivy-Ochs et al., 2009; Magny et al., 2009; Vorren et al., 1993), which could have promoted such erosive events by both descending the timberline and bringing more precipitation on an open landscape. While some studies suggested that warmer conditions can promote human activities (Tinner et al., 2003; Vorren et al., 1993), our pollen record does not allow conclusions about warmer or colder conditions. We can however argue that the large erosive event observed in the Kleinwalser Valley and the specific cultural pollen assemblage were a direct consequence of a strong and deliberate human land use rather than being the direct result of climate factors.

## 5.4 2800 cal BP to 600 cal CE: Iron Age and Roman period

The pressure of agro-pastoralism progressively disappeared from 2800 to 2500 cal BP as shown by the disappearance of *Artemisia, Fabacea, Cirsium* and *Plantago*. Cerealia pollen (*Hordeum/Triticum* and *Secale)* also go missing around 2500 cal BP. Forests progressively recovered in a stable landscape with minimum erosion, as also reflected in the low MAR. The decreasing human impact in the Kleinwalser Valley after the late Bronze Age may have been triggered by a cold phase (Ivy-Ochs et al., 2009), making harsh mountain environments less attractive. However, several studies discussed or contested a climate-deterministic view on the widespread decline of human activities around this period (e.g. Armit et al., 2014; Röpke et al., 2011; Tinner et al., 2003). Decreasing cultural indicators during this period were also documented elsewhere in the central Alps (Vorren et al., 1993). Yet, a general decline contrasts with human impact in the neighbouring Tannberg area (Walde and Oeggl, 2003, 2004). Why human impact in the Kleinwalser Valley decreased therefore remains unclear at this stage. We can however hypothesise that humans never abandoned the valley completely. The favourable warm and dry period starting around 2000 cal BP (Büntgen et al., 2011) attracted people again for hunting and pastoralism as suggested by pollen (*Artemisia, Plantago*) and by archaeological evidence (Leitner, 2003).

While anthropogenic impact in the Kleinwalser Valley declined from 2800 to 2000 cal BP, Pb EF suggests that metallurgical activities continued in the area. A Pb EF of up to 175 hints at intensive metallurgical activities not far from HFL between 2800 and 2600 cal BP. The exact locations of these activities remain unclear, but may be local to regional, as metallurgy became widespread in the eastern Alps around 3500 cal BP (Höppner et al., 2005; Lutz and Pernicka, 2013). The signal is in line with the technological introduction of the first Pb alloys (Tomedi et al., 2013). Afterwards (2600–2300 cal BP), short episodes of moderate Pb EF indicate ongoing metallurgy in the region. Part of it could have been connected to Celtic cultures (e.g. La Tène), as metal artefacts and metallurgy evidence were found in the northern central Alps (Bächtiger, 1982; Mansel, 1989).

During early Roman times (ca. 2000 cal BP in this region) HFL and LAD show a low MAR, indicating little erosion and therefore decreased land use, as Walde and Oeggl (2003, 2004) already suggested. In contrast, Friedmann and Stojakowits (2017) reported higher land use in the Alpine foreland. Later on, the study of Büntgen et al. (2011) suggested warm summers with moderately low precipitation from 200 to 300 cal CE. Simultaneously, rising mineral input in HFL indicates increased land use in the Kleinwalser Valley. The local and regional human activity and connectivity of the valley can only be inferred by connecting historical sources (Dertsch, 1974; Fink and von Klenze, 1891; von Raiser, 1830; Weber, 1995), archaeological finds (Gulisano, 1995) and a Roman trade route completion (Via Decia) through Sonthofen (20 km N) around 250 CE (Heuberger, 1955). We therefore suggest that people may have used the valley's slopes, which led to the observed MAR rise in HFL and LAD around the 3rd century cal CE. We also observe an elevated Pb EF around 100 cal CE, but in contrast to Mackensen (1995), we cannot firmly connect that to local Roman mining around Sonthofen. As strong Pb emissions of Roman origin are recorded across Europe (e.g. De Vleeschouwer et al., 2010b), we tend to attribute the enrichment in HFL to diffuse distal sources.

After 400 cal CE, increased *Abies alba* pollen indicate forest expansion in cool and humid conditions. The absence of herbs (e.g. *Plantago*) and *Corylus* suggests a low human influence in the Kleinwalser Valley. In parallel to the forest expansion and decreased anthropogenic pollen indicators, the MAR dropped significantly in the first half of the 6th century cal CE. Similar patterns were observed in the Kleinwalser Valley (Grosse-Brauckmann, 2002) as well as north of it (Rösch, 1992; Stojakowits, 2014). A wetter climate around 400 cal CE was directly followed by colder summer temperatures from 536 to 660 cal CE (Büntgen et al., 2011, 2016), called the Late Antique Little Ice Age (LALIA). Around this period, Holzhauser et al. (2005) observed glacier advances in the Swiss Alps. The comparison of our data with these palaeoclimate records suggests that due to a climatic deterioration between 500 and 600 cal CE, human activities in the Kleinwalser Valley and its surroundings declined significantly. Moreover, erosion decreased as a combined result of forest expansion and soil stabilisation.

### 5.5 600 cal CE to 2016 CE: from early Middle Ages to modern times

This period saw the expansion of the Frankish empire to higher elevations, but little is known about it in this part of the northern central Alps, as neither Roman nor Middle Age historical sources exist (Babucke, 1995). We nevertheless observe a growing human impact in HFL, reflected in increasing cultural pollen proportions (*Juglans*, Cerealia, *Plantago*), which fits to deforestation and settlement expansion in the Alpine foreland suggested by Friedmann and Stojakowits (2017). The MAR in HFL also increased sharply after the LALIA to peak around 700 cal CE, which is in accordance with observations in the Alps of Tinner et al. (2003). However, a sharp drop at 770 cal CE was then followed by a decreasing trend along with the Medieval climatic optimum (900 to 1300 CE) (Mann, 2002) until the onset of the Little Ice Age glacier progressions (1300 to 1850 CE) (Matthews and Briffa, 2005). The MAR decrease indicates a landscape stabilisation. Historical sources indeed suggested that the Kleinwalser Valley has been managed for cattle herding and hunting since at least the 11th century CE (Amann, 2013a). The Walser arrived in the early 14th century CE and should have been responsible for most of the changes since then (Wagner, 1950). The presence of macro-charcoal (> 1 mm) in HFL after 1350 cal CE is in line with the onset of Walser settlements and indicates intense use of fire across the valley. The uppermost pollen sample in HFL shows the highest proportion of cultural and open landscape indicators (Fig. 3). However, our palynological resolution is coarse and our age–depth model is limited for that period, placing this uppermost sample in the early period of industrialisation (ca 1880 cal CE). We can therefore assume that the Walser intensified deforestation until the mid-19th century, as shown on a land cover map from 1857 CE (State of Vorarlberg, 2018). The MAR progressively increased from the 13th century cal CE towards the industrial period, reflecting a growing population, increasing forestry and agro-pastoral activities (dairy and meat production). However, this accelerating trend to landscape opening may have been buffered by early land (forest) management regulations (Amann, 2014; Fink and von Klenze, 1891), mitigating further destabilisation of land cover.

In contrast to HFL, the MAR in LAD seems to have taken another development between the Middle Ages and industrialisation. Even if the accumulation rates in this part need to be considered with caution, the MAR rose quite strongly after around 1400 cal CE. Particularly this western side of the valley started to be used for cattle grazing after 1450 CE (Amann, 2013b). Consequently, the vulnerable slopes suffered from erosion, induced by timber cutting and cattle trampling.

Pb EF has also increased since around 1400 cal CE. Part of this increase may be attributed to the Sonthofen mining district, where exploitation was first documented for 1471 cal CE (Merbeler, 1995). However, the emergence of widespread European mining activities in the Middle Ages (e.g. Forel et al., 2010; Le Roux et al., 2005) could have contributed to the signal in HFL. The interpretation of the late Middle Ages in the LAD record is however limited by the age constraint. A more detailed discussion would therefore be speculative. We can however observe that the trends described above for Pb EF, the MAR, and pollen in HFL continued towards the 19th century. We can moreover suggest several interpretations from our geochemical data for the late 19th and 20th centuries. As a result of heavy industry and the introduction of leaded gasoline in Europe, the Pb EF in HFL strongly increased continuously from 1850 cal CE to a maximum of 250 in the 1980s and a sharp decline thereafter, perfectly fitting to the maximum use of leaded fuel and its subsequent ban (Pacyna and Pacyna, 2001). The chronology of the last centuries is however not well constrained. This could have been caused partly by drainage of Hoefle Mire, which temporarily reduced peat accumulation and enhanced decomposition at intermediate depth. However, our Pb EF profile is strikingly similar to the well-dated Pb EF profile of several Swiss mires (Shotyk et al., 1998; Weiss et al., 1999) and, hence, provides another chronological reference point for the topmost part of the Hoefle core. We can therefore say that, during the first half of the 20th century, the MAR remained low in both mires. The tourism intensification in the valley (Fritz, 1981) and the construction of related infrastructure increased the MAR in both mires again after 1950 cal CE.

## 6 Conclusions

We present two peat records of the central Alps covering the last 6200 years. By combining geochemical, palynological and chronological tools, we are able to understand the occupation and high human impact on the landscape in a valley of the northern central Alps and beyond. Calibrating a portable geochemical tool with ICP-MS also allows us to quantify geochemical elements in peat at a resolution that is rarely obtained and demonstrates its potential in (palaeo)environmental studies.

A cooler and wetter climate around 6200 cal BP promoted mire formation in the Kleinwalser Valley. Pollen spectra and erosion suggest human presence in the valley as early as around 5700 cal BP, lasting over several centuries, which is in line with studies on regional occupation. Increased Pb EF values around the same time suggest metallurgical activities in the area, which predates regional archaeological evidence by almost 2000 years. Large-scale deforestation and land use (agro-pastoralism) took place between 3500 and 2800 cal BP causing a drastic landscape opening and high initial erosion rates at both low and high elevations. At the end of this period, a prominent Pb EF points to metallurgical activities. However, landscape stabilised and forests recovered thereafter until well into the Roman period. A second period of increased erosion and land use started after 230 cal CE to a climax at around 700 cal CE. This increased land use period was interrupted by climatic deteriorations around 500 to 600 cal CE. Pb EF increased during the Roman period. It is however challenging to identify an origin as Roman Pb pollution was widespread. The Middle Ages saw progressive land management and the arrival of the Walser people. While historical sources point to a strong Walser influence on the area, our data only allow us to suggest that deforestation, agriculture and pastoralism continued during that period. The extent of those activities remains unclear however. The Pb EF increased during Late Middle Ages. It then rose faster during the industrial revolution and peaked before leaded gasoline was banned, allowing us to use it as a chronological marker to constrain the last century, which saw increasing tourism and its consequences taking place in the Kleinwalser Valley.

Although several archaeological findings and sites gave evidence for three prehistoric hotspots of human activity before, our pollen and geochemical data allow us to detail the evolution of the local and regional landscape and its use in the northern central Alps. The combination of historical sources with erosion indicators and pollen points to local land use and human presence in the valley thousands of years before the Walser arrival. Because the landscape had already undergone strong anthropogenic changes before, the recorded impact of the Walser was ultimately less prominent than could be expected.

**Data availability.** The geochemical data underlying this study are given either in the tables of the article or in the Supplement published with this article. The pollen data can be requested by contacting the first author.

**Supplement.** The supplement related to this article is available online at: https://doi.org/10.5194/egqsj-68-13-2019-supplement.

**Author contributions.** As corresponding author, CvS was responsible for planning and carrying out field work, geochemical analyses, data processing, and designing and writing of the paper. The pollen analyses were conducted by AL, whereas FDV contributed to sample preparation, geochemical analyses and designing of the paper. Both IU and JS helped in planning and conducting field sampling and contributed to the interpretation process.

**Competing interests.** The authors declare that they have no conflict of interest.

**Special issue statement.** This article is part of the special issue "Connecting disciplines – Quaternary archives and geomorphological processes in a changing environment". It is a result of the First Central European Conference on Geomorphology and Quaternary Sciences, Gießen, Germany, 23–27 September 2018.

**Acknowledgements.** We would like to thank Karl Keßler (landscape conservation Kleinwalser Valley), Alexander Suhm (Kiel University), Chuxian Li, Marie-Jo Tavella and Gaël Le Roux (all EcoLab) for their help and advice during field and laboratory phases. Clemens von Scheffer benefited from several travel grants from PPP (no. 57316724)/PHC-PROCOPE, no. 37646SG from DAAD/Campus-France (funded by the BMBF – German Federal Ministry of Education and Research), "*Soutien à la Mobilité Internationale 2017*" from the Institut National Polytechnique de Toulouse and a co-tutelle grant from the Deutsch-Französische Hochschule/Université franco-allemande (DFH/UFA). The project was co-funded through the graduate school *"Human development in landscapes"* (DFG-Excellence Initiative, GSC-208).

## References


Amann, A.: Alpleben im Walsertal – ein kulturhistorischer Abriss, in: Das Buoch soll Kraft und Macht haben, Alpbücher im Kleinwalsertal, 1541–1914, edited by: Amann, A. and Willand, D., 11–80, Brüüge, Riezlern/Kleinwalsertal, 2013a.

Amann, A.: Kaleidoskop der Alpbücher, in: Das Buoch soll Kraft und Macht haben, Alpbücher im Kleinwalsertal 1541–1914, edited by: Willand, D. and Amann, A., 103–164, Brüüge, Riezlern/Kleinwalsertal, 2013b.

Amann, A.: Alpgenossenschaften im Kleinwalsertal – Eine Vignette aus früherer Zeit "Berichte aus Alpbüchern des Alters 1592 AD", in: Genossenschaftswissenschaft zwischen Theorie und Geschichte: Festschrift für Prof. Dr. Johann Brazda zum 60. Geburtstag, edited by: Laurinkari, J., Schediwy, R., and Todev, T., 49–63, BoD – Books on Demand, 2014.

Armit, I., Swindles, G. T., Becker, K., Plunkett, G., and Blaauw, M.: Rapid climate change did not cause population collapse at the end of the European Bronze Age, P. Natl. Acad. Sci. USA, 111, 17045–17049, 2014.

Artioli, G., Angelini, I., Kaufmann, G., Canovaro, C., Dal Sasso, G., and Villa, I. M.: Long-distance connections in the Copper Age: New evidence from the Alpine Iceman's copper axe, edited by: Hart, J. P., PLoS One, 12, e0179263, https://doi.org/10.1371/journal.pone.0179263, 2017.

Babucke, V.: Das frühe Mittelalter, in Kempten und das Allgäu, Führer zu archäologischen Denkmälern in Deutschland 30, edited by: Czysz, W., Dietrich, H., and Weber, G., 70–78, Theiss, Stuttgart, 1995.

Bachnetzer, T.: Prähistorischer Feuersteinbergbau im Kleinwalsertal, Vorarlberg, Silex- und Bergkristallabbaustellen in Österreich, Praearchos, 5, 2017.

Bächtiger, K.: Die Erzvorkommen und Lagerstätten Graubündens und der ehemalige Bergbau, Mitteilungen, Verein der Freunde des Bergbaues Graubünden, 21, 2–12, 1982.

Baron, S., Lavoie, M., Ploquin, A., Carignan, J., Pulido, M., and De Beaulieu, J. L.: Record of metal workshops in peat deposits: History and environmental impact on the Mont Lozère Massif, France, Environ. Sci. Technol., 39, 5131–5140, https://doi.org/10.1021/es048165l, 2005.

Barry, R. G.: Changes in mountain environments: a review, in Mountain Environments in Changing Climates, edited by: Beniston, M., 496, Taylor & Francis, 2002.

Bartelheim, M., Eckstein, K., Huijsmans, M., Krauß, R., and Pernicka, E.: Kupferzeitliche Metallgewinnung in Brixlegg, Österreich, in: Die Anfänge der Metallurgie in der Alten Welt, edited by: Bartelheim,M., Pernicka, E., and Krause, R., 33–82, Rahden, Westfalia: Verlag Marie Leidorf, Rahden, 2002.

Bätzing, W.: Die Alpen: Geschichte und Zukunft einer europäischen Kulturlandschaft, 4th ed., C.H. Beck, Munich, 2015.

Blaauw, M.: Methods and code for "classical" age-modelling of radiocarbon sequences, Quat. Geochronol., 5, 512–518, 2010.

Blaauw, M. and Christen, J. A.: Flexible paleoclimate age-depth models using an autoregressive gamma process, Bayesian Anal., 6, 457–474, https://doi.org/10.1214/11-BA618, 2011.

Breitenlechner, E., Goldenberg, G., Lutz, J., and Oeggl, K.: The impact of prehistoric mining activities on the environment: A multidisciplinary study at the fen Schwarzenbergmoos (Brixlegg, Tyrol, Austria), Veg. Hist. Archaeobot., 22, 351–366, https://doi.org/10.1007/s00334-012-0379-6, 2013.

Büntgen, U., Tegel, W., Nicolussi, K., McCormick, M., Frank, D., Trouet, V., Kaplan, J. O., Herzig, F., Heussner, K. U., Wanner, H., Luterbacher, J., and Esper, J.: 2500 years of European climate variability and human susceptibility, Science, 80, 331, 578–582, https://doi.org/10.1126/science.1197175, 2011.

Büntgen, U., Myglan, V. S., Ljungqvist, F. C., McCormick, M., Di Cosmo, N., Sigl, M., Jungclaus, J., Wagner, S., Krusic, P. J., Esper, J., Kaplan, J. O., De Vaan, M. A. C., Luterbacher, J., Wacker, L., Tegel, W., and Kirdyanov, A. V.: Cooling and societal change during the Late Antique Little Ice Age from 536 to around 660 AD, Nat. Geosci., 9, 231–236, https://doi.org/10.1038/ngeo2652, 2016.

Carcaillet, C.: A spatially precise study of Holocene fire history, climate and human impact within the Maurienne valley, North French Alps, J. Ecol., 86, 384–396, https://doi.org/10.1046/j.1365-2745.1998.00267.x, 1998.

Clark, A. J. S., Merkt, J., and Muller, H.: Post-Glacial Fire, Vegetation, and Human History on the Northern Alpine Forelands, South-Western Germany, J. Ecol., 77, 897–925, 1989.

Clegg, E. J., Harrison, G. A. and Baker, P. T.: The impact of high altitudes on human populations, Hum. Biol., 42, 486–518, 1970.

Cornelissen, M. and Reitmaier, T.: Filling the gap: Recent Mesolithic discoveries in the central and south-eastern Swiss Alps, Quatern. Int., 423, 9–22, https://doi.org/10.1016/j.quaint.2015.10.121, 2016.

de Graaff, L. W. S., de Jong, M. G. G., Busnach, T., and Seijmonsbergen, A. C.: Geomorphologische Studie hinterer Bregenzerwald, Bericht an das Amt der Vorarlberger Landesregierung, Abt. Raumplanung und Baurecht Landhaus Bregenz, Amsterdam, 2003.

Della Casa, P.: Switzerland and the Central Alps, in The Oxford Handbook of the European Bronze Age, edited by: Harding, A. and Fokkens, H., 706–722, OUP Oxford, 2013.

Dertsch, R.: Ortsnamensbuch des Landkreises Sonthofen, Historisches Ortsnamenbuch von Bayern, Schwaben, Bd. 7, Kommission für Bayerische Landesgeschichte, München, 1974.

De Vleeschouwer, F., Chambers, F. M., and Swindles, G. T.: Coring and sub-sampling of peatlands for palaeoenvironmental research, Mires Peat, 7, 1–10, https://doi.org/10.1016/j.ssi.2010.01.014, 2010a.

De Vleeschouwer, F., Le Roux, G., and Shotyk, W.: Peat as an archive of atmospheric pollution and environmental change: A case study of lead in Europe, PAGES Mag., 18, 20–22, https://doi.org/10.22498/pages.18.1.20, 2010b.

Dieffenbach-Fries, H.: Zur spät- und postglazialen Vegetationsentwicklung bei Oberstdorf (Oberallgäu) und im kleinen Walsertal (Vorarlberg), Technische Hochschule Darmstadt, 1981.

Dietre, B., Walser, C., Kofler, W., Kothieringer, K., Hajdas, I., Lambers, K., Reitmaier, T., and Haas, J. N.: Neolithic to Bronze Age (4850–3450 cal. BP) fire management of the Alpine Lower Engadine landscape (Switzerland) to establish pastures and cereal fields, Holocene, 27, 181–196, https://doi.org/10.1177/0959683616658523, 2017.

El Balti, N., Christ, L., Kempke, M., Martens, T., Bork, H., and Schrautzer, J.: Die Moore im Kleinwalsertal – Aktueller Zustand und Entwicklungsmöglichkeiten, Ina. – Forsch. online, 40.1, 2017.

Festi, D., Putzer, A., and Oeggl, K.: Mid and late holocene land-use changes in the Ötztal alps, territory of the neolithic iceman "Ötzi", Quatern. Int., 353, 17–33, https://doi.org/10.1016/j.quaint.2013.07.052, 2014.

Fink, J. and von Klenze, H.: Der Mittelberg. Geschichte, Landes- und Volkskunde des ehemaligen gleichnamigen Gerichtes (Reprint), Kösel, Kempten, 1891.

Forel, B., Monna, F., Petit, C., Bruguier, O., Losno, R., Fluck, P., Begeot, C., Richard, H., Bichet, V., and Chateau, C.: Historical mining and smelting in the Vosges Mountains (France) recorded in two ombrotrophic peat bogs, J. Geochem. Explor., 107, 9–20, https://doi.org/10.1016/j.gexplo.2010.05.004, 2010.

Frank, C. and Pernicka, E.: Copper artefacts of the Mondsee group and their possible sources, in: Lake Dwellings after Robert Munro, Proceedings from the Munro International Seminar: The Lake Dwellings of Europe. 22nd 23rd October 2010, University of Edinburgh, edited by: Midgley, M. S. and Sanders, J., 113–138, Sidestone press, Leiden, 2012.

Friedmann, A. and Stojakowits, P.: Zur spät- und postglazialen Vegetationsgeschichte des Allgäu mit Alpenanteil, Kontrakpunkte: Festschrift für Manfred Rösch, edited by: Lechterbeck, J. and Fischer, E., Verlag Dr. Rudolf Habelt GmbH, Bonn, 2017.

Fritz, W.: Kleinwalsertal einst und jetzt: heimatkundliche Betrachtungen, Verlag Walserdruck, Erich Stöckeler, Riezlern/Kleinwalsertal, 1981.

Givelet, N., Le Roux, G., Cheburkin, A., Chen, B., Frank, J., Goodsite, M. E., Kempter, H., Krachler, M., Noernberg, T., Rausch, N., Rheinberger, S., Roos-Barraclough, F., Sapkota, A., Scholz, C., and Shotyk, W.: Suggested protocol for collecting, handling and preparing peat cores and peat samples for physical, chemical, mineralogical and isotopic analyses, J. Environ., 6, 481–492, https://doi.org/10.1039/B401601G, 2004.

Goldscheider, N.: Hydrogeologische Untersuchungen im alpinen Karstgebiet Gottesacker und Schwarzwassertal (Allgäu/Vorarlberg), Vor. Naturschau, 4, 247–294, available at: http://www.biologiezentrum.at (last access: 17 September 2018), 1998.

Grimm, E. C.: Tilia software v. 2.0.60, Illinois State Museum, Springf., 2018.

Grosse-Brauckmann, G.: Paläobotanische Befunde von zwei Mooren im Gebiet des Hohen Ifen, Vorarlberg (Österreich), Telma, 32, 17–36, 2002.

Gulisano, G.: Neue mittelsteinzeitliche Fundplätze im oberen Illertal und im Kleinwalsertal, Archäologische Informationen, 17, 79–84, https://doi.org/10.11588/ai.1994.1.35418, 1994.

Gulisano, G.: Die Besiedlung des Kleinwalsertales und seiner angrenzenden Gebiete in Bayern und Vorarlberg von der Steinzeit bis zur Einwanderung der Walser, Archäologische Informationen, 18, 53–65, https://doi.org/10.11588/ai.1995.1.35421, 1995.

Haas, J. N., Richoz, I., Tinner, W., and Wick, L.: Synchronous holocene climatic oscillations recorded on the Swiss plateau and at timberline in the alps, Holocene, 8, 301–309, https://doi.org/10.1191/095968398675491173, 1998.

HDÖ: Die Niederschläge, Schneeverhältnisse und Lufttemperaturen in Österreich im Zeitraum 1981–1991, Beiträge zur Hydrographie Österreichs, Vienna, 1994.

Heuberger, R.: Der Bodenseeraum im Altertum, in Aus Verfassungs- und Landesgeschichte, Festschrift für Theodor Mayer zum 70. Geb. Band 2. Geschichtliche Landesforschung, Wirtschaftsgeschichte u. Hilfswissenschaften, edited by: Büttner, H., Feger, O., and Meyer, B., 7–21, Lindau/Konstanz, 1955.

Hölzer, A. and Hölzer, A.: Silicon and titanium in peat profiles as indicators of human impact, Holocene, 8, 685–696, https://doi.org/10.1191/095968398670694506, 1998.

Holzhauser, H., Magny, M., and Zumbühl, H. J.: Glacier and lake-level variations in west-central Europe over the last 3500 years, Holocene, 15, 789–801, https://doi.org/10.1191/0959683605hl853ra, 2005.

Höppner, B., Bartelheim, M., Huijsman, M., Krauss, R., Martinek, K.-P., Pernicka, E., and Schwab, R.: Prehistoric copper production in the Inn Valley (Austria), and the earliest copper in Cental Europe, Archaeometry, 47, 293–315, https://doi.org/10.1111/j.1475-4754.2005.00203.x, 2005.

Hormes, A., Müller, B. U., and Schlüchter, C.: The Alps with little ice: Evidence for eight holocene phases of reduced glacier extent in the Central Swiss Alps, Holocene, 11, 255–265, https://doi.org/10.1191/095968301675275728, 2001.

Ivy-Ochs, S., Kerschner, H., Maisch, M., Christl, M., Kubik, P. W., and Schlüchter, C.: Latest Pleistocene and Holocene glacier variations in the European Alps, Quaternary Sci. Rev., 28, 2137–2149, https://doi.org/10.1016/j.quascirev.2009.03.009, 2009.

Jacomet, S.: Plant economy and village life in Neolithic lake dwellings at the time of the Alpine Iceman, Veg. Hist. Archaeobot., 18, 47–59, https://doi.org/10.1007/s00334-007-0138-2, 2009.

Kalnicky, D. J. and Singhvi, R.: Field portable XRF analysis of environmental samples, J. Hazard. Mater., 83, 93–122, https://doi.org/10.1016/S0304-3894(00)00330-7, 2001.

Le Roux, G., Aubert, D., Stille, P., Krachler, M., Kober, B., Cheburkin, A., Bonani, G., and Shotyk, W.: Recent atmospheric Pb deposition at a rural site in southern Germany assessed using a peat core and snowpack, and comparison with other archives, Atmos. Environ., 39, 6790–6801, https://doi.org/10.1016/j.atmosenv.2005.07.026, 2005.

Leitner, W.: Der Felsüberhang auf der Schneiderkürenalpe – Ein Jäger- und Hirtenlager der Vorzeit, Bergschau, 1, 1–32, 2003.

Löwemark, L., Chen, H. F., Yang, T. N., Kylander, M., Yu, E. F., Hsu, Y. W., Lee, T. Q., Song, S. R., and Jarvis, S.: Normalizing XRF-scanner data: A cautionary note on the interpretation of high-resolution records from organic-rich lakes, J. Asian Earth Sci., 40, 1250–1256, https://doi.org/10.1016/j.jseaes.2010.06.002, 2011.

Lutz, J. and Pernicka, E.: Prehistoric copper from the Eastern Alps, Open J. Archaeom., 1, 122–127, https://doi.org/10.4081/arc.2013.e25, 2013.

Mackensen, M.: Die spätrömische Grenze im Gebiet von Cambidano-Kempten, in: Kempten und das Allgäu, Führer zu archäologischen Denkmälern in Deutschland 30, edited by: Czysz, W., Dietrich, H., and Weber, G., 61–69, Theiss, Stuttgart, 1995.

Magny, M., Galop, D., Bellintani, P., Desmet, M., Didier, J., Haas, J. N., Martinelli, N., Pedrotti, A., Scandolari, R., Stock, A., and Vannière, B.: Late-Holocene climatic variability south of the Alps as recorded by lake-level fluctuations at Lake Ledro, Trentino, Italy, Holocene, 19, 575–589, https://doi.org/10.1177/0959683609104032, 2009.

Mann, M. E.: Medieval Climatic Optimum, Encycl. Glob. Environ. Chang., 1, 514–516, 2002.

Mansel, K.: Ein latènezeitlicher Schlüssel mit Stierplastik aus Sonthofen im Allgäu, Germania, 67, 572–587, 1989.

Matthews, J. A. and Briffa, K. R.: The "Little Ice Age": Re-evaluation of an evolving concept, Geogr. Ann. Ser. A, 87, 17–36, https://doi.org/10.1111/j.0435-3676.2005.00242.x, 2005.

McLennan, S. M.: Relationships between the trace element composition of sedimentary rocks and upper continental crust, Geochem. Geophy. Geosy., 2, 2000GC000109, https://doi.org/10.1029/2000GC000109, 2001.

Mejía-Piña, K. G., Huerta-Diaz, M. A., and González-Yajimovich, O.: Calibration of handheld X-ray fluorescence (XRF) equipment for optimum determination of elemental concentrations in sediment samples, Talanta, 161, 359–367, https://doi.org/10.1016/j.talanta.2016.08.066, 2016.

Merbeler, J.: Erzbergbau und Verhüttung im Starzlachtal, in: Kempten und das Allgäu, Führer zu archäologischen Denkmälern in Deutschland 30, edited by: Czysz, W., Dietrich, H., and Weber, G., 149–152, Theiss, Stuttgart, 1995.

Moore, P., Webb, J., and Collinson, M.: Pollen Analysis, Blackwell Scientific Publications Ltd, Oxford, 1991.

Nesbitt, H. W. and Markovics, G.: Weathering of granodioritic crust, long-term storage of elements in weathering profiles, and petrogenesis of siliciclastic sediments, Geochim. Cosmochim. Ac., 61, 1653–1670, https://doi.org/10.1016/S0016-7037(97)00031-8, 1997.

Oblinger, H.: Blei- und Zinkerz am Roßkopf (Ostrachtal/Allgäuer Alpen), Berichte des Naturwissenschaftlichen Vereins für Schwaben e.V., 100, 85–90, 1996.

O'Brien, W.: Prehistoric Copper Mining in Europe: 5500–500 BC, Oxford University Press, 2015.

Oeggl, K. and Nicolussi, K.: Prähistorische Besiedlung von zentralen Alpentälern in Bezug zur Klimaentwicklung, in: Klimawandel in Österreich: die letzten 20.000 Jahre und ein Blick voraus, edited by: Schmidt, R., Psenner, R., and Matulla, C., 77–86, Innsbruck university press, 2009.

Pacyna, J. M. and Pacyna, E. G.: An assessment of global and regional emissions of trace metals to the atmosphere from anthropogenic sources worldwide, Environ. Rev., 9, 269–298, https://doi.org/10.1139/er-9-4-269, 2001.

R Core Team: R: A Language and Environment for Statistical Computing, available at: https://www.r-project.org/ (last access: 14 April 2019), 2017.

Reimer, P. J., Bard, E., Bayliss, A., Beck, J. W., Blackwell, P. G., Ramsey, C. B., Buck, C. E., Cheng, H., Edwards, R. L., Friedrich, M., Grootes, P. M., Guilderson, T. P., Haflidason, H., Hajdas, I., Hatté, C., Heaton, T. J., Hoffmann, D. L., Hogg, A. G., Hughen, K. A., Kaiser, K. F., Kromer, B., Manning, S. W., Niu, M., Reimer, R. W., Richards, D. A., Scott, E. M., Southon, J. R., Staff, R. A., Turney, C. S. M., and van der Plicht, J.: IntCal13 and Marine13 Radiocarbon Age Calibration Curves 0–50 000 Years cal BP, Radiocarbon, 55, 1869–1887, https://doi.org/10.2458/azu_js_rc.55.16947, 2013.

Reitmaier, T., Doppler, T., Pike, A. W. G., Deschler-Erb, S., Hajdas, I., Walser, C., and Gerling, C.: Alpine cattle management during the Bronze Age at Ramosch-Mottata, Switzerland, Quatern. Int., 484, 19–31, https://doi.org/10.1016/j.quaint.2017.02.007, 2018.

Roepke, A. and Krause, R.: High montane-subalpine soils in the Montafon Valley (Austria, northern Alps) and their link to land-use, fire and settlement history, Quatern. Int., 308–309, 178–189, https://doi.org/10.1016/j.quaint.2013.01.022, 2013.

Roepke, A., Stobbe, A., Oeggl, K., Kalis, A. J., and Tinner, W.: Late-Holocene land-use history and environmental changes at the high altitudes of St Antönien (Switzerland, Northern Alps): Combined evidence from pollen, soil and tree-ring analyses, Holocene, 21, 485–498, https://doi.org/10.1177/0959683610385727, 2011.

Rösch, M.: Human impact as registered in the pollen record: some results from the western Lake Constance region, Southern Germany, Veg. Hist. Archaeobot., 1, 101–109, https://doi.org/10.1007/BF00206090, 1992.

Schmidl, A. and Oeggl, K.: Land Use in the Eastern Alps During the Bronze Age – an Archaeobotanical Case Study of a Hilltop Settlement in the Montafon (Western Austria), Archaeometry, 47, 455–470, https://doi.org/10.1111/j.1475-4754.2005.00213.x, 2005.

Schmidt-Thomé, P.: Zur Geologie und Morphologie des Ifengebirgsstockes (Allgäu): Erläuterungen zur topographisch-morphologischen Kartenprobe VI 3: Alpiner Karst und Bergsturz (On the Geology and Morphology of the Hohe Ifen), Erdkunde, 14, 181–195, 1960.

Schrautzer, J., Bork, H.-R., Christ, L., El-Balti, N., Martens, T., Kempke, M., von Scheffer, C., and Unkel, I.: Classification, ecological characterization and development of montane mires, Phytocoenologia – J. Veg. Ecol., in press, 2019.

Shand, C. A. and Wendler, R.: Portable X-ray fluorescence analysis of mineral and organic soils and the influence of organic matter, J. Geochem. Explor., 143, 31–42, https://doi.org/10.1016/j.gexplo.2014.03.005, 2014.

Shotyk, W., Weiss, D., Appleby, P. G., Cheburkin, A. K., Frei, R., Gloor, M., Kramers, J. D., Reese, S., and Van der Knaap, W. O.: History of atmospheric lead depostion since 12,370$^{14}$C yr BP from a Peat bog, Jura Mountains, Switzerland, Science, 281, 1635–1640, https://doi.org/10.1126/science.281.5383.1635, 1998.

Shotyk, W., Weiss, D., Kramers, J. D., Frei, R., Cheburkin, A. K., Gloor, M., and Reese, S.: Geochemistry of the peat bog at Etang de la Gruère, Jura Mountains, Switzerland, and its record of atmospheric pb and lithogenic trace metals (Sc, Ti, Y, Zr, and REE) since 12,370$^{14}$C yr bp, Geochim. Cosmochim. Ac., 65, 2337–2360, https://doi.org/10.1016/S0016-7037(01)00586-5, 2001.

Shuttleworth, E. L., Evans, M. G., Hutchinson, S. M., and Rothwell, J. J.: Assessment of lead contamination in peatlands using field portable XRF, Water Air. Soil Pollut., 225, https://doi.org/10.1007/s11270-013-1844-2, 2014.

State of Vorarlberg: VoGIS, Vorarlberg Atlas, Urmappe 1857, available at: http://vogis.cnv.at/, last access: 17 August 2018.

Stojakowits, P.: Pollenanalytische Untersuchungen zur Rekonstruktion der Vegetationsgeschichte im südlichen Iller-Wertach-Jungmoränengebiet seit dem Spätglazial (PhD-Thesis), Universität Augsburg, 2014.

Tinner, W., Lotter, A. F., Ammann, B., Conedera, M., Hubschmid, P., Van Leeuwen, J. F. N., and Wehrli, M.: Climatic change and contemporaneous land-use phases north and south of the Alps 2300 BC to 800 AD, Quaternary Sci. Rev., 22, 1447–1460, https://doi.org/10.1016/S0277-3791(03)00083-0, 2003.

Tomedi, G., Staudt, M., and Töchterle, U.: Zur Bedeutung des prähistorischen Bergbaus auf Kupfererze im Raum Schwaz-Brixlegg, in: Cuprum Tyrolense – 5550 Jahre Bergbau und Kupferverhüttung in Tirol, edited by: Oeggl, K. and Schaffer, V., 55–70, Edition Tirol, 2013.

Valese, E., Conedera, M., Held, A. C. C., and Ascoli, D.: Fire, humans and landscape in the European Alpine region during the Holocene, Anthropocene, 6, 63–74, https://doi.org/10.1016/j.ancene.2014.06.006, 2014.

Van der Knaap, W. O., van Leeuwen, J. F. N., and Ammann, B.: The first rise and fall of Fagus sylvatica and interactions with Abies alba at Faulenseemoos (Weiss Plateau) 6900–6000 cal yr BP, Acta Palaeobot., 44, 249–266, 2004.

Vanneste, H., De Vleeschouwer, F., Martínez-Cortizas, A., von Scheffer, C., Piotrowska, N., Coronato, A., and Le Roux, G.: Late-glacial elevated dust deposition linked to westerly wind shifts in southern South America, Sci. Rep., 5, 11670, https://doi.org/10.1038/srep11670, 2015.

Völk, H. R.: Geomorphologie des Kleinwalsertales und seiner Gebirgsumrahmung, Landschaftsformen zur Eiszeit und Nacheiszeit unter Einbeziehung der geologischen Verhältnisse, Vor. Naturschau, 10, 7–95, 2001.

von Gümbel, C. W.: Geognostische Beschreibung des Königreichs Bayern: Geognostische Beschreibung des bayerischen Alpengebirges und seines Vorlandes, bayer. Staatsministerium der Finanzen, Gotha, 1861.

von Raiser, J. N.: Der Ober-Donau-Kreis des Königreichs Bayern unter den Römern, Die Römer-Male von Augusta rauracum bis Augusta Vindelicorum: 1, Kranzfelder, Augsburg, 1830.

Vorren, K.-D., Mørkved, B,. and Bortenschlager, S.: Human impact on the Holocene forest line in the Central Alps, Veg. Hist. Archaeobot., 2, 145–156, https://doi.org/10.1007/BF00198585, 1993.

Wagner, G.: Rund um Hochifen und Gottesackergebiet, Verlag der Hohenloheschen Buchhandlung Ferdinand Rau, Öhringen, 1950.

Walde, C. and Oeggl, K.: Blütenstaub enthüllt 3000-jährige Siedlungsgeschichte im Tannberggebiet, Walserheimat Vor., Tirol und Liechtenstein, 73, 1–6, available at: https://www.vorarlberger-walservereinigung.at/vwvwp/bluetenstaub (last access: 6 March 2019), 2003.

Walde, C. and Oeggl, K.: Neue Ergebnisse zur Siedlungsgeschichte am Tannberg. Die Pollenanalysen aus dem Körbersee, Walserheimat Vor., Tirol und Liechtenstein, 75, 4–7, available at: https://www.vorarlberger-walservereinigung.at/vwvwp/neue-ergebnisse (last access: 6 March 2019), 2004.

Weber, L.: Handbuch der Lagerstätten der Erze, Industrieminerale und Energierohstoffe Österreichs: Erläuterungen zur metallogenetischen Karte von Österreich 1:500 000 unter Einbeziehung der Industrieminerale und Energierohstoffe, Geologische Bundesanstalt, 1997.

Weber, M.: Die frühe und mittlere römische Kaiserzeit, in Kempten und das Allgäu, Führer zu archäologischen Denkmälern in Deutschland 30, edited by: Czysz, W., Dietrich, H., and Weber, G., 49–60, Theiss, Stuttgart, 1995.

Weiss, D., Shotyk, W., Appleby, P. G., Kramers, J. D., and Cheburkin, A. K.: Atmospheric Pb Deposition since the Industrial Revolution Recorded by Five Swiss Peat Profiles: Enrichment Factors, Fluxes, Isotopic Composition, and Sources, Environ. Sci. Technol., 33, 1340–1352, https://doi.org/10.1021/es980882q, 1999.

Wick, L. and Tinner, W.: Vegetation Changes and Timberline Fluctuations in the Central Alps as Indicators of Holocene Climatic Oscillations, Arct. Alp. Res., 29, 445–458, https://doi.org/10.2307/1551992, 1997.

Wurth, G., Niggemann, S., Richter, D. K., and Mangini, A.: The Younger Dryas and Holocene climate record of a stalagmite from Hölloch Cave (Bavarian Alps, Germany), J. Quaternary Sci., 19, 291–298, https://doi.org/10.1002/jqs.837, 2004.

Zacher, W.: Geologische Karte von Österreich: Blatt 113 Mittelberg 1:50 000, Geologische Bundesanstalt, Wien, 1990.

E&G Quaternary Sci. J., 68, 29–46, 2019
https://doi.org/10.5194/egqsj-68-29-2019


Open Access E&G Quaternary Science Journal

Research article

# Grain-size distribution unmixing using the R package EMMAgeo

**Elisabeth Dietze[1,2] and Michael Dietze[3]**

[1]Alfred Wegener Institute for Polar and Marine Research, Research Unit Potsdam, 14473 Potsdam, Germany
[2]GFZ German Research Centre for Geosciences, Section 3.2 Organic Geochemistry, 14473 Potsdam, Germany
[3]GFZ German Research Centre for Geosciences, Section 5.1 Geomorphology, 14473 Potsdam, Germany

**Correspondence:** Elisabeth Dietze (edietze@awi.de)

**Relevant dates:** Received: 3 December 2018 – Accepted: 2 April 2019 – Published: 16 May 2019

**How to cite:** Dietze, E., and Dietze, M.: Grain-size distribution unmixing using the R package EMMAgeo, E&G Quaternary Sci. J., 68, 29–46, https://doi.org/10.5194/egqsj-68-29-2019, 2019.

**Abstract:** The analysis of grain-size distributions has a long tradition in Quaternary Science and disciplines studying Earth surface and subsurface deposits. The decomposition of multi-modal grain-size distributions into inherent subpopulations, commonly termed end-member modelling analysis (EMMA), is increasingly recognised as a tool to infer the underlying sediment sources, transport and (post-)depositional processes. Most of the existing deterministic EMMA approaches are only able to deliver one out of many possible solutions, thereby shortcutting uncertainty in model parameters. Here, we provide user-friendly computational protocols that support deterministic as well as robust (i.e. explicitly accounting for incomplete knowledge about input parameters in a probabilistic approach) EMMA, in the free and open software framework of R.

In addition, and going beyond previous validation tests, we compare the performance of available grain-size EMMA algorithms using four real-world sediment types, covering a wide range of grain-size distribution shapes (alluvial fan, dune, loess and floodplain deposits). These were randomly mixed in the lab to produce a synthetic data set. Across all algorithms, the original data set was modelled with mean $R^2$ values of 0.868 to 0.995 and mean absolute deviation (MAD) values of 0.06 % vol to 0.34 % vol. The original grain-size distribution shapes were modelled as end-member loadings with mean $R^2$ values of 0.89 to 0.99 and MAD of 0.04 % vol to 0.17 % vol. End-member scores reproduced the original mixing ratios in the synthetic data set with mean $R^2$ values of 0.68 to 0.93 and MAD of 0.1 % vol to 1.6 % vol. Depending on the validation criteria, all models provided reliable estimates of the input data, and each of the models exhibits individual strengths and weaknesses. Only robust EMMA allowed uncertainties of the end-members to be objectively estimated and expert knowledge to be included in the end-member definition. Yet, end-member interpretation should carefully consider the geological and sedimentological meaningfulness in terms of sediment sources, transport and deposition as well as post-depositional alteration of grain sizes. EMMA might also be powerful in other geoscientific contexts where the goal is to unmix sources and processes from compositional data sets.

Published by Copernicus Publications on behalf of the Deutsche Quartärvereinigung (DEUQUA) e.V.

# 1 Introduction

## 1.1 Mixing of grain-size subpopulations in sedimentary deposits

Many studies in Quaternary Science aim to reconstruct past Earth surface dynamics using sedimentary proxies. Earth surface dynamics include a variety of processes that mix process-related components (Buccianti et al., 2006). Sediment from different sources can be transported and deposited by a multitude of sedimentological processes that have been linked to climate, vegetation, geological and geomorphological dynamics (Bartholdy et al., 2007; Folk and Ward, 1957; Macumber et al., 2018; Stuut et al., 2002; Tjallingii et al., 2008; Vandenberghe, 2013; Vandenberghe et al., 2004, 2018). During transport, grain-size subpopulations are affected by different transport energies, and, thus, distinct grain-size distributions are created upon deposition. Accordingly, it is possible to infer source areas, transport pathways and transport processes as well as the related sedimentary environment from measured grain-size distributions. This basic concept has been exploited for more than 60 years (Flemming, 2007; Folk and Ward, 1957; Hartmann, 2007; Visher, 1969). However, the approach is limited when sediments are transported by more than one process and become mixed during and after deposition (Bagnold and Barndorff-Nielsen, 1980; Vandenberghe et al., 2018).

The advent of fast, high-resolution grain-size measurements through laser diffraction allows the assessment of grain-size distributions of large sample sets in a short time and reveals the sediment mixing effects in multiple modes or distinct shoulders in the grain-size distribution curves. Although widely used, classic measures of bulk distributions such as sand, silt and clay contents or mean grain size, $D_{50}$, sorting, skewness or kurtosis (Folk and Ward, 1957) are non-informative in non-Gaussian, multi-modal distributions and allow only a qualitative interpretation and comparison of sedimentary processes that contributed to sediment formation.

To overcome these limitations and to improve process interpretation and attribution of associated drivers from sedimentary archives (Dietze et al., 2014), two ways have been proposed to decompose multi-modal grain-size distributions and to quantify the dominant grain-size subpopulation: parametric and non-parametric approaches. Among the former, commonly used curve fitting approaches describe a sediment sample as a combination of a finite number of parametric distribution functions such as (skewed) log-normal, log-hyperbolic or Weibull distributions (Bagnold and Barndorff-Nielsen, 1980; Gan and Scholz, 2017; Sun et al., 2002). However, curve fitting solutions are non-unique, and subpopulations might not be detected if a fixed number of functions are fitted to individual samples (Paterson and Heslop, 2015; Weltje and Prins, 2003), whereas other parametric approaches such as non- and semi-parametric mixture models (Hunter et al., 2011; Lindsay and Lesperance, 1995) are still very poorly explored in the field of grain-size distribution analyses.

Non-parametric end-member modelling or mixing analysis (EMMA) aims to describe a whole data set as a combination of discrete subpopulations, based on eigenspace analysis and compositional data constraints (Aitchison, 1986). A multidimensional grain-size data set $\mathbf{X}$ (i.e. $m$ samples, each represented by $n$ grain-size classes) can be described as a linear combination of transposed end-member loadings ($\mathbf{V}^{\mathrm{T}}$, representing individual grain-size subpopulations), end-member scores ($\mathbf{M}$, the relative contribution of the end-member subpopulations to each sample) and an error matrix $\mathbf{E}$ using the function

$$\mathbf{X} = \mathbf{M} \cdot \mathbf{V}^{\mathrm{T}} + \mathbf{E}. \quad (1)$$

Hence, it is possible to identify (using end-member loadings) and quantify (using end-member scores) sediment sources, transport and depositional regimes from mixed grain-size data sets. EMMA has been successfully applied to interpret and quantify past sedimentary processes from sediment deposits, beyond classical measures, for example in marine, lacustrine, aeolian, fluvial, alluvial and periglacial environments, across multiple spatial and temporal scales (Borchers et al., 2015; Dietze et al., 2013, 2016; Schillereff et al., 2016; Strauss et al., 2012; Toonen et al., 2015; Varga et al., 2019; Vriend and Prins, 2005; Wündsch et al., 2016).

## 1.2 Non-parametric grain-size unmixing approaches

Five approaches of non-parametric EMMA have been proposed: Weltje (1997) has developed a FORTRAN algorithm based on simplex expansion, which has been translated to a set of scripts for R (R Core Team, 2017) called RECA (R-based Endmember Composition Algorithm), including a fuzzy c-means clustering approach (Seidel and Hlawitschka, 2015). Available as MATLAB scripts, the algorithm by Dietze et al. (2012) has included eigenvector rotation, whereas Yu et al. (2015) have introduced a Bayesian EMMA (BEMMA) and Paterson and Heslop (2015) have used approaches from hyperspectral image processing (AnalySize). Based on the MATLAB algorithm by Dietze et al. (2012), Dietze and Dietze (2016) compiled a prototype R package (EMMAgeo v. 0.9.4).

Most EMMA approaches are deterministic (i.e. one single model solution without any uncertainty estimates) and require the user to set a fixed number of end-members $q$ and further model parameters. In natural systems, however, $q$ is rarely known and, thus, often one of the reasons to employ EMMA. Different approaches have been proposed to estimate $q$, such as the inflection point in a $q$–$R^2$ plot (Paterson and Heslop, 2015; Prins and Weltje, 1999) or the iterative adjustment of model parameters such as the weight transformation limit (Dietze et al., 2012), maximum convexity error, number of iterations and weighting exponent (Weltje, 1997; Seidel and Hlawitschka, 2015).

Previous studies of EMMA performance (Weltje and Prins, 2007; Seidel and Hlawitschka, 2015; Paterson and Heslop, 2015) either used measured data without information on the true loadings and scores or were based on ideally designed synthetic data. However, natural process end-members can overlap substantially and may have a varying or multi-modal grain-size distribution shape due to unstable transport conditions (e.g. gradual fining of aeolian dust with transport distance) and deposition (e.g. reworking by soil formation; Dietze et al., 2016; Vandenberghe et al., 2018).

Recently, van Hateren et al. (2018) compared the concepts and performances of AnalySize, RECA, BEMMA, EMMAgeo and a diffuse reflectance spectroscopy (DRS) unmixing approach (Heslop et al., 2007). They used numerically mixed real-world grain-size samples and compared the modelled end-member loadings with the real-world distributions and modelled scores with randomised mixing ratios, as suggested by Schulte et al. (2014). Van Hateren and others confirmed former studies and highlighted that geological background knowledge is crucial for end-member interpretation, but they also pointed to strong differences in model performance. However, the descriptions of van Hateren et al. (2018) are mainly based on verbal comparisons of graphic data representations, and the validation data are not available for future comparative studies.

Here, we introduce new operational modes and protocols for the comprehensive open-source R package EMMAgeo as a tool for quantifying process-related grain-size subpopulations in mixed sediments. We aim to clarify information provided by the reference documentation of the first version of the package (v. 0.9.4; Dietze and Dietze, 2016) and by Dietze et al. (2014), regarding parameter estimation and optimisation, and we add a new approach of uncertainty estimation of the end-member scores. We evaluate the performance and validity of EMMAgeo using a real-world grain-size data set with fully known end-member compositions and unbiased quantitative measures. For comparison, the same data set is modelled with other available grain-size end-member algorithms. An evaluation and validation of both process end-member distribution shapes and mixing ratios are provided. Finally, general constraints for the interpretation of end-members are discussed. The detailed Supplement shall help users to apply the EMMAgeo protocols and to reproduce the results, making use of the raw data published along with this study.

## 2 The R package EMMAgeo

### 2.1 Background

EMMAgeo in its current version 0.9.6 (Dietze and Dietze, 2019) contains 22 functions (Table S1 in the Supplement), the example data set for this study and full documentation of these items. EMMAgeo provides a systematic chain of data pre-processing, parameter estimation and optimisation, the actual modelling and the inference of model uncertainties.

EMMAgeo is based on the EMMA MATLAB code by Dietze et al. (2012), which was slightly modified, i.e. vectorisation of looped calculations to increase computation speed, a new coding of the scaling procedure (Miesch, 1976) and additional measures of model performance. Following Dietze et al. (2012), the core function `EMMA()` rescales the grain-size data matrix $\mathbf{X}$ to constant row sums (i.e. $m$ rows of samples, $n$ columns of grain-size classes). Then, a weight transformation (Klovan and Imbrie, 1971) is performed using a weight constant $l$ to yield a weight matrix $\mathbf{W}$ that is not biased by variables with large standard deviations (Weltje, 1997). The similarity matrix $\mathbf{A}$ is returned as the minor product of $\mathbf{W}$. From the similarity matrix, the eigenspace is computed, and eigenvalues ($\mathbf{L}$) and their cumulative sums are calculated. Eigenvectors are inferred and sorted by decreasing explained variance ($\mathbf{V}_f$). These eigenvectors are then rotated, by default using the Varimax rotation (Dietze et al., 2012), in R using the package GPArotation (Bernaards and Jennrich, 2005). Their order is inverted to yield unscaled end-member loadings ($\mathbf{V}_q$). Then, normalised end-member loadings ($\mathbf{V}_{q\mathrm{n}}$) are computed by row-wise data normalisation of $\mathbf{V}_q$ or are user-defined; i.e. a known $\mathbf{V}_{q\mathrm{n}}$ can be used. A factor score matrix ($\mathbf{M}_q$) is calculated as a non-negative least squares estimate of $\mathbf{V}_{q\mathrm{n}}$ and $\mathbf{W}$. Then, the data set can be described as a minor product of $\mathbf{M}_q$ and $\mathbf{V}^{\mathrm{T}}$ to yield the modelled weight matrix $\mathbf{W}_{\mathrm{m}}$. These values are back-transformed and yield rescaled end-member loadings ($\mathbf{V}_{q\mathrm{sn}}$) and quantitative scores ($\mathbf{M}_{\mathrm{qs}}$). A linear combination of $\mathbf{M}_{\mathrm{qs}}$ and $\mathbf{V}^{\mathrm{T}}$ yields $\mathbf{X}'$, the modelled data set (see the mathematical formulation in Dietze et al., 2012). Model evaluation measures are calculated by comparing $\mathbf{X}$ and $\mathbf{X}'$: row-wise (sample) and column-wise (grain-size class) absolute model deviation, data variance and root mean square errors ($\mathrm{MAD}_m$ and $\mathrm{MAD}_n$, $R^2_m$ and $R^2_n$ and $\mathrm{RMSE}_m$ and $\mathrm{RMSE}_n$), explained variance of each end-member ($M_{\mathrm{qsvar}}$) and total mean $\mathrm{MAD}_{\mathrm{t}}$ and $R^2_{\mathrm{t}}$ of the model, as well as the number of overlapping end-member loadings (ol), defined as one end-member having its main mode within the area of another end-member.

### 2.2 Theory of operational modes and protocols

A deterministic and a robust operational EMMA mode can be run by a function and two protocols, respectively. First, EMMA can be performed with a user-based decision on all parameters, which is comparable to existing algorithms. This *deterministic EMMA* is mainly useful for exploratory studies, such as investigating the effect of different numbers of end-members $q$, weight transformation limits $l$ or factor rotation types. The function call `EM_det <- EMMA(X = X, q = 4, plot = TRUE)`, with `X` being the data set and `q` the number of suggested end-members, returns the final end-member loadings and scores, the modelled data set and several quality criteria. Additional function arguments can be provided, such as `l`, other factor rotation methods, predefined unscaled end-member loadings, the grain-size class limits of the input data set or a series of plot arguments in standard R language.

The second and third protocol of *robust EMMA* account for the real mixing conditions being generally unknown. In such cases, it is reasonable to evaluate different model realisations within meaningful parameter ranges; i.e. `q` and `l` can be varied to infer the range of uncertainty associated with the set of model scenarios in a probabilistic framework. The central goal of robust EMMA is to set the boundary conditions for these two parameters `q` and `l`, which allows all resulting scenarios to be modelled to identify emergent robust end-members and to describe these by statistical measures. There are two ways to run robust EMMA (Fig. 1). An extended protocol is suitable for more exploratory studies, in which parameter settings can be explored and manipulated in detail (Fig. 1a). A compact protocol allows calculation of all important input and output parameters in five steps (Fig. 1b). Both protocols follow the same workflow but with different requirements and possibilities to interact.

The *extended protocol of robust EMMA* (Fig. 1a) starts with defining $l_{\mathrm{min}}$, a lower limit for `l` (step 1). By default, $l_{\mathrm{min}}$ is set to zero (according to Miesch, 1976). The upper limit $l_{\mathrm{max}}$ (step 2) represents the maximum possible value that still allows eigenspace calculation and is either found by testing the possibility of eigenspace computation for a sequence of possible `l` values (function `test.l()`) or by iteratively approximating the highest possible `l` value (function `test.l.max()`). When `l` approaches $l_{\mathrm{max}}$, EMMA generates increasingly unreliable output (e.g. negative loadings), which is why $l_{\mathrm{max}}$ should be set to a lower value, for example, the default value 95 % of $l_{\mathrm{max}}$. Based on $l_{\mathrm{min}}$ and $l_{\mathrm{max}}$, a sequence of likely values for `l` is created (step 3). The number of these values (here $n = 20$) should balance sufficient `q` scenarios and reasonable computational time.

The range of the number of end-members $q$ is then modelled for each element of this sequence of `l`. Step 4 sets $q_{\mathrm{min}}$ by testing how much of the data variance can be explained with a given $q$ prior to eigenspace rotation. Dietze et al. (2012) suggested a minimum $R^2$ of 0.95. A reasonable estimate of the highest meaningful value $q_{\mathrm{max}}$ (step 5) can be the first local maximum of total mean $R_{\mathrm{t}}^2$ after all end-members were modelled. In EMMA (Dietze et al. 2012), $R_{\mathrm{t}}^2$ rises as more end-members are included until, after a local maximum, it drops again, which is related to the forced constant-sum constraints (Paterson and Heslop, 2015). Alternative criteria can be a fixed upper threshold of $R_{\mathrm{t}}^2$ or a fixed user-defined value for $q_{\mathrm{max}}$ (step 5). Note that this approach differs from the way that other models identify $q$. While Weltje (1997) and Prins and Weltje (1999) use the inflection point of the $q$–$R^2$ relationship to set one fixed $q$, robust EMMA provides a range of $\boldsymbol{q}$ that include this inflection point. In step 6, the ranges of `q` and `l` are combined to a parameter matrix `P`, used to model all likely end-member scenarios. In `P`, $\boldsymbol{q}_{\mathrm{min}}$ must be at least 2, $\boldsymbol{q}_{\mathrm{max}}$ must be at least as high as the corresponding $\boldsymbol{q}_{\mathrm{min}}$ and there must be no NA (not available) values (see Supplement).

End-member loadings from different model parameter settings tend to cluster at similar main mode positions, which Dietze et al. (2012, 2014) used to manually identify robust end-members. To identify these mode clusters within EMMAgeo (step 7), `EMMA()` is evaluated for each combination of $\boldsymbol{q}$ between $q_{\mathrm{min}}$ and $q_{\mathrm{max}}$ for each element of $\boldsymbol{l}$. Step 8 generates the limits around the mode clusters of the robust end-member loadings. The limits are a two-column matrix with the lower and upper limit class for each robust end-member. With these class limits, all robust end-member loadings can be extracted (step 9), and their class-wise means and standard deviations are calculated.

With the mean robust loadings, i.e. the unweighted mean of all similarly likely loadings of step 9, it is possible to optimise the model with respect to different quality criteria by changing `l` to yield an optimal EM solution ($l_{\mathrm{opt}}$, step 10). The default quality criterion is $R_{\mathrm{t}}^2$. Other possible criteria are thresholds in mean sample- and class-wise $R^2$ and $\boldsymbol{E}$ and the number of overlapping end-members. With the uncertainty ranges of robust loadings and $l_{\mathrm{opt}}$ (or any other user-defined $l$ values), it is possible to quantify the uncertainties of end-member scores using Monte Carlo simulations (step 11). The simulations generate many sets of unscaled end-member loadings, by default 100 times `q`. `EMMA()` is performed with each subset of loadings, and the scores are extracted. Their overall scatter is described by the sample-wise standard deviation. The Monte Carlo approach cannot propagate a specific $\boldsymbol{l}$ to the scores calculation because loadings are randomly sampled with no information about the initial $l$ with which they have been created. Hence, the Monte Carlo approach only delivers an estimate of the standard deviation of the scores (default) or asymmetric confidence intervals, whereas the mean derives from the optimal EM model.

The *compact protocol of robust EMMA* (Fig. 1b) combines steps of the extended protocol and automates the identification of plausible grain-size class limits for robust end-member extraction. After data input checks, the ranges of $\boldsymbol{l}$ (step 1) and $\boldsymbol{q}$ (step 2) are determined. These boundary conditions are used to evaluate multiple EMMA scenarios (step 3). Cluster limits can be identified by a kernel density estimate for all available grain-size modes (step 4) that are used to define robust end-members. Kernel density estimates are curves that depict the continuous empiric distribution of data, in this case grain-size mode classes, by sliding a window (the kernel) over the data and counting the number of values within it for each sliding step. The window size (or kernel bandwidth) is the parameter controlling the shape of the resulting curve. Here, a default kernel bandwidth of 1 % of the number of grain-size classes of the input data set is used. To identify mode cluster limits, the density curve needs to be cut off at a given threshold. Above that threshold, the limits bracketing

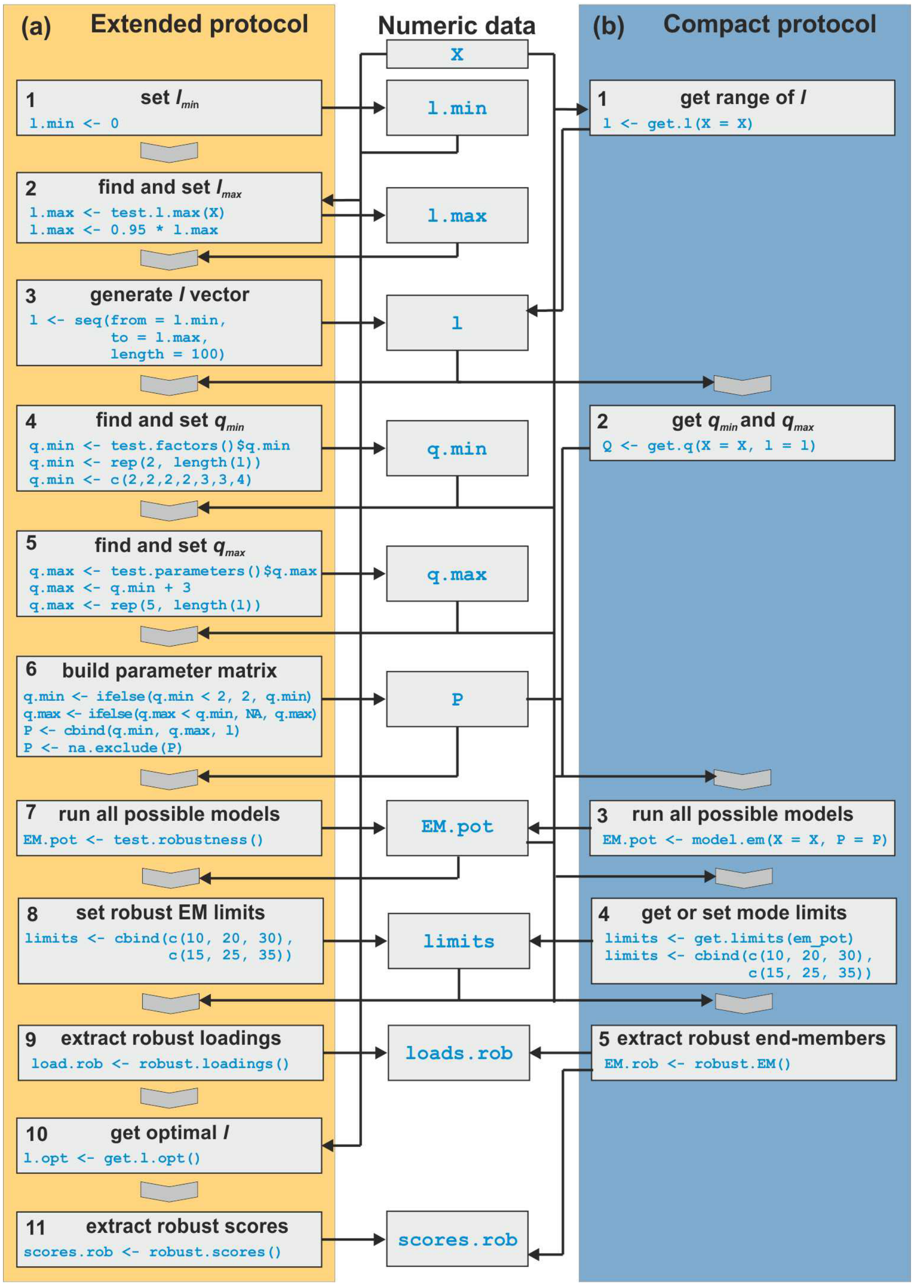


**Figure 1.** Flow chart of the two robust EMMA protocols. **(a)** Extended protocol with code for the entire modelling chain. **(b)** Compact protocol with minimal user input.

the modes can be derived. By default, the cut-off threshold is defined as the 0.7 quantile of the density values. These empirical default values were found to be appropriate during extensive tests with synthetic data sets during package development. However, they are not universal and may be adjusted when needed. With all modelled end-member loadings (from step 3) and the class limits (from step 4), the robust end-member loadings and scores can be extracted (step 5; Fig. 1).

## 3 Practical application: material and methods

### 3.1 Example data set

Sediment outcrops of four depositional environments were sampled near the city of Dresden, Germany (Fig. 2). These represent natural sedimentological end-members ($EM_{nat}$) of a floodplain section ($EM_{nat}1$, with main grain-size mode at 19 µm) of an Elbe River tributary, a loess deposit ($EM_{nat}2$, mode at 36 µm) of the Ostrau profile described by Meszner

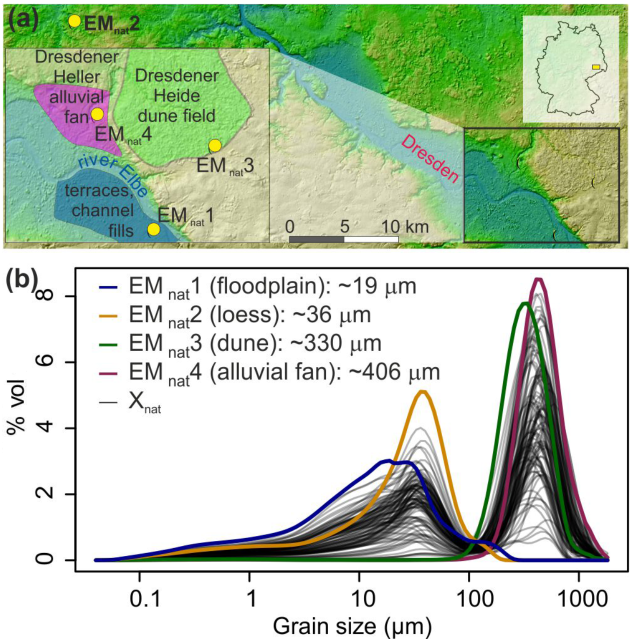


**Figure 2.** **(a)** Sample locations and sedimentological setting (according to the geological map, section Dresden, Sächsisches Landesamt für Umwelt, Landwirtschaft und Geologie; http://www.geologie.sachsen.de/geologische-karten-14041.html, last access: 10 May 2019); see kmz file in the Supplement. **(b)** Grain-size distributions of the four natural grain-size end-members ($EM_{nat}$) and the 100 resulting mixed samples ($X_{\mathrm{nat}}$), i.e. the example data set of the EMMAgeo R package (Dietze and Dietze, 2019).

et al. (2013), a sandur dune ($EM_{nat}3$, mode at 330 µm) and a Weichselian alluvial fan ($EM_{nat}4$, mode at 406 µm; Fig. 2). These natural environments were selected to cover a broad range of transport regimes, grain-size distribution shapes, degrees of mode overlapping ($EM_{nat}4$ and $EM_{nat}3$) and number of modes ($EM_{nat}1$). Note that these samples are potentially composed of multiple grain-size populations themselves and are far from "ideal" for synthetic unmixing. We decisively chose this approach not only to compare the performance of different EMMA methods but also to explore drawbacks in the modelling procedure under such conditions.

Three parallel samples (0.3–2.0 g) per outcrop were chemically treated with 10 % NaCl, 15 % $H_2O_2$ and 1.25 mL $Na_4P_2O_7$, each for 48 h, and measured with a Beckman Coulter LS 13 320 Laser Diffraction Particle Size Analyzer at RWTH Aachen, delivering 116 classes (0.04–2000 µm). Between 7 and 16 aliquots per sample were investigated in triplicates. Grain-size distributions were derived applying the Mie theory with the following parameters: fluid refraction index: 1.33; sample refraction index: 1.55; imaginary refraction index: 0.1. The resulting median grain-size distributions (Fig. 2) were manually mixed in the lab to generate 100 samples with randomly assigned individual contributions. Within this data set $\mathbf{X}_{\mathrm{nat}}$, 50 samples contained all four $EM_{nat}$, 25 were prepared without $EM_{nat}4$ material and a further 25 were prepared without $EM_{nat}1$. Hence, in contrast to other studies, we fully know the grain-size distributions of the underlying natural process end-members and their mixing ratios, which allows a detailed evaluation of performance and comparison of all available EMMA algorithms.

## 3.2 Model performance of different EM analyses

The example data set $\mathbf{X}_{\mathrm{nat}}$ was decomposed with deterministic EMMA of EMMAgeo using `q=4` and `l=0`. Robust EMMA was run with both the extended and the compact protocol. To be as conservative and as unbiased as possible, both protocols were executed with the default parameterisations as suggested above and were only modified when results obviously prompted manual parameter adjustments.

To run the FORTRAN-based approach by Weltje (1997), provided by Jan-Berendt Stuut (personal communication, 2017), the grain-size classes of $\mathbf{X}_{\mathrm{nat}}$ needed to be aggregated; i.e. the resolution decreased by a factor of 2. For consistent comparisons with the other approaches, the resulting end-member loadings were interpolated back to the initial grain-size resolutions (see Supplement). The down-sampling and subsequent up-sampling of all $EM_{nat}$ values resulted in negligible artefacts with an average $R^2 > 0.999$. The modelled data set $\mathbf{X}'$ was computed by combining loadings and scores according to Eq. (1), excluding the error matrix $\mathbf{E}$.

Running the collection of the five RECA R scripts (Seidel and Hlawitschka, 2015) required manual installation of the additional package compositions (Van den Boogaart et al., 2014), e1071 (Meyer et al., 2017) and nnls (Mullen and van Stokkum, 2012), loading all scripts and manual screen input of the model parameters. RECA needs to be run completely to the end until consequences of parameter changes can be inspected. The decision on $q$ is based on a $q$–$R_n^2$ plot (e.g. using the inflection point). Here, RECA was run with four end-members, a maximum convexity error of −6, confirmation of the first start model, 100 iterations and a weighting exponent of 1, as suggested by Seidel and Hlawitschka (2015).

AnalySize by Paterson and Heslop (2015) provides a MATLAB GUI, in which $q$ is set manually. The numeric MATLAB output, end-member loadings and scores, was imported to R using the package R.matlab (Bengtsson, 2018).

Bayesian EMMA (BEMMA) in MATLAB (Yu et al., 2015) does not allow a predefined $q$ to be specified. With repeated model runs, the number of output end-members changed unsystematically between two and four. Depending on $q$, the shape and mode positions of the unmixed distributions fluctuated, which prevented the output from different model runs from being grouped. Hence, we did not include BEMMA in this comparison.

### 3.3 Evaluation and validation criteria

The performance of all approaches was evaluated in two steps. First, we compared the original data set $\mathbf{X}_{\mathrm{nat}}$ and the modelled data sets $\mathbf{X}'$ using (i) coefficients of determination (mean total $R_{\mathrm{t}}^2$, sample-wise $R_m^2$, class-wise $R_n^2$) and (ii) the absolute differences between $\mathbf{X}_{\mathrm{nat}}$ and $\mathbf{X}'$ (total $\mathrm{MAD}_{\mathrm{t}}$, sample-wise $\mathrm{MAD}_m$, class-wise $\mathrm{MAD}_n$). This comparison resembles the classical evaluation step when the true natural end-member composition is unknown.

Second, knowing which natural end-members have been mixed to create the example data set $\mathbf{X}_{\mathrm{nat}}$, we compare (i) $R^2$ and MAD for $\mathrm{EM}_{\mathrm{nat}}$ distributions and loadings ($R_{n1}^2$ to $R_{n4}^2$ and $\mathrm{MAD}_{n1}$ to $\mathrm{MAD}_{n4}$), (ii) $R^2$ and MAD for mixing ratios and scores ($R_{m1}^2$ to $R_{m4}^2$ and $\mathrm{MAD}_{m1}$ to $\mathrm{MAD}_{m4}$) and (iii) the absolute deviations of the mode positions of $\mathrm{EM}_{\mathrm{nat}}$ distributions and loadings. For comparisons of $\mathrm{EM}_{\mathrm{nat}}$ distributions with modelled loadings, all results were truncated to grain-size classes of $\mathrm{EM}_{\mathrm{nat}}$ higher than 0.1 % vol and rescaled to 100 %. There are two reasons for this: first, due to the generally narrow grain-size distributions, $\mathrm{EM}_{\mathrm{nat}}$ contained many grain-size classes of only zeros, which biases the resulting measures (Ciemer et al., 2018). This bias is severe: correlating, for example, two sequences of random values (e.g. 3.1, 5.2, 4.0 and 9.2, 8.3, 3.5) typically yields a very low correlation coefficient (e.g. $r = -0.065$). However, padding these sequences with zeros strongly increases the correlation coefficient (e.g. $r = 0.87$, including five zeros). Second, it is known that EMMA (Dietze et al., 2012), but also other approaches, causes spurious secondary modes directly below the mode positions of other end-members (Paterson and Heslop, 2015). The spurious modes are obviously not related to the underlying sedimentation regime and are not intended to be interpreted genetically (Dietze et al., 2014). As they would also bias the model comparison measures, we excluded them from model evaluation.

## 4 Results: the different model performances

### 4.1 Evaluation of model performance

#### 4.1.1 Deterministic EMMA

Figure 3 shows the default graphical output after the EMMA algorithm has modelled the data set with four end-members. Panels a and b depict $R^2$ values (squared Pearson correlation coefficients) organised by grain-size class and sample. Overall, the data set was reproduced with a mean $R_{\mathrm{t}}^2$ of 0.969 and $\mathrm{MAD}_{\mathrm{t}}$ of 0.2 % vol (Table 1). Panels c and d show modelled end-member loadings and scores. End-member loadings (EM1-4) had modes at 16, 40, 310 and 450 µm. Spurious secondary modes of less than 2.5 % vol are visible below primary modes of other end-members. Apart from the multimodal EM4, all end-members have a log-normal shape. Figure 3a shows that grain-size class-wise $R_n^2$ decreases between 946 and 1830 and 117 and 177 µm, both grain-size class intervals that contribute less than 0.9 % vol to $\mathbf{X}$ (Fig. 2). Mean sample- and class-wise absolute deviations are shown in Table 1.

The scores of EM1 to EM4 accounted for 20 %, 20 %, 31 % and 29 % of the variance of $\mathbf{X}'$, respectively. Sample-wise $R_m^2$ is 0.98 on average (Table 1). Four outliers had $R_m^2 < 0.95$ (samples 16, 57, 64, 75; Fig. 3b). However, neither removing these samples nor changing the rotation type from Varimax to Quartimax or the oblique rotation Promax improved the modelling of loadings and scores (not shown).

#### 4.1.2 Robust EMMA – extended and compact protocol

In the extended protocol, an $l_{\mathrm{min}}$ of zero was used according to Miesch (1976), and $l_{\mathrm{max}}$ was set to 0.37, i.e. 95 % of the modelled absolute $l_{\mathrm{max}}$ of 0.39 (see methods in Sect. 3). However, when using this value, negative loadings occurred. Therefore, the value was set to 80 %, yielding a more realistic and valid $l_{\mathrm{max}}$ of 0.31. With 20 values between $l_{\mathrm{min}}$ and $l_{\mathrm{max}}$, $q_{\mathrm{min}}$ varied between 2 and 3 (Fig. 4a), and $q_{\mathrm{max}}$ showed a trend of decreasing $\boldsymbol{R}_{\mathrm{t}}^2$ with increasing $l$ (Fig. 4c, d), until even NA values were produced for some parameter combinations (blue graph, Fig. 4b). Accordingly, after a local optimum at $q_{\mathrm{max}}$ between 4 and 9 (open circles, Fig. 4b), adding more end-members leads to numerical instabilities.

Figure 5a shows all 223 end-member loadings from 96 EMMA runs that agree with the parameter space of `P`. Note that the protocol can be run with user-defined grain-size units (function argument classunits) or simply the raw grain-size class numbers (default, and used in the following sections for simplicity). Several end-members have main mode position clusters between grain-size class numbers 63 and 66, 74 and 77, 94 and 97 and 99 and 102 (orange polygons). These class limits were used to model the robust end-member loadings, excluding the negative loadings that were modelled due to $l_{\mathrm{max}}$ values that are too high. A fifth cluster at classes 71–73 exists (not marked), although the distribution of this end-member is rather broad and overlaps with the distribution shapes of the two other clusters in this range. It was rejected as a robust end-member (see below).

The resulting robust EM3 and EM4 loadings show high class-wise standard deviations (SDs) around the mode positions (Fig. 6a). EM1 has a continuously narrow uncertainty envelope (i.e. mean ± 1 SD), and EM2 shows the largest and most variable envelope. Mean class-wise SDs range from 0.06 (EM4) to 0.38 % vol (EM2). The main mode positions of the robust loadings are identical with those of deterministic EMMA; only the EM2 mode is one class off. Using the mean robust loadings, $l_{\mathrm{opt}}$ was 0.0163 when maximising $R_{\mathrm{t}}^2$. Based on this, mean robust scores were modelled (Fig. 6b) with an average SD of 9.9 % vol, 7.8 % vol, 11.3 % vol and 9.5 % vol for EM1 to EM4.

With the compact protocol, the same parameter space ($l_{\mathrm{min}}$, $l_{\mathrm{max}}$, $q_{\mathrm{min}}$ and $q_{\mathrm{max}}$) was calculated as with the extended protocol. Robust end-member definition is supported

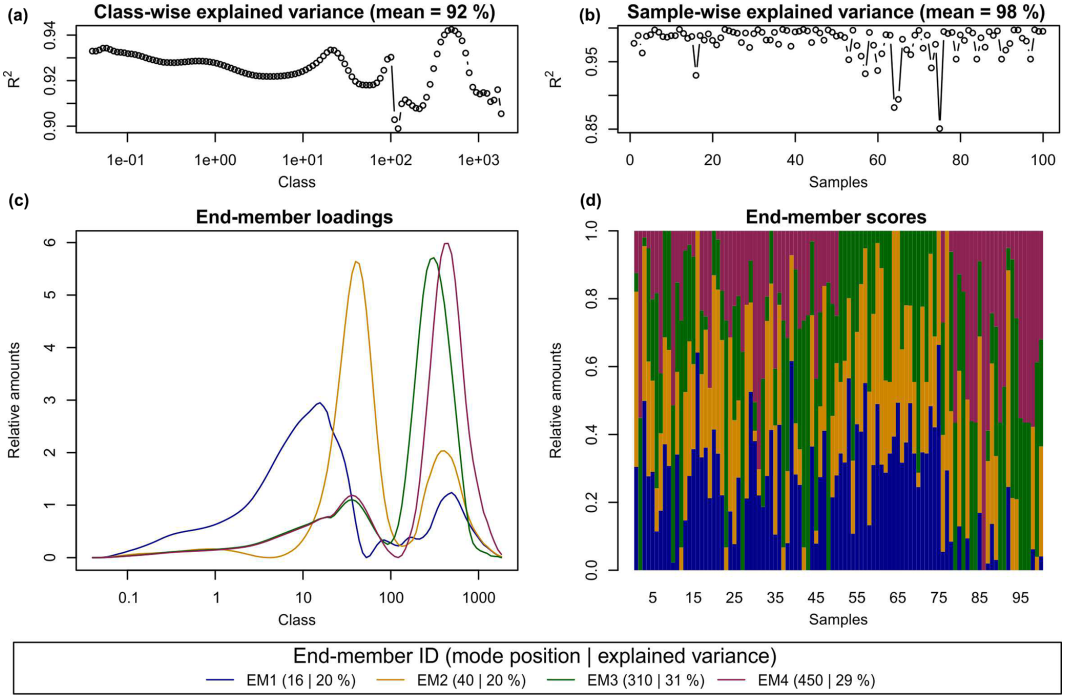


**Figure 3.** Default graphical output of the R function `EMMA()`. **(a, b)** Measures of model performance (i.e. class- and sample-wise $R^2$), **(c)** end-member loadings and **(d)** end-member scores. The legend presents the main mode positions (µm) and explained variance of each end-member (%).

**Table 1.** Comparison of model performance (total, sample-wise and grain-size class-wise coefficients of variation ($R_t^2$, $R_m^2$, $R_n^2$) and absolute deviation ($MAD_t$, $MAD_m$, $MAD_n$) of $X_{nat}$ versus $\mathbf{X}'$). $EMMA_{det}$, $EMMA_{rob\_ext}$ and $EMMA_{rob\_cmp}$ refer to EMMAgeo deterministic, extended and compact robust models (see text). $EMMA_{weltje}$, RECA and AnalySize refer to end-member approaches in FORTRAN (Weltje, 1997), R (Seidel and Hlawitschka, 2015) and MATLAB (Paterson and Heslop, 2015), respectively.

| Model | $R_t^2$ | $R_m^2$ | $R_n^2$ | $MAD_t$ | $MAD_m$ | $MAD_n$ |
|---|---|---|---|---|---|---|
| $EMMA_{det}$ | 0.969 | 0.98 | 0.925 | 0.15 | 0.155 | 0.145 |
| $EMMA_{rob\_ext}$ | 0.964 | 0.974 | 0.92 | 0.171 | 0.186 | 0.156 |
| $EMMA_{rob\_cmp}$ | 0.966 | 0.975 | 0.927 | 0.168 | 0.183 | 0.153 |
| $EMMA_{weltje}$ | 0.978 | 0.981 | 0.837 | 0.17 | 0.186 | 0.155 |
| RECA | 0.868 | 0.886 | 0.684 | 0.302 | 0.338 | 0.266 |
| AnalySize | 0.995 | 0.995 | 0.916 | 0.065 | 0.072 | 0.058 |

by the plot output of the function `robust.EM()`. Figure 5b shows five clusters with mode positions at 13–16, 27–33, 38–47, 250–320 and 390–500 µm (i.e. class numbers 63–66, 71–74, 75–77, 95–97 and 100–102). The colour scheme reveals that the cluster at 27–33 µm (grey bar, Fig. 5b) systematically occurs when EMMA was run with three end-members (red curves, Fig. 5a). Clusters at 13–20 and 38–47 µm emerge especially when four end-members were included in a model run (green curves). A similar case exists for the two coarse end-members, at 250–320 and 390–500 µm. Hence, models with a value for `q` that is too small systematically merge distinct grain-size distributions into spurious, broad curves. Values for `q` that are too high instead caused spikey loadings (blueish, pink curves, Fig. 5b).

Defining the limits by the automatic kernel density estimate approach suggested only three out of four natural end-members as robust ones, combining all loadings around class 100 (Fig. 5b, black line). Setting the kernel bandwidth arbitrarily to 0.5 would allow separation of the two overlapping modes around $EM_{nat}2$ while missing $EM_{nat}1$ and misinterpreting the cluster around the two coarsest end-members (not shown). Thus, for strongly overlapping mode clusters, automatic class limit detection was not appropriate. Hence, we set the mode limits similar to the extended protocol to class numbers 63–66, 75–77, 94–97 and 99–102, changing the definition of EM2 by just one grain-size class (extended protocol: 74–77) to better exclude the cluster at 27–

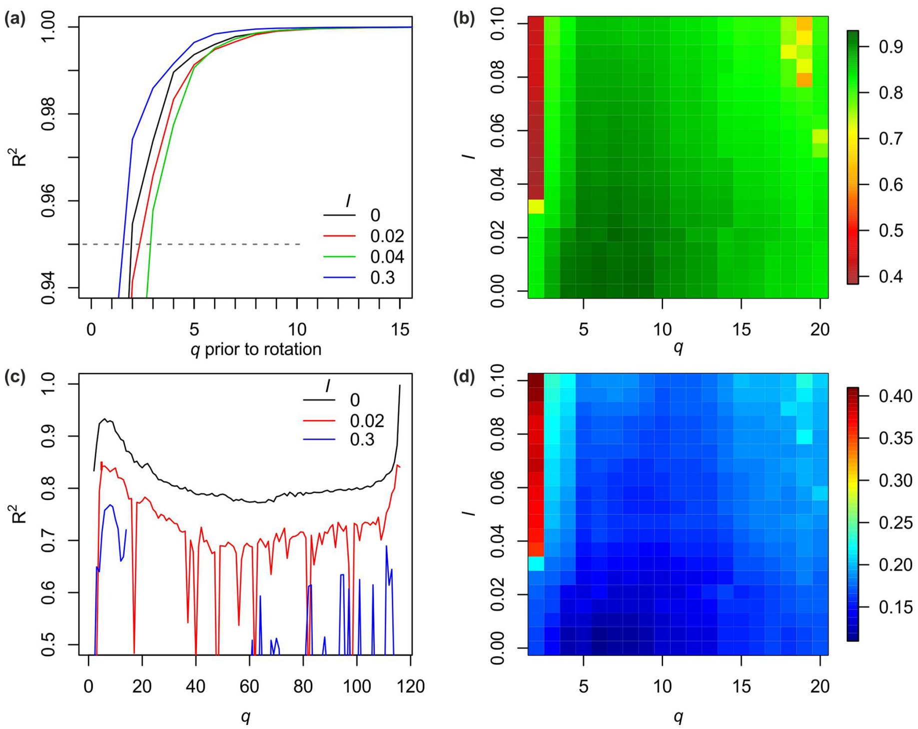


**Figure 4.** Parameter optimisation steps in the extended protocol of robust EMMA. **(a)** Model performance (coefficient of determination) with increasing number of factors prior to rotation (examples of weight transformation limits $l$; default output of the function `test.factors()`). **(b)** Mean total $R_t^2$ of all likely $q$ and $l$, default output of `test.parameter()`, 19 different $q$ (2 to 20). **(c)** Examples of total $R_t^2$ of EMMA-scenarios as a function of the number of end-members $q$ (along the $x$ axis) and three different $l$ values. **(d)** Mean sample-wise model error $E_n$ of all likely $q$ and $l$ values, optional output of `test.parameters()`, 20 different $l$ values (0 to 0.1).

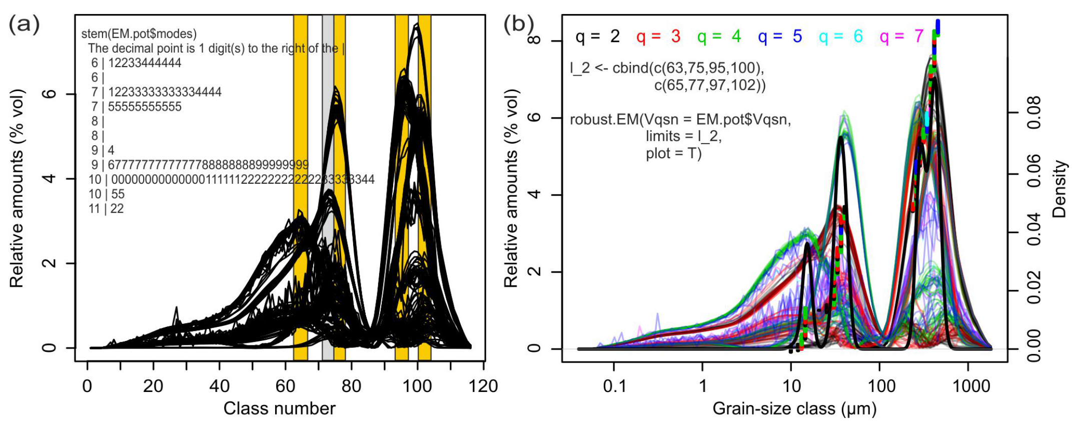


**Figure 5.** **(a)** Potential end-member loadings resulting from multiple EMMA runs with similarly likely parameter combinations. Distinct clusters of main mode positions define the grain-size class limits (orange bars) and allow calculation of the range of robust end-members by averaging the loadings with main modes that fall within the defined class limits. Note that there is no straightforward impression of the four input $EM_{nat}$ values and the few, spikey loadings resulting from values of $l$ that are too high. A stem-and-leaf plot of the mode clusters can be used to judge the appropriateness of the identified limits. **(b)** Default graphical output of the R function `model.EM()` assigns potential end-member loadings to the EMMA runs of **(a)**. Coloured lines show end-member loadings from EMMA models with different $q$ (dots at respective main mode positions) and varying $l$ values. The black line is a kernel density estimate of the main mode positions of all loadings, with a default bandwidth of 1.16, i.e. 1 % of the number of grain-size classes of the input data set and a default threshold to identify mode clusters (i.e. 0.016) that define three robust end-members (not shown). Manual setting of the limits avoids overlapping of the two coarse end-members and excludes the loadings of the grey bar.

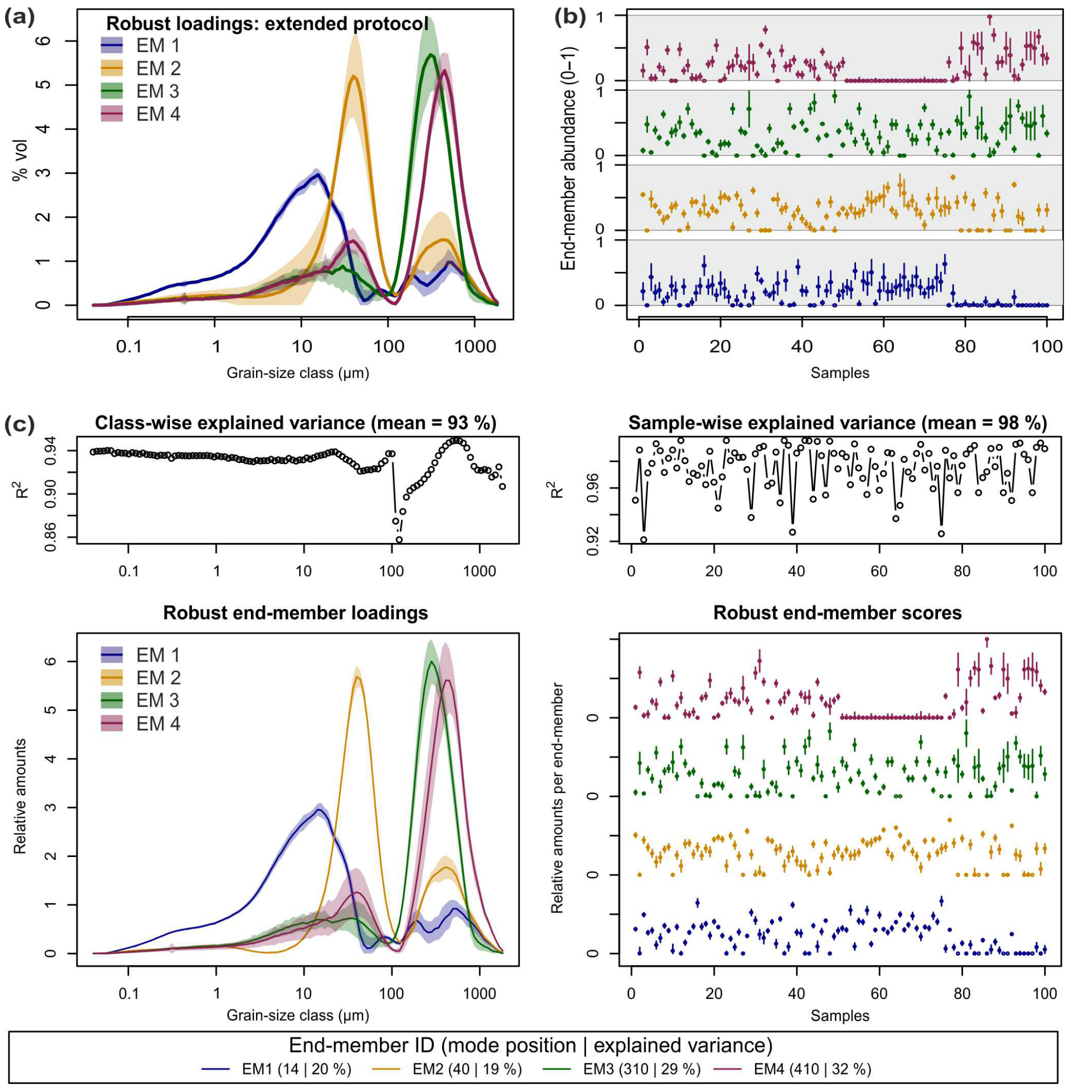


**Figure 6.** **(a)** Robust end-member loadings and **(b)** scores of the extended protocol. **(c)** Default graphical output of `robust.EM()` as part of the compact protocol, including class- and sample-wise explained variances **(a, b)** and a legend with main mode position and explained variance of each end-member. Mean robust loadings as line graphs, mean robust scores as panels of points. Polygons around loadings and bars around scores represent 1 standard deviation.

33 µm (red curves, Fig. 5b) and to assess varying robust end-member definitions.

The resulting end-members are shown in Fig. 6b. They are similar to the plotted output of the deterministic version (Fig. 3) but extended by uncertainty polygons, the different representation of scores and slightly different mode positions, grain-size class-wise $R_n^2$ (0.93) and sample-wise $R_m^2$ (0.98). Mean end-member contributions to the variance of the data set (20 %, 19 %, 29 % and 32 %) are almost identical to the deterministic version.

### 4.1.3 Comparison to other end-member unmixing algorithms

The full benchmark reveals that all approaches successfully model the data sets. The output of RECA shows difficulties in reaching the minimum convexity error of −6 with the initial 100 iterations, but by increasing the value to 200 iterations the issue was solved.

The average $R_t^2$ values were higher than 0.868 in all cases, up to 0.995 (Table 1). Sample-wise $R_m^2$ values were always higher than the grain-size class-wise $R_n^2$ values. Deterministic EMMA yielded slightly better results than the two robust EMMA protocols, which in turn were very similar. The lowest (highest) and highest (lowest) $R_t^2$ ($MAD_t$) values are related to RECA and AnalySize, respectively.

The main absolute deviations of $\mathbf{X}'$ from $\mathbf{X}_{nat}$ are associated with grain-size classes between 100 and 1000 µm, regardless of the model (Fig. 7). Except for AnalySize, all approaches show systematic underestimation of these grain-size classes of up to −2.5 % vol per class. Vice versa, finer grain-size classes between 1 and 100 µm are slightly overestimated by ca. 1 % vol per class. The effects of the applied sample mixing scheme of $X_{nat}$ are clearly visible in all model results (Fig. 7). Samples 51 to 75 (without coarse $EM_{nat}4$) show an overestimation of coarse and underestimation of fine classes. Samples 76 to 100 (without fine $EM_{nat}1$) show the opposite picture. AnalySize yielded the overall best unmixing, with average deviations of ca. ±1 % vol.

### 4.2 Validation against known data set composition

The above criteria quantify how well the approaches modelled the data set (Eq. 1), whereas their ability to reproduce the true "mixed ingredients" is addressed here. The $R^2$ values between loadings and input $EM_{nat}$ grain-size distributions (Table 2a) were on average between 0.4 and 0.99 and, thus, systematically larger than $R^2$ values linking scores and mixing ratios (0.77 to > 0.99; Table 2b). Both EMMAgeo and AnalySize performed less well in modelling one out of three $EM_{nat}$ distributions (EM1 for EMMAgeo and EM4 for AnalySize). The MAD was below 0.8 % vol for all models and end-members, except for EM4 scores (AnalySize).

A graphical comparison of the grain-size class-wise deviations of input end-member distributions and modelled loadings (Fig. 8) shows that all EMMAgeo-based models underestimate the main mode grain-size classes (i.e. curves are below the 1 : 1 line). This is the result of the emergence of spurious modes that shift class-wise percentages (up to −3.2 % vol) from the main modes to classes around the spurious modes (up to 1.3 % vol) that actually contain no grains (vertically aligned points at zero $x$ values). The other EMMA approaches also show mismatches between natural end-members and modelled loadings. Especially the alluvial fan $EM_{nat}4$ is affected, most severely in AnalySize. Percent volume (% vol) shifts due to spurious secondary modes also occur for the algorithm of Weltje (1997) and RECA. Overall, the latter approach yields the most accurate representations of the input distributions.

Concerning the reproduction of the initial mixing ratios (Fig. 9, Table 2b), variability among the models is higher, and all approaches show some unsystematic over- and underestimation, especially for EM in samples in which real mixing ratios were zero (vertical point clusters along the 0 % $x$ axis; Fig. 9). Except for RECA and AnalySize, the opposite effect is also visible: the models suggest zero contribution from end-members that are actually present in a sample with up to ca. 20 % (horizontal points along the 0 % $y$ axis; Fig. 9).

The modal grain-size classes of the four $EM_{nat}$ were modelled with different levels of success (Fig. 8, legends). The main modes of the coarse end-members were detected with only one or two grain-size classes' difference, whereas finer end-members differed by up to three classes. Modal classes of $EM_{nat}2$ and $EM_{nat}3$ were correctly depicted by EMMA of Weltje (1997), RECA and AnalySize. Most models yielded a value of $EM_{nat}1$ that is slightly too coarse, deviating by one or two grain-size classes. $EM_{nat}4$ caused the largest scatter among the models.

## 5 Discussion

### 5.1 Operational modes of EMMAgeo

The functionality of EMMA has improved significantly since the introduction of the MATLAB algorithm of Dietze et al. (2012). Not only an increase in computation speed, which was already 1 to 3 orders of magnitude faster than for other algorithms (Paterson and Heslop, 2015), but also many new and detailed ways to explore end-members (with deterministic EMMA) and to estimate and describe associated uncertainties of all end-member components (with robust EMMA) were implemented. The plot output of both EMMA modes is a comprehensive visualisation of all relevant information. It allows direct process interpretation in terms of plausibility of loadings and scores, model performance and identification of outliers.

Both EMMA modes, deterministic and robust, result in consistently similar outputs. Deviations of individual modes of robust loadings from known $EM_{nat}$ distributions by one or two grain-size classes are within the model uncertainty of robust EMMA. Therefore, a key step is the definition of robust end-members by setting the grain-size class limits that bracket robust, parameter-independent main modes, which overcomes the problem of relying on statistical measures like the inflection point of a $q$–$R^2$ graph (van Hateren et al., 2018). The workflow of robust EMMA offers ways to explore the ability of different kernel bandwidths and density thresholds, but in complicated cases, like the one provided in this study, expert knowledge-based limit definition might be the most practicable option. Hence, each data set should be considered individually, and deviations from common patterns may be significant in their own right (see discussion by van Hateren et al., 2018).

### 5.2 Performance test and validation

Unmixing quality is very high regardless of the model used, suggesting that all approaches in this benchmark are able to reproduce the input grain-size data set with unmixed end-member subpopulations. There is no model with an outstanding performance. Model deviations of < 1 % (especially for grain-size classes with > 0.1 % vol) are low in the light of uncertainties related to process interpretation (see below).

The validation against known input end-member composition showed that all EMMA approaches are equally applica-

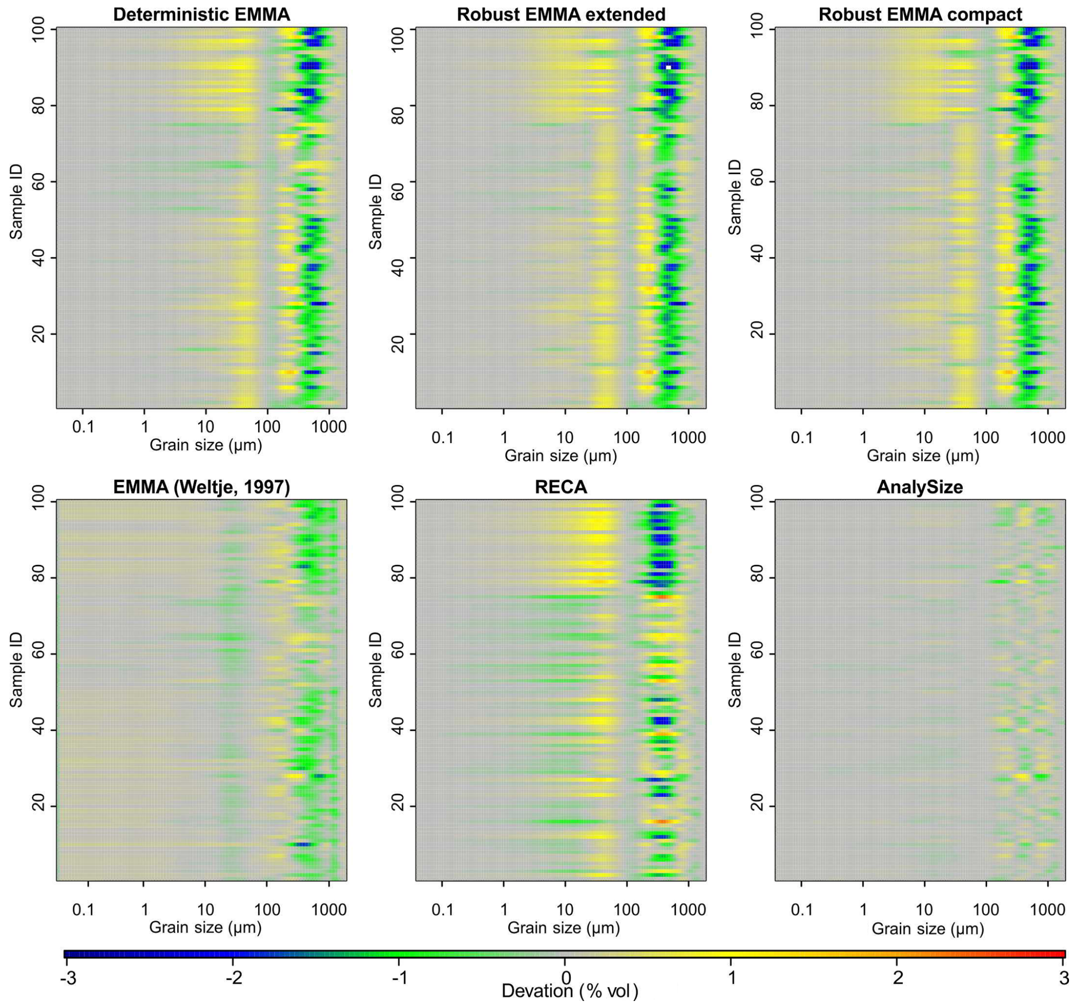


**Figure 7.** Model performance to unmix and reproduce the example data set $X_{nat}$. For each end-member model approach, the absolute difference MAD between modelled and original data set is shown.

ble. When comparing end-member loadings with the $EM_{nat}$ distributions, $R^2$ mainly represents shifts in mode positions, whereas MAD reacts to both shifts in the modes of individual grain-size distributions and differences in the volume percentages per class. Yet, each algorithm has certain strengths depending on the specific dimension of the investigation: if the main goal is to identify the most likely $q$ that builds an empirical data set, robust EMMA provides a set of tools that go beyond classical approaches (e.g. the inflection point of the $q$–$R^2$ plot) – allowing the inclusion of expert knowledge in the quantification and interpretation of grain-size subpopulations.

If the correct grain-size distribution shape of underlying process end-members is targeted, RECA of Seidel and Hlawitschka (2015) and EMMA by Weltje (1997) are most suitable from our benchmark study (Table 2a). RECA had problems with reaching the convexity error threshold, which could result from our data set with largely overlapping natural process end-members.

When quantifying the contribution of end-members to a given sample, robust EMMA, EMMA according to Weltje (1997) and AnalySize performed best (Table 2b). Robustly estimated scores using EMMAgeo reproduced original mixing proportions very well and in a range comparable to the other available end-member algorithms. However, as all approaches and earlier EMMA evaluations showed, very low and high scores ($< 20\,\%$ and $> 80\,\%$) of one end-member might be under- or overestimated within the compositional mixture (McGee et al., 2013). Hence, extremely high (e.g. 100 %) contributions of one end-member to a sample should not be interpreted as complete absence of the other end-members but rather as the dominance of this one end-member (and vice versa).

If uncertainty estimates for both loadings and scores are considered important, then only robust EMMA is suitable. The inclusion of uncertainties for loadings and scores is a key precondition for propagating model results to further data analysis, for example to interpret grain-size end-members

**Table 2.** **(a)** Grain size class-wise coefficients of variation ($R_n^2$) and absolute deviation ($\mathrm{MAD}_n$) of modelled end-member loadings compared to natural end-member distributions. **(b)** Sample-wise coefficients of variation ($R_m^2$) and absolute deviation ($\mathrm{MAD}_m$) of modelled end-member scores compared to natural end-member mixing ratios.

**(a)**

| Model | $R_n^2 1$ | $R_n^2 2$ | $R_n^2 3$ | $R_n^2 4$ | $\mathrm{MAD}_n 1$ | $\mathrm{MAD}_n 2$ | $\mathrm{MAD}_n 3$ | $\mathrm{MAD}_n 4$ |
|---|---|---|---|---|---|---|---|---|
| $\mathrm{EMMA}_{\mathrm{det}}$ | 0.765 | 0.811 | 0.922 | 0.872 | 0.094 | 0.082 | 0.076 | 0.084 |
| $\mathrm{EMMA}_{\mathrm{rob\_ext}}$ | 0.752 | 0.807 | 0.941 | 0.884 | 0.096 | 0.081 | 0.068 | 0.097 |
| $\mathrm{EMMA}_{\mathrm{rob\_cmp}}$ | 0.744 | 0.821 | 0.901 | 0.867 | 0.096 | 0.078 | 0.082 | 0.095 |
| $\mathrm{EMMA}_{\mathrm{weltje}}$ | 0.988 | 0.975 | 0.723 | 0.702 | 0.04 | 0.051 | 0.096 | 0.095 |
| RECA | 0.745 | 0.403 | 0.595 | 0.837 | 0.116 | 0.165 | 0.125 | 0.072 |
| AnalySize | 0.98 | 0.974 | 0.761 | 0.701 | 0.045 | 0.049 | 0.088 | 0.091 |

**(b)**

| Model | $R_m^2 1$ | $R_m^2 2$ | $R_m^2 3$ | $R_m^2 4$ | $\mathrm{MAD}_m 1$ | $\mathrm{MAD}_m 2$ | $\mathrm{MAD}_m 3$ | $\mathrm{MAD}_m 4$ |
|---|---|---|---|---|---|---|---|---|
| $\mathrm{EMMA}_{\mathrm{det}}$ | 0.773 | 0.93 | 0.989 | 0.999 | 0.5 | 0.827 | 0.303 | 0.097 |
| $\mathrm{EMMA}_{\mathrm{rob\_ext}}$ | 0.778 | 0.925 | 0.97 | 0.978 | 0.477 | 0.83 | 0.499 | 0.531 |
| $\mathrm{EMMA}_{\mathrm{rob\_cmp}}$ | 0.772 | 0.925 | 0.979 | 0.98 | 0.485 | 0.831 | 0.416 | 0.513 |
| $\mathrm{EMMA}_{\mathrm{weltje}}$ | 0.975 | 0.993 | 0.988 | 0.92 | 0.166 | 0.133 | 0.478 | 0.906 |
| RECA | 0.917 | 0.966 | 0.978 | 0.947 | 0.272 | 0.284 | 0.427 | 0.686 |
| AnalySize | 0.985 | 0.999 | 0.97 | 0.787 | 0.116 | 0.037 | 0.625 | 1.633 |

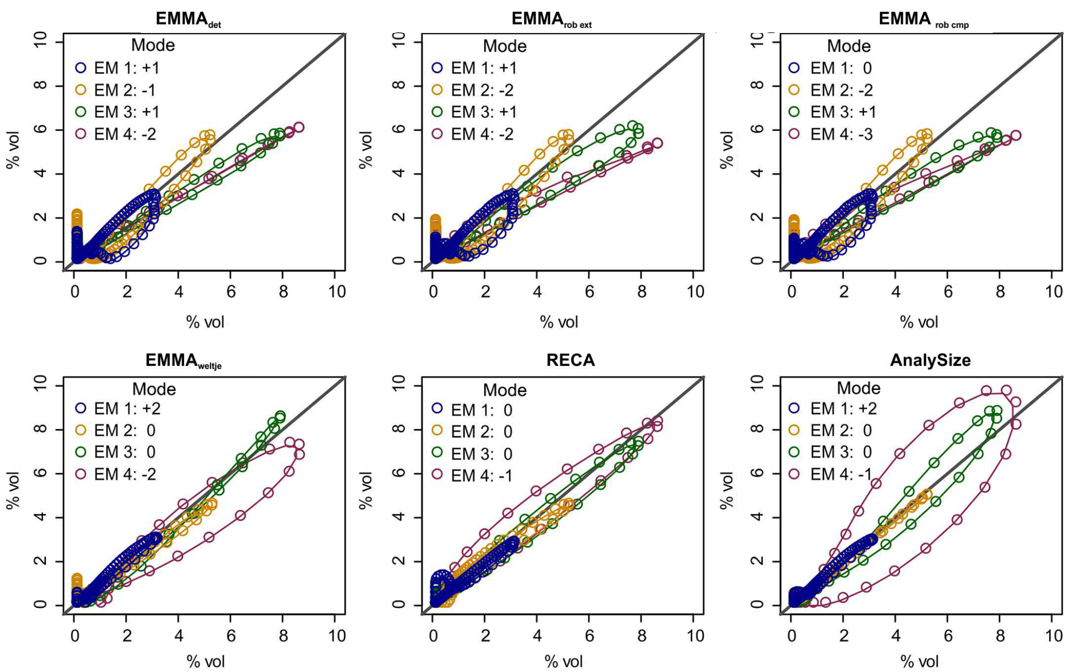


**Figure 8.** Natural versus modelled end-member grain-size distributions for all evaluated models. Deviation of main mode (in number of classes). $x$ axes show $\mathbf{X}_{\mathrm{nat}}$ and $y$ axes modelled $\mathbf{X}'$ values.

as proxies for sediment sources (loadings) in environmental archives as they evolve with time (scores). As van Hateren et al. (2018) emphasise, changes in the model results will inevitably result in diverging interpretations of the assumed sedimentary processes. Also, the interpretations of the scores in their spatial (samples across a landscape) or temporal (samples downcore) context will be affected. Thus, it is extremely important to provide some estimate of the inherent uncertainty in both the proxy definition and in the sample domain. So far only robust EMMA can deliver such information. Yet, necessary parameter estimates and diverging start conditions evidently exist in the other models too.

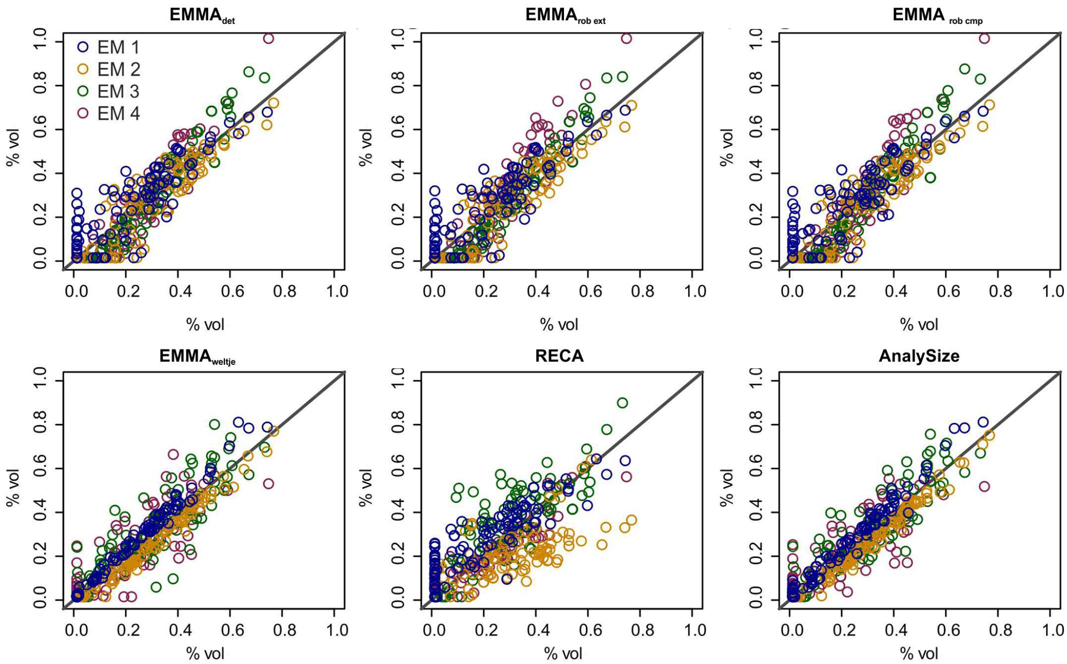


**Figure 9.** Natural versus modelled end-member mixing ratios for all evaluated models. $x$ axes show $\mathbf{X}_{\mathrm{nat}}$ and $y$ axes modelled $\mathbf{X}'$ values.

If the distribution shape of an inherent natural grain-size end-member is known, EMMAgeo allows quantification of its contribution to the data set by including it as unscaled loadings in both deterministic and robust EMMA or by assigning the known main mode class limits when selecting robust end-members (step 4; Fig. 1b). Finally, if free and open-source software is a criterion – which is increasingly the case for journals and funding agencies (David et al., 2016; Munafò et al., 2017) – RECA and EMMAgeo remain the only options.

## 5.3 Comparison with other benchmark studies

In previous benchmark studies, EMMAgeo performed less well, which Paterson and Heslop (2015) attributed to the implementation of the non-negativity and sum-to-one constraints. van Hateren et al. (2018) pointed to the secondary modes as cause of the deviations of scores from the mixing ratios. We cannot confirm the poor performance of EMMAgeo in our study, as it is not fully clear how van Hateren et al. (2018) determined the EMMAgeo loading curves, which they evaluate graphically. They note that in EMMAgeo the $q$ is not set by the inflection point of the $q$–$R^2$ relationship, but robust EMMA would lead to one $q$, and not a sequence of 2 to 5, as discussed in their study. Additionally, it is unclear which realisation from within the robust EMMA uncertainty range was evaluated by van Hateren et al. (2018). Accordingly, detailed introduction of the EMMA protocols is essential to avoid future misinterpretations.

Yet, the occurrence of artificial secondary modes below the main modes of the end-members is more pronounced in EMMAgeo compared to other unmixing algorithms. The inherent compositional data constraints lead to an intimate linkage of the distribution shape of one end-member with the distribution shapes of other loadings. However, when excluding hardly interpretable secondary modes from global measures of model quality, the performance of EMMA is well within the range of other available algorithms. As repeatedly noted in articles applying EMMAgeo (Dietze et al., 2012, 2014) but also highlighted for other approaches in the benchmark study of Paterson and Heslop (2015), secondary modes are model artefacts and should not be interpreted genetically.

However, to test the impact of artificial secondary modes on model performance, we modelled the $\mathrm{EM_{nat}}$ data set with user-defined end-members. We manually set the unscaled loadings outside the known primary end-member modes to zero and used these updated loadings for the modelling process (see Supplement for R code). Although the resulting end-member loadings are now free of secondary modes, the mixing ratios are only marginally better modelled ($-1$ % to 4 % deviation). Thus, such a truncation may help in tuning the shape of the modelled end-members but cannot improve deviations of the scores from mixing ratios. Still, the uncertainty ranges of the robust scores included the expected $\mathrm{EM_{nat}}$ mixing ratios (66.5 % of the samples are within the modelled 1 standard deviation range).

## 5.4 Constraints on end-member interpretation

Going beyond classical measures of grain-size properties, EMMA is well suited to quantify sedimentary processes from mixed sediment sequences in space and time. However, interpretation of grain-size end-members requires expert knowledge about the investigated sedimentary system. Hence, when applying EMMA to any set of grain-size data, the interpretability of the resulting end-members needs to be checked. For this, both end-member components should be considered: the shape and position of the main modes of the loadings and the spatio-temporal or stratigraphic context of the scores. For example, the effectiveness of a process in sorting sediment could be interpreted in the classical sense from the shape of the end-member loadings (excluding artificial modes), with broader peaks being more poorly sorted than narrow peaks (Friedman, 1961).

As any other statistical method, EMMA is a tool, and interpretation of grain-size end-members relies on contextual knowledge. There may be processes that contribute to the overall sediment composition and that are not size-selective or sort sediment of various grain-size classes in a typical way. For example, event-triggered turbidity currents in lakes caused problems in attributing a single sedimentary process to end-members in the study by Dietze et al. (2014) because the typical fining-upwards trend was also reflected by several end-members that contributed to samples of "normal" deposition.

Closely related is the constraint of stationarity in processes, which implies that through space and time each transport process must create an identical grain-size distribution. For example, fining of aeolian material from one distinct source area with downwind transport distance (Pye, 1995) might rather be explored by a gradual approach, e.g. by running EMMA in a moving window over a data set to detect shifts in stationarity.

Post-depositional processes that change grain-sizes, e.g. due to permafrost conditions or soil formation, could strongly disturb the original grain-size characteristics. In the worst case, a lacustrine sediment archive composed of different aeolian and fluvial sediment end-members (Dietze et al., 2013) can be affected by ongoing cryogenic and active-layer dynamics in a way that all modelled end-members were overlapping and peaking in similar grain-size classes – "erasing" primary signals related to sediment deposition. If post-depositional activity overprints the original depositional processes, EMMA can detect them as single end-members and would allow quantification of the intensity of the overprint, e.g. soil formation (Dietze et al., 2016) or weathering (Sun et al., 2002; Xiao et al., 2012).

Sediments affected by the processes mentioned above can affect end-member modelling in manifold ways. For example, EMMA could result in rather low explained variances, and the modes of affected end-member loadings would become broader and/or may even be better represented by additional but nevertheless spurious end-members. In the worst case, modes of end-member loadings overlap strongly or cannot be unmixed at all.

## 6 Conclusions

EMMAgeo allows the characterisation of multi-modal grain-size distributions by end-member subpopulations. New protocols allow a quick analysis, including modelling of associated uncertainties for both end-member loadings and scores. Using four known natural end-members, which represent typical sediment types found in terrestrial systems, the performance of EMMAgeo in unmixing the correct end-member distribution shapes and mixing ratios is within the same order as the performance of other available end-member modelling algorithms, which all perform very well. Hence, all of these algorithms are powerful tools for characterisation of different sediment source, transport, depositional and even post-depositional processes. In comparison to other algorithms, EMMAgeo is the only available open-source grain-size unmixing approach that includes uncertainty estimates. An inherent strength of the fully free R package is a large flexibility for users to modify the parameter settings and workflows with the new protocols, reproduce results and continue data evaluation.

Once genetically interpretable grain-size end-members are derived, their loadings can be described by classical descriptive measures (Folk and Ward, 1957; Blott and Pye, 2001). This allows a statistically robust determination and comparison of mean, sorting and shape measures across sites and data sets by describing and quantifying processes that sort sediment better or poorer than other processes.

Many future applications in the fields of Quaternary Science, sedimentology, geology, geomorphology and hydrology could gain new insights from applying EMMAgeo to compositional data sets that represent mixtures. In contrast to classical linear decomposition methods such as principle component analysis, EMMA has the potential to quantify (and not just qualify) different sources or processes of modern and past sedimentary environments that contribute to a sample set, including associated model uncertainties.

**Code and data availability.** The Supplement contains the example data set, end-member measurement data, mixing ratios and output of the other approaches included in the comparison. The R package EMMAgeo in its latest release version 0.9.6 (Dietze and Dietze, 2019; https://doi.org/10.5880/GFZ.4.6.2019.002) is available on the Comprehensive R Archive Network (R Core Team, 2017) and on GitHub. Please report any bugs and improvements to the maintainers of the package.

**Supplement.** The supplement related to this article is available online at: https://doi.org/10.5194/egqsj-68-29-2019-supplement.

**Author contributions.** ED and MD improved the original EMMA algorithm, workflows and auxiliary functionalities. ED compiled the operational modes of EMMA and MD established the EMMAgeo package. Both authors wrote the paper.

**Competing interests.** The authors declare that they have no conflict of interest.

**Special issue statement.** This article is part of the special issue "Connecting disciplines – Quaternary archives and geomorphological processes in a changing environment". It is a result of the First Central European Conference on Geomorphology and Quaternary Sciences, Gießen, Germany, 23–27 September 2018.

**Acknowledgements.** Thomas Hösel and Claudia Ziener prepared the example data set. Philip Schulte performed grain-size analysis using the Laser particle sizer at RWTH Aachen. Jan-Berend Stuut provided the data from the FORTRAN code of Weltje (1997), and Mitch D'Arcy provided language editing. Kai Hartmann and Andreas Borchers supported the initial development of EMMA and Kirsten Elger the DOI and landing page coordination. Many users of former versions of the MATLAB and R scripts greatly helped to improve EMMAgeo.

**Financial support.** The article processing charges for this open-access publication were covered by a Research Centre of the Helmholtz Association.

## References

Aitchison, J.: The statistical analysis of compositional data, Chapham and Hall, London, New York, 1986.

Bagnold, R. A. and Barndorff-Nielsen, O.: The pattern of natural size distributions, Sedimentology, 27, 199–207, 1980.

Bartholdy, J., Christiansen, C., and Pedersen, J. B. T.: Comparing spatial grain-size trends inferred from textural parameters using percentile statistical parameters and those based on the log-hyperbolic method, Sedimentary Geology From Particle Size to Sediment Dynamics, 202, 436–452, 2007.

Bengtsson, H.: R.matlab: Read and Write MAT Files and Call MATLAB from Within R, available at: https://CRAN.R-project.org/package=R.matlab (last access: 10 May 2019), 2018.

Bernaards, C. A. and Jennrich, R. I.: Gradient Projection Algorithms and Software for Arbitrary Rotation Criteria in Factor Analysis, Educ. Psychol. Meas., 65, 676–696, 2005.

Blott, S. J. and Pye, K.: GRADISTAT: a grain size distribution and statistics package for the analysis of unconsolidated sediments, Earth Surf. Process. Landforms, 26, 1237–1248, https://doi.org/10.1002/esp.261, 2001.

Borchers, A., Dietze, E., Kuhn, G., Esper, O., Voigt, I., Hartmann, K., and Diekmann, B.: Holocene ice dynamics and bottom-water formation associated with Cape Darnley polynya activity recorded in Burton Basin, East Antarctica, Mar. Geophys. Res., 2015, 1–22, https://doi.org/10.1007/s11001-015-9254-z, 2015.

Buccianti, A., Mateu-Figueras, G., and Pawlowsky-Glahn, V.: Compositional Data Analysis in the Geosciences: From Theory to Practice, Geological Society of London, London, 212 pp., 2006.

Ciemer, C., Boers, N., Barbosa, H. M. J., Kurths, J., and Rammig, A.: Temporal evolution of the spatial covariability of rainfall in South America, Clim. Dynam., 51, 371–382, 2018.

David, C. H., Gil, Y., Duffy, C. J., Peckham, S. D., and Venayagamoorthy, S. K.: An introduction to the special issue on Geoscience Papers of the Future, Earth Space Sci., 3, 441–444, 2016.

Dietze, E., Hartmann, K., Diekmann, B., Ijmker, J., Lehmkuhl, F., Opitz, S., Stauch, G., Wünnemann, B., and Borchers, A.: An end-member algorithm for deciphering modern detrital processes from lake sediments of Lake Donggi Cona, NE Tibetan Plateau, China, Sediment. Geol., 243–244, 169–180, 2012.

Dietze, E., Wünnemann, B., Hartmann, K., Diekmann, B., Jin, H., Stauch, G., Yang, S., and Lehmkuhl, F.: Early to mid-Holocene lake high-stand sediments at Lake Donggi Cona, northeastern Tibetan Plateau, China, Quaternary Res., 79, 325–336, 2013.

Dietze, E., Maussion, F., Ahlborn, M., Diekmann, B., Hartmann, K., Henkel, K., Kasper, T., Lockot, G., Opitz, S., and Haberzettl, T.: Sediment transport processes across the Tibetan Plateau inferred from robust grain-size end members in lake sediments, Clim. Past, 10, 91–106, https://doi.org/10.5194/cp-10-91-2014, 2014.

Dietze, M. and Dietze, E.: EMMAgeo: End-Member Modelling of Grain-Size Data, available at: https://cran.r-project.org/web/packages/EMMAgeo/ (last access: 10 May 2019), 2016.

Dietze, M. and Dietze, E.: EMMAgeo – R package. V. 0.9.6, GFZ Data Services, https://doi.org/10.5880/GFZ.4.6.2019.002, 2019.

Dietze, M., Dietze, E., Lomax, J., Fuchs, M., Kleber, A., and Wells, S. G.: Environmental history recorded in aeolian deposits under stone pavements, Mojave Desert, USA, Quaternary Res., 85, 4–16, 2016.

Flemming, B. W.: The influence of grain-size analysis methods and sediment mixing on curve shapes and textural parameters: Implications for sediment trend analysis, Sedimentary Geology From Particle Size to Sediment Dynamics, 202, 425–435, 2007.

Folk, R. L. and Ward, W. C.: Brazos River bar [Texas]; a study in the significance of grain size parameters, J. Sediment. Res., 27, 3–26, 1957.

Friedman, G. M.: Distinction between dune, beach, and river sands from their textural characteristics, J. Sediment. Res., 31, 514–529, 1961.

Gan, S. Q. and Scholz, C. A.: Skew Normal Distribution Deconvolution of Grain-size Distribution and Its Application To 530 Samples from Lake Bosumtwi, Ghana, J. Sediment. Res., 87, 1214–1225, 2017.

Hartmann, D.: From reality to model: Operationalism and the value chain of particle-size analysis of natural sediments, Sedimentary Geology From Particle Size to Sediment Dynamics, 202, 383–401, 2007.

Heslop, D., von Dobeneck, T., and Höcker, M.: Using non-negative matrix factorization in the "unmixing" of diffuse reflectance spectra, Mar. Geol., 241, 63–78, 2007.

Hunter, D. R., Richards, D. S. P., and Rosenberger, J. L.: Non-parametric Statistics and Mixture Models, World Scientific, The Pennsylvania State University, 2011.

Klovan, J. E. and Imbrie, J.: An algorithm and Fortran-iv program for large-scale Q-mode factor analysis and calculation of factor scores, J. Int. Ass. Math. Geol., 3, 61–77, 1971.

Lindsay, B. G. and Lesperance, M. L.: A review of semiparametric mixture models, J. Stat. Plan. Infer., 47, 29–39, 1995.

Macumber, A. L., Patterson, R. T., Galloway, J. M., Falck, H., and Swindles, G. T.: Reconstruction of Holocene hydroclimatic variability in subarctic treeline lakes using lake sediment grain-size end-members, Holocene, 28, 845–857, 2018.

McGee, D., deMenocal, P. B., Winckler, G., Stuut, J. B. W., and Bradtmiller, L. I.: The magnitude, timing and abruptness of changes in North African dust deposition over the last 20 000 yr, Earth Planet. Sc. Lett., 371–372, 163–176, 2013.

Meszner, S., Kreutzer, S., Fuchs, M., and Faust, D.: Late Pleistocene landscape dynamics in Saxony, Germany: Paleoenvironmental reconstruction using loess-paleosol sequences, Quaternary Int., 296, 94–107, 2013.

Meyer, D., Dimitriadou, E., Hornik, K., Weingessel, A., and Leisch, F.: e1071: Misc Functions of the Department of Statistics, Probability Theory Group (Formerly: E1071), available at: https://CRAN.R-project.org/package=e1071 (last access: 10 May 2019), TU Wien, 2017.

Miesch, A. T.: Q-mode factor analysis of compositional data, Comput. Geosci., 1, 147–159, 1976.

Mullen, K. M. and van Stokkum, I. H. M.: nnls: The Lawson-Hanson algorithm for non-negative least squares (NNLS), available at: https://CRAN.R-project.org/package=nnls (last access: 10 May 2019), 2012.

Munafò, M. R., Nosek, B. A., Bishop, D. V. M., Button, K. S., Chambers, C. D., Percie du Sert, N., Simonsohn, U., Wagenmakers, E.-J., Ware, J. J., and Ioannidis, J. P. A.: A manifesto for reproducible science, Nature Human Behaviour, 1, 0021, Tulsa, Oklahoma, USA, 2017.

Paterson, G. A. and Heslop, D.: New methods for unmixing sediment grain size data, Geochem. Geophys. Geosyst., 16, 4494–4506, 2015.

Prins, M. A. and Weltje, G. J.: End-member modeling of siliciclastic grain-size distributions: The late Quaternary record of aeolian and fluvial sediment supply to the Arabian Sea and its paleoclimatic significance, in: SEPM Special Publication, edited by: Harbaugh, J., 62, Society for Sedimentary Geology, 1999.

Pye, K.: The nature, origin and accumulation of loess, Quaternary Sci. Rev., 14, 653–667, 1995.

R Core Team: R: A language and environment for statistical computing, R Foundation for Statistical Computing, Vienna, 2017.

Schillereff, D. N., Chiverrell, R. C., Macdonald, N., and Hooke, J. M.: Hydrological thresholds and basin control over paleoflood records in lakes, Geology, 44, 43–46, 2016.

Schulte, P., Dietze, M., and Dietze, E.: How well does end-member modelling analysis of grain size data work?, EGU General Assembly Conference Abstracts, 1903, 2014.

Seidel, M. and Hlawitschka, M.: An R-Based Function for Modeling of End Member Compositions, Math. Geosci., 47, 995–1007, 2015.

Strauss, J., Schirrmeister, L., Wetterich, S., Borchers, A., and Davydov, S. P.: Grain-size properties and organic-carbon stock of Yedoma Ice Complex permafrost from the Kolyma lowland, northeastern Siberia, Global Biogeochem. Cy., 26, 1–12, 2012.

Stuut, J.-B. W., Prins, M. A., Schneider, R. R., Weltje, G. J., Jansen, J. H. F., and Postma, G.: A 300-kyr record of aridity and wind strength in southwestern Africa: inferences from grain-size distributions of sediments on Walvis Ridge, SE Atlantic, Mar. Geol., 180, 221–233, 2002.

Sun, D., Bloemendal, J., Rea, D. K., Vandenberghe, J., Jiang, F., An, Z., and Su, R.: Grain-size distribution function of polymodal sediments in hydraulic and aeolian environments, and numerical partitioning of the sedimentary components, Sediment. Geol., 152, 263–277, 2002.

Tjallingii, R., Claussen, M., Stuut, J.-B. W., Fohlmeister, J., Jahn, A., Bickert, T., Lamy, F., and Rohl, U.: Coherent high- and low-latitude control of the northwest African hydrological balance, Nat. Geosci., 1, 670–675, 2008.

Toonen, W. H. J., Winkels, T. G., Cohen, K. M., Prins, M. A., and Middelkoop, H.: Lower Rhine historical flood magnitudes of the last 450 years reproduced from grain-size measurements of flood deposits using End Member Modelling, CATENA, 130, 69–81, 2015.

Vandenberghe, J.: Grain size of fine-grained windblown sediment: A powerful proxy for process identification, Earth-Sci. Rev., 121, 18–30, 2013.

Vandenberghe, J., Lu, H., Sun, D., van Huissteden, J., and Konert, M.: The late Miocene and Pliocene climate in East Asia as recorded by grain size and magnetic susceptibility of the Red Clay deposits (Chinese Loess Plateau), Palaeogeogr. Palaeocl., 204, 239–255, 2004.

Vandenberghe, J., Sun, Y., Wang, X., Abels, H. A., and Liu, X.: Grain-size characterization of reworked fine-grained aeolian deposits, Earth-Sci. Rev., 177, 43–52, 2018.

Van den Boogaart, K. G., Tolosana, R., and Bren, M.: compositions: Compositional Data Analysis, available at: https://CRAN.R-project.org/package=compositions (last access: 10 May 2019), 2014.

van Hateren, J. A., Prins, M. A., and van Balen, R. T.: On the genetically meaningful decomposition of grain-size distributions: A comparison of different end-member modelling algorithms, Sediment. Geol., 375, 49–71, 2018.

Varga, G., Újvári, G., and Kovács, J.: Interpretation of sedimentary (sub)populations extracted from grain size distributions of Central European loess-paleosol series, Quaternary Int., 502, 60–70, https://doi.org/10.1016/j.quaint.2017.09.021, 2019.

Visher, G. S.: Grain size distributions and depositional processes, J. Sediment. Res., 39, 1074–1106, 1969.

Vriend, M. and Prins, M. A.: Calibration of modelled mixing patterns in loess grain-size distributions: an example from the northeastern margin of the Tibetan Plateau, China, Sedimentology, 52, 1361–1374, 2005.

Weltje, G.: End-member modeling of compositional data: Numerical-statistical algorithms for solving the explicit mixing problem, Math. Geol., 29, 503–549, 1997.

Weltje, G. J. and Prins, M. A.: Muddled or mixed? Inferring palaeoclimate from size distributions of deep-sea clastics, Sediment. Geol., 162, 39–62, 2003.

Weltje, G. J. and Prins, M. A.: Genetically meaningful decomposition of grain-size distributions, Sediment. Geol., 202, 409–424, 2007.

Wündsch, M., Haberzettl, T., Kirsten, K. L., Kasper, T., Zabel, M., Dietze, E., Baade, J., Daut, G., Meschner, S., Meadows, M. E., and Mäusbacher, R.: Sea level and climate change at the southern Cape coast, South Africa, during the past 4.2 kyr, Palaeogeogr. Palaeocl., 446, 295–307, 2016.

Xiao, J., Chang, Z., Fan, J., Zhou, L., Zhai, D., Wen, R., and Qin, X.: The link between grain-size components and depositional processes in a modern clastic lake, Sedimentology, 59, 1050–1062, 2012.

Yu, S.-Y., Colman, S. M., and Li, L.: BEMMA: A Hierarchical Bayesian End-Member Modeling Analysis of Sediment Grain-Size Distributions, Math. Geosci., 2015, 1–19, https://doi.org/10.1007/s11004-015-9611-0, 2015.

E&G Quaternary Sci. J., 68, 47–51, 2019
https://doi.org/10.5194/egqsj-68-47-2019


Open Access E&G Quaternary Science Journal

Express report

# Archaeology and agriculture: conflicts and solutions

**Richard Vogt**[1] **and Inga Kretschmer**[2]

[1]Landesamt für Denkmalpflege im Regierungspräsidium Stuttgart, Fischersteig 9, 78343 Gaienhofen-Hemmenhofen, Germany
[2]Landesamt für Denkmalpflege im Regierungspräsidium Stuttgart, Moltkestraße 74, 76133 Karlsruhe, Germany

**Correspondence:** Richard Vogt (richard.vogt@rps.bwl.de) and Inga Kretschmer (inga.kretschmer@rps.bwl.de)

**Relevant dates:** Received: 16 January 2019 – Revised: 5 March 2019 – Accepted: 21 March 2019 – Published: 13 June 2019

**How to cite:** Vogt, R., and Kretschmer, I.: Archaeology and agriculture: conflicts and solutions, E&G Quaternary Sci. J., 68, 47–51, https://doi.org/10.5194/egqsj-68-47-2019, 2019.

## 1 Introduction

The archaeological soil archive that has been preserving information on human activities over thousands of years is extremely endangered by increasing land use and intensive agriculture in highly frequented regions.

Many archaeological cultural monuments are located in regions which have been settled since prehistory because of various positive location factors, such as fertile soils and sufficient water supply. In these areas modern agriculture produces high yields also today, and the arable land is therefore affected by intensive farming practices. This, in turn, puts the preservation of cultural heritage and soil archives at risk and could result in their irreversible destruction.

This paper reports common problems and approaches for problem-solving strategies that derive from daily practice and experience in cultural heritage management, as a contribution to further discussion in an international context.

The industrialization and intensification of agriculture since the 19th century has resulted in increasing losses of archaeological soil archives. Moreover, intensive soil cultivation leads to erosion in many regions, which has had a strong impact on soil conservation and on remaining archaeological structures. Land consolidation, removing boundaries of fields and terraces, has facilitated the use of large agricultural machines and enhanced erosion processes.

As a result, above-ground archaeological monuments such as tumuli fields, ramparts and ditches, which are better preserved in grassland or in the forest, will be completely flattened and disappear in agricultural landscapes (Fig. 1). Modern ploughs dig deeply into the ground and destroy any remaining structures. Large farming machines remove or shred stones and bricks including archaeological stone structures and walls. Ploughing also leads to the removal of soil and artefacts outside of the context of archaeological features and sites. Machinery use, fertilization and usage of chemical pesticides damage finds, which is particularly evident in heavily corroded metal objects. Also drainage of moorland for peat extraction and land reclamation is a substantial danger to the preservation of wetland sites with their wooden and organic objects that can be thousands of years old (Kretschmer, 2014).

## 2 Prospection and evaluation

One method to detect erosion as well as archaeological features is the evaluation of aerial photographs. Variances in height and vegetation colour can display archaeological features like ramparts, pits or burials. However, the clearer archaeological remains are visible in aerial photographs; the closer these remains are to the surface, the more vulnerable they are to total destruction (Fig. 2). A large number of archaeological remains picked up during field prospections indicate exposure and translocation of archaeological sites.

Soil mapping by soil coring is an appropriate method for the evaluation of archaeological site conditions. The devel-

**Figure 1.** The rampart of the Celtic oppidum Finsterlohr (Creglingen, Baden-Württemberg) was partially flattened by ploughing (Landesamt für Denkmalpflege im Regierungspräsidium Stuttgart, LAD, Baden-Württemberg/I. Kretschmer).

**Figure 2.** Aerial photograph of the remains of the Gothic church and abandoned medieval monastery in Remchingen-Wilferdingen (Baden-Württemberg) (LAD, Baden-Württemberg/O. Braasch).

opment of a soil profile helps to estimate the amounts of erosion and accumulation, especially in landscapes where Luvisols are widespread, e.g. in the German loess regions. These Luvisols are characterized by clay transfer processes from upper (elluvial) to lower (illuvial) horizons. This is very important for archaeological research questions because of their nearly constant thickness. The average thickness usually reaches around 40–50 cm for the elluvial and 50–70 cm for the illuvial horizon. Depending on the morphological situation the original soil profiles have changed due to forest clearing and the use of hills and other exposed terrain for agriculture, where erosion processes start. The large variation of current soil types in hilly areas is a result of human influence through agricultural activity over the last 6000 years. In some cases no remains of the original soil profiles were preserved, which means that more than 1 m of soil was lost by erosion. Eroded material will be deposited in depressions and at slope foots. A pedological survey can result in a soil map that shows the present distribution of these different kinds of soils. Assignment and depth of soil horizons and type and the determination of soil colour, content of organic material and carbonates and the moisture level are the most important parameters to be gathered by fieldwork (Behm et al., 2011). Areas of archaeological sites and their surroundings, which are strongly influenced by erosion, can be detected by soil mapping, as well as the accumulation zones, where sites are protected by a cover of colluvial deposits. Specific protection strategies can be developed in connection with land owners and the farmers by delineating erosion zones and erosion amounts.

Two case studies from the loess-covered hilly area northwest of Dresden in the surroundings of the small town Lommatzsch in Saxony will be presented in the following to exemplify our approach and the research method.

## 2.1 Case study Piskowitz-Tanzberg

Piskowitz-Tanzberg is a large area situated on a hill and attached ridge with pits and ditches of the Linear and Stroke-Ornamented Pottery Culture, as well as with burials of the late Bronze Age, early Iron Age and Roman Iron Age. The site is situated to the west of the hamlet Piskowitz. It was discovered during arable farming and was partly excavated by Johannes Deichmüller between the years 1905 and 1909. Since that time more than 100 years of agricultural land use has occurred there, and the question arose as to where it is still possible to find preserved burial remains (Behm et al., 2011).

Based on hand drillings and mapping, the analysis showed a compartmentalized mosaic of different areas of soil preservation. Promising areas with less erosion and hence potential for archaeological features could be identified. These are distributed at the nearly flat crest, where less ($Le'$) or a little more eroded Luvisols ($Le^{+}$) occur (Fig. 3). There, east of the top, a later excavation was successful and revealed some burial remains. To the north and west, we found calcaric Regosols (pararendzinas) and calcaric Cambisols (coloured in lilac and brown) that mark areas with a nearly complete erosional loss of the original soil profiles (Ender et al., 2012). In the east, larger parts of the area were covered with colluvial deposits (coloured in orange). In the north-eastern section, a small area with total profile loss can be recognized (coloured in lilac). From there to the south, a thin cover of colluvial deposits lies above brown soil. That brown soil indicates a former phase of erosion.

Soil profiles are not the only way to obtain information about the extent of erosion. The depth of the calcareous layers can also indicate it because the loess has high lime content. But calcaric components are leached and transported to lower parts of the profile during soil development. Therefore, the line of decalcification in developed Luvisols could usually be observed at a depth of about 1.20 m or more. In areas where profiles are shortened by erosion, the calcareous parts are closer to the surface, depending on the amount of eroded soil. In the case of pararendzinas and calcaric Cambisols, the substrate on top includes lots of calcaric components.

The evaluation of this site showed that a complete loss of the original soil profile can be observed and that the preservation at the central ridge and hilltop is rather endangered in some areas. Widespread ceramic findings in the plough horizon are also a sign for the ongoing destruction of archaeological remains. Therefore, a negative prediction for the future development needs to be given for most parts of the site. Our recommendation to protect the archaeological remains is that farmers should cultivate crops with a high degree of soil covering and implement consequent mulch tillage (Strobel et al., 2009).

### 2.2 Case study Burgberg Zschaitz

The site Burgberg Zschaitz, well known for its ramparts and ditches, is situated on a wide plateau of a hill spur and adjoins directly to the small village Zschaitz. Several remains and findings date to Middle and Late Neolithic, Late Bronze and early Iron Age. The two impressive great ramparts were constructed in Early to High Middle Ages. The rampart and ditch system separates the spur from the plateau and divides the area into an inner and outer bailey (Bromme et al., 2010). Soil mapping of the inner bailey showed that the soil profiles are completely destroyed. Only parts of the formerly very deeply buried archaeological remains are still preserved. This is due to soil erosion as a consequence of intensive agricultural land use on the one hand and man-made plantations during the Middle Ages on the other hand. Shifted soil material was deposited around the inner bailey in the north-west and south to build a rampart. The height of the main rampart in the east of the inner bailey was measured exactly during the 1950s. The comparison with a current measurement showed that during the last 60 years the rampart has levelled by about 60 cm due to agricultural use and ploughing (Bens et al., 2012). Moreover, the large number of archaeological findings in the plough horizon indicates rampart destruction.

The preservation state of the inner bailey and the main rampart is very poor. Fortunately it was possible to take this area out of agricultural land use and to convert it to grassland. To obtain this result, the land had to be purchased on behalf of the preservation of sites of historic interest and nature protection. An intensive cooperation between the administration, NGOs and private landowners was necessary to realize this preservation concept.

## 3 Protecting sites in farm- and wetland

### 3.1 Solutions to protect sites in farmland

Land use such as grassland delivers the best site preservation because barely any soil erosion occurs, and no farming machines disturb deeper soil layers. Several possibilities exist to take an area with archaeological remains out of agricultural farming and ploughing, such as (i) the land purchase of archaeological cultural monument sites, (ii) the swapping of areas with field areas without archaeological remains or (iii) the financial support of pasture management. In cooperation with the departments of nature conservation, soil protection, land consolidation or road construction, archaeological sites can be used as compensation areas. Compensation measures, such as the growing of green spaces to preserve nature and landscape, are demanded when construction projects use space. Such extensification solutions are not often realisable; however it is important to test all possible options to convert farmland with archaeological sites into grassland (Kretschmer, 2016).

Another protection measure is to apply no-till methods with specific and commonly available machines. These machines reduce the risk of soil erosion by leaving plant remains on the soil surface after harvesting and covering the top. Sowing new crops can be done by mulch tillage or direct seeding without tillage. The costs for purchasing such machines could be reduced by governmental incentives.

Both pasture management and conservation soil tillage are the only measures that protect the archaeological record as a permanent solution by excluding deep ploughing after any change of agricultural management.

Invisible archaeological monuments that are at risk from ploughing could also be covered, or the terrain could be filled with additional sediments or soil material, depending on soil conservation requirements.

Last but not least, technical equipment for arable farming has developed very fast during recent years, e.g. precision agriculture with GPS and newly constructed field machines for special functional requirements. Precision farming allows the protection of archaeological sites to be managed by treating these areas differently from other parts of the same field. Shapes of archaeological monuments can be seen on computer screens on board the machine. If the tractor reaches the site the cultivator may automatically lift to continue with more shallow tillage, preventing artefacts from being pulled out of deeper layers (Kretschmer, 2014).

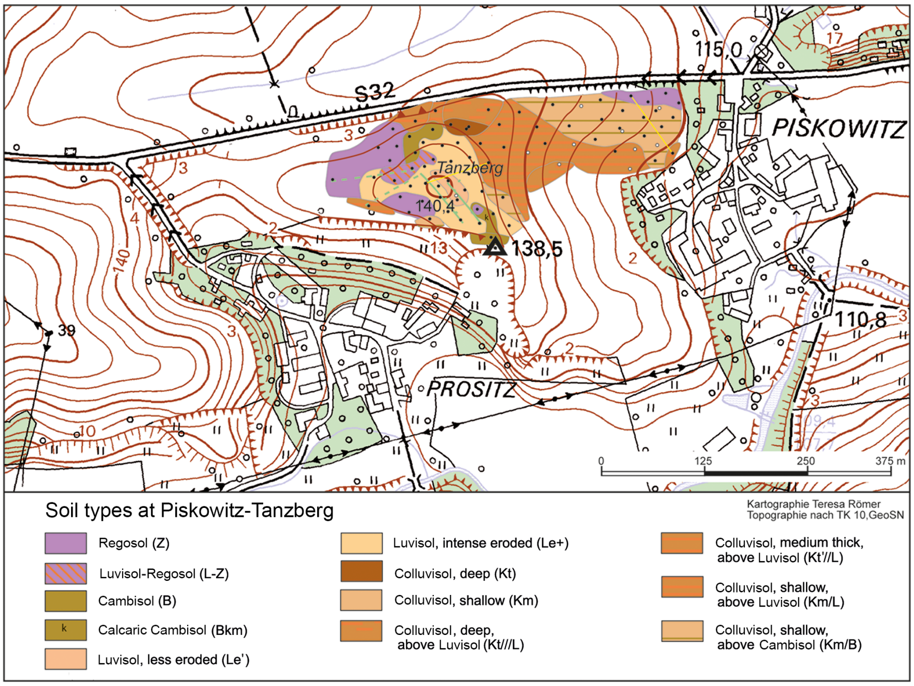


**Figure 3.** Detailed soil map of the surroundings of the site Piskowitz-Tanzberg (Saxony) (LfA Sachsen, T. Römer/R. Vogt).

## 3.2 Endangered wetland sites

Archaeological sites are not only threatened by agricultural use on farmland. Numerous bogs were meliorated in the past to obtain more and better grassland. Ditches or pipes were constructed to drain such areas. Descending groundwater levels resulted in humification and mineralization of peats, which often includes organic archaeological remains (Fig. 4). Thus, important information and archaeological remains could be destroyed, like famous sites of pile dwellings as well as wooden plank roads or outstanding findings like the 5000-year-old wooden disc wheels from the sites Alleshausen and Olzreute in Baden-Württemberg.

Organic material can survive thousands of years due to special preservation conditions under water and in an oxygen-free environment. The information content about pile dwellers' lives in the past and their related environment is inestimable (Aichele et al., 1999). This is why pile dwellings of six countries received UNESCO world heritage status in 2011. Most German sites are found in the south-west around Lake Constance and the Federsee region in Upper Swabia.

An area of nearly 400 ha of bog in the Federsee region was bought by the government of Baden-Württemberg to preserve archaeological cultural monuments for the future and to generate better conditions in this nature reserve. Ownership allowed the possibility to raise the groundwater level in this zone by building weirs and closing ditches. The original bog water supply could be restored, and preservation conditions of the archaeological sites were enhanced (Möllenberg and Schlichtherle, 2013).

**Figure 4.** Wooden disc wheel in the wetland site Olzreute-Enzisholz (Baden-Württemberg) beside wooden house construction elements (LAD, Baden-Württemberg/W. Hohl).

Yet, bog melioration remains a problem in other places. The Bodnegg site in the Allgäu region, discovered in 2014, serves as a good example. A fireplace with stony and loamy material was excavated beneath the dry soil surface. Settlement structures on this site were built on peat around 3900 BCE. This peat today has been totally transformed by the influence of oxygen in its upper parts because of the lower groundwater level. Thus, wooden parts of the houses and non-carbonized organic remains of the cultural layers have only survived in the lower parts (Ebersbach et al., 2017). Special protection strategies for such places need to be developed in every region.

## 4 Conclusions

The preservation of archaeological sites is endangered by many different effects of agricultural use, such as the deep ploughing of soils during cultivation, soil migration by machines, soil erosion by rainfall, drying wetlands by decreasing water levels or by the use of pesticides and fertilizers.

It can be shown that every site is different from another and inhomogeneous in itself. Therefore, an individual evaluation and development of solutions is needed for every single archaeological site. A joint concept for solutions and for protection strategies is necessary, incorporating the interests of landowners and farmers (Strobel et al., 2009). To obtain good results, many stakeholders from different departments need to be involved: agriculture, forestry, heritage management, nature conservation, sustainable soil protection and land consolidation (for more information, see, for example, https://www.denkmalpflege-bw.de/fileadmin/media/denkmalpflege-bw/publikationen/infobroschueren/informationen-praktische-denkmalpflege/10_archaeologie-landwirtschaft-forstwirtschaft/Broschuere_Archaeologie-Landwirtschaft-Forstwirtschaft.pdf (last access:14 December 2018).

Every single method helps to preserve the archaeological heritage, yet maximum protection is usually not achievable.

**Data availability.** All raw data of the drillings are stored at the Landesamt für Denkmalpflege im Regierungspräsidium Stuttgart (Richard Vogt) and can be obtained upon reasonable request.

**Author contributions.** RV carried out the fieldwork (drillings, observations and descriptions). The manuscript was written by IK and RV.

**Competing interests.** The authors declare that they have no conflict of interest.

**Special issue statement.** This article is part of the special issues "Geoarchaeology and past human–environment interactions".

**Acknowledgements.** A part of the research was done during the model study in Saxony "Archäologie und Landwirtschaft", funded by the Deutsche Bundesstiftung Umwelt (DBU). Thanks are expressed to Thomas Westphalen and Michael Strobel for project management.

## References

Aichele, G., Banghard, K., Billamboz, A., Einstein, J., Maier, U., Schlichtherle, H., Schwab, S., Strobel, M., and Wernicke, K.: Archäologie und Naturschutz im Federseemoor, Landesdenkmalamt Baden-Württemberg, Stuttgart, 47 pp., 1999.

Behm, H., Bräunig, A., Ende, F., Hartsch, K., Schmidt, W.-A., Schob, A., Strobel, M., Ueberfuhr, F., Vogt, R., Voss, J., and Westphalen, T.: Archäologie und Landwirtschaft, Wege zu einem partnerschaftlichen Verhältnis in Hochertragslandschaften, Erfahrungen aus einem Modellprojekt in der Lommatzscher Pflege (Freistaat Sachsen), Deutsche Bundesstiftung Umwelt, Sächsisches Landesamt für Archäologie, Sächsisches Landesamt für Umwelt, Landwirtschaft und Geologie, Verband der Landesarchäologen in der Bundesrepublik Deutschland e.V., Osnabrück, 87 pp., 2011.

Bens, S., Olkusznik, A., Schulze, H., Strobel, M., Ullrich, B., Vogt, R., Voss, J., Weißenbern, P., and Westphalen, T.: Zukunft für ein bedeutendes archäologisches Kulturdenkmal – der Burgberg Zschaitz, Ausgrabungen in Sachsen 3, 92–100, Dresden, 2012.

Bromme, V., Ende, F., Hardtke, H.-J., Kinne, A., Slobodda, S., Strobel, M., Ullrich, B., Vogt, R., Westphalen, T., and Winkler, C.: Der Burgberg Zschaitz in der Lommatzscher Pflege – Landschaft, Natur und Archäologie, Archaeonaut 9, Dresden, 24 pp., 2010.

Ebersbach, R., Kleinmann, A., Maier, U., Mainberger, M., Merkt, J., Million, S., Nelle, O., Schlichtherle, H., Stephan, E., Vogt, R., and Wick, L.: Das BELAVI-Projekt erschließt eine neue Fundlandschaft des Neolithikums im Westallgäu, Archäologische Ausgrabungen in Baden-Württemberg 2016, Darmstadt, 22–25, 2017.

Ender, W., Kinne, A., Strobel, M., and Vogt, R.: Das Gräberfeld auf dem Tanzberg bei Piskowitz/Prositz (Stadt Lommatzsch, Kr. Meißen) – eine archäologisch-bodenkundliche Nachlese, Ausgrabungen in Sachsen 3, Dresden, 75–81, 2012.

Kretschmer, I.: Archäologie – Landwirtschaft – Forstwirtschaft, Ein Projekt zur integrativen Nutzung von Bodendenkmalen in der Kulturlandschaft, Archäologische Ausgrabungen in Baden-Württemberg 2013, Darmstadt, 20–23, 2014.

Kretschmer, I.: Zum Fortgang des Projekts Archäologie – Landwirtschaft – Forstwirtschaft, Schutz und Erhalt von Bodendenkmalen in land- und forstwirtschaftlichen Nutzungsgebieten, Archäologische Ausgrabungen in Baden-Württemberg 2015, Darmstadt, 22–25, 2016.

Möllenberg, S. and Schlichtherle, H.: Archäologische Denkmale, Bodenerosion und Mineralisierung, Über das leise Verschwinden von Bodendenkmalen, Denkmalpflege in Baden-Württemberg 1/2013, Stuttgart, 9–14, 2013.

Strobel, M., Vogt, R., and Westphalen, T.: Die Lommatzscher Pflege – eine sächsische Altsiedellandschaft, Mitteilungen Landesverein Sächsischer Heimatschutz 2/2009, Mügeln, 4–12, 2009.

E&G Quaternary Sci. J., 68, 53–73, 2019
https://doi.org/10.5194/egqsj-68-53-2019


Open Access E&G Quaternary Science Journal

Research article

# New chronological constraints on the timing of Late Pleistocene glacier advances in northern Switzerland

**Dorian Gaar[1,a], Hans Rudolf Graf[2], and Frank Preusser[3]**

[1]Institute of Geological Sciences and Oeschger Centre for Climate Change Research, University of Bern, Baltzerstrasse 1+3, 3012 Bern, Switzerland
[2]Dr. von Moos AG, Dorfstrasse 40, 8214 Gächlingen, Switzerland
[3]Institute of Earth and Environmental Sciences, University of Freiburg, Albertstraße 23b, 79104 Freiburg, Germany
[a]present address: Baugeologie und Geo-Bau-Labor AG, Bolettastrasse 1, 7000 Chur, Switzerland

**Correspondence:** Frank Preusser (frank.preusser@geologie.uni-freiburg.de)

**Relevant dates:** Received: 10 January 2018 – Revised: 23 April 2019 – Accepted: 15 May 2019 – Published: 21 June 2019

**How to cite:** Gaar, D., Graf, H. R., and Preusser, F.: New chronological constraints on the timing of Late Pleistocene glacier advances in northern Switzerland, E&G Quaternary Sci. J., 68, 53–73, https://doi.org/10.5194/egqsj-68-53-2019, 2019.

**Abstract:** Deposits of the Reuss Glacier in the central northern Alpine foreland of Switzerland are dated using luminescence methodology. Methodological considerations on partial bleaching and fading correction of different signals imply the robustness of the results. An age of ca. 25 ka for sediment directly overlying basal lodgement till corresponds well with existing age constraints for the last maximal position of glaciers of the northern Swiss Alpine Foreland. Luminescence ages imply an earlier advance of Reuss Glacier into the lowlands during Marine Isotope Stage 4. The presented data are compared to findings from other parts of the Alps regarding glacier dynamics and palaeoclimatological implications, such as the source of precipitation during the Late Pleistocene.

**Kurzfassung:** Ablagerungen des Reuss-Gletschers im zentralen Teil des nördlichen Alpenvorlandes der Schweiz wurden mit Lumineszenzmethodik datiert. Methodische Überlegungen bezüglich unvollständiger Bleichung und Fadingkorrektur verschiedener Signale bekräftigen die Robustheit der Ergebnisse. Ein Alter von ca. 25 ka für Sedimente oberhalb eines basalen Tills stimmt gut mit der existierenden Chronologie für den letzten Maximalstand der Gletscher im nördlichen Alpenvorland der Schweiz überein. Die Lumineszenzalter weisen zudem auf einen früheren Gletschervorstoß während des marinen Isotopenstadiums 4 hin. Die hier präsentierten Daten werden mit Befunden aus anderen Gebieten der Alpen verglichen, mit Bezug auf Gletscherdynamik und paläoklimatologische Implikationen, wie z.B. die Herkunft von Niederschlägen während des späten Pleistozäns.

## 1 Introduction

Investigating the extent, geometry and timing of past ice sheets and glacier networks allows for the detection of atmospheric circulation patterns during the Late Pleistocene, as an important contribution for a better understanding of natural climate dynamics (Stokes et al., 2015). For example, Florineth and Schlüchter (2000) as well as Kuhlemann et al. (2008) deduce a more southward position of the polar front over the North Atlantic during the Last Glacial Maximum (LGM) from glacial records. However, it has to be noted that the term LGM is ambiguous: it is either used to refer to the maximum of global cooling during Marine Isotope Stage (MIS) 2 (ca. 29–14 ka ago; Lisiecki and Raymo, 2005) or the last maximum of global ice volume (ca. 22–19 ka on a global scale; Yokoyama et al., 2000), both of which are inferred from deep marine sediment records. Continental records indicate that most ice sheets and glaciers reached their last most extensive position between 26.5 and 19 ka ago, with the onset of deglaciation mainly just after 20 ka (Clark et al., 2009). Interestingly, it appears that in some regions the maximum extent of glaciers after the Last Interglacial was not synchronous with the peak of MIS 2 (cf. Hughes et al., 2013), with important and not yet entirely deciphered indications for past circulation. For example, Jimenez-Sanchez et al. (2013) suggest that the last local glacial maximum in the Pyrenees occurred during MIS 4 and that glaciers during MIS 2 were of substantially smaller extent.

Besides the timing it is also of interest to reconstruct the nature of past glaciations, i.e. the rate of ice advance and the related question of if these were temperate or cold-based glaciers. Answering these questions will be of importance when modelling glaciations (e.g. Haeberli and Schlüchter, 1987; Becker et al., 2016; Seguinot et al., 2018) and their potential to deeply erode into bedrock (e.g. Headly and Ehlers, 2015). Beside pure scientific interests, the question of possibly future glacial erosion is of high interest for the siting of nuclear waste disposal sites (Haeberli, 2010; McEvoy et al., 2016).

For the Alps, the timing of the last maximum extent of glaciers (Fig. 1) at first appears fairly well constrained (e.g. Ivy-Ochs et al., 2008). However, direct dating is actually limited to a few sites and the available data do, when analysed closely, reveal several discrepancies with regard to the exact timing. For the Lyonnais lobe of the French Alps (Fig. 1), the largest extension of glaciers since the Last Interglacial appears to be older than 40 ka, with a less extensive, polyphase terminal moraine radiocarbon dated to around 23 and 19 ka (Mandier, 2003; Mandier et al., 2003). In the SW Italian Alps, at Ponte Murato (Fig. 1), $^{10}$Be dated boulders on terminal moraines have a mean age of $20 \pm 2$ ka (Federici et al., 2012), apparently in concert with the global isotopic signal. According to Ravazzi et al. (2014), glacier collapse in the Lake Garda area (Fig. 1) occurred soon after $17.5 \pm 0.2$ ka cal BP. For the Tagliamento end-moraine system (Fig. 1), a two-fold glacial advance is recorded with the larger extent between 26.5 and 23 ka and the second, slightly smaller extent to 24–21 ka by radiocarbon dating (Monegato et al., 2007). A similar pattern is found in the former Salzach Glacier of the NE Alps, at Duttendorf (Fig. 1), with continuous loess accumulation dated to ca. 30 to 21 ka by luminescence dating (Starnberger et al., 2011). The inner Alpine position of Baumkirchen (Fig. 1) was reached by ice 33–32 ka ago according to both radiocarbon (Spötl et al., 2013) and luminescence dating (Klasen et al., 2007). $^{10}$Be exposure dating of terminal moraines of the type locality of the Würmian glaciation at Starnberg (Fig. 1) gives only a minimum age ca. 18 ka due to post-depositional instability of the dated boulders (Reuther et al., 2011). Luminescence dating of glaciofluvial sediments of the last Würmian ice advance in the Würm Valley reveals ages of ca. 29 ka, constraining the maximum age for this ice advance (Klasen et al., 2007). An early phase of ice decay inside the Alps is recorded by kame deposits at Rahmstätt (Fig. 1), with a mean luminescence age of ca. 19 ka (Klasen et al., 2007).

For the NW Alps, Keller and Krayss (2005a, b) established a model of the last advance and decay of the Rhine Glacier lobe into the foreland (Fig. 1) based on previously published radiocarbon data. However, this study lacks information on the dating uncertainties and is not up to date with regard to calibration. For the present study, the uncalibrated $^{14}$C data were collected from the original sources and calibrated using OxCal 4.2 (Bronk Ramsey, 2009), applying the IntCal13 calibration curve (Reimer et al., 2013; Table 1). According to these data (Fig. 2), ice build-up of the LGM Rhine Glacier started around 29 ka and reached its maximum between 26 and 22 ka ago, with the decaying ice front reaching the inner Alpine valleys before 17 ka. The radiocarbon chronology is confirmed by quartz luminescence ages for an outcrop at Hüntwangen (Fig. 1), ca. 4 km downstream of the maximum terminal moraine of the last glacier advance (Preusser et al., 2007). Outwash gravel in an ice proximal position has an age of $25.0 \pm 2.0$ ka and overbank deposits attributed to a melting phase date between $22.2 \pm 1.6$ and $17.1 \pm 1.3$ ka.

For the Reuss Glacier lobe (Fig. 1), several radiocarbon ages of large mammal finds from glaciofluvial gravels constrain the last ice advance (Graf, 2009). Their calibrated (IntCal13) ages range between 26.9 and 21.6 ka BP but their position with regard to glacier advance or retreat is not known precisely. Glaciofluvial gravel from Gebenstorf (Fig. 3 GE) has luminescence ages of $32.9 \pm 4.6$ and $26.1 \pm 3.4$ ka (Gaar et al., 2014). According to $^{10}$Be and $^{36}$Cl dating, the minimum age of ice decay is $22.2 \pm 1.0$ ka at the frontal position and $20.4 \pm 1.0$ ka at the lateral position. By latest $18.6 \pm 0.9$ ka Reuss Glacier was approximately 12 km behind the maximal extent position (Reber et al., 2014). Gravel aggradation of the Low Terrace in the Hochrhein Valley dates to ca. 30 to 15 ka (quartz luminescence) and a second phase between 13 and 11 ka (Kock et al., 2009a, b).

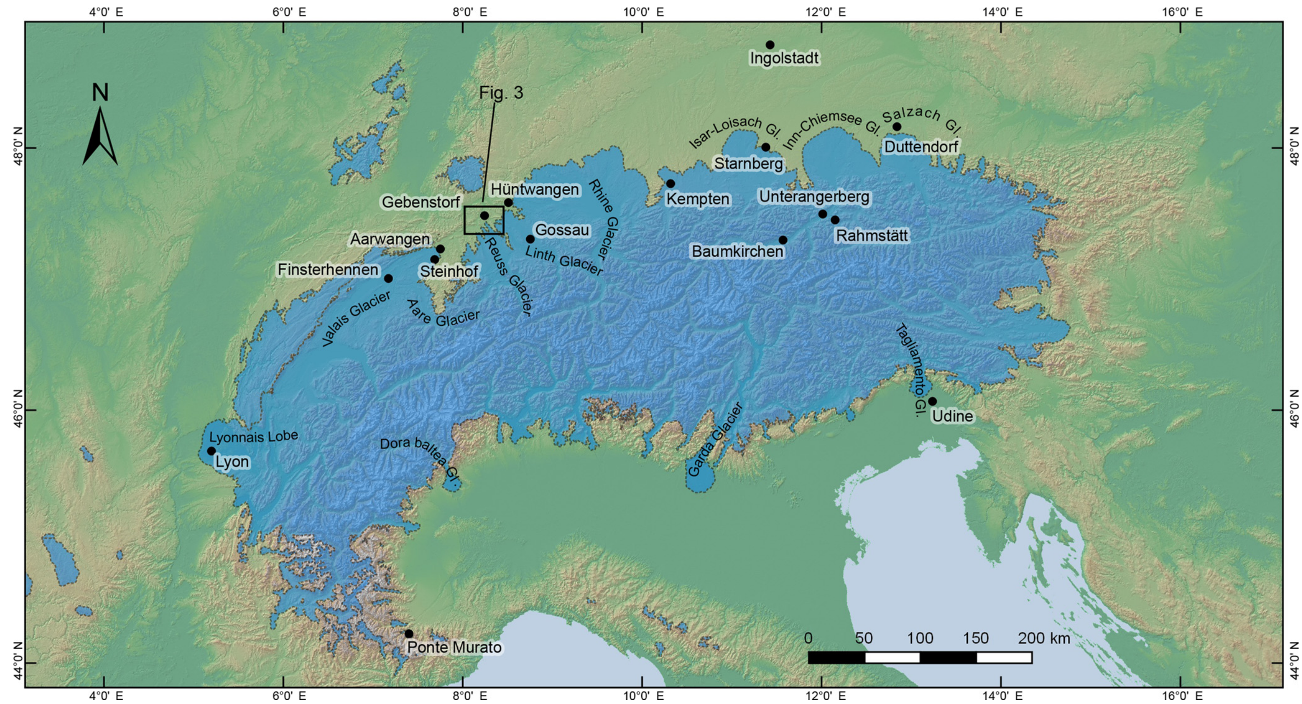


**Figure 1.** Overview of the Alps with the ice extent ca. 24 ka ago according to Ehlers and Gibbard (2004) with sites mentioned in the text. Elevation data from Jarvis et al. (2008). References for the sites are as follows: Lyon – Mandier et al. (2003); Ponte Murato – Federici et al. (2012); Udine – Monegato et al. (2007); Duttendorf – Starnberger et al. (2011); Baumkirchen – Klasen et al. (2007) and Spötl et al. (2013); Starnberg – Reuther et al. (2011); Steinhof – Ivy-Ochs et al. (2004); Ingolstadt – Fiebig and Preusser (2003); Gossau – Preusser et al. (2003); Kempten – Link and Preusser (2005); Hüntwangen, Aarwangen, and Finsterhennen – Preusser et al. (2007); Unterangerberg – Starnberger et al. (2013); Rahmstätt – Klasen et al. (2007).

For the Swiss lobe of the Valais Glacier, the terminal moraine near Steinhof (Fig. 1) was dated by $^{10}$Be, $^{26}$Al and $^{36}$Cl (Ivy-Ochs et al., 2004). The original data are recalculated here by applying the NE North America production rate (Balco et al., 2009), no snow correction and an erosion rate to 1 mm ka$^{-1}$, using the CRONUS Earth calculator 2.2 (Balco et al., 2008). This yields an age of $24.1 \pm 1.9$ ka for the maximum terminal position and $22.8 \pm 1.8$ ka for the onset of deglaciation. In the same region (Aarwangen gravel pit, Fig. 1), luminescence dating suffers from partial bleaching and the resulting ages of $27.4 \pm 2.8$ and $25.7 \pm 4.2$ ka are interpreted as maximum estimates for the ice advance (Preusser et al., 2007). At Finsterhennen (Fig. 1), radiocarbon (mammoth tusk) and quartz luminescence ages for the basal part of LGM glaciofluvial accumulation are between 30 and 25 ka (Preusser et al., 2007).

Already Köppen and Wegener (1924) discuss an extensive glaciation during the Würmian prior to the LGM, based on the astronomical parameters calculated by Milanković (1941). The same authors later referred to these expected glacier advances as Würm I (ca. 115 ka) and Würm II (ca. 70 ka) (Köppen and Wegener, 1940). This concept was originally entirely based on theoretical considerations and not supported by evidence from the geological record. Based on pollen records and correlations with marine isotope stratigraphy, Welten (1981) designates an early Würmian cold stage and supposes a substantial glacial advance (called Turicum 1a) shortly after the Last Interglacial, followed by mild climatic conditions and another glacial advance between 70 and 55 ka. Schlüchter (1986) discusses the possibility that the MIS 4 glacier extent is larger than MIS 2, and Frenzel (1991) postulates a large advance of the Rhine Glacier shortly after the Eemian Interglacial based on pollen records. Keller and Krayss (1998) compile lithostratigraphic indications for a Middle Würmian glacier advance and reconstruct its dimensions, tentatively placed into MIS 4. Luminescence dating of (glacio?)-fluvial sediments in the area of Ingolstadt (Fig. 1) indicates that parts of the deposits, originally interpreted as the distal part of outwash plains of the penultimate glacial cycle (Rissian), might actually be younger than the Last Interglacial (Fiebig and Preusser, 2003). Link and Preusser (2005) describe evidence for a possible MIS 4 glaciation in SW Germany (Kempten, Fig. 1), based on luminescence dating of proglacial lake deposits. Preusser et al. (2003) luminescence dated sediments at the gravel pit of Gossau (Fig. 1), which were interpreted as MIS 4 (glacial) delta sediments. However, the dating results rather point towards a deposition during MIS 5d, i.e. the

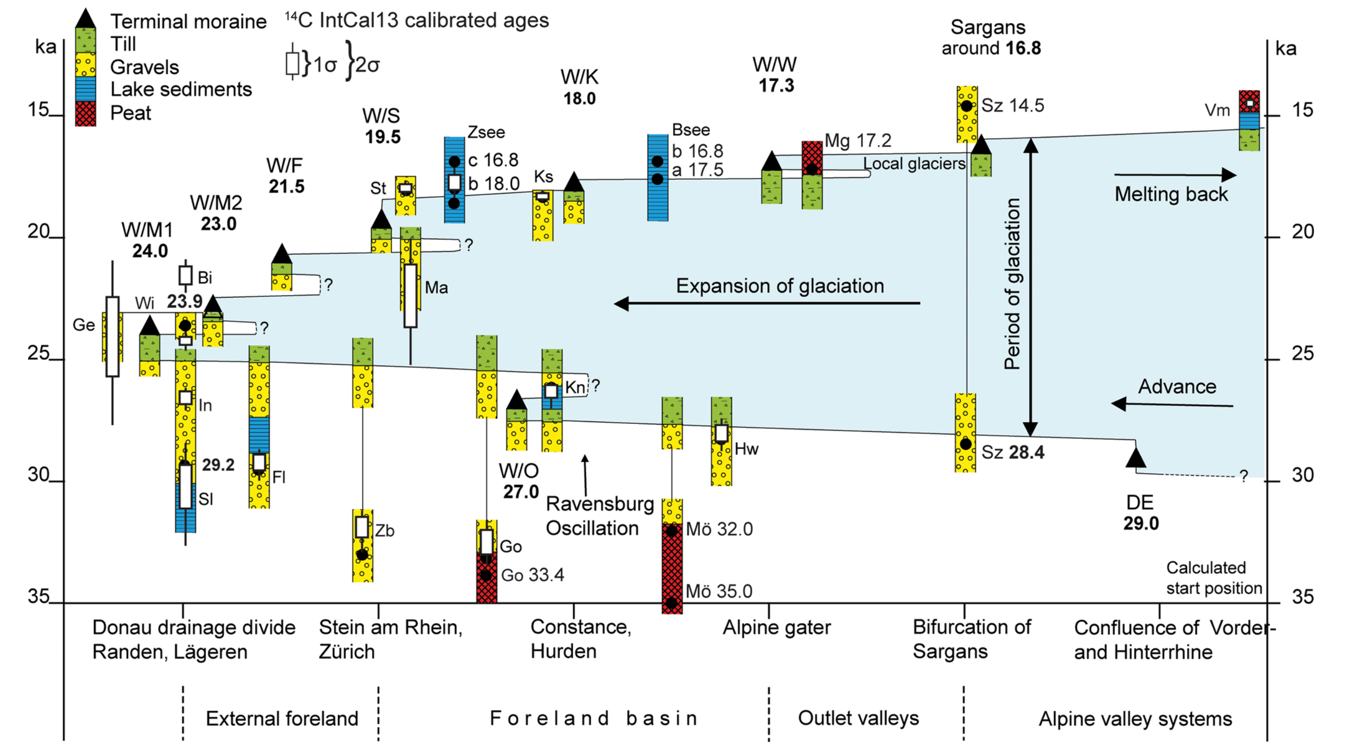


**Figure 2.** Chronology of the last glacial advance of the Rhine–Linth Glacier (Birrfeld/Würm) complemented with recalibrated radiocarbon ages (white boxes) using IntCal13; figure taken from Preusser et al. (2011) and redrawn after Keller and Krayss (2005a, b). Ice marginal positions: DE – Domat/Ems, W/O – Obersee, W/M1 – outer maximum, W/M2 – inner maximum, W/F – Feuerthalen, W/S – Stein am Rhein, W/K – Konstanz, W/W – Weissbad.

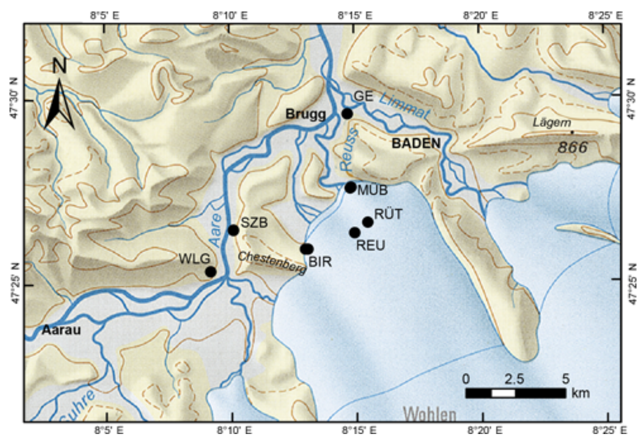


**Figure 3.** Map of the Birrfeld area during the LGM with sampling sites of this study and samples of earlier studies (WLG: Gaar and Preusser, 2012, and GE: Gaar et al., 2014). Background map by Bini et al. (2009). Source: Swiss Federal Office of Topography.

Turicum 1a of Welten (1981). Gravel attributed to an advancing glacier in the Reuss Valley close to Mülligen (Fig. 3) has a mean luminescence age of $66 \pm 9$ ka (Preusser and Graf, 2002). Probably the most compelling evidence for the Valais Glacier, reaching the lowlands of Switzerland during MIS 4, is given by Preusser et al. (2007). In the Finsterhennen gravel pit (Fig. 1), the age of a lower till is older than 30 ka according to radiocarbon and luminescence dating. Glaciofluvial deposits from just below the till have a quartz luminescence age of ca. 70 ka.

In this article, we present a new set of luminescence ages further constraining the timing of glacial advances in the Reuss Glacier system, situated in between the areas occupied by the main lobes of the Rhine Glacier and Valais Glacier during the Late Pleistocene (Figs. 1, 3). For this area, a revised system of Quaternary glaciations was developed by Graf (2009; summarised in Preusser et al., 2011), as the scheme by Penck and Brückner (1901–1909) does not fully reflect the complex pattern observed in sediment sequences of northern Switzerland. The type location of the last glacial advance (Würm sensu stricto), the Birrfeld Glacial of Graf (2009), is investigated in this article. Furthermore, recent developments in luminescence methodology led us to redate the Müllingen outcrop previously investigated by Preusser and Graf (2002). Besides the implications for the chronology of Late Pleistocene glacier advances in northern Switzerland, and in comparison to other parts of the Alps, a detailed discussion of methodological aspects is provided. This aims to, firstly, corroborate the reliability of the presented results and, secondly, add connotations to the performance of different

**Table 1.** Radiocarbon ages used for the ice build-up and decay model of the Rhine glacier, only showing samples for which the original radiocarbon ages are available and that therefore allow calibration.

| | Site | Stratigraphic meaning | Sample material | Lab code | $^{14}$C age (a BP) | cal ka BP 1$\sigma$ range | | cal ka BP 2$\sigma$ range | | Reference | Cited in |
|---|---|---|---|---|---|---|---|---|---|---|---|
| | | | | | | from | to | from | to | | |
| Bi | Binningen | Recessional complex I | Mammoth | HV 14390 | 20 195 ± 140 | 24.44 | 24.09 | 24.66 | 23.88 | Schreiner (1992) | |
| Fl | Flurlingen | Above basal till | Wood | – | 25 210 ± 270 | 29.57 | 28.92 | 30.04 | 28.67 | Frank and Rey (1996) | |
| Ge | Geisslingen | Lower Terrace | Mammoth | HV 14486 | 19 895 ± 1450 | 25.75 | 22.46 | 27.69 | 20.98 | Bausch et al. (1989) | Schreiner (1992) |
| Go | Gossau ZH | Upper foliated peat | Peat | ETH 2205 | 28 550 ± 310 | 33.02 | 32.00 | 33.43 | 31.63 | Schlüchter et al. (1987) | |
| Hw | Hochwacht/Bregenz | Pre-max. glaciation | Mammoth | UtC-1292 | 23 900 ± 400 | 28.38 | 27.68 | 28.78 | 27.41 | De Graaf (1992) | de Graaf and de Jong (1995) |
| In | Ingoldingen | | Mammoth | | 22 330 ± 185 | 26.90 | 26.33 | 27.12 | 26.14 | Moegle (1994) | |
| Kn | Knollengraben | Pre-max. glaciation | Humics | | 22 130 ± 225 | 26.61 | 26.07 | 27.01 | 25.94 | Weinhold (1973) | de Graaf and de Jong (1995) |
| Ks | Karsee | Late-phase Rhine | ? | GrN-11836 | 15 090 ± 80 | 18.47 | 18.23 | 18.57 | 18.09 | De Jong (1983) | de Graaf and de Jong (1995) |
| Ma | Markelfingen | Pre-max. glaciation | Mammoth | HV 10655 | 18 530 ± 1045 | 23.70 | 21.15 | 25.25 | 20.12 | Geyh and Schreiner (1984) | |
| Sl | Saulgau | Below 1. Würmian till | Coal | | 26 195 ± 970 | 31.18 | 29.32 | 32.65 | 28.45 | Werner (1974) | Schreiner (1992) |
| St | Steisslingen | Recessional complex II | Bone | HV 10654 | 14 800 ± 120 | 18.17 | 17.86 | 18.32 | 17.70 | Geyh and Schreiner (1984) | |
| Vm | Viamala/Crapteig | | | | 12 400[a] | 14.57[a] | 14.29[a] | 14.71[a] | 14.22[a] | Burga (1981) | |
| Wi | Wil/Rafz ZH | | | | 17 850 ± 265 | 21.95 | 21.23 | 22.30 | 20.93 | Hünermann (1985) | |
| Zb | Zürichberg | Between tills | Peat | ETH5192 | 28 060 ± 340 | 32.37 | 31.45 | 32.90 | 31.24 | Schlüchter and Röthlisberger (1995) | |
| Zsee | Zürichsee Bohrung | Post ice recession | Twig | GL 2 | 14 600 ± 250 | 18.08 | 17.47 | 18.39 | 17.13 | Lister et al. (1984) | |

[a] No measurement uncertainty indicated in original publication.

luminescence techniques for the dating of proglacial sediments in general.

## 2 Context and sampling sites

### 2.1 Regional setting

Birrfeld, i.e. the mainly flat area between the rivers Aare and Reuss (with the village of Birr), is situated between the two most easterly surface fold structures of the Jura Mountains. The oldest Quaternary sediments of the region are scarce occurrences of Early Pleistocene gravel sheet (Deckenschotter) deposits (Graf, 1993). As the result of subglacial erosion, overdeepened valleys formed during the Middle Pleistocene (cf. Preusser et al., 2010), which often contain complex sequences of multiphase sediment successions (e.g. Graf, 2009; Dehnert et al., 2012). At the base, the valley fillings comprise coarse-grained subglacial gravel and till intercalating with or overlain by water-lain till or thick post-glacial lacustrine sediments. The geometrical and chronological relationship between the different types of deposit is yet poorly understood due to the limited data available, as the sedimentary records are only accessible via coring and have seen a limited application of modern sedimentological approaches and dating methods (e.g. luminescence). However, there appears to be evidence for four superimposed glacial successions in the area, at least two of which are older than the Last Interglacial, as indicated by palaeosols (Graf, 2009; Preusser et al., 2011). Exposed in outcrops are mainly deposits of the younger glaciations that are the focus of the present study.

### 2.2 Gravel pit Joriacher (BIR)

The gravel pit Joriacher (47°25′50″ N, 8°12′59″ E), near the village Birr, is located at the SW end of Birrfeld (Fig. 3). The basal unit is composed of sandy, mainly coarse and partly open-worked gravel intercalated by cobbles and blocks (Fig. 4). The petrographic composition represents an alpine spectrum with crystalline components (e.g. granodiorites), strongly weathered into loose aggregates of detritus. Due to its rather coarse components and petrographic composition the gravel is interpreted to be of glaciofluvial origin. The gravel is topped by a yellow-brownish decalcified silty gravel of about 2 m thickness, interpreted as fBt horizon (Graf, 2009; Fig. 4). Locally, black precipitation occurs and deeper parts of this palaeosol reach about 1 m into the underlying unweathered gravel in a cone-shaped pattern. A clayey–silty fine sediment of about 1 m thickness is found above the palaeosol without a change of colour. Whether this continuity in colour indicates a deposition of the fine sediment synchronous with soil formation or whether there is a hiatus remains unclear. The fine-sediment layer is interpreted as low-energy fluvial (overbank?) deposits and sample BIR-1 was taken from it. Another coarse-grained gravel intercalated by blocks (up to > 1.5 m in diameter) and sand layers

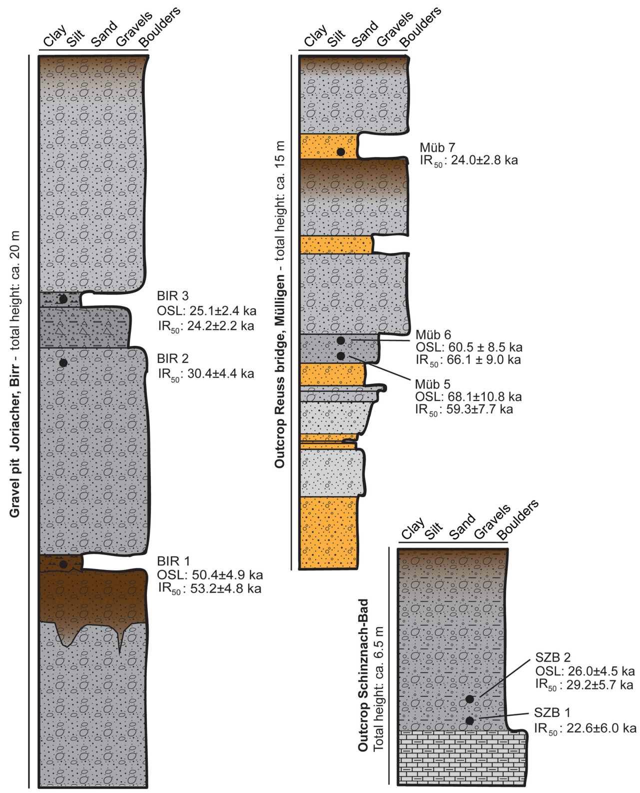


**Figure 4.** Schematic logs of the sections at the gravel pit Joriacher in Birr (BIR), outcrop by the bridge over river Reuss close to Mülligen (MÜB) and outcrop close to Schinznach-Bad (SZB).

tops the brown palaeosol with a sharp contact. It has the same petrographic composition as the lower gravel unit but without indication of weathering. Sample BIR-2 was taken from a 40 cm thick, massive sand layer found within this gravel. Other sand layers in this gravel show cross-bedding structures. The succession of gravel is interrupted by a ca. 80 cm thick diamicton with angular components, interpreted as a basal lodgement till, directly indicating a past glacier presence at this position. The top of this diamicton bears locally fine silty-clayey sediment of ca. 40 cm thickness. This fine sediment likely represents the infill of a pond in front of a retreating glacier. The age of sample BIR-3 from this fine-grained sediment will mark the retreat of ice from its maximum position in this part of Birrfeld, as no other till is found above.

## 2.3 Low Terrace in the Aare Valley (SZB)

In the valley of the River Aare, just to the west of Birrfeld, a succession of gravel builds up the Low Terrace, which is attributed to the last glacial advance. At Schinznach-Bad (47°26′22″ N, 8°10′4″ E; Fig. 3 SZB) it is composed of silty, sandy gravel with cobbles and scarce boulders (< 50 cm) directly overlying the bedrock (Fig. 4). Two samples were taken, one (SZB-1) from a 30 cm thick sand layer at the base of the gravel, 80 cm above the bedrock, and one (SZB-2) from a 20 cm thick sand layer about 2 m above the bedrock. To account for the possible inhomogeneity in the radiation field in this thin sand layer, a second sample from the surrounding sandy gravel was taken 10 cm below the sand layer for determination of dose-rate-relevant elements.

## 2.4 Outcrop Mülligen (MÜB)

This outcrop is located close to the bridge between the villages of Mülligen and Birmenstorf, on the left-hand side of River Reuss (47°27′29″ N, 8°14′46″ E; Fig. 3). The outcrop shows a coarsening upwards succession of medium-sized sand towards gravel (Fig. 4). The sequence is interpreted to be of fluvial origin with a decreasing transport distance; thus it most likely represents an advancing glacier. Considering the rather fine sediment and good sorting, the sediment source has to be assumed a few kilometres upstream for the sampled sandy units (MÜB-5 and 6). About 4 m below the present surface, a brown layer is interpreted as the remains of a palaeosol (Preusser and Graf, 2002) and sample MÜB-7 has been taken from a sandy layer just above. In a neighbouring gravel pit (Niderhard, Birmenstorf), the molar of a mammoth found at a similar depth to the palaeosol was dated to ca. 36 ka cal BP (ETH-17251, Graf, 2009).

## 2.5 Reuss Valley (RÜT and REU)

Sample RÜT-1 was taken from a natural outcrop situated in a small valley (Fig. 5), west of the sewage plant of Rütihof (47°26′33″ N, 8°15′26″ E; Fig. 3). The lower part of the outcrop is classified as diamicton, consisting of clayey, sandy silt interbedded with clayey silty sand (alternating in the decimetre range), both containing calcite. Coarse-gravel layers occur as a frequent accessory in both types of deposit. The pebbles are subangular to subrounded and partly show weak striations; large boulders (> 1 m) are scarce. The lithology of the components reflects both alpine and local origin. Bedding is inclined by 25–30° towards 280° west, steepening in the westernmost part. Based on these observations, the sediment is interpreted as melt-out till (Graf, 2009) and sample RÜT-1 was taken from a sandy bed. The diamicton is topped by sandy coarse gravel with subrounded cobbles, interpreted as outwash deposited in proximity to a glacier.

The two samples REU-1 and REU-2 were taken on the left-hand side of the River Reuss, close to the village of Birrhard (47°26′15″ N, 8°14′53″ E, Fig. 3). The sampled unit is mica-rich and composed of clayey to silty fine sand, which is horizontally bedded with wave or climbing ripples. Calcitic concretions are abundant in parallel strata, which are tilted locally. Graf (2009) interprets this sand as deposit of a shallow lake with strong currents. Accordingly, occasional desiccation led to the calcitic concretions and cementation. The tilting of the concretions is interpreted to be caused by later glaciotectonical processes. The total thickness of this sand

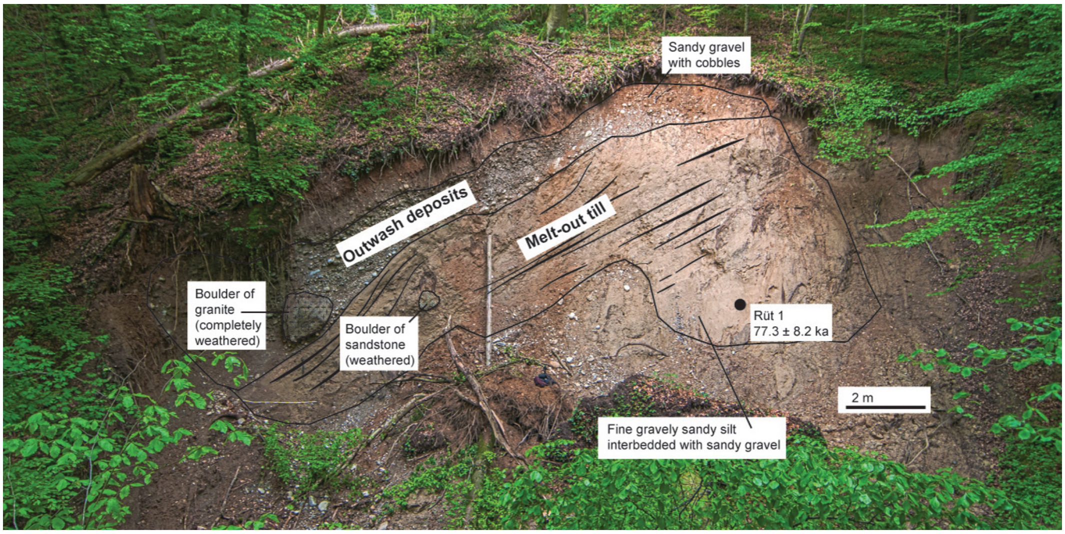


**Figure 5.** The melt-out till close to Rütihof with position of sample RÜT-1.

is probably exceeding 20 m (borehole data). This outcrop is interpreted to represent the basal and more distal part of the coarsening upward sequence already sampled at Müllingen (MÜB-5 and 6).

## 3 Methodology

### 3.1 Sampling and sample preparation

Most samples were taken from homogeneous layers of several decimetres thickness composed of either sand or silt. Sampling faces were cleaned by removing some decimetres of sediment. A metal cylinder, closed at one end, was forced into the sediment immediately, minimising exposition to daylight. The cylinders were then emptied into opaque plastic bags by avoiding daylight exposition.

All sample preparation was performed in the laboratory under subdued red-light (peak emission at 660 nm) conditions. Samples were chemically cleaned with HCl (32 %) and $H_2O_2$ (30 %) to remove carbonates and organic material. From the fine-grain samples, the 4–11 µm fraction was obtained by applying the settling technique using Stokes' law. A part of the polymineral fraction was subsequently etched for 10 days in $H_2SiF_6$ (34 %) to remove feldspars and HCl (32 %) was used to dissolve fluorite precipitates that formed during etching. The coarse-grain samples were separated for their 200–250 µm fraction by dry sieving. The chemical cleaning with HCl and $H_2O_2$ was followed by density separation using an aqueous sodium polytungstate solution at two densities ($\rho = 2.70$ and $2.58\,\mathrm{g\,cm^{-3}}$) to remove heavy minerals and to obtain a quartz-rich and a K-feldspar-rich fraction. The quartz fraction was etched for 60 min in HF (40 %) to remove remaining feldspar and the outer rim of the quartz grains, followed by HCl treatment to dissolve fluoride precipitates formed during the HF treatment. Final sieving of the etched quartz was carried out to remove feldspar grains that will have substantially reduced in size during etching.

### 3.2 Dose rate determination

The concentrations of dose-rate-relevant elements (U, K, Th) were determined using high-resolution gamma spectrometry (Preusser and Kasper, 2001) on bulk sediment samples of ca. 450 g; results are shown in Table 2. Indications of radioactive disequilibria in the uranium decay chain have been observed for samples RÜT-1 and SZB-1 when comparing the activity of $^{238}U$ and $^{226}Ra$ (Preusser and Degering, 2007). For these two samples a polyphase U depletion model was applied using ADELE software (Kulig, 2005) to account for the loss of U over time. In this model, we assume a depletion of water soluble U since the beginning of the Holocene, when climate is known to be changing towards warmer conditions and hence water is mobilised. The difference in effective dose rate between a conservative approach with no U depletion and modelled dose rates is minor for the feldspar fractions of SZB-1 (less than 0.3 %) and moderate for RÜT-1 (5.7 %). For the coarse-grain quartz fraction, the difference is negligible because the influence of U on the total dose rate is low, as the rim affected by the alpha radiation is removed during HF etching. Sample SZB-2 has been taken from a thin sand layer and an influence on the radiation field of the sample from the surrounding sediment has to be assumed. A second sample taken 10 cm below the sampled sand layer allowed the calculation of the effective radiation field using a model with several layers of different content of dose-rate-relevant elements (using ADELE software).

The cosmogenic dose rate was assessed by ADELE software, following Prescott and Hutton (1994) for cosmic dose estimation, using modern burial depth and a density of

**Table 2.** Results of high-resolution gamma spectrometry and resulting dose rates during burial. ($W_{eff}$ is effective water content relative to dry mass, Q is quartz and F is feldspar).

| Sample | Site | Grain size (µm) | K (%) | Th (ppm) | U (ppm) | $W_{eff}$ (%) | Overburden (m) | Dose rate F ($Gy\,ka^{-1}$) | Dose rate Q ($Gy\,ka^{-1}$) |
|---|---|---|---|---|---|---|---|---|---|
| BIR-1 | Birr Joriacher | 4–11 | $1.73 \pm 0.05$ | $11.59 \pm 0.25$ | $2.74 \pm 0.09$ | $20 \pm 4$ | 14 | $3.27 \pm 0.26$ | $3.02 \pm 0.24$ |
| BIR-2 | Birr Joriacher | 200–250 | $1.10 \pm 0.02$ | $3.48 \pm 0.28$ | $1.23 \pm 0.01$ | $6 \pm 4$ | 8 | $2.37 \pm 0.16$ | $1.54 \pm 0.09$ |
| BIR-3 | Birr Joriacher | 4–11 | $1.18 \pm 0.03$ | $6.77 \pm 0.48$ | $2.27 \pm 0.06$ | $20 \pm 5$ | 6 | $2.33 \pm 0.20$ | $2.15 \pm 0.20$ |
| MÜB-5 | Mülligen Brücke | 200–250 | $1.36 \pm 0.04$ | $3.16 \pm 0.14$ | $0.95 \pm 0.05$ | $6 \pm 4$ | 9 | $2.51 \pm 0.17$ | $1.68 \pm 0.10$ |
| MÜB-6 | Mülligen Brücke | 200–250 | $1.20 \pm 0.04$ | $2.61 \pm 0.12$ | $0.80 \pm 0.01$ | $10 \pm 5$ | 8 | $2.24 \pm 0.16$ | $1.42 \pm 0.09$ |
| MÜB-7 | Mülligen Brücke | 200–250 | $1.45 \pm 0.05$ | $9.22 \pm 0.23$ | $2.60 \pm 0.08$ | $10 \pm 5$ | 5 | $3.31 \pm 0.23$ | $2.47 \pm 0.17$ |
| REU-2 | Reusstal Birrhard | 200–250 | $1.01 \pm 0.02$ | $5.09 \pm 0.09$ | $1.65 \pm 0.03$ | $7 \pm 4$ | 15 | $2.44 \pm 0.15$ | $1.62 \pm 0.09$ |
| RÜT-1 | Reusstal Rütihof | 200–250 | $1.06 \pm 0.01$ | $7.61 \pm 0.30$ | $1.76 \pm 0.38$[a] | $10 \pm 5$ | 8 | $2.69 \pm 0.25$[a] | $2.01 \pm 0.15$[a] |
| SZB-1 | Schinznach-Bad | 200–250 | $1.17 \pm 0.02$ | $2.66 \pm 0.14$ | $0.45 \pm 0.12$[a] | $15 \pm 5$ | 5 | $2.19 \pm 0.13$[a] | $1.38 \pm 0.07$[a] |
| SZB-2 | Schinznach-Bad | 200–250 | $1.17 \pm 0.01$ | $2.85 \pm 0.09$ | $0.90 \pm 0.04$ | $15 \pm 5$ | 4 | $2.21 \pm 0.15$[b] | $1.39 \pm 0.09$[b] |

[a] U disequilibrium detected and time-dependent depletion modelled. [b] Possible inhomogeneous radiation field modelled using a second sample from surrounding sediment.

$2\,g\,cm^{-3}$. The calculated contribution from cosmic radiation is taken into account with a relative uncertainty of 10 %.

Potassium content of feldspar and polymineral samples was assumed to be $12.5 \pm 1.0$ % following the estimates of Huntley and Baril (1997) and our own measurements (Gaar et al., 2014). This was cross-checked for one sample (RÜT-1) by analysing randomly selected grains of the feldspar separate by electron microprobe analysis (see Gaar et al., 2014, for technical details). Of the 200 grains, 35 grains were identified as quartz; the rest was identified as feldspar. Backscattered electron microscopy imagery reveals scarce perthitic grains, but the vast majority of grains are homogeneous. While 16 grains have an albite (Na-feldspar) or intermediate composition, the large majority of 167 grains are orthoclase (K-feldspar). The average K content of the measured feldspars is $12.77 \pm 0.25$ % (standard error). The mean measured for the orthoclase only is $13.57 \pm 0.09$ %.

The efficiency of alpha particles in causing radiation damage (alpha efficiency, $a$-value) is assumed based on literature values. For coarse feldspar and polymineral fine grains an $a$-value of $0.05 \pm 0.01$ was used following Preusser (1999) and Preusser et al. (2001), representing the geographically closest $a$-value assessments. For fine-grain quartz an $a$-value of $0.03 \pm 0.01$ was used (Mauz et al., 2006). Since the outer rim is removed by HF etching for coarse-grain quartz, the $a$-value is not considered for palaeodose estimates on this fraction. Modern sediment water content was assessed by drying the sample the laboratory at 50 °C until a constant mass was reached. In order to account for varying water contents, large uncertainty was given to the assessed water content values.

## 3.3 Equipment and equivalent dose determination

Luminescence measurements were made on automated Risø TL/OSL DA-20 readers equipped with 9235QA photomultiplier tubes. For single-grain measurements a Risø single-grain laser attachment with dual lasers was used (Bøtter-Jensen et al., 2003). The $\beta$ source of the reader has been checked for inhomogeneity using a $\beta$ radiation sensitive self-developing film (Lapp et al., 2012). As non-uniformity of the $\beta$ source is minor, no correction on the single-grains measurements was applied. Optically stimulated luminescence (OSL) from quartz multigrain aliquots was stimulated with blue LEDs and single grains with a green laser. Signal detection was in the near-UV emission spectrum (Hoya U-340 filter). Infrared stimulated luminescence (IRSL) from feldspars was stimulated in the near infrared (LEDs for multigrain aliquots, laser for single grains) and signal detection was in the blue emission band (Schott BG-39 with 410 nm interference filter). Palaeodoses were determined using modified single-aliquot regenerative-dose (SAR) protocols after Murray and Wintle (2000), Blair et al. (2005) and Thomsen et al. (2008) (Table 3). Preheat temperatures were checked using dose recovery tests (discussed below) and an appropriate preheat temperature was chosen where dose recovery ratios are within 10 % of unity and sensitivity change during the SAR protocol is low. Preheating to 230 °C for 10 s after all irradiation steps was chosen for both quartz and feldspar. Equivalent doses ($D_e$) were calculated using Luminescence Analyst 4.11 (Duller, 2013). While the majority of aliquots have sufficiently bright OSL signals, in some the OSL intensity is too low to allow for proper analyses (Fig. 6). In the bright aliquots, quartz signals are dominated by the fast component, as shown exemplarily in Fig. 7. For quartz multigrain aliquots (single grains) the first 0.4 s (0.04 s) of the signal, minus the signal 40–60 s (2–5 s) as background, was used for calculations. For feldspar multigrain aliquots (single grains) using the $IR_{50}$ protocol, the first 10 s (1 s) were used, minus the final 50 s (2 s) as background.

As the $IR_{50}$ signal is often considered to be unstable, but applying a second stimulation at 225 °C ($pIRIR_{225}$) after $IR_{50}$ is expected to isolate a low- or even non-fading signal (Thomsen et al., 2008; Buylaert et al., 2009). For the $pIRIR_{225}$ protocol, $D_e$ calculation of multigrain aliquots (single grains) was based on the first 2 s (1 s) of the decay curve,

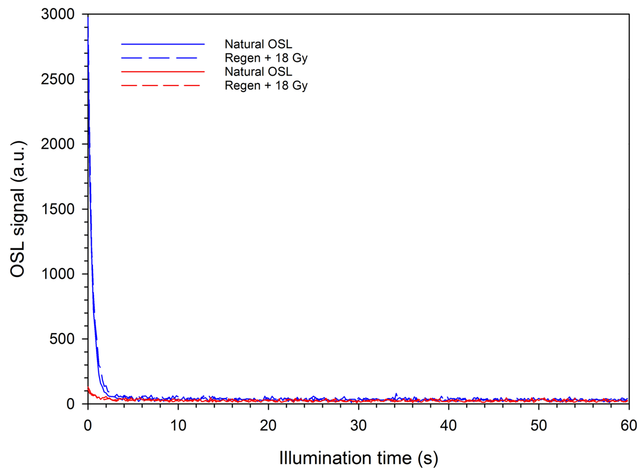


**Figure 6.** While most OSL decay curves from the study area are relatively bright, some aliquots emit very low OSL intensities that make them unsuitable for $D_e$ determination.

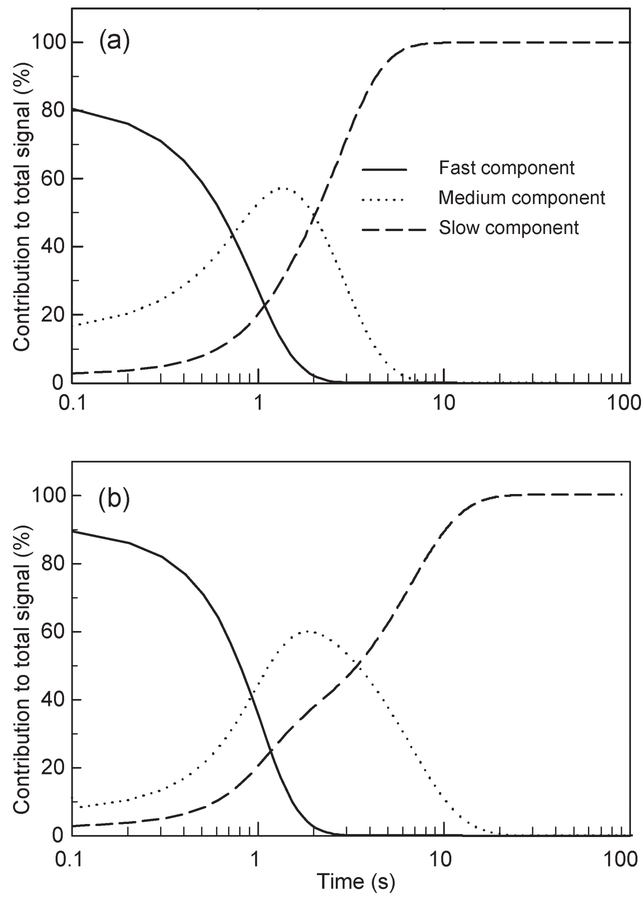


**Figure 7.** Component stripping of quartz OSL signals reveals domination of the fast component. **(a)** BIR-3 fine-grain quartz, **(b)** MÜB-5 coarse-grain quartz.

and the last 20 s (2 s) were subtracted as background (Table 3). A major disadvantage of the pIRIR$_{225}$ approach is its much slower resetting compared to IR$_{50}$ (Buylaert et al., 2012) and hard-to-bleach natural residual doses are often observed. As natural residuals are constant and not a function of $D_e$, the problem of natural residuals decreases, while accumulated doses increase (Buylaert et al., 2009; Sohbati et al., 2012). While the applicability in glacial environments with low bleaching probabilities has proven problematic in previous studies (Blomdin et al., 2012; Lowick et al., 2012, 2015; Gaar et al., 2014), it is here further tested for completeness.

Validity of the above parameters for samples from the area of interest has been outlined by Gaar et al. (2014) and confirmed by dose recovery experiments on selected samples, as detailed below. Dose response curves were fitted using a single saturating exponential function for both quartz and feldspar, examples being displayed in Fig. 8. A measurement error of 1.5 % was included in the $D_e$ determination for single-aliquot measurements and 2.4 % for single grains according to Trauerstein et al. (2012); the error on curve fitting based on Monte Carlo simulation is included.

## 3.4 Partial bleaching

In glaciofluvial environments, incomplete signal resetting due to short transport distances is a common phenomenon (e.g. Fuchs and Owen, 2008). This means that many grains were only reset to a certain degree and not accounting for it would lead to age overestimation (e.g. Duller, 2006). However, it is usually assumed that there is a portion of grains that were exposed to daylight sufficiently long enough to fully reset the signal (Duller, 1994). When partial bleaching is recognised, the population of the fully reset grains can be obtained, for example, by using the Minimum Age Model (unlogged MAM-3) by Galbraith et al. (1999).

A basic assumption for the application of the MAM is that $D_e$ is derived from individual grains and not as an average from several grains. In the latter case, averaging effects will likely mask the spread of $D_e$ values caused by differential bleaching and it might hence not be possible to extract the dose accumulated during burial (Wallinga, 2002). This would, in principle, require the exclusive use of a single-grain over multigrain methodology for partially bleached samples, but single-grain dating is not only laborious but also subject to some methodological concerns (e.g. Thomsen et al., 2016). In this context, it is important to note that it has repeatedly been shown that only a small proportion of all grains emit luminescence (e.g. Duller, 2008), and averaging effects will be proportional to the number of grains contributing to the signal (Wallinga, 2002). For samples from the study area, Gaar et al. (2014) and the data presented here (Table 4) reveal that on average 2.6 % of all measured quartz grains and about 20 % of all feldspar grains have OSL and IRSL signals significantly above background. Calculating the number of grains on a multigrain disc following Heer et al. (2012), for the grain size (200–250 µm) and aliquot

**Table 3.** Protocols used in this study. OSL was applied to quartz, IR50 and pIRIR225 were applied to feldspar. OSL is a stimulation with blue LEDs and SG OSL with a green laser. IRSL is a stimulation with IR LEDs and SG IRSL with an IR laser.

| Observed | OSL – multiple-grain aliquots | OSL – single grains | $IR_{50}$ – multiple-grain aliquots | $IR_{50}$ – single grains | $pIRIR_{225}$ – single grains |
|---|---|---|---|---|---|
| | Dose[a] | Dose[a] | Dose[a] | Dose[a] | Dose[a] |
| | Preheat at 230 °C for 10 s | Preheat at 230 °C for 10 s | Preheat at 230 °C for 60 s | Preheat at 230 °C for 60 s | Preheat at 230 °C for 60 s |
| | IRSL at 50 °C for 60 s[b] | SG IRSL at 50 °C for 5 s[b] | | | IRSL at 50 °C for 100 s |
| $L_n/L_x$ | OSL at 125 °C for 60 s | SG OSL at 125 °C for 5 s | IRSL at 50 °C for 300 s | SG IRSL at 50 °C for 5 s | SG IRSL at 225 °C for 5 s |
| | Test dose | Test dose | Test dose | Test dose | Test dose |
| | Preheat at 230 °C for 10 s | Preheat at 230 °C for 10 s | Preheat at 230 °C for 60 s | Preheat at 230 °C for 60 s | Preheat at 230 °C for 60 s |
| | | | | | IRSL at 50 °C for 100 s |
| $T_n/T_x$ | OSL at 125 °C for 100 s | SG OSL at 125 °C for 5 s | IRSL at 50 °C for 300 s | SG IRSL at 50 °C for 5 s | SG IRSL at 225 °C for 5 s |

[a] Omitted in first cycle to measure Ln. [b] Only applied in last cycle.

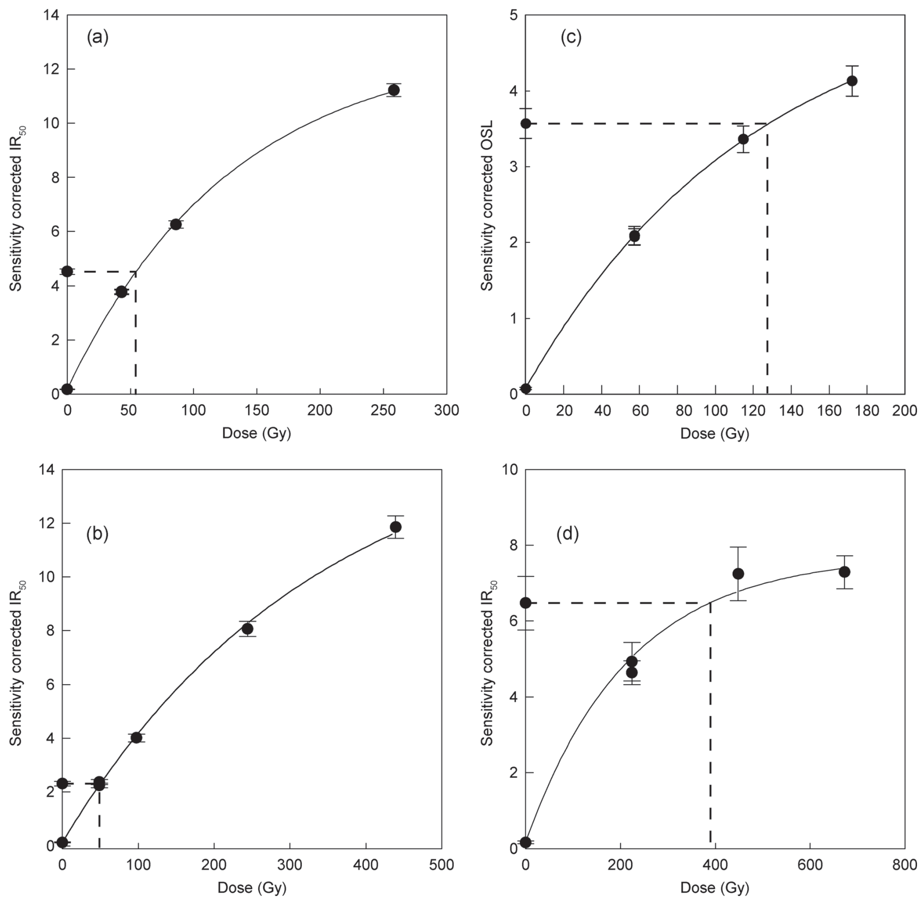


**Figure 8.** Examples of dose response curves. **(a)** BIR-3 polymineral $IR_{50}$, **(b)** SZB-1 feldspar, multiple-grain $IR_{50}$, **(c)** MÜB-6 quartz, multiple-grain OSL and **(d)** RÜT-1 feldspar, single-grain $IR_{50}$.

sizes used here, results in average numbers of 72 (quartz, 2 mm) and 18 (feldspar, 1 mm) grains per disc. Using the number of grains contributing significantly to the signal emitted from a multigrain disc as given above indicates that the signal of multigrain aliquots used in the present study should on average originate from ca. 2 (quartz) and ca. 3.5 (feldspar) grains, respectively. This implies that averaging effects for the geometry chosen here should be quite limited. This is confirmed by Gaar et al. (2014), who could clearly distinguish between a well and poorly bleached sample base on the spread of $D_e$ values for both single grains and 1 mm aliquots of K-feldspar.

Here, identification of partial bleaching is mainly based on Gaar et al. (2014), who investigated glaciofluvial samples within the same source area. A critical value is $\sigma b$, which is used in the statistical models to define the expected variation of data. In this study, $\sigma b$ values exceeding 0.18 for 1 mm feldspar aliquots, 0.19 for 2 mm quartz aliquots, 0.32 for sin-

**Table 4.** Doses and ages.

| Sample | Mineral | Protocol | Aliquot size (mm) | $n_{total}$ | $n$ | od. | $\sigma$ Skew | Palaeodose (CAM) (Gyr) | Palaeodose (MAM) (Gyr) | Age (CAM) (ka) | Age (MAM) (ka) | Age (CAM) fading corrected (ka) | Age (MAM) fading corrected (ka) |
|---|---|---|---|---|---|---|---|---|---|---|---|---|---|
| BIR-1 | Poly. | $IR_{50}$ | 9.7 | 7 | 7 | 12 | −0.59 | 173.6 ± 7.2 | – | 53.2 ± 4.8 | – | 59.1 ± 6.0 | – |
| BIR-1 | Qtz | OSL | 9.7 | 7 | 7 | 9 | −0.25 | 152.3 ± 8.7 | – | 50.4 ± 4.9 | – | – | – |
| BIR-2[a] | Fsp | $IR_{50}$ | 1 | 48 | 36 | 53 | 0.40 | 156.7 ± 13.9 | 72.1 ± 9.1 | 66.2 ± 7.3 | 30.4 ± 4.4 | 89.5 ± 10.6 | 40.6 ± 5.8 |
| BIR-2 | Qtz | OSL | 2 | 91 | 17 | 31 | −0.30 | 88.9 ± 7.2 | 65.8 ± 10.0 | 57.6 ± 5.8 | 42.6 ± 7.0 | – | – |
| BIR-3 | Poly. | $IR_{50}$ | 9.7 | 7 | 7 | 3 | 0.30 | 56.3 ± 0.99 | – | 24.2 ± 2.2 | – | 30.2 ± 3.0 | – |
| BIR-3 | Qtz | OSL | 9.7 | 7 | 7 | 6 | −0.93 | 53.92 ± 1.59 | – | 25.1 ± 2.4 | – | – | – |
| MÜB-5 | Fsp | $IR_{50}$ | SG | 270 | 62 | 35 | 1.67 | 198.4 ± 10.0 | 148.5 ± 16.6 | 79.2 ± 6.6 | 59.3 ± 7.7 | 107.0 ± 9.9 | 80.1 ± 11.4 |
| MÜB-5 | Fsp | $pIRIR_{225}$ | SG | 450 | 39 | 35 | 0.27 | 233.2 ± 13.9 | 184.6 ± 26.3 | 93.0 ± 8.4 | 73.6 ± 11.6 | 106.9 ± 9.6 | 84.6 ± 13.8 |
| MÜB-5 | Qtz | OSL | 2 | 96 | 23 | 26 | 0.09 | 138.8 ± 8.6 | 114.7 ± 16.7 | 82.4 ± 7.2 | 68.1 ± 10.8 | – | – |
| MÜB-6 | Fsp | $IR_{50}$ | SG | 270 | 57 | 44 | 0.45 | 228.4 ± 13.8 | 148.1 ± 17.2 | 102.1 ± 9.5 | 66.1 ± 9.0 | 139.7 ± 14.82 | 89.4 ± 12.8 |
| MÜB-6 | Fsp | $pIRIR_{225}$ | SG | 540 | 38 | 28 | 0.18 | 211.6 ± 10.6 | 195.3 ± 26.1 | 94.5 ± 8.2 | 87.2 ± 13.2 | – | – |
| MÜB-6 | Qtz | OSL | 2 | 60 | 40 | 26 | 0.65 | 104.8 ± 4.9 | 85.8 ± 10.5 | 73.8 ± 6.0 | 60.5 ± 8.5 | – | – |
| MÜB-7 | Fsp | $IR_{50}$ | SG | 630 | 153 | 35 | 1.65 | 71.5 ± 2.1 | 58.7 ± 6.9 | 21.6 ± 1.6 | 17.7 ± 2.4 | 29.9 ± 2.0 | 24.0 ± 2.8 |
| REU-2 | Fsp | $IR_{50}$ | SG | 270 | 40 | 28 | 0.13 | 247.0 ± 12.3 | 226.7 ± 31.9 | 101.2 ± 8.0 | 92.9 ± 14.3 | – | – |
| REU-2 | Qtz | OSL | 2 | 96 | 57 | 33 | 0.44 | 164.7 ± 8.2 | 123.2 ± 16.2 | 101.7 ± 7.6 | 76.0 ± 10.9 | – | – |
| RÜT-1 | Fsp | $IR_{50}$ | 1 | 72 | 48 | 36 | 0.07 | 336.5 ± 17.9 | 212.6 ± 18.9 | 125.1 ± 13.4 | 79.0 ± 10.2 | 166.8 ± 18.1 | 105.4 ± 14.1 |
| RÜT-1 | Fsp | $IR_{50}$ | SG | 1800 | 300 | 46 | 0.39 | 328.3 ± 9.0 | 207.8 ± 10.5 | 122.1 ± 11.8 | 77.3 ± 8.2 | 156.5 ± 15.8 | 99.0 ± 11.1 |
| RÜT-1 | Fsp | $pIRIR_{225}$ | SG | 450 | 20 | 32 | −0.96 | 339.9 ± 27.5 | 303.4 ± 55.9 | 126.4 ± 15.6 | 112.8 ± 23.3 | – | – |
| RÜT-1 | Qtz | OSL | SG | 2700 | 31 | 37 | 0.15 | 190.0 ± 15.6 | 163.0 ± 35.4 | 94.5 ± 10.5 | 81.0 ± 18.6 | – | – |
| SZB-1 | Fsp | $IR_{50}$ | 1 | 48 | 47 | 57 | 1.91 | 70.8 ± 5.9 | 49.5 ± 12.8 | 32.3 ± 3.3 | 22.6 ± 6.0 | 36.3 ± 4.3 | 25.4 ± 6.8 |
| SZB-2 | Fsp | $IR_{50}$ | 1 | 45 | 42 | 57 | 0.78 | 107.9 ± 9.7 | 46.1 ± 5.6 | 48.8 ± 5.5 | 29.2 ± 5.7 | 55.7 ± 6.8 | 32.8 ± 6.6 |
| SZB-2[a] | Qtz | OSL | 2 | 60 | 33 | 34 | 0.83 | 43.1 ± 2.3 | 36.1 ± 5.9 | 31.0 ± 2.6 | 26.0 ± 4.5 | – | – |

[a] Dose distribution has been manually changed by removing single outliers from the lowermost end.

gle grains of quartz and 0.28 for single feldspar grain are interpreted as indicative of partial bleaching. These values have been used as threshold and input parameter when applying the MAM. For samples with $\sigma b$ values smaller than the above and for all fine-grain samples, the Central Age Model (CAM; Galbraith et al., 1999) was used.

The SZB samples are from the Aare Valley and thus from another sediment source to the rest of the samples. Hence, the $\sigma b$ parameter derived for Birrfeld samples cannot be expected a priori to be valid for samples from another area. For the SZB feldspar samples, an approximation to a realistic $\sigma b$, representative of the natural spread of $D_e$ values for bleached samples was possible by manually removing the uppermost values from the $D_e$ distribution of SZB-1 that were clearly separated from the rest of the $D_e$ distribution, assuming these values derive from grains that were incompletely bleached. This resulted in a $\sigma b$ value of 0.39 for feldspar IR50 multigrain aliquots, which is substantially higher than for the Birrfeld samples, and is considered to possibly overestimate the real $\sigma b$ value of a well-bleached sample. Using this as input parameter in the MAM may hence result in an overestimated, maximum age estimate.

While the choice of the input parameter for the MAM is based on the information available, it is not unproblematic to assume that values observed for one sample automatically applied to another. As an independent test, we additionally follow Murray et al. (2012), who suggest that partial bleaching can be tested by comparing results for feldspar and quartz, as the minerals have different bleaching rates.

### 3.5 Fading of IR signals

Fading tests on multigrain aliquots were carried out on the feldspar and polymineral fraction of samples from all sites in order to detect and quantify anomalous fading of the $IR_{50}$ signals (and in one case $pIRIR_{225}$). The fading tests were based on delayed $L_x/T_x$ measurements, with preheating directly following irradiation (similar to natural dose) and different storage times prior to $L_x$ measurements (Auclair et al., 2003). Delay of the measurements was up to 40 h after irradiation. The $L_x/T_x$ ratios measured after different delays are plotted against the time delay between irradiation and $IR_{50}$ measurement on a log scale. The calculated percentage of signal loss per decade is referred to as the $g$-value (Aitken, 1985). Results of the fading tests are given in Table 5. These $g$-values are used for fading correction using the R package Luminescence (Kreutzer et al., 2012), which corrects according to Huntley and Lamothe (2001). This correction, however, is restricted to doses which lie within the linear part of the dose response curve (Huntley and Lamothe, 2001). In general, there is controversy around whether the assessment of $g$-values through laboratory experiments reflects the fading behaviour of samples in nature and if the correction always leads to accurate ages (e.g. Wallinga et al., 2007; Reimann et al., 2011; Lowick et al., 2012). Furthermore, it is has been questioned if $g$-values assessed on multigrain aliquots reflect the fading behaviour of the IRSL signal excited by a laser in single-grain measurements (Trauerstein et al., 2012). Nevertheless, the correction after Huntley and Lamothe (2001) was applied, although most of the samples are in the non-linear part of signal growth. This theoretically leads to undercorrection of the signal loss; hence, even corrected $IR_{50}$ age may underestimate the real deposition age.

**Table 5.** Fading rates of feldspar and polymineral samples.

| Sample | Mineral | Protocol | $g$-value (% decade$^{-1}$) |
|---|---|---|---|
| BIR-1 | Polymineral | $IR_{50}$ | $1.1 \pm 0.4$ |
| BIR-2 | Fsp | $IR_{50}$ | $2.9 \pm 0.2$ |
| BIR-3 | Polymineral | $IR_{50}$ | $2.4 \pm 0.2$ |
| MÜB-5 | Fsp | $IR_{50}$ | $2.9 \pm 0.3$ |
| MÜB-5 | Fsp | $pIRIR_{225}$ | $1.4 \pm 0.1$ |
| MÜB-7 | Fsp | $IR_{50}$ | $3.2 \pm 0.1$ |
| RÜT-1 | Fsp | $IR_{50}$ | $2.7 \pm 0.1$ |
| SZB-2 | Fsp | $IR_{50}$ | $1.5 \pm 0.6$ |

For samples from northern Switzerland, observations regarding fading correction are controversial. Gaar et al. (2014) found fading-corrected $IR_{50}$ ages in good agreement with quartz OSL ages for two samples with a known age between 30 and 20 ka. On the other hand, several other studies found an age overestimation after fading correction and/or good agreement with independent age control from radiocarbon dating or quartz OSL (e.g. Preusser et al., 2003; Gaar and Preusser, 2012; Lowick et al., 2012, 2015; Veit et al., 2017). For this reason, we present both uncorrected and fading-corrected $IR_{50}$ ages.

## 4 Results

Results of luminescence dosimetry, statistical age models and calculated ages are given in Table 4. All $D_e$ distributions are found in the Supplement of this article.

### 4.1 Gravel pit Joriacher (BIR)

Samples BIR-1 and BIR-3 are the only fine-grain samples presented in this study. Dose recovery tests yield recovery values of $96.8 \pm 3.7$ % for BIR-1 and $94.5 \pm 4.1$ % for BIR-3. Fading rates of the $IR_{50}$ signal on the polymineral fraction were estimated to $g = 1.1 \pm 0.4$ % per decade for BIR1 and $2.4 \pm 0.2$ % for BIR3, which are relatively low and will have only a minor effect when applying age corrections. For fine grains it is not possible to detect partial bleaching by inspecting $D_e$ distributions due to the large number of grains on each aliquot.

For BIR-1, a quartz OSL age of $50.4 \pm 4.9$ ka is within uncertainties in good agreement with both the uncorrected ($53.2 \pm 4.8$ ka) and the fading-corrected ($59.1 \pm 6.0$ ka) $IR_{50}$

ages. The same applies for sample BIR-3, with a quartz OSL age of 25.1 ± 2.4 ka and polymineral $IR_{50}$ ages of 24.2 ± 2.2 ka (uncorrected) and 30.2 ± 3.0 ka (fading corrected). BIR-2 bears some difficulty for interpretation as the quartz has low sensitivity and its data set contains only 17 $D_e$ values. The $IR_{50}$ on the feldspar fraction yielded more values, with a broad and skewed distribution indicating partial bleaching. One single outlier at the lower end of the distribution observed during visual inspection was discarded for further analysis to avoid strong biasing by this value (Fig. 9a). The quartz MAM age (42.6 ± 7.0 ka) of this samples is based on rather few $D_e$ values and should be taken with precaution. $IR_{50}$ yields a MAM age of 30.4 ± 4.4 ka (40.6 ± 5.8 ka, corrected for fading).

## 4.2 Low Terrace in the Aare Valley (SZB)

The quartz data for sample SZB-1 had to be discarded due to a machine failure. Dose recovery of the quartz fraction is 97.4 ± 6.8 % and the fading rate of the $IR_{50}$ on the feldspar fraction was estimated to a low $g = 1.5 \pm 0.6$ % per decade for SZB2.

For sample SZB-1, the $D_e$ distribution of the $IR_{50}$ 1 mm feldspar aliquots show a tail of high doses. We interpret this as a typical distribution of a partially bleached sample, where a substantial part of the aliquots has been completely reset. The MAM age of this sample is 22.6 ± 6.0 ka (25.4 ± 6.8 ka, when corrected for fading).

For SZB-2, the quartz aliquot measurements show one clear single outlier at the lower end of the dose distribution that was discarded from further analysis (Fig. 9b). The remaining $D_e$ distribution has an overdispersion of 27 %, larger than the value of 19 % expected for 2 mm quartz aliquots of a well-bleached sample in this area (Gaar et al., 2014). We consider the quartz fraction of this sample being reset to a large extent but still having an unbleached component. The MAM age of this sample 26.0 ± 4.5 ka. The $D_e$ distribution of the 1 mm feldspar aliquots ($IR_{50}$) displays a wide range (overdispersion of 58 %) with some values at the upper end, implying the presence of partial bleaching. The MAM ages are 29.2 ± 5.7 ka (uncorrected) and 32.8 ± 6.6 ka (fading corrected).

## 4.3 Outcrop Mülligen (MÜB)

The $D_e$ distribution of MÜB-5 quartz OSL 2 mm aliquots has an overdispersion of 26 %, slightly larger than the value of 19 % expected for a completely reset sample. Furthermore, the distribution is significantly positively skewed, and a partially bleached component is likely to be present in this distribution. A MAM age of 68.1 ± 10.8 ka has been calculated. Single-grain feldspar measurements using the $IR_{50}$ and $pIRIR_{225}$ protocols return $D_e$ distributions with higher overdispersion values of 38 % ($IR_{50}$) and 35 % ($pIRIR_{225}$) implying partial bleaching for these signals as well. Fading tests on the $IR_{50}$ signal give a $g$-value of 2.9 ± 0.3 % and 1.4 ± 0.1 % per decade for the $pIRIR_{225}$ signal. For $IR_{50}$ an uncorrected MAM age of 59.3 ± 7.7 ka was calculated, a correction (in the non-linear dose range) returns 80.1 ± 11.4 ka. The $pIRIR_{225}$ MAM age (73.6 ± 11.6 ka) agrees with the quartz MAM age, whereas the corrected age (84.6 ± 13.8 ka) tends to rather overestimate. Regarding the question of signal resetting it is noteworthy that, while some degree of partial bleaching is observed, in some the grains the $pIRIR_{225}$ signal was completely bleached. A good performance of $pIRIR_{225}$ is observed in the dose recovery test, where a given dose was recovered to 99 %.

Sample MÜB-6 is similar to MÜB-5, the overdispersion values of the $D_e$ distributions are 26 % (quartz OSL, 2 mm aliquots), 44 % (feldspar $IR_{50}$, single grains) and 28 % ($pIRIR_{225}$, single grains). No fading test was done for this sample and $IR_{50}$ is corrected using the fading rate obtained for MÜB-5. The MAM ages obtained for this sample are 60.5 ± 8.5 ka (quartz OSL), 66.1 ± 9.0 ka ($IR_{50}$, uncorrected), 89.4 ± 12.8 ka ($IR_{50}$, corrected) and 87.2 ± 13.2 ka ($pIRIR_{225}$).

MÜB-7 was only measured using single feldspar grains with the $IR_{50}$ protocol. Its distribution is positively skewed, and a couple of outliers can be identified at the upper end of the distribution. We interpret this sample as not being completely reset. The measured fading rate (3.2 ± 0.1 g per decade) is the highest observed in this study and the fading-corrected MAM age is 24.0 ± 2.8 ka, while the uncorrected age is 17.7 ± 2.4 ka.

## 4.4 Reuss Valley (RÜT and REU)

For sample RÜT-1, only about 1 % of the investigated single quartz grains are acceptable for $D_e$ analyses. The MAM age obtained for quartz OSL is 81.0 ± 18.6 ka. The $IR_{50}$ single-grain data set (Fig. 9c) of the same sample allows a solid estimation of the degree of bleaching as it offers a large number of $D_e$ values. Its shape does not show a strongly positively skewed distribution but a very wide spread, spanning 1 order of magnitude between ca. 50 and over 800 Gyr. Since fading rates in the region are usually very similar (Gaar et al., 2014; Lowick et al., 2015) and internal K content of feldspars appears to be quite uniform (Gaar et al., 2014, and this study), the spread is most likely explained by different degrees of bleaching. The fading rate of the $IR_{50}$ was estimated to 2.7 ± 0.1 % g per decade with a dose recovery of 99 %. The $IR_{50}$ MAM on the single feldspar grains yields an age of 77.3 ± 8.2 ka (uncorrected) and 99.0 ± 11.1 ka (fading corrected). For the 1 mm aliquots, very similar MAM ages of 79.0 ± 10.2 ka (uncorrected) and 105.4 ± 14.1 ka (fading corrected) are calculated; similarly to the distributions of BIR-2 and SZB-2, a single outlier at the lower end of the distribution was identified and removed for further analysis.

The $pIRIR_{225}$ analysis on single grains of RÜT-1 yielded a low sensitivity, with ca. 4 % of the grains giving accept-

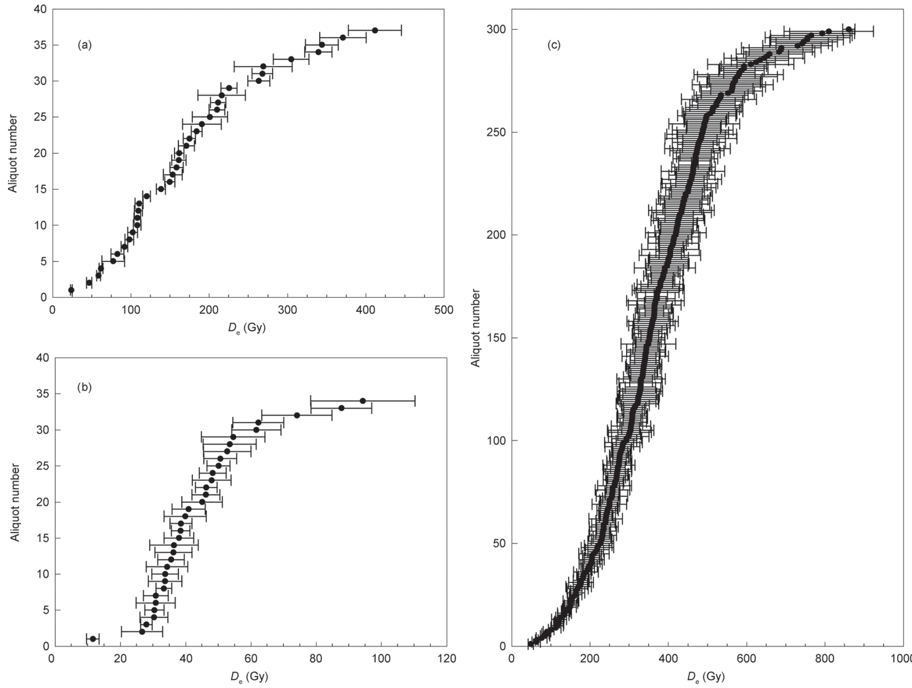


**Figure 9.** $D_e$ distributions of selected samples. **(a)** BIR-2 feldspar multiple-grain $IR_{50}$, **(b)** SZB-2 quartz multiple-grain OSL, **(c)** RÜT-1 single-grain feldspar $IR_{50}$.

able signals. Dose recovery of $pIRIR_{225}$ single grains is 100 %. The data set of 20 $D_e$ values does likely not reflect a representative dose distribution and the MAM age of $112.8 \pm 23.3$ ka overestimates the ages obtained for OSL and $IR_{50}$. This might be explained either by lower resetting probability of the $pIRIR_{225}$ signal and/or the small data set not covering a sufficiently large population of fully reset grains.

Sample REU-1 is a replicate sample of REU-2 and due a shortage of machine time, this sample was not further investigated. The single-grain $IR_{50}$ $D_e$ distribution of sample REU-2 has an overdispersion of 28 %, which is similar to the overdispersion of other well-bleached samples in the area. We consider this sample to be well bleached and the single-grain $IR_{50}$ CAM age of $101.2 \pm 8.0$ ka agrees very well with the CAM age obtained from 2 mm quartz aliquots of $101.7 \pm 7.6$ ka.

## 5 Discussion

### 5.1 Methodological considerations

For our samples, we did not encounter the problem with an absence of quartz OSL sensitivity as reported in other studies from glacially derived sediments (Spencer and Owen, 2004; Lukas et al., 2007; Rowan et al., 2012; Klasen et al., 2016). One reason for low OSL sensitivity appears to be related to the sedimentary history of the quartz grains with repeated cycles of erosion, transport, deposition and burial increasing sensitivity (Preusser et al., 2006; Pietsch et al., 2008). While the glaciers responsible for the deposition of the sediments investigated here have their origin in the central Alps, a large number of the grains will originate from Molasse sediments, as has been shown for other sediments from the Swiss Alpine Foreland (e.g. Preusser et al., 2001). Molasse sediments were eroded and deposited in the foreland during growth of the Alps (Oligocene-Miocene) and therefore have undergone several sedimentary cycles prior to their initial deposition. Practically problematic is the small fraction of quartz grains giving an OSL signal, which increases measurement time for single-grain quartz analyses.

Fading rates of the $IR_{50}$ signals are relatively low with values between ca. 1 % and 3 %. The comparison of uncorrected and corrected $IR_{50}$ age estimates with the corresponding quartz OSL ages is plotted in Fig. 10, revealing that fading-corrected $IR_{50}$ ages have a tendency to overestimate the OSL ages. Assuming the effect of partial bleaching has been adequately considered, this implies little if any fading in the $IR_{50}$ feldspar signal during burial. As already stated by Lowick et al. (2012) and others, $g$-values may not fully represent the potential signal loss occurring in nature, at least for the samples investigated here and in other parts of the northern Alpine foreland. Hence, while not applying a correction may cause age underestimation, the fading correction can lead to an overestimation in the real age of deposition, as reported by Klasen et al. (2016) and Lowick et al. (2015). This issue will require further systematic investigations.

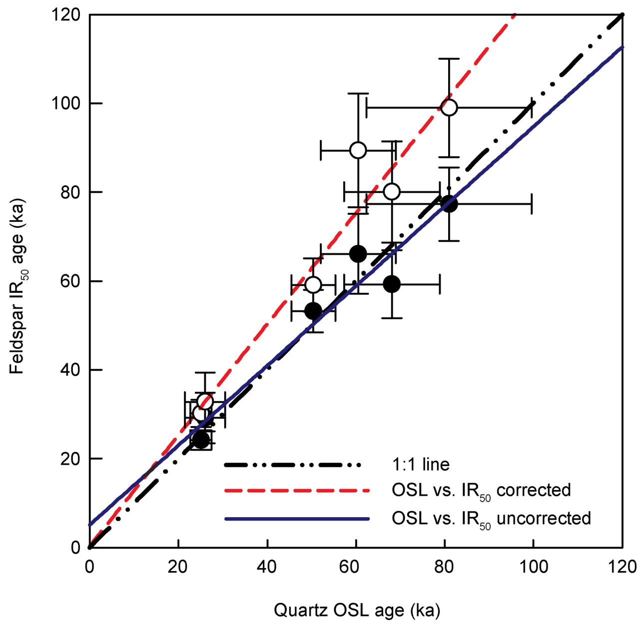


**Figure 10.** Quartz OSL age plotted vs. uncorrected (black circles) and fading-corrected (open circles) feldspar $IR_{50}$ age (both multiple and single grain). Note the consistency of quartz OSL ages with uncorrected $IR_{50}$ ages. Functions of the regressions lines are $IR_{50}$ uncorrected $= 5.039 + 0.897 \times$ OSL and $IR_{50}$ corrected $= 0.263 + 1.250 \times$ OSL ($r^2 = 0.95$ for both regressions).

A substantial portion of our samples that show indication of partial bleaching (BIR-2, MÜB-5-7, SZB-1 and 2) was sampled from homogeneous sand layers in gravel successions, which indicate proximal, high-energetic meltwater. Our findings are in contrast with observations from the southern Scandinavian Ice Sheet, where good bleaching is found for glaciofluvial samples after short transport distances (e.g. Alexanderson and Murray, 2012). A possible explanation would be that glaciers from the foreland of the Swiss Alps were characterised by meltwater channels with relatively small surfaces, often limited by pronounced relief. For the margin of the Scandinavian Ice Sheet, extended outwash plains with low relief (sandur) are expected. The large surface of the ice shield likely also induced katabatic winds and related aeolian reworking in the outwash plains, greatly increasing the probability of signal resetting as discussed by Lüthgens et al. (2011).

## 5.2 The last glacial advance

Sample BIR-1 (OSL: 50.4±4.9 ka; $IR_{50}$: 53.2±4.8 ka) gives a minimum age estimate for soil formation and the massive gravel deposition below but, due to the lack of suitable layers for dating, the age of this horizon is not further constrained. Sample BIR-2 represents an early phase of aggradation ($IR_{50}$: 30.4 ± 4.4 ka) of glaciofluvial gravel, similar to ages of ca. 27 to 29 ka reported from the northern part of Birrfeld (Gaar et al., 2014). Gravel aggradation in the neighbouring Aare Valley (SZB-1: $IR_{50}$: 22.6±6.0 ka, SZB-2 OSL: 26.0 ± 4.5 ka, $IR_{50}$: 29.2 ± 5.7 ka) also occurred during this early phase. The maximum ice extent at the type locality of the Birrfeld glaciation is constrained by sample BIR-3 with consistent OSL ages of 25.1 ± 2.4 ka and $IR_{50}$ 24.2 ± 2.2 ka consistent for sediment just above till. This implies that the maximum ice extent in the study was reached earlier than the global LGM (Fig. 11), dated to 22–19 ka (Yokoyama et al., 2000). This offset is also observed in many other parts of the Alps, as discussed above. It appears that Alpine glaciers reacted faster to climate change compared to the large ice sheets that reached their maximum about 21 ka ago (e.g. Hughes et al., 2016).

Analysing the temporal and spatial reconstruction of Rhine Glacier (Fig. 2) indicates that ice advanced over ca. 160 km, the distance from Chur to the maximal extent, within 6000 years. This corresponds to an advance of the ice front of some 10 m per year, which represents the fastest advance rates estimated for late Holocene Alpine glaciers (Holzhauser, 1995). Such a rapid rate of advance implies that glaciers were warm based, as cold-based glaciers are unlikely to move at such a speed. In this context it is interesting to note that typical outcrops in the northern Alpine foreland often show massive accumulation of glaciofluvial gravel covered by thick till layers that form the present land surface in many areas (e.g. Preusser et al., 2003, 2007, 2011). By contrast, gravel associated with the recession phase, as observed at Birrfeld (Fig. 4), is relatively scarce. It is to hypothesise that the massive aggradation of glaciofluvial sediment below till reflects the warm-based nature of alpine glaciers during their advance. The common absence of such deposits on top of till, representing maximum extent and subsequent meltdown, may indicate that several parts of the glaciers had cold-based ice. An explanation for such a hypothesis might be that the southward shift of the polar front turned the northern foreland into an arctic desert, cutting off the moisture supply with lowering temperatures at the same time. This would have also led to a situation in which humid air from the south precipitates over the main chain and crosses the Alps into the northern foreland as warm dry fall winds (foehn). Reduction in precipitation on the northern side of the Alps combined with dry winds from the south could have led to substantial sublimation of the ice (desiccation of the foreland glaciers), explaining the common lack of meltwater deposits during ice decay.

## 5.3 Evidence for earlier glacier advances

The melt-out till at Rütihof (RÜT-1) reveals consistent quartz and feldspar ages of about 80 ka that may overestimate rather than underestimate the real deposition age. Considering the environmental history of the Alps (cf. Preusser, 2004) implies a likely correlation to the cold phase of MIS 4 (71–54 ka). At Mülligen, sediments interpreted to indicate an

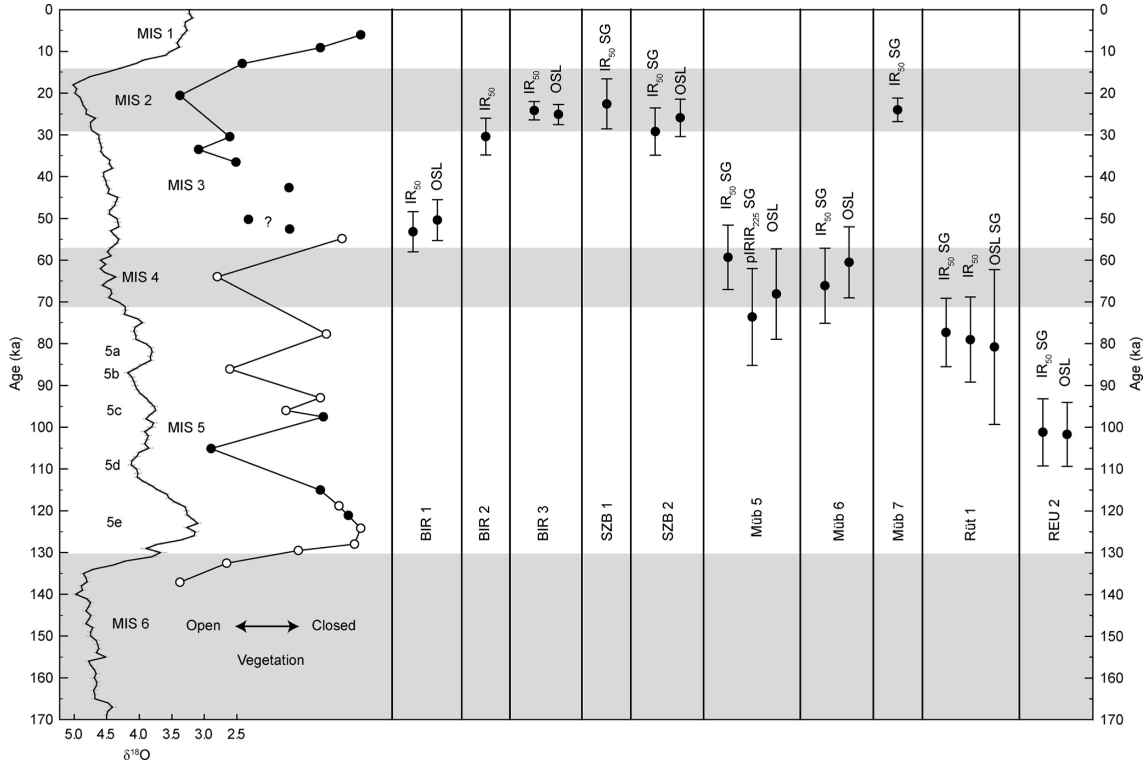


**Figure 11.** Ages obtained in this study compared to the LR04 global stack of benthic $\delta^{18}$O data as a proxy for global ice volume (Lisiecki and Raymo, 2005) and the climatic history of the northern Alpine foreland according to palynostratigraphy (closed circles indicate dated periods, open circles non-dated vegetational periods) compiled by Preusser (2004).

approaching glacier (MÜB-5, MÜB-6) also have consistent quartz and feldspar ages, representing a mean of ca. 64 ka. All available ages are clearly younger than MIS 6 when compared to other studies from the region (e.g. Lowick et al., 2015). Our evidence for substantial glaciation of the Swiss Alpine Foreland during MIS 4 is in concert with other reports from the Western Alps (e.g. Mandier et al., 2003; Preusser et al., 2007), but it is in contradiction to findings from the Eastern Alps. For example, Starnberger et al. (2013) explicitly state that there is no indication of an ice advance into the Inn Valley between the Last Interglacial and MIS 2. If all these observations are correct, the apparent discrepancy might be explained by a different source of humidity during MIS 4 compared to MIS 2. Possibly, the southward shift of the polar front, as to be expected for MIS 4, did not reach as far south as during MIS 2. This could have resulted in a large moisture delivery to the western Alps. This excess of humidity would explain a larger MIS 4 glacier extent in the Lyon area compared to MIS 2, as this ice is expected to originate mainly from the Savoyan Alps (Coutterand et al., 2009), the first orographic obstacle where high precipitation would have occurred. The west–east trend of decreasing MIS 4 glaciation extension could also have had an additional topographic reason, as the accumulation areas in the eastern Alps are about 1000 m lower than in the west.

The age of ca. 100 ka for the REU sample (OSL: $101.7 \pm 7.6$ ka, $IR_{50}$: $101.2 \pm 8.0$ ka) falls in the transition from MIS 5d to MIS 5c, a time considered to be cold, with open vegetation (Welten, 1981), for which a glacier advance in eastern Switzerland has been postulated (Preusser et al., 2003). However, a direct link between glacier presence in the foreland and the deposition of the dated sand is not possible.

## 6 Conclusions

Luminescence dating of glacial sediments remains challenging, as partial bleaching has to be identified and statistical age models need to be applied cautiously. It is shown here that the fading correction of feldspar $IR_{50}$ ages tends to age overestimation compared to quartz OSL, whereas the uncorrected $IR_{50}$ ages are mainly in better agreement with the latter. This confirms previous observations that fading determined in the laboratory rates may not necessarily represent signal loss occurring in nature. As in previous studies, there are indications that feldspar $pIRIR_{225}$ is of limited use in sedimentary environments with low bleaching probabilities.

In this study, the last glacier advance of the Reuss Glacier into the Swiss Alpine Foreland at the type locality of the Birrfeld glacial is consistently dated by quartz OSL and feldspar $IR_{50}$ to about 25 ka. This age is in good agreement with other age estimates, indicating that the maximum of the last glacier advance into the foreland of the NW Alps was reached before the global LGM. An earlier glacier advance is likely constrained to MIS 4. The apparent absence of this advance in the Eastern Alps might be explained by only a moderate southward shift of the polar front during MIS 4, bringing humidity mainly to the Western Alps.

**Data availability.** All data relevant for this contribution are presented within the article itself or the Supplement.

**Supplement.** The supplement related to this article is available online at: https://doi.org/10.5194/egqsj-68-53-2019-supplement.

**Author contributions.** DG carried out field work and processed, measured and analysed the samples. He wrote the first draft of the manuscript and developed most of the illustrations. HRG suggested field sites and joined the sampling. He contributed with text about the sampling sites and the regional geology. FP designed the project, secured funding and supervised DG during his PhD. He re-wrote part of the manuscript and developed Fig. 6 and the Supplement. All authors contributed to the discussion and interpretation of the presented research results.

**Competing interests.** The authors declare that they have no conflict of interest.

**Acknowledgements.** Naki Akçar is thanked for help with the recalculation of $^{10}$Be ages. Martin Robyr is thanked for guidance with the electron microprobe analysis. We thank Tony Reimann and two anonymous reviewers for their detailed constructive comments on earlier versions of the article.

**Financial support.** This research has been supported by the Swiss National Science Foundation (grant no. 200021_126784 and 200020_144456). The article processing charge was funded by the German Research Foundation (DFG) and the University of Freiburg in the funding programme Open Access Publishing.

## References

Aitken, M. J.: Thermoluminescence dating, Academic Press, London, 359 pp., 1985.

Alexanderson, H. and Murray, A. S.: Problems and potential of OSL dating Weichselian and Holocene sediments in Sweden, Quaternary Sci. Rev., 44, 37–50, 2012.

Auclair, M., Lamothe, M., and Huot, S.: Measurement of anomalous fading for feldspar IRSL using SAR, Radiat. Meas., 37, 487–492, 2003.

Balco, G., Stone, J. O., Lifton, N. A., and Dunai, T. J.: A complete and easily accessible means of calculating surface exposure ages or erosion rates from $^{10}$Be and $^{26}$Al measurements, Quat. Geochronol., 3, 174–195, 2008.

Balco, G., Briner, J., Finkel, R. C., Rayburn, J. A., Ridge, J. C., and Schaefer, J. M.: Regional beryllium-10 production rate calibration for late-glacial northeastern North America, Quat. Geochronol., 4, 93–107, 2009.

Bausch, W., Geyer, O. F., Schober, T., and Schreiner, A.: Zur Geologie des badischen Klettgaus, Jahresb. Mitt. Oberrhein. Geol. Ver. NF, 71, 199–224, 1989.

Becker, P., Seguinot, J., Jouvet, G., and Funk, M.: Last Glacial Maximum precipitation pattern in the Alps inferred from glacier modelling, Geogr. Helv., 71, 173–187, https://doi.org/10.5194/gh-71-173-2016, 2016.

Bini, A., Buoncristiani, J.F., Coutterand, S., Ellwanger, D., Felber, M., Florineth, D., Graf, H. R., Keller, O., Kelly, M., Schlüchter, C., and Schoeneich, P.: Die Schweiz während des letzteiszeitlichen Maximums (LGM) (Map 1 : 500 000), swisstopo, Wabern, 2009.

Blair, M. W., Yukihra, E. G., and McKeever, S. W. S.: Experiences with single-aliquot OSL procedures using coarse-grain feldspars, Radiat. Meas., 39, 361–374, 2005.

Blomdin, R., Murray, A., Thomsen, K. J., Buylaert, J. P., Sohbati, R., Jansson, K. N., and Alexanderson, H.: Timing of the deglaciation in southern Patagonia: Testing the applicability of K-Feldspar IRSL, Quat. Geochronol., 10, 264–272, 2012.

Bøtter-Jensen, L., Andersen, C. E., Duller, G. A. T., and Murray, A. S.: Developments in radiation, stimulation and observation facilities in luminescence measurements, Radiat. Meas., 37, 535–541, 2003.

Bronk Ramsey, C.: Bayesian Analysis of Radiocarbon Dates, Radiocarbon, 51, 337–360, 2009.

Burga, C. A.: Glazialmorphologische Untersuchungen im Hinterrhein-Tal und am Bernhardina-Pass, Vierteljahrsschr. Naturforsch. Ges. Zürich, 126, 237–267, 1981.

Buylaert, J. P., Murray, A. S., Thomsen, K. J., and Jain, M.: Testing the potential of an elevated temperature IRSL signal from K-feldspar, Radiat. Meas., 44, 560–565, 2009.

Buylaert, J. P., Jain, M., Murray, A. S., Thomsen, K. J., Thiel, C., and Sohbati, R.: A robust feldspar luminescence dating method for Middle and Late Pleistocene sediments, Boreas, 41, 435–451, 2012.

Clark, P. U., Dyke, A. S., Shakun, J. D., Carlson, A. E., Clark, J., Wohlfarth, B., Mitrovica, J. X., Hostetler, S. W., and McCabe, A. M.: The Last Glacial Maximum, Science, 325, 710–714, 2009.

Coutterand, S., Schoeneich, P., and Nicoud, G.: Le lobe glaciaire lyonnais au maximum würmien: glacier du Rhône ou/et glaciers savoyards?, in: Neige et glace de montagne. Reconstitution, dynamique, pratiques, edited by: Deline, P. and Ravanel, L., 9–20, Cahiers de Géographie ed. EDYTEM, Université de Savoie, Le Bourget du Lac Cedex, 2009.

de Graaf, L. W. S.: Zur Altersbestimmung eines Mammut-Stosszahns (Kiesgrube Hochwacht) und ihre Bedeutung für die mophostratigraphische Einstufung der Quartärablagerungen zwischen Bregenz und Langen, Schriften des Vorarlberger Landesmuseums, A5, 23–28, 1992.

de Graaf, L. W. S. and de Jong, M. G. G.: Notes on the Alpine Rhine glacier and the chronostratigraphy of the Upper Würm, Mededelingen Rijks Geologische Dienst, 52, 317–330, 1995.

Dehnert, A., Lowick, S. E., Preusser, F., Anselmetti, F. S., Drescher-Schneider, R., Graf, H. R., Heller, F., Horstmeyer, H., Kemna, H. A., Nowaczyk, N. R., Züger, A., and Furrer, H.: Evolution of an overdeepened trough in the northern Alpine Foreland at Niederweningen, Switzerland, Quaternary Sci. Rev., 34, 127–145, 2012.

de Jong, M. G. G.: Quaternary deposits and landforms of Western Allgäu (Germany) and the deglaciation after the last major Pleistocene ice advance, 186 pp., PhD thesis, Amsterdam, 1983.

Duller, G. A. T.: Luminescence dating of poorly bleached sediments from Scotland, Quaternary Sci. Rev., 13, 521–524, 1994.

Duller, G. A. T.: Single grain optical dating of glacigenic deposits, Quat. Geochronol., 1, 296–304, 2006.

Duller, G. A. T.: Single-grain optical dating of Quaternary sediments: why aliquot size matters in luminescence dating, Boreas, 37, 589–612, 2008.

Duller, G. A. T.: Luminescence Analyst, 4.11 edn., Aberystwyth University, Aberystwyth, 2013.

Ehlers, J. and Gibbard, P. L.: Quaternary Glaciations Extent and Chronology Part I: Europe, Developments in Quaternary Sciences, Elsevier, Amsterdam, 2004.

Federici, P. R., Granger, D. E., Ribolini, A., Spagnolo, M., Pappalardo, M., and Cyr, A. J.: Last Glacial Maximum and the Gschnitz stadial in the Maritime Alps according to $^{10}$Be cosmogenic dating, Boreas, 41, 277–291, 2012.

Fiebig, M. and Preusser, F.: The age of fluvial sediments from the Ingolstadt area (Bavaria) and their significance for the stratigraphy of the ice age in the Alpine foreland, Zeitschr. f. Geomorph, 47, 449–467, 2003.

Florineth, D. and Schlüchter, C.: Alpine evidence for atmospheric circulation patterns in Europe during the last glacial maximum, Quaternary Res., 54, 295–308, 2000.

Frank, S. and Rey, R.: N4 Flurlingen: Durch Tunnelbau beschleunigte Kriechbewegungen und deren Konsequenzen für die Bauausführung, in: Instabile Hänge und andere risikorelevante natürliche Prozesse, edited by: Verità, M., Birkhäuser, Basel, 1996.

Frenzel, B.: Über einen frühen letzteiszeitlichen Vorstoß des Rheingletschers in das deutsche Alpenvorland, in: Klimageschichtliche Probleme der letzten 130 000 Jahre, edited by: Frenzel, B., 377–400 pp., Gustav Fischer, Stuttgart, 1991.

Fuchs, M. and Owen, L. A.: Luminescence dating of glacial and associated sediments: review, recommendations and future directions, Boreas, 37, 636–659, 2008.

Gaar, D. and Preusser, F.: Luminescence dating of mammoth remains from northern Switzerland, Quat. Geochronol., 10, 257–263, 2012.

Gaar, D., Lowick, S. E., and Preusser, F.: Performance of different luminescence approaches for the dating of known-age glaciofluvial deposits from northern Switzerland, Geochronometria, 41, 65–80, 2014.

Galbraith, R. F., Roberts, R. G., Laslett, G. M., Yoshida, H., and Olley, J. M.: Optical dating of single and multiple grains of quartz from jinmium rock shelter, northern Australia, part 1, Experimental design and statistical models, Archaeometry, 41, 339–364, 1999.

Geyh, M. A. and Schreiner, A.: $^{14}$C-Datierungen an Knochen- und Stoßzahnfragmenten aus würmeiszeitlichen Ablagerungen im westlichen Rheingletschergebiet, Eiszeit. U. Gegenw., 34, 155–161, 1984.

Graf, H. R.: Die Deckenschotter der zentralen Nordschweiz, Diss. ETH Zürich, Zürich, 10205, 1993.

Graf, H. R.: Stratigraphie von Mittel- und Spätpleistozän in der Nordschweiz, 198 p. Landesgeologie, Wabern, 2009.

Haeberli, W.: Glaciological conditions in northern Switzerland during recent Ice Ages, NAGRA NAB 10–18, 28 pp., 2010.

Haeberli, W. and Schlüchter, C.: Geological evidence to constrain modelling of the Late Pleistocene Rhonegletscher (Switzerland), IAHS, Wallingford, 170, 333–346, 1987.

Headley, R. M. and Ehlers, T. A.: Ice flow models and glacial erosion over multiple glacial–interglacial cycles, Earth Surf. Dynam., 3, 153–170, https://doi.org/10.5194/esurf-3-153-2015, 2015.

Heer, A. J., Adamiec, G., and Moska, P.: How many grains are there on a single aliquot?, Ancient TL, 30, 9–16, 2012.

Holzhauser, H.: Gletscherschwankungen innerhalb der letzten 3200 Jahre am Beispiel des grossen Aletsch- und des Gornergletschers: neue Ergebnisse, in: Gletscher im ständigen Wandel, edited by: SANW, 101–122 pp., vdf Hochschulverlag AG an der ETH Zürich, Zürich, 1995.

Hughes, A. L. C., Gyllencreutz, R., Lohne, O. S., Mangerud, J., and Svendsen, J. I.: The last Eurasian ice sheets a chronological database and time-slice reconstruction, DATED-1, Boreas, 45, 1–45, 2016.

Hughes, P. D., Gibbard, P. L., and Ehlers, J.: Timing of glaciation during the last glacial cycle: evaluating the concept of a global "Last Glacial Maximum" (LGM), Earth-Sci. Rev., 125, 171–198, 2013.

Hünermann, K. A.: Eiszeit-Säugetiere aus dem Kanton Zürich, Vierteljahrsschr. Naturforsch. Ges. Zürich, 130, 229–250, 1985.

Huntley, D. J. and Baril, M. R.: The K content of the K-feldspars being measured in optical dating or in thermoluminescence dating, Ancient TL, 15, 11–14, 1997.

Huntley, D. J. and Lamothe, M.: Ubiquity of anomalous fading in K-feldspars and the measurement and correction for it in optical dating, Can. J. Earth Sci., 38, 1093–1106, 2001.

Ivy-Ochs, S., Schäfer, J., Kubik, P., Synal, H.-A., and Schlüchter, C.: Timing of deglaciation on the northern Alpine foreland (Switzerland), Eclogae Geol. Helv., 97, 47–55, 2004.

Ivy-Ochs, S., Kerschner, H., Reuther, A., Preusser, F., Heine, K., Maisch, M., Kubik, P. W., and Schlüchter, C.: Chronology of the last glacial cycle in the European Alps, J. Quat. Sci., 23, 559–573, 2008.

Jarvis, A., Reuter, H. I., Nelson, A., and Guevara, E.: Hole-filled seamless SRTM data V4. International Centre for Tropical Agriculture (CIAT), available at: http://srtm.csi.cgiar.org (last access: April 2012), 2008.

Jimenez-Sanchez, M., Rodriguez-Rodriguez, L., Garcia-Ruiz, J. M., Dominguez-Cuesta, M. J., Farias, P., Valero-Garces, B., Moreno, A., Rico, M., and Valcarcel, M.: A review of glacial geomorphology and chronology in northern Spain: Timing and regional variability during the last glacial cycle, Geomorphology, 196, 50–64, 2013.

Keller, O. and Krayss, E.: Datenlage und Modell einer Rhein-Linth-Vorlandvergletscherung zwischen Eem-Interglazial und Hochwürm, GeoArchaeoRhein, 2, 121–138, 1998.

Keller, O. and Krayss, E.: Der Rhein-Linth-Gletscher im letzten Hochglazial 1. Teil: Einleitung, Aufbau und Abschmelzen des Rhein-Linth-Gletscher im Oberen Würm, Vierteljahrsschr. Naturforsch. Ges. Zürich, 150, 19–32, 2005a.

Keller, O. and Krayss, E.: Der Rhein-Linth-Gletscher im letzten Hochglazial 2. Teil: Datierung und Modelle der Rhein-Linth-Vergletscherung, Klima Rekonstruktionen, Vierteljahrsschr. Naturforsch. Ges. Zürich, 150, 69–85, 2005b.

Klasen, N., Fiebig, M., Preusser, F., Reitner, J. M., and Radtke, U.: Luminescence dating of proglacial sediments from the Eastern Alps, Quaternary Int., 164–165, 21–32, 2007.

Klasen, N., Fiebig, M., and Preusser, F.: Applying luminescence methodology to key sites of Alpine glaciations in Southern Germany, Quaternary Int., 420, 249–258, 2016.

Kock, S., Huggenberger, P., Preusser, F., Rentzel, P., and Wetzel, A.: Formation and evolution of the Lower Terrace of the Rhine River in the area of Basel, Swiss J. Geosci., 102, 307–321, 2009a.

Kock, S., Kramers, J. D., Preusser, F., and Wetzel, A.: Dating of Late Pleistocene terrace deposits of the River Rhine using Uranium series and luminescence methods: Potential and limitations, Quat. Geochronol., 4, 363–373, 2009b.

Köppen, W. and Wegener, A.: Die Klimate der geologischen Vorzeit, 257 pp., Gebrüder Borntraeger, Berlin, 1924.

Köppen, W. and Wegener, A.: Die Klimate der geologischen Vorzeit – Ergänzungen und Berichtigungen, 38 pp., Gebrüder Borntraeger, Berlin, 1940.

Kreutzer, S., Schmidt, C., Fuchs, M.C., Dietze, M., Fischer, M., and Fuchs, M.: Introducing an R package for luminescence dating analysis, Ancient TL, 30, 1–8, 2012.

Kuhlemann, J., Rohling, E.J., Krumrei, I., Kubik, P., Ivy-Ochs, S., and Kucera, M.: Regional synthesis of Mediterranean atmospheric circulation during the last glacial maximum, Science, 321, 1338–1340, 2008.

Kulig, G.: Erstellung einer Auswertesoftware zur Altersbestimmung mittels Lumineszenzverfahren unter spezieller Berücksichtigung des Einflusses radioaktiver Ungleichgewichte in der $^{238}$U-Zerfallsreihe, BSc thesis, Technische Bergakademie Freiberg, Freiberg, 2005.

Lapp, T., Jain, M., Thomsen, K. J., Murray, A. S., and Buylaert, J.-P.: New luminescence measurement facilities in retrospective dosimetry, Radiat. Meas., 47, 803–808, 2012.

Link, A. and Preusser, F.: Hinweise auf eine Vergletscherung des Kemptener Beckens (Südwest-Bayern) im Mittleren Würm, Eiszeit und Gegenw., 55, 64–87, 2005.

Lisiecki, L. E. and Raymo, M. E.: A Pliocene-Pleistocene stack of 57 globally distributed benthic delta O-18 records, Paleoceanography, 20, PA1003, 2005.

Lister, G., Kelts, K., Schmid, R., Bonani, G., Hofmann, H., Morenzoni, E., Nessi, M., Suter, M., and Wolfli, W.: Correlation of the Paleoclimatic Record in Lacustrine Sediment Sequences – $^{14}$C Dating by AMS, Nucl. Instrum. Meth B, 5, 389–393, 1984.

Lowick, S. E., Trauerstein, M., and Preusser, F.: Testing the application of post IR-IRSL dating to fine grain waterlain sediments, Quat. Geochronol., 8, 33–40, 2012.

Lowick, S. E., Büchi, M., Gaar, D., Graf, H. R., and Preusser, F.: Luminescence dating of Middle Pleistocene proglacial deposits from northern Switzerland: methodological aspects and stratigraphical conclusions, Boreas, 44, 459–482, 2015.

Lukas, S., Spencer, J. Q. G., Robinson, R. A. J., and Benn, D. I.: Problems associated with luminescence dating of Late Quaternary glacial sediments in the NW Scottish Highlands, Quat. Geochronol., 2, 243–248, 2007.

Lüthgens, C., Böse, M., and Preusser, F.: Age of the Pomeranian ice-marginal position in northeastern Germany determined by Optically Stimulated Luminescence (OSL) dating of glaciofluvial sediments, Boreas, 40, 598–615, 2011.

Mandier, P.: Reconstitution de l'expansion glaciaire de peidmont des stades. A et D des glaciers würmiens du Rhône et de l'Isère: implication et origine de leur disparité, Quaternaire 14, 129–133, 2003.

Mandier, P., Petiot, R., Argant, J., and Evin, J.: Chronostratigraphie des accumulations würmiennes dans la moyenne vallée du Rhône. L'apport des dates radiocarbon, Quaternaire, 14, 113–127, 2003.

Mauz, B., Packman, S., and Lang, A.: The alpha effectiveness in silt-sized quartz: New data obtained by single and multiple aliquot protocols, Ancient TL, 24, 47–52, 2006.

McEvoy, F. M., Schofield, D. I., Shaw, R. P., and Norris, S.: Tectonic and climatic considerations for deep geological disposal of radioactive waste: A UK perspective, Sci. Total Environ., 571, 507–521, 2016.

Milanković, M.: Kanon der Erdbestrahlung und seine Anwendung auf das Eiszeitenproblem, 655 pp., Königlich Serbische Akademie, Belgrad, 1941.

Moegle, E.: Supermaximalphasen des würmhochglazialen Rhein-Vorland-Gletschers, Jahresb. Mitt. Oberrh. Geol. Ver. NF, 76, 335–351, 1994.

Monegato, G., Ravazzi, C., Donegana, M., Pini, R., Calderoni, G., and Wick, L.: Evidence of a two-fold glacial advance during the last glacial maximum in the Tagliamento end moraine system (eastern Alps), Quaternary Res., 68, 284–302, 2007.

Murray, A. S. and Wintle, A. G.: Luminescence dating of quartz using an improved single-aliquot regenerative-dose protocol, Radiat. Meas., 32, 57–73, 2000.

Murray, A. S., Thomsen, K. J., Masuda, N., Buylaert, J. P., and Jain, M.: Identifying well-bleached quartz using the different bleaching rates of quartz and feldspar luminescence signals, Radiat. Meas., 47, 688–695, 2012.

Penck, A. and Brückner, E.: Die Alpen im Eiszeitalter, 1157 pp., Tauchnitz, Leipzig, 1901–1909.

Pietsch, T. J., Olley, J. M., and Nanson, G. C.: Fluvial transport as a natural luminescence sensitiser of quartz, Quat. Geochronol., 3, 365–376, 2008.

Prescott, J. R. and Hutton, J. T.: Cosmic ray contributions to dose rates for luminescence and ESR dating: Large depths and long-term time variations, Radiat. Meas., 23, 497–500, 1994.

Preusser, F.: Luminescence dating of fluvial sediments and overbank deposits from Gossau, Switzerland: fine grain dating, Quaternary Sci. Rev., 18, 217–222, 1999.

Preusser, F.: Towards a chronology of the Late Pleistocene in the northern Alpine Foreland, Boreas, 33, 195–210, 2004.

Preusser, F. and Degering, D.: Luminescence dating of the Niederweningen mammoth site, Switzerland, Quaternary Int., 164–165, 106–112, 2007.

Preusser, F. and Graf, H.: Erste Ergebnisse von Lumineszenzdatierungen eiszeitlicher Ablagerungen der Nordschweiz, Jahresb. Mitt. Oberrh. Geol. Ver. NF, 84, 419–438, 2002.

Preusser, F. and Kasper, H. U.: Comparison of dose rate determination using high-resolution gamma spectrometry and inductively coupled plasma-mass spectrometry, Ancient TL, 19, 19–23, 2001.

Preusser, F., Müller, B. U., and Schlüchter, C.: Luminescence dating of sediments from the Luthern Valley, central Switzerland, and implications for the chronology of the last glacial cycle, Quaternary Res., 55, 215–222, 2001.

Preusser, F., Geyh, M. A., and Schlüchter, C.: Timing of late pleistocene climate change in lowland Switzerland, Quaternary Sci. Rev., 22, 1435–1445, 2003.

Preusser, F., Ramseyer, K., and Schlüchter, C.: Characterisation of low luminescence intensity quartz from Westland, New Zealand, Radiat. Meas., 41, 871–877, 2006.

Preusser, F., Blei, A., Graf, H., and Schlüchter, C.: Luminescence dating of Würmian (Weichselian) proglacial sediments from Switzerland: methodological aspects and stratigraphical conclusions, Boreas, 36, 130–142, 2007.

Preusser, F., Reitner, J., and Schlüchter, C.: Distribution, geometry, age and origin of overdeepened valleys and basins in the Alps and their foreland, Swiss J. Geosci., 103, 407–426, 2010.

Preusser, F., Graf, H. R., Keller, O., Krayss, E., and Schlüchter, C.: Quaternary glaciation history of northern Switzerland, E&G Quaternary Sci. J., 60, 21, https://doi.org/10.3285/eg.60.2-3.06, 2011.

Ravazzi, C., Pini, R., Badino, F., De Amicis, M., Londeix, L., and Reimer, P. J.: The latest LGM culmination of the Garda Glacier (Italian Alps) and the onset of glacial termination. Age of glacial collapse and vegetation chronosequence, Quaternary Sci. Rev., 105, 26–47, 2014.

Reber, R., Akçar, N., Ivy-Ochs, S., Tikhomirov, D., Burkhalter, R., Zahno, C., Lüthold, A., Kubik, P. W., Vockenhuber, C., and Schlüchter, C.: Timing of retreat of the Reuss Glacier (Switzerland) at the end of the Last Glacial Maximum, Swiss J. Geosci., 107, 293–307, 2014.

Reimann, T., Tsukamoto, S., Naumann, M., and Frechen, M.: The potential of using K-rich feldspars for optical dating of young coastal sediments A test case from Darss-Zingst peninsula (southern Baltic Sea coast), Quat. Geochronol., 6, 207–222, 2011.

Reimer, P. J., Bard, E., Bayliss, A., Beck, J. W., Blackwell, P. G., Ramsey, C. B., Grootes, P. M., Guilderson, T. P., Haflidason, H., Hajdas, I., Hatté, C., Heaton, T. J., Hoffmann, D. L., Hogg, A. G., Hughen, K. A., Kaiser, K. F., Kromer, B., Manning, S. W., Niu, M., Reimer, R. W., Richards, D. A., Scott, E. M., Southon, J. R., Staff, R. A., Turney, C. S. M., and van der Plicht, J.: IntCal13 and Marine13 Radiocarbon Age Calibration Curves 0–50 000 Years cal BP, Radiocarbon, 55, 1869–1887, 2013.

Reuther, A. U., Fiebig, M., Ivy-Ochs, S., Kubik, P. W., Reitner, J. M., Jerz, H., and Heine, K.: Deglaciation of a large piedmont lobe glacier in comparison with a small mountain glacier – new insight from surface exposure dating. Two studies from SE Germany, E&G Quaternary Sci. J., 60, 18, https://doi.org/10.3285/eg.60.2-3.03, 2011.

Rowan, A. V., Roberts, H. M., Jones, M. A., Duller, G. A. T., Covey-Crump, S. J., and Brocklehurst, S. H.: Optically stimulated luminescence dating of glaciofluvial sediments on the Canterbury Plains, South Island, New Zealand, Quat. Geochronol., 8, 10–22, 2012.

Schlüchter, C.: The Quaternary Glaciations of Switzerland, with Special Reference to the Northern Alpine Foreland, Quaternary Sci. Rev., 5, 413–419, 1986.

Schlüchter, C. and Röthlisberger, C.: 100 000 Jahre Gletschergeschichte, in: Gletscher im ständigen Wandel, edited by: SANW, 47–63, vdf Hochschulverlag AG an der ETH Zürich, Zürich, 1995.

Schlüchter, C., Maisch, M., Suter, J., Fitze, P., Keller, W. A., Burga, C. A., and Wynistorf, E.: Das Schieferkohlen-Profil von Gossau (Kanton Zürich) und seine stratigraphische Stellung innerhalb der letzten Eiszeit, Vierteljahrsschr. Naturforsch. Ges. Zürich, 132, 135–174, 1987.

Schreiner, A.: Einführung in die Quartärgeologie, 257 pp., E. Schweizerbart, Stuttgart, 1992.

Seguinot, J., Ivy-Ochs, S., Jouvet, G., Huss, M., Funk, M., and Preusser, F.: Modelling last glacial cycle ice dynamics in the Alps, The Cryosphere, 12, 3265–3285, https://doi.org/10.5194/tc-12-3265-2018, 2018.

Sohbati, R., Murray, A. S., Buylaert, J. P., Ortuno, M., Cunha, P. P., and Masana, E.: Luminescence dating of Pleistocene alluvial sediments affected by the Alhama de Murcia fault (eastern Betics, Spain) – a comparison between OSL, IRSL and post-IR IRSL ages, Boreas, 41, 250–262, 2012.

Spencer, J. Q. and Owen, L. A.: Optically stimulated luminescence dating of Late Quaternary glaciogenic sediments in the upper Hunza valley: validating the timing of glaciation and assessing dating methods, Quaternary Sci. Rev., 23, 175–191, 2004.

Spötl, C., Reimer, P. J., Starnberger, R., and Reimer, R. W.: A new radiocarbon chronology of Baumkirchen, stratotype for the onset of the Upper Würmian in the Alps, J. Quat. Sci., 28, 552–558, 2013.

Starnberger, R., Rodnight, H., and Spötl, C.: Chronology of the Last Glacial Maximum in the Salzach Palaeoglacier Area (Eastern Alps), J. Quaternary Sci., 26, 502–510, 2011.

Starnberger, R., Drescher-Schneider, R., Reitner, J. M., Rodnight, H., Reimer, P. J., and Spötl, C.: Late Pleistocene climate change and landscape dynamics in the Eastern Alps: the inner-alpine Unterangerberg record (Austria), Quaternary Sci. Rev., 68, 17–42, 2013.

Stokes, C. R., Tarasov, L., Blomdin, R., Cronin, T. M., Fisher, T. G., Gyllencreutz, R., Hättestrand, C., Heyman, J., Hindmarsh, R., Hughes, A., Jakobsson, M., Kirchner, N., Livingstone, S. J., Margold, M., Murton, J., Noormets, R., Peltier, R. W., Peteet, D. M., Piper, D., Preusser, F., Renssen, H., Roberts, D. H., Roche, D., Saint-Ange, F., Stroeven, A. P., and Teller, J. T.: On the reconstruction of palaeo-ice sheets: Recent advances and future challenges, Quaternary Sci. Rev., 125, 15–49, 2015.

Thomsen, K. J., Murray, A. S., Jain, M., and Botter-Jensen, L.: Laboratory fading rates of various luminescence signals from feldspar-rich sediment extracts, Radiat. Meas., 43, 1474–1486, 2008.

Thomsen, K. J., Murray, A. S., Buylaert, J. P., Jain, M., Hansen, J. H., and Aubry, T.: Testing single-grain quartz OSL methods using sediment samples with independent age control from the Bordes-Fitte rockshelter (Roches d'Abilly site, Central France), Quat. Geochronol., 31, 77–96, 2016.

Trauerstein, M., Lowick, S., Preusser, F., Rufer, D., and Schlunegger, F.: Exploring fading in single grain feldspar IRSL measurements, Quat. Geochronol., 10, 327–333, 2012.

Veit, H., Trauerstein, M., Preusser, F., Messmer, T., Gnägi, C., Zech, R., and Wüthrich, L.: Late Glacial/Early Holocene slope deposits on the Swiss Plateau: Genesis and palaeo-environment, Catena, 158, 102–112, 2017.

Wallinga, J.: On the detection of OSL age overestimation using single-aliquot techniques, Geochronometria, 21, 17–26, 2002.

Wallinga, J., Bos, A. J. J., Dorenbos, P., Murray, A. S., and Schokker, J.: A test for anomalous fading correction in IRSL dating, Quat. Geochronol., 2, 216–221, 2007.

Weinhold, H.: Beiträge zur Kenntnis des Quartärs im württembergischen Allgäu zwischen östlichem Bodensee und Altdorfer Wald, PhD thesis, Universität Tübingen, Tübingen, 1973.

Welten, M.: Verdrängung und Vernichtung der anspruchsvollen Gehölze am Beginn der letzten Eiszeit und die Korrelation der Frühwürm-Interstadiale in Mittel- und Nordeuropa, Eiszeit und. Gegenw., 31, 187–202, 1981.

Werner, J.: Über die Zeit zwischen Riss- und Würmglazial, insbesondere im deutschen Rheingletschergebiet, Heidelberger geograph. Arb., 40, 121–130, 1974.

Yokoyama, Y., Lambeck, K., De Deckker, P., Johnston, P., and Fifield, L. K.: Timing of the Last Glacial Maximum from observed sea-level minima, Nature, 406, 713–716, 2000.

E&G Quaternary Sci. J., 68, 75–93, 2019
https://doi.org/10.5194/egqsj-68-75-2019


Open Access E&G Quaternary Science Journal

Research article

# Neolithic settlement dynamics derived from archaeological data and colluvial deposits between the Baar region and the adjacent low mountain ranges, southwest Germany

**Jan Johannes Miera[1,2,*], Jessica Henkner[2,3], Karsten Schmidt[2,3,4], Markus Fuchs[5], Thomas Scholten[2,3], Peter Kühn[2,3], and Thomas Knopf[2,6]**

[1]Historisches Seminar, Professur für Ur- und Frühgeschichte, Universität Leipzig, Ritterstrasse 14, 04109 Leipzig, Germany
[2]Sonderforschungsbereich 1070 RessourcenKulturen, Universität Tübingen, Gartenstrasse 29, 72074 Tübingen, Germany
[3]Research Area Geography, Soil Science and Geomorphology Working Group, Eberhard Karls Universität Tübingen, Rümelinstrasse 19–23, 72070 Tübingen, Germany
[4]eScience-Center, Eberhard Karls Universität Tübingen, Wilhelmstrasse 32, 72074 Tübingen, Germany
[5]Department of Geography, Justus Liebig University Giessen, Senckenberstrasse 1, 35390 Giessen, Germany
[6]Institute for Prehistory, Early History and Medieval Archaeology, Department of Early History, Eberhard Karls Universität Tübingen, Schloss Hohentübingen, 72070 Tübingen, Germany
[*]previously published under the name Jan Johannes Ahlrichs

**Correspondence:** Jan Johannes Miera (jan@miera.de)

**Relevant dates:** Received: 14 January 2019 – Accepted: 21 May 2019 – Published: 27 June 2019

**How to cite:** Miera, J. J., Henkner, J., Schmidt, K., Fuchs, M., Scholten, T., Kühn, P., and Knopf, T.: Neolithic settlement dynamics derived from archaeological data and colluvial deposits between the Baar region and the adjacent low mountain ranges, southwest Germany, E&G Quaternary Sci. J., 68, 75–93, https://doi.org/10.5194/egqsj-68-75-2019, 2019.

**Abstract:** The present study combines archaeological data with archaeopedological data from colluvial deposits to infer Neolithic settlement dynamics between the Baar region, the Black Forest and the Swabian Jura. A review of the state of archaeological research and an analysis of the processes leading to the discovery of the Neolithic sites and thereby the formation of the current archaeological site distribution in these landscapes is presented. The intensity of land use in the study area is compared with other landscapes in southern Germany using site frequencies. Phases of colluvial deposition are dated using AMS $^{14}C$ ages of charcoals and luminescence ages of sediments and interpreted as local proxies for a human presence. Archaeological source criticism indicates that the distribution of the Neolithic sites is probably distorted by factors such as superimposition due to erosion and weathering effects limiting the preservation conditions for Neolithic pottery. A reconstruction of Neolithic settlement dynamics is achieved by complementing the archaeological data with phases of colluviation. Evidence for a continuous land use in the Baar region throughout the Neolithic is provided and sporadic phases of land use on the Swabian Jura and in the Black Forest are identified. In the late and final Neolithic, an intensification of colluvial formation can be noticed in the low mountain ranges.

**Kurzfassung:** In der vorliegenden Studie werden archäologische Daten mit bodenkundlichen Daten aus kolluvialen Ablagerungen verknüpft, um Phasen der Landnutzung während des Neolithikums zu ermitteln und somit neolithische Siedlungsdynamiken zwischen der Baar, dem Schwarzwald und der

Schwäbischen Alb beschreiben zu können. Ausgehend von einer Auswertung der lokalen archäologischen Forschungsgeschichte und einer quellenkritischen Betrachtung des Fundstoffes erfolgt eine Evaluierung der Verbreitung der gegenwärtig bekannten neolithischen Fundstellen. Auf der Basis von Fundstellenfrequenzen wird eine überregionale Einordnung der Intensität der lokalen Siedlungsaktivität vorgenommen. Phasen der Kolluvienbildung werden durch Radiokohlenstoffdatierungen von Holzkohlen und Lumineszenzalter von Sedimenten datiert und als Hinweise auf eine Anwesenheit des Menschen interpretiert. Die quellenkritische Auswertung des Fundstoffes legt den Verdacht nahe, dass die Verbreitung der neolithischen Fundstellen im Arbeitsgebiet durch verschiedene Faktoren beeinflusst wird. Demnach wird die Zugänglichkeit neolithischer Fundstellen durch Über- und Umlagerung aufgrund von Erosion verzerrt und die Erhaltung von Keramik durch lokale Witterungsbedingungen eingeschränkt. Die Beschreibung neolithischer Siedlungsdynamiken gelingt letztlich durch die Korrelation der archäologischen und bodenkundlichen Daten. Für den gesamten Verlauf des Neolithikums lässt sich auf diese Weise eine neolithische Besiedlung der Baar aufzeigen. Im Schwarzwald und auf der Schwäbischen Alb lassen sich hingegen nur sporadische Landnutzungsphasen aufzeigen. Im Spät- und Endneolithikum lässt sich in den Mittelgebirgen eine Verstärkung der Kolluvienbildung beobachten.

## 1 Introduction

The transition from a mobile subsistence based on hunting and gathering to sedentary farming communities marks a turning point in human history. As this shift had far-reaching consequences for the further development of societies, it is often referred to as the "Neolithic Revolution" (Childe, 1936; Teuber et al., 2017). This transition changed not only the human perception of landscapes, but it also had a major impact on the environment (Gerlach, 2003, 2006). The vegetation was affected by local deforestation carried out in order to establish settlements and introduce fields for plant cultivation and for livestock. As soils became an important resource for survival, they needed maintenance with manure and had to be worked with ploughs to ensure sufficient yields (Lüning, 2000). Already in the Early Neolithic, both changes in vegetation and ploughing resulted in the erosion of soils in the vicinity of the settlements (Saile, 1993; Semmel, 1995). The correlate sediments of soil erosion caused by human activities are called colluvial deposits and can be seen as pedosedimentary archives of human activities in the landscape (Leopold and Völkel, 2007; Kadereit et al., 2010; Kühn et al., 2017). Because they are proxies for land use, they can be used to study pre- and early historic human–environment interactions (Dotterweich, 2008; Fuchs et al., 2011; Pietsch and Kühn, 2017; Voigt, 2014). Colluvial deposits always represent the adjacent upward slope areas and therefore provide local "site biographies" with a high resolution (Henkner et al., 2017, 2018a, c).

So far, colluvial deposits have been used mainly to investigate the long-term consequences of pre- and early historic agriculture in the lowlands in southwestern Germany. Prehistoric land use in low mountain ranges has rarely been investigated using archaeopedological methods (Fuchs et al., 2011; Ahlrichs, 2017; Henkner et al., 2018a, c). Especially in these landscapes, pedological datasets from colluvial deposits are an important supplement to archaeological data. Low mountain ranges such as the Black Forest in southwestern Germany are often densely forested and cannot be adequately investigated solely by using archaeological methods. As a consequence, the kind and intensity of prehistoric land use in this landscape has been a matter of speculation for decades (Lais, 1937; Valde-Nowak, 2002). Due to the climate, relief and soils, the agricultural potential of the Black Forest is fairly limited in comparison to adjacent lowlands, where fertile soils on loess are abundant (Gradmann, 1931, 1948). Therefore, it has been suspected for a long time that this unfavourable landscape was basically avoided in prehistoric times and not colonized before the High Middle Ages (e.g. Schreg, 2014; Ahlrichs, 2017).

However, research from recent decades has provided increasing evidence for early phases of land use dating back to the Neolithic (Frenzel, 1997; Valde-Nowak, 1999; Rösch, 2009). Consequently, the archaeological and archaeobotanical research from the last three decades opens the demand for a reassessment of the relationship between favourable and unfavourable landscapes in the Neolithic. Currently, an interdisciplinary research project at the University of Tübingen takes up this issue using methods from prehistoric archaeology and soil science. The research presented in this paper focuses on the following objectives:

- evaluation of the archaeological data and an identification of factors that influenced the current distribution of the Neolithic sites

- discussion of Neolithic settlement dynamics between the Baar region, the Black Forest and the Swabian Jura with a high spatial and chronological resolution by synchronizing archaeological and pedological data.

## 2 Regional setting

The study area is located northwest of Lake Constance in the federal state of Baden-Württemberg, southwestern Germany. Geographically, it includes three landscapes: the southeastern part of the central Black Forest, the Baar region and the southwestern part of the Swabian Jura (Fig. 1). The topography changes significantly between these landscapes (Gradmann, 1931; Reichelt, 1977; Schröder, 2001). Deeply cut valleys with steep slopes characterize the Black Forest with an elevation of up to 1100 m a.s.l., while the southwestern part of the Swabian Jura consists of several high plateaus such as the Heuberg and Lindenberg with elevations up to 1000 m a.s.l., separated by wide river valleys. The Baar region, however, is an elevated basin-shaped landscape (German: *Hochmulde*) with an average elevation of 600–800 m a.s.l. and gentle rolling slopes. In contrast to the Baar region, the two low mountain ranges represent agriculturally unfavourable regions with an oceanic climate (Reichelt, 1977; Tanha, 1986). This is due to high amounts of annual precipitation between 1000 and 1900 mm, low average temperatures ranging from 4 to 6 °C as well as long periods of winter and frost (Gradmann, 1931; Knoch, 1953). The climate in the Baar region is more continental with an average annual temperature of 7–8 °C and an average precipitation of 850 mm per year (Siegmund, 1999, 2006). In addition, the landscapes can be differentiated with regard to their pedology (Kösel and Rilling, 2002; Lazar, 2005; Lazar and Rilling, 2006). Due to fertile soils on loess, the local population used to describe the Baar region as the breadbasket of Baden (Reich, 1859; Deecke, 1921). This is in contrast to the Black Forest, where low-yielding and acidic soils limit the agricultural potential. The Swabian Jura is characterized by a karst landscape with low-yielding soils as well.

## 3 Methods

### 3.1 Assessment of archaeological site distributions

In order to study the pre- and early historic settlement dynamics in this regional setting, an archaeological database was set up in 2014. In total, we recorded 1826 archaeological sites using local area files (German: *Ortsakten*) from the State Office for Cultural Heritage Baden-Württemberg. The sites date from the late Upper Palaeolithic to the end of the 12th century CE (Ahlrichs et al., 2016; Ahlrichs, 2017). The database includes 107 sites that can be used for a discussion of Neolithic land use and settlement dynamics. In large study areas like this, changes in settlement patterns can be described and investigated by comparing distribution maps with different time frames (Schier, 1990; Saile, 1998; Pankau, 2007). However, as suggested by Sommer (1991), Gerhard (2006) and Eggert (2012), it is necessary to examine the archaeological data in detail in order to evaluate distribution patterns and thus to provide a reliable analysis of settlement dynamics.

#### 3.1.1 State of local research

First of all, it is necessary to discuss the genesis of the archaeological record. This includes a literature review with respect to the local history of archaeological research. Within this framework, the general nature of the available data will be presented with focus on geographical as well as chronological aspects. To visualize changes in settlement patterns in a geographic information system (GIS), we digitized the position (EPSG: 31 467) of each recorded site if it could be located within a radius of ±250 m based on recent map information. The detection of settlement dynamics requires an accurate dating for the sites of interest with a chronological resolution as high as possible. Therefore, for each recorded site, the available literature was screened for information regarding its chronological position. We distinguished four degrees of chronological precision: epoch, period, phase and sub-phase (Eggert, 2012; Eggert and Samida, 2013).

#### 3.1.2 Intentionality of site discoveries

In addition, quantitative analyses of the circumstances leading to the discovery of the recorded Neolithic sites are necessary. It is crucial to distinguish intentional discoveries from accidental ones (Wilbertz, 1982; Schier, 1990; Pankau, 2007). Intentional discoveries can be the result of field surveys, aerial photography, analysis of airborne light detection and ranging (lidar) data, research excavations, rescue excavations and small prospections. On the other hand, archaeological sites can be discovered accidentally in the course of construction measures, agricultural and forestry activities, land consolidation (German: *Flurbereinigung*), the extraction of raw materials, or randomly when people go for a walk or go hiking. Finally, historical records mentioning prehistoric sites are also included in this category as well as sites that were already known for a long time by local residents before archaeologists discovered their significance – this applies especially to easily accessible structures such as (burial) mounds, ditches or remnants of walls. For a better assessment of the data for the Neolithic, the interpretation of the analyses will also consider the data for the Bronze Age and the pre-Roman Iron Age.

#### 3.1.3 Depth of sites

In addition, the depth of a site in relation to the modern surface can be inferred from the circumstances of its discovery (Schier, 1990; Saile, 1998). They can be grouped in a way which allows a differentiation between sites discovered below, close to or on the modern surface (see Table 2). This analysis takes the data for the Bronze Age and the pre-Roman Iron Age into account as well.

#### 3.1.4 Site distribution in relation to modern land use

Furthermore, modern land use strategies have an impact on the conservation and visibility of prehistoric sites (Schiffer, 1987; Sommer, 1991). Therefore, an analysis of site distributions against the background of different land use types is recommended (Pankau, 2007; Ahlrichs, 2017). For a study of this kind, we use CORINE Land Cover data, provided by the European Environment Agency (EEA) (European Environment Agency, 2007). This raster dataset with a resolution of 100 m contains 44 types of modern land use classes. However, for archaeological purposes, it is appropriate to aggregate these classes to seven main types: urban areas, forests, arable land, grassland, water bodies, bogs or swamps, and landfills or dumpsites (Ahlrichs, 2017). In order to assess whether certain types of land use may lead to distortions in the distribution of prehistoric sites, we use the $\chi^2$ test (Shennan, 1988).

#### 3.1.5 Weathering effects on pottery, stone and coins

The local topography has an influence on the preservation and accessibility of archaeological sites. At certain relief positions, such as upper slopes or crests, artefacts are exposed to weathering for longer time periods and thus have worse conservation conditions than artefacts on foot slopes or in valleys, where they are covered (and thus protected) by sediment due to erosion (Pasda, 1994, 1998; Saile, 2002). Another important factor is the material the artefacts are made of, i.e. pottery, is less resistant to weathering than stone or metal (Geilmann and Spang, 1958; Schiffer, 1987). Therefore, we defined three groups: pottery, stone artefacts and coins. We used artefacts from settlement contexts and single finds dating to “prehistory”, the Palaeo-, Meso- and Neolithic, the Bronze Age, the pre-Roman Iron Age and the Roman Empire (Table 4). We deliberately excluded artefacts from graves because they are directly buried after deposition and less exposed to weathering. In order to establish whether the local topography does indeed influence the preservation of prehistoric artefacts, we analysed the distribution of the three material groups using a non-dimensional unit called morphometric protection index (MPI) from Yokoyama et al. (2002) in the System for Automated Geoscientific Analyses (SAGA) geographic information system (GIS) (Conrad et al., 2015). This analysis is based on a revised and error-corrected version of a digital elevation model (DEM) with a resolution of 90 m derived from the Shuttle Radar Topography Mission (SRTM) carried out by the National Aeronautics and Space Administration (NASA) (Jarvis et al., 2008). However, due to the chronological composition of the three material groups, this analysis provides only general information regarding the effect of weathering due to topographic openness. Because of the small number of Neolithic sites in this study area, it is not possible to perform such an analysis only for the Neolithic.

#### 3.1.6 Local site frequencies in relation to other study areas

The local site frequency (German: *Fundstellenfrequenz*) is determined and compared with other regions in southern Germany (Fig. 6) in order to evaluate local changes in demography and settlement intensity. This statistical value indicates how many sites came into existence in the course of a century and thus represents an indicator of the intensity of settlement. The site frequency is calculated by multiplying the number of archaeological sites of a period by 100 and then dividing it by the duration of the period in years (Saile, 1998; Schefzik, 2001; Pankau, 2007).

### 3.2 Investigation of colluvial deposits

#### 3.2.1 Field methods

The archaeological database was used to select 13 locations for the investigation of colluvial deposits in the study area (Fig. 1). In the Black Forest, colluvial deposits were investigated at the spring sources of the Breg and the Brigach rivers as well as at Bubenbach and Lehmgrubenhof. In the Baar region, colluvial deposits were studied at Magdalenenberg, Grüningen, Fürstenberg, Geisingen and Spaichingen. Phases of colluvial deposition were studied on the Lindenberg and the Heuberg (Böttingen, Königsheim and Rußberg). Humans can force phases of colluviation through a variety of activities affecting the vegetation, such as grazing and farming, deforestation, mining, building settlements, ramparts or other infrastructures (Starkel, 1987; Leopold and Völkel, 2007). However, it is difficult to conclude directly from a colluvial deposit the activities leading to its formation. In general, colluvial deposits lacking archaeological finds are more likely to be the result of agricultural activities or deforestation than of settlement activities. Colluvial deposits containing scattered archaeological finds qualify as relocated material from a settlement located in the catchment area of the colluvial deposit (Wunderlich, 2000; Niller, 1998). It is possible to correlate phases of colluviation with archaeological data because the deposits can be dated as well (Ahlrichs et al., 2016; Ahlrichs, 2017; Henkner et al., 2017, 2018a, c).

In total, 68 soil profiles were described between 2013 and 2015 in the field (Henkner et al., 2018a) according to the German soil classification system (Ad-hoc-AG Boden, 2005), the Food and Agriculture Organization of the United Nations (FAO, 2006) as well as the world reference base for soil resources (IUSS Working Group WRB, 2015). A main characteristic for anthropogenic colluvial deposits is a lack of autochthonous pedogenic properties; hence their horizons are designated M (M = Latin *Migrare*, to migrate) in the German soil classification system. In our studies, we use the M horizon together with the FAO nomenclature in order to distinguish between colluvial horizons and others with different pedogenic development (Henkner et al., 2017, 2018a, c). To understand the local stratigraphy of colluvial deposits at each

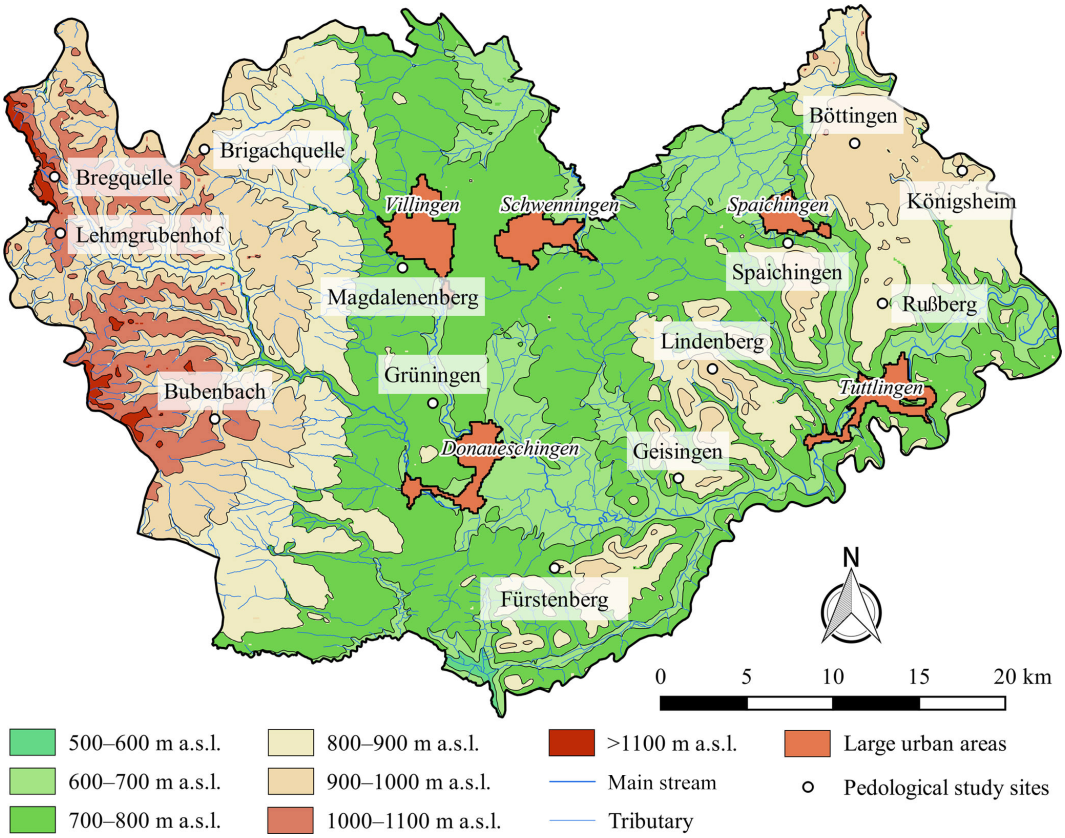


**Figure 1.** Study area and sites of investigated colluvial deposits. The topography is based on a digital elevation model provided by NASA (Jarvis et al., 2008). The mapping of rivers is based on Amtliches Digitales Wasserwirtschaftliches Gewässernetz (AWGN) provided by Landesanstalt für Umwelt, Messungen und Naturschutz Baden-Württemberg (LUBW).

site, we used catenas, i.e. a sequence of soil profiles extending from the upper slope to foot slope positions, thus covering differences in topography, elevation and drainage as well as erosion or deposition. Samples for dating phases of colluvial deposition were taken from profiles regarded as the most characteristic for a site due to their detailed pedostratigraphy (Henkner et al., 2017, 2018a, c).

### 3.2.2 Laboratory methods

All soil chemical analyses were done in the Laboratory of Soil Science and Geoecology at the University of Tübingen. Total C and N contents (mass %) were analysed using oxidative heat combustion at 1150 °C in a He atmosphere (element analyser "vario EL III", Elementar Analysensysteme GmbH, Germany, in CNS mode). Soil organic C content (SOC) was determined using $SOC = C_{total} - CaCO_3 \times 0.1200428$, and soil organic matter (SOM) was calculated using the factor 1.72 (Ad-hoc-AG Boden, 2005; Eberhardt et al., 2013; Henkner et al., 2018c).

To estimate the deposition ages of colluviation, we used two methods: charcoal samples were taken for radiocarbon dating by means of accelerator mass spectrometry (AMS). The samples were processed in the $^{14}C$ laboratories in Jena, Mannheim, Erlangen and Poznań. When interpreting AMS $^{14}C$ from colluvial deposits, it has to be taken into account that the ages represent the point in time at which the carbon exchange between the wood and the biosphere broke off, i.e. the year in which the sampled tree ring was formed (Taylor and Bar-Yosef, 2014). This age does not necessarily coincide with the time when the charcoal was formed. Subsequently, the AMS $^{14}C$ dates usually represent the maximum age of the colluvial deposition from which they were taken (Ahlrichs et al., 2016; Henkner et al., 2017). The calibration of the data was done with OxCal 4.2 and the calibration curve IntCal13 (Bronk Ramsey, 2009; Reimer et al., 2013).

Furthermore, optical stimulated luminescence (OSL) dating was applied, using opaque steel cylinders with a diameter of 4.5 cm for sampling. For equivalent dose (De) determinations, the coarse-grain (90–200 µm) quartz fraction was prepared and measured with a single-aliquot regenerative-dose (SAR) protocol after Murray and Wintle (2000). All luminescence measurements were carried out at the luminescence laboratory of the Justus Liebig University in Giessen, using a Freiberg Instruments Lexsyg reader (Lomax et al., 2014). For data analysis, the R luminescence package (Kreutzer et al.,

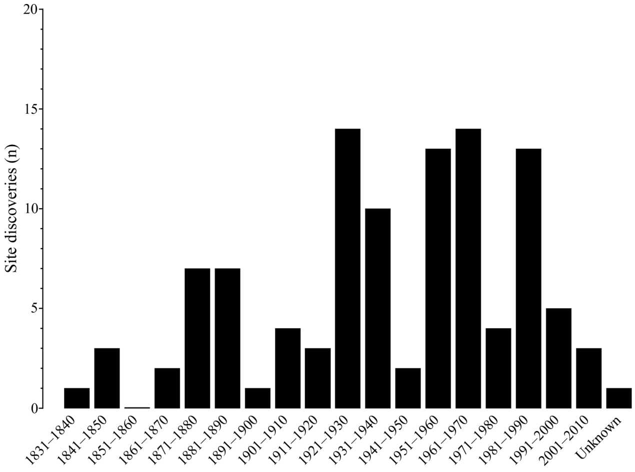


**Figure 2.** Distribution of Neolithic site discoveries.

2016) was used. In contrast to radiocarbon dating, OSL is assumed to date the time of colluvial deposition because it determines the period of time when the sampled sediment was last exposed to sunlight. Postsedimentary reworking (e.g. by bioturbation), however, should generally not be neglected when luminescence ages are interpreted as ages of colluvial deposition (see Reimann et al., 2017). A prerequisite for the successful application of this method is that the sampled sediments were sufficiently exposed to sunlight during their relocation. In case of insufficient daylight exposure, OSL dating would result in an age overestimation (Bußmann, 2014; Henkner et al., 2018a). Nevertheless, colluvial deposits can generally be dated successfully by OSL as demonstrated in numerous studies from various landscapes and cultural periods (Fuchs and Lang, 2009; Kadereit et al., 2010).

## 4 Results

### 4.1 Archaeological data

#### 4.1.1 State of local research

Since the mid-thirties of the 19th century, Neolithic sites have been known in the study area (Fig. 2). Several decades later, Wagner (1908), Haug and Sixt (1914) published the first comprehensive archaeological catalogues which included these early discovered sites. From the 1920s onwards until the 1950s, Paul Revellio led the archaeological research in the Baar region (Hall, 1968). He carried out rescue excavations at construction sites as well as field surveys and small prospections. Revellio recorded and published most of the Neolithic sites discovered during these three decades (Revellio, 1924, 1932 and 1938). In the 1930s, Fischer (1936) and Stoll (1941 and 1942) also studied the Neolithic settlement dynamics in the region. When Revellio retired in the 1950s, Rudolf Ströbel continued his work (Benzing, 1974). After his death, Spindler (1977) and Schmid (1991 and 1992) were the only researchers who provided analyses of the Neolithic sites discovered since the 1960s. In addition, few Neolithic sites were discussed in studies with a supra-regional focus (Paret, 1961; Itten, 1970; Pape, 1978). In general, it has to be noted that very few Neolithic sites in the study area have been investigated in the field (for exceptions see Wagner, 2014; Seidel, 2015). The vast majority were merely registered and published in the form of short site reports (see Schmid, 1992; Ahlrichs, 2017). In this context, it is noteworthy that in the course of the 20th century, several researchers carried out field surveys in the Baar region and adjacent landscapes. Although the surveyed territories cover a large part of the study area (Fig. 3), only one Neolithic site was actually discovered in the course of these surveys (Ahlrichs, 2017).

Against the background of this research history, we recorded 107 archaeological sites dating to the Neolithic. Based on the available data in the local area files and the literature we were able to assign a point coordinate to 75 sites (Fig. 7). In the remaining 32 cases this was not possible due to a lack of geographical information. Furthermore, after a review of the sites with regard to their archaeological dating, we were able to assign 49 sites to different Neolithic periods. Due to the nature of the artefacts, it was not possible to date the Neolithic sites on the level of phases or even sub-phases. The remaining 58 sites date to the "Neolithic" in general because the artefacts recovered at these sites are too fragmented or atypical for any further chronological specification. Therefore, more than half of the recorded sites are not suitable for the description of local-settlement dynamics. These results mirror the state of archaeological research of the individual sites: out of 107 registered Neolithic sites, no more than 12 sites were studied in the course of research excavations. Out of those 12 sites, 9 had to be excavated because they were discovered during excavations of archaeological sites dating to later periods. Furthermore, rescue excavations took place at four Neolithic sites after their initial discovery. This unbalanced ratio between excavated and not excavated sites has been observed in other study areas too (Schmotz, 1989). With respect to the state of research in the Baar region and adjacent landscapes, 20 sites qualify as settlements due to the presence of grinding stones and/or features such as pits or postholes. At five sites, human remains were recovered, classifying these locations as burial sites. The remaining 82 sites are composed of single finds or small artefact assemblages that currently do not allow a more detailed description of the activities that took place at these sites (Ahlrichs, 2017).

#### 4.1.2 Intentionality of site discoveries

In contrast to the Bronze Age and the pre-Roman Iron Age, an extraordinarily large number of Neolithic sites were discovered accidentally (Table 1). In total, 87 out of 107 sites are associated with non-intentional modes of discovery. Most of them were found randomly ($n = 38$) during agricultural and forestry activities ($n = 18$) or in the course of construc-

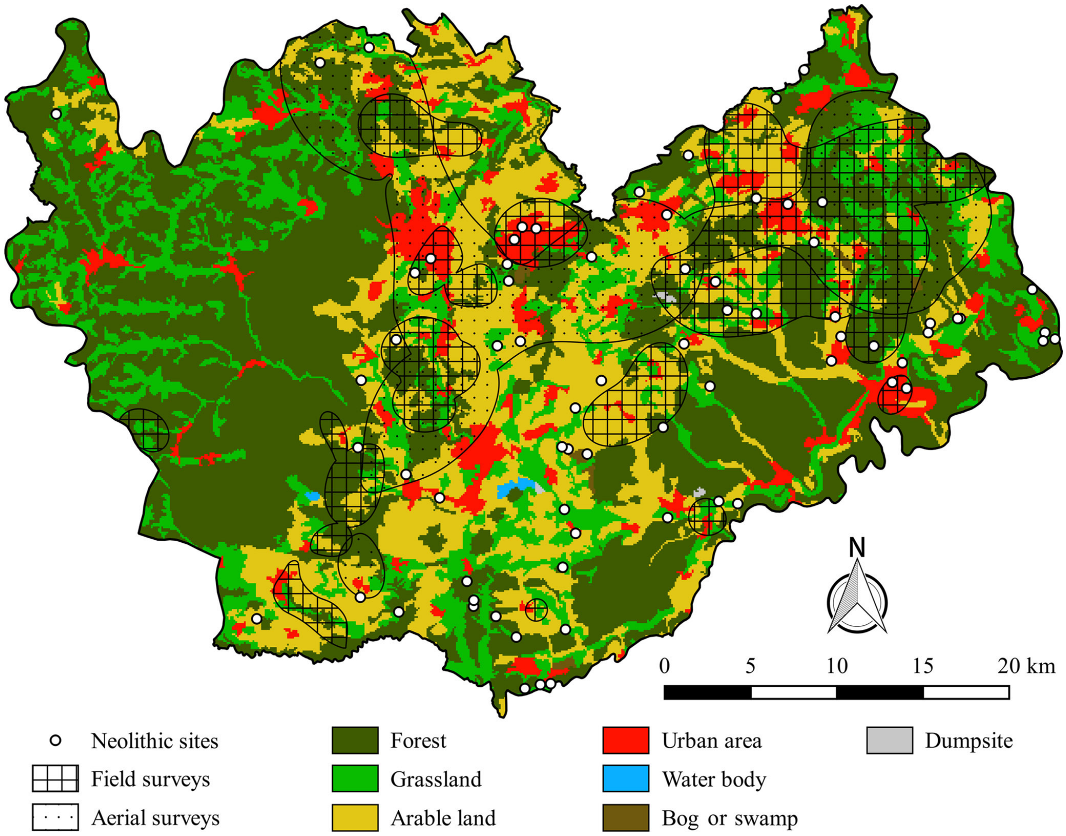


**Figure 3.** Modern land use according to CORINE Land Cover data (European Environment Agency, 2007) and areas studied by field surveys (Ahlrichs, 2017).

**Table 1.** Intentionality of archaeological site discoveries.

| Intentionality | Modes of discovery | Neolithic | | Bronze Age | | Pre-Roman Iron Age | |
|---|---|---|---|---|---|---|---|
| | | (*n*) | (%) | (*n*) | (%) | (*n*) | (%) |
| Non-intentional | Long known | 1 | 1 | 3 | 2 | 17 | 8.5 |
| | Random discovery | 38 | 35.5 | 22 | 16 | 28 | 14 |
| | Working measure | 16 | 15 | 48 | 34 | 47 | 23.5 |
| | Land consolidation | 1 | 1 | 1 | 1 | 2 | 1 |
| | Extraction of raw materials | 8 | 7.5 | 6 | 4 | 3 | 1.5 |
| | Historical records | 0 | 0 | 0 | 0 | 0 | 0 |
| | Agricultural and forestry activities | 18 | 17 | 10 | 7 | 8 | 4 |
| Intentional | Field survey | 1 | 1 | 18 | 13 | 47 | 23.5 |
| | Lidar data | 0 | 0 | 0 | 0 | 0 | 0 |
| | Aerial photography | 0 | 0 | 0 | 0 | 3 | 1.5 |
| | Research excavation | 9 | 8 | 8 | 6 | 7 | 3.5 |
| | Rescue excavation | 0 | 0 | 0 | 0 | 2 | 1 |
| | Prospection | 0 | 0 | 0 | 0 | 1 | 0.5 |
| Unknown | Unknown | 15 | 14 | 24 | 17 | 35 | 17.5 |
| | Sum | 107 | 100 | 140 | 100 | 200 | 100 |

tion measures ($n = 16$). Less than 10 % of the Neolithic sites are associated with intentional modes of discovery. These include the nine Neolithic sites mentioned earlier that were registered during excavations of archaeological sites dating to later periods and a single site that was discovered in a field survey. These results are even more indicative of potential gaps in the distribution of the sites when compared to younger epochs. The numbers of intentionally discovered sites are approximately 19 % for the Bronze Age and 30 % for the pre-Roman Iron Age. Altogether, 18 Bronze Age sites and 47 sites dating to the pre-Roman Iron Age were registered during field surveys (Table 1). This indicates that the material remains from these epochs may be more resistant to weathering compared to the ones dating to the Neolithic. In addition, the numerous discoveries during field surveys can be used to correct potential distortions in the Bronze Age and Iron Age site distributions caused by construction sites in urban areas. However, there is no such balance for the Neolithic sites.

### 4.1.3 Depth of sites

In total, 40 Neolithic sites were discovered on the modern surface, 19 were just slightly below the surface and about another 33 below the surface (Table 2). Initially, these results are quite similar with those for the Bronze Age and the pre-Roman Iron Age. However, a closer look at the archaeological data shows that at just one site Neolithic pottery was found on the recent surface. Overall, at 37 out of 38 sites discovered on the surface the artefacts were made of stone, which is far more resistant to weathering. This is in contrast to the Bronze Age and the pre-Roman Iron Age (Table 2). In total, 43 Bronze Age sites were discovered on the modern surface and at 27 of them pottery was present. In the case of the pre-Roman Iron Age, 92 sites were registered on the modern surface; pottery was found at 60 of them (Ahlrichs, 2017). These results suggest that Neolithic pottery may be less resistant to weathering on the surface than pottery from the Bronze Age and the pre-Roman Iron Age. Consequently, a distortion in the distribution of Neolithic sites is possible, as a preservation of pottery is more likely at topographic positions where it is superimposed shortly after its deposition.

### 4.1.4 Site distribution in relation to modern land use

On arable land, grassland as well as in bogs and at dumpsites about as many Neolithic sites were registered as would be expected with an even distribution over the land use classes (Fig. 3, Table 3). Consequently, these land use classes do not have much influence on the distribution of the sites. In contrast, urban areas and forests seem to have an influence on the distribution of Neolithic sites. In urban areas, the number of registered sites exceed the number of expected sites. This result can be attributed to the fact that construction measures are more likely to occur in settlements than in the other

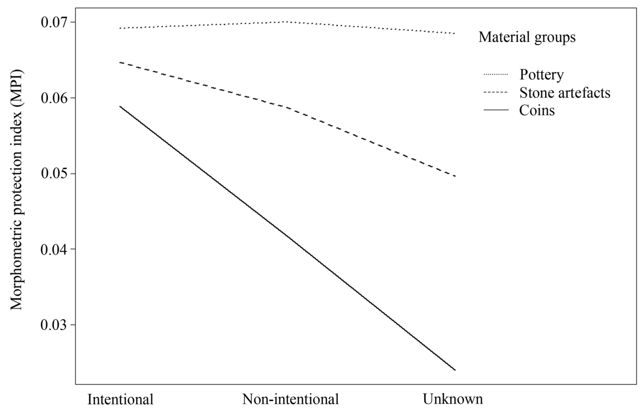


**Figure 4.** Comparison of average MPI values for pottery, stone artefacts and coins with regard to the intentionality of the site discoveries

land use classes. As the frequency of construction measures increases, so does the probability of discovering new sites. This can lead to artificial clusters of prehistoric sites in urban areas (Schier, 1990; Gerhard, 2006). As Fig. 3 indicates, this does not apply to the Neolithic sites in this study area, since none of the modern settlements correlates with a remarkably large number of Neolithic sites. However, it is noticeable that several sites in the valleys of the Swabian Jura were discovered during construction measures. It has been suggested in earlier research that the density of prehistoric sites in the valleys of the Swabian Jura is low because their archaeological visibility and accessibility are reduced due to erosion (Paret, 1961; Wahle, 1973). This seems to apply to our study area as well. In addition, the visibility of prehistoric sites is limited by dense vegetation in areas covered by forests. As a result, fewer Neolithic sites were registered in forests than expected. This is a crucial factor in understanding the absence of Neolithic sites in Black Forest and in large parts of the Swabian Jura (Lais, 1937; Valde-Nowak, 2002; Pankau, 2007).

### 4.1.5 Weathering effects on pottery, stone and coins

Each of the three material groups shows a specific frequency distribution over the morphometric protection index (MPI). In fact, pottery and coins can be differentiated due to their distinct trends (Table 5). As can be seen in Fig. 5, pre- and early historic pottery has often been registered in topographical positions with a high MPI such as foot slopes or valleys. In contrast, the frequency distribution of coins concentrates in topographic areas with a fairly small MPI, while stone artefacts take an intermediate position between these groups. Compared to pottery, however, there is also a trend towards areas with small MPIs for stone artefacts (Fig. 5). Since these trends might have been influenced by the circumstances leading to the discovery of the sites, an additional analysis was carried out taking into account the intentionality of the site discoveries. Figure 4 shows the average MPI values of the

**Table 2.** Relation of archaeological sites to the modern surface.

| Relation to surface | Modes of discovery | Neolithic | | Bronze Age | | Pre-Roman Iron Age | |
|---|---|---|---|---|---|---|---|
| | | ($n$) | (%) | ($n$) | (%) | ($n$) | (%) |
| Above surface | Field survey | 1 | 0.93 | 18 | 12.86 | 47 | 23.5 |
| | Random discovery | 38 | 35.51 | 22 | 15.71 | 28 | 14 |
| | Long known | 1 | 0.93 | 3 | 2.14 | 17 | 8.5 |
| | Historical records | 0 | 0 | 0 | 0 | 0 | 0 |
| Close to surface | Agricultural or forestry activities | 18 | 16.82 | 10 | 7.14 | 8 | 4 |
| | Lidar data | 0 | 0 | 0 | 0 | 0 | 0 |
| | Aerial photo | 0 | 0 | 0 | 0 | 3 | 1.5 |
| | Land consolidation | 1 | 0.93 | 1 | 0.71 | 2 | 1 |
| Below surface | Working measure | 16 | 14.95 | 48 | 34.3 | 47 | 23.5 |
| | Research excavation | 9 | 8.41 | 8 | 5.71 | 7 | 3.5 |
| | Rescue excavation | 0 | 0 | 0 | 0 | 2 | 1 |
| | Prospection | 0 | 0 | 0 | 0 | 1 | 0.5 |
| | Extraction of raw materials | 8 | 7.5 | 6 | 4.29 | 3 | 1.5 |
| Unknown | Unknown | 15 | 14.02 | 24 | 17.14 | 35 | 17.5 |
| | Sum | 107 | 100 | 140 | 100 | 200 | 100 |

**Table 3.** Distribution of Neolithic sites over modern land use.

| Land use | Spatial abundance (%) | Recorded sites ($n$) | Expected sites ($n$) | $\chi^2$ value |
|---|---|---|---|---|
| Water bodies | 0.1 | 0 | 0.08 | 0.08 |
| Urban areas | 7.88 | 16 | 5.91 | 17.23 |
| Arable land | 24.43 | 22 | 18.32 | 0.74 |
| Grassland | 20.16 | 15 | 15.12 | 0 |
| Forest | 47.1 | 22 | 35.33 | 5.03 |
| Bogs or swamps | 0.25 | 0 | 0.19 | 0.19 |
| Dumpsites or landfills | 0.08 | 0 | 0.06 | 0.06 |
| Sum | 100 | 75 | 75 | 23.33 |

The critical $\chi^2$ value for 6 degrees of freedom is at 22.46 (significance level: 0.001 %).
In this case, the site distribution is highly significantly unequal (see Ihm et al., 1978, p. 595).

intentional and non-intentional site discoveries for each material group. The results demonstrate that pottery was registered in topographic positions with a very specific MPI, regardless of whether they were recorded in the course of intentional or non-intentional modes of discovery. This cannot be seen in the other groups. These results suggest that the topography has an influence on the preservation and accessibility of pre- and early historic pottery and thus constitutes a crucial factor with respect to the understanding of site distributions in the study area.

#### 4.1.6 Local site frequencies in relation to other study areas

According to the available archaeological data, the Neolithic settlement of the Baar region and adjacent landscapes are characterized by extremely low site frequencies (Table 6).

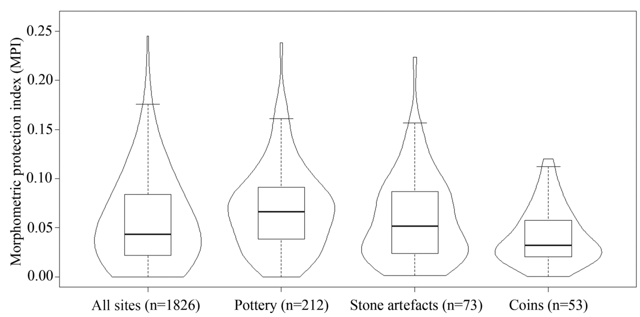


**Figure 5.** General comparison of average MPI values for pottery, stone artefacts and coins (see also Table 5).

**Table 4.** Distribution of material groups over different epochs and types of archaeological sites.

| Epoch | Type of site | Pottery | Stone artefacts | Coins | Sum |
|---|---|---|---|---|---|
| "Prehistory" | Settlement | 18 | 1 | 0 | 19 |
| | Single finds | 1 | 0 | 0 | 1 |
| Palaeolithic | Settlement | 0 | 0 | 0 | 0 |
| | Single finds | 0 | 2 | 0 | 2 |
| Mesolithic | Settlement | 0 | 1 | 0 | 1 |
| | Single finds | 0 | 3 | 0 | 3 |
| Neolithic | Settlement | 9 | 10 | 0 | 19 |
| | Single finds | 1 | 47 | 0 | 48 |
| Bronze Age | Settlement | 50 | 2 | 0 | 52 |
| | Single finds | 6 | 2 | 0 | 8 |
| Pre-Roman Iron Age | Settlement | 94 | 3 | 0 | 97 |
| | Single finds | 5 | 0 | 6 | 11 |
| Roman Empire | Settlement | 15 | 1 | 12 | 28 |
| | Single finds | 13 | 1 | 35 | 49 |
| Sum | | 212 | 73 | 53 | 338 |

**Table 5.** Comparison of average MPI values for pottery, stone artefacts and coins (see also Fig. 5).

| Material group | Minimum | First quartile | Median | Mean | Second quartile | Maximum | Standard deviation |
|---|---|---|---|---|---|---|---|
| All sites ($n = 1826$) | 0 | 0.0217 | 0.0431 | 0.0557 | 0.0839 | 0.245 | 0.0429 |
| Pottery ($n = 212$) | 0 | 0.0388 | 0.066 | 0.069 | 0.091 | 0.2381 | 0.0436 |
| Stone artefacts ($n = 73$) | 0.0012 | 0.024 | 0.0515 | 0.0588 | 0.0866 | 0.2236 | 0.0435 |
| Coins ($n = 53$) | 0.0003 | 0.0204 | 0.032 | 0.0416 | 0.0573 | 0.1198 | 0.0283 |

The Early Neolithic and the Final Neolithic are the only periods for which we could calculate site frequencies of one and nearly two sites per hundred years. The other Neolithic periods are characterized by even smaller site frequencies. In fact, similar results cannot be observed in any other study area in southern Germany (Table 6, Fig. 6). On the contrary, in landscapes such as the Wetterau or Maindreieck, frequencies of up to 30 sites per century can be demonstrated. The Brenz–Kocher Valley on the Swabian Jura is the only landscape with similarly low site frequencies. In general, it can be assumed that the calculated site frequencies do reflect regional trends in Neolithic settlement dynamics, even though the results may be affected to a certain degree by local research traditions. Altogether, we assume that the Neolithic settlement density must have been very low in the study area. This probably results from the limited accessibility of Neolithic sites as well as poor conditions for the conservation of pottery due to the topography and modern land use.

## 4.2 Colluvial deposits

### 4.2.1 Archaeopedological dataset

The entire dataset includes 93 AMS $^{14}C$ datings of charcoals, 47 luminescence datings of colluvial deposits and laboratory results of 728 bulk soil samples (Henkner et al., 2018b). Since this paper deals with the Neolithic land use, this section will focus on those 21 AMS $^{14}C$ ages (Table 7) and 9 luminescence ages (Table 8) associated with the Neolithic. In the following, the results for each of the three landscapes are presented.

### 4.2.2 The Baar region

At the beginning of the Neolithic, phases of land use triggered colluvial formation at Magdalenenberg and Fürstenberg. A luminescence age from Mag1_14 (GI0132) and a radiocarbon age from Fue9 (Erl-20278) date the related colluvial deposits into the Early Neolithic period. This is supplemented by three OSL samples covering the entire time frame from the early to the Younger Neolithic due large standard errors (GI0183, GI0184, GI0248). There are few sam-

**Table 6.** Supra-regional comparison of Neolithic site frequencies (see also Fig. 6).

| Region | Early Neolithic | Middle Neolithic | Younger Neolithic | Late Neolithic | Final Neolithic | Reference |
|---|---|---|---|---|---|---|
| Baar | 1.2 | 0.83 | 0.11 | 0.86 | 1.85 | This study |
| Brenz–Kocher Valley | 5 | 1.5 | 2.33 | – | 1.23 | Pankau (2007) |
| Estuary of the Isar river | 5.2 | 13.5 | 3.22 | – | 3.54 | Schmotz (1997, 2001) |
| Northwestern Maindreieck | 11.8 | 2.33 | 4.33 | – | 5.08 | Obst (2012) |
| Groß-Gerau | 11.8 | 20.83 | 5 | – | 10.62 | Gebhard (2007) |
| Danube Valley near Regensburg | 13.4 | 20.5 | 3.89 | – | 6.46 | Schier (1985) |
| Ries | 17.6 | 6 | 5.56 | – | 1.23 | Krippner (1995) |
| Maindreieck | 28 | 30 | 5.67 | 5 | 12.46 | Schier (1990) |
| Wetterau | 29.8 | 15.83 | 7.22 | – | – | Saile (1998) |

**Table 7.** Neolithic AMS $^{14}$C radiocarbon dates from charcoals in colluvial deposits from Fürstenberg (Fue), Magdalenenberg (Mag), Spaichingen (Spa), Geisingen (Gei), Grüningen (Gru), Lehmgrubenhof (Leh), Brigach spring (Bri), Königsheim (Koe), Lindenberg (Lin) and Böttingen (Boe). The data calibrations were done with OxCal 4.2 and the calibration curve IntCal13 (Bronk Ramsey, 2009; Reimer et al., 2013).

| Lab code | Landscape | Site | Profile | Depth (cm) | Horizon | BP (a ± error) | cal BCE or CE ($1\sigma$) | cal BCE or CE ($2\sigma$) | Neolithic period(s) |
|---|---|---|---|---|---|---|---|---|---|
| Erl-20278 | Baar | Fue | 9 | 135 | M4 | 6526 ± 66 | cal BCE 5560–5380 | cal BCE 5620–5360 | Early Neolithic |
| Poz-36954 | Baar | Mag | 1_10 | 65 | M2 | 4970 ± 40 | cal BCE 3800–3690 | cal BCE 3930–3650 | Younger Neolithic |
| Erl-20132 | Baar | Mag | 1_14 | 75 | 2 M4 | 5071 ± 51 | cal BCE 3950–3800 | cal BCE 3980–3710 | Younger Neolithic |
| P 12878 | Baar | Spa | 1 | 185 | 2 MBl | 5040 ± 18 | cal BCE 3950–3780 | cal BCE 3960–3710 | Younger Neolithic |
| Erl-20276 | Baar | Fue | 9 | 90 | M2 | 4557 ± 67 | cal BCE 3490–3100 | cal BCE 3520–3020 | Late Neolithic |
| Erl-20277 | Baar | Fue | 9 | 115 | M3 | 4477 ± 58 | cal BCE 3340–3030 | cal BCE 3360–2930 | Late Neolithic |
| P 14445 | Baar | Gei | 2 | 137 | 5 BgM3 | 4278 ± 14 | cal BCE 2910–2880 | cal BCE 2920–2880 | Late Neolithic |
| P 13418 | Baar | Gei | 2 | 144 | 3 MBg | 4070 ± 26 | cal BCE 2840–2490 | cal BCE 2860–2480 | Final Neolithic |
| Erl-20137 | Baar | Gru | 8_14 | 105 | 2 M3 | 3889 ± 40 | cal BCE 2470–2300 | cal BCE 2480–2210 | Final Neolithic |
| Erl-20275 | Baar | Fue | 9 | 60–70 | M1 | 3918 ± 61 | cal BCE 2480–2290 | cal BCE 2580–2200 | Final Neolithic |
| P 12871 | Black Forest | Leh | 3 | 58 | 2 M3 | 5354 ± 55 | cal BCE 4330–4050 | cal BCE 4440–3960 | Younger Neolithic |
| P 12865 | Black Forest | Bri | 1 | 111 | 4 BgM2 | 4394 ± 63 | cal BCE 3330–2900 | cal BCE 3370–2710 | Late Neolithic |
| P 12920 | Black Forest | Bri | 4 | 90 | M4 | 3783 ± 14 | cal BCE 2280–2140 | cal BCE 2290–2140 | Final Neolithic |
| P 12910 | Swabian Jura | Koe | 3 | 29 | M2 | 6191 ± 51 | cal BCE 5300–5010 | cal BCE 5380–4840 | Early and middle Neolithic |
| P 12903 | Swabian Jura | Lin | 3 | 80 | M5 | 5685 ± 18 | cal BCE 4550–4460 | cal BCE 4670–4440 | Middle Neolithic |
| P 12896 | Swabian Jura | Lin | 2 | 58 | 2 M3 | 5464 ± 45 | cal BCE 4450–4230 | cal BCE 4470–4050 | Younger Neolithic |
| P 12897 | Swabian Jura | Lin | 2 | 90 | 3 M4 | 4623 ± 17 | cal BCE 3500–3360 | cal BCE 3520–3340 | Late Neolithic |
| P 12900 | Swabian Jura | Lin | 3 | 43 | M2 | 3937 ± 52 | cal BCE 2570–2290 | cal BCE 2840–2140 | Final Neolithic |
| P 12907 | Swabian Jura | Koe | 2 | 243 | M4 | 4326 ± 51 | cal BCE 3270–2870 | cal BCE 3340–2670 | Late and Final Neolithic |
| P 12925 | Swabian Jura | Lin | 2 | 74 | M4 | 3770 ± 14 | cal BCE 2280–2140 | cal BCE 2290–2060 | Final Neolithic |
| P 12888 | Swabian Jura | Boe | 2 | 32–36 | M | 3869 ± 49 | cal BCE 2470–2210 | cal BCE 2570–2060 | Final Neolithic |

ples dating to the Middle Neolithic. These include the above mentioned OSL samples from Fue8 (GI0183, GI0184) and Fue9 (GI0248) as well as one OSL sample from Mag1_14 (GI0131). The archaeopedological results indicate no significant change in the settlement pattern in the Baar region until the end of the Middle Neolithic. The transition to the Younger Neolithic is marked by a significant increase in radiocarbon ages. In this period, land use continues at Magdalenenberg (Poz-36954, Erl-20132, GI0131) and Fürstenberg (GI0183, GI0184, GI0247, GI0248). Furthermore, an AMS $^{14}$C age from Spaichingen (P 1278) dates into this period, thus suggesting local settlement dynamics that went along with the human impact on the eastern Baar. For the Late Neolithic, a distinctive human influence can be demonstrated in several soil profiles. While there are no more indications of land use at Spaichingen and Magdalenenberg, a continuation of land use can be seen in soil profiles at Fürstenberg (GI0247, Erl-20276, Erl-20277). An additional phase of colluviation was detected at Geisingen (P 14445) in the southeastern Baar region. These results indicate both an intensification of land use in the southern Baar region but also point to the cultural significance of the Danube Valley for the Late Neolithic farming societies as an important geographical element with respect to traffic and communication. This is also indicated by imported objects such as an axe made of jadeite found at the Fürstenberg and a hatchet made of copper discovered in the Danube Valley (Wagner, 2014; Seidel, 2015; Ahlrichs, 2017). For the Final Neolithic,

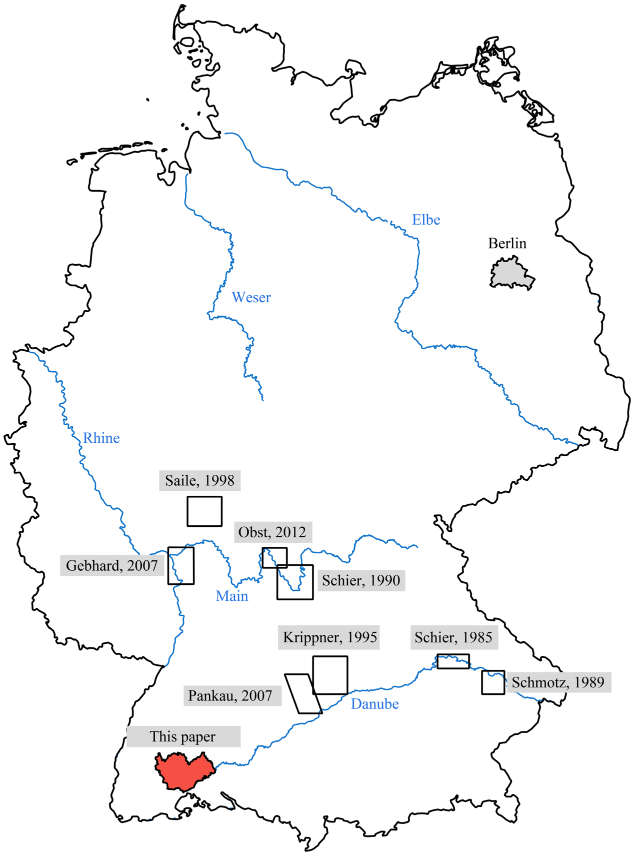


**Figure 6.** Location of study areas used in discussion on local site frequencies (see Table 6).

the archaeopedological studies indicate settlement dynamics on the western Baar region. At Grüningen, both an AMS $^{14}C$ age (Erl-20137) and a luminescence age (GI0296) from Gru8_14 point to the formation of a colluvial deposit during the Final Neolithic. Furthermore, AMS $^{14}C$ dating of charcoals demonstrates a human presence at Fürstenberg (Erl-20275) and Geisingen (P 13418).

### 4.2.3 The Swabian Jura

The archaeopedological studies suggest similar developments in the Baar region and on the Swabian Jura, even though the number of AMS $^{14}C$ and luminescence datings are significantly smaller on the Swabian Jura. A radiocarbon age from Königsheim (P 12910) points to land use on the Heuberg in the Early Neolithic. The Middle Neolithic is represented by two radiocarbon ages from the Swabian Jura. Whereas the AMS $^{14}C$ dating from Königsheim (P 12910) covers both the early and the Middle Neolithic, and the charcoal sample from Lindenberg (P 12903) dates into this period suggesting a more frequent human presence in the eastern Baar and in the small river valleys between the high plateaus of the Swabian Jura. Younger Neolithic land use on the Swabian Jura can be demonstrated by using a charcoal

**Table 8.** Neolithic luminescence ages of sediments from colluvial deposits at Magdalenenberg (Mag), Fürstenberg (Fue), Grüningen (Gru) and Lehmgrubenhof (Leh). Age refers to the year of dating rounded to 2010.

| Lab code | Landscape | Site | Profile | Horizon | Depth | Model | De (Gyr) | Age (ka) | cal BCE or CE | Neolithic period(s) |
|---|---|---|---|---|---|---|---|---|---|---|
| GI0132 | Baar | Mag | 1_14 | M2 | 69 | Central age model | 30.5 ± 1.5 | 8.2 ± 0.8 | BCE 6990–5390 | Early Neolithic |
| GI0183 | Baar | Fue | 8 | M5 | 135 | Bootstrap minimum age model 3 | 20.1 ± 0.9 | 6.9 ± 0.6 | BCE 5490–4290 | Early, Middle and Younger Neolithic |
| GI0184 | Baar | Fue | 8 | M6 | 162 | Bootstrap minimum age model 3 | 22.3 ± 0.7 | 6.5 ± 0.7 | BCE 5190–3790 | Early, Middle and Younger Neolithic |
| GI0248 | Baar | Fue | 9 | M6 | 155 | Central age model | 21.35 ± 0.96 | 6.61 ± 0.62 | BCE 5220–3980 | Early, middle and younger Neolithic |
| GI0131 | Baar | Mag | 1_14 | M2 | 62 | Central age model | 25 ± 1.5 | 6.1 ± 0.6 | BCE 4690–3490 | Middle and Younger Neolithic |
| GI0247 | Baar | Fue | 9 | M4 | 125 | Central age model | 15.71 ± 0.54 | 5.26 ± 0.42 | BCE 3670–2830 | Younger and Late Neolithic |
| GI0296 | Baar | Gru | 8_14 | M2 | 72 | Central age model | 13.48 ± 0.66 | 4.4 ± 0.4 | BCE 2790–1990 | Final Neolithic |
| GI315 | Black Forest | Leh | 3 | 2 M3 | 71 | Central age model | 14.02 ± 0.94 | 4.3 ± 0.4 | BCE 2690–1890 | Final Neolithic |

sample from the Lindenberg soil profile (P 12896). So far, there have been no indications of a formation of colluvial deposits during this period on the Heuberg. The transition to the Late Neolithic is characterized by a continuous formation of colluvial deposits on the Lindenberg (P 12897) and a new phase of land use on the Heuberg at Königsheim (P 12907). In the Final Neolithic, an intensification of land use on the Heuberg is indicated as the formation of colluvial deposits can be demonstrated in soil profiles at Böttingen (P 12888) and Königsheim (P 12907). In addition, charcoal fragments from a colluvial deposit point to an ongoing land use on the Lindenberg (P 12900, P 12925).

#### 4.2.4 The Black Forest

In general, the archaeopedological studies indicate a low human impact in the Black Forest during the Neolithic. Nevertheless, it is striking that the earliest indications of an anthropogenically triggered formation of colluvial deposits in this landscape date to the Younger Neolithic (P 12871). This period is characterized by a significant increase in data for colluviation in the adjacent Baar region suggesting an intensification and expansion of land use. Apparently this was accompanied by a more frequent human presence in the Black Forest. Furthermore, Late Neolithic land use in the Black Forest is indicated by an AMS $^{14}$C age from the spring source of the river Brigach (P 12865). Radiocarbon ages from both the river Brigach (P 12920) and Lehmgrubenhof (GI0315) also point to phases of human presence in the Final Neolithic. The fact that charcoal samples from the spring source area of the river Brigach date into the Late and Final Neolithic may be an indication that humans followed the larger rivers as they entered this landscape. This is also suggested by archaeological finds from the western Baar (Ahlrichs et al., 2016) and by the fragment of a Neolithic blade made of Cretaceous chert found in the colluvial deposits at the spring source of the river Breg (Henkner et al., 2018c).

## 5 Discussion of Neolithic settlement dynamics

### 5.1 Early Neolithic (5500–5000 cal BCE)

During the Early Neolithic, the study area was sparsely populated (Fig. 7). The archaeological record demonstrates human land use in the vicinity of Villingen-Schwenningen at the river Brigach and the spring source of the river Neckar as well as at the Danube in the southern Baar and in the valleys of the Swabian Jura. The pedological data support these archaeological results. Both at the Magdalenenberg (GI0132) and the Fürstenberg (GI0183, GI0184, GI0248, Erl-2027), phases of colluviation were detected dating to the Early Neolithic. In addition, the dating of charcoal sample P 12910 from Königsheim indicates a phase of land use on the Heuberg, a landscape, where no Early Neolithic sites are known so far. The location of Early Neolithic settlements in the immediate vicinity of large rivers in other areas was interpreted in a way that the early farmers followed large rivers when they colonized new territories (Schier, 1990; Bofinger, 2005). Similar locations of settlements were discovered at the river Neckar and in close proximity to the Danube in the Baar region (Ahlrichs, 2017). The artefacts from the settlement at the river Neckar indicate that Neolithic farmers penetrated the Black Forest to extract raw materials. Several grinding stones found in the settlement were made of a type of rock that occurs only in the Black Forest. Furthermore, chunks of haematite were recovered at the site (Schmid, 1992) which was mined in the Black Forest (Ahlrichs, 2015).

### 5.2 Middle Neolithic (5000–4400 cal BCE)

Archaeologically, the Middle Neolithic is characterized by a low site density (Fig. 7). However, the site distribution indicates a continuation of the settlement patterns introduced in the Early Neolithic. In contrast to the Early Neolithic, there is archaeological evidence for hilltop settlements in the southern and eastern Baar. Trends like these have also been observed in the Maindreieck (Schier, 1990) and the Obere Gäue (Bofinger, 2005). In addition, there are archaeological indications of a human presence in the northern Baar and an expansion into the northeastern Baar. However, the artefacts recovered from these four sites cannot be assigned to the Middle Neolithic with absolute certainty as they are also typical for later periods (Ahlrichs, 2017). The pedological data are consistent with the site distribution: radiocarbon and luminescence ages point to a formation of colluvial deposits in the northern Baar (GI0131) and on the Swabian Jura (P 12896, P 12903, P 12910).

### 5.3 Younger Neolithic (4400–3500 cal BCE)

The transition to the Younger Neolithic is characterized by significant reduction in the archaeological data (Fig. 7). This is in strong contrast to other landscapes in southwest Germany where Neolithic farmers expanded their territories (Bofinger, 2005). So far, only one site from the northeastern Baar can be dated directly to this period. Furthermore, there are four sites in the northern Baar and two in the southern Baar dating to the Younger Neolithic. In contrast to the archaeological data, both AMS $^{14}$C ages and OSL ages from colluvial deposits indicate land use at the Magdalenenberg (Poz-36954, Erl-20132, GI0131), in the vicinity of Spaichingen (P 12878), at the Fürstenberg (GI0183, GI0184, GI0247, GI0248) and on the Swabian Jura (P 12896). So far, there are neither archaeological nor pedological indications of land use on the Heuberg. However, pollen analysis of a bog profile from Elzhof and a radiocarbon age from Lehmgrubenhof (P 12871) in the southeastern Black Forest point to changes in the vegetation caused by land use during the Younger Neolithic (Henkner et al., 2018a, c). These developments are in line with archaeological and archaeobotanical studies

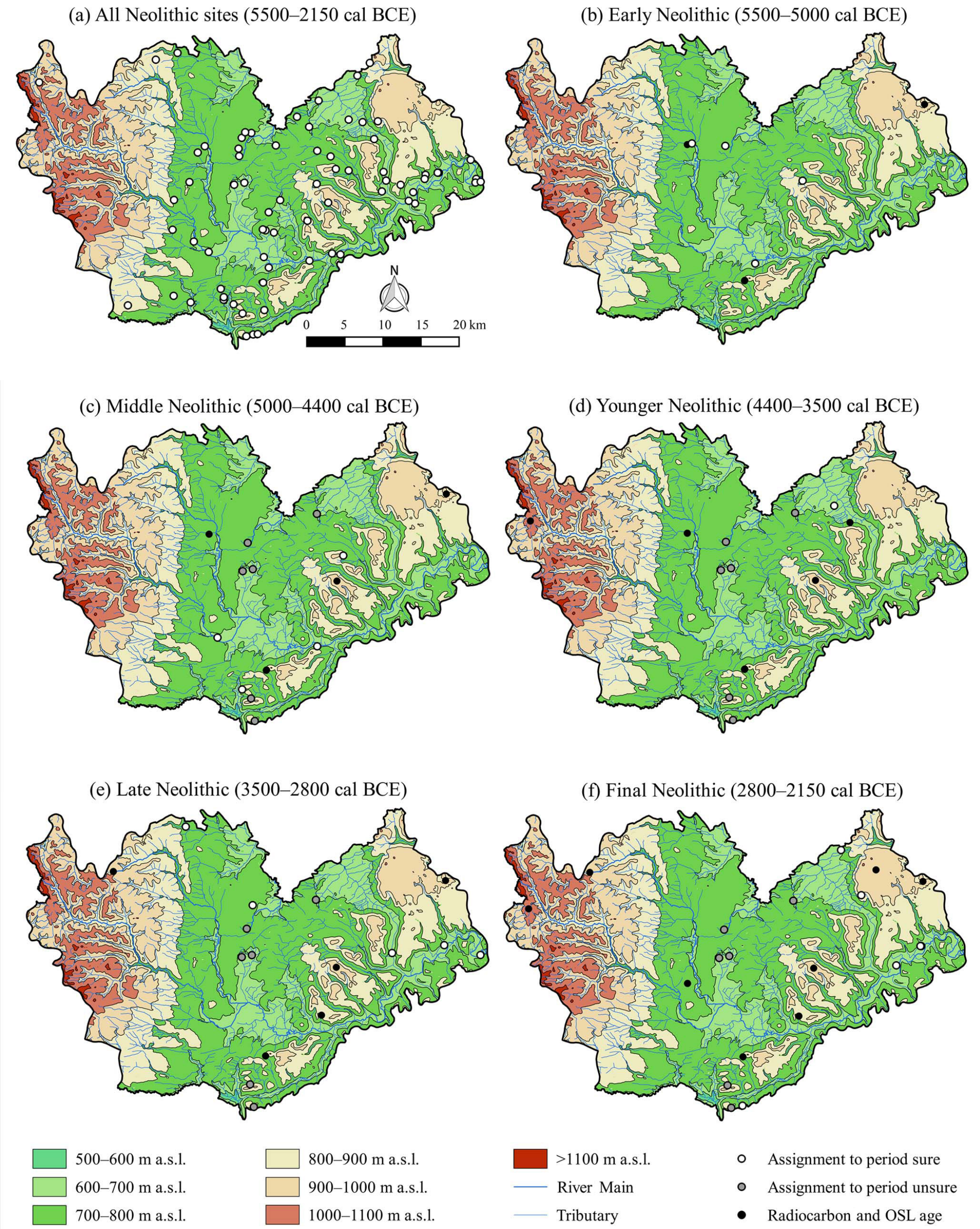


**Figure 7.** Distribution of all recorded Neolithic sites **(a)** and reconstruction of Neolithic settlement dynamics during the **(b)** Early Neolithic, **(c)** Middle Neolithic, **(d)** Younger Neolithic, **(e)** Late Neolithic and **(f)** Final Neolithic.

from other parts of the Black Forest. Based on archaeological field surveys (Valde-Nowak, 1999; Kienlin and Valde-Nowak, 2004; Valde-Nowak and Kienlin, 2002) and pollen records (Frenzel, 1982, 1997; Rösch, 2009), human presence can be demonstrated in the western and northern areas of the Black Forest during the Younger Neolithic. Basically, the archaeological and archaeobotanical results are interpreted as an indication of seasonal land use in the Black Forest, i.e. in the context of a transhumance (Valde-Nowak, 2002). This form of land use leaves few archaeological traces because of its seasonal character and the fact that small mobile groups of shepherds are travelling along with the livestock. In addition, these sites are difficult to find due to the recent reforestation of the Black Forest and sites may have been redeposited or covered by slope deposits (Lais, 1937; Paret, 1961; Pasda, 1998).

Henkner et al. (2017) calculated the summed probability density (SPD) of the radiocarbon and luminescence ages for the Baar region. The oldest phase of increased colluvial deposition dates to the Younger Neolithic, where the increase in formations of colluvial deposits took place in a wetter- and colder-climate period. Therefore, higher erosion rates may have been caused by higher amounts of precipitation. Furthermore, the agricultural technology went through major changes during the Younger Neolithic. During the early and Middle Neolithic fields were ploughed manually, whereas farming became more efficient in the Younger Neolithic since new types of ploughs (pulled by cattle) were introduced (Lüning, 2000). This change opens up the possibility of cultivating larger fields, which may have increased local soil erosion processes.

### 5.4 Late Neolithic (3500–2800 cal BCE)

The transition to the Late Neolithic is marked by significant changes in the local settlement pattern (Fig. 7). In contrast to previous periods, several sites were established in the Danube Valley. In the northwestern Baar, a site is situated in a small river valley leading into the Black Forest. This can be taken as an indicator for a temporary human presence in this landscape. Additionally, archaeobotanical analysis of pollen profiles from Elzhof and Moosschachen documented a small human impact during the Late Neolithic in the Black Forest (Henkner et al., 2018c). Furthermore, pedological analysis of colluvial deposits point to human activities on the Heuberg at Königsheim (P 12907) and on the Lindenberg (P 12897, P 12900). Consequently, the Late Neolithic is the first period in which Neolithic societies expanded simultaneously their territories into the eastern Black Forest and western Swabian Jura. The pedological investigations of colluvial deposits at Fürstenberg (Erl-20276, Erl-20277, GI0247) and Geisingen (P 13418, P 14445) point to a human presence in the southern and southeastern Baar during the Late Neolithic for which archaeological evidence still has to be provided.

### 5.5 Final Neolithic (2800–2150 cal BCE)

The general Late Neolithic settlement pattern prevailed during the Final Neolithic (Fig. 7). However, for the first time, there is archaeological evidence for a Neolithic settlement on the Heuberg. The analysis of a colluvial deposit at Böttingen points to human presence near this settlement (P 12888). Furthermore, AMS $^{14}$C and OSL dates indicate a phase of colluvial deposition at Grüningen in the western Baar (Erl-20137, GI0296).

## 6 Conclusion

We investigated Neolithic settlement dynamics by using an integrated archaeological–archaeopedological approach with a focus on archaeological source criticism and colluvial deposits. Our results lead to the following conclusions.

- Archaeological source criticism indicates that Neolithic settlement dynamics in our study area cannot be described based on the archaeological data alone. The distribution pattern of the sites especially in the low mountain ranges seems to be influenced by various factors: (i) a restricted accessibility of sites due to dense vegetation in forests in the Black Forest and on the Swabian Jura, (ii) a superimposition of sites by colluvial deposits and (iii) weathering effects on the preservation of pottery. These factors contribute to the difficulty of discovering new Neolithic sites by field surveys. Consequently, the Neolithic site frequencies are very low compared to other regions in southwestern Germany.

- A more reliable picture of Neolithic settlement dynamics is achieved by complementing archaeological data and chronological data from colluvial deposits. Thus, we were able to describe settlement dynamics not only between the Baar region and the adjacent low mountain ranges but also within the Baar region for the different chronological levels of the Neolithic.

- Archaeopedological results indicate a continuous land use at the Fürstenberg throughout the Neolithic. This site might have been a particular favourable location because of its proximity to the Danube, which probably served as an important route for communication and trade. This is also suggested by rare imported objects found at the Fürstenberg and in the Danube Valley.

- Archaeological finds point to expeditions into the Black Forest for the extraction of raw material for stone tools and haematite in the Early Neolithic. The formation of colluvial deposits in the eastern Black Forest and western Swabian Jura was triggered most probably by transhumance and small-scale farming in the Late and Final Neolithic.

**Data availability.** The data used in this paper are stored at Dryad (https://doi.org/10.5061/dryad.rh67h, Henkner, 2018b). Additional information and supplementary data about this project are published (Ahlrichs et al., 2016, 2018a, b; Ahlrichs, 2017; Henkner et al., 2017, 2018a, c).

**Author contributions.** JJM, JH, PK, TS and TK designed the study, and JJM carried it out. JJM prepared the manuscript with contributions from all co-authors. MF was responsible for OSL dating. KS contributed to the interpretation and discussion of the results of the quantitative analyses.

**Competing interests.** The authors declare that they have no conflict of interest.

**Special issue statement.** This article is part of the special issue "Geoarchaeology and past human—environment interactions". It is not associated with a conference.

**Acknowledgements.** We acknowledge financial support by the German Research Foundation (DFG) and the SFB 1070 ResourceCultures at the University of Tuebingen. Furthermore, we acknowledge support from the DFG and Leipzig University within the program of Open Access Publishing. We also thank our anonymous reviewers for their helpful comments and suggestions on an earlier draft of this paper.

**Financial support.** This research has been supported by the German Research Foundation (DFG), the University of Tuebingen (SFB 1070 ResourceCultures), and the Leipzig University (Open Access Publishing).

## References

Ad-hoc-AG Boden: Bodenkundliche Kartieranleitung, KA5, 5th edn., Schweizerbart, Stuttgart, Germany, 2005.

Ahlrichs, J. J.: Ocker im Paläolithikum, Universitätsforschungen zur prähistorischen Archäologie 265, Habelt, Bonn, Germany, 2015.

Ahlrichs, J. J.: Ur- und frühgeschichtliche Siedlungsdynamiken zwischen Gunst- und Ungunsträumen in Südwestdeutschland – Eine Fallstudie zur Baar und den angrenzenden Naturräumen des Schwarzwaldes und der Schwäbischen Alb, PhD thesis, Eberhard Karls University Tübingen, Germany, 726 pp., 2017.

Ahlrichs, J., Henkner, J., Teuber, S., Schmidt, K., Scholten, T., Kühn, P., and Knopf, T.: Archaeological and archaeopedological approaches to analyze the development of marginal areas in prehistory: a case study from the western Baar, SW Germany, in: Landscape as impulsion for culture: research, perception & protection. Landscape in the past & forgotten landscapes 2, edited by: Kołodziejczyk, P. and Kwiatkowska-Kopka, B., Institute of Archeology Kraków, Institute of Landscape Architecture Kraków, Kraków, Poland, 39–49, available at: https://www.clc.edu.pl/wp-content/uploads/2016/09/VOL_2_CLC2016.pdf (last access: 18 June 2019), 2016.

Ahlrichs, J. J., Henkner, J., Schmidt, K., Scholten, T., Kühn, P., and Knopf, T.: Bronzezeitliche Siedlungsdynamiken zwischen der Baar und angrenzenden Naturräumen, in: Bronzezeitlicher Transport. Akteure, Mittel und Wege. RessourcenKulturen 8, edited by: Neumann, D., Nessel, B., and Bartelheim, M., Tübingen University Press, Tübingen, Germany, 269–303, 2018a.

Ahlrichs, J. J., Henkner, J., Schmidt, K., Scholten, T., Kühn, P., and Knopf, T.: L'utilisation des terres pendant la période néolithique sur la colline du Fürstenberg à la bordure sud du Baar en Allemagne du sud-ouest, in: Habitations et habitat du Néolithique à l'âge du Bronze en France et ses marges. Actes des IIe Rencontres Nord/Sud de Préhistoire récente, Dijon, 19–21 November 2015, edited by: Lemercier, O., Sénépart, I., Besse, M., and Mordant, C., Archives d'Écologie Préhistorique, Toulouse, France, 619–622, 2018b.

Benzing, A. G.: Dr. Rudolf Ströbel, Schriften des Vereins für Geschichte und Naturgeschichte der Baar, 30, 15–19, 1974.

Bofinger, J.: Untersuchungen zur neolithischen Besiedlungsgeschichte des Oberen Gäus, Materialhefte zur Archäologie in Baden-Württemberg 68, Theiss, Stuttgart, Germany, 2005.

Bronk Ramsey, C.: Bayesian analysis of radiocarbon dates, Radiocarbon, 51, 337–360, https://doi.org/10.1017/S0033822200033865, 2009.

Bußmann, J.: Holozäne Sedimentdynamik im Umfeld der Varusschlacht, PhD thesis, University of Osnabrück, Germany, 113 pp., 2014.

Childe, V. G.: Man makes himself, Watts & Co., London, UK, 1936.

Conrad, O., Bechtel, B., Bock, M., Dietrich, H., Fischer, E., Gerlitz, L., Wehberg, J., Wichmann, V., and Böhner, J.: System for Automated Geoscientific Analyses (SAGA) v. 2.1.4, Geosci. Model Dev., 8, 1991–2007, https://doi.org/10.5194/gmd-8-1991-2015, 2015.

Deecke, W.: Natur, Oberflächengestaltung und Wirtschaftsformen der Baar. Vom Bodensee zum Main – Heimatblätter herausgegeben vom Landesverein badische Heimat 16, Müller, Karlsruhe, Germany, 1921.

Dotterweich, M.: The history of soil erosion and fluvial deposits in small catchments of central Europe: Deciphering the long-term interaction between humans and the environment – A review, Geomorphology, 101, 192–208, https://doi.org/10.1016/j.geomorph.2008.05.023, 2008.

Eberhardt, E., Schad, P., Berner, T., Lehmann, C., Walthert, L., and Pietsch, D.: Ableitungsschlüssel zur Klassifizierung von Böden nach WRB 2007: aus Daten der KA 5-Nomenklatur, Berlin, Germany, available at: http://eprints.dbges.de/id/eprint/980 (last access: 18 June 2019), 2013.

Eggert, M. K. H.: Prähistorische Archäologie: Konzepte und Methoden, UTB 2092, Francke, Tübingen, Germany, 2012.

Eggert, M. K. H. and Samida, S.: Ur- und frühgeschichtliche Archäologie, UTB 3254, Francke, Tübingen, Germany, 2013.

European Environment Agency: CLC2006 technical guidelines, EEA Technical report 17, Office for Official Publications of the European Communities, Luxembourg, https://doi.org/10.2800/12134, 2007.

FAO: Guidelines for soil description, 4th edn., Food and Agriculture Organization of the United Nations, Rome, Italy, 2006.

Fischer, E.: Beiträge zur Kulturgeographie der Baar. Badische Geographische Abhandlungen 16, Waibel, Freiburg im Breisgau, Germany, 1936.

Frenzel, B.: Über eine vormittelalterliche Besiedlung in einigen Teilen des nördlichen Schwarzwaldes, in: Geschichte und Naturwissenschaft in Hohenheim Beiträge zur Natur-, Agrar-, Wirtschafts- und Sozialgeschichte Südwestdeutschlands: Festschrift für Günther Franz zum 80. Geburtstag, edited by: Winkel, H., Thorbecke, Sigmaringen, Germany, 239–263, 1982.

Frenzel, B.: Vegetationsgeschichtliche und paläoökologische Probleme des Schwarzwaldes, in: Erstes Nordschwarzwald-Symposium: Siedlungsgeschichte und Waldnutzungsformen, Baiersbronn 1994. Veröffentlichungen des Alemannischen Instituts 64, edited by: Lohrenz, S. and Matzke, M., Heimat- und Museumsverein für Stadt und Kreis Freudenstadt, Freudenstadt, Germany, 11–40, 1997.

Fuchs, M. and Lang, A.: Luminescence dating of hillslope deposits – a review, Geomorphology, 109, 17–26, https://doi.org/10.1016/j.geomorph.2008.08.025, 2009.

Fuchs, M., Will, M., Kunert, E., Kreutzer, S., Fischer, M., and Reverman, R.: The temporal and spatial quantification of Holocene sediment dynamics in a meso-scale catchment in northern Bavaria/Germany, Holocene, 21, 1093–1104, https://doi.org/10.1177/0959683611400459, 2011.

Gebhard, K.: Die vorgeschichtliche Besiedlung des Kreises Groß-Gerau. Materialien zur Vor- und Frühgeschichte von Hessen 25, Selbstverlag des Landesamtes für Denkmalpflege Hessen, Wiesbaden, Germany, 2007.

Geilmann, W. and Spang, A.: Eine Beobachtung zur Schnelligkeit der Zerstörung keramischer Scherben auf der Erdoberfläche. Die Kunde, Neue Folge, 9, 93–94, 1958.

Gerhard, S.: Beiträge zur archäologischen Quellenkritik an Beispielen aus dem Neolithikum und der Frühbronzezeit Südbayerns, Arbeiten zur Archäologie Süddeutschlands 18, Faustus, Büchenbach, Germany, 2006.

Gerlach, R.: Wie dynamisch sind die geogenen Grundlagen einer archäologischen Prognose? Die Veränderungen von Relief, Boden und Wasser seit dem Neolithikum, in: Archäoprognose Brandenburg I. Symposium Landschaftsarchäologie und geographische Informationssysteme. Forschungen zur Archäologie im Land Brandenburg 8, edited by: Kunow, J. and Müller, J., Brandenburgisches Landesamt für Denkmalpflege und Archäologisches Landesmuseum, Wünsdorf, Germany, 89–96, 2003.

Gerlach, R.: Holozän: Die Umgestaltung der Landschaft durch den Menschen seit dem Neolithikum, Jahrbuch des Rheinischen Vereins für Denkmalpflege und Landschaftsschutz, 2005, 87–98, 2006.

Gradmann, R.: Süddeutschland II. Die einzelnen Landschaften, Gentner, Darmstadt, Germany, 1931.

Gradmann, R.: Altbesiedeltes und jungbesiedeltes Land, Studium Generale, 1–3, 163–177, 1948.

Hall, A.: Dr. Paul Revellio. Schriften des Vereins für Geschichte und Naturgeschichte der Baar, 27, V–IX, 1968.

Haug, F. and Sixt, G.: Die römischen Inschriften und Bildwerke Württembergs, second edn., Kohlhammer, Stuttgart, Germany, 1914.

Henkner, J., Ahlrichs, J. J., Downey, S., Fuchs, M., James, B. R., Knopf, T., Scholten, T., Teuber, S., and Kühn, P.: Archaeopedology and chronostratigraphy of colluvial deposits as a proxy for regional land use history (Baar, southwest Germany), Catena, 155, 93–103, https://doi.org/10.1016/j.catena.2017.03.005, 2017.

Henkner, J., Ahlrichs, J., Downey, S., Fuchs, M., James, B., Junge, A., Knopf, T., Scholten, T., and Kühn, P.: Archaeopedological analysis of colluvial deposits in favourable and unfavourable areas: reconstruction of land use dynamics in SW Germany, Roy. Soc. Open Sci., 5, 171624, https://doi.org/10.1098/rsos.171624, 2018a.

Henkner, J., Ahlrichs, J., Downey, S., Fuchs, M., James, B., Junge, A., Knopf, T., Scholten, T., and Kühn, P.: Archaeopedological analysis of colluvial deposits in favourable and unfavourable areas: reconstruction of land use dynamics in SW Germany, Dryad Digital Repository, https://doi.org/10.5061/dryad.rh67hb, 2018b.

Henkner, J., Ahlrichs, J., Fischer, E., Fuchs, M., Knopf, T., Rösch, M., Scholten, T., and Kühn, P.: Land use dynamics derived from colluvial deposits and bogs in the Black Forest, Germany, J. Plant Nutr. Soil Sci., 181, 240–260, https://doi.org/10.1002/jpln.201700249, 2018c.

Ihm, P., Lüning, J., and Zimmermann, A.: Statistik in der Archaeologie: Probleme der Anwendung, allgemeine Methoden, Seriation und Klassifikation, Archaeo-Physika 9, Habelt, Bonn, Germany, 1978.

Itten, M.: Die Horgener Kultur. Monographien zur Ur- und Frühgeschichte der Schweiz 17, Die Schweizerische Gesellschaft für Ur- und Frühgeschichte, Basel, Switzerland, 1970.

IUSS Working Group WRB: World reference base for soil resources 2014, update 2015. International soil classification system for naming soils and creating legends for soil maps, World soil resources reports 106, Rome, Italy, 2015.

Jarvis, A., Reuter, H. I., Nelson, A., and Guevara, E.: Hole-filled SRTM for the globe Version 4, CGIAR-CSI SRTM 90m Database, available at: http://srtm.csi.cgiar.org (last access: 18 June 2019), 2008.

Kadereit, A., Kühn, P., and Wagner, G. A.: Holocene relief and soil changes in loess-covered areas of south-western Germany: The pedosedimentary archives of Bretten-Bauerbach (Kraichgau), Quaternary Int., 222, 96–119, https://doi.org/10.1016/j.quaint.2009.06.025, 2010.

Kienlin, T. L. and Valde-Nowak, P.: Neolithic Transhumance in the Black Forest Mountains, SW Germany, J. Field Archaeol. 29, 29–44, https://doi.org/10.1179/jfa.2004.29.1-2.29, 2004.

Knoch, K.: Klima-Atlas von Baden-Württemberg, Deutscher Wetterdienst, Bad Kissingen, Germany, 1953.

Kösel, M. and Rilling, K.: Die Böden der Baar – ein Beitrag zur regionalen Bodenkunde Südwestdeutschlands, Schriften des Vereins für Geschichte und Naturgeschichte der Baar, 45, 99–128, 2002.

Kreutzer, S., Dietze, M., Burow, C., Fuchs, M. C., Schmidt, C., Fischer, M., Firedrich, J., Mercier, N., Smedley, R. K., Durcan, J., and King, G.: Comprehensive Luminescence Dating Data Analysis (R package), available at: https://cran.r-project.org/web/packages/Luminescence/index.html (last access: 18 June 2019), 2016.

Krippner, F.: Siedlungskundliches aus dem Ries. Eine erste Zusammenfassung der systematischen Begehungen, Bayerische Vorgeschichtsblätter, 60, 63–80, 1995.

Kühn, P., Lehndorff, E., and Fuchs, M.: Lateglacial to Holocene pedogenesis and formation of colluvial deposits in a loess landscape of Central Europe (Wetterau, Germany), Catena, 154, 118–135, https://doi.org/10.1016/j.catena.2017.02.015, 2017.

Lais, R.: Die Steinzeit im Schwarzwald, Badische Fundberichte, 13, 29–66, 1937.

Lazar, S.: Bodenzustandsbericht Baar. Bodenschutz 19, Landesanstalt für Umweltschutz Baden-Württemberg, Karlsruhe, Germany, 2005.

Lazar, S. and Rilling, K.: Die Böden der Baar, in: Faszination Baar, edited by: Siegmund, A., Mory's Hofbuchhandlung, Donaueschingen, Germany, 37–56, 2006.

Leopold, M. and Völkel, J.: Colluvium: Definition, differentiation, and possible suitability for reconstructing Holocene climate data, Quaternary Int., 162–163, 133–140, https://doi.org/10.1016/j.quaint.2006.10.030, 2007.

Lomax, J., Kreutzer, S., and Fuchs, M.: Performance tests using the Lexsyg luminescence reader, Geochronometria, 41, 327–333, https://doi.org/10.2478/s13386-013-0174-x, 2014.

Lüning, J.: Steinzeitliche Bauern in Deutschland. Die Landwirtschaft im Neolithikum, Universitätsforschungen zur prähistorischen Archäologie 58, Habelt, Bonn, Germany, 2000.

Murray, A. S. and Wintle, A. G.: Luminescence dating of quartz using an improved singlealiquot regenerative-dose protocol, Radiat. Meas., 32, 57–73, https://doi.org/10.1016/S1350-4487(99)00253-X, 2000.

Niller, H.-P.: Niller, Prähistorische Landschaften im Lößgebiet bei Regensburg, Kolluvien, Auenlehme und Böden als Archive der Paläoumwelt, Regensburger Geographische Schriften 31, Institut für Geographie, Regensburg, Germany, 1998.

Obst, R.: Die Besiedlungsgeschichte am nordwestlichen Maindreieck vom Neolithikum bis zum Ende des Mittelalters, Würzburger Arbeiten zur prähistorischen Archäologie 4, Leidorf, Rahden, Germany, 2012.

Pankau, C.: Die Besiedlungsgeschichte des Brenz-Kocher-Tals (östliche Schwäbische Alb) vom Neolithikum bis zur Latènezeit, Universitätsforschungen zur prähistorischen Archäologie 142, Habelt, Bonn, Germany, 2007.

Pape, W.: Bemerkungen zur relativen Chronologie des Endneolithikums am Beispiels Südwestdeutschlands und der Schweiz, Tübinger Monographien zur Urgeschichte 3, Archaeologica Venatoria, Tübingen, Germany, 1978.

Paret, O.: Württemberg in vor- und frühgeschichtlicher Zeit. Veröffentlichungen der Kommission für Geschichtliche Landeskunde in Baden Württemberg, Reihe B, Band 17, Kohlhammer, Stuttgart, Germany, 1961.

Pasda, C.: Altensteig und Ettlingen – Mesolithische Fundstellen am Rand des Nordschwarzwalds, Fundberichte aus Baden-Württemberg, 19, 99–174, 1994.

Pasda, C.: Zur Erhaltung steinzeitlicher Fundstellen in Flußtälern der Mittelgebirge – Ein Beispiel aus dem Nordschwarzwald, in: Aktuelle Forschungen zum Mesolithikum, in: Urgeschichtliche Materialhefte 12, edited by: Conard, N. J. and Kind, C.-J., Mo-Vince, Tübingen, Germany, 223–228, 1998.

Pietsch, D. and Kühn, P.: Buried soils in the context of geoarchaeological research – two examples from Germany and Ethiopia, Archaeol. Anthropol. Sci., 9, 1571–1583, https://doi.org/10.1007/s12520-014-0180-9, 2017.

Reich, L.: Die badische Landschaft Baar, Badenia oder das badische Land und Volk, 1, 431–461, 1859.

Reichelt, G.: Die Landschaft und ihr natürliches Gefüge, in: Der Schwarzwald-Baar-Kreis, edited by: Gutknecht, R., Theiss, Stuttgart, Germany, 37–55, 1977.

Reimann, T., Román-Sánchez, A., Vanwalleghem, T., and Wallinga, J.: Getting a grip on soil reworking – Single-grain feldspar luminescence as a novel tool to quantify soil reworking rates, Quat. Geochronol., 42, 1–14, https://doi.org/10.1016/j.quageo.2017.07.002, 2017.

Reimer, P., Bard, E., Bayliss, A., and Beck, J. W.: IntCal13 and Marine13 radiocarbon age calibration curves 0–50 000 years cal BP, Radiocarbon, 55, 1869–1887, https://doi.org/10.2458/azu_js_rc.55.16947, 2013.

Revellio, P.: Die Baar in vor- und frühgeschichtlicher Zeit. Neue und alte Funde, Schriften des Vereins für Geschichte und Naturgeschichte der Baar, 14, 35–53, 1924.

Revellio, P.: Aus der Ur- und Frühgeschichte der Baar, Link, Schwenningen a. N., Germany, 1932.

Revellio, P.: Die Baar in vor- und frühgeschichtlicher Zeit, in: Die Baar: Donaueschingen – Villingen, Badische Heimat 25, edited by: Busse, H. E., Haus Badische Heimat, Freiburg im Breisgau, Germany, 58–71, 1938.

Rösch, M.: Botanical evidence for prehistoric and medieval land use in the Black Forest, in: Medieval Rural Settlement in Marginal Landscapes, Ruralia VII, 8–14 September 2007, Cardiff, Wales, UK, edited by: Klápšte, J., Brepols, Turnhout, UK, 335–343, 2009.

Saile, T.: Holozäner Bodenabtrag im Bereich einer bandkeramischen Siedlung am Rande des Reinheimer Beckens bei Wembach, Archäol. Korresponden., 23, 187–196, 1993.

Saile, T.: Untersuchungen zur ur- und frühgeschichtlichen Besiedlung der nördlichen Wetterau. Materialien zur Vor- und Frühgeschichte von Hessen 21, Selbstverlag des Landesamtes für Denkmalpflege Hessen, Wiesbaden, Germany, 1998.

Saile, T.: Relief Intensity and the Formation of the Archaeological Record, in: Classification, Automation, and New Media. Studies in Classification, Data Analysis, and Knowledge Organization, edited by: Gaul, W. and Ritter, G., Springer, Berlin, Germany, 479–489, https://doi.org/10.1007/978-3-642-55991-4_52, 2002.

Schefzik, M.: Die bronze- und eisenzeitliche Besiedlungsgeschichte der Münchner Ebene: eine Untersuchung zu Gebäude- und Siedlungsformen im süddeutschen Raum, Internationale Archäologie 68, Leidorf, Rahden/Westfalen, Germany, 2001.

Schier, W.: Zur vorrömischen Besiedlung des Donautales südöstlich von Regensburg, Bayerische Vorgeschichtsblätter, 50, 9–80, 1985.

Schier, W.: Die vorgeschichtliche Besiedlung im südlichen Maindreieck. Materialhefte zur bayerischen Vorgeschichte 60, Lassleben, Kallmünz/Opf, Germany, 1990.

Schiffer, M. B.: Formation Processes of the Archaeological Record, University of New Mexico Press, Albuquerque, USA, 1987.

Schmid, B.: Die urgeschichtlichen Funde und Fundstellen der Baar: Eine Auswertung des Bestandes. Band 1: Text und Tafeln, Schäuble, Rheinfelden, Germany, 1991.

Schmid, B.: Die urgeschichtlichen Funde und Fundstellen der Baar: Eine Auswertung des Bestandes. Band 2: Katalog, Schäuble, Rheinfelden, Germany, 1992.

Schmotz, K.: Die vorgeschichtliche Besiedlung im Isarmündungsgebiet, Materialhefte zur bayerischen Vorgeschichte 58, Lassleben, Kallmünz/Opf, Germany, 1989.

Schmotz, K.: Kritische Anmerkungen zur Kenntnis vorgeschichtlicher Siedlungsabläufe am Beispiel des Isarmündungsgebietes, in: Archäologische Arbeitsgemeinschaft Ostbayern/West- und Südböhmen, 6. Treffen 12. bis 15. Juni 1996 in Hluboká nad Vltavou, Resümees der Vorträge, edited by: Michálek, J., Schmotz, K., and Zápotocká, M., Leidorf, Espelkamp, Germany, 54–62, 1997.

Schmotz, K.: Zur Besiedlung im Umfeld der Isarmündung während des 4. und 3. Jahrtausends v. Chr.: Quellenlage und Grenzen der Interpretation, in: Mensch und Umwelt während des Neolithikums und der Frühbronzezeit in Mitteleuropa, Internationale Archäologie: Arbeitsgemeinschaft, Symposium, Tagung, Kongress 2, edited by: Lippert, A., Leidorf, Rahden/Westfalen, Germany, 61–72, 2001.

Schreg, R.: Uncultivated landscapes or wilderness? Early medieval land use in low mountain ranges and flood plains of Southern Germany, European Journal of Post-Classical Archaeologies, 4, 69–98, 2014.

Schröder, K. H.: Naturräumliche Grundlagen der Landesgeschichte, in: Handbuch der baden-württembergischen Geschichte. Band 1: Von der Urzeit bis zum Ende der Staufer, edited by: Schaab, M. and Schwarzmaier, H., Klett-Cotta, Stuttgart, Germany, 1–27, 2001.

Seidel, U.: Fürstenberg (Schwarzwald-Baar-Kreis), Fundberichte aus Baden-Württemberg, 35, 895–906, 2015.

Semmel, A.: Bodenkundliche Hinweise auf Ackernutzung und intensive Bodenerosion um 8000 B.P. im Rhein-Main-Gebiet, Archäol. Korresponden., 25, 157–163, 1995.

Shennan, S.: Quantifying archaeology, Edinburgh University Press, Edinburgh, UK, 1988.

Siegmund, A.: Das Klima der Baar: regionalklimatische Studien einer Hochmulde zwischen Schwarzwald und Schwäbischer Alb, PhD thesis, University of Mannheim, Germany, 1999.

Siegmund, A.: Der Klimacharakter der Baar – ein regionales Querprofil, in: Faszination Baar, edited by: Siegmund, A., Mory's Hofbuchhandlung, Donaueschingen, Germany, 57–74, 2006.

Sommer, U.: Zur Entstehung archäologischer Fundvergesellschaftungen: Versuch einer archäologischen Taphonomie, Universitätsforschungen zur prähistorischen Archäologie 6, Habelt, Bonn, Germany, 1991.

Spindler, K.: Aus der Geschichte: Vor- und Frühgeschichte, in: Der Schwarzwald-Baar-Kreis, edited by: Gutknecht, R., Theiss, Stuttgart, Germany, 56–84, 1977.

Starkel, L.: Man as Cause of Sedimentological Changes in the Holocene, Striae, 26, 5–12, 1987.

Stoll, H.: Die früheste Besiedlung der deutschen Mittelgebirge, ein Vergleich: Schwarzwald – Sudeten, Schlesische Blätter, Ausgabe B. Mitteilungen des Landesamtes für Geschichte und des Schlesischen Altertumsvereins, 3, 181–185, 1941.

Stoll, H.: Urgeschichte des Oberen Neckargebietes und der Baar, Habilitation thesis, University of Freiburg, Freiburg im Breisgau, Germany, 1942.

Tanha, A.: Das Schichtstufenrelief der Baar: Morphodynamik und Morphogenese, PhD thesis, Eberhard Karls University Tübingen, Germany, 244 pp., 1986.

Taylor, R. E. and Bar-Yosef, O.: Radiocarbon Dating: An Archaeological Perspective, Left Coast Press, Walnut Creek, USA, 2014.

Teuber, S., Ahlrichs, J. J., Henkner, J., Knopf, T., Kühn, P., and Scholten, T.: Soil cultures – the adaptive cycle of agrarian soil use in Central Europe: an interdisciplinary study using soil scientific and archaeological research, Ecol. Soc., 22, 13, https://doi.org/10.5751/ES-09729-220413, 2017.

Valde-Nowak, P.: Neolithic penetration of European Mid Mountains, Archaeologia Polona, 37, 3–12, 1999.

Valde-Nowak, P.: Siedlungsarchäologische Untersuchungen zur neolithischen Nutzung der mitteleuropäischen Gebirgslandschaften, Internationale Archäologie 69, Rahden/Westf., 2002.

Valde-Nowak, P. and Kienlin, T. L.: Neolithische Transhumanz in den Mittelgebirgen: Ein Survey im westlichen Schwarzwald, Praehist. Z., 77, 29–75, https://doi.org/10.1515/prhz.2002.77.1.29, 2002.

Voigt, R.: Kolluvien als Archive für anthropogen ausgelöste Landschaftsveränderungen an Beispielen aus der westlichen Bodenseeregion, Materialhefte zur Archäologie in Baden-Württemberg 99, Theiss, Stuttgart, Germany, 2014.

Wagner, E.: Fundstätten und Funde aus vorgeschichtlicher, römischer und alamannisch-fränkischer Zeit im Grossherzogtum Baden. Band 1: Das badische Oberland: Kreise Konstanz, Villingen, Waldshut, Lörrach, Freiburg, Offenburg, Mohr, Tübingen, Germany, 1908.

Wagner, H.: Von der Steinzeit zur Stadt: Neue Forschungen zur Besiedlungsgeschichte des Fürstenbergs, Schriften des Vereins für Geschichte und Naturgeschichte der Baar, 57, 33–62, 2014.

Wahle, E.: Beiwort zu den Karten III, 1–2. Historischer Atlas von Baden-Württemberg, Band III: Vor- und Frühgeschichte, edited by: Kommission für Geschichtliche Landeskunde in Baden-Württemberg and Landesvermessungsamt Baden-Württemberg, Landesvermessungsamt Baden-Württemberg, Stuttgart, Germany, available at: https://www.leo-bw.de/detail-gis/-/Detail/details/DOKUMENT/kgl_atlas/HABW_03_01/Das+b%C3%A4uerliche+Neolithikum (last access: 18 June 2019), 1973.

Wilbertz, O. M.: Die Urnenfelderkultur in Unterfranken, Materialhefte zur Bayerischen Vorgeschichte 49, Lassleben, Kallmünz/Opf, Germany, 1982.

Wunderlich, J.: Prähistorische und historische Bodenerosion im Amöneburger Becken – Abgeleitet aus einer Sequenz datierter Kolluvien, Berichte der Kommission für Archäologische Landesforschung in Hessen, 5, 9–15, 2000.

Yokoyama, R., Shirasawa, M., and Pike, R. J.: Visualizing Topography by Openness: A New Application of Image Processing to Digital Elevation Models, Photogramm. En. Rem. S., 68, 257–265, 2002.

E&G Quaternary Sci. J., 68, 95–105, 2019
https://doi.org/10.5194/egqsj-68-95-2019


Open Access E&G Quaternary Science Journal

Research article

# Holocene floodplain evolution in a central European loess landscape – geoarchaeological investigations of the lower Pleiße valley in NW Saxony

**Christian Tinapp[1,4], Susann Heinrich[2], Christoph Herbig[3], Birgit Schneider[1], Harald Stäuble[4], Jan Miera[5], and Hans von Suchodoletz[6,1]**

[1]University of Leipzig, Institute of Geography, Johannisallee 19a, 04103 Leipzig, Germany
[2]Max-Planck-Institute for Evolutionary Anthropology, Deutscher Platz 6, 04103 Leipzig, Germany
[3]Am Dorf 12, 63517 Rodenbach, Germany
[4]Saxonian Archaeological Heritage Office, Zur Wetterwarte 7, 01109 Dresden, Germany
[5]University of Leipzig, Historical Seminar, Ritterstraße 14, 04109 Leipzig, Germany
[6]University of Technology Dresden, Institute of Geography, Helmholtzstraße 10, 01069 Dresden, Germany

**Correspondence:** Christian Tinapp (christian.tinapp@lfa.sachsen.de)

**Relevant dates:** Received: 8 March 2019 – Revised: 17 May 2019 – Accepted: 13 June 2019 – Published: 15 July 2019

**How to cite:** Tinapp, C., Heinrich, S., Herbig, C., Schneider, B., Stäuble, H., Miera, J., and von Suchodoletz, H.: Holocene floodplain evolution in a central European loess landscape – geoarchaeological investigations of the lower Pleiße valley in NW Saxony, E&G Quaternary Sci. J., 68, 95–105, https://doi.org/10.5194/egqsj-68-95-2019, 2019.

**Abstract:** Undisturbed sediments are an important source for the reconstruction of the Holocene development of valleys. Wide floodplains with relatively small rivers in a region settled since 5500 BCE offer opportunities for investigations regarding climatic and anthropogenic landscape change. In the context of a motorway construction, excavations were carried out by the Saxonian Heritage Office in the year 2015. At one of the sites it was possible to get a view of the sediments of the Pleiße valley less than 100 m distance from large cross sections described by Neumeister (1964) in a former open cast mine. Archaeological finds and features, plant remains and radiocarbon dating as well as micromorphological and geochemical investigations helped to decipher the age and the characteristics of the Holocene sediments: above Weichselian loamy sands a sedge peat developed in small depressions during the Preboreal and Boreal. The sands and the sedge peat are covered by a "black clay", which was still the topsoil during the Atlantic period. The sedimentation of 2.3 m thick overbank fines began after 4000 BCE. A depth of 1 m below the surface a medieval Slavic find layer was excavated. These results show that sedimentation processes in the lower Pleiße valley significantly changed after 4000 BCE. It is obvious that the increase in silty material in the floodplain is caused by the land clearance in the Neolithic period. More than half of the silty overbank fines were deposited before the Middle Ages began.

**Kurzfassung:** Ungestörte Sedimente in fluvialen Systemen sind ein wichtiges Archiv zur Rekonstruktion der holozänen Talentwicklung. Seit 5500 BCE besiedelte Altsiedellandschaften mit breiten, von relativ kleinen Flüssen durchflossenen Tälern bieten besonders gute Voraussetzungen für die Untersuchung klimatischer und anthropogener Einflüsse auf Landschaftsveränderungen. Im Rahmen eines Autobahnprojektes südlich von Leipzig wurden vom Landesamt für Archäologie Sachsen Ausgrabungen durchgeführt. An einer der Grabungsflächen konnten die Sedimente des Pleißetales in weniger als 100 m Entfernung zu den von Neumeister (1964) in einem Tagebau beschriebenen Profilen aufgenommen und beprobt werden. Archäologische Befunde und Funde, Pflanzenreste, Radiocarbondatierungen, mikromorphologische und geochemische Untersuchungen führten zur Eingrenzung des Alters der holozänen Sedimente: Über weichselzeitlichem lehmigen Sand lagern in kleinen Vertiefungen Seggentorflagen aus dem Präboreal und Boreal. Sand sowie Torf werden von einem "Schwarzen Ton" überdeckt, der bis weit in das Atlantikum hinein den Oberboden bildete. Nach 4000 BCE begann die Sedimentation von etwa 2,3 m Auenlehm. Einen Meter unter der Geländeoberfläche befindet sich eine mittelalterliche, slawische Fundschicht. Die Ergebnisse belegen, dass sich nach der Ankunft der ersten Ackerbauern die Sedimentationsprozesse im Tal der unteren Pleiße nach 4000 BCE signifikant änderten. Der deutliche Anstieg von schluffreicherem Material in der Aue geht auf die Unterkulturnahme weiter Teile des Einzugsgebietes im Neolithikum zurück. Mehr als die Hälfte der Auenlehmdecke entstand vor dem Mittelalter.

## 1 Introduction

Alluvial valley sediments are important archives of the Holocene landscape evolution, since besides internal processes the dynamics of rivers are controlled by external factors such as base level changes, tectonic activity, climate changes and anthropogenic activity (Bridgland and Westaway, 2008; Faust and Wolf, 2017). Therefore, to investigate the Holocene landscape evolution of central Europe, alluvial sediments of several rivers have been studied during recent years (Starkel et al., 2006; Hoffmann et al., 2008; Erkens et al., 2009; Kaiser et al., 2012; Houben et al., 2013; Notebaert et al., 2018).

Considering central Germany with a long settlement history since ca. 7.5 ka (Heynowski and Reiß, 2010), only sediments of the lower Weiße Elster River were intensively studied during recent decades (Händel, 1967; Hiller et al., 1991; Fuhrmann, 1999; Tinapp, 2002; Tinapp et al., 2008). However, given that the fluvial dynamics can show individual behaviour even between neighbouring river systems (Faust and Wolf, 2017; von Suchodoletz et al., 2018a), the results from the lower Weiße Elster should ideally be complemented by investigations from other regional river systems to derive sound conclusions about the regional paleoenvironmental evolution. Generally, the Holocene landscape evolution of central Germany is not well known so far: besides investigations of the alluvial sediments from the lower Weiße Elster valley, current knowledge is based on non-continuous pollen, snail or ostracod data from different archives, as well as on lacustrine sediments from the former lake Salziger See (Litt, 1992; Mania, 1980; Fuhrmann, 2008; Wennrich et al., 2005).

In contrast to the Weiße Elster River, the lower part of its eastern tributary Pleiße has rarely been investigated so far (Neumeister, 1964; Händel, 1967). According to Neumeister (1964) the stratigraphy for large parts of the lower Pleiße valley is as follows: the base is formed by Late Weichselian silty fine sand that is sporadically covered by peat, and both are covered by a so-called "black clay" ("Schwarzer Ton"; Neumeister, 1964) that is overlain by older and younger overbank fines. New geoarchaeological investigations of a long-known site in the lower Pleiße valley in 2015 offered the chance to re-evaluate and reanalyse the fluvial stratigraphy of the lower Pleiße valley with modern radiocarbon, sedimentological and micromorphological methods.

Therefore, the goal of this study was to reconstruct environmental change in the lower Pleiße floodplain and to compare these results with those from the neighbouring lower Weiße Elster valley (Figs. 1 and 2) but also with other floodplains from central Europe. This will allow sound conclusions about the regional paleoenvironmental evolution of central Germany compared with other regions of central Europe.

## 2 Study area

The area south of Leipzig belongs to the North German Plain, and the mostly flat landscape is covered with Pleistocene sediments: in the northern part, glacial till, gravel and sand deposits of Elsterian and Saalian age are covered by Weichselian sandy loess with a thickness of ca. 50 cm. Towards the south, the sandy loess grades into typical loess and increases its thickness to more than 7 m in the Altenburg-Zeitz loess hills (Eissmann, 2002).

The once 115 km long Pleiße River is a right-hand tributary of the Weiße Elster. Most of its former valley was destroyed by mining activities during the 20th century. Therefore the river flows through a canal today, and only small parts of its original floodplain are still preserved. The courses of the Weiße Elster and Pleiße River were formed during the Elsterian glaciation more than 400 000 years ago (Eissmann, 2002; Lauer and Weiss, 2018). Subsequently, fluvial gravels and sand were deposited under periglacial conditions

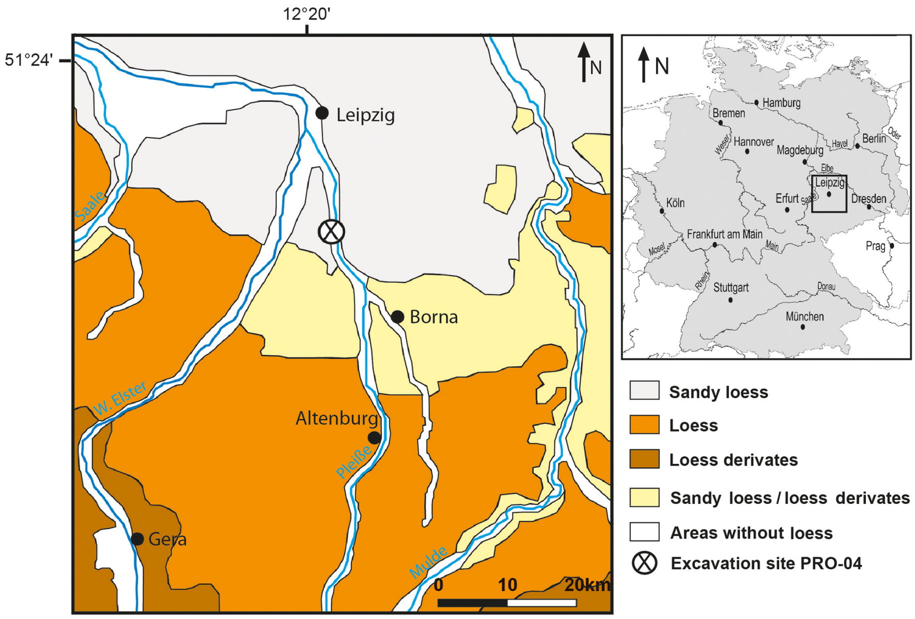


**Figure 1.** The excavation site near the Pleiße River south of Leipzig with the distribution of loess and loess-like deposits (according to Eissmann, 2002).

during the Saalian and Weichselian glacial periods. In both river systems the current floodplains are found at the eastern sides of the once wider valleys, whereas the western parts are mainly occupied by Saalian gravel terraces. In the remaining smaller floodplains Weichselian gravels and sands form the bases of the Holocene deposits. The branched Weichselian river systems changed towards meandering systems during the latest Weichselian period (Mol, 1995). After the Younger Dryas cold spell, the so far dominant steppe vegetation was replaced by open forests that developed in the floodplains and the surrounding areas (Litt, 1994). The first Neolithic settlers already arrived in the region 7500 years ago (Heynowski and Reiß, 2010). This was the start of a long history of land use in the region with varying intensities during different periods (Tinapp and Stäuble, 2000).

## 3 Methods

In the context of a motorway construction, archaeological excavations were carried out by the Saxonian Heritage Office in 2015. In one of the four excavation sites east of the village Großdeuben, sediments of the lower Pleiße floodplain were exposed probably less than 100 m distance from the cross sections that were described by Neumeister (1964) in the open cast lignite mine Espenhain more than 50 years ago.

In preparation for the excavation, the topsoil was removed in a 20 × 83 m wide area by an excavator up to 1 m below the current surface. At this level a small channel and a lot of Slavic remnants (900–1000 CE) were discovered. During the excavations of the Slavic features three cross sections were opened by the excavator: Profile 1 was 15 m long and 2.1 m deep, and Profile 2 was 10 m long and 1.8 m deep. Both east–west directed parallel cross sections started on the level of the Slavic features, while the smaller (2 m long) and 1.6 m deep Profile 3 was dug at the edge of the excavation area (Fig. 3). From the sediments in Profile 3, 6 samples were taken for geochemical analyses, and in Profile 2, 22 samples were taken for geochemical analyses and another 6 for radiocarbon dating. In Profile 1, 1 sample was taken for thin section analysis.

Plant macro remains were extracted from two sediment samples each in Profile 1 and 2 by flotation and wet sieving (mesh width: 2, 0.5 and 0.25 mm), and determined under magnifications from ×6.3 to ×40 using standard literature (e.g. Cappers et al., 2012) and the reference collection at the Laboratory of Archaeobotany, Institute of Prehistoric Archaeology, Goethe University Frankfurt. Attribution of the taxa to ecological units followed Oberdorfer (2001). Several discovered fruits and seeds, as well as pieces of charcoal from two layers of the overbank fines under the Slavic surface at Profile 2, were used for radiocarbon dating (Table 1).

A thin section for micromorphological analysis was prepared from an oriented and undisturbed soil sample taken from the transition of the black clay to the overlying overbank deposits in Profile 1 and was impregnated with resin. The thin section was analysed using a petrographic microscope under plane-polarized light (PPL), crossed polarized light (XPL) and oblique incident light (OIL). The microscopic description mainly followed the terminology according to Bullock et al. (1985) and Stoops (2003).

The particle size distribution was determined by dry sieving of the sand fraction, and silt and clay were measured

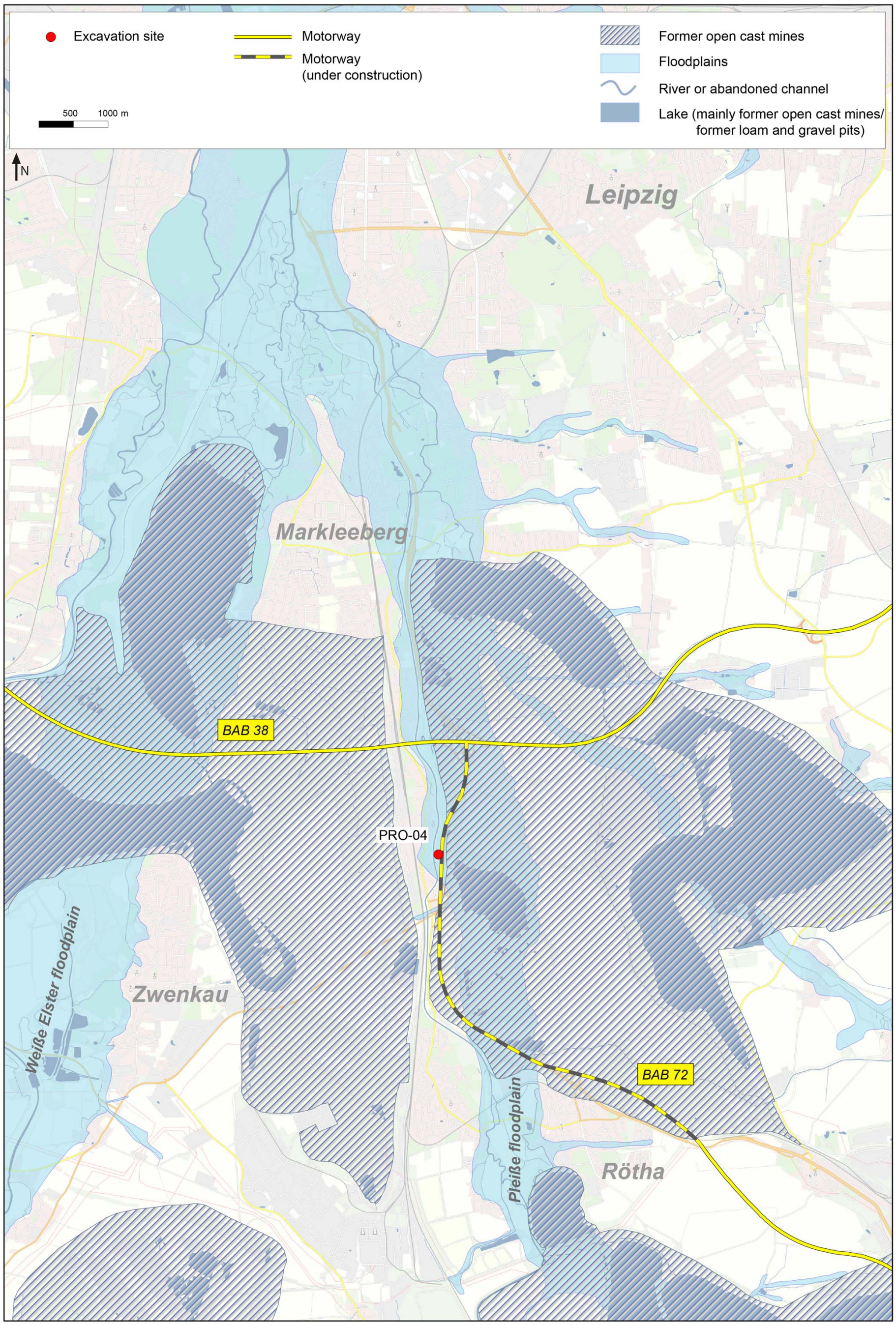


**Figure 2.** Location of the excavation site (PRO-04) with mining areas and the floodplains of Weiße Ester and Pleiße (map: Geodaten© Staatsbetrieb Geoinformation und Vermessung Sachsen 2018).

based on settling velocities using a sedigraph (Micrometrics). An element analyser was used for the determination of the total contents of carbon, nitrogen and sulfur. The determination of the carbonate content was carried out using the volumetric method with a Eijkelkamp calcimeter according to Scheibler. Subtraction of the inorganic carbon from the total carbon resulted in the organic carbon.

## 4 Results

In the following, the stratigraphic succession of the lower Pleiße valley with analytical and dating results is described from the base to the top (Fig. 4):

– The base of the Holocene floodplain is formed by Late Weichselian loamy sands. These are waterlogged and do

**Table 1.** Results of $^{14}C$ analyses, performed by Ronny Friedrich, Curt-Engelhorn-Zentrum Archäometrie in Mannheim (CEZ), and calibrated using INTCAL 13 and SwissCal 1.0.

| MAMS | Material | $^{14}C$ age (years) | Error (years) | $\delta^{13}C$ ($^0/00$) | $1\sigma$ Cal. BCE (years) | $2\sigma$ Cal. BCE (years) | C (%) |
|---|---|---|---|---|---|---|---|
| 27 110 | peat | 9876 | 35 | −25.0 | 9353–9283 | 9402–9265 | 52.8 |
| 27 111 | charcoal | 9408 | 34 | −30.7 | 8730–8638 | 8785–8612 | 59.7 |
| 27 112 | wood fragments | 8702 | 33 | −26.6 | 7736–7613 | 7811–7599 | 56.4 |
| 27 113 | wood fragments | 5152 | 27 | −27.7 | 3984–3951 | 4038–3816 | 51.5 |
| 27 114 | charcoal | 4474 | 27 | −31.7 | 3327–3095 | 3337–3029 | 2.2 |
| 27 115 | charcoal | 3604 | 25 | −28.1 | 2015–1924 | 2026–1895 | 38.4 |

not contain any organic remnants, with the exception of fine roots.

- The loamy sands are sporadically covered by peat layers, where $C_{org}$ values reach $>30\,\%$, and the pH is $<3$ (Fig. 5). The peat is compacted and contains plant material mostly consisting of *Carex* species. Other plants which could be identified were *Betula* spec. and some herbs like *Comarum palustre* and *Filipendula ulmaria*, indicating the existence of a *Carex* peat. Radiocarbon dates prove a Preboreal age of the peat layers (Fig. 4 and Table 1): peat fragments date between 9402 and 9265 cal. BCE, while the charcoal has a younger age of 8785–8612 cal. BCE. In contrast, dated wood pieces probably have their origin in roots and are about 1000 years younger.

- A black clay ca. 25 cm thick covers the loamy sand and the peat. Clay contents $>80\,\%$ demonstrate calm sedimentation conditions during its deposition. pH values rise to $>4$, and $C_{org}$ values are $>6\,\%$. Root traces start at the top and pass downwards through the black clay layer. Plant macro remains could not be found, with the exception of root fragments and one charcoal piece. The root fragments gave a radiocarbon age of 4038–3816 cal. BCE (Fig. 4). The lowest part of the thin section, representing the upper part of the black clay, was made up of dark-grey-coloured, very fine-grained material (fine silt and clay). The microstructure of the sediment was spongy, as it mainly consisted of more or less oval and round-shaped voids that were encircled by filigree sediment covers and bridges between the covered voids (Fig. 6a, b). Their shape implies its genesis by plant pseudomorphs: plants (stems) were embedded into the sediments and subsequently completely decomposed so that only the embedding material was preserved. Plants standing upright would have created vertical structures. Therefore, the horizontal pseudomorphs suggest a surface-parallel bedding of the plant stems. This process is regularly observed during flood events. Obviously, the thin section illustrates the remnants of the last vegetation that covered the black clay before the deposition of overbank fines began.

- The black clay is overlain by overbank fines with a thickness of ca. 2.3 m. The deposits directly overlying the black clay already have a much higher silt content, while clay percentages drop from 80 % to around 50 % (Fig. 5). The colour changes from black (2.5Y2.5/1) to dark greyish brown (10YR4/2), while the pH values are between 4 and 5. The $C_{org}$ content of the overbank fines fluctuates between 0.5 % and 1 %, and redoximorphic features prove temporal waterlogging. Charcoal pieces were taken from two levels of the overbank fines of Profile 2, i.e. at 117.1 and 117.8 m a.s.l. (Fig. 4). Both radiocarbon ages prove a Subboreal age (3337–3029, 2026–1895 cal. BCE; Table 1). The upper part of the thin section, representing the lowest overbank fines, shows closely packed fine-grained sediments. The material has a light grey colour with dark-grey-coloured channel infillings, consisting of the underlying black clay that was mixed in by bioturbation (Fig. 6). Furthermore, abundant biogenic voids underline a high intensity of bioturbation processes. The grey colour of the sediments is mainly a consequence of reducing conditions due to a high groundwater level. Nevertheless, the thin section reveals features of groundwater oscillations: larger voids allowing oxygen intrusion into the sediment display coatings, hypocoatings and fibrous crystals of ferric oxides and hydroxides (Fig. 6e, f).

- Above the lower level of overbank fines with an Atlantic to Subboreal age, a lot of potsherds of the Slavic period (ca. 900–1000 CE) mark the base of ca. 1 m of loamy material that was deposited during the last ca. 1000 years (Fig. 3). Higher sand values below and above the Slavic layer prove less calm conditions during the sedimentation process (Fig. 5). Missing settlement features give evidence for just a short period of human activity on the valley floor during the Slavic period.

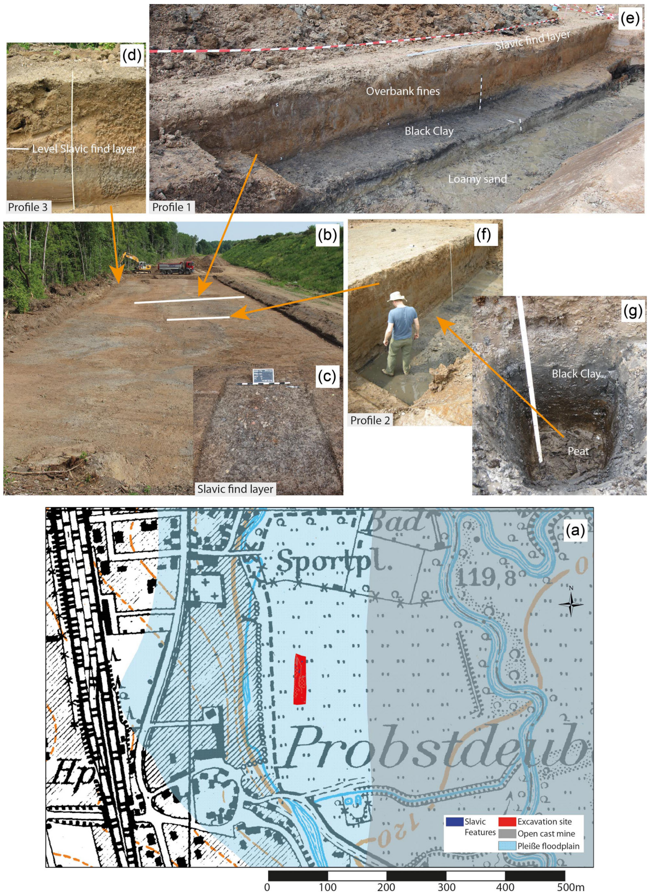


**Figure 3.** The excavation site, the profiles and the sediments near Probstdeuben. **(a)** The excavation site in the floodplain and the topographic situation during the first half of the last century (Geodaten© Staatsbetrieb Geoinformation und Vermessung Sachsen 2018). **(b)** The excavation site after removal of ca. 1 m of overbank fines by an excavator with the positions of the three profiles. **(c)** Slavic finds in the overbank fines ca. 1 m below the recent surface. **(d)** The uppermost overbank fines with the level of the Slavic find layer in Profile 3. **(e)** Profile 1 with the waterlogged loamy sands that are covered by the black clay and overbank fines. **(f)** Profile 2 with the black clay at the bottom. In a small hand-dug pit beneath the base of the profile a peat layer was found under the black clay **(g)**.

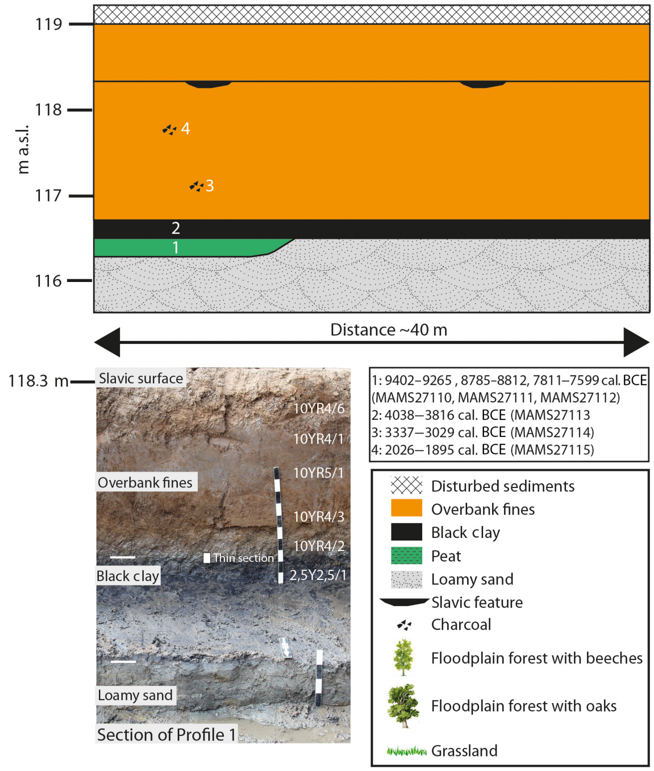


**Figure 4.** The valley sediments of the Pleiße according to Profile 1 to 3 with $^{14}$C ages and the position of the thin section.

## 5 Discussion

### 5.1 Deposition of peat and black clay sediments during the Early to Middle Holocene

The oldest Holocene sediments in the lower Pleiße valley are peats that developed in small depressions of the Weichselian valley floor during the Preboreal period (Fig. 7a). Similar layers were formerly also described by Neumeister (1964) and Händel (1967). Organic sediments in the same stratigraphic position are also known from the lower Weiße Elster valley (Hiller et al., 1991; Tinapp, 2002), and organic deposition since that period is also known from other European catchments (Rittweger, 2000; Notebaert et al., 2018). Probably wetter conditions and higher groundwater levels in the valleys during the Preboreal resulted in the formation of many small peat layers on the Weichselian sediment base.

Sedimentation of the black clay in the Pleiße valley started during the Boreal and stopped during the Atlantic period when it was covered by overbank fines. According to the high clay content we assume mainly limnic conditions during the time of its sedimentation. According to Neumeister (1964) our investigations confirm that the black clay is pedologically a gyttja; i.e. it was formed under waterlogging conditions. The black clay discordantly covers the Weichselian sand and the Preboreal peat (Fig. 7b). Deposition of these more limnic sediments with a lower organic content during the Boreal compared with the Preboreal indicates a change towards more humid environmental conditions on the valley floor of the lower Pleiße River. However, iron and manganese features and roots that start in the black clay and reach the underlying loamy Weichselian sands also prove temporal drier periods. It is likely that the repeated changes of wetter and drier conditions on the valley floor were caused by fluctuations of the water table of the river. A similar black clay layer was not found in the neighbouring lower Weiße Elster river system. There, overbank fines directly cover Weichselian sand and gravel and sporadically also Preboreal peats (Hiller et al., 1991; Tinapp, 2002). We assume that the val-

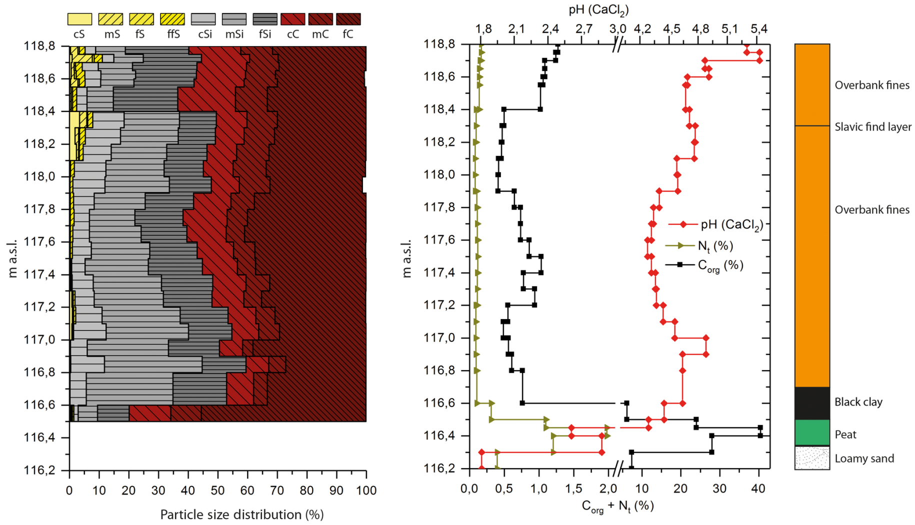


**Figure 5.** Particle size distribution, pH values and organic carbon of the sediments of Profile 1 to 3.

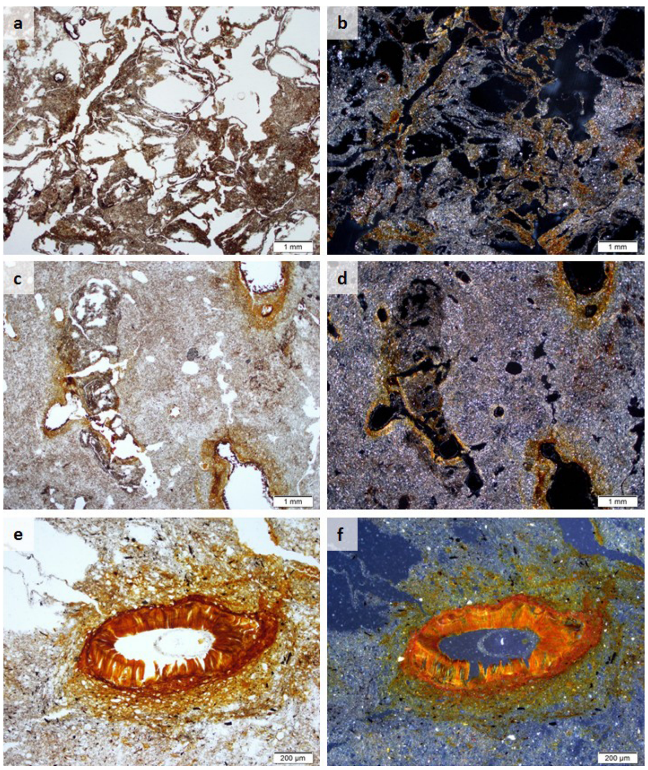

**Figure 6.** Microphotographs of the black clay (**a**, **b**) and the oldest overbank fines (**c**–**f**). **(a)** Voids encircled by filigree sediment covers and bridges between the covered voids (PPL). **(b)** Like **(a)** (XPL). **(c)** Light-grey-coloured material with dark-grey-coloured channel infillings consisting of the underlying black clay mixed in by bioturbation (PPL). **(d)** Like **(c)** (XPL). **(e)** Ferric coating, hypocoating and fibrous crystals of goethite (PPL). **(f)** Like **(e)** (OIL).

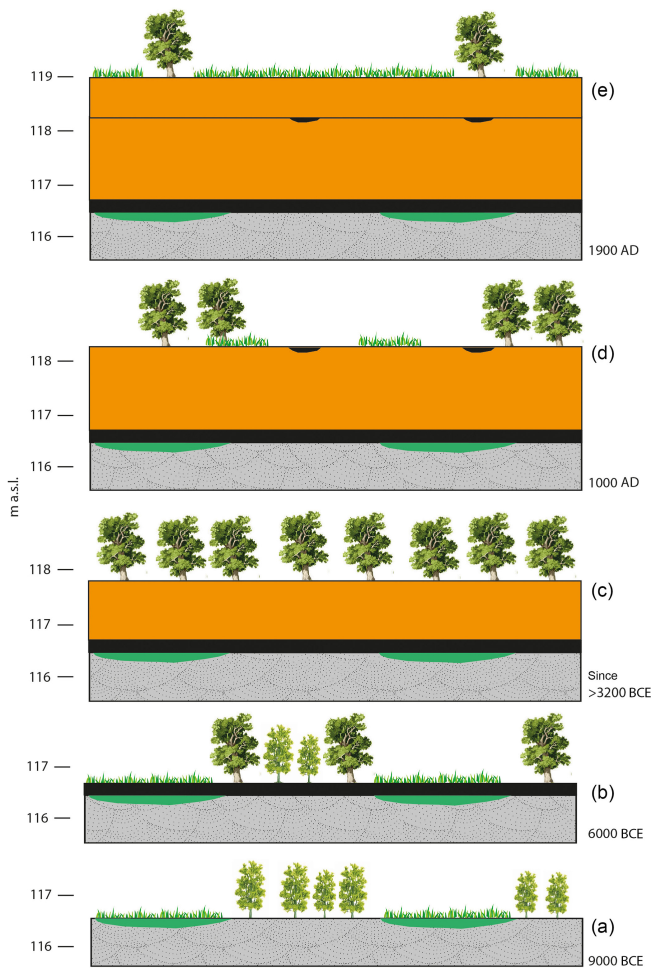


**Figure 7.** Holocene floodplain development of the lower Pleiße in five stages (legend in Fig. 4).

ley of the lower Weiße Elster, 2 km wide, was better drained than the lower Pleiße valley with a width of only ca. 1 km, and therefore a black clay could not develop in the former. It is also possible that the very slight slope of less than 1 % from here towards the drainage base a few kilometres in the north that is formed by the Weiße Elster valley stimulated the temporary development of limnic conditions in the lower Pleiße valley, allowing the deposition of the black clay layer.

It can be questioned whether black Holocene floodplain sediments should generally be interpreted as "Black Floodplain Soils" (Rittweger, 2000). However, the widespread existence of black-coloured organic-rich and clayey sediments in the same stratigraphic positions of different loess-influenced central European floodplains (Brunnacker, 1959; Schirmer, 1983; Bork, 1983; Brosche, 1984; Pretzsch, 1994; Schellmann, 1994; Hilgart, 1995; Rittweger, 2000; Bos et al., 2008; Brown et al., 2018) suggests similar conditions during the Boreal and Atlantic period for central Europe: wet valley floors and high organic load obviously caused the formation of clay-rich limnic layers with high contents of organic carbon. Rittweger (2000) discussed Chernozem-derived material as one factor in the formation of these dark layers. However, Chernozem and Phaeozem soils are found in the catchment of the lower Weiße Elster valley where no black clay was formed (Tinapp et al., 2008). In contrast, for the Pleiße catchment where a black clay exists such soils do not exist today. Instead, Stagnogleys and Luvisols are the main soil types in the catchment of the lower Pleiße River and probably also existed prior to Neolithic settlement (von Suchodoletz et al., 2019). Therefore, for the lower Pleiße valley a genesis of the black clay from Chernozem- and Phaeozem-derived material can clearly be rejected.

## 5.2 Alluvial overbank sedimentation since the Neolithic period

The covering of the black clay by ca. 2.3 m of younger overbank deposits indicates an environmental change at all sites: the sedimentation of the black clay in an environment with fluctuating water tables in the floodplain passed over into the deposition of more silty and sandy material. Human deforestation and agricultural land use in the catchment of the Pleiße river since 5500 BCE obviously resulted in the aggradation of coarser-grained and less organic overbank deposits that started between since ca. 4000 and ca. 3200 BCE (Fig. 7c and d). The growing thickness of the overbank fines led to less wet conditions and a more frequently dry topsoil. Similar to our results Rittweger (2000) dated the so-called Black Floodplain Soil into the Boreal and Atlantic period. He suggested relatively dry conditions after its formation, since the Black Floodplain Soil was strongly overprinted by soil development, and archaeological features on its surface proved human activities in the floodplain. However, that could be denied for the lower Pleiße valley: during the Early Neolithic period the floodplain was muddy and wet, and only the continuous rise of the valley floors by subsequent overbank deposition allowed longer-lasting anthropogenic activities in the floodplain during a later period. Accordingly, the oldest archaeological features in the lower Pleiße valley originate from the Bronze Age (Grahmann and Braune, 1933). The moment of sedimentation change from the black clay to the overlying overbank deposits could obviously be detected by our thin section analysis: holes at the surface of the black clay must have been caused by rotten plant material (Fig. 6). These should derive from sedges that were bent over during a flood event and buried by the oldest overbank fines. During subsequent drier periods the organic material was decomposed, whereas the holes remained since bioturbation was prevented by the new sediment cover.

Similar to the neighbouring lower Weiße Elster floodplain where significant overbank sedimentation was recorded in ca. 4500 to 4000 BCE (Tinapp et al., 2008), this demonstrates a start of overbank sedimentation during the Neolithic period. Therefore, the fairly early start of overbank sedimentation obviously represents a regional reaction of the landscape in this part of central Germany following Neolithic settlement activities (Fig. 8). This demonstrates the dominant influence of quite intensive human activity on the development of overbank fines (Hiller et al., 1991; Tinapp, 2002; Tinapp et al., 2008), especially against the background that major climatic changes are not detectable in central Germany for this time (Litt, 1994; Wennrich, 2005).

The start of overbank sedimentation in central Germany already during the Neolithic period was significantly earlier than in many other catchments of central Europe, where despite Neolithic settlement activities this process started at the earliest between ca. 4.2 and ca. 2 ka (Rittweger, 2000; Niller, 2001; Mäckel et al., 2002; Fuchs et al., 2011; Houben et al., 2013; Notebaert et al., 2018; Brown et al., 2018). Delayed overbank sedimentation compared with the onset of Neolithic land use and the deposition of corresponding colluvial slope sediments in the latter is explained with temporally variable hydrosedimentary connectivity between hillslopes and floodplains, leading to a sediment cascade in the landscape (Brown, 2009; Fuchs et al., 2011; Houben et al., 2013). In contrast, the early start of overbank deposition in the Weiße Elster catchment was explained with good hillslope–channel coupling due to missing small sediment traps along the lower Weiße Elster valley since the Neolithic period (Tinapp et al., 2008). However, given the obviously regional character of early overbank sedimentation in this part of central Germany we think that other factors could have also caused the high regional Neolithic sediment connectivity. Possible factors could, for example, have been the spatial structure of regional Neolithic settlement activity or climatic factors in this relatively dry area with precipitation down to 500 mm $a^{-1}$. However, these are only hypotheses so far that need further investigations.

No clear sediment unconformities were detected in the overbank fines, although geomorphologically stable periods

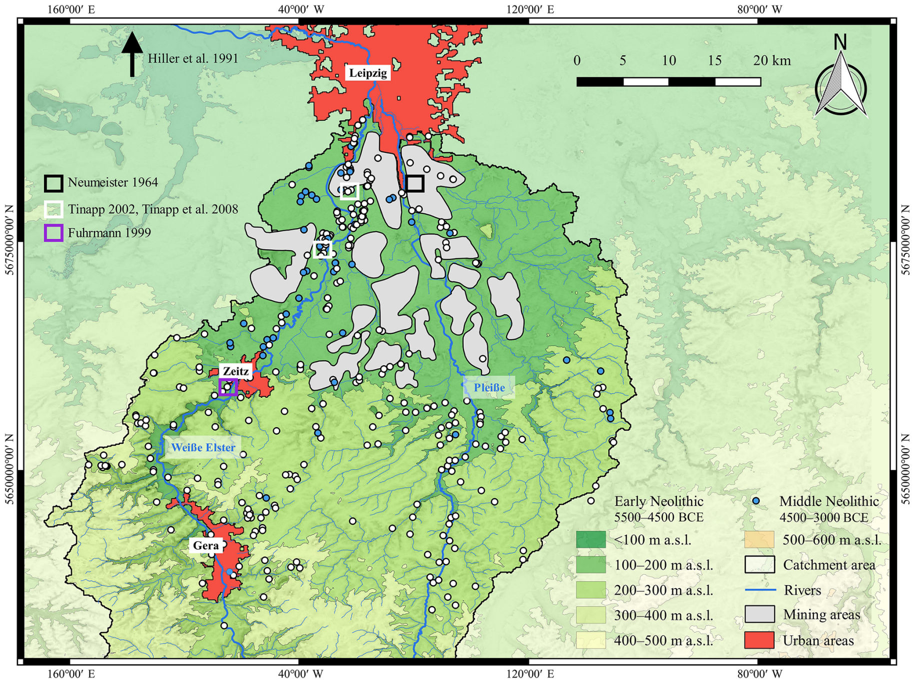


**Figure 8.** Early and Middle Neolithic find spots around the valleys of Weiße Elster and Pleiße and the positions of the main study sites. Mining activities destroyed great parts of the lower Pleiße floodplain and the surrounding plains, and most of these areas were archaeologically not investigated prior to 1993. The extent of the open cast mines on the map dates back to the year 1990 (Standke et al., 2010).

with less flooding often led to soil formation with the accumulation of organic material in floodplains of other regions (Zielhofer et al., 2009; May et al., 2015; von Suchodoletz et al., 2018b). Even at the Slavic level initial enrichment of organic material could not be detected (Fig. 5). Generally, unlike in many other river systems of western central Europe (Hoffmann et al., 2008; Fuchs et al., 2011; Houben et al., 2013; Notebaert et al., 2018) no strong increase of overbank sedimentation during the last 1000 years was observed along the lower Pleiße and Weiße Elster River: whereas at the lower Weiße Elster River ca. 0.8–1 m of overbank sediments compared with a total thickness of ca. 3–4 m was deposited over the last 1000 years (Fig. 7e), along the lower Pleiße River ca. 1 m of overbank sediments compared with a total thickness of ca. 2.3 m was observed. Thus, more than half of the fine-grained sediment cover of these valleys was formed prior to the Middle Ages. Therefore, unlike in most other river systems of central Europe this demonstrates a relatively continuous high regional sediment connectivity in this part of central Germany since the Neolithic period.

## 6 Conclusions

Our investigations in the lower Pleiße valley were conducted at a mostly undisturbed site with predominant sedimentation and negligible erosion processes during the Holocene. We compared our results with those of Neumeister (1964) that were carried out less than 100 m east of our study site and that were based on field investigations that extended over ca. 900 m. This comparison demonstrates that our investigated stratigraphy is representative of this part of the lower Pleiße valley, so we were able to build up a well-based reconstruction of its Holocene landscape development. In doing so, it was possible to define the turning point from extremely clayey and organic-rich, mostly limnic sedimentation (black clay) in the Boreal and Atlantic periods towards the deposition of coarser-grained and less organic overbank fines during the following period. This change occurred more than 1000 years after the beginning of Early Neolithic settlement between 4000 and 3300 BCE and was obviously linked with land clearance by these first farmers. The fairly early start of overbank sedimentation during the Neolithic period seems to be the exception rather than the rule in central Europe. During the following 6000 years sedimentation conditions did not change significantly (Fig. 4). Even initial organic enrichment could not be detected, although some geomorphologically stable periods with less flooding should have led to initial soil development. We also did not find a strong increase of the sediment deposition rates during and after the Middle Ages that was detected in many other catchments of central Europe, since more than half of the sediment cover of the lower Pleiße valley was deposited prior to that period. Further research in other river catchments of central Europe is needed to prove or to deny the singularity of the Holocene sedimentation history in the river catchments of lower Pleiße and Weiße Elster.

**Data availability.** Data relating to this paper can be found in the Supplement.

**Supplement.** The supplement related to this article is available online at: https://doi.org/10.5194/egqsj-68-95-2019-supplement.

**Author contributions.** CT and HS organized the project. CT, SH and HvS carried out the fieldwork. The concept and structure of the paper were organized by CT and HvS. The laboratory work was done by CH (plant macro remains) and BS (geochemistry, particle size distribution). Thin section analysis were carried out by SH. Archaeological investigations were performed by HS and JM. CT and HvS took the lead in writing the manuscript, with input from SH, CH, BS and HS. All authors discussed the results and contributed to the final manuscript.

**Competing interests.** The authors declare that they have no conflict of interest.

**Special issue statement.** This article is part of the special issue "Connecting disciplines – Quaternary archives and geomorphological processes in a changing environment". It is a result of the First Central European Conference on Geomorphology and Quaternary Sciences, Gießen, Germany, 23–27 September 2018.

**Acknowledgements.** We thank Yvonne Heine and the excavation team. Constructive comments by Knut Kaiser and an anonymous reviewer helped us to improve the manuscript.

## References

Bork, H.-R.: Die holozäne Relief- und Bodenentwicklung in Lössgebieten, Catena, Suppl.-Band, 1–93, 1983.

Bos, J. A. A., Dambeck, R., Kalis, A. J., Schweizer, A., and Thiemeyer, H.: Palaeoenvironmental changes and vegetation history of the northern Upper Rhine Graben (southwestern Germany) since the Lateglacial, Netherlands J. Geosc. Geol. Mijnb., 87, 65–88, 2008.

Bridgland, D. and Westaway, R.: Climatically controlled river terrace staircases: A worldwide Quaternary phenomenon, Geomorphology, 98, 285–315, 2008.

Brosche, K. H.: Zur jungpleistozänen und holozänen Entwicklung des Werratales zwischen Hannoversch Münden und Phillipsthal, Eiszeitalter u. Gegenwart, 34, 105–129, 1984.

Brown, A. G.: Colluvial and alluvial response to land use change in Midland England: an integrated geoarchaeological approach, Geomorphology, 108, 92–106, 2009.

Brown, A. G., Lespez, L., Sear, D. A., Macaire, J.-J., Houben, P., Klimek, K., Brazier, R. E., Van Oost, K., and Pears, B.: Natural vs anthropogenic streams in Europe: History, ecology and implications for restoration, river-rewilding and riverine ecosystem services, Earth-Sci. Rev., 180, 185–205, 2018.

Brunnacker, K.: Junge Deckschichten und 'schwarzerdeähnliche' Böden bei Schweinfurt, Geol. Bl. Nordost-Bayern, 9, 2–14, 1959.

Bullock, P., Fedoroff, N., Jongerius, A., Stoops, G., and Tursina, T. (Eds.): Handbook for soil thin section description, Waine Research Publications, Albrighton, Wolverhampton, 1985.

Cappers, R. T. J., Bekker, R. M., and Jans, J. E. A.: Digitale zadenatlas van Nederland – Digital seed atlas of the Netherlands, Groningen Archaeological Studies 4, 2nd edn., Barkhuis Publishing, Eelde, 2012.

Eissmann, L.: Quaternary geology of eastern Germany (Saxony, Saxon-Anhalt, South Brandenburg, Thüringia, type area of the Elsterian and Saalian stages in Europe, Quat. Sci. Rev., 21, 1275–1346, 2002.

Erkens, G., Dambeck, R., Volleberg, K. P., Bouman, M. T. I. J., Bos, J. A. A., Cohen, K. M., Wallinga, J., and Hoek, W. Z.: Fluvial terrace formation in the northern Upper Rhine Graben during the last 20 000 years as a result of allogenic controls and autogenic evolution, Geomorphology, 103, 476–495, 2009.

Faust, D. and Wolf, D.: Interpreting drivers of change in fluvial archives of the Western Mediterranean – A critical review, Earth-Sci. Rev., 174, 53–83, 2017.

Fuchs, M., Will, M., Kunert, E., Kreutzer, S., Fischer, M., and Reverman, R.: The temporal and spatial quantification of Holocene sediment dynamics in a meso-scale catchment in northern Bavaria, Germany, The Holocene, 21, 1093–1104, 2011.

Fuhrmann, R.: Klimaschwankungen im Holozän nach Befunden aus Talsedimenten Mitteldeutschlands – Beiträge zur Klimageschichte und Stratigraphie des jüngeren Quartärs, Altenbg. nat.wiss. Forsch., 11, 3–41, 1999.

Fuhrmann, R.: Die Ostrakoden- und Molluskenfauna des Auelehmprofils Zeitz (Landkreis Burgenland) und ihre Aussage zum Klima sowie zur Landnutzung im jüngeren Holozän Mitteldeutschlands, Mauritiana, 20, 253–281, 2008.

Grahmann, R. and Braune, K.: Braune, Bronzezeitliche und slawische Herdstellen in der Pleißeaue bei Markkleeberg, "Die Fundpflege", Jg. 1, H. 6, Beitrag d. Mitteldt. Bl. f. Volkskunde, 1933.

Händel, D.: Das Holozän in den nordwestsächsischen Flußauen, Hercynia, Bd. 4 Leipzig, 2, 152–198, 1967.

Heynowski, R. and Reiß, R. (Eds): Atlas zur Geschichte und Landeskunde von Sachsen, Beiheft zur Karte BI 1.1-1.5, Ur- und Frühgeschichte Sachsens, Leipzig/Dresden, 2010.

Hilgart, M.: Die geomorphologische Entwicklung des Altmühl- und Donautales im Raum Dietfurt-Kelheim-Regensburg im jüngeren Quartär, Forschungen zur deutschen Landeskunde, 242, Deutsche Akademie für Landeskunde, Trier, 1995.

Hiller, A., Litt, T., and Eissmann, L.: Zur Entwicklung der jungquartären Tieflandstäler im Elbe-Saale-Gebiet unter besonderer Berücksichtigung von $^{14}C$-Daten, Eiszeitalter u. Gegenwart, 41, 26–46, 1991.

Hoffmann, T., Lang, A., and Dikau, R.: Holocene river activity: Analysing $^{14}C$-dated fluvial and colluvial sediments from Germany, Quaternary Sci. Rev., 27, 2031–2040, 2008.

Houben, P.: Sediment budget for five millennia of tillage in the Rockenberg catchment (Wetterau loess basin, Germany), Quaternary Sci. Rev., 52, 12–23, 2012.

Houben, P., Schmidt, M., Mauz, B., Stobbe, A., and Lang, A.: Asynchronous Holocene colluvial and alluvial aggradation: A matter of hydrosedimentary connectivity, The Holocene, 23, 544–555, 2013.

Kaiser, K., Lorenz, S., Germer, S., Juschus, O. Küster, M, Libra, J., Bens, O. and Hüttl, R. F.: Late Quaternary evolution of rivers, lakes and peatlands in northeast Germany reflecting past climatic and human impact – an overview, Quaternary Sci. J., 61, 2, 103–132, 2012.

Lauer, T. and Weiss, M.: Timing of the Saalian- and Elsterian glacial cycles and the implications for Middle- Pleistocene hominin presence in central Europe, Nature, Sci. Rep., 8, 5111, https://doi.org/10.1038/s41598-018-23541-w, 2018.

Litt, T.: Fresh investigations into the natural and anthropogenically influenced vegetation of the earlier Holocene in the Elbe-Saale Region, Central Germany, Veg. Hist. Archaeobot., 1, 69–74, 1992.

Litt, T.: Paläoökologie, Paläobotanik und Stratigraphie des Jungquartärs im nord-mitteleuropäischen Tiefland unter besonderer Berücksichtigung des Elbe-Saale-Gebietes, Dissertationes Botanicae, Halle, 227, 1994.

Mäckel, R., Schneider, R., Friedmann, A., and Seidel, J.: Envionmental changes and human impact on the relief development in the Upper Rhine valley and Black Forest (South-West Germany) during the Holocene, Z. Geomorphol., Supplement 128, 31–45, 2002.

Mania, D.: Zur spät- und nacheiszeitlichen Besiedlung in ihrer Beziehung zur natürlichen Umwelt, in: Wissenschaftliche Beiträge der Martin-Luther-Universität Halle-Wittenberg 1980/6, Halle/S, 29–31, 1980.

May, J.-H., Plotzki, A., Rodrigues, L., Preusser, F., and Veit, H.: Holocene floodplain soils along the Río Mamoré, northern Bolivia, and their implications for understanding inundation and depositional patterns in seasonal wetland settings, Sediment. Geol., 330, 74–89, 2015.

Mol, J.: Weichselian and Holocene river dynamics in relation to climate change in the Halle-Leipziger Tieflandsbucht (Germany), Eiszeitalter und Gegenwart, 45, 32–41, 1995.

Neumeister, H.: Beiträge zum Auenlehmproblem des Pleiße- und Elstergebietes, Wiss. Veröff. Dt. Inst. Länderkde., 21, 65–132, 1964.

Niller, H. P.: Wandel prähistorischer Landschaften, Erdkunde, 55, 32–48, 2001.

Notebaert, B., Broothaerts, N., and Verstraeten, G.: Evidence of anthropogenic tipping points in fluvial dynamics in Europe, Global Planet. Change, 164, 27–38, 2018.

Oberdorfer, E.: Pflanzensoziologische Exkursionsflora für Deutschland und angrenzende Gebiete, 8th edn., Ulmer, Stuttgart, 2001.

Pretzsch, K.: Spätpleistozäne und holozäne Ablagerungen als Indikatoren der fluvialen Morphodynamik im Bereich der mittleren Leine, Göttinger Geogr. Abh., Göttingen, 99, 1994.

Rittweger, H.: The “Black Floodplain Soil” in the Amöneburger Becken, Germany: a lower Holocene marker horizon and indicator of an upper Atlantic to Subboreal dry period in Central Europe?, Catena, 41, 143–164, 2000.

Schellmann, W.: Die Talentwicklung der unteren Oberweser im jüngeren Quartär, Düsseld. Geogr. Schr., 34, 11–43, 1994.

Schirmer, W.: Die Talentwicklung an Main und Regnitz seit dem Hochwürm, Geol. Jahrb., 71, 11–43, 1983.

Standke, G., Escher, D., Fischer, J., and Rascher, J: Das Tertiär Nordwestsachsens, Ein geologischer Überblick, LfULG Sachsen, Dresden, 2010.

Starkel, L., Soja, R., and Michczynska, D. J.: Past hydrological events reflected in Holocene history of Polish rivers, Catena, 66, 24–33, 2006.

Stoops, G.: Guidelines for analysis and description of soil and regolith thin sections, Soil Science Society of America, Inc., Madison, 2003.

Tinapp, C: Geoarchäologische Untersuchungen zur holozänen Landschaftsentwicklung der südlichen Leipziger Tieflandsbucht, Trierer Geographische Studien, 26, Trier, 2002.

Tinapp, C. and Stäuble, H.: Auenentwicklung und Besiedlungsgeschichte im Tal der Weissen Elster südlich von Leipzig, Trierer Geographische Studien, 23, 31–48, 2000.

Tinapp, C., Meller, H., and Baumhauer, R.: Holocene accumulation of colluvial and alluvial sediments in the Weiße Elster river valley in Saxony, Germany, Archaeometry, 50, 696–709, 2008.

von Suchodoletz, H., Gärtner, A., Zielhofer, C., and Faust, D.: Eemian and post-Eemian fluvial dynamics in the Lesser Caucasus, Quaternary Sci. Rev., 191, 189–203, 2018a.

von Suchodoletz, H., Zielhofer, C., Hoth, S., Umlauft, J., Schneider, B., Zeeden, C., Sukhishvili, L., and Faust, D.: North Atlantic influence on Holocene flooding in the southern Greater Caucasus, The Holocene, 28, 609–620, 2018b.

von Suchodoletz, H., Tinapp, C., Lauer, T., Glaser, B., Stäuble, H., Kühn, P., and Zielhofer, C.: Distribution of Chernozems and Phaeozems in Central Germany during the Neolithic period, Quat. Int., in press, https://doi.org/10.1016/j.quaint.2017.10.041, 2019.

Wennrich, V., Wagner, B., Melles, M., and Morgenstern, P.: Late Glacial and Holocene history of former Salziger See, Central Germany, and its climatic and environmental implications, Int. J. Earth Sci. (Geol Rundsch), 94, 275–284, 2005.

Zielhofer, C., Recio-Espejo, J. M., Nunez-Granados, M. A., and Faust, D.: Durations of soil formation and soil development indices in a Holocene Mediterranean floodplain, Quaternary Int., 209, 44–65, 2009.

E&G Quaternary Sci. J., 68, 107–117, 2019
https://doi.org/10.5194/egqsj-68-107-2019


Open Access E&G Quaternary Science Journal

Research article

# Archaeological dating of colluvial and lacustrine deposits in a GIS environment investigating the multi-period site Gortz 1 on Oberer Beetzsee, Brandenburg

**Janko Reichel[1], Sophie F. Heisig[2], Thomas Schenk[1], and Thomas Schatz[3]**

[1]Landscape Archaeology, University of Applied Sciences, Berlin, Germany
[2]Prehistoric Archaeology, Freie Universität, Berlin, Germany
[3]Soil Science, Berlin, Germany

**Correspondence:** Janko Reichel (janko-reichel@gmx.net)

**Relevant dates:** Received: 22 February 2019 – Revised: 11 May 2019 – Accepted: 26 May 2019 – Published: 18 July 2019

**How to cite:** Reichel, J., Heisig, S. F., Schenk, T., and Schatz, T.: Archaeological dating of colluvial and lacustrine deposits in a GIS environment investigating the multi-period site Gortz 1 on Oberer Beetzsee, Brandenburg, E&G Quaternary Sci. J., 68, 107–117, https://doi.org/10.5194/egqsj-68-107-2019, 2019.

**Abstract:** From the mid-14th century CE onwards, extensive soil erosion, caused by intensive agricultural practices, has led to the destruction of landscape structures in Central Europe. In 2016, the University of Applied Sciences in Berlin investigated the colluvial deposits at the site of Gortz in western Brandenburg (Germany), which had accumulated on the lower slopes and were caused by the processes just mentioned.

The mapping of each individual archaeological find made it possible to project all finds onto one profile running along the slope. Transformation of the finds' coordinates from profile view to plan view enabled the visualization in a Geographical Information System (GIS). The combination of adjacent strata into larger units using a pedological and sedimentological approach enabled an improved dating of colluvial deposits. In addition, the method facilitated the dating of historical water levels in the Beetzsee chain of lakes, which are part of the Havel river system.

As a result, it could be demonstrated that substantial anthropogenic activity, such as clay quarrying and bank straightening, took place during the Late Slavic Period. An interlocking horizon of colluvial and lacustrine deposits indicates that the water level of the lake Oberer Beetzsee rose from a value under 29.4 m above sea level (a.s.l.) in the 11th/12th century CE to approximately 29.8 m a.s.l. in the 13th century CE. However, isolated flooding events during the 13th century CE can be recorded up to a height of 30.5 m a.s.l. A modern colluvial deposit of 1 m in thickness indicates an acute endangerment of the archaeological site by modern agriculture.

**Kurzfassung:** Flächenhafte Bodenerosion, ausgelöst durch intensive landwirtschaftliche Nutzung, führte ab Mitte des 14. Jahrhunderts u.Z. zur Zerstörung von Landschaftsstrukturen und in Mitteleuropa. Kolluvien, welche durch diese Prozesse entstanden und am Unterhang akkumulierten, wurden auf dem Fundplatz Gortz (westliches Brandenburg, Deutschland) durch die Hochschule für Technik und Wirtschaft Berlin im Jahr 2016 untersucht.

Konsequente Einzelfundeinmessung ermöglichte die Projizierung aller Funde auf eines der längs zum Hang verlaufenden Profile. Koordinatentransformation der Funde von der Profilansicht in die Draufsicht, ermöglichte die Visualisierung in einem GIS. Die Zusammenfassung benachbarter Schichten auf Basis der bodenkundlich-sedimentologischen Ansprache ermöglichte eine verbesserte Datierung der Kolluvien. Zusätzlich ermöglichte diese Methode die Datierung historischer Pegelstände der Beetzseekette, eines Teils des Flusssystems der Havel.

Im Ergebnis ließen sich für die spätslawische Zeit starke anthropogene Aktivitäten wie Mergelabbau und eine Uferbegradigung nachweisen. Über einen Verzahnungshorizont limnischer und kolluvialer Sedimente. ließ sich ein Pegelanstieg des Oberen Beetzsees von einem Wert unterhalb von 29.4 m Normalhöhennull (NHN) im 11./12. Jahrhundert u.Z. auf etwa 29.8 m NHN im 13. Jahrhundert u.Z. feststellen. Es lassen sich für das 13. Jahrhundert u.Z. jedoch auch vereinzelte Überschwemmungsereignisse bis in eine Höhe von 30.5 m NHN fassen.

Ein modernes Kolluvium von einem Meter Mächtigkeit zeigt die akute Gefährdung des Bodendenkmals durch die moderne Landwirtschaft.

## 1 Introduction and objectives

The combination of archaeological and soil-sedimentological investigations into erosion processes at archaeological sites enables reliable conclusions to be made about historical settlement phases and their paleoenvironmental context. At the same time, erosion can be used to draw conclusions about the sub-recent to recent destruction of archaeological sites. In the best case, this can be used to derive scientific recommendations for the agricultural use of the land.

The Gortz 1 site, which is the focus of this study, has been subject to intensive agricultural use since the middle of the 20th century and is therefore subject to extensive soil erosion. Systematic field walking on sections of the site resulted in the collection of 7600 surface finds from 2.6 ha (Schenk, 2018). This accumulation can be seen as a clear indicator of the destruction of associated archaeological features. However, erosion processes are not just the result of modern agriculture alone; rather, they are associated with many anthropogenic interventions in existing landscape structures since the Neolithic Age. The consequence of soil erosion is a shift of the topsoil from the upper slopes to the lower slopes and the foot of the slope and beyond. These relocated soils are referred to as colluvia. Almost every anthropogenic activity phase leads to the formation of a colluvial deposit. It often contains material remains from when the deposit was first laid down. The colluvial deposit thus represents a sort of archive of the activity phase, which can be dated archaeologically via the associated ceramics. The thickness of the colluvia gives an indication of the intensity of the activity phase. If very little or no ceramics can be found for an epoch, this is an indication of an anthropogenic resting phase, i.e. a period in which no ceramics were used or relocated which could indicate less intensive human activity. The terms activity and resting phase are used according to the definition of Bork (Bork et al., 1998).

For the investigation presented here, the shore location of the archaeological site plays a significant role. The site is connected to the Havel river system via the Beetzsee chain of lakes. Therefore, dating of lacustrine deposits enables us to draw conclusions about the former spatial extension of water bodies in the wider landscape. These conclusions extend far beyond the boundaries of the site.

The aim of the study is to determine the former erosion history, paleo-environmental context and sub-recent to recent history of the destruction of this archaeological site. The research presented in this paper focuses on the following objectives:

1. dating of colluvial and lacustrine deposits,
2. categorization of phases of anthropogenic activity and resting,
3. investigation of historical water levels in the Beetzsee chain of lakes and the associated landscape development, and
4. assessment of the present-day risk to the archaeological site.

## 2 Research area

Located within the wider Havel river system, the archaeological site of Gortz 1 lies on the banks of a lake which is part of the Beetzsee chain of lakes. The lake chain was formed during the Brandenburg glacial stage (24–17 ka BP) in the Weichselian High Glacial, as a subglacial drainage channel (Lippstreu and Hermsdorf, 2010). The maximal extent and intermediate positions of the ice sheet were located south of or probably through this channel during this period (Stackebrandt and Lippstreu, 2010). The Beetzsee chain of lakes ex-

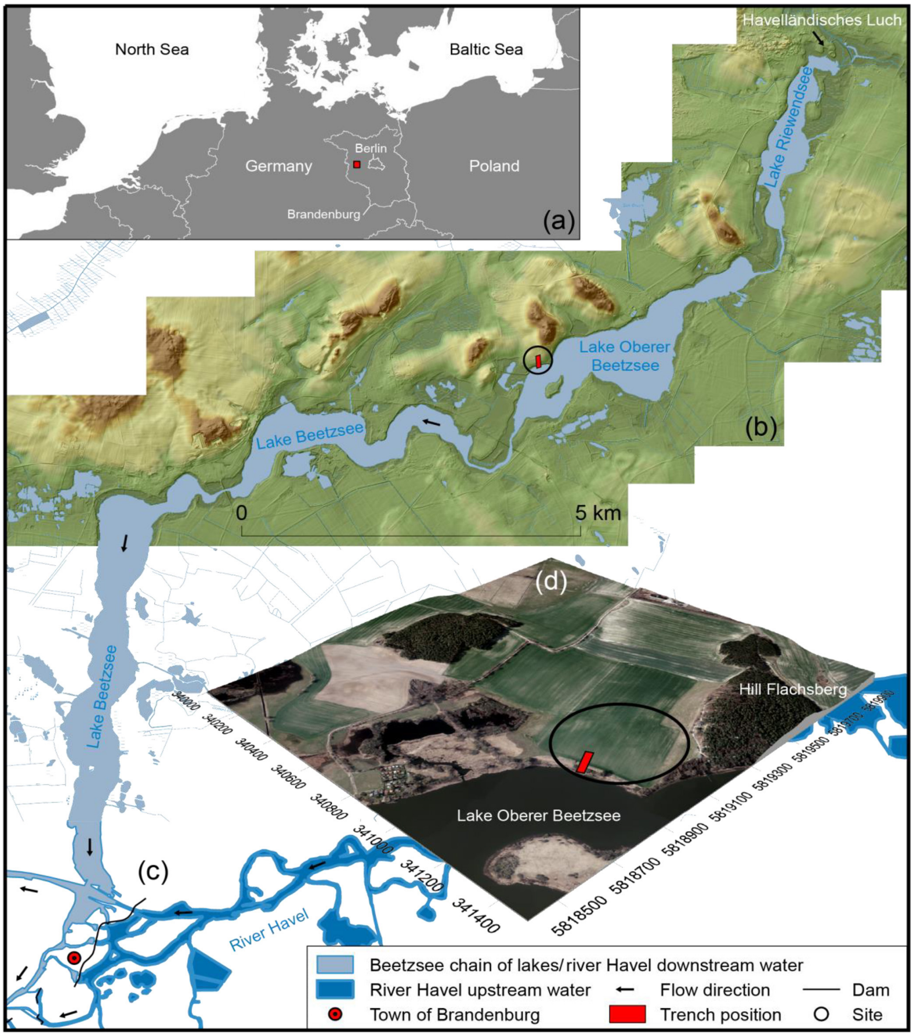


**Figure 1.** The Beetzsee chain of lakes in northeastern Germany **(a)** with a floodplain and moraine landscape encompassing it **(b)**. The lakes drain into the river Havel at the town of Brandenburg **(c)**. Within the town, the river Havel is divided into an upper and lower water level due to a mill dam system. They are referred to as the upstream and downstream water **(c)**. The position of the trench at the shore of the lake Oberer Beetzsee in a slightly elevated terrain model with view to the northwest is shown in panel **(d)**.

tends over more than 30 km from the wetland area Havelländisches Luch in the north to the town of Brandenburg in the south, where it drains into the river Havel (Fig. 1b, c). The chain is thus part of the lowland and floodplain landscape of the river Havel. On the northern and northwestern banks, the lowlands merge into an undulating, partly hilly, moraine landscape (Lippstreu, 2010). Within this transitional area, the site of Gortz extends from the southwest slope of the Flachsberg hill to the shore of the lake Oberer Beetzsee (Fig. 1d). In the riparian zone, colluvial deposits resulting from different settlement phases are interwoven with lacustrine deposits, both of which lie above boulder clay and gravelly sands. The most common soils around the lake chain are Brunic Arenosols, which also occur as Brunic, Endogleyic Arenosols or Cutanic Luvisols (Abrubtic, Arenic). In the riparian zone, the geological subsoil is mostly formed by Hemic Histosols (Eutric, Drainic) and Mollic Gleysols (Arenic) (LBGR, 2018).

Archaeological evidence of anthropogenic activities in the region can be found from the Mesolithic Period (9600–5300 BCE) onwards and for the entire Holocene (BLDAM, 2019). Based on the available sources of information, the study focuses primarily on the period of the last 1000 years. A particular focus is on the period from the late 11th century to the early 13th century CE. In this period the areas east of the river Elbe were strongly influenced by the colonization of land, which was organized by German regional rulers and supported by the Christian clergy. During this process, from the mid-12th century CE, German settlers were brought into the area, which had previously been inhabited by Slavic people. For the Slavs this meant the end of their political independence (Brather, 2001).

In archaeological features, the colonization of the Slavic region is highlighted by a slow transition to a new type of ceramic (Brather, 2001). Belt decorations are typical of ceramics from the Late Slavic Period. The Late Slavic Period roughly covers the 11th and 12th centuries CE for the area east of the river Elbe (Brather, 2001). From the middle of the 12th century the German settlement took place, which is also called the Early German Period. This was accompanied by a soft, blue-grey earthenware, which was already being replaced by the higher-quality hard grey earthenware as early as 1200 CE (Mangelsdorf, 1994b). The introduction of new technologies, such as the heavy plough, or the founding of new towns, led to far-reaching changes on the economic and infrastructural level (Brather, 2001). Large-scale agricultural cultivation, damming and hydro-melioration projects began to influence the water level of the middle and lower Havel, which led to lasting changes that are still visible in the landscape today (Kaiser et al., 2018). This raises the question of the extent to which the Gortz site was affected by these changes.

In Slavic times, the banks of the Beetzsee chain of lakes was one of the most densely settled areas in the Havelland area, with the large settlement chamber of Brandenburg in the south and Riewend in the northeast (Sasse, 1987). The Gortz site is situated half way up in an elevated position, from where there is a wide view over the lakes. Due to its surface finds, the site is referred to in the literature as a medieval deserted village, which must have existed at least from the Late Slavic to the Early German Period (Krenzlin, 1956; Mangelsdorf 1994a). Today there is an extensive field in this location. The village of Gortz, which still exists today, was founded about 2 km away in a higher location, although the tract of land on which the site sits has retained the name "Die alten Dörfer" (the old villages) (Krenzlin, 1956). These field names like "Dorfstelle", "Wüste Dorfstätte" and "altes Dorf" (village place, desert village site and old village) indicate that the original location was abandoned in the Late Slavic/Early German transition period (Krenzlin, 1956).

The archaeological investigations, carried out by Professor Thomas Schenk from the University of Applied Sciences Berlin since 2014, show a multi-period settlement history, which stretches from the Neolithic to the High Middle Ages. This is reflected in the numerous finds, some of which are unique in the Brandenburg region. The settlement character and the special significance of the site are reflected in the numerous metal finds covering a broad spectrum, as well as a large number of recognizable pits and hearths (Schenk, 2018).

## 3 Methods

Since 2014 the University of Applied Sciences Berlin has been researching the landscape archaeology of the region around the Beetzsee chain of lakes. This includes geophysical prospection, field-walking surveys, sieving, and counting material from test pits and excavations. The Gortz site has been a special focus, due to its diachronic settlement history, its location and the acute threat posed by its agricultural use. In order to investigate the colluvial deposits which have accumulated on the foot of the slope, a 20 m long trench was cut following the direction of the slope, from the foot of the slope down to the riparian zone of the lake Beetzsee (Figs. 1d, 2). The trench was dug down to the C horizon. This resulted in two longitudinal profiles following the direction of the slope with a length of 20 m and a depth of over 2 m. The longitudinal profiles show the stratigraphy of the colluvial deposits. Only the western profile was used for the post-excavation evaluation (Fig. 2a, b).

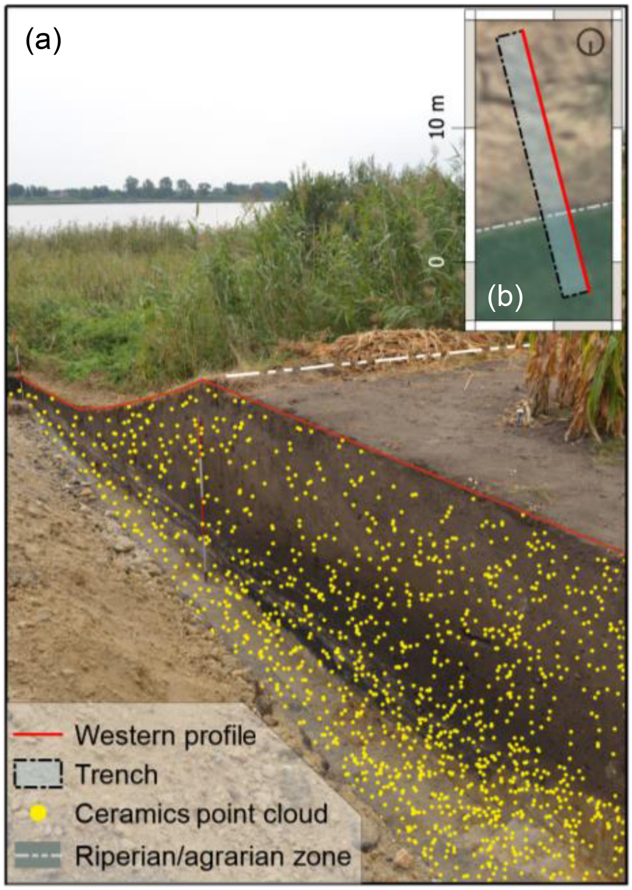


**Figure 2.** Photo of the investigated trench which extends from the foot of the slope into the riparian zone of Oberer Beetzsee with view to the south. The point cloud represents the ceramics recorded tachymetrically during the excavation, which was later projected onto the western profile of the trench during the post-excavation evaluation **(a)**. The position of the western profile in the plan view (plan was oriented to the south), which served as the visualization layer for the point cloud, is shown in panel **(b)**.

In order to date the colluvial deposits, not only the finds from the profile wall but all finds from the trench should be

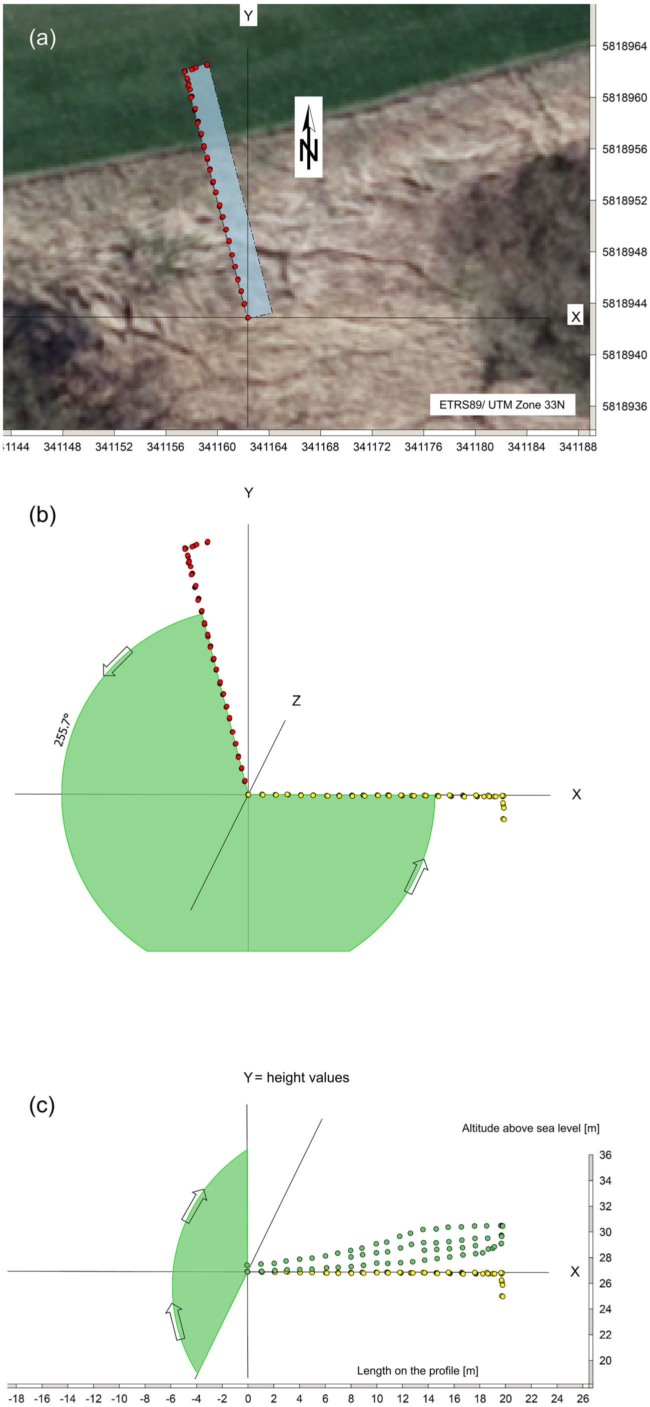


**Figure 3.** Rotation of the point cloud by matrix multiplication using the photogrammetry points of the western longitudinal profile as an example.

used[1]. For this reason, the position of every find was recorded using a total station (Fig. 2a). During the post-excavation evaluation, all identifiable ceramic fragments were archaeologically dated.

The visualization of the western longitudinal profile and the subsequent dating of the layers was achieved using QGIS 2.18.3. In order to enable the visualization in a GIS, the first step was to project the tachymetrically recorded point cloud of all finds of the trench onto the profile wall (Fig. 2a). In a second step, the profile was tilted from the profile view to plan view. A matrix multiplication in Excel served as an aid for this process, in which points with $xyz$ coordinates can be rotated around the three spatial axes ($X$, $Y$, $Z$) at will (Kühnlein, 2019). This manipulation of the coordinates becomes necessary if the profile is not aligned with one of the cardinal axes (north–south $= Y$, west–east $= X$) shown in Fig. 3a. Prerequisites are that

A: the angle of deviation from one of the cardinal axes is known and

B: the complete dataset of a trench is summarized in one Excel table.

For the projection onto the profile, the point cloud was rotated around the $Z$ axis until it had an east–west orientation. The points thus receive a new artificial easting, which lies exactly on the $X$ axis (Fig. 3b). Without this step, the finds could only be displayed distorted in GIS. In a second step, the tilting into the plan view took place by defining the height values as the new northing (Fig. 3c). The easting coordinates are then reset to an artificial zero point so that profile metres (metres on the profile) can be displayed on the $X$ axis (Fig. 3c). In order to generate a visualization layer, the western profile following the direction of the slope was recorded photogrammetrically and the photos were georeferenced in QGIS. This method of rotating coordinates allows an unlimited number of profiles with their real height values to be displayed side by side and compared within one project file. The layers were then redrawn and dated based on the ceramic. Many of the thin layers proved particularly difficult to reliably date. Where finds were measured further away from the profile wall, they could be considered as belonging to any number of adjacent layers. Therefore, the 58 recorded strata were combined, using a pedological and sedimentological approach, into five phases of anthropogenic activity (Fig. 4).

## 4 Results and discussions

The elevation heights refer to the German Main Elevation Network (DHHN92) and are given here as metres above sea level (a.s.l.). The easting coordinates are given here as metres on the profile (o.t.p.). Of the approximately 1600 diagnostic fragments, about half could be dated (Reichel and

[1]The background is that finds within colluvial deposits have often been displaced and therefore have less significance regarding the exact timing and circumstances (archaeological features) of their deposition. However, with a greater number of finds, even if they are potentially predominantly relocated, a more reliable dating of a layer can be made.

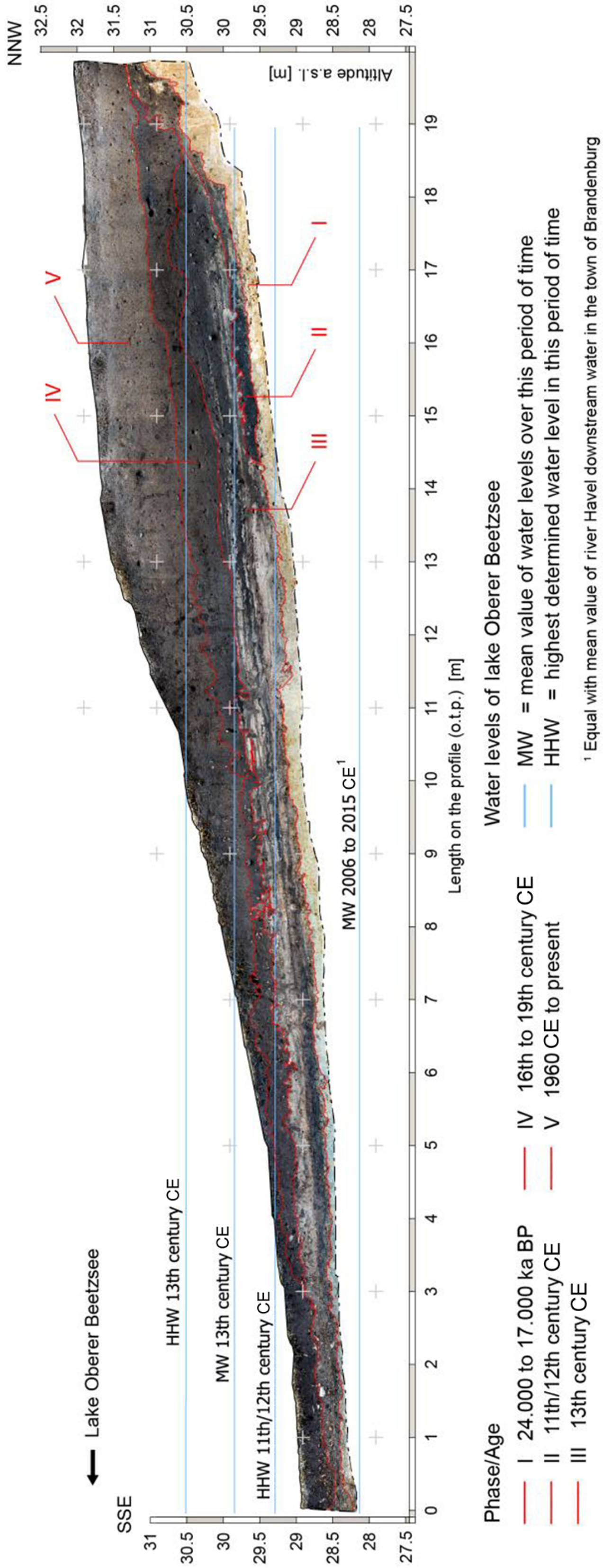


**Figure 4.** Photogrammetry of the western profile following the direction of the slope. The trench extends into the riparian zone of Oberer Beetzsee. The five phases were combined, using a pedological–sedimentological approach, and dated via the diagnostic ceramics of the entire trench. The dating allowed historical water levels to be determined for the periods of the 11th/12th and 13th centuries.

Schenk, 2019). This archaeological identification of ceramic fragments formed the basis for the dating of the different phases. In cases where bioturbation could be ruled out, the most recent ceramics give the terminus post quem for the deposition of a layer (Bork et al., 1998). Phase I contains no ceramics and corresponds to the C horizon consisting of boulder clay and gravelly sands. Between 11.5 and 18 m o.t.p., the sequence of layers is strikingly even and straight. Gravelly sands dominate here. From 18 to 20 m o.t.p., the sequence of layers is reminiscent of a staircase that, in several steps, changes the height level by more than 1 m. This part of phase 1 consists of boulder clay. The transition to phase II, which lies above, is sharply defined. Characteristic features of soil formation are missing. The straight, even upper edge of the C horizon can be interpreted as a result of ground levelling and the steps as remains of clay quarrying. The latter in particular demonstrates an anthropogenic intervention here (Fig. 4).

Phase II can be dated to the 11th/12th century CE on the basis of 42 % of all ceramic sherds from this phase being Late Slavic (Reichel and Schenk, 2019). Two fragments from the German Middle Ages and a sherd from the Early Modern Period (1500–1700 CE) (Verband der Landesarchäologen, 2014) were probably introduced to these layers by strong bioturbation. The only stratum from the entire profile that can be interpreted as an in situ culture layer, due to the presence of lenses of ash and a high proportion of charcoal pieces, lies directly on the straightened C horizon between 14 and 17 m o.t.p. (Fig. 4). The absence of colluvial deposits, which are older than Slavic ones, is conspicuous, since much older settlement phases are documented on the site, in particular from the Early Bronze Age (2100–1500 BCE), the Roman Period (9 BCE–375 CE) and the Migration Period (375–565 CE) (Verband der Landesarchäologen, 2014). All older colluvial deposits were obviously removed in the course of clay quarrying. Therefore, the in situ layer can be used for dating the clay quarrying and ground levelling into the Late Slavic Period.

On the side that borders the lake, the culture layer is cut possibly by wave erosion. There are several thin layers of light lacustrine sand running up to this stratum and covering it. Furthermore, a series of holes filled with lacustrine sands can be seen impressed into the culture layer. These holes can be interpreted as cattle hoof prints and delineate the shoreline during the Late Slavic Period in this area. At 11 m o.t.p., the straightened C horizon is interrupted by a 0.2 m high sill (Fig. 4). Here the blue-grey earthenware of the German Middle Ages appears in large numbers. The sill obviously marks the edge of the riparian zone that had been levelled. In the 11th/12th century CE, the lake level must have been below this sill, suggesting a height of 29.4 m a.s.l. ±0.2 m. Otherwise, no culture layer interspersed with ash lenses could have formed and been preserved between 14 and 17 m o.t.p. (Fig. 4).

Phase III is dominated by Slavic ceramics with 35 % of all ceramic sherds from this phase. Blue-grey earthenware is represented by 7 % of all ceramic sherds from this phase and allows the phase to be dated to the 13th century CE (Reichel and Schenk, 2019). The colluvial deposits in phase III between 16 and 19 m o.t.p. can be interpreted as Slavic. Strong indicators are the high humus content when compared to the other colluvial deposits of the profile and the charcoal particles, which cause a darker-coloured sediment (Schatz, 2011).

The hydrochloric acid test (10 % HCl) showed a carbonate content of > 10 %. Thus, the colluvium is rich in carbonates (Ad-hoc-AG Boden, 2005). A high calcium carbonate content also indicates significant, if partial, erosion on the upper slope. This suggests intensive settlement activity in this phase. Due to finds of the commonly associated grey earthenware and Pingsdorfer Ware in other trenches of the site, it is likely that the German settlement started in the late 12th or early 13th century CE. So far no finds can be classified as dating back to the 14th and 15th centuries CE, probably because the village had already been relocated during the 13th century CE. However, the colluvial deposits indicate that the German settlement probably existed for less than a hundred years.

The reason for the abandonment of the settlement of Gortz remains unknown. However, erosion processes could have played a role, which is indicated by the partially high carbonate content in phase III. Between 1150 and 1250 CE, the colonization of the Havelland area led to an extensive settlement and restructuring of the landscape, the like of which had never been seen before. In the sequel, many newly founded settlements in the Havelland area were abandoned from the turn of the 12th to 13th centuries CE. Taking into account the fact that the settlers did not know the terrain and the soils, it is likely that in many cases they became victims of erosion processes they caused and had to give up the site (Mangelsdorf, 1994a).

In phase III, on the side that borders the lake, between 8 and 17 m o.t.p., there is a horizon of interlocking dark colluvial deposits and lighter-coloured lacustrine sediments (Figs. 4 and 5). Incorporation of swirled dark humus material within the entire interlocking horizon indicates that sedimentation took place in an area of slightly moving standing water. Thus, the interlocking horizon can be interpreted as a riparian zone. Each of the thin, light-coloured layers was formed during a flooding event, whereby the deposition may have occurred at short intervals. Straight above the aforementioned sill (Fig. 4, 11 m o.t.p) blue-grey earthenware of the German Middle Ages appears in large numbers. Thus, the interlocking horizon can be clearly dated to the 13th century CE and is therefore part of phase III. The flood events indicate rising water levels during this period. The interlocking horizon reaches up to a height of at least 29.8 m a.s.l. (Fig. 4). Evidently, in the 13th century CE, the level of Oberer Beetzsee rose to this height. However, isolated flooding events

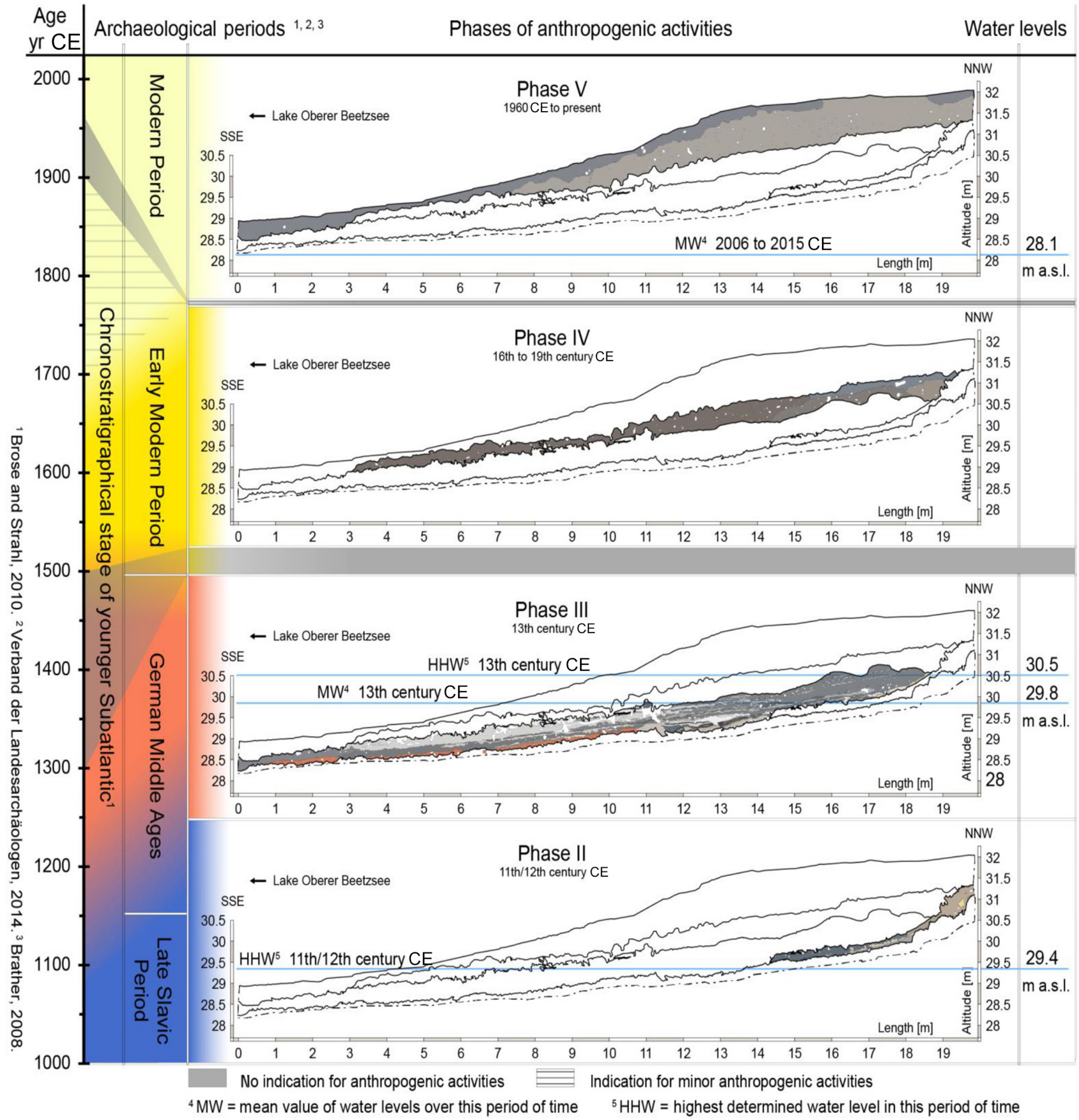


**Figure 5.** Development of the anthropogenic activities at the site Gortz from the Late Slavic Period to the present day, and the associated development of water level changes of the lake Beetzsee.

during the 13th century CE can be recorded up to a height of 30.5 m a.s.l. (Fig. 4).

This increase has regional significance, as the Beetzsee chain of lakes is connected to the lower Havel river (Fig. 1). Historical sources indicate that water levels in the river Havel region rose by an average of 1–2 m due to medieval mill dams (Driescher, 2003). The Beetzsee chain of lakes drains into the river Havel at the town of Brandenburg. Since the first half of the 13th century CE the river Havel has been divided into an upper and lower water level by a mill dam system (Müller, 2009). They are referred to in this study as the upstream and downstream water. The most recent study assumes that the dam system caused a water level rise of 1.5 m in the upstream water (Kaiser et al., 2018). However, the Beetzsee chain of lakes drains into the river Havel downstream from the dam system (Fig. 1) The dams associated with medieval mills may not have played a direct role in the rise of Beetzsee, whereas fish weirs could be responsible for rising water levels (Kaiser et al., 2012). Nowadays the downstream water level values in the town of Brandenburg are also valid for the Beetzsee chain of lakes. Between 2006 and 2015, the mean value of the downstream water level was at 28.13 m a.s.l. (WSA Brandenburg, 2015). Thus the water level of Oberer Beetzsee in the 13th century CE was 1.6 m above the present-day level.

Phase IV features the highest number of archaeological finds in the whole trench (Reichel and Schenk, 2019). Yellow-glazed and occasionally also brick-red earthenware date the colluvia to the 16th/17th century CE at the earliest. This was a time when the settlement had already been abandoned for about 300 years and the site was being used agriculturally. A later origin of phase IV is also conceivable, provided that in the 18th/19th century CE only little domestic waste had reached the fields (Fig. 5). The transition between the foot of the slope and the shore area was until this period less steep than today (Schenk, 2018).

Phase V contains a balanced spectrum of ceramics from Bronze Age to current times. Thus this is the only phase with recent ceramics (Reichel and Schenk, 2019). In addition, associated finds, such as plastic bands and the light colour of the substrate, typical of recent deposits, also suggest a Modern Period colluvia (Fig. 5). Its deposition can be associated with agro-structural measures that had a strong influence on landscape development from the 1960s to the 1980s. Land consolidation and collectivization led to destructions of important soil-protecting landscape structures (Bork et al., 1998). These measures have probably also been implemented in Gortz by the local agricultural producer cooperative. Within > 70 years a colluvial deposit of 1 m thickness has formed. This impressively demonstrates the endangerment of the archaeological site by modern agriculture.

## 5 Conclusions

Consistent tachymetric mapping of the finds of a trench and their projection onto one of the longitudinal profiles within a GIS environment, in combination with a sedimentological–pedological approach to combine neighbouring layers into phases, led to new insights into the settlement and landscape development of the studied site and its surroundings. The advantages of our approach are an unambiguous spatial allocation of the finds. In addition, not only the ceramic embedded in the profile wall but also the datable ceramic from the entire trench can be used to date the phases. The larger number of ceramic fragments that can be used for dating can provide a more reliable determination of the age of the phases.

On the basis of the recovered ceramics, it was feasible to approximate the sedimentation time of the differing colluvial phases. The timing of the sedimentation of the shoreline deposits in the interlocking horizon could thus be dated indirectly.

From the Late Slavic Period onwards, phases with settlement processes as well as phases with anthropogenic resting can be observed at the site. Especially in the Late Slavic settlement phase, it can be proved that intensive activities in the shore area such as the straightening of the bank and clay quarrying took place. Cattle hoof prints show the course of the riparian zone at that time. The interlocking horizon indicates a change in the shoreline from the 11th/12th to 13th centuries CE. During this time, the lake water level rose from < 29.4 m a.s.l. to approximately 29.8 m a.s.l. Thus the water level of Oberer Beetzsee in the 13th century CE was 1.6 m above the present-day level.

Up to now no colluvial deposits could be assigned to the 14th and 15th centuries CE, so that a resting phase on the site can be assumed (Fig. 5). This is probably because the settlement had already been deserted in the 13th century CE.

The modern colluvial deposit of 1 m thickness indicates an acute endangerment of the archaeological site. The cultivation of maize, which has been practised here for years, is also responsible for the high erosion rates. But also the cultivation of asparagus, which is widespread in the region, would entail far-reaching soil interventions, which would lead to the irreparable destruction of archaeological features in a short time. It is clear that a continuation of agricultural use in its present form will inevitably mean the loss of remaining archaeological features in the coming decades.

**Data availability.** The data presented here are available online at https://opus4.kobv.de/opus4-htw/frontdoor/index/index/docId/363 (last access: 7 July 2019) (Reichel and Schenk, 2019).

**Supplement.** The supplement related to this article is available online at: https://doi.org/10.5194/egqsj-68-107-2019-supplement.

**Author contributions.** Fieldwork was performed by JR and SFH under the project supervision of TSche. Pedological and sedimentological expertise came from TScha; archaeological dating of ceramics was done by TSche. JR and SFH prepared the manuscript and JR the figures.

**Competing interests.** The authors declare that they have no conflict of interest.

**Special issue statement.** This article is part of the special issue “Geoarchaeology and past human—environment interactions”. It is not associated with a conference.

**Acknowledgements.** We thank the Ministry of Science, Research and Culture Brandenburg for funding the 2016 Gortz 1 campaign partly.

We thank an anonymous reviewer as well as the guest editor, Hans von Suchodoletz, who made very helpful comments on an earlier version of the manuscript.

We would like to thank Fiona Vernon, who contributed very helpful comments regarding the English translation.

Stefan Dalitz (Heritage Conservation, Municipal Office Brandenburg/Havel) and his family, Alessandra Mancinelli, Diana Catalina Acosta Parsons, Andrey Jostes and Leroy Fischer (all University of Applied Sciences Berlin), are acknowledged for their participation in field work during the 2016 Gortz 1 campaign.

## References

Ad-hoc-Arbeitsgemeinschaft Boden: Bodenkundliche Kartieranleitung, 5, edited by: Bundesanstalt für Geowissenschaften und Rohstoffe, Staatliche Geologische Dienste der Bundesrepublik Deutschland, Schweizerbart, Hannover, 2005.

BLDAM, Brandenburg Department of Cultural Heritage and Archaeological State Museum: Fundplaetze FZK (Fundart/Zeitstellung/Kultur), Wünsdorf, 2019.

Bork, H. R., Bork, H., Dalchow, C., Faust, B., Piorr, H. P., and Schatz, T.: Landschaftsentwicklung in Mitteleuropa: Wirkung des Menschen auf Landschaften, 1, Gotha, Stuttgart, Germany, 1998.

Brather, S.: Archäologie der westlichen Slawen: Siedlung, Wirtschaft und Gesellschaft im früh- und hochmittelalterlichen Ostmitteleuropa, 2, Ergänzungsbände zum Reallexikon der Germanischen Altertumskunde, 61, edited by: Beck, H., Geuenich, D., and Steuer, H., Walter de Gruyter, Berlin, New York, 2008.

Brose, F. and Strahl, J.: Die Gliederung des Holozäns im Land Brandenburg, The Brandenburg State Office for Mining, Geology and Raw Materials, Germany, 135, available at: https://www.geobasis-bb.de/geodaten/lbgr/4_geoatlas.htm (last access: 7 July 2019), 2010.

Driescher, E.: Veränderungen an Gewässern Brandenburgs in historischer Zeit, Studien und Tagungsberichte, 47, Potsdam Landesumweltamt, Potsdam, 2003.

Kaiser, K., Günther, K., Lorenz, S., Merz, B., Bens, O., and Hüttl, R., F.: Historische Veränderungen des Wasserhaushalts und der Wassernutzung in Nordostdeutschland, in: Historische Perspektiven auf Wasserhaushalt und Wassernutzung in Mitteleuropa, edited by: Kaiser, K., Merz, B., Bens, O., and Hüttl, R. F., Waxmann Verlag, Münster, Germany, 73–102, 2012.

Kaiser, K., Keller, N., Brande, A., Dalitz, S., Hensel, N., Heußner, K.-U., Kappler, C., Michas, U., Müller, J., Schwalbe, G., Weiße, R., and Bens, O.: A large-scale medieval dam-lake cascade in central Europe: water level dynamics of the Havel River, Berlin-Brandenburg region, Germany, Geoarchaeology, 33, 237–259, https://doi.org/10.1002/gea.21649, 2018.

Kühnlein, K.: Punkte mit xyz–Koordinaten um drei Achsen drehen, available at: http://www.excelformeln.de/tips.html?welcher= (last access: 7 July 2019), 53, 2019.

Krenzlin, A.: Deutsche und slawische Siedlungen im inneren Havelland, Ausgrabungen und Funde: Nachrichtenblatt der Landesarchäologie, 1, 174–185, 1956.

LBGR: Bodengeologische Übersichtskarte im Maßstab 1 : 300 000 (BÜK 300), The Brandenburg State Office for Mining, Geology and Raw Materials, Germany, available at: http://www.geo.brandenburg.de/lbgr/bergbau (last access: 7 July 2019), 2018.

Lippstreu, L.: Landschaftsgenese, The Brandenburg State Office for Mining, Geology and Raw Materials, Germany, 157, available at: https://www.geobasis-bb.de/geodaten/lbgr/4_geoatlas.htm (last access: 7 July 2019), 2010.

Lippstreu, L. and Hermsdorf, N.: Die Gliederung des Pleistozäns im Land Brandenburg, The Brandenburg State Office for Mining, Geology and Raw Materials, Germany, 134, available at: https://www.geobasis-bb.de/geodaten/lbgr/4_geoatlas.htm (last access: 7 July 2019), 2010.

Mangelsdorf, G.: Die Ortswüstungen des Havellandes, Ein Beitrag zur historisch-archäologischen Wüstungskunde der Mark Brandenburg, Veröffentlichungen der Historischen Kommission zu Berlin, 86, edited by: Mangelsdorf, G., Walter de Gruyter, Berlin, New York, 1994a.

Mangelsdorf, G.: Untersuchungen zur Formenkunde spätmittelalterlicher Keramik im westlichen Brandenburg, Europäische Hochschulschriften, 50, edited by: Mangelsdorf, G., Peter Lang, Frankfurt/M, 1994b.

Müller, J.: Wasserbau als Infrastruktur der mittelalterlichen Planstadt: Brandenburg an der Havel, in: Mitteilungen der deutschen Gesellschaft für Archäologie des Mittelalters und der Neuzeit, 21, Untermann, M., Paderborn, 2009.

Reichel, J. and Schenk, T.: 2016_Gortz1_trench5_finds_data record, University of Applied Sciences Berlin, data set, available at: https://opus4.kobv.de/opus4-htw/frontdoor/index/index/docId/363 (last access: 7 July 2019), 2019.

Sasse, B.: Die spätslawische und frühdeutsche Zeit, in: Das Havelland im Mittelalter: Untersuchungen zur Struktur einer ostelbischen Landschaft in slawischer und deutscher Zeit, Germania Slavica, 5, Berliner historische Studien, 13, edited by: Ribbe, W., Dunker und Humblot, Berlin, 1987.

Schatz, T.: Bodenkundlich-geoarchäologische Untersuchungen zur historischen Gewässerdynamik in der Aue der unteren Mittelelbe (Lkr. Lüchow–Dannenberg ), in: Slawen an der Elbe, edited by: Willroth, K.–W. and Schneeweiß, J., Wachholtz Verlag, Neumünster, 2011.

Schenk, T.: Südhang mit Seeblick. Mehrphasiger Siedlungsplatz am Beetzsee, Lkr. Potsdam–Mittelmark, in: Archäologie in Berlin und Brandenburg, edited by: Archaeological Society in Berlin and Brandenburg e.V. in cooperation with the Brandenburg Department of Cultural Heritage and Archaeological State Museum and Landesdenkmalamt Berlin, Theiss, Stuttgart, Germany, 80–83, 2018.

Stackebrandt, W. and Lippstreu, L.: Brandenburg–Eisrandlagen in Brandenburg und ihre möglichen Verknüpfungen, The Brandenburg State Office for Mining, Geology and Raw Materials, Germany, 157, available at: https://www.geobasis-bb.de/geodaten/lbgr/4_geoatlas.htm (last access: 7 July 2019), 2010.

Verband der Landesarchäologen: Kommission Archäologie und Informationssysteme: Zeitstrahl, available at: http://www.landesarchaeologen.de/fileadmin/Dokumente/Dokumente_Kommissionen/Dokumente_Archaeologie-Informationssysteme/Dokumente_AIS_Thesauri/Zeitstrahl_V01.pdf (last access: 7 July 2019), 2014.

WSA Brandenburg: Aktuelle Wasserstandshauptwerte, Zehnjahesreihe 2006 bis 2015 einiger Pegelstationen des WSA Brandenburg, Brandenburg Waterways and Shipping Authority, Germany, available at: http://www.wsa-brandenburg.wsv.de/service/Wasserstaende/index.html (last access: 7 July 2019), 2015.

E&G Quaternary Sci. J., 68, 119–139, 2019
https://doi.org/10.5194/egqsj-68-119-2019


Open Access E&G Quaternary Science Journal

Research article

# Coastal lowland and floodplain evolution along the lower reaches of the Supsa River (western Georgia)

**Hannes Laermanns**[1], **Simon Matthias May**[1], **Daniel Kelterbaum**[1], **Giorgi Kirkitadze**[2], **Stephan Opitz**[1], **Levan Navrozashvili**[2], **Mikheil Elashvili**[2], and **Helmut Brückner**[1]

[1]Institute of Geography, University of Cologne, Albertus-Magnus-Platz, 50923 Cologne, Germany
[2]Ilia State University, K. Cholokashvili Ave 3/5, Tbilisi 0162, Georgia

**Correspondence:** Hannes Laermanns (h.laermanns@uni-koeln.de) and Helmut Brückner (h.brueckner@uni-koeln.de)

**Relevant dates:** Received: 5 December 2018 – Revised: 21 May 2019 – Accepted: 30 May 2019 – Published: 24 July 2019

**How to cite:** Laermanns, H., May, S. M., Kelterbaum, D., Kirkitadze, G., Opitz, S., Navrozashvili, L., Elashvili, M., and Brückner, H.: Coastal lowland and floodplain evolution along the lower reaches of the Supsa River (western Georgia), E&G Quaternary Sci. J., 68, 119–139, https://doi.org/10.5194/egqsj-68-119-2019, 2019.

**Abstract:** In the southernmost part of the Colchian plain (Georgia), the Supsa and Rioni rivers represent important catchments for reconstructing Holocene landscape changes. Using granulometric methods, geochemical analyses and radiocarbon dating, we demonstrate that significant palaeoenvironmental changes have taken place in the surroundings of the Supsa fan since at least 4000 BCE. The initial foothill fan accumulation was prolonged by delta plain progradation. Due to continued fluvial sediment supply, mainly from the Rioni, the lagoon silted up and extended peat bogs formed east of the beach ridge complex. The Supsa fan first prograded northwards (since the third millennium BCE) and later shifted westwards, eventually following an avulsion of the Rioni. While Supsa deposits remain limited to the area of the fan and the modern estuary, the alluvial fines of the Rioni dominate the surrounding areas. The relative sea-level (RSL) index points of the region suggest a gradual RSL rise from $\sim -9$ m between 4000 and 3500 BCE to $-3/-2$ m below the modern sea level in the second half of the first millennium BCE, the period during which Greek colonization and Colchian settlements are attested by archaeological remains.

**Kurzfassung:** Im südlichsten Teil der kolchischen Tiefebene (Georgien) stellen die Einzugsgebiete von Rioni und Supsa wichtige Areale zur Rekonstruktion des holozänen Landschaftswandels dar. Mittels granulometrischer und geochemischer Analysen sowie Radiokohlenstoffdatierungen lässt sich der signifikante Landschaftswandel im Bereich des Supsa-Schwemmfächers seit etwa 4000 v. Chr. nachweisen. Das Areal wurde von einer Sandbarre vom offenen Meer getrennt, hinter der sich große Stillwasserbereiche bildeten. Der anhaltende fluviale Sedimenteintrag, hauptsächlich durch den Rioni, begünstigte die allmähliche Verlandung und die Entstehung von Torfmooren. Gleichzeitig baute sich – zunächst nach Norden (etwa ab dem 3. Jahrtausend v. Chr.) und später durch den Rioni nach Westen abgelenkt – der Schwemmfächer des Supsa vor. Während sich die Supsa-Ablagerungen im Wesentlichen auf den Schwemmfächer und die aktuelle Mündung beschränken, dominieren die feinkörnigen Ablagerungen des Rioni die Umgebung. Die Indexpunkte für den relativen Meeresspiegel deuten auf einen anhaltenden Anstieg des Meeres hin, ausgehend von etwa $-9$ m unter dem heutigen Niveau um 4000 bis 3500 v. Chr. auf −3 bis −2 m in der zweiten Hälfte des 1. Jahrtausends v. Chr. Für den letztgenannten Zeitraum sind kolchische und griechische Siedlungen durch archäologische Funde in der Umgebung der Supsa-Mündung belegt.

## 1 Introduction

Deltas, estuaries and low-lying coastal plains render important information about the postglacial coastal evolution and the Holocene sea-level rise (Arslanov et al., 2007; Marriner et al., 2010; Haghani et al., 2015). At the same time deltaic regions played an important role for the ancient colonization (e.g. by Greeks, Romans and Phoenicians; Anthony et al., 2014; Giaime et al., 2019), providing access to the hinterland as well as to the open sea. Especially in the Mediterranean many important ancient cities were founded on the coast of large embayments and estuaries, e.g. Troy (Kraft et al., 2003), Ephesus (Stock et al., 2013, 2016), Miletus and Priene (Brückner et al., 2002, 2017) and their respective gulfs, and Aquileia near Laguna di Grado in northeastern Italy (Arnaud-Fassetta et al., 2003).

While a significant amount of research on both sea-level evolution and human–environment interactions exists from Mediterranean coastal lowlands and delta regions (e.g. Lario et al., 2002; Pavlopoulos et al., 2006; Carozza et al., 2011; Brückner et al., 2017; Herda et al., 2019) – many of them in geoarchaeological contexts and at ancient harbour sites especially(Marriner and Morhange, 2007; e.g. for Rome's harbours Portus and Ostia: Delile et al., 2014; Goiran et al., 2014; for Miletus: Brückner et al., 2014; for Alexandria: Flaux et al., 2017; for Ephesus Stock et al., 2013, 2014) – studies on the sea-level evolution of the Black Sea are scarce. Only during the last decade, the number of publications has increased for particular areas (e.g. Danube delta: Giosan et al., 2006; Taman and Kerch peninsulas: Kelterbaum et al., 2011, 2012) and in the context of the controversial debate about sea-level evolution and fluctuations (e.g. Brückner et al., 2010; Fouache et al., 2012; Erginal et al., 2013; Bolikhovskaya et al., 2018).

In particular, the Georgian Black Sea coast remains understudied so far, although it stands out with its unique vegetation history and long-time human occupation, with the ancient Kingdom of Colchis and several Greek colonies of which the lost city of Phasis is the most famous (Lordkipanidze, 1991). Overall, the Georgian coast and its central section, the Colchian plain, offer – with estuaries of numerous rivers and extensive wetlands – promising geo-bio-archives. The potential of the Colchian plain (i.e. the area between the rivers Supsa and Enguri, Fig. 1) for palaeoenvironmental and geoarchaeological studies has been shown only in the very recent past by elucidating the mid-Holocene to late Holocene development of the Rioni delta (Laermanns et al., 2017a) and presenting new data on the evolution of Bronze Age settlements (Laermanns et al., 2017b).

While most of the major rivers in the northern and central Colchian plain are sourced in the Greater Caucasus in the north and have formed the vast alluvial Colchian plain, the southernmost river, the Supsa, is fed by the Lesser Caucasus in the south (Fig. 1). While presently flowing into the Black Sea, it has built a prominent, semi-circular alluvial fan at the interface between the mountains and the southern Colchian plain, which constitutes an arable area along the southern margin of Lake Paliastomi (Fig. 2). Colchian and Greek amphorae, as well as graves, were found at several sites in the surroundings of the river course (Lordkipanidze 1985; Miron and Orthmann, 1995; Sens, 2009); thus, the area may have represented a favourable settlement place due to its slightly elevated position near Lake Paliastomi; even speculations on a possible location of Phasis in this area exist (see an overview in Gamkrelidze, 2012). Yet, to date there is neither detailed information about the Holocene evolution of the Supsa fan and its environs nor on its occupation history.

Against this background, the overall aim of our study is to provide the first data on the Holocene evolution of the Supsa alluvial fan and its surroundings during the past millennia. Therefore, we aim to (i) document the chronostratigraphy of the fan, (ii) reconstruct the palaeogeographical and palaeoenvironmental evolution of the delta area, and (iii) differentiate between the sediments originating from the Supsa and the Rioni catchments. Furthermore, we intend to (iv) probe if archaeological findings can testify that the former conditions favoured human occupation in this particular area.

## 2 Regional setting

### 2.1 Physical setting

The Kolkheti lowlands or Colchian plain, which roughly correspond to the historical region of Colchis, form a triangular-shaped coastal plain of western Georgia (Fig. 1). They are limited by the Black Sea in the west, the slopes of the Greater Caucasus in the northeast and the Lesser Caucasus in the southeast (Fig. 1). The lower Likhi range connects both Caucasian ranges and forms the easternmost border, separating the Colchian lowlands from the Kura catchment in eastern Georgia, which discharges eastwards into the Caspian Sea (Eppelbaum and Khesin, 2012).

Like the whole of Georgia, the Colchian plain is located in the convergence zone between the Arabian and Eurasian plates (Dhont and Chorowicz, 2006). During the closure of

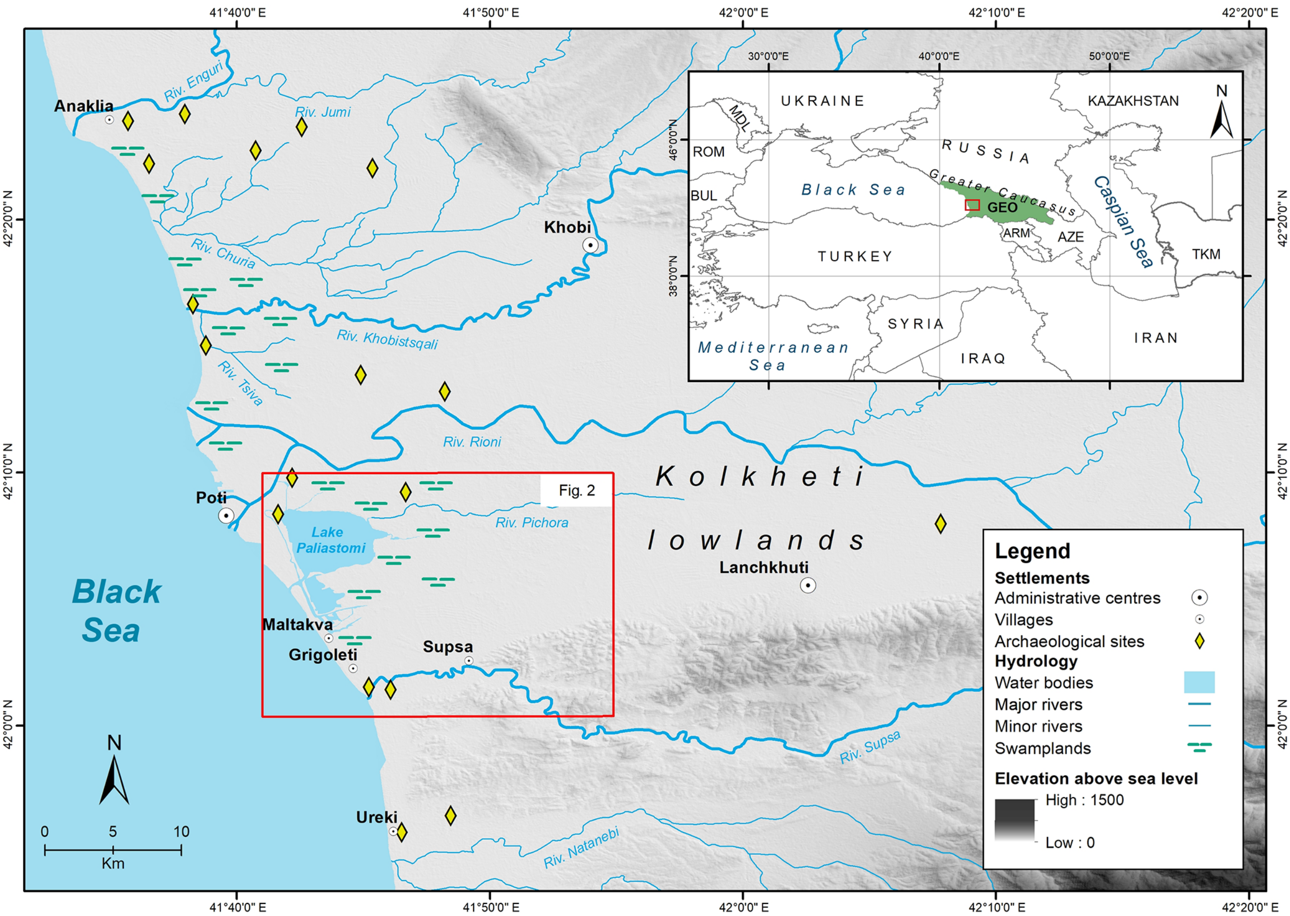


**Figure 1.** Map of the central part of the Georgian Black Sea coast, also known as Colchian plain or Kolkheti lowlands. It is dominated by a vast alluvial plain, swamplands and several rivers of which the Enguri, Khobistsqali, Rioni and Supsa are the most important. The red frame indicates the area shown in Fig. 2 (based on the ASTER digital elevation model, shaded model).

the northern Neo-Tethys Ocean (Sosson et al., 2010) and the subsequent Alpine–Himalayan orogeny, this former Mesozoic to Cenozoic back-arc marginal extensional basin was closed and the folded mountains of the Caucasus evolved (Adamia et al., 2011; Forte et al., 2014). Triggered by the northward drift of the Arabian plate, the ongoing continent–continent collision between the Lesser Caucasus arc and the Eurasian basement still has convergence rates between ∼ 12 mm per year in the eastern part and ∼ 2 mm per year in the western part, e.g. the Colchian plain (Avdeev and Niemi, 2011; Yılmaz et al., 2013). There, convergence occurs along the Adjara–Trialeti Thrust Belt (ATTB) in the south and the Chaladidi–Tsaishi Thrust (CTT) in the north (Reilinger et al., 2006; Forte et al., 2014) (Fig. 1).

Though the Caucasus mountains evolved from the same tectonic processes they differ in their geology from the Colchian plain: the Greater Caucasus in the north is a polycyclic, folded-nappe formation (Okrostsvaridze et al., 2016) and consists of a pre-alpine crystalline basement complex and a younger cover of Mesozoic to Neogene ophiolites, (marine) sedimentary and volcanic rocks. The Lesser Caucasus inherits additional andesitic pyroclastica and effusiva (Mitchell and Westaway, 1999), as well as granite and gneiss intrusions (Yılmaz et al., 2013).

In contrast, the Colchian plain primarily consists of Cretaceous and Palaeogene sediments and by volcanoclastics (Bazhenov and Burtman, 2002). These deposits are overlain by Quaternary molasses and river terraces of eroded material from the surrounding mountains and their foothills (Adamia et al., 2011). Due to high fluvial sedimentation and tectonic subsidence, the deposits reach a thickness of up to 30–40 m in the western area (Adamia et al., 2011). During the Holocene, these deposits and the large-scale sea-level rise dominated the morphology on the Colchian plain. Here, massive coastline changes were provoked, especially by the reconnection of the Black Sea with the Mediterranean Sea ∼ 8400 years ago (Ryan, 2007; Giosan et al., 2009), and vast areas of former dry land drowned. Probably around 3000 BCE, sea level nearly reached its present posi-

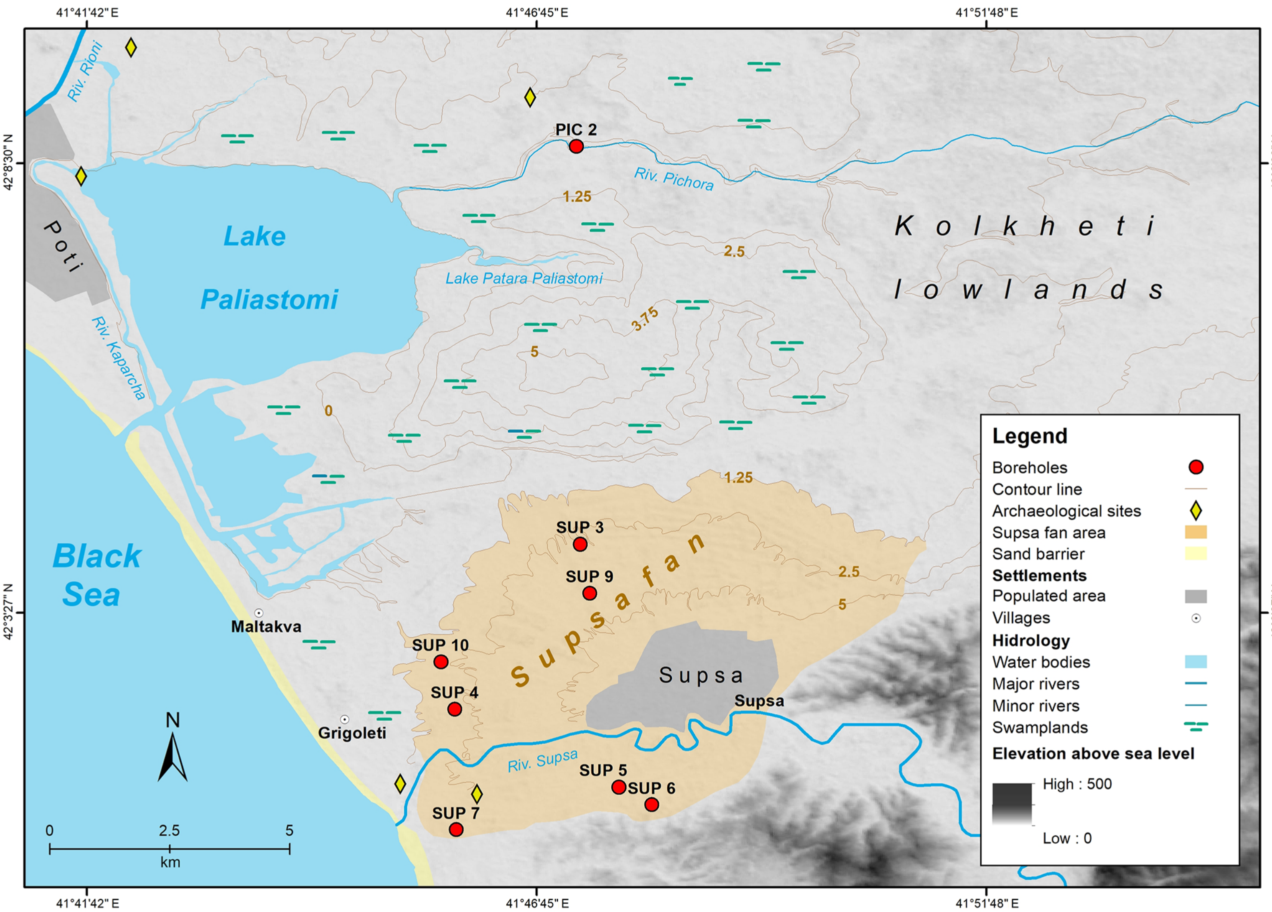


**Figure 2.** Map of the research area. The Supsa fan is highlighted in light brown. The sites of the boreholes are indicated by red dots (based on the ASTER digital elevation model, shaded model).

tion (∼ 1.5–0 m) (Brückner et al., 2010; Fouache et al., 2012; Kelterbaum et al., 2012; Laermanns et al., 2017a).

Today, the central plain is dominated by four rivers (from north to south): Enguri, Khobistsqali, Rioni and Supsa. While the former three have their source areas in the Greater Caucasus, the latter originates from the Lesser Caucasus (Fig. 1). While the Rioni has a catchment of ca. 13 400 $km^2$, an average water volume of 13.38 $km^3\,a^{-1}$ and a sediment load of $6.02 \times 10^6\,t\,a^{-1}$ before debouching into the Black Sea (Berkun et al., 2015), the Supsa is considerably smaller: with a catchment of ca. 1100 $km^2$, a discharge of less than 3 $km^3\,a^{-1}$ and a sediment load of $0.246 \times 10^6\,t\,a^{-1}$, the Supsa can be considered as a river of regional importance only. However, it contributes more water than the two northernmost rivers Enguri and Khobistsqali with 1.25 and 1.89 $km^3$ discharge and catchment areas of 460 and 1340 $km^2$, respectively (Jaoshvili, 2002; Berkun et al., 2015). The sediment load of the Khobisqali is comparable ($0.221 \times 10^6\,t\,a^{-1}$), and the load of the Enguri is significantly higher ($0.45 \times 10^6\,t\,a^{-1}$. In general, the sediment load of the four rivers predominantly consists of sand and silt (Jaoshvili, 2002).

The Supsa is the only river which has built a major lobate fan in the Kolkheti lowlands, which in its centre rises up to several metres over the surrounding swamp areas while its outermost edges are of almost the same elevation (Fig. 2). It is located directly north of the foothills where the Supsa discharged into the former lagoon, the recent open plain. This protected location may be the reason why the sediments were not affected by longshore drift and, therefore, not transported further along the coast. In this paper, the term "Supsa fan" refers to this morphological feature. In contrast, the recent river mouth of the Supsa is located further to the west, forming an estuary which is comparable to those of the Enguri and Khobistsqali rivers.

The Colchis shelf is only 10–15 km wide. It is dissected by submarine canyons that were formed during sea-level lowstands and are extensions of the (later) estuaries of Supsa, Rioni and Enguri (Jaoshvili, 2002). While the dominant coastal surface current runs anti-clockwise, annual fluctuations occur especially in front of the Rioni delta (Jaoshvili, 2002; Korotaev et al., 2003). During the last millennia, the long-shore drift has formed the wave-dominated Colchian coastline with long-stretched, wide sandy beaches.

The regional climate is characterized by high precipitation (> 2000 mm per year) and average annual temperatures around 14 °C, without regular winter frosts (the mean January temperature is 6 °C in Batumi) (Box et al., 2000; see also Denk et al., 2000; Hijmans et al., 2005). This warm and humid climate, combined with the high relief in the upper river courses, led to high rates of weathering and erosion, which in turn result in the high sediment load of the rivers.

Extensive wetlands with swamps, peat bogs, shallow lakes, open reed areas and forests of evergreen understory cover huge parts of the Colchian plain, while mixed forests dominate the neighbouring foothills (Box et al., 2000). As a result of centuries-long deforestation and drainage activities, most of the natural vegetation along the coast, rivers and foothills has been replaced by open grassland and farmland (de Klerk et al., 2009). Thus, an extensive system of drainage ditches and ridge-and-furrow fields forms a significant part of the recent relief on the Colchian plain (Nikolaishvili et al., 2015). This holds especially true for the slightly elevated Supsa fan where drier conditions exist in contrast to the swampier surroundings.

### 2.2 Human occupation

Georgia has been populated since the Palaeolithic; bones discovered at the site of Dmanisi are presently the oldest hominid remains outside of Africa (Lordkipanidze et al., 2007). During the Holocene, an early transition from hunting and gathering to farming and animal husbandry set in between 10 000 and 9000 BCE (Arslanov et al., 2007). People spread from the foothills into the plain where the oldest settlement sites of Ontsakoshia (Janelidze and Tatashidze, 2010) and Ispani (Connor et al., 2007; de Klerk et al., 2009) date back to the transition between the Chalcolithic and the early Bronze Age in the mid-third millennium BCE. Since the early Bronze Age settlement mounds in the northern part of the Colchis have yielded evidence for the evolving Colchian culture (Lordkipanidze, 1991; Sens, 2009; Laermanns et al., 2017b). The region experienced its heyday between the sixth and fourth centuries BCE under the Kingdom of Colchis – a time of intensive trade contact with (mainly Milesian) Greek merchants, who had founded several colonies along the Colchian Black Sea coast (Sens, 2009; Gamkrelidze, 2012). In the late second to early first century BCE, Colchis fell into the sphere of influence of the Kingdom of Pontus. Later it became a client state of the Roman Empire (Gamkrelidze, 2012) and finally a Roman province (Rayfield, 2013).

Our knowledge of ancient Colchis is to some extent based on ancient Greek and Roman writers. One of the oldest accounts is the mythical journey of Jason and the Argonauts, a small band of heroes named after their ship Argo, who embarked for the Kingdom of Colchis on their quest to find the "Golden Fleece". Described in Homer's *Odyssey* (eighth–seventh century BCE), as background of Euripides' play *Medea* (fifth century BCE) and as subject of the epic poem *Argonautica* (Greek: *Αργοναυτικά*) by Apollonius Rhodius (third century BCE), this myth is one of the most important narratives of Antiquity (Okrostsvaridze et al., 2016). Besides its adventurous story of Jason and his comrades, the saga reflects the impressions of Mycenaean Greeks from their first voyages to the Colchis in the late second millennium BCE (Okrostsvaridze et al., 2016). In the literature, opinions differ as to whether the Golden Fleece represents sheep skins which were used for the extraction of placer gold, as described by Strabo (Book XIII), Pliny the Elder and Appian of Alexandria, who all praise the gold and silver richness of the Colchian rivers (Okrostsvaridze et al., 2016), or if it symbolizes the wealth of Colchis in general (Braund, 1994).

### 2.3 Research area

Our investigations focus on the Supsa delta region and its adjacent areas, i.e. on the southernmost part of the Colchian plain (Fig. 1). Here, the Supsa River leaves the foothills and forms its lobe-shaped alluvial fan. The eponymous village covers the central part of the fan, while its surroundings are dominated by farmland (Fig. 3b). The prevailing ridge-and-furrow fields, which are divided by an extensive network of drainage channels, have overprinted the natural fluvial structures (cf. Fig. 2). Only in few swampy grassland areas have near-natural conditions prevailed. The recent river mouth is located ca. 6.5 km west of the fan apex. The graded shoreline is formed by a straight beach with several beach ridges behind, and it is strongly influenced by the northbound long-shore current (Korotaev et al., 2003). North of the river mouth, the villages Maltakva and Grigoleti stretch atop the linear structure of the coast-parallel beach ridges. The coast section is separated from the alluvial fan by swamplands and peat bogs which extend to the southern shores of Lake Paliastomi (Figs. 2, 3a). On the southern side of the river mouth, the foothills reach close to the graded shoreline.

Within this area several archaeological sites are known. Whole amphorae and fragments from Heraclea Pontica and Sinope were unearthed between the village Maltakva and the Supsa river mouth (Figs. 1, 2); they date to the fourth and third centuries BCE (Sadzradze et al., 1999). At the villages of Ureki and Maltakva, several Colchian amphorae (second and first centuries BCE) were found (Miron and Orthmann, 1995; Gamkrelidze, 2012). Some historians (e.g. Shafranov, 1880, in Gamkrelidze, 2012) even speculate that the ancient city of Phasis was located on the southern shore of Lake Paliastomi at the river mouth of the Supsa. Further upstream, many smelting furnaces were discovered through different surveys (Khakhutaishvili, 2008, 2009; Erb-Satullo et al., 2014). Their spatial concentration can be explained by the occurrence of chalcopyrite, the dominant copper-bearing mineral in quartz veins or iron oxide matrices (Gugushvili

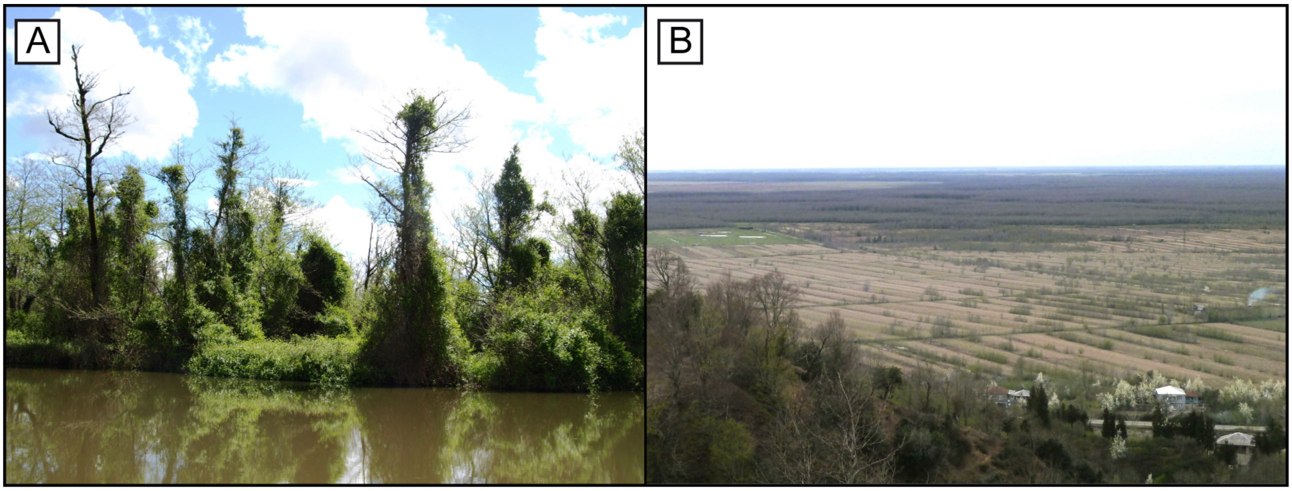


**Figure 3.** **(a)** Natural swamp forest vegetation close to the site of sediment core PIC 2 on the banks of the Pichora River. **(b)** Northward view from the foothills to the south of the village of Supsa. The ridge-and-furrow system of the agrarian areas is contrasted by the swamplands in the background (photos: Hannes Laermanns, 2014, 2015).

et al., 2010; Erb-Satullo et al., 2014). Chalcopyrite outcrops due to tectonic faults and erosion at the Adjara–Trialeti Thrust Belt (Okrostsvaridze et al., 2016).

## 3 Methods

### 3.1 Geochemical and sedimentological analyses

The coring sites of the delta area were chosen due to their accessibility and relevance. The sediment cores were retrieved using a Cobra TT (Atlas Copco) percussion-coring device. Only sediment core PIC 2 was taken further north, at the riverside of the Pichori, which discharges into Lake Paliastomi (Figs. 1, 2). The diameter of the drill heads were 6 and 5 cm, respectively, and coring reached a maximum depth of 12 m below surface (b.s.). These sediment cores form the basis for further stratigraphic and geochemical analyses and interpretations. Core description in the field encompassed sediment texture, colour and $CaCO_3$ test (with HCl, 10 %) of the different sediment units. Samples were taken with intervals of ca. 20 cm for further treatment in the laboratory.

All analyses were conducted in the laboratory of the Institute of Geography, University of Cologne, Germany. The samples were oven-dried at 40 °C for 48 h, subsequently sieved < 2 mm and gently crushed with a mortar to disintegrate the aggregates.

For granulometric analyses, the samples were pre-treated with hydrogen peroxide ($H_2O_2$, 15 %) to remove organic matter and with sodium pyrophosphate ($Na_4P_2O_7$, 46 g $L^{-1}$) to avoid coagulation. Before measurement, the samples were shaken for at least 12 h in an overhead shaker. Granulometric analyses were performed in 116 channels from 0.04 to 2000 µm with a Laser Diffraction Particle Size Analyzer (LS 13320 Beckmann Coulter™), where each sample was measured three times using the optical Fraunhofer model. Grain-size parameters based on Folk and Ward (1957) were calculated using the GRADISTAT software version v8 (Blott and Pye, 2001). All grain-size categories are given according to the norm based on AG Boden (2005).

After separating the < 63 µm fraction by sieving, the grain shape of samples from the sandy beds was analysed using a Retsch CAMSIZER® P4. This fraction was measured in 52 channels up to 22.4 mm to define roundness, sphericity and elongation using the principle of dynamic image analysis (ISO 13322-2) to identify different deposition modes and possible sources. The results were calculated using the software CAMSIZER® 4.4.1.

Loss on ignition (LOI) was measured to estimate the organic matter content of the sediments. A total of 5 g of sample material were oven-dried at 105 °C for 12 h, and subsequently ignition was determined in a muffle furnace (Carbolite ELF) at 550 °C for 5 h. Although possible uncertainties may result from the combustion of clay minerals, sulfates and/or carbonates, LOI is often used to estimate the organic matter content (e.g. Barsch et al., 2000; Heiri et al., 2001).

Element concentrations (Ca, Al, Fe, K, S, Cu, Zn and Pb) were measured by a portable XRF Analyzer (NITON XL3t, Thermo Scientific, analyticon) to draw conclusions on the depositional environment (marine or terrestrial origin) and on human influence (Oonk et al., 2009; Dung et al., 2013; Dirix et al., 2015). Triplicate measurements were performed on pellets of dried and ground sample aliquots, which were pressed into a Teflon ring with 12 N $mm^{-2}$ and subsequently covered with a 4 µm polypropylene film (X-ray film, TF-240-255). A gold anode emitted X-ray (70 kV) needed to perform measurements within the "mining-minerals-mode", which uses four different filters for 40 s each. The secondary X-rays of element-specific wavelength are detected and processed by a digital signal processor. Si concentrations (in ppm) are calculated from the element-specific fluorescence energies and compared with external and internal reference materials (STDS-4, BCR142R, BCR-CRM 277). Magnetic susceptibility (MagSus) measurements were performed three times for each sample using a Bartington MS2B sensor.

Principal component analyses (PCAs) were applied using the software PAST (version 3.1.1, Hammer et al., 2001) to establish a statistically validated distinction of the different depositional facies (e.g. Zhang et al., 2002; Borůvka et al., 2005; Zhang and Mischke, 2009; Laermanns et al., 2017a). Therefore, standardized values of the granulometric parameters (mean grain size, sorting, kurtosis and skewness) were used to differentiate between the depositional modes (Folk and Ward, 1957). Additionally, a selection of the measured geochemical parameters, Ca, K, Fe and Cu, that provided information about the origin of the sediments and, in the case of Cu, possible human activity were standardized and added to the PCA (Oonk et al., 2009; Dung et al., 2013; Dirix et al., 2015). An additional PCA was applied for the sandy layers to differentiate their origins. The distribution of the data was explained by the first two components of each PCA.

### 3.2 Dating techniques

A total of 12 samples (plant remains and charcoal) from the three sediment cores SUP 3, 4 and 10 were taken for radiocarbon dating (Table 1) at the $^{14}$CHRONO Centre, Queens University Belfast, Northern Ireland, UK. All ages were calibrated using Calib 7.1 (calibration data set: intcal13.14c; Stuiver and Reimer, 1993; Reimer et al., 2013). An age–depth model was calculated for the sediment core SUP 4 using the R-based software Bacon 2.2 (Blaauw and Christen, 2011).

## 4 Results

### 4.1 Sediment cores

#### 4.1.1 SUP 3

SUP 3 was cored in the northern part of the Supsa fan (Figs. 2, 4, 5). The lowermost section (11.00–10.16 m b.s.) is composed of brown to dark brown silty to sandy peat. The layer is characterized by a heterogeneous grain-size composition, poor sorting and low values for all of the measured parameters. Between 10.16 and 8.75 m b.s., (dark) brownish grey clayey silt occurs with a more homogeneous grain size (< 7 µm). The layer of fine to medium sand at 8.75–6.33 m b.s. is characterized by sharp boundaries, also indicated by the sudden rise in the mean grain size with values of > 100 µm and elevated values of Ca, K, magnetic susceptibility (MagSus), Ca/K and Ca/Fe ratios. In contrast, the S content remains low. From 6.33 m b.s. to the surface, greyish brown to grey silts dominate with changing sand and clay contents and low values of LOI, MagSus, Ca/K and Ca/Fe. Only between 4.53 and 4.00 m b.s., two layers of peat and sand are interdigitated, each ∼ 25 cm thick and confined by sharp boundaries. While the peat shows high LOI values (up to ∼ 47 %), the sand is characterized by a sharp peak in its Ca/Fe ratio.

#### 4.1.2 SUP 9

The sediment core SUP 9 was taken 150 m south of the SUP 3 site (Fig. 2). The lowermost part (10–9.55 m b.s.) consists of organic-rich (brownish) clayey silt. Then follows heterogeneous grey silt to silty sand. From 7.13 to 3.41 m b.s., homogeneous (brownish) grey clayey silts dominate once again; the mean grain size does not exceed 10 µm. Only an intercalation of brownish silt between 5.75 and 5.33 m b.s. stands out with coarser grain size and different colour. At 3.41 m b.s., an abrupt disconformity occurs with a shift to a 2 m thick heterogeneous brownish grey to grey fine to medium sand. The main grain size slightly decreases towards the upper facies limit at 1.41 m b.s., where brown sandy silt was deposited. The uppermost part (0.72–0 m b.s.) is formed of brown to reddish brown loamy silt.

#### 4.1.3 SUP 4

SUP 4 was cored at the western margin of the Supsa fan (Figs. 2, 6). The basal part consists of (brownish) grey silty fine sand with very poor sorting, low MagSus and relatively low Ca/Fe and Ca/K ratios but high LOI values. This layer gradually merges into the subsequent peat, which stands out with high Ca/Fe and Ca/K ratios and low MagSus values. Above a sharp boundary, well-sorted clayey silt shows high concentrations of Pb, Zn and P as well as low values of S. At 9.46–9.23 m b.s. another peat occurs, which differs from the lower peat in terms of smaller matrix grain size, better sorting and very high S values. While its lower boundary is hard to define due to the gradual transition from the silt below, the upper boundary is rather sharp. Between 9.23 and 2.31 m b.s. grey silt occurs. The lowermost (9.23–7.53 m b.s.) and uppermost (4.62–2.31 m b.s.) parts of this unit are characterized by relatively low Ca/K and Ca/Fe ratios, while S, Pb and Zn reach very high levels. By contrast, the in-between section (7.53 and 4.62 m b.s.) shows higher sand content, poorer sorting, elevated Ca/K and Ca/Fe ratios, as well as a high MagSus. After a disconformity follows silty sand with elevated values of Ca/K, Ca/Fe and MagSus. The uppermost part of the core (1.88–0 m b.s.) is silty loam with a similar geochemical composition as the sand below.

#### 4.1.4 SUP 10

Northwest of SUP 4, SUP 10 was cored beyond the western margin of the alluvial fan of the Supsa (Figs. 2, 7). The stratigraphy is dominated by fine to medium sand with interdigitated peats. From the maximum depth at 12 to 10.46 m b.s. (dark) grey fine sand shows high Ca/Fe and Ca/K ratios. After a disconformity follows a sequence of

**Table 1.** Radiocarbon data set. Measurements were carried out at the $^{14}$CHRONO Centre, Queens University Belfast, Northern Ireland, UK. All ages are calibrated using Calib 7.1 (calibration data set: IntCal13.14c; Stuiver and Reimer, 1993; Reimer et al., 2013) and are presented with $2\sigma$.

| Sample ID | Lab code | Depth below surface (m) | $\delta^{13}$C (‰) | Material | Conventional $^{14}$C age BP | Calibrated $^{14}$C age (cal BCE/CE), $2\sigma$ |
|---|---|---|---|---|---|---|
| SUP 3/14 | UBA-34221 | 4.32 | −30.5 | Wood | 2180 ± 27 | 359–171 BCE |
| SUP 3/22 | UBA-34222 | 6.40 | −28.5 | Wood | 3818 ± 30 | 2434–2143 BCE |
| SUP 3/34 | UBA-34223 | 10.50 | −26.1 | Wood | 4423 ± 58 | 3336–2913 BCE |
| SUP 4/6 | UBA-26767 | 1.35 | −28.3 | Plant fragment | 854 ± 28 | 1053–1257 CE |
| SUP 4/11 | UBA-26768 | 2.35 | −21.0 | Wood | 1214 ± 34 | 690–891 CE |
| SUP 4/19 | UBA-26769 | 4.70 | −30.9 | Wood | 2281 ± 37 | 404–209 BCE |
| SUP 4/23 | UBA-26770 | 5.70 | −24.7 | Wood | 2404 ± 39 | 749–396 BCE |
| SUP 4/36 | UBA-26771 | 9.27 | −26.3 | Wood | 4699 ± 42 | 3631–3370 BCE |
| SUP 4/39 | UBA-26772 | 9.75 | −27.6 | Wood | 5111 ± 74 | 4045–3711 BCE |
| SUP 4/41 | UBA-26773 | 10.50 | −24.9 | Wood | 4983 ± 38 | 3795–3660 BCE |
| SUP 10/23 | UBA-34224 | 6.72 | −26.4 | Wood | 1126 ± 27 | 778–990 CE |
| SUP 10/29 | UBA-34225 | 7.52 | −25.7 | Wood | 3492 ± 29 | 1893–1701 BCE |

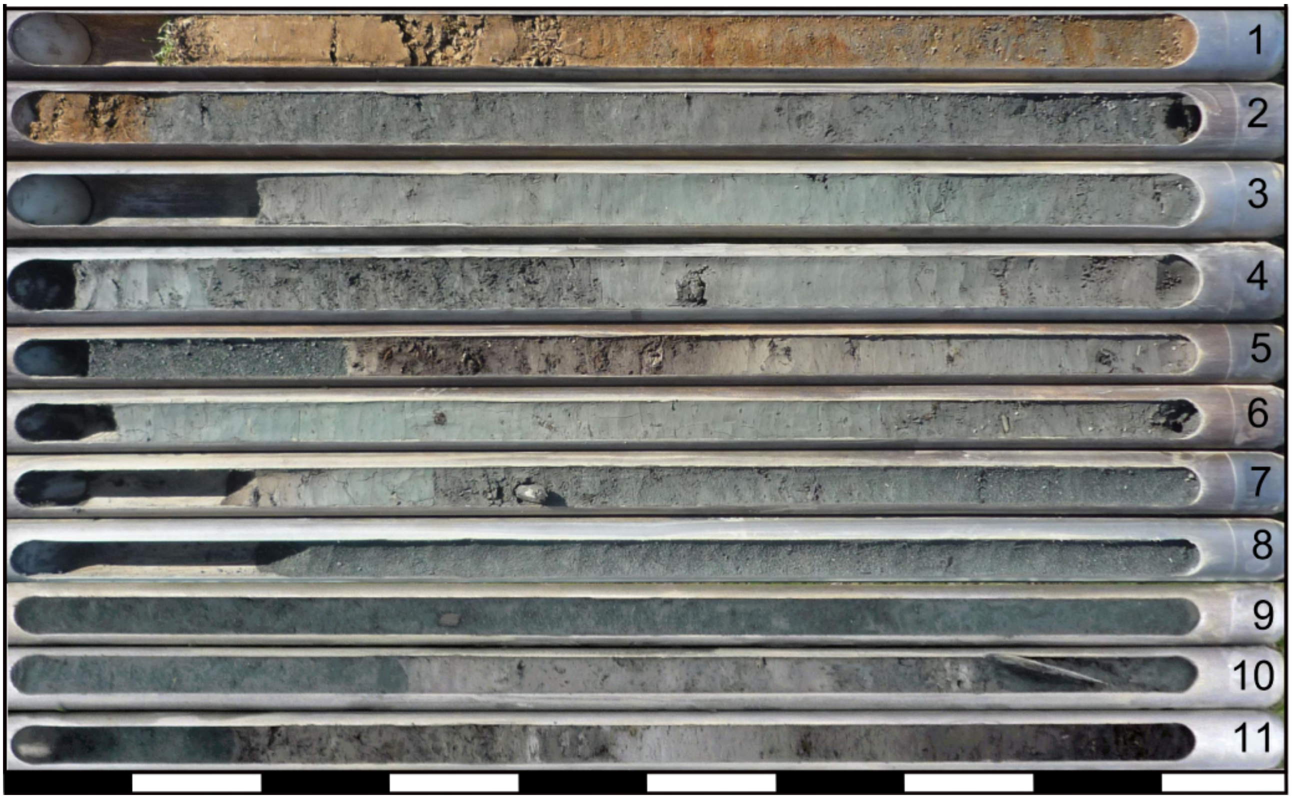


**Figure 4.** Sediment core SUP 3 from the maximum depth at 11 m b.s. (bottom right) to the surface (top left). Outer diameter of auger heads: 6 cm (0–4 m) and 5 cm (4–11 m) (photo: Hannes Laermanns, 2013).

several peat and organic-rich greyish brown strata with low Ca/Fe and Ca/K ratios, while LOI rises up to > 20 %. In general, this sequence is characterized by heterogeneous but generally low values of Fe, Cu, Zn, Pb and Ca. At 7.91–7.51 m b.s., massive wood occurs. Between 7.51 and 6.56 m, the brownish grey silt contains many ceramic fragments, up to 2 cm long. In this unit Ca/Fe and Ca/K reach their minimum values, while Fe, Al, Pb, Zn and Cu rise significantly. Then grey medium sand follows with a changing mean grain size of 90 to 450 µm. The sand unit is characterized by sharp lower and upper boundaries, low LOI contents, as well as low Ca/K and Ca/Fe ratios. The upper 2 m consists of grey

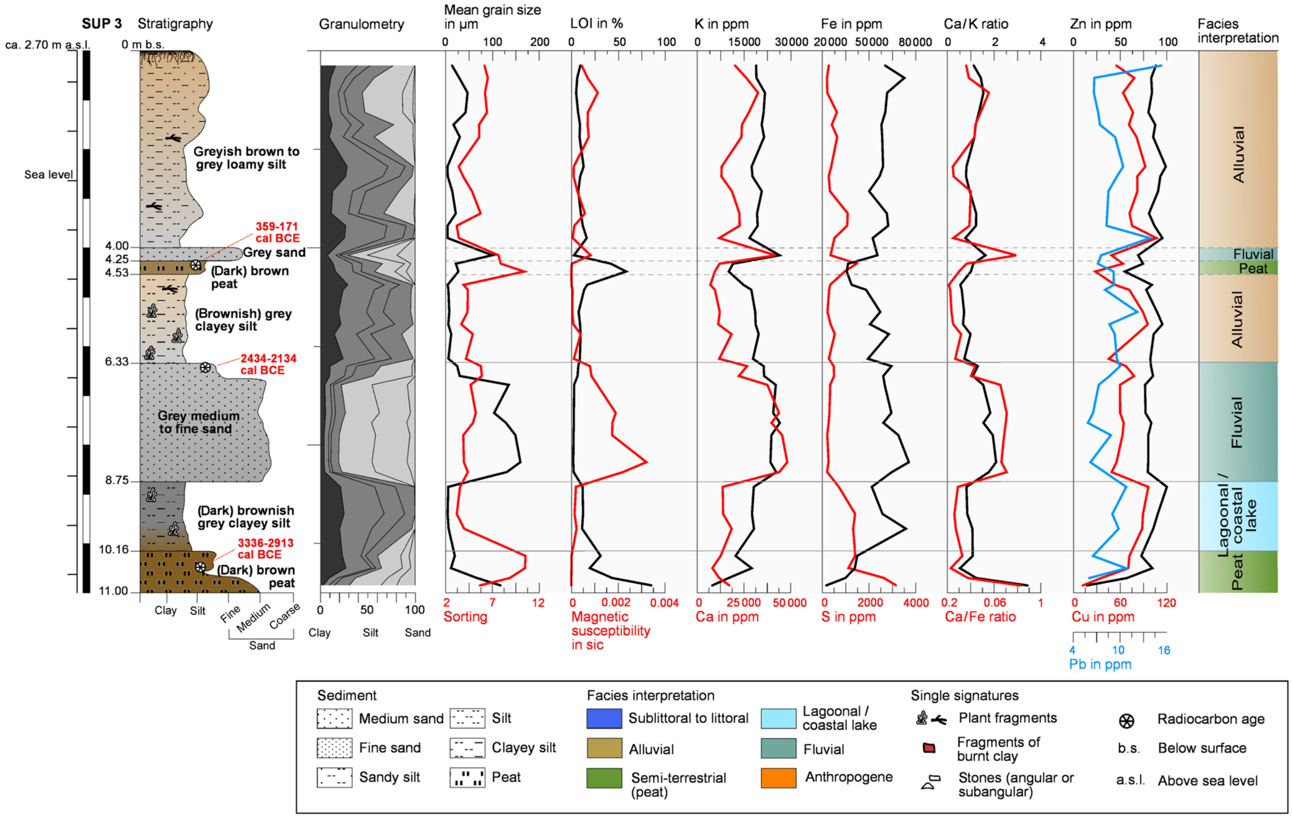


**Figure 5.** Profile, facies interpretation, granulometry, geochemistry and $^{14}$C age estimates of sediment core SUP 3 from the northern part of the Supsa fan (location in Fig. 2). The sediment core is dominated by fine-grained alluvial layers, which are interdigitated with peats in the lower part of the fluvial deposits (see Fig. 3).

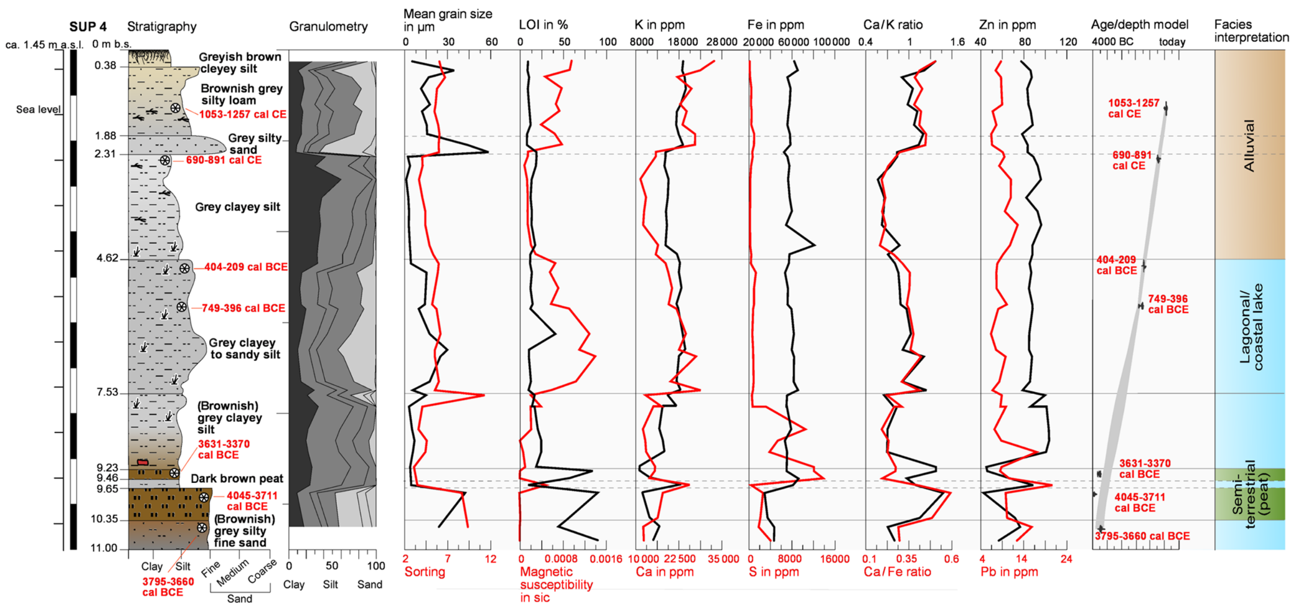


**Figure 6.** Profile, facies interpretation, granulometry, geochemistry and $^{14}$C age estimates of sediment core SUP 4 from the western edge of the Supsa fan (for the legend, see Fig. 5). Except from the peat interdigitations below 9 m b.s., the entire sediment core consists of fine-grained lagoonal to alluvial deposits, documenting the gradual change from a lagoon to a floodplain environment. The age–depth model was established with the R-based software Bacon 2.2 (Blaauw and Christen, 2011).

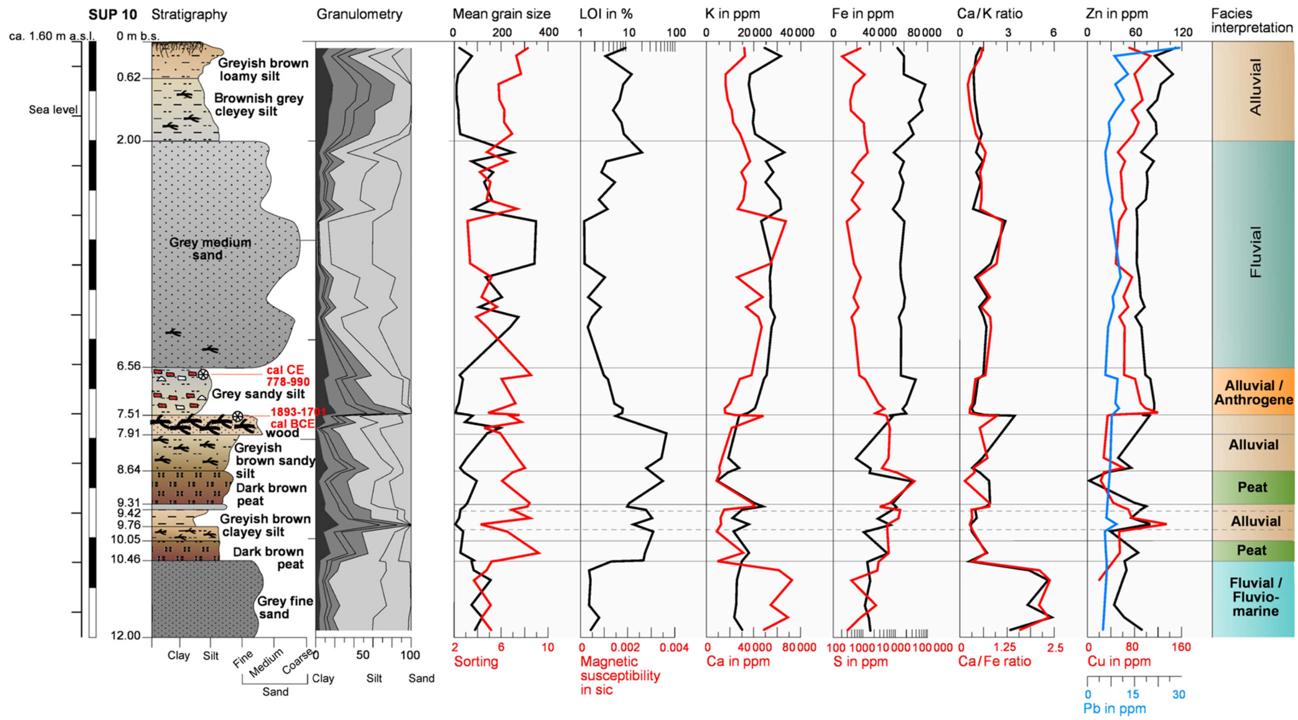


**Figure 7.** Profile, facies interpretation, granulometry, geochemistry and $^{14}$C age estimates of sediment core SUP 10 from the area between the coast and the Supsa fan (see Fig. 2). Above fluvio-littoral deposits, peat is interdigitated with alluvial silts and topped by a layer with many ceramic finds at 7.51–6.56 m b.s. Then fluvial sand dominates until 2 m b.s. (for the legend, see Fig. 5).

to greyish brown loamy to clayey silt, in which Zn and Pb rise up to the surface.

#### 4.1.5 SUP 5

Sediment core SUP 5, conducted on a grassland ca. 200 m north of the foothills (Fig. 2), is one of the two sediment cores taken on the southern riverside of the Supsa. The entire 10 m core consists of clayey to loamy silt. Its lowermost part contains several plant fragments. The sand content increases slightly between 8.31 and 4.56 m b.s. In the upper 2 m, the grey to dark grey colour of the core changes to a greyish brown.

#### 4.1.6 SUP 6

SUP 6, the second core taken from the southern side of the Supsa, originates from an outlet of a small tributary valley ca. 600 m southeast of the SUP 5 site (Fig. 2). In contrast to the fine-grain-dominated stratigraphy of SUP 5, SUP 6 contains several layers of medium sand (mean grain size varies between ca. 100 and 380 µm) from its maximum depth at 8 to 0.88 m b.s. The single sand layers can be divided by the occurrence of pebbles (< 3 cm) at different depths. Above a small silt layer at 3.58–3.52 m b.s., the Ca/K and Ca/Fe ratios fall to lower levels, while the concentrations of Zn and Cu rise. The uppermost 0.88 m of the core consists of brown sandy loam with some pebbles and coarse plant fragments.

#### 4.1.7 SUP 7

SUP 7, the westernmost sediment core, is from a grassland between the coast and the village of Ureki (Fig. 2). The lowermost part (5–1.91 m b.s.) consists of dark grey medium sand with a mean grain size between ∼ 140 and 300 µm. Above, grey clayey silt was deposited between 1.91 and 1.16 m b.s. Homogeneous grey fine sand (mean grain size ∼ 50 µm) follows at 1.16–0.77 m b.s. The uppermost part is built up of (greyish) brown loamy silt.

#### 4.1.8 PIC 2

PIC 2 was cored on the banks of the Pichora River (Figs. 2, 3a). Its lowermost part consists of dark grey to greyish brown medium sand. While P, Zn and S remain at low levels, a marked decrease in Ca, Ca/Fe and Ca/K values occurs within this layer. The subsequent stratum (2.93–1.26 m b.s.) of poorly sorted loamy silt is clearly separated from the previous and subsequent sand layers; it reveals slightly increased values of Pb, Zn, P and S, while Ca/K and Ca/Fe ratios remain at low levels. The upper sand layer stands out with a mean grain size of up to ∼ 320 µm, comparable to the sand layer in the lower part of the core. Most of the geochemical values are close to the loam layer in between. The uppermost part is a humus-rich fine-grained deposit.

### 4.2 Radiocarbon dating results

Altogether, 12 samples from the sediment cores SUP 3, SUP 4 and SUP 10 were $^{14}$C AMS dated (see Figs. 5 to 7, Table 1). The results are given with $2\sigma$ confidence interval.

The seven age estimates from SUP 4 cover a time span of roughly 5000 years (3756 BCE to 1261 CE; mean ages). Though the $2\sigma$ ranges of the two lowermost samples, SUP 4/39 and SUP 4/41, overlap, an age inversion cannot be excluded. The age estimates from SUP 3 cover $\sim$ 3000 years and ca. 6 m of sediment. For SUP 10, only two samples were used for radiocarbon dating. They derive from the lower and upper facies limit of the archaeological layer at 7.51–6.56 m b.s., covering a time span between 1893–1701 BCE and 778–990 CE ($\sim$ 2480 to 2900 years).

### 4.3 Statistical analyses of the sedimentological and geochemical data

By means of a principal component analysis using granulometric parameters (mean grain size, sorting, kurtosis and skewness) and the geochemical parameters Ca, K, Fe and Cu, the three main components were estimated as follows: PC 1: 41.4 %; PC 2: 24.9 %; and PC 3: 11.6 % (Fig. 10a, b). The majority of samples in Fig. 10a cluster on the left side of the $y$ axis (quadrants I and III) and refer to high values of Cu, Fe and skewness. They are considered to be of lagoonal or alluvial origin. The poor sorting and scattered distribution in quadrant III coincide with high values of loss on ignition (cf. Figs. 5–9), and, therefore, an enrichment of organic matter. In quadrant II, samples with high values of Ca, mean grain size and (to a certain extent) K are considered to be of fluvial origin. Quadrant IV shows samples of the sediment core PIC 2 and the lower part of SUP 10. Between these two groups sandy samples that derive from SUP 7 are situated.

Further, a PCA (Fig. 10c, d) that focuses on the sandy sediments was calculated with 25 representative samples. Besides the factors used in the former model, the grain shape parameters of roundness (RNDS), sphericity (SPHR) and elongation (the length–width ratio $b/l$) (Kasper-Zugbillaga et al., 2005; Eamer et al., 2017) were included. Within this PCA, the first three axes explain 40.3 %, 25.5 % and 14.5 %, respectively. The outlier position of the samples of sediment core PIC 2 and the lower part of SUP 10 is confirmed, as well as the exception of the samples of SUP 7.

## 5 Discussion

### 5.1 Facies determination

Based on the granulometric, geochemical and statistical results, six different depositional facies units were defined.

– Facies A: sublittoral to littoral.

  The majority of the relatively well-sorted medium sand of SUP 7 stands out with very coarse mean grain size up to $\sim$ 300 µm and a unimodal grain-size distribution. This points to hydrodynamic conditions with rather high sediment transport capacities, consistent with wave-dominated coastal conditions (Folk and Ward, 1957; Hesp, 2002; Dingler, 2005). The geochemistry is characterized by relatively high values of Ca and K and low values of Fe. In Fig. 10 A they scatter between the two outlier groups in quadrants II and IV. However, a separation from facies D remains challenging due to the proximity of the Supsa river mouth and its fluvial deposits. Nonetheless, the littoral deposits show a slightly better sorting.

– Facies B: alluvial (overbank deposits).

  Although they are of riverine origin, similar to facies E, these deposits are listed separately due to their different characteristics and deposition modes. Facies B is characterized by silty to clayey sediments with elevated K and Ca contents and relatively low LOI values. It can be found in all of the analysed drill cores and dominates the stratigraphy of SUP 3, SUP 4 and SUP 6. It was deposited as a suspended sediment load across the floodplain surface by diffuse and channelized flows (Dunne and Aalto, 2013). These overbank fines are accumulated in slack waters of floodplain depressions (Blair and McPherson, 1994). In this facies, coarser layers with varying fine sand content and Ca/Fe and Ca/K values represent fluctuating hydrodynamic conditions during the outflow of fluvial deposits, e.g. during the formation of crevasse splays by breaching of levees of the Supsa (or Rioni) River (North and Davidson, 2012).

– Facies C: semi-terrestrial (peat and organic-rich deposits).

  Facies C is characterized by poor sorting and considerably elevated LOI and K values. The numerous well-preserved macroscopic plant remains and, to some extent, elevated Fe and S values point to anoxic conditions (Turney et al., 2005). The high TOC/N ratios (Joosten et al., 2003) indicate the dominance of cellulosic plants of peat bogs (Meyers and Teranes, 2001). Although there are many layers with high LOI values and plant fragments, real peat layers were only found in drill cores SUP 3, SUP 4 and SUP 10, where LOI rises above 30 %–40 % (AG Boden, 2005).

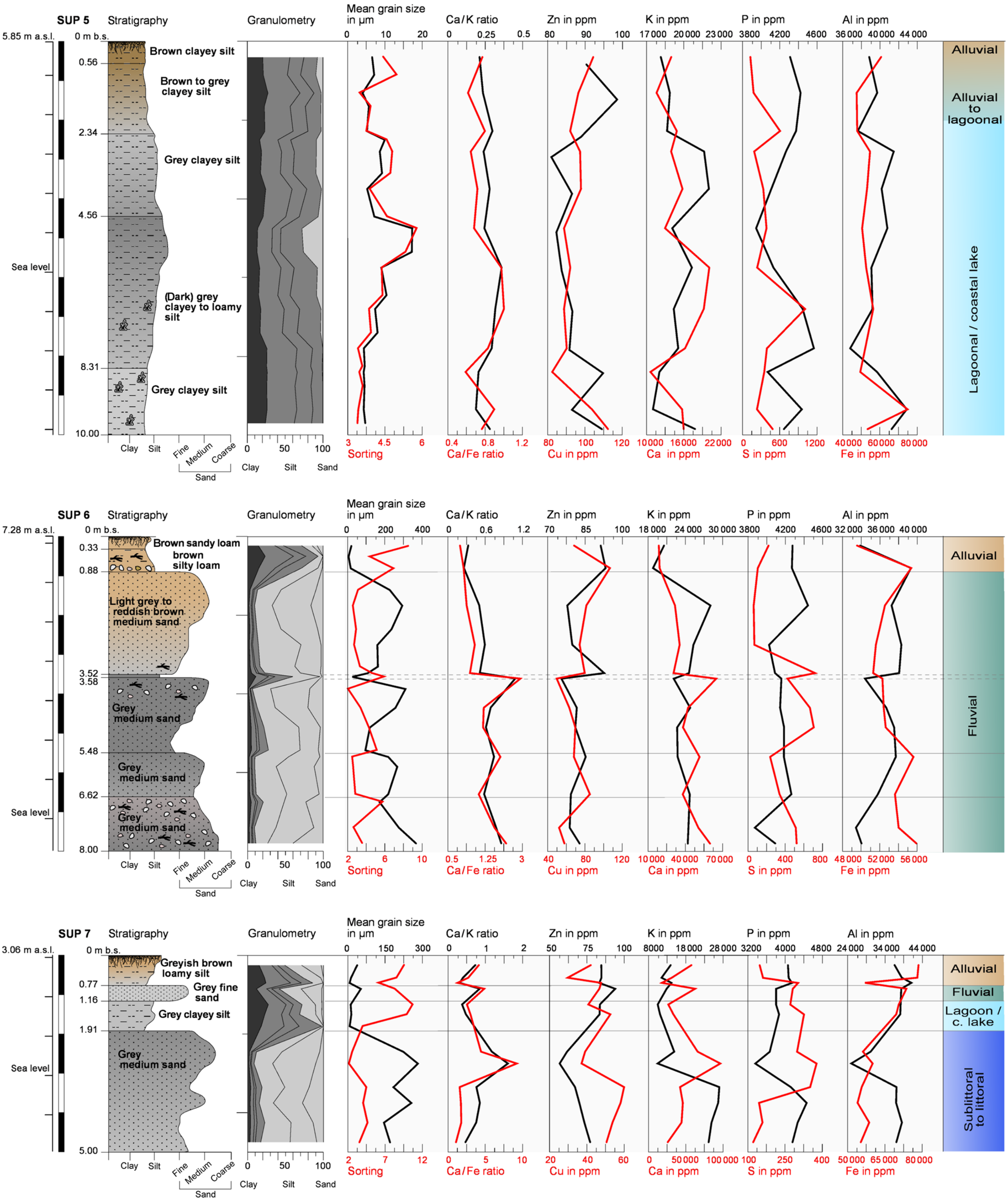


**Figure 8.** Profiles, facies interpretation, granulometry and geochemistry of the sediment cores SUP 5, SUP 6 and SUP 7. The former two are located at southern banks of the Supsa in the vicinity of a smaller tributary, the latter is located close to the coastline south of the recent river mouth (cf. Fig. 2).

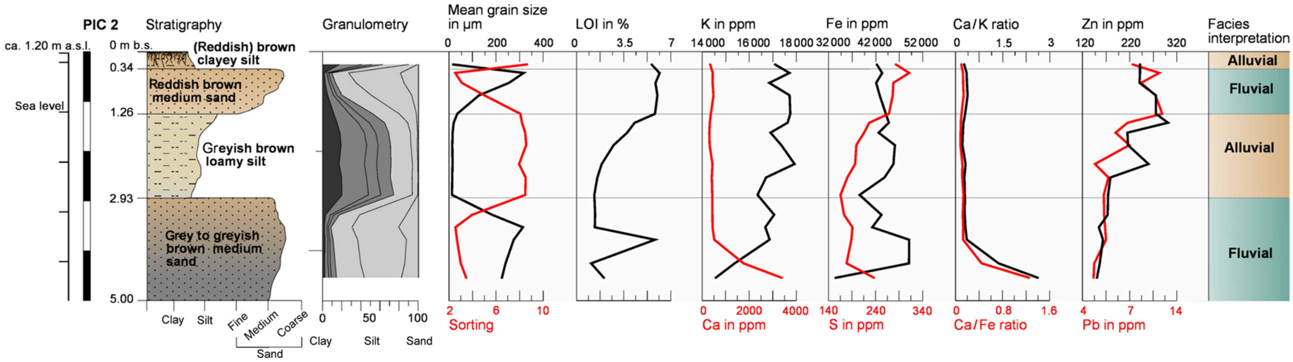


**Figure 9.** Profile, facies interpretation, granulometry, and geochemistry of sediment core PIC 2 from the banks of the Pichora River ca. 7 km north of the Supsa fan (Figs. 2, 3a). The sand-dominated core is strongly influenced by Pichora and Rioni deposits.

– Facies D: lagoonal or coastal lake.

In terms of grain size and geochemistry, the sediments of this facies closely resemble the sediments of Facies B. However, facies D stands out for slightly higher Ca/Fe and Ca/K ratios and lower Si and Ti contents (Cuven et al., 2011; Martin-Puertas et al., 2011). The strong resemblance to Facies B can be explained by the slow transition from a still water environment to deltaic semi-dry conditions. Since there is no microfaunal evidence, it remains challenging to estimate the salinity. Therefore, we cannot differentiate between a lagoon and coastal lake. Although deposited under low-energy conditions, several samples from the lagoonal or coastal lake strata reveal a coarser grain size. The granulometric variations may be explained by changing conditions within the water body, such as the floods from the landward side and storm surges or tsunamis from the seaward side.

– Facies E: fluvial.

A large portion of the sandy deposits in the sediment cores are characterized by moderate to poor sorting and slightly elevated Fe and K values, which hints at an increased input of terrestrial material (Arz et al., 1998; Kujau et al., 2010). They were found in sediment cores SUP 3, SUP 4, SUP 6, SUP 7, SUP 10 and PIC 2 and can be assumed to be of fluvial origin, primarily linked to sediment input by distributary channels of the Supsa. The varying grain size, for instance, can be explained by river avulsion and channel migration, as well as deposition during larger floods in areas close to distributary channels. Though there are some terrestrial markers (e.g. increased Fe and K values; cf. Davies et al., 2015), and, in general, this facies is quite heterogeneous (Dunne and Aalto, 2013), the differentiation from facies A remains challenging. The similar characteristics can be explained by the close proximity of the river mouth to the shoreline. Many littoral deposits derive from the Supsa, are only transported for a short distance along the shore and are then redeposited by the sea. By means of the lower values of roundness and sphericity (Fig. 10c), an approximate separation can be achieved (cf. Kasper-Zubillaga et al., 2005). The lowermost stratum of sediment core SUP 10 shows a slightly better sorting than most other layers of this facies. A certain marine or littoral influence may be assumed; this will be discussed in Sect. 5.3. Furthermore, facies E is differentiated from facies B, although both derive from the rivers and may also have the same origins. However, the fine-grained facies B is deposited as suspended sediment load across the floodplain surface (Dunne and Aalto, 2013), while facies E is limited to areas close to the stream currents where coarser sands are accumulated.

– Facies F: anthropogenic.

This facies occurs only in the sediment core SUP 10 between 6.56 and 7.51 m b.s. The fine-grained matrix closely resembles facies B. However, the large number of burnt clay, ceramic fragments and charcoal indicates a human-induced deposition or, at least, a strong post-depositional human influence. In the other cores, only random finds of burnt clay fragments and charcoal indicate a possible human activity.

## 5.2 Implications for the local relative sea-level evolution

As for reconstructing former sea levels, the most reliable samples of this research derive from peat layers, which are directly related to the back-barrier groundwater table and, thus, to the local relative sea level (Pirazzoli, 1996; Vött, 2007; Brückner et al., 2010; Laermanns et al., 2017a). Regarding the stratigraphical position of most peat layers – they are superimposed by lagoonal or coastal lake deposits – a peat growth in a situation comparable to the swamps and peat bogs of floodplains today and a subsequent drowning in the course of relative sea-level (RSL) rise seems most likely. Although the peat might also derive from riverine en-

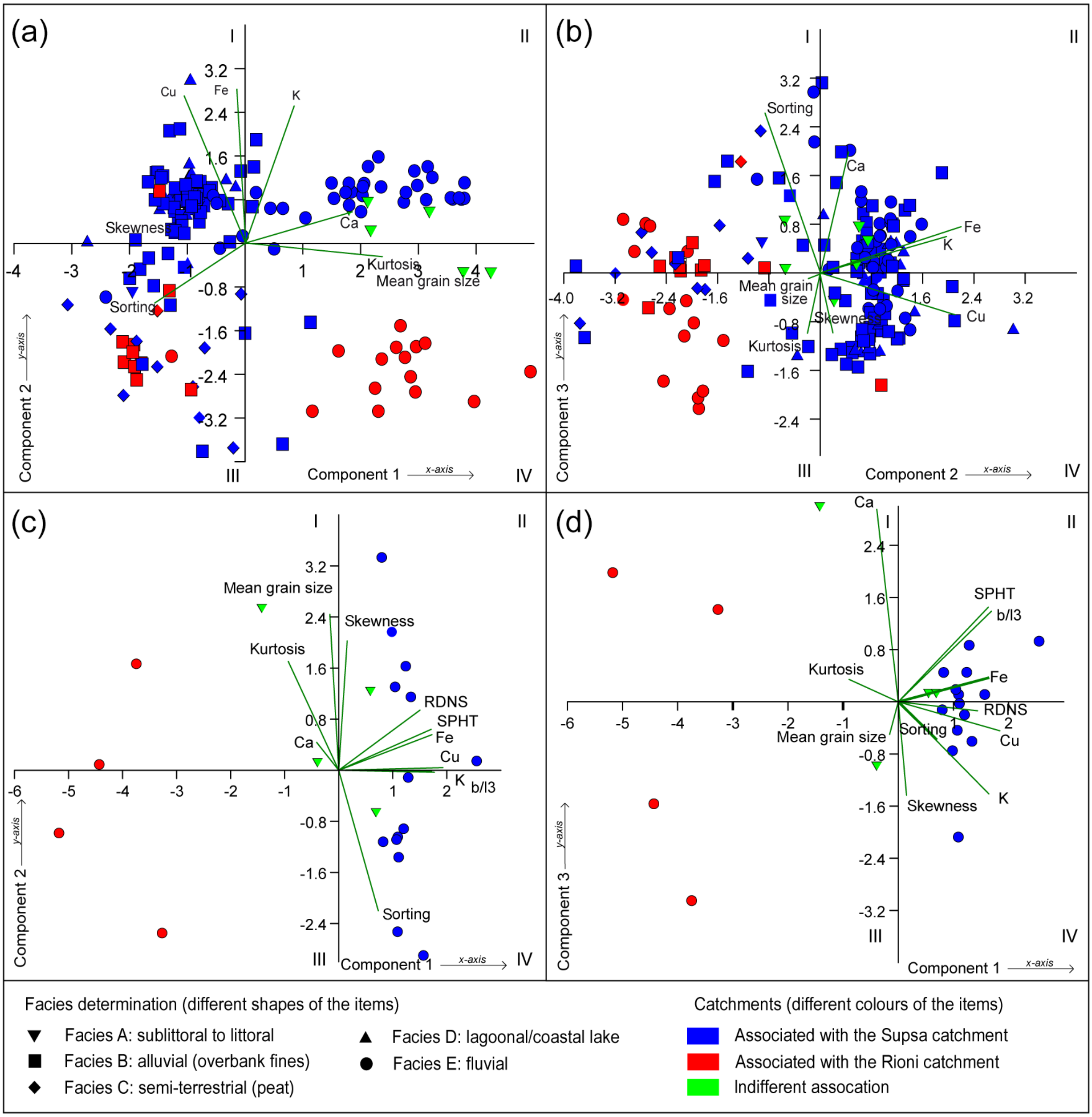


**Figure 10.** Principal component analyses (PCAs) to decipher the origins and depositional modes of the sediments. **(a)** PCA uses the geochemical parameters Ca, Fe, K and Cu, as well as the granulometric parameters mean grain size, sorting, skewness and kurtosis (PC 1: 41.4 %; PC 2: 24.9 %; PC 3: 11.6 %). The axes represent components 1 and 2, while PCA B is based on the components 1 and 3. Panels **(c)** and **(d)** show PCAs on a selection of sandy samples using the parameters of PCA A plus the grain-shape parameters roundness (RNDS), sphericity (SPHR) and elongation ($b/l$) (PC 1: 40.3 %; PC 2: 25.5 %; PC 3: 14.5 %), plotted on the components 1 and 2 (PCA C) and components 1 and 3 (PCA D).

vironments of the Supsa fan, such as oxbows, we assume a comparable groundwater table due to the proximity to coast and floodplain environments and, therefore, an indirect sea-level indicator even if marine layers were not reached. In any case, a vertical error range should be considered for RSL reconstructions based on these peat layers, the extent of which is still debated. Only limited data exist to compare and quantify compaction (Törnquist et al., 2008). While Pirazzoli (1996) calculated a general vertical error bar of ca. 0.5 m, recent publications instead hint to varying rates,

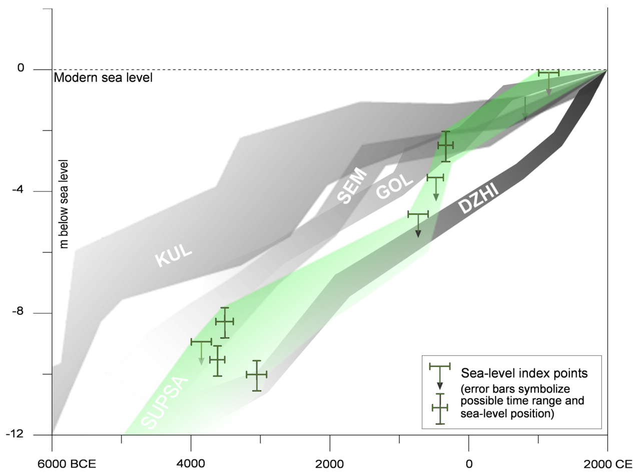


**Figure 11.** Sea-level index points based on radiocarbon dating of the Supsa delta region with the first estimated sea-level trend (SUPSA, in green). An arrow pointing downwards indicates $^{14}$C-dated material from an alluvial context; a cross indicates $^{14}$C-dated paralic peat. For comparison, sea-level curves from the central part of the Colchian plain (KUL) and from sites on the Taman Peninsula (southwestern Russia, northeastern Black Sea: SEM, GOL, DZHI) are also shown. KUL: Kulevi area north of Poti (Laermanns et al., 2017a); SEM: Semebratnee (Brückner et al., 2010); GOL: Golubitskaya (Kelterbaum et al. 2011) and DZHI: Dschiginka (Fouache et al., 2012).

depending on grain size distribution, organic matter and water content (Horton and Shennan, 2009). These factors affect not only the peat layers but also with varying influence the (fine-grained) Holocene sediments below (Bungenstock and Weerts, 2010). From such layers derive the samples that were taken from alluvial facies. These index points serve as indicators for the maximum sea-level position at a certain time. Besides compaction, other mechanisms, such as tectonic subsidence, must be taken into consideration (Bungenstock and Weerts, 2010). Therefore, the sea-level position for each data point can only be seen as a relative indicator (Fig. 11) and must not be transferred to other locations, where different sedimentary and tectonic settings may prevail (Bungenstock and Weerts, 2012).

Although establishing a relative sea-level curve for the Supsa area remains challenging due to the small number of radiocarbon-dated index points of the former sea levels, a local relative sea-level position at about −10 to −8 m can be reconstructed for the time between 4000 and 3500 BCE. Later, during the first millennium BCE, a gradual but relatively steep rise from −5 to −3/−2 m is suggested. During the second millennium CE, the RSL approximates the modern level. We are aware that these $^{14}$C-dated sea-level indicators and the limited knowledge about tectonics, compaction and subsidence rates (Gamkrelidze, 1998; Adamia et al., 2011) include several uncertainties (Brückner et al., 2010). Furthermore, changes in the coastline, e.g. opening or closing of the lagoon (Lake Paliastomi) or dislocations of the palaeochannel of the Supsa, might have had a major influence on the samples' setting as well. However, the comparison with earlier studies of the region reveals at least similar trends. In general, the sea-level evolution in the Supsa area mirrors the investigations between the rivers Rioni and Khobistskali (Laermanns et al., 2017a). However, the steeper RSL rise from the fourth to the first millennium BCE presented there (Fig. 11) might be attributed to the different location closer to the Rioni and the resulting different compaction and subsidence.

There are several similarities between these RSL data from Georgia and those from the Taman Peninsula at the sites of Semebratnee (Brückner et al., 2010), Golubitskaya (Kelterbaum et al., 2011) and Dschiginka (Fouache et al., 2012). Especially when compared to the RSL curves of Semebratnee and Golubitskaya for the last ∼ 3000 years, these curves look much like the one from the Supsa delta region. Before 2000 BCE, our RSL indicators fit well with the curves of Semebratnee and Dschiginka. In general, the RSL curve from the Colchian coast of Georgia resembles those of the Taman Peninsula and others of the Mediterranean quite well (Vött, 2007; Vött et al., 2007; Brückner et al., 2010). As already stated, the differences between the single curves most likely originate from local effects, such as different subsidence and compaction rates as well as local tectonics. It is in any case noteworthy that no hints for significant sea-level oscillations during the mid-Holocene to late Holocene, as proposed by various authors (especially Balabanov, 2007), were detected in our data.

### 5.3 Palaeo-environmental evolution of the Supsa delta area

The sediment record elucidated by the drilling from the Supsa area yields some hints for the landscape change that has taken place since the mid-Holocene. While being a contribution to the complex formation of the fan, the data from individual cores can only provide local information. However, several repetitive patterns were identified, so that the general process pattern can be revealed.

The sands in the lowermost part of sediment core SUP 10 closely resemble, in terms of geochemistry, sorting and grain shape parameters (Figs. 7, 9 and 11), those of sediment core PIC 2, suggesting a littoral relocation of deposits originating from the Rioni; this may explain their differentiation from the Supsa fan deposits. Due to their slightly better sorting and a possible relocation, they were considered not to be deposits of the alluvial fan sensu stricto and were classified as fluvio-marine deposits instead (Fig. 7). Considering the 25-times higher sediment load of the Rioni today (Berkun et al., 2015), this seems quite likely. However, there is no evidence for a progradation of the Supsa fan to any of the investigated sites before 3000 BCE (Fig. 12a). Instead, the growth of paralic (coastal) peat continued, comparable to the Rioni area

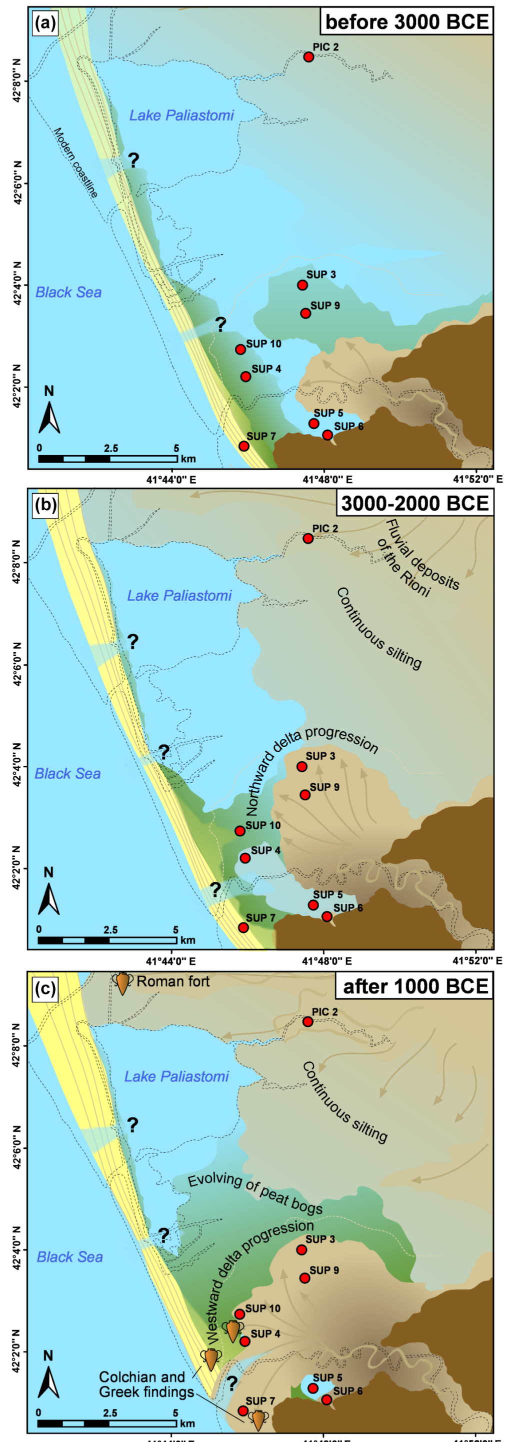


**Figure 12.** Palaeoenvironmental evolution of the Supsa delta region and adjacent areas. The transformation from lagoonal conditions **(a)** to an alluvial plain took place since at least 3000 BCE. The Supsa River built a remarkable fan that prograded first northwards **(b)** and later shifted westwards **(c)**. During the first millennium BCE, Colchians and Greeks settled between the fan and the coastline which is documented by ceramic finds and graves, among other sources.

further north (Laermanns et al., 2017a). This holds true for northern and western parts of the Supsa fan, where at the sites of the sediment cores SUP 3 and SUP 4 peat growth is indicated since the mid-fifth to the mid-fourth millennium BCE (Figs. 5, 6 and 12, Table 1). This indicates that at least since some time before 3000 BCE, a sand spit had evolved by the longshore drift, which separated the research area from the open sea. Since then, lagoonal conditions represented the continuation of the Holocene transgression (Ryan, 2007; Giosan et al., 2009; Fouache et al., 2012). When the growth of the paralic peat could not keep pace with the ongoing rise in sea level, it was covered by fine-grained sediments related either to standing water bodies, such as shallow lagoons or coastal lakes, or to alluvial deposits (for SUP 4, see Fig. 6).

In contrast to this general process, which can be assumed for the entire Colchian plain during the mid-Holocene, the evolution of the Supsa fan forms an outstanding element of the local geomorphology. While in the open plain fine-grained material dominated the stratigraphy, the Supsa River introduced an exceptional share of coarser sediments on the plain, related to the formation of the semi-circular alluvial fan just north of the foothills of the Lesser Caucasus. Its natural shape is clearly visible and protrudes beyond the surrounding plain, although the intensive agricultural use and drainage systems have strongly reshaped the terrain.

Furthermore, the sandy sediment of the Supsa fan can be separated from sandy deposits of the Rioni-dominated floodplain sediments by higher K and Fe contents, a higher grade of sphericity and slightly poorer sorting (Fig. 10), which most likely derived from the different geologic settings and transport distances. The typical interdigitations of alluvial fan-related distributary channels and fine-grained alluvial deposits are reflected in sediment core SUP 3 and in the upper part of SUP 10. The chronostratigraphy of SUP 3 in the northern part of the fan indicates that channel deposits of $\sim 2.40$ m thickness reached that site after the mid-third millennium BCE (Fig. 12b). Similar deposits were found in sediment cores SUP 4 and SUP 10 in the western section of the fan, although of different thickness and grain size; here, these channel deposits accumulated considerably later, i.e. in the first millennium CE (Fig. 12c). A comparable layer recurs in the northern sediment core SUP 3 as well, just above a peat layer, which dates to the second half of the first millennium BCE. These results indicate that the main activity and progradation of the Supsa fan shifted between the second millennium BCE and the first millennium CE from north to west.

Besides this general fan evolution several areas were only marginally affected by the progradation. Sediment core SUP 5, where only fine sediments were found, exemplifies that close to the foothills of the Lesser Caucasus the quiescent depositional conditions of the central Colchian plain have prevailed over a longer period. However, the neighbouring sediment core SUP 6 shows river-dominated deposits from the small tributary valley (Figs. 1, 12).

In contrast, the area west of the Supsa fan, around the modern river mouth, reveals a different stratigraphy. In the sediment core SUP 7 (Fig. 2), coarse sand that is most likely of littoral origin dominates, which is reflected by the relatively high Ca/K and Ca/Fe ratios and the low Fe contents (Davies et al., 2015). However, the lower sections resemble, to a certain extent, the (fluvial) deposits of the sediment cores taken from the Supsa fan, although the main grain size is coarser and comparable to the fluvial deposits of sediment core PIC 2 in the Rioni catchment. Plus, the sand is better sorted, which indicates littoral relocation and reworking through longshore drift (Folk and Ward, 1957; Hesp, 2002). The location in the PCAs in Fig. 10 confirms the different composition and deposition. Conditions gradually change upwards, documenting the increasing influence of the Supsa River at the site of SUP 7.

Considering the sediment successions at all the investigated sites we can assume that already before 3000 BCE the research area was already characterized by standing water bodies, likely related to lagoonal environments with fine-grained sediments, separated from the open sea by a continuously evolving beach barrier complex. Due to continued riverine sediment input, the lagoons silted up (Berkun et al., 2015) and extended peat bogs formed landwards of the beach ridges. Comparable processes are known from the central Kolkheti lowlands (Laermanns et al., 2017a), as well as from areas further south (Connor et al., 2007; de Klerk et al., 2009). The formation of the Supsa fan has advanced at least since the third millennium BCE, first to the north and later to the west.

### 5.4 Human occupation

Traces of human occupation in the research area can be found in sediment core SUP 10, where the entire layer between 7.51 and 6.56 m b.s. is full of brick fragments, ceramic remains and charcoal fragments. Obviously, a human settlement existed at or close to this coring site. The radiocarbon ages from the uppermost part of the layer below and the uppermost part of the archaeological stratum, indicate an occupation between 1893–1701 BCE and 778–990 CE (Table 1). The huge age gap within a rather small vertical distance could have been caused by the removal of sediments at the beginning and during the settlement periods. Although the homogeneity of the brick fragments hints at a same origin, it remains unclear if this settlement is of Colchian, Greek or Roman and/or Byzantine origin. In any case, besides the artefacts, the geochemical evidence, namely the sharp increase in Cu and Zn values, confirms human activities.

The area of the findings is located between the present shoreline in the west and the northern part of the Supsa fan in the east. This suggests that ancient people settled in the vicinity of the swampy but fertile back-barrier areas, which had been built up by alluvial deposits since at least ca. 2000 BCE (in the case of the SUP 10 site). According to the radiocarbon ages, the gradual shift to a floodplain environment was completed between the 9th and the 11th centuries CE (Figs. 5, 6). Such settlement locations are known from different sites along the Colchian coast, e.g. close to Ureki (Miron and Orthmann, 1995; Gamkrelidze, 2012) or near Kobuleti, where the ancient settlement of Ispani was situated in a similar back-barrier position (Connor et al., 2007; de Klerk et al., 2009); it was later covered by sands.

## 6 Conclusions

Based on the analysis of eight sediment cores a significant landscape change could be proven for the Supsa delta fan and the adjacent areas on the Colchian plain. By using a combination of sedimentological and geochemical parameters, different depositional facies were identified. Their succession reflects the palaeoenvironmental evolution of the area over the last 6000 years. The southern part of the Colchian plain underwent a similar morphogenesis as the areas of the Rioni and other rivers further north (Laermanns et al., 2017a). Although the complex setting of the delta forms a challenging geo-archive, several general trends can be assumed.

After the deceleration of the postglacial sea-level rise around 7000 years ago (Brückner et al., 2010), deltaic progradation became the dominant landscape-forming coastal process (Anthony et al., 2014). In the research area, a beach barrier complex evolved, which led to the formation of extended lagoons. Thus, the area was separated from the open sea by longshore-transported sediments. The Supsa River debouched into this vast lagoon and later floodplain environment. It has formed a remarkable alluvial fan at least since the third millennium BCE. This fan stands out with its elevated relief and a sediment stratigraphy that can well be differentiated from the Rioni-dominated deposits of the Colchian plain by grain-shape characteristics and geochemical parameters. The beach barrier complex first developed with material that had been eroded from cliff sections to the south and later also by sediments that originated from the Rioni and the Supsa rivers.

The indicated sea-level evolution must be considered with caution due to limited information about subsidence and compaction rates, the complex delta setting, and only a few index points. Nevertheless, an overall continuous rise is suggested, and the sea-level trend resembles the RSL curves from the Taman Peninsula (Fouache et al., 2012) and the central parts of the Colchian plain (Laermanns et al., 2017a). However, considering the mentioned challenges, our results should rather be taken as an indication for the sea-level trend, not as a sea-level curve.

**Data availability.** All data presented in this study were collected, analysed, and interpreted by the authors and are published here. If single amounts of concentrations are not given in tables, they are shown in the graphs (e.g. Fig. 5) so values are publicly accessible.

For further information please see the dissertation of Hannes Laermanns which is accessible at https://kups.ub.uni-koeln.de/9129/ (last access: 26 June 2019).

**Author contributions.** All authors and co-authors have approved the final version of the paper and agreed to submission. All authors and co-authors substantially contributed to the presented research. HL, DK, GK, LN, and ME contributed to fieldwork and lab work. HL designed the study, and HL, SMM, DK, SO, and HB interpreted the data. Finally, HL wrote the manuscript with contributions of GK. The paper was amended and corrected by all co-authors.

**Competing interests.** The authors declare that they have no conflict of interest.

**Acknowledgements.** Hannes Laermanns gratefully acknowledges the funding of his PhD project by the Heinrich Böll Foundation and by the Graduate School of Geosciences (GSGS) of the University of Cologne. He also thanks the Albertus Magnus Graduate Center (University of Cologne) for funding his research stay at the Université de Franche-Comté in Besançon. We thank the colleagues and students from the Ilia State University and Javakishvili University at Tbilisi, who were involved in fieldwork in 2013 and 2015, for their scientific, administrative and logistical help, as well as for providing accommodation at the Grigoleti Marine Research Centre of the Ilia State University during fieldwork.

**Financial support.** This research has been supported by the Heinrich Böll Foundation (grant no. P106171 awarded to Hannes Laermanns).

## References

Adamia, S., Zakariadze, G., Chkhotua, T., Sadradze, N., Tsereteli, N., Chabukiani, A., and Gventsadze, A.: Geology of the Caucasus: A Review, Turkish Journal of Earth Sciences, 20, 489–544, 2011.

AG Boden: Bodenkundliche Kartieranleitung, Hannover, Germany, 2005.

Anthony, E. J., Marriner, N., and Morhange, C.: Human influence and the changing geomorphology of Mediterranean deltas and coasts over the last 6000 years: From progradation to destruction phase?, Earth-Sci. Rev., 139, 336–361, 2014.

Arnaud-Fassetta, G., Carre, M.-B., Marocco, R., Maselli Scotti, F., Pugliese, N., Zaccaria, C., Bandelli, A., Bresson, V., Manzoni, G., Montenegro, M.E., Morhange, C., Pipan, M., Prizzon, A., and Siché, I.: The site of Aquileia (northeastern Italy): example of fluvial geoarchaeology in a Mediterranean deltaic plain, Géomorphologie, 4, 227–246, 2003.

Arslanov, K. A., Dolukhanov, P. M., and Gei, N. A.: Climate, Black Sea levels and human settlements in Caucasus Littoral 50 000–9000 BP, Quaternary Int., 167–168, 121–127, 2007.

Arz, H. W., Pätzold, J., and Wefer, G.: Correlated millennial-scale changes in surface hydrography and terrigenous sediment yield inferred from last-glacial marine deposits off Brazil, Quaternary Res., 50, 157–166, 1998.

Avdeev, B. and Niemi, N. A.: Rapid Pliocene exhumation of the central Greater Caucasus constrained by low-temperature thermochronometry, Tectonics, 30, 1–16, 2011.

Balabanov, I. P.: Holocene sea-level changes of the Black Sea, in: The Black Sea Flood question: Changes in coastline, climate and human settlement, edited by: Yanko-Hombach, V., Gilbert, A. S., Panin, N., and Dolukhanov, P., Springer, Dordrecht, the Netherlands, 711–730, 2007.

Barsch, H., Billwitz, K., and Bork, H.: Arbeitsmethoden in der Physiogeographie und Geoökologie, Klett-Perthes, Gotha, Germany, 2000.

Bazhenov, M. L. and Burtman, V. S.: Eocene paleomagnetism of the Caucasus (southwest Georgia): Oroclinal bending in the Arabian syntaxis, Tectonophysics, 344, 247–259, 2002.

Berkun, M., Aras, E., and Akdemir, U.: Water runoff, sediment transport and related impacts in the southeastern Black Sea rivers, Environ. Eng. Manag. J., 14, 781–791, 2015.

Blaauw, M. and Christen, J. C.: Flexible paleoclimate age-depth models using an autoregressive gamma process, Bayesian Analysis, 6, 457–474, 2011.

Blair, T. C. and McPherson, J. G.: Alluvial fans and their natural distinction from rivers based on morphology, hydraulic processes, sedimentary processes, and facies assemblages, J. Sediment. Res., A64, 450–489, 1994.

Blott, S. J. and Pye, K.: Technical communication, GRADISTAT: A grain size distribution and statistics package for the analysis of unconsolidated sediments, Earth Surf. Processes Landf., 26, 1237–1248, 2001.

Bolikhovskaya, N. S., Porotov, A. V., Richards, K., Kaitamba, M. D., Faustov, S. S., and Korotaev, V. N.: Detailed reconstructions of Holocene climate and environmental changes in the Taman Peninsula (Kuban River delta region) and their correlation with rapid sea-level fluctuations of the Black Sea, Quaternary Int., 465, 22–36, 2018.

Borůvka, L., Vacek, O., and Jehlička, J.: Principal component analysis as a tool to indicate the origin of potentially toxic elements in soils, Geoderma, 128, 289–300, 2005.

Box, E. O., Fujiwara, K., Nakhutsrishvili, G., Zazanashvili, N., Liebermann, R. J., and Miyawaki, A.: Vegetation and landscape of Georgia (Caucasus) as a basis for landscape restoration, Bulletin of the Institute of Environmental Science and Technology, Yokohama National University, 26, 69–102, 2000.

Braund, D.: Georgia in Antiquity: a history of Colchis and Transcaucasian Iberia, 550 BC–AD 562, Oxford University Press, 359 pp., Oxford, UK, 1994.

Brückner, H., Müllenhoff, M., Handl, M., and van der Borg, K.: Holocene landscape evolution of the Büyük Menderes alluvial plain in the environs of Myous and Priene (Western Anatolia, Turkey), Ann. Geomorphology, 127, 47–65, 2002.

Brückner, H., Kelterbaum, D., Marunchak, O., Porotov, A. and Vött, A.: The Holocene sea level story since 7500 BP – lessons from the Eastern Mediterranean, the Black and the Azov Seas, Quaternary Int., 225, 160–179, 2010.

Brückner, H., Herda, A., Müllenhoff, M., Rabbel, W., and Stümpel, H.: On the Lion Harbour and other harbours in Miletos: recent historical, archaeological, sedimentological, and geophysical research, Proceedings of the Danish Institute at Athens, 7, 49–103, Aarhus, Denmark, 2014.

Brückner, H., Herda, A., Kerschner, M., Müllenhoff, M., and Stock, F.: Life cycle of estuarine islands – From the formation to the landlocking of former islands in the environs of Miletos and Ephesos in western Asia Minor (Turkey), J. Archaeol. Sci. Reports, 12, 876–894, 2017.

Bungenstock, F. and Weerts, H. J. T.: The high-resolution Holocene sea-level curve for Northwest Germany: global signals, local effects or data-artefacts?, Int. J. Earth Sci., 99, 1687–1706, 2010.

Bungenstock, F. and Weerts, H. J. T.: Holocene relative sea-level curves for the German North Sea coast, Int. J. Earth Sci., 101, 1083–1090, 2012.

Carozza, J.-M., Puig, C., Odiot, T., Valette, P., and Passarius, V.: Geoarchaeological insight in the Tech basin (Roussillon, Gulf of Lion, Western Mediterranean), Quaternary Int., 266, 94–104, 2011.

Connor, S., Thomas, I., and Kvavadze, E.: A 5600-yr history of changing vegetation, sea levels and human impacts from the Black Sea coast of Georgia, The Holocene, 17, 25–37, 2007.

Cuven, S., Francus, P., and Lamoureux, S.: Mid to Late Holocene hydroclimatic and geochemical records from the varved sediments of East Lake, Cape Bounty, Canadian High Arctic, Quaternary Sci. Rev., 30, 2651–2665, 2011.

Davies, S. J., Lamb, H. F., and Roberts, S. J.: Micro-XRF Core Scanning in Palaeolimnology: Recent Developments, in: Micro-XRF Studies of Sediment Cores, edited by: Croudace, I. W. and Rothwell, R. G., Springer Nature, Switzerland, 189–226, 2015.

De Klerk, P., Haberl, A., Kaffke, A., Krebs, M., Matchutadze, I., Minke, M., Schulz, J., and Joosten, H.: Vegetation history and environmental development since ca 6000 cal yr BP in and around Ispani 2 (Kolkheti lowlands, Georgia), Quaternary Sci. Rev., 28, 890–910, 2009.

Delile, H., Mazzini, I. Blichert-Toft, J., Arnaud-Godet, F., Salomon, F., and Albarède, F.: Geochemical investigation of a sediment core from the Trajan basin at Portus, the harbor of ancient Rome, Quaternary Sci. Rev., 87, 34–45, 2014.

Denk, T., Frotzler, N., and Davitashvili, N.: Vegetational patterns and distribution of relict taxa in humid temperate forests and wetlands of Georgia (Transcaucasia), Biol. J. Linn. Soc., 72, 287–332, 2000.

Dhont, D. and Chorowicz, J.: Review of the neotectonics of the Eastern Turkish-Armenian Plateau by geomorphic analysis of digital elevation model imagery, Int. J. Earth Sci., 95, 34–49, 2006.

Dingler, J. R.: Beach processes, in: Encyclopedia of Coastal Sciences, edited by: Schwartz, M. L., Springer, Dordrecht, the Netherlands, 161–168, 2005.

Dirix, K., Muchez, P., Degryse, P., and Poblome, J.: Spatial distribution of elemental enrichments around archaeological sites: Insights from the ancient city of Sagalassos in Southwest Turkey, Geoarchaeology, 31, 34–48, 2015.

Dung, T. T. T., Cappuyns, V., Swennen, R., and Phung, N. K.: From geochemical background determination to pollution assessment of heavy metals in sediments and soils, Reviews in Environmental Science and Biotechnology, 12, 335–353, 2013.

Dunne, T. and Aalto, R. E.: Larger River Floodplains, in: Fluvial Geomorphology, edited by: Wohl, E., 9, 645–678, 2013.

Eamer, J. B. R., Shugar, D. H., Walker, I. J., Lian, O. B., and Neudorf, C. M.: Distinguishing depositional setting for sandy deposits in coastal landscapes using grain shape, J. Sediment. Res., 87, 1–11, 2017.

Eppelbaum, L. and Khesin, B.: Geophysical Studies in the Caucasus. Lecture Notes in Earth System Sciences, Springer, Berlin, Heidelberg, Germany, 2012.

Erb-Satullo, N., Gilmour, B., and Khakhutaishvili, N.: Late Bronze and Early Iron Age copper smelting technologies in the South Caucasus: the view from ancient Colchis c. 1500–600 BC, J. Archaeol. Sci., 49, 147–159, 2014.

Erginal, A. E., Ekinci, Y. L., Demirci, A., Bozcu, M., Ozturk, M. Z., Avciglu, M., and Oztura, E.: First record of beachrock on Black Sea coast of Turkey: Implications for Late Holocene sea-level fluctuations, Sediment. Geol., 294, 294–302, 2013.

Flaux, C., El-Assal, M., Shaalan, C., Marriner, N., Morhange, C., Torab, M., Goiran, J. P., and Empereur, J. Y.: Geoarchaeology of Portus Mareoticus: Ancient Alexandria's lake harbour (Nile Delta, Egypt), J. Archaeol. Sci., 13, 669–681, 2017.

Folk, R. L. and Ward, W. C.: Brazos river bar: A study in the significance of grain size parameters, J. Sediment. Petrol., 27, 3–26, 1957.

Forte, A., Cowgill, E., and Whipple, K. X.: Transition from a singly vergent to doubly vergent wedge in a young orogeny: The Greater Caucasus, Tectonics, 33, 2077–2101, 2014.

Fouache, E., Kelterbaum, D., Brückner, H., Lericolais, G., Porotov, A., and Dikarev, V.: The Late Holocene evolution of the Black Sea – a critical view on the so-called Phanagorian regression, Quaternary Int., 266, 162–174, 2012.

Gamkrelidze, G.: Stress vector orientations and movement of the Earth's crust of the territory of Georgia on the neotectonic stage, Bulletin of the Georgian Academy of Science, 158, 284–287, 1998.

Gamkrelidze, G.: Researches in the Iberia-Colchology (History and Archaeology of ancient Georgia), Georgian National Museum Tbilisi, Georgia, 2012.

Giaime, M., Marriner, N., and Morhange, C.: Evolution of ancient harbours in deltaic contexts: A geoarchaeological typology, Earth-Sci. Rev., 191, 141–167, 2019.

Giosan, L., Donnelly, J. P., Filip, F., Ovejanu, I., Vespremeanu-Stroe, A., Vespremeanu, E., and Duller, G. A. T.: Young Danube delta documents stable Black Sea level since the middle Holocene: Morphodynamic, paleogeographic, and archaeological implications, Geology, 34, 757–760, 2006.

Giosan, L., Filip, F., and Constantinescu, S.: Was the Black Sea catastrophically flooded in the early Holocene?, Quaternary Sci. Rev., 28, 1–6, 2009.

Goiran, J. P., Salomon, F., Mazzini, I., Bravard, J. P., Pleuger, E., Vittori, C., Boetto, G., Christiansen, J., Arnaud, P., Pellegrino, A., Pepe, C., and Sadori, L.: Geoarchaeology confirms location of the ancient harbour basin of Ostia (Italy), J. Archaeol. Sci., 41, 389–398, 2014.

Gugushvili, V., Popkhadze, N., Beridze, T., and Khutsishvili, S.: Sources of base, precious and rare metals during the Tethyan Phanerozoic evolution of the Caucasus and Pontides, in: Proceedings of the XIX CBGA Congress, Thessaloniki, School of Geology, Aristotle University of Thessaloniki, Special vol. 100, 333–341, 2010.

Haghani, S., Leroy, S., Khdir, S., Kabiri, K., Beni, A. N., and Lahijani, H. A. K.: An early 'Little Ice Age' brackish water invasion along the south coast of the Caspian Sea (sediment of Langarud wetland) and its wider impacts on environment and people, The Holocene, 26, 3–16, 2015.

Hammer, Ø., Harper, D. A. T., and Ryan, P. D.: PAST: Paleontological Statistics Software Package for Education and Data Analysis, Palaeontol. Electron., 4, 9–11, 2001.

Heiri, O., Lotter, A., and Lemcke, G.: Loss on ignition as a method for estimating organic and carbonate content in sediments: reproducibility and comparability of results, J. Paleolimnol., 25, 101–110, 2001.

Herda, A., Brückner, H., Müllenhoff, M., and Knipping, M.: From the Gulf of Latmos to Lake Bafa: On the history, geoarchaeology, and palynology of the lower Maeander Valley at the foot of the Latmos Mountains, Hesperia, The Journal of the American School of Classical Studies at Athens, 88, 1–86, 2019.

Hesp, P.: Foredunes and blowouts: initiation, geomorphology and dynamics, Geomorphology, 48, 245–268, 2002.

Hijmans, R. J., Cameron, S. E., Parra, J. L., Jones, P. G., and Jarvis, A.: Very high resolution interpolated climate surface for global land areas, Int. J. Climatol., 25, 1965–1978, 2005.

Horton, B. P. and Shennan, I.: Compaction of Holocene strata and the implications for relative sea-level change on the east coast of England, Geology, 37, 1083–1086, 2009.

Janelidze, Z. and Tatashidze, Z.: Palaeogeographical interpretation of archaeological site of swamps of the Black Sea Coast of Georgia, Bulletin of the Georgian National Academy of Sciences, 4, 159–161, 2010.

Jaoshvili, S.: The rivers of the Black Sea, EEA Technical report 71, European Environmental Agency, Copenhagen, 2002.

Joosten, H., Kaffke, A., and Matchutadze, I.: The mires of the Kolkheti lowlands (Georgia), IMCG Newsletter, 2003/3, 19–23, 2003.

Kasper-Zubillaga, J. J., Dickinson, W. W., Carranza-Edwards, A., and Hronelas-Orozco, Y.: Petrography of quartz grains in beach and dune sands of Northland, North Island, New Zealand, New Zealand Journal of Geology and Geophysics, 48, 649–660, 2005.

Kelterbaum, D., Brückner, H., Porotov, A., Schlotzhauer, U., and Zhuravlev, D.: Geoarchaeology of Taman Peninsula (SW Russia) – the example of the ancient Greek settlement of Golubitskaya 2, Die Erde, 142, 235–258, 2011.

Kelterbaum, D., Brückner, H., Dikarev, V., Gerhard, S., Pint, A., Porotov, A., and Zin'ko, V.: Palaeogeographic changes at Lake Chokrak on the Kerch Peninsula, Ukraine, during the Mid- and Late-Holocene, Geoarchaeology, 27, 206–219, 2012.

Khakhutaishvili, D. A.: The Manufacture of Iron in Ancient Colchis, Archaeopress, Oxford, UK, 2009.

Khakhutaishvili, N.: An ancient Colchian center of iron metallurgy at Chorokhi: excavations in 2001, in: Archaeology in Southern Caucasus: Perspectives from Georgia, edited by: Sagona, A. and Abramashvili, M., Peters, Leuven, Belgium, 397–405, 2008.

Korotaev, G., Oguz, T., Nikiforov, A., and Koblinsky, C.: Seasonal, interannual, and mesoscale variability of the Black Sea upper layer circulation derived from altimeter data, J. Geophys. Res., 108, 19.1–19.15, 2003.

Kraft, J. C., Rapp, G., Kayan, İ., and Luce, J. V.: Harbor areas at ancient Troy: Sedimentology and geomorphology complement Homer's Iliad, Geology, 31, 163–166, 2003.

Kujau, A., Nürnberg, D., Zielhofer, C., Bahr, A., and Röhl, U.: Mississippi River discharge over the last ∼ 560 000 years – indications from X-ray fluorescence core-scanning, Palaeogeogr. Palaeocl., 298, 311–318, 2010.

Laermanns, H., Kelterbaum, D., May, S. M., Elashvili, M., Opitz, S., Hülle, D., Rölkens, Verheul, J., Riedesel, S., and Brückner, H.: Mid- to Late Holocene landscape changes in the Rioni Delta area (Kolkheti lowlands, W Georgia), Quaternary Int., 465, 85–98, 2017a.

Laermanns, H., Kirkitadze, G., May, S. M., Kelterbaum, D., Opitz, S., Heisterkamp, A., Basilaia, G., Elashvili, M., and Brückner, H.: Bronze Age settlement mounds on the Colchian plain at the Black Sea coast of Georgia – a geoarchaeological perspective, Geoarchaeology, 33, 453–469, 2017b.

Lario, J., Zazo, C., Goy, J. L., Dabrio, C. J., Borja, F., Silva, P. G., Sierro, F., González, A., Soler, V., and Yill, E.: Changes in the sedimentation trends in SW Iberia Holocene estuaries (Spain), Quaternary Int., 93–94, 171–176, 2002.

Lordkipanidze, D., Jashashvili, T., Vekua, A., Ponce de León, M., Zollikofer, C., Rightmire, G. P., Pontzer, H., Ferring, R., Oms, O., Tappen, M., Bukhsianidze, M., Agusti, J., Kahlke, R., Kiladze, G., Martinez-Navarro, B., Mouskhelishvili, A., Nioradze, M., and Rook, L.: Postcranial evidence from early Homo from Dmanisi, Georgia, Nature, 449, 305–310, 2007.

Lordkipanidze, O.: Das alte Kolchis und seine Beziehungen zur griechischen Welt vom 6. zum 4. Jh. v. Chr., in: XENIA – Konstanzer Althistorische Vorträge und Forschungen, 14, edited by: Schuller, W., Konstanz, Germany, 49 pp., 1985.

Lordkipanidze, O.: Archäologie in Georgien. Von der Altsteinzeit zum Mittelalter, VCH Verlagsgesellschaft mbH, Weinheim, Germany, 1991.

Marriner, N. and Morhange, C.: Geoscience of ancient Mediterranean harbours, Earth-Sci. Rev., 80, 137–194, 2007.

Marriner, N., Morhange, C., and Goiran, J. P.: Coastal and ancient harbour geoarchaeology, Geology Today, 26, 21–27, 2010.

Martin-Puertas, C., Valero-Garcés, B., Mata, M. P., Moreno, A., Giralt, S., Martinez-Ruiz, F., and Jimenéz-Espejo, F.: Geochemical processes in a Mediterranean lake: a high-resolution study of the last 4,000 years in Zoñar Lake, southern Spain, J. Paleolimnol., 46, 405–421, 2011.

Meyers, P. A. and Teranes, J. L.: Sediment organic matter, in: Tracking Environmental Change Using Lake Sediments, edited by: Last, W. M. and Smol, J. P., Kluwer Academic Publishers, Dordrecht, the Netherlands, 239–269, 2001.

Miron, A. and Orthmann, W.: Unterwegs zum Goldenen Vlies – archäologische Funde aus Georgien, Museum für Vor- und Frühgeschichte Saarbrücken, Saarbrücken, 1995.

Mitchell, J. and Westaway, R.: Chronology of Neogene and Quaternary uplift and magmatism in the Caucasus: constraints from K-Ar dating of volcanism in Armenia, Tectonophysics, 304, 157–186, 1999.

Nikolaishvili, D. A., Elizbarashvili, N., and Meladze, G. G.: Evaluation of degree of landscape's anthropogenic transformation (landscapes of Georgia), Procedia – Social and Behavioral Sciences, 19, 547–555, 2015.

North, C. P. and Davidson, S. K.: Unconfined alluvial flow processes: recognition and interpretation of their deposits, and the significance for palaeogeographic reconstruction, Earth-Sci. Rev., 111, 199–223, 2012.

Okrostsvaridze, A., Gagnidze, N., and Akimidze, K.: A modern field investigation of the mythical "gold sands" of the ancient Colchis Kingdom and "Golden Fleece" phenomena, Quaternary Int., 409, 61–69, 2016.

Oonk, S., Slomp, C. P., and Huisman, D. J.: Geochemistry as an aid in archaeological prospection and site interpretation: Current issues and research directions, Archaeol. Prospect., 16, 35–51, 2009.

Pavlopoulos, K., Karkanas, P., Triantaphyllou, M., Karymbalis, E., Tsourou, T., and Palyvos, N.: Paleoenvironmental evolution of the coastal plain of Marathon, Greece, during the Late Holocene: Depositional environment, climate, and sea level changes, J. Coast. Res., 22, 424–438, 2006.

Pirazzoli, P. A.: Sea-level Changes. The Last 20,000 Years, Wiley and Sons, Chichester, UK, 1996.

Rayfield, D.: Edge of Empires: A History of Georgia, Reaktion Books, London, UK, 2013.

Reilinger, R., McClusky, S., Vernant, P., Lawrence, S., Ergintav, S., Cakmak, R., Ozener, H., Kadirov, F., Guliev, I., Stepanyan, R., Nadariya, M., Hahubia, G., Mahmoud, S., Sakr, K., Arrajehi, A., Paradissis, D., Al-Aydrus, A., Prilepin, M., Guseva, T., Evren, E., Dmitrotsa, A., Filikov, S. V., Gomez, F., Al-Ghazzi, R., and Karam, G.: GPS constraints on continental deformation in the Africa-Arabia-Eurasia continental collision zone and implications for the dynamics of plate interactions, J. Geophys. Res., 111, 405–411, 2006.

Reimer, P. J., Bard, E., Bayliss, A., Beck, J. W., Blackwell, P. G., Bronk Ramsey, C., Buck, C. E., Cheng, H., Edwards, R. L., Friedrich, M., Grootes, P. M., Guilderson, T. P., Haflidason, H., Hajdas, I., Hatté, C., Heaton, T. J., Hogg, A. G., Hughen, K. A., Kaiser, K. F., Kromer, B., Manning, S. W., Niu, M., Reimer, R. W., Richards, D. A., Scott, E. M., Southon, J. R., Turney, C., and van der Plicht, J.: InterCal13 and Marine 13 radiocarbon age calibration curves 0–50,000 years cal BP, Radiocarbon, 55, 1869–1887, 2013.

Ryan, W. B. F.: Status of the Black Sea Flood Hypothesis, in: The Black Sea Flood Question, edited by: Yanko-Hombach, V., Gilbert, A. S., Panin, N., and Dolukhanov, P. M., Springer, Dordrecht, the Netherlands, 63-88, 2007.

Sadzradze, V., Davlianidze, R., and Murvanidze, B.: Archaeological investigation of Supsa terminal and adjacent area, Pipeline Archaeology, 1, 104–115, 1999.

Sens, U.: Kulturkontakt an der östlichen Schwarzmeerküste, in: Schriften des Zentrums für Archäologie und Kulturgeschichte des Schwarzmeerraumes, 15, edited by: Bertemes, F. and Furtwängler, A., Beier & Beran, Stuttgart, Germany, 2009.

Sosson, M., Rolland, Y., Müller, C., Danelian, T., Mekonyan, R., Kekelia, S., Adamia, S., Babazadeh, V., Kangarli, T., Avagyan, A., Galoyan, G., and Mosar, J.: Subduction, obduction and collision in the Lesser Caucasus (Armenia, Azerbaijan, Georgia) – new insights, Geological Society, London Special Publications, 340, 329–352, 2010.

Stock, F., Pint, A., Horejs, B., Ladstätter, S., and Brückner, H.: In search of the harbours – new evidence of Late Roman and Byzantine harbours of Ephesus, Quaternary Int., 312, 57–69, 2013.

Stock, F., Kerschner, M., Kraft, J. C., Pint, A., Frenzel, P., and Brückner, H.: The palaeogeographies of Ephesos (Turkey), its harbours, and the Artemision – a geoarchaeological reconstruction for the timespan 1500–300 BC, Ann. Geomorphol., 58, 33–66, 2014.

Stock, F., Knipping, M., Pint, A., Ladstätter, S., Delile, H., Heiss, A., Laermanns, H., Mitchell, P., Ployer, R., Steskal, M., Thanheiser, U., Urz, R., Wennrich, V., and Brückner, H.: Human impact on Holocene sediment dynamics in the Eastern Mediterranean – the example of the Roman harbour of Ephesus, Earth Surf. Processes Landf., 41, 980–996, 2016.

Stuiver, M. and Reimer, P.: Extended $^{14}$C data base and revised Calib 3.0 $^{14}$C age calibration program, Radiocarbon, 35, 215–230, 1993.

Törnqvist, T. E., Wallace, D. J., Storms, J. E. A., Wallinga, J., Dam, R. L., Blaauw, M., Derksen, M. S., Klerks, C. J. W., Meijneken, C., and Snijders, E. M. A.: Mississippi Delta subsidence primarily caused by compaction of Holocene strata, Nat. Geosci., 1, 173–176, 2008.

Turney, C., Canti, M., Branch, N., and Clark, P.: Environmental archaeology: theoretical and practical approaches, Routledge, London, UK, 2005.

Vött, A.: Relative sea level changes and regional tectonic evolution of seven coastal areas in NW Greece since the mid-Holocene, Quaternary Sci. Rev., 26, 894–919, 2007.

Vött, A., Schriever, A., Handl, M., and Brückner, H.: Holocene palaeogeographies of the central Acheloos River delta (NW Greece) in the vicinity of the ancient seaport Oiniadai, Geodinamica Acta, 20, 241–256, 2007.

Yılmaz, A., Adamia, S., and Yılmaz, H.: Comparisons of the suture zones along a geotraverse from the Scythian Platform to the Arabian Platform, Geosci. Frontiers, 5, 855–875, 2013.

Zhang, C. and Mischke, S.: A Late glacial and Holocene lake record from the Nianbaoyeze Mountains and inferences of lake, glacier and climate evolution on the eastern Tibetan Plateau. Quaternary Sci. Rev., 28, 1970–1983, 2009.

Zhang, C., Wang, L., Li, G., Dong, S., Yang, J., and Wang, X.: Grain size effect on multi-element concentrations in sediments from the intertidal flats of Bohai Bay, China, Appl. Geochem., 17, 59–68, 2002.

E&G Quaternary Sci. J., 68, 141–164, 2019
https://doi.org/10.5194/egqsj-68-141-2019


Open Access E&G Quaternary Science Journal

Research article

# The formation of Middle and Upper Pleistocene terraces (*Übergangsterrassen* and *Hochterrassen*) in the Bavarian Alpine Foreland – new numeric dating results (ESR, OSL, $^{14}$C) and gastropod fauna analysis

**Gerhard Schellmann**[1], **Patrick Schielein**[1], **Wolfgang Rähle**[2], **and Christoph Burow**[3]

[1]Department of Physical Geography and Landscape Studies, University of Bamberg, Bamberg, Germany
[2]Engelfriedshalde 102, 72076 Tübingen, Germany
[3]Institute of Geography, University of Cologne, Cologne, Germany

**Correspondence:** Gerhard Schellmann (gerhard.schellmann@uni-bamberg.de)

**Relevant dates:** Received: 27 March 2019 – Accepted: 24 June 2019 – Published: 25 July 2019

**How to cite:** Schellmann, G., Schielein, P., Rähle, W., and Burow, C.: The formation of Middle and Upper Pleistocene terraces (*Übergangsterrassen* and *Hochterrassen*) in the Bavarian Alpine Foreland – new numeric dating results (ESR, OSL, $^{14}$C) and gastropod fauna analysis, E&G Quaternary Sci. J., 68, 141–164, https://doi.org/10.5194/egqsj-68-141-2019, 2019.

**Abstract:** Until now, reliable chronological classifications based on numerical ages for many Pleistocene fluvial deposits in the Alpine Foreland were rare. In this study, new numeric data (ESR, OSL, $^{14}$C) from Middle and Upper (Late) Pleistocene *Hochterrassen* (high terraces) and *Übergangsterrassen* (transitional terraces) in the Bavarian Alpine Foreland are presented. The dating results imply that the *Hochterrassen* gravel sensu stricto were deposited during the penultimate glacial (MIS 6, Rissian), and that underlying older gravel accumulation are predominantly of penultimate interglacial (MIS 7, Riss–Riss interglacial) age. In some areas of the *Hochterrassen* in the Danube valley south of Regensburg (interglacial *Hartinger Schichten*, Harting layers), and in some areas of the *Rainer Hochterrasse* (basal gravel unit I), *Hochterrassen* gravels are underlain by much older interglacial gravel deposits. These interglacial basal gravel deposits illustrate that the downcutting of these valleys far away from areas of Pleistocene foreland glaciations happened predominantly during warm-temperate interglacial or late-glacial periods. One last interglacial (MIS 5e, Riss–Würm interglacial) *Hochterrasse* is morphologically preserved in the Isar valley. This *Jüngere Moosburger Hochterrasse* is composed of the *Fagotienschotter* (Fagotia gravel, named after the gastropod *Fagotia acicularis*). The next younger terraces are the Early to Middle Würmian (MIS 5d to MIS 3?) *Übergangsterrassen* (transitional terraces), whereas the younger one of the two *Übergangsterrassen* was formed most probably during the Middle Würmian (MIS 3).

**Kurzfassung:** Chronostratigraphischen Einstufungen pleistozäner fluvialer Ablagerungen und Formen im Alpenvorland mangelt es bis heute an verlässlichen numerischen Altersdaten. Um diese Lücke etwas zu schließen, werden in diesem Beitrag neue numerische Altersdatierungen (ESR, OSL, $^{14}$C) von den mittel- und ober (jung)-pleistozänen Hochterrassen und Übergangsterrassen im Bayerischen Alpenvorland vorgestellt. Danach wurden die Hochterrassenschotter sensu stricto im vorletzten Glazial

(MIS 6, Riss) und eventuell erhaltene ältere Sockelschotter vor allem im vorletzten Interglazial (MIS 7, inner-RißInterglazial) abgelagert. Das schließt allerdings nicht aus, dass unter einzelnen Hochterrassenschottern wie im Donautal südlich von Regensburg (interglaziale *Hartinger Schichten*) oder im Bereich der Rainer Hochterrasse (basaler Schotterkörper I) auch noch ältere interglaziale Kieskörper erhalten sein können. Die Relikte warmzeitlicher Sockelschotter weisen darauf hin, dass die Tieferlegung der Talsohlen in Tälern, die weiter von den alpinen Vorlandvergletscherungen entfernt sind, verstärkt in den Inter- und Spätglazialen stattgefunden hat. Letztinterglazialer (Eem, MIS 5e) Herkunft ist die im Isartal erhaltene Jüngere Moosburger Hochterrasse, deren Kieskörper nach den manchmal enthaltenen Schneckenschalen der Gattung *Fagotia acicularis* auch als Fagotienschotter bezeichnet wird. Die nächst jüngeren Terrassen sind die früh- bis mittelwürmzeitliche (MIS 5d bis MIS 3?) ältere Übergangsterrasse 1 und die mittelwürmzeitliche (MIS 3) jüngere Übergangsterrasse 2.

## 1 Introduction

In the Northern Alpine Foreland, large river valleys like the Danube (German: *Donau*) valley and its tributaries Iller, Lech and Isar (Fig. 1) are characterised by well-developed stepped fluvial terrace systems, which are partly connected to terminal moraines of Quaternary glaciations in front of the Alps. Penck and Brückner (1901–1909) described these morphostratigraphic relationships between terminal moraines and associated fluvial terraces (respectively fluvial gravel deposits) of different elevations for the first time. They named the four glaciations (from old to young) *Günz, Mindel, Riss*, and *Würm* and the associated terrace levels (from old to young) *Älterer Deckenschotter* (Older Cover Gravel), *Jüngerer Deckenschotter* (Younger Cover Gravel), *Hochterrasse* (HT, high terrace, high terrace gravels) and *Niederterrasse* (NT, lower terrace; lower terrace gravel). In later studies, additional glaciations like the "*Donau* glaciation" (Eberl, 1930) and "*Biber* glaciation" (Schaefer, 1957) as well as further fluvial terrace levels like the *Hochschotter* (highest cover gravel) by Graul (1943) or the *Übergangsterrassen* (ÜT, transitional terraces; transitional terrace gravel) by Schellmann (1988) have been differentiated.

This article focuses on the Middle to Upper (Late) Pleistocene *Hochterrassen* and *Übergangsterrassen* of the Danube, Isar, Lech and Iller rivers. It was Penck (1884) who for the first time used the morphostratigraphic term *Hochterrasse* for fluvial terraces that are situated some metres (mostly 7 to 15 m) above the valley floors, and the term *Niederterrasse* for those that are located in the valley floor usually up to 2.5 m above the floodplains. Penck and Brückner (1901–1909) attributed all *Hochterrassen* to the Rissian (penultimate glaciation, late Middle Pleistocene) and all *Niederterrassen* to the Würmian glaciation (last glaciation, Upper Pleistocene) of the Alpine Foreland. In more recent studies, further loess-covered terrace levels, the Lower to Middle Würmian *Übergangsterrassen* (e.g. Schellmann, 1988, 2010; Unger, 1999; Kroemer, 2010; Doppler et al., 2011; Schielein and Schellmann, 2016b), were described between the levels of the *Hochterrassen* and the *Niederterrassen* in some valleys (e.g. Danube, Isar, Lech valley). In general, the locally specific morphological position of the *Übergangsterrassen* and the loess cover is the reason for an occasionally incorrect stratigraphic interpretation of the *Übergangsterrassen* as *Niederterrasse* or *Hochterrasse*, respectively.

Each of these different levels of fluvial terraces within the range of some metres above the modern valley floors can be subdivided additionally into further terrace sublevels with individual fluvial gravel deposits: in some valleys of the Bavarian Alpine Foreland the *Hochterrassen* can be subdivided morphologically into two (e.g. Penck and Brückner, 1901–1909; Miara, 1996; Miara and Rögner, 1996) or three sublevels (e.g. Schellmann, 1988, 2017b, and further references therein). The terrace gravels are sometimes superimposed on older basal gravel units (e.g. Bibus and Strahl, 2000; Leger, 1988; Schellmann 1988, 1990, 2016b, 2017b; Schellmann et al., 2010; Schielein et al., 2015). Likewise, the Lower to Middle Würmian *Übergangsterrassen* are sporadically subdivided in two different sublevels (Schellmann, 2010, 2018b; Doppler et al., 2011).

A detailed review of the current stratigraphical system for Quaternary terrace units and for different terminal moraines in southern Bavaria was presented by Doppler et al. (2011). Here, we followed the stratigraphic nomenclature of the Bavarian Geological Survey, which correlates the Würmian to MIS 5d up to MIS 2, the Rissian to MIS 10 up to MIS 6, and the Mindelian to MIS12 and older (cf. Doppler et al., 2011: Table 3).

All in all, Doppler et al. (2011) showed that secure chronological classifications based on numerical ages are rare for many Pleistocene fluvial deposits in the Alpine Foreland. Whereas the age of the Holocene terrace gravels (H) and the Upper Würmian (MIS 2) *Niederterrassen* gravels in the Bavarian Alpine Foreland is relatively well established by numerous radiocarbon and dendrochronological data from river channel sediments, palaeochannel fills or overlaying floodplain deposits (e.g. Schellmann, 2010, 2016a, 2017a, 2018a; Doppler et al., 2011), numerical ages of the Middle Pleistocene *Hochterrassen* deposits (e.g. Schielein et al., 2015; Rades et al., 2018, and further references therein) and of the Lower to Middle Würmian *Übergangsterrassen* deposits are much scarcer (e.g. Doppler et al., 2011; Schellmann, 2010).

The earliest attempts to numerically date the *Übergangsterrassen* and *Hochterrassen* in the Bavarian Alpine Foreland started in the late 1980s. Luminescence dating techniques were used focusing on the age determination of the loess cover and the palaeosols on top of the *Hochterrassen* (Rögner et al., 1988; Zöller, 1995; Miara, 1996; Miara and Rögner, 1996; Becker-Haumann and Frechen, 1997) or the *Übergangsterrassen* (Buch and Zöller, 1990, see also discussion by Schellmann, 2010; Zöller, 1995). Later, Fiebig and Preusser (2003) presented the first infrared stimulated luminescence (IRSL) measurements on feldspar extracted from sandy layers in *Hochterrassen* (see Sect. 5) deposits near Ingolstadt, Neuburg and Rain. Thus far, luminescence dating remains the mainly used dating method in the Northern Alpine Foreland. However, luminescence data from fluvial deposits in the Northern Alpine Foreland often suffer from a large scatter in equivalent dose estimates either due to insufficient signal intensities, aberrant luminescence properties, incomplete bleaching of the samples, fading phenomena or a combination of these (e.g. Klasen, 2008; Schielein et al., 2015; Klasen et al., 2016; Trauerstein et al., 2017; Rades et al., 2018).

In the light of these problems when dating fluvial sediments using luminescence, during the last few years we concentrated on electron spin resonance (ESR) dating of small gastropods from the aeolian loess cover on top of the fluvial gravel deposits and from shell-bearing clods of sandy loam and marl in the gravel deposits of the *Übergangsterrassen* and the *Hochterrassen*.

First ESR data have already been obtained by dating a relatively large land-snail shell from a clod of marl in the basal gravel of the *Langweider Hochterrasse* in the Lech valley northwest of Augsburg (Schielein et al., 2015). At that location, the upper gravel was dated by IRSL to the penultimate glaciation (Rissian, MIS 6) around $160 \pm 15$ to $179 \pm 20$ ka. One sample from the basal gravel unit yielded an IRSL age of $263 \pm 29$ ka, whereas four further samples could not be dated by IRSL. The land-snail shell of *Succinea putris*, embedded in a loamy clod at a depth of approximately 11 m below the surface, was dated by ESR to $204 \pm 27$ ka (Schielein et al., 2015), which indicates a deposition of this basal gravel most likely during MIS 7. The difficulty in dating this basal gravel unit by luminescence and the discrepancy between IRSL and ESR data illustrate the need for further investigations.

Recent ESR dating studies on small land-snail shells demonstrate that ESR is a valuable additional method whose upper dating limit supposedly extends beyond MIS 7, an age range similar to that of mollusc shells or corals (e.g. Schellmann et al., 2018). While the ESR dating method can also encounter methodological problems, the most severe problem of its application in this context is to find gastropods bearing sediments, especially in the investigated fluvial gravel deposits, with sufficient amount of dating material (> 5 g shell material), if present at all.

Here, we focused on the age of the *Übergangsterrassen* and the *Hochterrassen* deposits in the Bavarian Alpine Foreland in the light of new numerical dating results (ESR, OSL, and $^{14}$C). We also present some new information about the gastropod fauna, which was found in the sampled aeolian and fluvial sediments leading to the question of the climatic conditions during terrace formation and its different gravel deposits.

## 2 Regional context and investigated areas

All sample sites are located in the Bavarian Alpine Foreland (Fig. 1) and were sampled during geological field mappings of larger parts of the valley floors of the Danube, Lech, Wertach and Isar rivers in the past years (Schellmann, 2010, 2016a, 2017a, 2018a). In these valleys, prominent flights of Middle Pleistocene *Hochterrassen* and of early to middle Late Pleistocene *Übergangsterrassen* are preserved. All of them are accumulation terraces and consist of some metres (mostly 4 to 7 m) thick deposits of fluvial gravels and sands which are often overlain by fine-grained aeolian loess or sandy loess deposits. In particular, in areas with unusually thick fluvial gravel accumulations, the *Hochterrassen* deposits are composed of two stacked gravel deposits with an older fluvial facies at the base and a cold climate *Hochterrassen* deposit sensu stricto at the top. This was described for the first time in the Danube valley downstream of Regensburg (Fig. 1), where an interglacial fluvial facies (determined by pollen analysis) named the *Hartinger Schichten* is preserved at the base of the oldest of three *Hochterrassen* levels (Schellmann, 1988, 1990; Schellmann et al., 2010). In the same area, the unusually thick (up to 11.5 to 13.5 m) fluvial gravel deposits of the youngest *Hochterrasse* consist of a basal, approximately 8 m thick sand-rich gravel unit with numerous limestone cobbles dislocated from the nearby Jurassic Alb. This basal gravel unit was overlain by an approximately 4 m thick, very coarse-grained gravel deposit (the younger *Hochterrassen* deposit sensu stricto) with numerous pebbles from the Alps, and with boulders up to 1.2 m × 0.8 m × 0.4 m in diameter (Schellmann, 1988). Schellmann (1988, p. 124) did not address the question of whether the two gravel units have been deposited under different climatic conditions or if they only represent a local phenomenon.

A predominantly sandy gravel unit at the base of coarse-grained and cobble-rich *Hochterrassen* deposits has been found during geological mapping of the upper Danube valley (Fig. 1: *Dillinger Hochterrasse*) and in the Lech valley (Fig. 1: *Langweider Hochterrasse* and *Rainer Hochterrasse*. Geological maps of these areas including explanations were published by Schellmann (2016b, 2017b) and Schielein

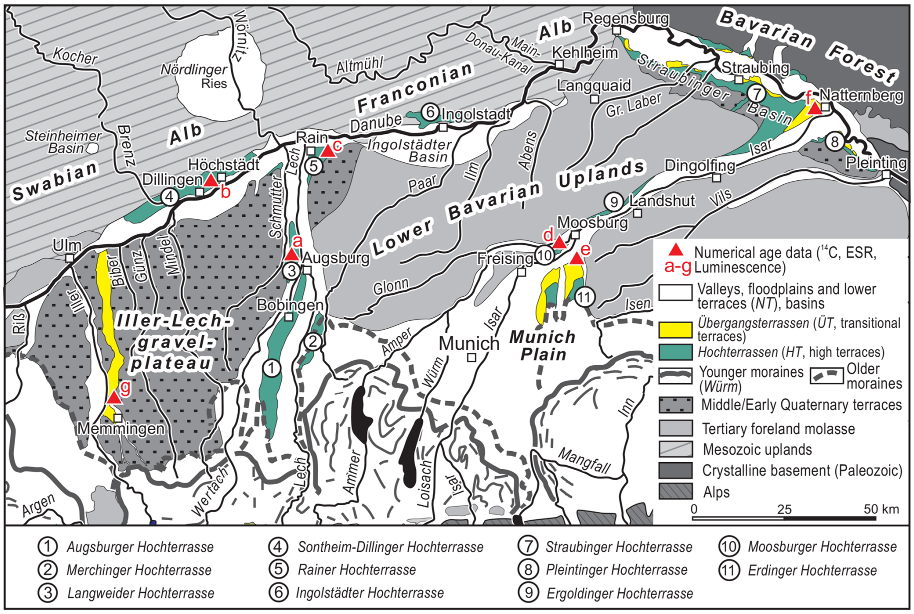


**Figure 1.** Location of Middle Pleistocene (Rissian) *Hochterrassen* and lower to middle Upper Pleistocene (Würmian) *Übergangsterrassen* in the Bavarian Alpine Foreland including sampling sites mentioned in the text.

and Schellmann (2016a, b). From a lithostratigraphic point of view, these basal gravel units could either be only several hundreds to several thousands years older or even one or more glacial–interglacial periods older than the superimposed penultimate glacial accumulation of the *Hochterrassen* gravel sensu stricto. In this respect, only numeric dating methods can give a more accurate chronostratigraphical classification.

Numeric dating results are also essential for a geochronological classification of the *Jüngere Moosburger Hochterrasse* in the Isar valley west of Moosburg (Fig. 1: sample site d). A geological map of this area including explanations has been published by Schellmann (2018b). Here, Nathan (1953) for the first time found sand lenses with an interglacial gastropod fauna like *Fagotia acicularis* embedded in the *Hochterrassen* gravel. Therefore, this *Hochterrassen* deposit is also known by the name "*Fagotienschotter*" (Fagotia gravel). Whereas Nathan (1953), Brunnacker and Brunnacker (1962), Brunnacker (1966), and Jerz (1993) postulated a last interglacial age, Kovanda (2006) assumed a much older age, older than *Mindel*.

More numeric age data are also needed for the loess-covered Lower to Middle Würmian *Übergangsterrassen* (e.g. Doppler et al., 2011, and further references therein). They are older than the pleniglacial (MIS 2) deposition of the oldest *Niederterrasse* (i.e. NT1), younger than the youngest penultimate glacial *Hochterrassen* deposits, and younger than the accumulation of the interglacial *Jüngere Moosburger Hochterrasse*. *Übergangsterrassen* are well preserved in the Danube valley near Dillingen (e.g. Schellmann, 2017b) and downstream of Regensburg (e.g. Schellmann, 2010), in the Isar valley near Moosburg (Schellmann, 2018b) and at the confluence of the Isar and Danube valley (e.g. Kroemer, 2010; Unger, 1999; Schellmann, 1988) for example.

## 3 Sample sites and methods

Samples of ESR dating (snail shells and the surrounding sediment within 30 cm in diameter) and for luminescence dating were collected during geological field mapping of Holocene, Late and Middle Pleistocene fluvial terraces along the Danube, Lech, Wertach and Isar rivers over the past 10 years (Schellmann, 2010, 2016a, 2017a, 2018a).

Shells from land snails were sampled from loamy or marly clods, which were embedded in fluvial gravel and sands of the *Langweider* and *Rainer Hochterrasse* (Fig. 1: sample site a and c), of the *Dillinger Hochterrasse* west of Höchstädt (Fig. 1: sample site b), and of the *Jüngere Moosburger Hochterrasse* west of Moosburg (Fig. 1: sample site d). These clods were eroded from the adjacent floodplain or from islands in the riverbed during the deposition of the terrace gravels. Shells from gastropods were also collected from the sandy loess cover on the *Übergangsterrasse* in the Isar valley south of Moosburg (Fig. 1: sample site e), and in the Danube valley west of Natternberg near the Isar–Danube confluence (Fig. 1: sample site f). Luminescence samples were collected and dated from the sandy loess cover on the *Übergangsterrasse* in the Iller valley northeast of Memmingen (Fig. 1: sample site g). Here, Schaefer (1940, 1953) and Brunnacker (1953) postulated that this loess-covered terrace (named *Fellheimer Feld*) is older than the Würmian pleniglacial *Niederterrasse* (named *Erolzheimer Feld*).

The accuracy of the ESR dating results was checked by parallel dating of two Upper Würmian snail shells by the accelerated mass-spectrometric (AMS) radiocarbon method (Table 1). In addition, at three localities, the ESR data could be compared with luminescence data (Fig. 1: sample sites a, f, g). A further check was made by ESR dating of land-snail shells from different clods of sandy loam, which were embedded in the basal facies of the *Dillinger Hochterrasse* of the Danube (Fig. 1: sample site b). The composition of the gastropod fauna at some sample sites gave helpful palaeoecological information on whether they lived in an interglacial or glacial period. This is also useful to verify the reliability of numeric dating results in general.

Samples for ESR dating were prepared in the sediment laboratory of the University of Bamberg. After cleaning manually, the thickness of the shell fragments was measured using a micrometer or reflection electron microscope (REM) measurements. REM investigations of some shell thicknesses were undertaken in the laboratory of the Department of Building Preservation Sciences of the University of Bamberg. Both techniques yielded congruent results after having measured the thickness from about 20 points per sample. Afterwards, the shells were carefully ground by hand and sieved with a final grain size of 125 to 250 µm. The ESR signals were measured in the ESR laboratory of the Institute of Geography at the University of Cologne. Due to the small amount of shell material it was necessary to put together a mixture of different individuals to obtain sufficient material for a single sample. In five cases, mixtures of different specimens from one sample site had to be used (Table 1: Ba32, Ba33, Ba42, Ba43, Ba56).

At some locations, particle sizes and carbonate content of the loess cover were determined using the pipette method after Köhn and Köttgen and volumetrically after Scheibler.

## 3.1 ESR measurements and equivalent dose ($D_E$) calculations

A multiple aliquot additive-dose procedure was applied for ESR $D_E$ determination. Depending on the amount of available sample material, 18 to 20 aliquots per sample were used. For sample K5838 material for only 10 aliquots was available. Due to limited sample material each aliquot has a weight between 0.02 and 0.07 g (Table 1) instead of the commonly used 0.2 g. All aliquots were re-weighed after ESR measurement to correct the corresponding ESR signal amplitudes if needed.

All samples were $\gamma$-irradiated by a $^{60}Co$ source (Helmholtz Center in Munich, effective dose rates of 0.8–5.2 Gy min$^{-1}$) prior to ESR measurements with maximal doses up to 784 Gy for the Middle Pleistocene shells (Table 1).

The ESR measurements were performed at room temperature on a Bruker ESP 300E X-band spectrometer or on a Bruker ELEXSYS 500 X-band spectrometer working at a frequency of 9.7–9.8 GHz. Measurement conditions were microwave power of 10, 25 or 101 mW, modulation amplitude of 0.485 G, conversion time of 20.48 ms, time constant of 163.84 ms and sweep time of 20.972 s. Depending on the individual signal-to-noise ratio, between 5 and 40 scans were used to record the ESR spectra. The $D_E$ was derived from the analysis of the dating signal at $g = 2.0007$ (Fig. 2), which was successfully used by Schellmann and Kelletat (2001) in the context of ESR dating of snail shells from aeolianites in Cyprus. The investigated shells are largely composed of aragonite, whereas some shells also contain some calcite layers (Table 1; Fig. 2). Already the smallest traces of calcite (< 2 %) exhibit six triplets of hyperfine $Mn^{2+}$ lines in the ESR spectra (Fig. 2a; e.g. Low and Zeira, 1972; Molodkov, 1988, 1993; Inoue et al., 2000), which may overlap with the left shoulder of the ESR signal at $g = 2.0007$. In such cases ESR dating is not possible with the method used here. The signal peak at $g = 2.0007$ was determined by additional measurements of a DPPH standard, an aragonitic coral (*Acropora palmata*) from Cuba and an aragonitic mollusc shell (*Protothaca antiqua*) from the Patagonian Atlantic coast (Fig. 2b).

The $D_E$–$D_{max}$ plot (DDP) procedure was used for $D_E$ determination (Fig. 2c). This plateau screening method for $D_E$ determination and some further details of ESR measurement parameters, number of aliquots and irradiations steps, timing of major U-uptake processes in mollusc shells and corals have been described in detail by Schellmann and Radtke (1999, 2001), and Schellmann et al. (2008). The $D_E$ was calculated using a single saturation exponential function with the program "simplex-fit" (version 1993) written by Rainer Grün.

## 3.2 Dose rate and age calculations

The natural radioactivity of the surrounding sediments (external dose rate) was determined by measuring the radioactive elements uranium (U), thorium (Th) and potassium (K), and the radioactivity of the snail shells (internal dose rate) by measuring the internal U content. U and Th contents were determined at the Jülich Research Centre and some samples at the Landeslabor Berlin-Brandenburg by inductively coupled plasma mass spectrometry (ICP-MS). The K content was measured at the University of Bayreuth via inductively coupled plasma optical emission spectroscopy (ICP-OES) and partly at the Bavarian Geological Survey via X-ray fluorescence (XRF) analysis. For some samples double analyses of U, Th and K were performed and their mean value was used for ESR age calculations (Table 1). Cosmic dose rates were calculated following Prescott and Hutton (1994) using the current depth of the sample below terrain surface. These estimates were used in the "ESR-Data V-6" software (Grün,

**Table 1.** Samples and dose rate data, equivalent doses, ESR ages and AMS radiocarbon data.

| Sample no. | Ba08 | Ba13 | Ba32 | Ba33 | Ba43 | Ba55 | Ba56 |
|---|---|---|---|---|---|---|---|
| Locality | Do14/8b | Do14/8b | Is16/4 | Is16/5 | Is16/7 | Is17/1b*1 | Is17/1b*2 |
| Stratigraphy | ÜT | ÜT | ÜT | ÜT | Jüngere Moosburger HT | Jüngere Moosburger HT | Jüngere Moosburger HT |
| Sample depth (cm) | 380 ± 10 | 380 ± 10 | 50 ± 10 | 105 ± 10 | 250 ± 20 | 200 ± 30 | 200 ± 30 |
| Species | *Succinea putris* | *Succinea putris* | *Succinea putris*<br>*Succinella oblonga* | *Trochulus* sp.<br>*Succinea putris*<br>*Stagnicola* sp. | *Arianta arbustorum*<br>*Aegopinella* cf. *nitens*<br>*Succinella oblonga*<br>*Trochulus hispidus* | *Arianta arbustorum* | *Aegopinella* cf. *nitens*<br>*Trochulus hispidus* |
| [a] Calcite (ESR, XRD) | ∼ 2 % | ∼ 2 % | yes | yes | no | yes | yes |
| Thickness (µm) | 290 ± 90 | 290 ± 90 | 100 ± 41 | 117 ± 39 | 214 ± 88 | 390 ± 104 | 112 ± 38 |
| [b] Removed size (µm) | 120 | 120 | – | – | – | – | – |
| Weight/aliquot (g) | 0.070 | 0.070 | 0.020 | 0.020 | 0.030 | 0.020 | 0.020 |
| Aliquots (*n*) | 20 | 20 | 19 | 18 | 20 | 20 | 20 |
| Dmax (Gy) | 784 | 592 | 140.2 | 131.9 | 562.9 | 544.25 | 544.25 |
| U shell (ppm) | 1.015 ± 0.015 | 1.015 ± 0.015 | 0.470 ± 0.130 | 0.530 ± 0.010 | 0.463 ± 0.012[f] | 0.449 ± 0.006 | 0.430 ± 0.300 |
| U sediment (ppm) | 1.59 ± 0.015 | 1.59 ± 0.015 | 1.800 ± 0.040 | 1.000 ± 0.040 | 1.405 ± 0.065[f] | 1.520 ± 0.030 | 1.520 ± 0.030 |
| Th sediment (ppm) | 7.70 ± 0.20 | 7.70 ± 0.20 | 3.10 ± 0.70 | 8.60 ± 0.50 | 6.50 ± 0.25[f] | 5.10 ± 0.20 | 5.10 ± 0.20 |
| K sediment (wt. %) | 1.18 ± 0.03[f] | 1.18 ± 0.03[f] | 0.844 ± 0.02[f] | 1.006 ± 0.06[f] | 0.859 ± 0.02[f] | 0.981 ± 0.07[f] | 0.981 ± 0.07[f] |
| $H_2O$ (wt. %) | 21 ± 4 | 21 ± 4 | 16 ± 3 | 14 ± 3 | 10 ± 3 | 12 ± 2 | 12 ± 2 |
| $D'$ (µGy $a^{-1}$) total | 1429 ± 83 | 1429 ± 83 | 1858 ± 77 | 1583 ± 69 | 1407 ± 75 | 1288 ± 68 | 1499 ± 74 |
| $D'_{int}$ (µGy $a^{-1}$) | 94 ± 14 | 94 ± 14 | 32 ± 10 | 40 ± 7 | 66 ± 12 | 69 ± 11 | 55 ± 39 |
| $D'_{cos}$ (µGy $a^{-1}$) | 127 ± 2 | 127 ± 2 | 199 ± 4 | 182 ± 3 | 147 ± 4 | 156 ± 7 | 156 ± 7 |
| $D_E$ (Gy) | 43.6 ± 2.6 | 43.7 ± 2.6 | 30.4 ± 4.7 | 36.7 ± 1.6 | 182.3 ± 20.3 | 168.6 ± 16.4 | 177.6 ± 20 |
| Age (EU) | 30.5 ± 2.6 ka | 30.6 ± 1.9 ka | 16.4 ± 2.6 ka | 23.2 ± 1.4 ka | 130 ± 16 | 131 ± 14 | 119 ± 15 |
| Age (LU) | 31.6 ± 2.7 ka | 31.8 ± 2.0 ka | 16.4 ± 2.6 ka | 23.5 ± 1.4 ka | 130 ± 16 | 131 ± 14 | 119 ± 15 |
| [c] $^{14}C$ age (years) | | | 16 160 ± 40 $^{14}C$ BP | 18 680 ± 60 $^{14}C$ BP | | | |
| [d] cal BP (2$\sigma$) | | | 19 324–19 670 cal BP | 22 385–22 715 cal BP | | | |
| [e] $^{14}C$ Lab. no. | | | Beta 470 771 | Beta 485 050 | | | |
| **Sample no.** | **Ba12** | **Ba09** | **Ba11** | **Ba14** | **Ba15** | **Ba42** | **K5838** |
| Locality | Le14/3 | Do13/8 | Do13/8li | Do13/8 | Do14/9 | Le16/5c | Le11/31 |
| Stratigraphy | Langweider HT | Dillinger HT | Dillinger HT | Dillinger HT | Dillinger HT | Rainer HT, unit II | Rainer HT, unit II |
| Sample depth (cm) | 200 ± 50 | 530 ± 15 | 530 ± 20 | 530 ± 15 | 560 ± 10 | 480 ± 20 | 660 ± 15 |
| Species | *Trochulus hispidus* | *Arianta arbustorum* | *Arianta arbustorum* | *Fruticicola fruticum* | unknown | *Helicodonta obvoluta*<br>*Aegopis verticillus* | unknown |
| [a] Calcite (ESR, XRD) | yes | ∼ 2 % | no | no | no | yes | no |
| Thickness (µm) | 53 ± 10 | 283 ± 68 | 283 ± 68 | 220 ± 80 | 250 ± 30 | 168 ± 126 | 550 ± 50 |
| [b] Removed size (µm) | – | – | – | – | – | – | – |
| Weight/aliquot (g) | 0.020 | 0.060 | 0.050 | 0.026 | 0.035 | 0.020 | 0.022 |
| Aliquots (*n*) | 20 | 20 | 20 | 20 | 20 | 20 | 10 |
| Dmax (Gy) | 640 | 784 | 784 | 640 | 592 | 562.9 | 534 |
| U shell (ppm) | 1.140 ± 0.030 | 0.197 ± 0.006 | 0.183 ± 0.006 | 0.173 ± 0.004 | 0.330 ± 0.030 | 0.350 ± 0.020 | 0.500 ± 0.010 |
| U sediment (ppm) | 1.23 ± 0.01 | 1.59 ± 0.09 | 0.74 ± 0.06 | 0.68 ± 0.06 | 0.33 ± 0.10 | 1.906 ± 0.014 | 2.070 ± 0.030 |
| Th sediment (ppm) | 1.82 ± 0.01 | 4.70 ± 0.80 | 4.80 ± 0.20 | 4.75 ± 0.50 | 3.03 ± 0.10 | 5.10 ± 0.20 | 3.19 ± 0.10 |
| K sediment (wt. %) | 0.42 ± 0.10 | 1.11 ± 0.03[f] | 1.12 ± 0.02[f] | 1.12 ± 0.02[f] | 1.02 ± 0.10 | 0.981 ± 0.07[f] | 0.750 ± 0.020 |
| $H_2O$ (wt. %) | 15 ± 5 | 17 ± 3 | 17 ± 3 | 20 ± 4 | 20 ± 4 | 21 ± 4 | 25 ± 5 |
| $D'$ (µGy $a^{-1}$) total | 963 ± 73 | 1102 ± 62 | 1132 ± 53 | 1122 ± 72 | 926 ± 57 | 1391 ± 110 | 893 ± 43 |
| $D'_{int}$ (µGy $a^{-1}$) | 152 ± 29 | 34 ± 6 | 32 ± 6 | 32 ± 6 | 56 ± 11 | 58 ± 11 | 96 ± 4^ |
| $D'_{cos}$ (µGy $a^{-1}$) | 160 ± 10 | 106 ± 2 | 106 ± 3 | 106 ± 2 | 102 ± 1 | 111 ± 3 | 88 ± 2 |
| $D_E$ (Gy) | 150.7 ± 16.6 | 222.1 ± 13.7 | 240.6 ± 19.5 | 223.2 ± 21.2 | 190.8 ± 13.8 | 291.7 ± 35.8 | 191.5 ± 18.5 |
| age (EU) | 156 ± 21 ka | 202 ± 17 ka | 213 ± 20 ka | 199 ± 23 ka | 206 ± 20 ka | 210 ± 31 | 214 ± 23 |
| age (LU) | 172 ± 23 ka | 202 ± 17 ka | 213 ± 20 ka | 199 ± 23 ka | 206 ± 20 ka | 210 ± 31 | 214 ± 23 |

[a] Calcite (ESR) yes or no indicates with $Mn^{2+}$ or without $Mn^{2+}$ lines. [b] Thickness (µm) reduced by etching with 2 % HCl approximately 1 to 2 min. [c] AMS $^{14}C$ ages (Beta Analytic Florida). [d] Calibrated with IntCal13 (CALIB Rev. 7.0.4); due to hard-water effect the real age is most probably younger than the atmospheric calibrated $^{14}C$ age. [e] Beta – Beta Analytic Florida. MAMS – Curt-Engelhorn-Zentrum Archäometrie Mannheim. [f] Mean value of double or triple analysis; U, Th analysis by ICP-MS, K analyses by ICP-OES or RFA. ESR age calculation uses: *k* factor of 0.07 ± 0.01 (Grün, 2007; Grün and Katzenberger, 1994); initial $^{234}U/^{238}U$ ratio 1.0 ± 0.2; density of shell 2.95 ± 0.02 g $cm^{-3}$ EU – age calculation assuming early U uptake or LU – linear (continuous) U uptake.

2009) to calculate the age of a sample. The water content of the surrounding sediments was measured in the field using an electronic soil moisture meter. Measured values were used for ESR age calculations with relative errors of 15 % to 30 % (Table 1).

Fortunately, all dated snail shells have low internal U contents, often below 0.5 ppm (Table 1). Thus, ESR ages are the same or do not differ significantly when they are calculated under the assumption of an early (EU) or a linear (LU) U uptake model (Table 1). Even so, mollusc shells seem to incorporate U after death very quickly in a few thousand years (e.g. Schellmann et al., 2008), and consequently ESR age calculation of Pleistocene shells should prefer an early U uptake model, whereas ESR age calculations of Holocene shells should be checked with different U-uptake models.

In the context of ESR age calculation we further used (a) an alpha efficiency (*k* factor) of 0.07 ± 0.01 following Grün (2007) and Grün and Katzenberger (1994), and we assumed (b) an initial $^{234}U/^{238}U$ value of 1.0 ± 0.2, a value commonly found in soils and sediments (e.g. Borylo and Skwarzec, 2014; Vigier and Bourdon, 2012; Srivastava et al., 2012, and further references therein). Weißhaar (2000, Fig. 4.11) for example reported $^{234}U/^{238}U$ values of about 0.95 to 1.18 for fluvial gravel, sand, silts and clays in a 280 m

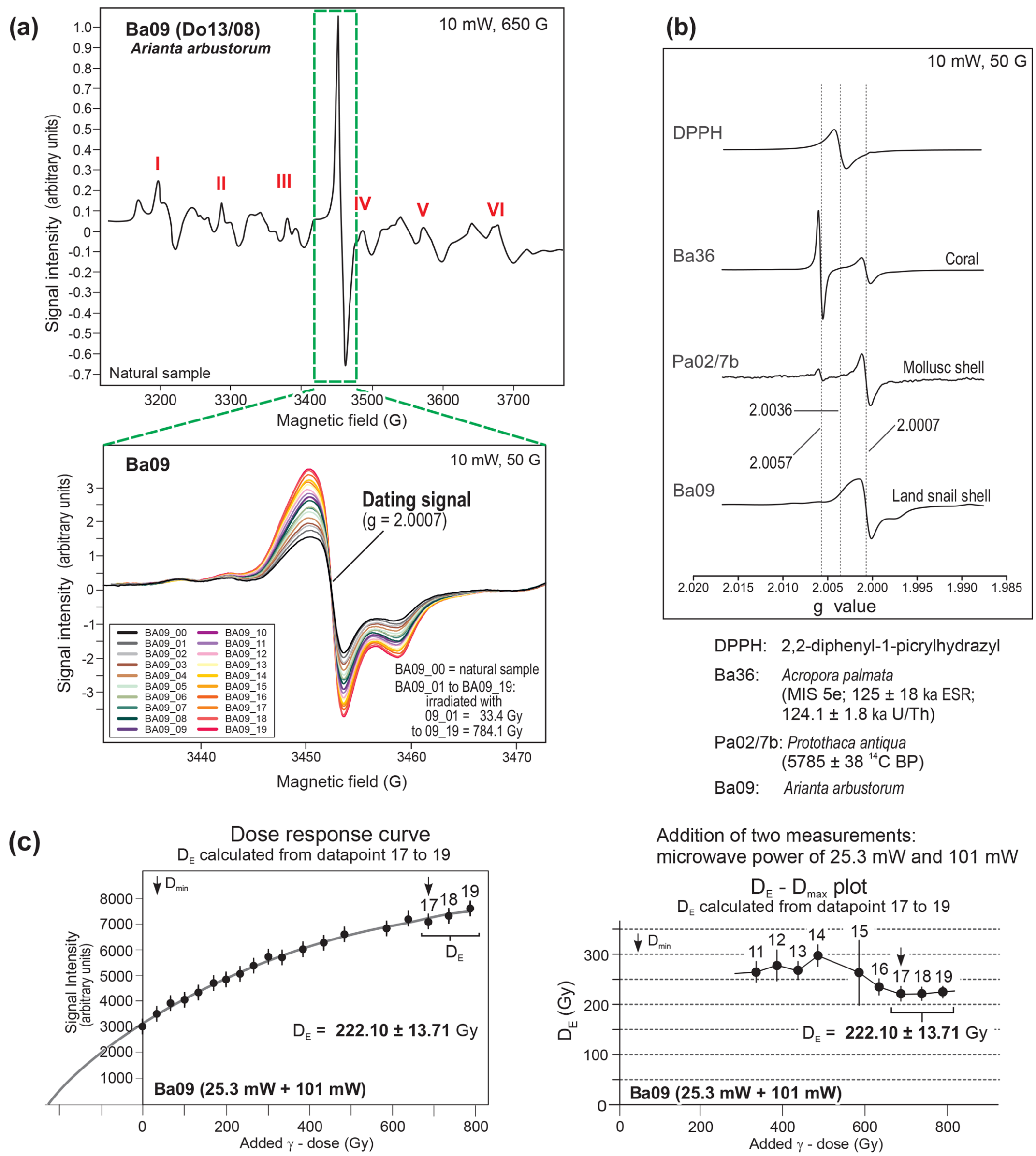


**Figure 2.** ESR spectra of a penultimate interglacial (MIS 7) land-snail shell (*Arianta arbustorum*) with aragonite and minor calcite crystal structure (calcite content approx. 2 % measured by XRD); **(a)** ESR screenings with a 650 G (top), and 50 G (bottom) scan width. The latter shows a strong signal growth of the dating signal at $g = 2.0007$ after gamma irradiation to doses of up to 784.1 Gy. The extra-wide ESR screening of 650 G shows six triplets (I to VI) of ESR hyperfine $Mn^{2+}$ lines in the ESR spectrum; **(b)** $g$-value determination of the dating signal of Ba09 using a DPPH, a MIS 5e aragonite coral sample, and a Holocene aragonite mollusc shell for calibration; **(c)** additive dose response curve and $D_E$–$D_{max}$ plot (DDP) of the sample Ba09. Only for this sample, the ESR signal amplitude is the mean value of two separate ESR measurements using different microwave powers of 25.3 and 101 mW, respectively.

deep sediment core of the Quaternary river Neckar alluvial fan deposit (southern Germany).

## 3.3 Radiocarbon and luminescence data

To check the reliability of the ESR dating results, two Late Würmian snail shells were also dated using the radiocarbon ($^{14}C$) method (Table 1). Data were calibrated without a hard-water correction using the atmospheric "IntCal13" calibration set (Reimer et al., 2013) and the software CALIB (version 7.0.2; Stuiver and Reimer, 1993). It needs to be considered that the hard-water effect, which may occur as a result of incorporating $^{14}C$-free inorganic carbon from dissolved ancient carbonates during shell crystallisation (e.g. Xu et al., 2011, and further references therein), limits the reliability of land-snail $^{14}C$ age dating results. Measured $^{14}C$ ages can be a few years, some hundreds of years or even up to 2000 or 3000 years too old (e.g. Goodfriend and Stipp, 1983; Pigati et al., 2010; Xu et al., 2011). In our research area, the river channel and floodplain deposits of the Danube, Isar, and Lech rivers have high carbonate contents; hence $^{14}$C ages should be influenced by a hard-water effect of some hundreds of years. This assumption is derived from radiocarbon dates of reworked charcoal or organic plant fragments and associated snail shells in fluvial deposits of the Alpine Foreland rivers Lech (Gesslein, 2013, p. 43) and Danube (Schellmann, 2017b), which have shown age differences of 570 and 500 years, respectively. Since the exact value of the hard-water effect is unknown, the calendar age should be younger than the atmospheric calibrated $^{14}$C ages in Table 1.

ESR data are compared to published luminescence dating results from the same or neighbouring outcrops (Kroemer, 2010; Schielein et al., 2015). Additionally, we present two new OSL data (Table 2), sampled from the sandy loess cover on the *Übergangsterrasse* (i.e.,*Fellheimer Feld*) in the Iller valley (Fig. 1: sample site g). The luminescence samples were taken from the loess deposits in opaque tubes and prepared under subdued red light in the luminescence laboratory at the University of Bayreuth. Both samples were sieved and treated with 10 % HCl and 10 % $H_2O_2$ to remove any carbonates and organic material. The fine-grain (4–11 µm) quartz fraction was segregated by etching with $H_2SiF_6$ and enriched by settling using Stokes law. The suspension of demineralised water and 1.5 mg of fine-grain quartz was dispensed onto 9.8 mm wide stainless-steel discs. The measurements for $D_E$ estimation were conducted on Risø DA-20 luminescence readers following the standard SAR protocol of Murray and Wintle (2003). OSL emission was filtered through a U-340 filter after stimulation with blue LEDs (125 °C, 40 s). The seven or nine measured aliquots of each sample were all accepted and yielded dose values from which median $D_E$ values were calculated. For dose rate estimation, uranium and thorium concentrations were measured by alpha-counting and the potassium contents by ICP-OES. Conversion factors from Adamiec and Aitken (1998) were used. Furthermore, the geographic position, recent depth below surface, altitude, and density of the overlying sediment were included in the cosmic dose rate calculations (Prescott and Hutton, 1994) as well as water contents, which were measured in the field considering a relative error of 25 %. Dose rate and age calculations were conducted in ADELE software (Kulig, 2005).

## 4 Results

### 4.1 ESR, radiocarbon and luminescence data from the *Übergangsterrasse* in the Danube, Isar and Iller valley

Ages are obtained from the Upper Würmian sand loess cover on the *Übergangsterrasse* (ÜT) in the Danube valley north of the Isar valley mouth (Fig. 1: sample site f; Fig. 3 and Table 1: sample Ba33), in the Isar valley near Moosburg (Fig. 1: sample site e; Figs. 4, 5 and Table 1: sample Ba32), and in the Iller valley southwest of Fellheim (Fig. 7: sample site g; Table 2).

The ÜT in the Danube valley west of the Natternberg was first described by Schellmann (1988, 1990) and Unger (1999), and then later by Kroemer (2010), who published first numeric age data based on luminescence dating of feldspar (Fsp.) and quartz (Qu.) (Fig. 3). The luminescence dating was by Nicole Klasen (University of Cologne). The luminescence data from the base of the loess cover on the ÜT confirm an Upper Würmian (MIS 2) age of around $18.8 \pm 1.0$ ka (Fsp.) and $23.1 \pm 2.8$ ka (Qu.). Furthermore, a sandy layer in the fluvial gravel deposits of the ÜT was dated to $36.0 \pm 1.9$ ka (Fsp.) and $30.4 \pm 3.7$ ka (Qu.), implying a late Middle Würmian (MIS 3) age of the fluvial aggradations of the ÜT in this area (Kroemer, 2010).

In the current study, land-snail shells were sampled from the base of the sandy loess covering the unweathered sandy gravel deposits of the *Übergangsterrasse* (Fig. 3) and were dated by ESR and $^{14}$C. Due to the small amount of shell material, sample Ba33 represents a mixture of the three species *Trochulus* sp., *Succinea putris* and *Stagnicola* sp. (Table 1). The resulting ESR age of $23.2 \pm 1.4$ ka agrees very well with the quartz age of ca. $23.1 \pm 2.8$ ka published by Kroemer (2010). Within error, it also agrees well with the AMS $^{14}$C age of $18\,680 \pm 60$ BP of the gastropod collected in this study. The atmospheric calibrated age without hard-water correction is about 22 966 to 22 525 cal BP (Table 1: Ba33). If a hard-water effect of a few hundreds of years is assumed, the radiocarbon age would also be within the error range of the ESR age.

Further small terrestrial gastropods for ESR and radiocarbon dating were taken from the gravel pit Schulz in the younger *Übergangsterrasse 2* (ÜT2) of the Isar (Fig. 1: sample site e) west of Langenpreising (Figs. 4, 5). Some kilometres south of the location an older *Übergangsterrasse* (ÜT1) is preserved (Fig. 4), 0.5 to 2 m above the ÜT2. Details about the distribution and stratigraphy of the *Übergangsterrassen* and other Middle and Upper Pleistocene terraces of the Isar in this region, including some numeric data, are published in Schellmann (2018b). Similar to other valleys of the Bavarian Alpine Foreland, the gravelly, horizontal and occasionally also trough-bedded braided river deposits of the *Übergangsterrassen* are covered by sandy loess of fine to medium grain sizes (Fig. 5). The upper part of the 7 to 9 m thick gravel deposit of the ÜT2 and its loess cover are exposed in the gravel pit west of Langenpreising (Fig. 5; Table 1: sample Ba32). The calcareous, often sandy loess deposit is between 0.6 and 1.3 m thick and lies on top of the unweathered sandy gravel deposits of the *Übergangsterrasse*. A fossil palaeo-soil in the form of a very weak Gelic Gleysol and the high content of sandy grain sizes (Fig. 5) are characteristic of many Upper Würmian loess deposits in Bavaria.

An Upper Würmian age of this loess cover is confirmed by the ESR and $^{14}$C dating results of land-snail shells. They

**Table 2.** Samples and dose rate data, equivalent doses, and OSL ages.

| Sample | Location | Depth (m) | Grain size (µm) | Radionuclide concentrations | | | Water content (%) | Dose rate (Gy/ka) | No. aliquots | $D_e$ (Gy) | Age (ka) |
|---|---|---|---|---|---|---|---|---|---|---|---|
| | | | | U (ppm) | Th (ppm) | K (%) | | | | | |
| Iller12/1 | ÜT (*Fellheimer Feld*) | 1.65 | 4–11 | 3.05 ± 0.19 | 6.41 ± 0.63 | 1.23 ± 0.12 | 20 ± 5 | 2.46 ± 0.34 | 9 | 76.2 ± 4.0 | 31 ± 4 |
| Iller12/3 | ÜT (*Fellheimer Feld*) | 1.50 | 4–11 | 3.59 ± 0.20 | 6.30 ± 0.64 | 1.25 ± 0.13 | 20 ± 5 | 2.60 ± 0.40 | 7 | 75.4 ± 5.3 | 29 ± 4 |

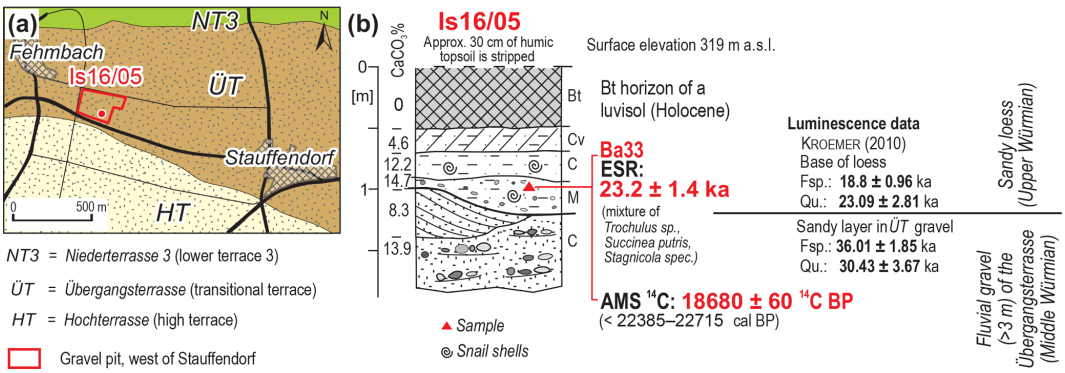


**Figure 3.** ESR, $^{14}$C and luminescence data from the *Übergangsterrasse* in the Danube valley west of the village Stauffendorf; **(a)** geological map with location of sample site; **(b)** geological profile with ESR and $^{14}$C dating results, and some luminescence data from Kroemer (2010) (Fig. 1: sample site f; Table 1: sample Ba33).

were sampled from the unweathered sandy loess layers above and below the weak Gelic Gleysol. The sample Ba32 is a mixture of several individuals of the species *Succinea putris* (Fig. 5; Table 1). The ESR age of 16.4 ± 2.6 ka seems underestimated compared to the atmospheric calibrated AMS $^{14}$C age of 19 670–19 324 cal BP. Considering a hard-water effect of a few hundred years, the radiocarbon age would possibly agree with the ESR age within error range.

These data from the *Übergangsterrassen* in the Danube and Isar valley indicate an Upper Würmian age of the loess cover. This is also the case for the loess cover on the *Übergangsterrasse* in the Iller valley southwest of Fellheim (Fig. 1: sample site g). A formation prior to the Würmian pleniglacial of this loess-covered transitional terrace was first assumed by Schaefer (1940, 1953) and Brunnacker (1953). They demonstrated that the 1 to 2 m, sometimes more than 4 m thick, layers of Würmian loess and loess loam overlay the unweathered gravel deposit without any fossil interglacial soil horizon. In a gravel pit southwest of Fellheim, the more than 10 m thick, horizontally and trough-bedded gravel deposits (Fig. 6: Photo 1) and its up to 1.6 m thick cover of sandy loess (Fig. 7) were recently exposed. Only the upper 20 to 30 cm of the gravel layers were very slightly weathered with some mellow sandstones and dolomites, but without any significant decalcification (Fig. 7). A few species of cold-climate land-snail shells of *Succinella oblonga* ($n = 8$) and *Pupilla muscorum* ($n = 6$), and one shell of *Cochlicopa lubrica* were sampled from the bottom layer of the loess sediments. Unfortunately, not enough material for ESR dating could be sampled. However, two OSL samples of the bottom loess itself yielded ages of 29 ± 4 and 31 ± 4 ka, respectively (Fig. 7, Table 2).

All in all, the fluvial gravel deposits of the described *Übergangsterrassen* areas in the valleys of the Iller, Isar and Danube rivers are older than the Upper Würmian loess cover on top of their gravel deposits. Most probably, the younger one of the currently known two *Übergangsterrassen*, the ÜT2, is at least of late Middle Würmian age (MIS 3). This is indicated by the luminescence data of Kroemer (2010) from the *Übergangsterrasse* of the Danube west of Natternberg (Fig. 3). The age of the older ÜT1 is still unknown. This terrace is younger than the last interglacial Fagotia gravel (see next section), most probably of Early Würmian age (MIS 5d to MIS 4).

## 4.2 ESR data and gastropod fauna from the *Jüngere Moosburger Hochterrasse* (*Fagotienschotter*, Isar valley)

Two different levels of *Hochterrassen* are preserved between the Isar and lower Amper valley in the vicinity of Moosburg (Fig. 4) and were described in detail by Schellmann (2018b). The *Ältere Moosburger Hochterrasse* (Older Moosburger high terrace) is elevated about 15 to 16 m above the flood-

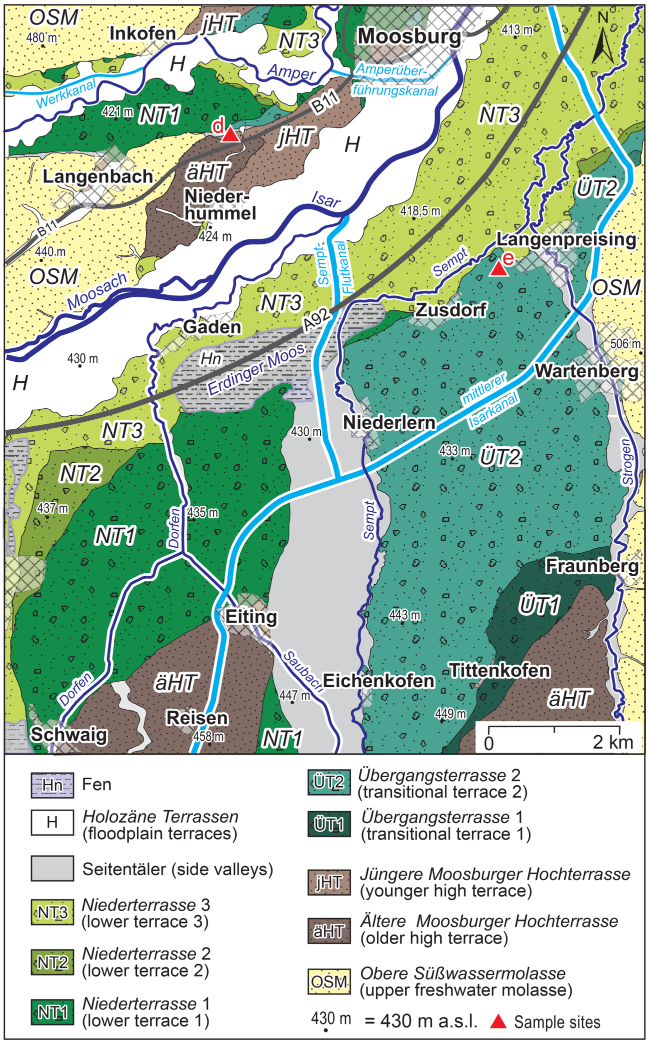


**Figure 4.** Middle and Late Pleistocene terraces of the Isar valley west and south of Moosburg modified after Schellmann (2018b).

plain of the river Isar, the *Jüngere Moosburger Hochterrasse* (Younger Moosburger high terrace) about 10 to 14 m.

The fluvial gravel deposits of both *Hochterrassen* have thicknesses of about 5 to 7 m, which are covered by Würmian loess mostly with thicknesses of 1 to 5 m. The Middle Pleistocene gravel deposits underlying the *Hochterrassen* are elevated above the fluvial gravel deposits of the adjacent Würmian and Holocene terraces of the Isar valley.

The *Jüngere Moosburger Hochterrasse* is situated between the valleys of Isar and Amper (Fig. 4). This terrace deposit has been known for many years under the name *Fagotienschotter* (Fagotia gravel), named after the gastropod *Fagotia acicularis*. Biostratigraphically (mollusc content) these gravel deposits are supposed to be as old as the last interglacial (Nathan, 1953; Brunnacker and Brunnacker, 1962; Brunnacker, 1966; Jerz, 1993) or older than the Elsterian glaciation in northern Germany as postulated by Kovanda (2006). All these authors agree on the interglacial habitus of the gastropod fauna; only the age interpretation is controversial.

Gastropod samples for dating were collected from a small gravel pit west of Moosham (Fig. 1: sample site d; Fig. 8). Here, marly clods bearing land-snail shells are intercalated in the *Fagotienschotter*. This new collection of land-snail species is similar to the collection of Nathan (1953). The interglacial character of the gastropod fauna is demonstrated by some interglacial species like *Aegopinella nitens* and by some further species that prefer warm temperate climatic conditions (Table 3). The floodplain of the river Isar, containing small standing waters and swamps and rich in high shrubs, could have been the habitat from which the snails derive. Species indicating dryness or open landscapes are almost completely absent.

Land-snail shells were collected from two separate marly clods (Fig. 8: Is 16/7 and Is17/1b) and dated by ESR. A mixture of land-snail shells of the species *Aegopinella* cf. *nitens*, *Arianta arbustorum, Succinella oblonga* and *Trochulus hispidus* yielded a last interglacial ESR age of $130 \pm 16$ ka (Table 1: Ba43). In the other marly clod, a few individuals of *Arianta arbustorum* also resulted in a last interglacial ESR age of $131 \pm 14$ ka (Table 1: Ba55) and a shell mixture of *Aegopinella* cf. *nitens* and *Trochulus hispidus* in an ESR age of $119 \pm 15$ ka (Table 1: Ba56).

From a morphostratigraphic point of view, the *Jüngere Moosburger Hochterrasse* (or Fagotia gravel) is older than both *Übergangsterrassen* deposits of Lower to Middle Würmian age southwest of Moosburg. And it also is younger than the Rissian *Ältere Moosburger Hochterrasse*, which is preserved in the west of the *Jüngere Moosburger Hochterrasse* (Fig. 4; details in Schellmann, 2018b). The gastropod fauna, which is preserved in marly or sandy clods or in sand lenses in the gravel deposits of the *Jüngere Hochterrassen*, indicates a warm temperate interglacial age of this deposit (Nathan; 1953, Brunnacker and Brunnacker, 1962; Brunnacker, 1965; Kovanda, 2006); the three ESR ages provide clear evidence for a deposition during the last interglacial (MIS 5e).

## 4.3 ESR data and gastropod fauna from the basal gravel unit of the *Dillinger Hochterrasse*

In the Danube valley between the villages Sontheim, Dillingen and Höchstädt (Fig. 9), *Hochterrassen* are widely preserved, especially north of the river. Graul (1962) was the first one to separate this extensive *Hochterrassen* area into three sublevels, and Leger (1988) and Bibus and Strahl (2000) found that the middle level of these three *Hochterrassen* levels, the *Dillinger Hochterrasse*, is composed of two stacked gravel deposits. This is the case in areas where the otherwise typically 5 to 8 m thick *Dillinger Hochterrassen* gravel reaches unusual thicknesses of about 10 to 13.5 m (Fig. 9). For details about the *Dillinger Hochterrasse* including the history of research, a geological map and

**Table 3.** Shells from gastropods collected from sand lenses and clods of marl and sand embedded in the *Jüngere Moosburger Hochterrassen* gravel (Fagotia gravel).

| | | Nathan (1953) | A | B1 | B2 |
|---|---|---|---|---|---|
| | 1. Forest snails sensu stricto | | | | |
| ! | *Aegopinella nitens* | × | × | – | 65 |
| ! | *Helicodonta obvoluta* | × | – | – | – |
| ! | *Monachoides incarnatus* | × | – | – | – |
| ! | *Platyla polita* | × | – | – | – |
| | 2. Further shade-preferring species | | | | |
| | *Arianta arbustorum* | – | × | 1 | 17 |
| ! | *Cepaea* sp. | – | – | – | 1 |
| ! | *Cepaea nemoralis* | × | – | – | – |
| ! | *Discus rotundatus* | × | – | – | – |
| (!) | *Fruticicola fruticum* | × | – | – | – |
| | *Trochulus striolatus* | × | – | – | – |
| ! ? | *Trochulus villosus* | – | – | – | 1 |
| | *Vitrea crystallina* | – | – | – | 1 |
| | *Vitrea* sp. | × | – | – | – |
| ! | *Vitrinobrachium breve* | × | – | – | 1 |
| | 3. Ubiquists | | | | |
| | Agriolimacidae/Limacidae | × | – | – | – |
| ! | *Carychium tridentatum* | × | – | – | – |
| | *Cochlicopa lubrica* | × | × | | 48 |
| | *Nesovitrea hammonis* | – | – | – | 17 |
| | *Nesovitrea petronella* | – | × | – | 1 |
| | *Succinella oblonga* | – | × | – | 17 |
| | *Trochulus hispidus* | × | × | 2 | 31 |
| | 4. Open-land species | | | | |
| ! | *Cecilioides acicula* | × | – | – | – |
| | *Vallonia costata* | – | × | – | 1 |
| | 5. Water- and swamp-preferring molluscs | | | | |
| (!) | *Ancylus fluviatilis* | × | – | – | – |
| | *Anisus leucostoma* | × | – | – | – |
| | *Anisus vortex* | × | – | – | – |
| (!) | *Bithynia tentaculata* | × | – | – | – |
| (!) | *Carychium minimum* | × | – | – | – |
| !! | *Esperiana daudebartii* (*Fagotia acicularis*) | × | – | – | – |
| | *Galba truncatula* | × | – | 1 | – |
| | *Gyraulus acronicus* | × | – | – | – |
| | *Gyraulus laevis* | × | – | – | – |
| !! | *Lithoglyphus* sp. | × | – | – | – |
| (!) | *Oxyloma elegans* | – | – | 12 | 1? |
| | *Pisidium amnicum* | × | – | – | – |
| (!) | *Pisidium moitessierianum* | × | – | – | – |
| | *Pisidium ponderosum* | × | – | – | – |
| | *Planorbis planorbis* | × | – | – | – |
| | *Radix balthica* | × | – | – | – |
| (!) | *Segmentina nitida* | × | – | – | – |
| | *Stagnicola corvus* | × | – | – | – |
| | *Valvata cristata* | × | – | – | – |
| (!) | *Valvata piscinalis* | × | – | – | – |
| | Unionacea | × | – | – | – |
| | 6. Indifferent | | | | |
| | Clausiliidae | × | – | – | – |

A – sample Is 16/97 collected 2016; B1 – sample Is 17/1a collected 2017; B2 – sample Is 17/1b collected 2017 in the gravel pit west of Moosham. !! interglacial indicator species: ! interglacial species; (!) predominately warm temperate species, sometimes also distributed in interstadials.

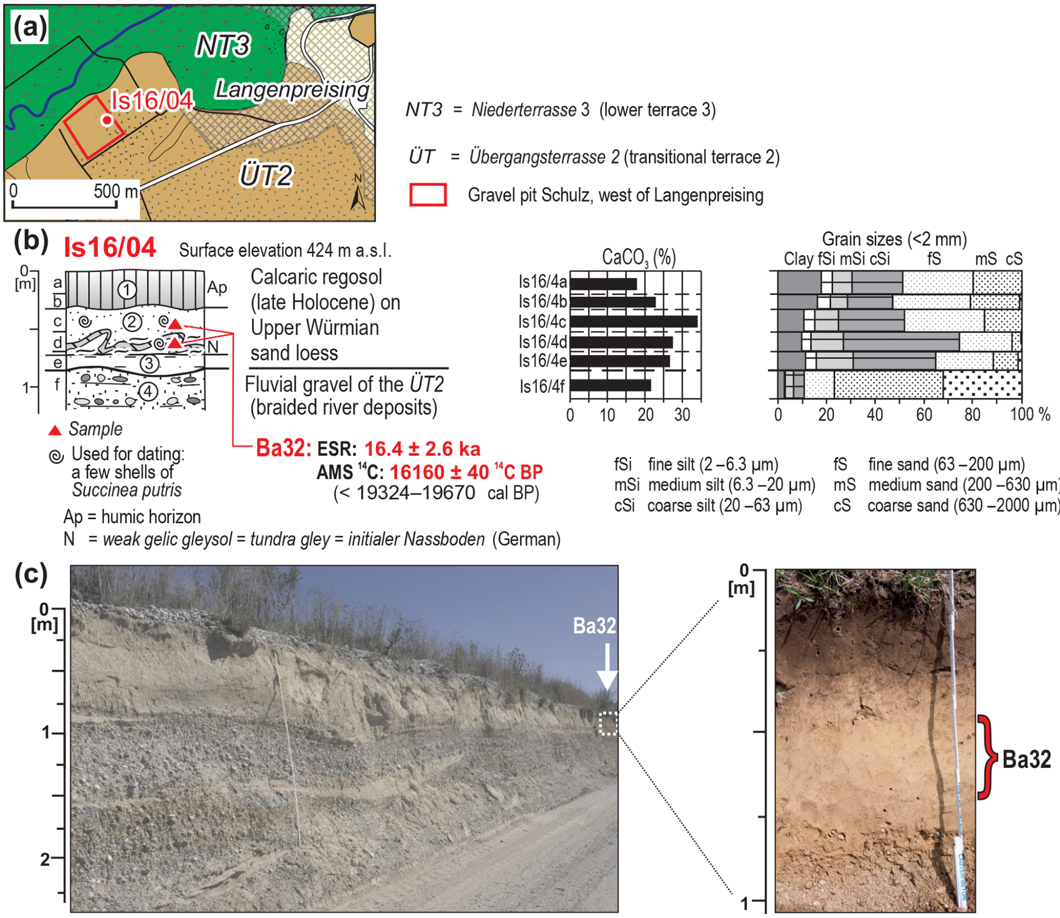


**Figure 5.** ESR and $^{14}$C dating results of small terrestrial gastropods from the sand loess cover on the *Übergangsterrasse 2* west of Langenpreising, Isar valley (Fig. 1: sample site e; Table 1: sample Ba32); **(a)** geological map modified after Schellmann (2018b) with location of the sample site Ba32; **(b)** geological profile with dating results and some laboratory analysis (carbonate content, grain sizes); **(c)** photo of the *Übergangsterrassen* gravel (left) and its sandy loess cover with sample location Ba32 (right).

a revised fluvial terrace stratigraphy of the Danube valley in this region, see Schellmann (2017a, b).

Like the *Fagotienschotter* in the Isar valley, the basal gravel formation of the *Dillinger Hochterrasse* in the Danube valley west of Höchstädt (Fig. 1: sample site b, Fig. 9) also contains a warm-temperate interglacial mollusc fauna, which is embedded in sandy layers and predominantly in loamy and sandy clods. It was Leger (1988) who for the first time described an interstadial or interglacial gastropod fauna embedded in sandy gravel deposits of the *Dillinger Hochterrasse* west of the village of Höchstädt.

Gastropods shells have been collected from sandy layers and loamy and sandy clods at different sections in a gravel pit on the *Dillinger Hochterrasse* west of Höchstädt (Fig. 10). This location is only some hundred metres away from the site sampled by Leger (1988). The clods were deposited in frozen state in the basal gravel formation of the *Dillinger Hochterrasse* and have been reworked from a nearby former floodplain. Only in the eastern part of the gravel pit, this large-scale cross-bedded basal gravel unit reaches up to the gravel surface below the last glacial (Würmian) loess cover (Fig. 10b). In most parts of the gravel pit, the basal gravel unit is overlain by another few-metres-thick gravel unit deposited by a braided river (Fig. 10c). Gastropod shells were sampled in the eastern part of the gravel pit from two sandy layers (Table 4) and from two loamy and sandy clods (Fig. 10b). The collected gastropod fauna contain a few interglacial index species like *Discus perspectivus* and *Esperiana daudebartii* (*Fagotia acicularis*) and some other warm temperate species like *Helicodonta obvoluta* and *Monachoides incarnatus* (Table 4).

ESR dating of *Arianta arbustorum* (Ba09) and of *Fruticicola fruticum* species (Ba14) gave almost identical ages of 202 ± 17 and 199 ± 23 ka, respectively (Fig. 10b: Do13/8; Table 1: Ba09 and Ba14). The ESR age of 213 ± 20 ka of a further *Arianta arbustorum* shell from a neighbouring clod of loamy sand in this part of the gravel pit is within the error range of the other ages from this gravel unit (Fig. 10b:

**Table 4.** Shells from gastropods collected from sandy gravel deposits of the *Dillinger Hochterrasse* in the eastern part of the gravel pit Höchstädt.

| | | (1) | (2) | (3) | (4) | (5) | Total |
|---|---|---|---|---|---|---|---|
| | 1. Shade-preferring species | | | | | | |
| | 1a. Forest snails | | | | | | |
| ! | *Acanthinula aculeata* | – | – | 1 | – | – | 1 |
| ! | *Aegopinella* sp. | – | – | – | – | 1 | 1 |
| !! | *Discus perspectivus* | – | – | 3 | – | – | 3 |
| ! | *Helicodonta obvoluta* | – | – | 2 | – | – | 2 |
| ! | *Monachoides incarnatus* | – | – | 1 | 2 | – | 3 |
| | 1b. Other shade-preferring species | | | | | | |
| | *Arianta arbustorum* | | – | 5 | 5 | 6 | 16 |
| ! | *Cepaea hortensis* | 1 | – | ? | – | – | 1 |
| | *Clausilia pumila* | – | – | 3 | 3 | – | 6 |
| (!) | Fruticicola fruticum | 1 | – | 3 | 3 | 2 | 9 |
| ? | *Trochulus* cf. *coelomphalus* | – | – | 4 | 6 | 4 | 14 |
| | 2. Ubiquists | | | | | | |
| ! | *Carychium tridentatum* | – | – | – | 2 | 1? | 2 |
| | *Eucobresia diaphana* | – | – | – | 1 | – | 1 |
| | 3. Open-land species | | | | | | |
| (!) | *Vallonia pulchella* | – | – | 1 | – | 2 | 3 |
| | 4. Water- and swamp-preferring mollusc | | | | | | |
| !! | *Esperiana daudebartii (Fagotia acicularis)* | 1 | – | – | – | – | 1 |
| | *Pisidium amnicum* | – | 1 | – | – | – | 1 |
| | *Succinea putris* | 1 | – | – | – | – | 1 |
| | *Helicidarum* (indet.) | – | × | ××× | × | ×× | |

!! interglacial index species ! interglacial species (!) predominately warm temperate species. (1) gastropods collected from sandy layer during July 2013. (2) gastropods collected from sandy layer during October 2013 (Do 13/5). (3) gastropods collected from a loamy and sandy clod during October 2013 (Do 13/8li). (4) gastropods collected from another loamy and sandy clod during October 2013 (Do 13/8re). (5) gastropods collected from both loamy and sandy clods during October 2013 (Do 13/8).


**Figure 6.** Horizontally and trough-bedded gravel deposits of the *Übergangsterrasse* (*Fellheimer Feld* in the Iller valley south of the village Fellheim (Fig. 1: sample site g).

Do13/8li; Table 1: Ba11). Gastropod shells from the western part of the gravel pit (Fig. 10c: Do14/9, Ba15; Table 1: Ba15) also yield a MIS 7 age of $206 \pm 20$ ka. This shell-bearing clod was also deposited in the sandy and large-scale cross-bedded basal gravel unit. The overlying unit of a medium- to coarse-gravel facies is horizontally bedded, which is typical of braided river deposits. This overlying gravel unit was deposited by the Danube under cold climate conditions most probably during MIS 6. Under warm climate conditions like the Holocene the Danube is a meandering river in this region with sandy gravel channel deposits, which are large-scale cross-bedded (Schellmann, 2017b).

In general, these ESR dating results from the *Dillinger Hochterrasse* illustrate that ESR ages of different species of land-snail shells and from different clods of sandy loam in a gravel pit yield highly congruent ages. All ESR data from the basal gravel unit in the gravel pit west of the village Höchstädt are of penultimate interglacial (MIS 7) age. These

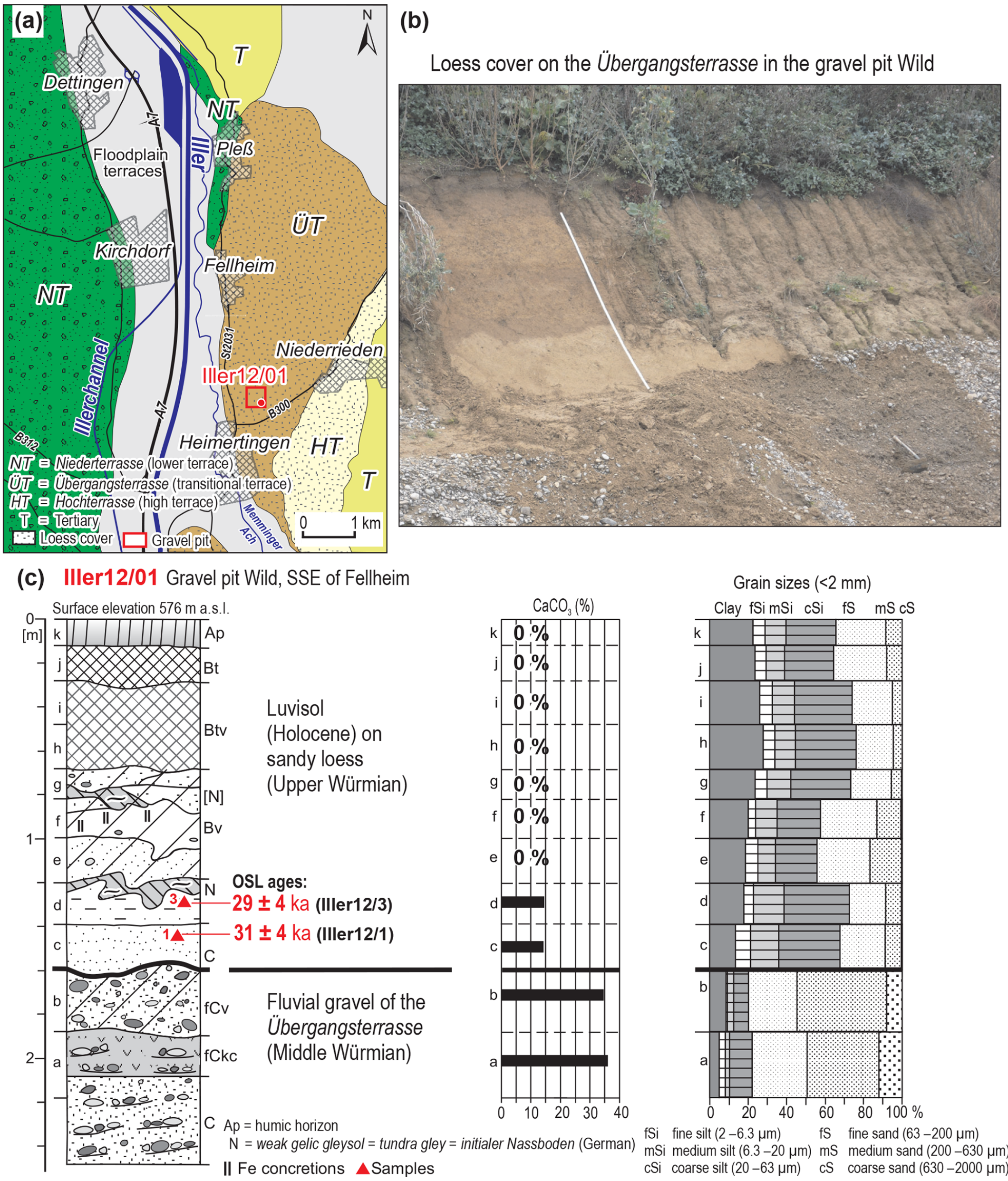


**Figure 7.** Luminescence dating results from the base of the sandy loess cover on top of the *Übergangsterrassen* gravel south of the village Fellheim (Fig. 1: sample site g; luminescence data are listed in Table 2); **(a)** geological map with location of the sample site Iller 12/01; **(b)** photo of the loess cover in the gravel pit Wild; **(c)** soil profile with some laboratory analysis (carbonate content, grain sizes), and two luminescence ages.

dating results confirm the regional stratigraphy (Schellmann, 2017b) and match the warm temperate climate indicated by the gastropod species. The 2 to 5 m thick superimposed gravel unit with its braided river facies type is most probably of penultimate glacial age (Rissian, MIS 6).

### 4.4 ESR and luminescence data from the *Langweider Hochterrasse* (Lech valley)

Similar to the *Dillinger Hochterrasse* in the Danube valley, a subdivision of the Middle Pleistocene fluvial gravel deposits of the *Langweider Hochterrasse* between Lech and Schmutter valley in two different gravel formations has been discussed for decades (Schäfer, 1957; Scheuenpflug, 1979, 1981; Aktas and Frechen, 1991; Schellmann, 2016b; Schielein and Schellmann, 2016a). All these studies assume

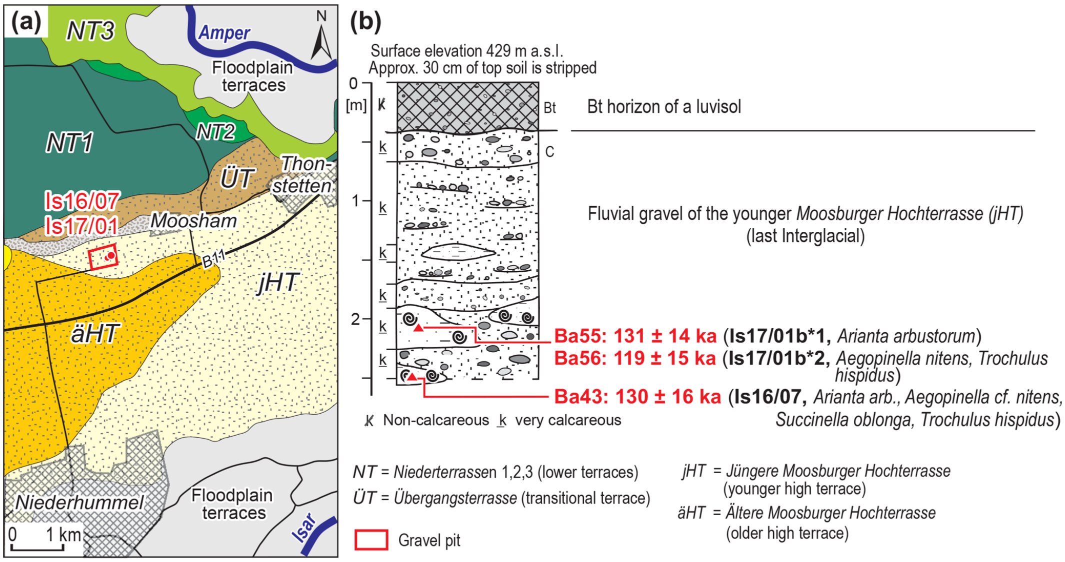


**Figure 8.** Marly and fine-sandy clods in the gravel deposits of the *Jüngere Moosburger Hochterrasse* (Fagotia gravel) west of Moosham, Amper valley (Fig. 1: sample site d; Table 1: samples Ba43, Ba55, Ba56). Small gastropods were collected and ESR dated from two separate clods in the years 2016 (sample Is16/07, Ba43) and 2017 (sample Is17/1, Ba55, Ba56); **(a)** geological map (modified after Schellmann, 2018b) with location of sample sites; **(b)** soil profile with ESR dated gastropod shells (species are listed in Table 3).

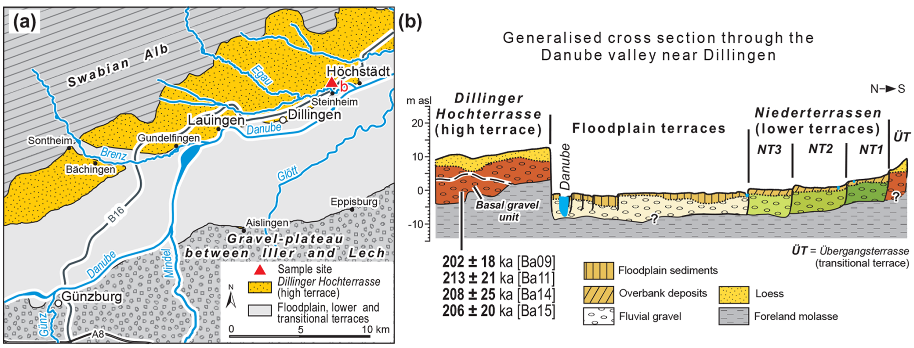


**Figure 9.** Distribution **(a)** and geological cross section **(b)** of the *Dillinger Hochterrasse* on the northern valley side of the river Danube between the villages Sontheim, Dillingen and Höchstädt (modified after Schellmann, 2017b).

a deposition of the 6 to 8 m thick top unit of the *Langweider Hochterrasse* during the penultimate glacial (Rissian), whereas the age of the basal gravel unit with thicknesses of 2 to 4 m remained uncertain. It was Schielein et al. (2015) who presented first luminescence data from both gravel units (Fig. 11) and one ESR age from the basal gravel deposit (Fig. 11: Le 11/26c; sample site: A11 Nachwegäcker). The luminescence data indicate a Rissian age of the superimposed gravel. Four IRSL samples from the basal gravel unit imply an age older than MIS 6, whereas the ESR dating of one large shell of *Succinea putris* refers to a deposition during the penultimate interglacial (MIS 7).

Small shells of the land-snail species *Trochulus hispidus* were collected from a clod of marl in the superimposed gravel (Fig. 11: sample site A7; Table 1: sample Ba12). The ESR age of 156 ± 21 ka is similar to IRSL ages of 160 ± 15 ka and of 163 ± 19 ka from sandy layers in the same gravel unit. Within error range, the ESR and luminescence ages also fit to two IRSL dates of 170 ± 18 and 179 ± 20 ka from the superimposed gravel in the neighbouring outcrop A8 Burghof W (Fig. 11). It can be stated that the superimposed gravel of the *Langweider Hochterrasse* was most likely accumulated during the penultimate glacial (MIS 6, Rissian), whereas the basal gravel unit has a minimum age of MIS 7 (Schielein et al., 2015). Most probably, the basal gravel formation may be correlated with the basal gravel deposit of the *Dillinger Hochterrasse*.

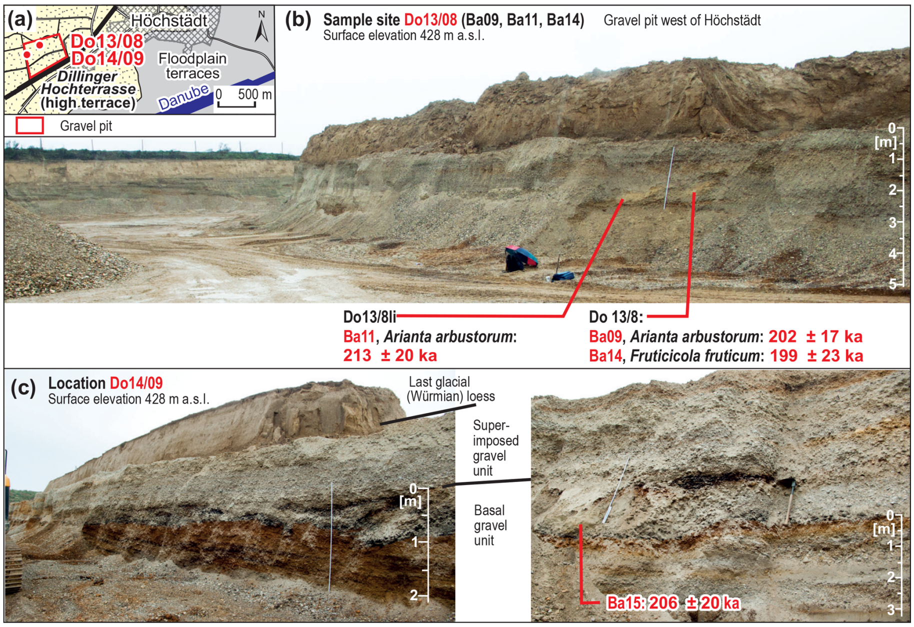


**Figure 10.** ESR dating results of an interglacial gastropod fauna from the basal gravel unit of the *Dillinger Hochterrasse* in the gravel pit Höchstädt W (Fig. 1: sample site b; Table 1: samples Ba09, Ba11, Ba14, Ba15); **(a)** geological map (modified after Schellmann, 2016b) with location of sample sites Do13/8 and Do14/9; **(b)** photo of sample site Do13/8 and ESR ages of the samples Ba09, Ba11, Ba14; **(c)** photos of the location Do14/9 with a large scale cross-stratified basal gravel unit and a horizontally bedded (braided river) top gravel unit (left), and the location and ESR age of sample Ba15 (right).

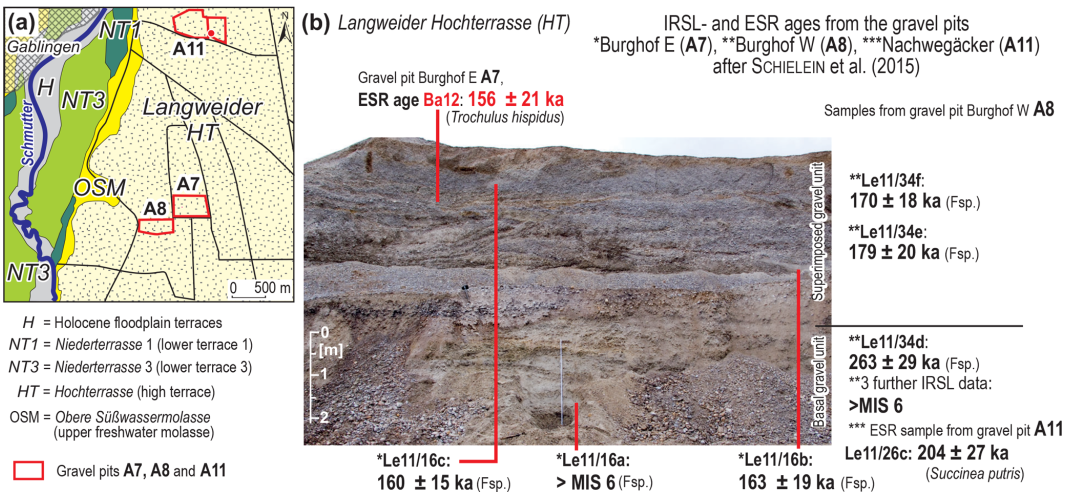


**Figure 11.** ESR and luminescence data from the stacked gravel deposits of the *Langweider Hochterrasse* in the gravel pit A7 Burghof E (Fig. 1: sample site a); **(a)** geological map (modified after Schellmann, 2018b; Schielein and Schellmann, 2016a) with location of sample sites; **(b)** photo with the newly dated ESR sample Ba12, and with some luminescence and ESR ages from Schielein et al. (2015). The latter are from the same outcrop (*), or from the nearby gravel pits A8 Burghof W (**) and A11 Nachwegäcker (***).

## 4.5 ESR and luminescence data from the *Rainer Hochterrasse* and from its loess cover (Lech valley)

Following the Lech valley downstream, a further high terrace is conserved near the confluence of Lech and Danube rivers: the *Rainer Hochterrasse* (Fig. 1: sample site c; Fig. 12). In contrast to Schaefer (1966), a clear morphostratigraphic subdivision of the Rainer Hochterrasse could not be confirmed (Schielein and Schellmann, 2016b) as already stated by Kilian and Löscher (1979). Only small areas of the significantly lower elevated surfaces of the *Übergangsterrasse* can be differentiated from the higher elevated areas of the *Rainer Hochterrasse* (Fig. 12).

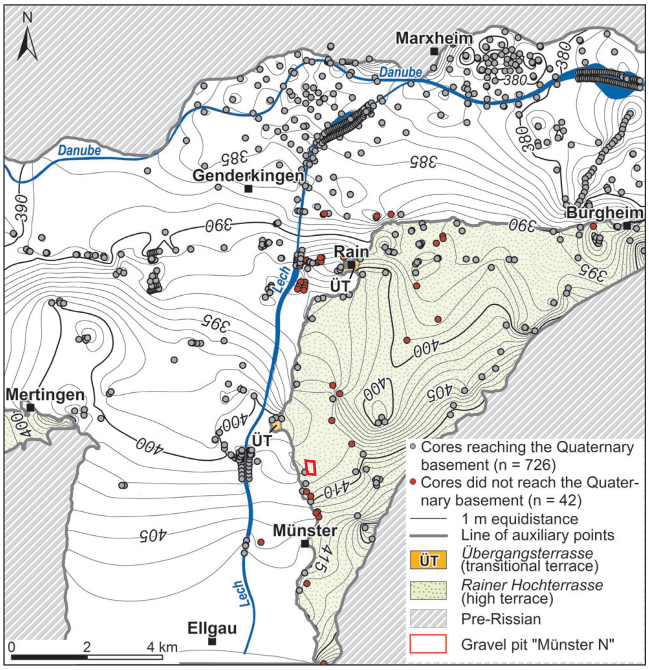


**Figure 12.** Geological map of the *Rainer Hochterrasse* with contour lines of the base level (m a. s.l.) of the Quaternary gravel deposits and location of the gravel pit Münster N mentioned in the text.

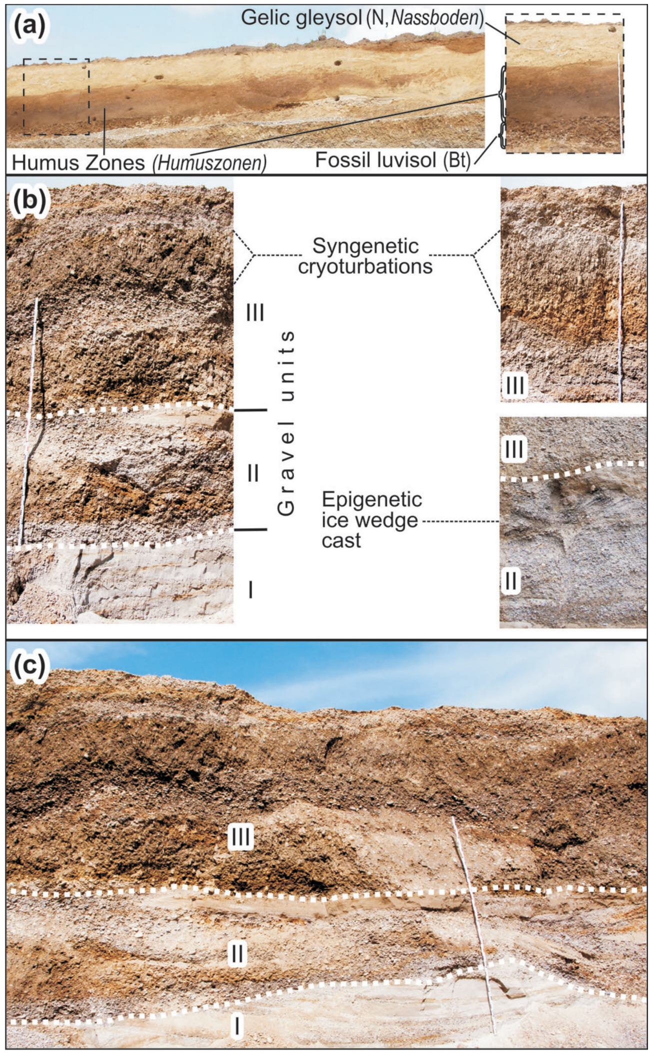


**Figure 13.** Images of the different fluvial gravel deposits of the *Rainer Hochterrasse* and the Würmian loess cover exposed in the gravel pit Münster N (Fig. 1: sample site c) during the last few years; **(a)** images of the loess cover exposed during the year 2009; **(b)** images of the three gravel units I to III exposed during the years 2016 and 2017; **(c)** image of the three gravel units I to III exposed during the year 2017.

The uniform terrace level of the *Rainer Hochterrasse* including some periglacial dry valleys is elevated about 10 to 14 m above the valley floor of the Lech and Danube rivers and its Würmian and Holocene terraces. The gravel deposits and the 1 to 3 m thick loess and sand loess cover reach thicknesses of 7 to 13 m in total. The base of the gravel deposits in the area of the *Rainer Hochterrasse* is about 8 to 10 m higher than the base level in the adjacent Upper Würmian and Holocene valley bottom (Fig. 12). In a southwest–northeast-orientated elongated depression extending in the central areas of the high terrace, a maximum thickness of the Quaternary sediments up to 15 m is reached (Fig. 12; Kilian and Löscher, 1979).

In one gravel pit north of the small village of Münster (gravel pit Münster N), which has been investigated by different researchers (e.g. Tillmanns et al., 1982, 1983; Schielein et al., 2015; Schielein and Schellmann, 2016b), the following summarised section has been exposed since 2016. Here, the *Hochterrassen* gravel is covered by 1 to 2.5 m thick loess sediments. In periglacial depressions, some decimetres thick layers of solifluidal reworked silts, sands and gravels (Fig. 14) are present. Up to three slightly rusty and grey Gelic Gleysols (tundra gley, *Nassboden*) may be preserved in the upper part of the fine-sandy loess cover. Similar weak Gelic Gleysols are most common in Upper Würmian loess deposits in Germany. In the lower part of a 2.6 m thick fine-grained infill of a periglacial trough valley, a stack of two humic horizons (*Humuszonen*) was preserved (details in Schielein and Schellmann, 2016b), which are comparable to the Lower (Early) Würmian *Mosbacher Humuszonen* (e.g. Semmel, 1968). Light reddish-brown spots in the upper part of the lower humic horizon correlate most probably to the "*gefleckten Horizont*" (spotted horizon) of Rohdenburg (1964) and might have been developed through acidic conditions by bleaching along plant roots. The Upper to Lower Würmian age of this loess cover is confirmed by the luminescence ages of 19.3 ± 2.2 ka (Fsp.) and 19.8 ± 2.7 ka (Qu.) from the top of the sandy loess cover, and of 95 ± 12 ka

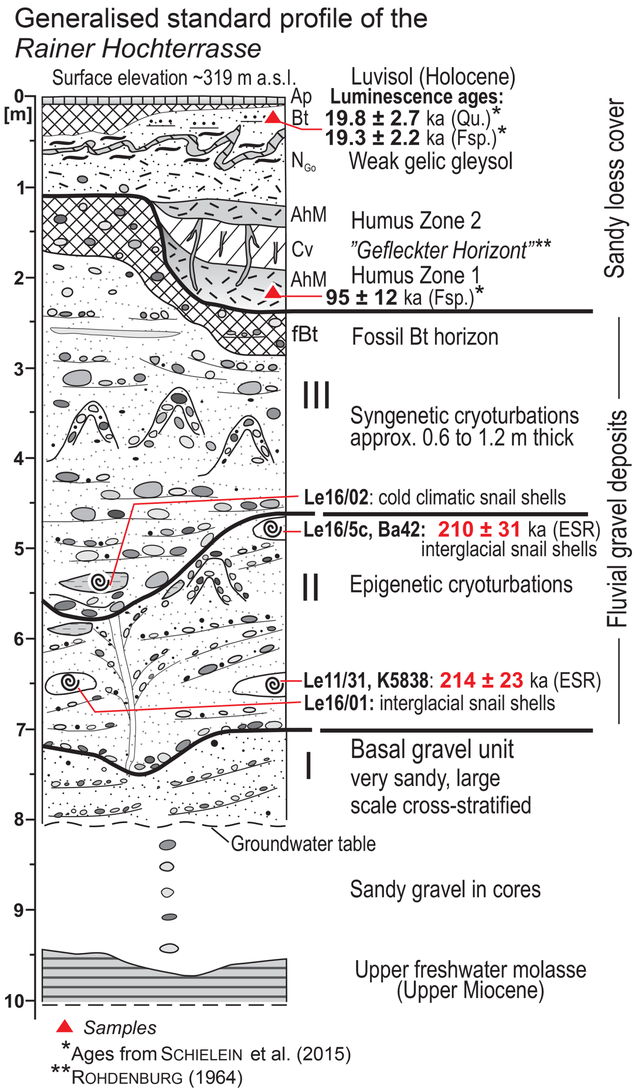


| Wet sieving, one vertical sample per gravel unit | Gravel I | Gravel II | Gravel III |
|---|---|---|---|
| | wt.% | wt.% | wt.% |
| Sand, silt, clay (<0.2 cm) | 35.5 | 16.2 | 19.5 |
| Fine - middle gravel (0.2–2.0 cm) | 64.3 | 61 | 32.6 |
| Coarse gravel (2.0–6.3 cm) | 0.2 | 19 | 26.3 |
| Stones (>6.3 cm) | | 3.8 | 21.1 |
| Max. diameter (cm) | | 8.5 | 11.5 |

**Figure 14.** Generalised standard profile of the different sediment units of the *Rainer Hochterrasse* exposed in the gravel pit Münster N (Fig. 1: sample site c) during the last few years. IRSL data from the loess cover are from Schielein et al. (2015); the ESR dating results of an interglacial gastropod fauna from the gravel unit II and the faunae collections are new.

(Fsp.) from the base of the lower humic horizon (Fig. 14; Schielein et al., 2015).

Below the loess cover, a fossil interglacial soil horizon (Bt horizon of a Luvisol; Fig. 14) with a mean thickness of 0.3 to 0.5 m is widely preserved on top of the *high terrace* gravels. In several outcrops, the 8 to 14 m thick sandy gravel deposits of the *Rainer Hochterrasse* can be subdivided into two stacked gravel units as previously mentioned by Tillmanns et al. (1982, 1983) and Schielein et al. (2015). In the aforementioned gravel pit Münster N, a third gravel unit is exposed below the other units near the groundwater table (Fig. 13). This very sandy and often large-scale cross-bedded or sometimes trough-bedded gravel unit I is often preserved approximately up to 1 to 2 m above the groundwater level (Fig. 14). The light colour of unit I is due to its high sand content of about 35 % and allows a clear separation from both superimposed gravel units, whose sand content is significantly lower (Fig. 14). The more than 1.5 m thick gravel unit II is predominately composed of fine to medium gravels but may contain coarse- and medium-sand layers with thicknesses of up to 1 m (Schielein et al., 2015). Sometimes epigenetic cryoturbations or small ice-wedge casts (Fig. 13) are preserved at the top of the gravel unit II. These periglacial features are overlain discordantly by the 2 to 5 m thick gravel deposits of unit III. The latter consists of medium and coarse gravel with many stones in a sandy matrix (Fig. 14), shows horizontal and trough-bedding, and exhibits strong syngenetic cryoturbations within the upper part of the unit (Fig. 13) as already described by Tillmanns et al. (1982, 1983).

In general, gravel units I and II are both large-scale cross-bedded, which indicate a deposition by a meandering or a moderate branching river like the Holocene river Lech. In contrast, the superimposed gravel unit III was accumulated by a braided river as it is characteristic of river morphology in this region under Pleistocene cold climate conditions.

Single clods of marl or sand can be preserved from the groundwater level up to the top of the gravel deposits. A separation of the whole gravel deposit by one significant layer of marly clods ("*Mergelbatzenhorizont*") as described by Tillmanns et al. (1982, 1983) was not comprehensible. All gravel units contain marly or loamy clods sometimes concentrated near the base of a gravel unit but often irregular within the gravel unit. As already described by Tillmanns et al. (1982, 1983) these clods sometimes contain shells of predominately cold (*Columella columella*, *Pupilla muscorum*, *Succinea oblonga*, *Trichia hispida*) and rarely warm (*Ena montana*, *Discus rotundatus*, *Aegopinella* sp., *Helicondonta obvoluta*, *Cepaea* sp.) gastropod fauna. A cold climatic or interstadial gastropod fauna could be sampled from a marly clod embedded at the base of gravel unit III at approx. 5.5 m below terrace surface (Fig. 14: Le16/2). This clod contained shells from the following species: *Cochlicopa lubrica*, *Pupilla muscorum*, *Neostyriaca corynodes*, *Succinella oblonga*, *Trochulus hispidus*, *Vallonia costata* and *Vallonia pulchella*. Shells from *Cochlicopa lubrica*, *Pupilla muscorum*, *Succinella oblonga*, *Vallonia costata* and *Vallonia pulchella* have been sampled also from marly clods with cold climatic gastropod fauna in 5 to 6 m below terrace surface by Tillmanns et al. (1982).

Both the cold climatic habitus of the gastropod fauna and the strong syngenetic cryoturbations clearly point to a deposition of gravel unit III under periglacial, stadial or interstadial climatic conditions older than the Early to Late Würmian loess and older than the interglacial Bt horizon on top of the gravel deposits. The upper gravel unit is most probably of penultimate glacial (Rissian, MIS 6) age.

In contrast, two loamy clods from gravel unit II contain interglacial fauna. The following warm temperate species could be sampled from a loamy clod from gravel unit II in 4.8 m below surface (Fig. 14: Le16/5c): *Aegopis verticillus*, *Cepaea* sp. (*nemoralis*?), *Cochlodina laminata*, *Helicodonta obvoluta*, *Isognomostoma isognomostomos* and *Monachoides incarnatus*. A further loamy clod from gravel unit II in a depth of 6.5 m below surface contains shells of the warm temperate species *Aegopinella* sp., *Helicodonta obvoluta*, and *Monachoides incarnatus* (Fig. 14: Le16/1). These species have already been sampled by Tillmann et al. (1982) in this outcrop area from a marly clod with warm climatic gastropod fauna at approx. 5 m below terrace surface.

*Helicodonta obvoluta* and *Aegopis verticillus* shells from a loamy clod (Fig. 14: Ba42) and one large shell fragment from a layer of fine-sandy loam (Fig. 14: K5838) yielded almost identical ESR ages of 210 ± 31 and 214 ± 23 ka, respectively. Hence, the formation of gravel unit II during penultimate interglacial (MIS 7) is very likely. Schielein et al. (2015) published four luminescence (IRSL, OSL) ages from one sand layer at the top of gravel unit II in a nearby gravel pit, but the data scatter between MIS 7 and MIS 9.

The age of the underlying gravel unit I is still open. It could have been deposited under warm climate conditions as indicated by the sedimentological observations, perhaps during the MIS 7 interglacial period.

**Table 5.** Stratigraphical overview for the formation of Middle and Upper Pleistocene gravel deposits in the Bavarian Alpine Foreland.

| International: Age (Ka) | Marine Isotop. Stage | System | (Sub-)Series | Bavaria: Strati-graphy | | Terraces |
|---|---|---|---|---|---|---|
| 11,5 | 1 | QUATERNARY | Holocene | Würmian | | H7 to H1 *Holozänterrassen* (Holocene terraces) |
| 30 | 2 | | Upper (Late) Pleistocene | | Upper | NT3 NT2 NT1 *Niederterrassen* (lower terraces) |
| 70 | 3 - 4 | | | | Middle | ÜT2 loess cover is as old as 29 to 31 ka gravel deposition: 30.4 ± 3.7 (Qu.); 36.0 ± 1.9 (Fsp.)* *Übergangsterrassen* (transitional terraces) |
| 115 | 5a - 5d | | | | Lower | ÜT1 |
| 130 | 5e | | | *Riß/ Würmian* | | JHT *Jüngere Moosburger Hochterrasse* (*Fagotia* gravel) (approx. 119 to 131 ka; ESR) |
| | 6 - 10 | | Middle Pleistocene | Rissian | | HT *Langweider, Dillinger, Rainer Hochterrasse* (high terraces) top gravel unit: MIS 6 (approx. 156 to 179 ka; ESR, luminescence) basal gravel, gravel unit II: MIS 7 (approx. 199 to 214 ka; ESR) |
| | 11 | | | *Mindel/ Rissian* | | |

* luminescence data from Kroemer (2010)

International and Bavarian stratigraphic nomenclature modified after Doppler et al. (2011)

## 5 Discussion

Numerical age data (ESR, OSL, $^{14}$C) indicate that the formation of the two *Übergangsterrassen* (ÜT1, ÜT2) in the Bavarian Alpine Foreland took place before the Upper Würmian (MIS 2) and thus before the formation of the oldest *Niederterrasse* 1 (NT1) and the loess accumulation on top of the fluvial gravel deposit during MIS 2 (Table 5). In the valley of the river Isar in the vicinity of the village of Moosburg, it could be shown by geological mapping that both *Übergangsterrassen* are younger than the *Jüngere Moosburger Hochterrasse* (i.e. Fagotia gravel) of MIS 5e age. Luminescence data by Kroemer (2010) from a sandy layer in the fluvial gravel deposit of the ÜT2 in the Danube valley west of the Natternberg imply a late Middle Würmian age (MIS 3). This correlates well with the fact that only Upper Würmian loess covers the *Übergangsterrassen* gravel. Previously, Buch and Zöller (1990; see also discussion by Schellmann, 2010) published early Upper Würmian luminescence ages of 25.4 ± 2.4 and 24.1 ± 2.4 ka respectively from the base of the loess cover on the younger *Übergangsterrasse* (ÜT2; Schellmann, 2010) of the Danube southeast of Regensburg (Fig. 1). Buch and Zöller (1990) called this loess-covered terrace level "*Deckniveau der Niederterrasse*".

In contrast to the younger *Übergangsterrasse* (ÜT2), the age of the older ÜT1 is still unknown. But the ÜT1 is younger than the MIS 5e old *Jüngere Moosburger Hochterrasse*. Therefore, the ÜT1 is most likely of Early Würmian age (MIS 5d to MIS 4). Doppler et al. (2011, p. 354) assume that the relatively young OSL data of ∼ 70 to ∼ 90 ka by Fiebig and Preusser (2003) for parts of the *Rainer Hochterrasse*, for the *Neuburger* as well as the *Ingolstädter Hochterrasse* most likely point to a classification as *Übergangsterrasse*.

At this point, a short but stratigraphically important digression to northern Germany may be excused. In the Upper Weser valley between the villages of Hamelin (Hameln in German) and Rinteln, an *Übergangsterrasse* is preserved (Schellmann, 1994). The terrace is younger than the Drenthe glaciation (MIS 6; Lang et al., 2018) of the valley and older than the Upper Weichselian (Upper Pleistocene) *Niederterrasse 1*. At the gravel pit Franke (geological map in Schellmann, 1994: Fig. 6), Winsemann et al. (2015) postulated on the basis of one luminescence dated sample (79 ± 3 ka) a loess-covered lower middle terrace (*Untere Mittelterrasse*), which can likely be correlated to the *Übergangsterrasse* mapped by Schellmann (1994) in this area.

Until now, the only known terrace of last interglacial age in the Bavarian Alpine Foreland was the *Jüngere Moosburger Hochterrasse* (Fagotia gravel). The interglacial formation of this gravel deposit has been known for many years by the finding of shells from interglacial gastropod fauna embedded in sand lenses and loamy clods. They were described first by Nathan (1953), Brunnacker and Brunnacker (1962), and Brunnacker (1965). The ESR data (Table 1) of three shell samples with ages of 131±14, 130±16 and 119±15 ka point to a last interglacial (MIS 5e) age of this terrace (Table 5) instead of an age older than the Elsterian glaciation in northern Germany as postulated by Kovanda (2006).

Generally, the *Hochterrassen* in the Bavarian Alpine Foreland were formed under cold climatic conditions during the Rissian period. Therefore, they are covered by loess sediments of Würmian age only, and just a relict of one interglacial soil (Bt horizon of a Luvisol) may be preserved at the top of their fluvial gravel deposits. Most recently, Mayr et al. (2017) published new numeric age data with Würmian ages from the loess cover and its palaeosoils preserved on an interglacial soil relict (Bt horizon of a Luvisol) at the top of the fluvial gravel deposit of the *Augsburger Hochterrasse* (Fig. 1). In some river valleys, especially in such areas with unusual thick fluvial sediment accumulations, older gravel deposits (basal gravel) may have been covered by the extensive *Hochterrassen* gravel accumulations (top gravel) during the Rissian. IRSL and ESR data from the top gravel of the *Langweider Hochterrasse* in the Lech valley indicate a penultimate glacial (MIS 6) age of the top gravel unit (Table 5). Similar old luminescence data have been published by Becker-Haumann and Frechen (1997) and Frechen (1999) from the gravel deposits of the *Augsburger Hochterrasse*. This penultimate glacial age (MIS 6) corresponds very well with the MIS 6 age of the high terrace in the type locality of the Rissian (Penck and Brückner, 1901–1909) at the northeastern margin of the former Rhine glacier. There, Rades et al. (2018) dated "high terrace gravels" in the gravel pit Scholterhausen (Biberach am Riß) via single-grain feldspar luminescence to an age range between 149 ± 15 and 179 ± 17 ka. These ages may correspond with luminescence data of 116 ± 17 ka and 142 ± 15 (OSL), and 122 ± 18 and 210±24 ka (IRSL) by Bickel et al. (2015) on sediments from glaciofluvial deposits linked to penultimate glaciation in the Eastern Alps. In contrast, Fiebig and Preusser (2003) dated sediments from the gravel pit Münster via IRSL, which they associated with the *Rainer Hochterrasse*. They yielded Early Würmian ages between ∼ 66 and ∼ 81 ka. Whereas Rades et al. (2018) assume an anomalous fading of these samples, Schielein et al. (2015) state that these samples could be derived from gravel deposits of the *Übergangsterrasse* and not of the *Rainer Hochterrasse*.

A penultimate glacial age of the superimposed top gravel unit in the *Langweider*, *Dillinger* and *Rainer Hochterrasse* is also implied by penultimate interglacial ages of the underlying older gravel units. But the luminescence (IRSL) dating of sandy layers in the basal gravel of the *Langweider Hochterrasse* seems to reach its upper dating limit (Schielein et al., 2015). Only one of the five luminescence samples allowed a proper age estimation. Its age of 263 ± 29 ka indicates a deposition between MIS 7 and MIS 8. In contrast, the ESR age of a *Succinea putris* shell of 204 ± 27 ka (Schielein et al., 2015) implies a deposition during the penultimate interglacial MIS 7. The latter agrees very well with the MIS 7 ESR ages of four land-snail shells from the basal gravel unit of the *Dillinger Hochterrasse* with ages of 199 ± 23, 202 ± 17, 206 ± 20, and 213 ± 20 ka, and two ESR ages of 210 ± 31 and 214 ± 23 ka from the medium-gravel unit II of the *Rainer Hochterrasse* (Table 1). The reliability of these MIS 7 dating results is additionally strengthened by the interglacial character of gastropod fauna collected from the basal, medium-gravel deposits of the *Dillinger* and *Rainer Hochterrasse*. Most probably, the basal gravel formation of the *Jüngere Hochterrasse* (HT1 sensu Schellmann, 1988) in the Danube valley downstream of Regensburg, which is also preserved in some metres deep troughs eroded in the Tertiary basement, may correlate with these older penultimate interglacial gravel deposits at the base of the *Rainer* and *Dillinger Hochterrasse*.

The oldest gravel units at the base of *Hochterrassen* deposits are the sand-rich gravel unit I of the *Rainer Hochterrasse* and the interglacial peat and gravel deposits of the "*Hartinger Schichten*" at the base of the oldest *Hochterrasse* south of Regensburg (Schellmann, 1988; Schellmann et al., 2010). Their ages are still unknown.

Interglacial gravel units at the base of superimposed cold climatic *Hochterrassen* gravels illustrate that fluvial downcutting in some valley parts far away from areas of Pleistocene glaciations happened not only in the Würmian late glacial and Early Holocene (e.g. Schellmann, 2010; Schielein et al., 2011), but also during older interglacial periods. In some valley parts, this erosion reached down to the surface of the recent valley floor or even below. In the Lech valley south of Augsburg, the deepest valley erosion most probably was reached during the last interglacial. There, older gravel deposits embedded in a deep trough in the Miocene molasse basement are distributed below calcareous sinter sediments, the "*Hurlacher Kalktuff*" (Jerz and Mangelsdorf, 1989; Gesslein, 2013). Both the fluvial and the sinter sediments contain an interglacial mollusc fauna (Kovanda, 1989). They were dated by uranium–thorium (U–Th) to approx. 120 ka (MIS 5e) (Jerz and Mangelsdorf, 1989). However, in many valleys of the Bavarian Alpine Foreland (Danube, lower Lech, Isar, Amper, Schmutter, Große Laber), the Würmian late glacial and Holocene erosion undercut the base level of older Pleistocene river dynamics (e.g. Schellmann, 2010; Schielein, 2012; Schellmann, 2016a, 2017a, 2018a).

As demonstrated, ESR dating of gastropods appears to be a viable alternative to luminescence methods applied to quartz (OSL) and feldspar (IRSL). The latter are the usually used methods for dating fluvial and glaciofluvial deposits in the Northern Alpine Foreland. However, luminescence data from Pleistocene fluvial deposits often show a large scattering of the dating results, and often show a low accuracy (e.g. Klasen, 2008; Klasen et al., 2016; Schielein et al., 2015; Rades et al., 2018; Trauerstein et al., 2017). In addition to providing an independent age control, ESR dating of gastropods also offers the advantage of a higher upper dating limit, which is supposedly larger than MIS 7, most probably similar to that of marine mollusc shells and corals (e.g. Schellmann et al., 2018). But in most fluvial–glaciofluvial and aeolian deposits, often only very small gastropod shells are preserved, which necessitates the reduction of the sample size of individual aliquots to a minimum (up to ca. 0.02 g instead of the commonly used 0.2 g). In some instances, it is even necessary to mix some specimen from the same or even different species. However, the mixture of individuals or different species as well as the reduction of sample weight seems not to influence the dating results.

## 6 Conclusions

In summary, the here presented new numeric age data permit a more accurate chronostratigraphic classification of the Würmian *Übergangsterrassen* ÜT1 and ÜT2, and of some of the stacked *Hochterrassen* deposits in the Bavarian Alpine Foreland. ESR, $^{14}$C and luminescence data imply that loess sedimentation on the ÜT starts in the early Upper Würmian (MIS 2), and luminescence data by Kroemer (2010) imply an accumulation of the younger ÜT2 gravel deposit during the late Middle Würmian (MIS 3). The ÜT1 is older than the ÜT2 and younger than the last interglacial (MIS 5e) formation of the *Jüngere Moosburger Hochterrasse*. In this respect, the ÜT1 was formed after MIS 5e and before MIS 3. MIS 5e old ESR data from interglacial gastropod fauna embedded in the *Jüngere Moosburger Hochterrasse* (Fagotia gravel) indicate a formation during the last interglacial as it was already assumed on basis of morphostratigraphy (e.g. Brunnacker, 1965; Schellmann, 2018b) and gastropod assemblages (Nathan, 1953; Brunnacker and Brunnacker, 1962; Brunnacker, 1966). Most of the *Hochterrassen* deposits in the Bavarian Alpine Foreland were formed during the penultimate glacial (MIS 6). This is pointed out by luminescence and ESR data from the youngest gravel deposits (top gravel unit) of the *Langweider Hochterrasse*. A deposition under cold climate conditions is indicated by the occurrence of syngenetic cryoturbations and cold gastropod fauna, which were already described by many studies in the past. However, most remarkable are the ESR dating results of snail shells from the gravel unit below the MIS 6 top gravel unit in some areas of the *Langweider*, *Dillinger* and *Rainer Hochterrasse*. All ESR data imply a deposition of these sandy basal gravel units during the penultimate interglacial (MIS 7), and the warm temperate habitus of the gastropod assemblages supports this assumption.

All in all, the ESR ages and their error ranges are mostly within the age interval of luminescence (IRSL, OSL) or radiocarbon dating results. The ESR dating of small terrestrial gastropods allows differentiating land-snail shells of Upper or Middle Würmian (last glacial), penultimate glacial (MIS 6) or penultimate interglacial (MIS 7) age and with error ranges between ca. 10 % and 15 %.

**Data availability.** Most of the data are included in the paper. ESR raw data are stored at the Department of Physical Geography of the University of Bamberg. They are still part of further research but can be obtained upon reasonable request.

**Author contributions.** Fieldwork (geological mapping, descriptions, sampling) was carried out by GS and PS. ESR measurements were performed by CB and PS under the supervision of GS. ESR age calculations were done by GS and luminescence age calculations by PS. Analysis of the gastropod fauna remains was carried out by WR. GS prepared the manuscript and figures.

**Competing interests.** The authors declare that they have no conflict of interest.

**Special issue statement.** This article is part of the special issue “Connecting disciplines – Quaternary archives and geomorphological processes in a changing environment”. It is a result of the First Central European Conference on Geomorphology and Quaternary Sciences, Gießen, Germany, 23–27 September 2018.

**Acknowledgements.** This study was funded by the Bavarian Environment Agency (LfU) in the framework of the EU-funded project “Informationsoffensive Oberflächennahe Geothermie” and by the University of Bamberg. We thank Ernst Kroemer and Gerhard Doppler (Bavarian Geological Survey) for numerous field excursions and technical support. We also would like to greatly thank Helmut Brückner (University of Cologne) for permission to use his ESR facilities and Rainer Drewello (University of Bamberg) for permission to use his REM facilities. We are also very thankful to Roland Beer (University of Bamberg), who did much of the necessary laboratory work, including thickness measurements of the shells and $\gamma$ irradiation of the aliquots at the Helmholtz Center in Munich, and to Matthias Will, who did some luminescence measurements at the ”Zöller” laboratory at the University of Bayreuth. Last but not least, we would also like to thank Silke Schwieger (Bamberg) for the very dedicated GIS and graphic work. The helpful comments of Ernst Kroemer, Johanna Lomax and an anonymous reviewer contributed to improving the manuscript.

## References


Adamiec, G. and Aitken, M.: Dose-rate conversion factors: update, Ancient TL, 16, 37–50, 1998.

Aktas, A. and Frechen, M.: Mittel- bis jungpleistozäne Sedimente der Hochterrassen in der nördlichen Iller-Lech-Platte, Sonderveröff, Geol. Inst. Univ. zu Köln, 82, 19–41, 1991.

Becker-Haumann, R. and Frechen, M.: Vergleichende Lumineszenzdatierungen mit IRSL und TL am Deckschichtenprofil Bobingen/Lechtal, Z. Geol. Wiss., 25, 617–633, 1997.

Bibus, E. and Strahl, M.: Zur Gliederung und Altersstellung der bayerischen Hochterrassen nördlich des Donauriedes, Z. Geomorph. N.F., 44, 211–232, 2000.

Bickel, L., Luthgens, C., Lomax, J., and Fiebig, M.: Luminescence dating of glaciofluvial deposits linked to the penultimate glaciation in the Eastern Alps, Quaternary Int., 357, 110–124, 2015.

Borylo, A. and Skwarzec, B.: Activity disequilibrium between $^{234}U$ and $^{238}U$ isotopes in natural environment, J. Radioanal. Nucl. Chem., 300, 719–727, 2014.

Brunnacker, K.: Die bodenkundlichen Verhältnisse der würmeiszeitlichen Schotterfluren im Illergebiet, Geologica Bavarica, 18, 113–130, 1953.

Brunnacker, K.: Die Deckschichten und Paläoböden über dem Fagotien-Schotter westlich von Moosburg, N. Jb. Geol. Paläont. Mh., 1966, 214–227, 1966.

Brunnacker, M. and Brunnacker, K.: Weitere Funde pleistozäner Molluskenfaunen bei München, Eiszeitalter u. Gegenwart, 13, 129–137, 1962.

Buch, M. W. and Zöller, L.: Gliederung und Thermolumineszenz-Chronologie der Würmlösse im Raum Regensburg, Eiszeitalter u. Gegenwart, 40, 63–84, 1990.

Doppler, G., Kroemer, E., Rögner, K., Wallner, J., Jerz, H., and Grottenthaler, W.: Quaternary Stratigraphy of Southern Bavaria, E&G Quaternary Sci. J., 60, 23, https://doi.org/10.3285/eg.60.2-3.08, 2011.

Eberl, B.: Die Eiszeitenfolge im nordlichen Alpenvorlande – Ihr Ablauf, ihre Chronologie auf Grund der Aufnahmen des Lech- und Illergletschers, Benno Filser Verlag, Augsburg, 427 pp., 1930.

Fiebig, M. and Preusser, F.: Das Alter fluvialer Ablagerungen aus der Region Ingolstadt (Bayern) und ihre Bedeutung für die Eiszeitenchronologie des Alpenvorlandes, Z. Geomorph. N.F., 47, 449–467, 2003.

Frechen, M.: Upper Pleistocene loess stratigraphy in Southern Germany, Quat. Geochronol., 18, 243–269, 1999.

Gesslein, B.: Zur Stratigraphie und Altersstellung der jungquartären Lechterrassen zwischen Hohenfurch und Kissing unter Verwendung hochauflösender Airborne-LiDAR-Daten, Bamberger Geographische Schriften, SF 10, 148 pp., 2013.

Goodfriend, G. A. and Stipp, J. J.: Limestone and the problem of radiocarbon dating of land-snail shell carbonate, Geology, 11, 575–577, 1983.

Graul, H.: Zur Morphologie der Ingolstädter Ausräumungslandschaft, Forschungen zur deutschen Landeskunde, 43, 114 pp., 1943.

Graul, H.: Eine Revision der pleistozänen Stratigraphie des schwäbischen Alpenvorlandes, Petermann Geogr. Mitt., 106, 253–271, 1962.

Grün, R.: Electron Spin Resonance Dating, Encyclopedia of Quaternary Science, 2, 1505–1516, 2007.

Grün, R.: The DATA program for the calculation of ESR age estimates on tooth enamel, Quat. Geochronol., 4, 231–232, 2009.

Grün, R. and Katzenberger, O.: An alpha irradiator for ESR dating, Ancient TL, 12, 35–38, 1994.

Inoue, K., Hirai, M., Ikeya, M., and Yim, W.: Calibration method for ESR Signal intensity of calcitic shells, Appl. Magn. Reson., 19, 255–269, 2000.

Jerz, H.: Das Eiszeitalter in Bayern – Erdgeschichte, Gesteine, Wasser, Boden, Schweizerbart, Stuttgart, 243 pp., 1993.

Jerz, H. and Mangelsdorf, J.: Die interglazialen Kalksinterbildungen bei Hurlach nördlich Landsberg am Lech, Eiszeitalter u. Gegenwart, 39, 29–32, 1989.

Kilian, R. and Löscher, M.: Zur Stratigraphie des Rainer Hochterrassen-Schotters östlich des unteren Lechs, Heidelberger Geographische Arbeiten, 49, 210–217, 1979.

Klasen, N.: Lumineszenzdatierung glazifluvialer Sedimente im nördlichen Alpenvorland, Ph.D. thesis, University of Cologne, Germany, 209 pp., 2008.

Klasen, N., Fiebig, M., and Preusser, F.: Applying luminescence methodology to key sites of Alpine glaciations in Southern Germany, Quaternary Int., 420, 249–258, 2016.

Kovanda, J.: Fossile Mollusken in Kalksinterbildungen (Dauchen) am Lechufer östlich von Hurlach (nördlich Landsberg/Lech), Eiszeitalter u. Gegenwart, 39, 33–41, 1989.

Kovanda, J.: "Fagotia-Faunen" und quadriglazialistisches stratigraphisches System des Pleistozäns im nördlichen Alpenvorland im Vergleich zu einigen Fundorten im Bereich der nordischen Vereisung Deutschlands, J. Geol. Sci. Anthrop., 26, 5–37, 2006.

Kroemer, E.: Fluviale Geomorphodynamik der Donau im Bereich des Rückstaus durch das Isarmündungsgebiet bei Deggendorf (Niederbayern) und Aussagen zur späthochglazialen und spätglazialen Entwicklung, Bamberger Geographische Schriften, 24, 79–87, 2010.

Kulig, G.: Erstellung einer Auswertsoftware zur Altersbestimmung mittels Lumineszenzverfahren unter besonderer Berücksichtigung des Einflusses radioaktiver Ungleichgewichte in der 238U-Zerfallsreihe, B.Sc. Thesis, TU Bergakademie Freiberg, Germany, 2005.

Lang, J., Lauer, T., and Winsemann, J.: New age constraints for the Saalian glaciation in northern central Europe: Implication for the extent of ice sheets and related proglacial lake systems, Quaternary Sci. Rev., 180, 240–259, 2018.

Leger, M.: Géomorphologie de la vallée subalpine du Danube entre Sigmaringen et Passau, Thèse du doctorat, Univ. Paris VII, 621 pp., 1988.

Low, S. and Zeira, S.: ESR spectra of $Mn^{2+}$ in heat-treated Aragonite, Am. Mineral., 57, 1115–11124, 1972.

Mayr, C., Matzke-Karasz, R., Stojakowits, P., Lowick, S. E., Zolitschka, B., Heigl, T., Mollath, R., Theuerkauf, M., Weckend, M.-O., Bäumler, R., and Gregor, H.-J.: Palaeoenvironments during MIS 3 and MIS 2 inferred from lacustrine intercalations in the loess–palaeosol sequence at Bobingen (southern Germany), E&G Quaternary Sci. J., 66, 73–89, https://doi.org/10.5194/egqsj-66-73-2017, 2017.

Miara, S.: Deckschichtenuntersuchungen zur Gliederung der Rißeiszeit beiderseits der Iller im Gebiet des Rhein- und Illergletschers (westliches Alpenvorland, Deutschland), Jahresberichte und Mitteilungen des oberrheinischen geologischen Vereins N.F., 78, 359–374, 1996.

Miara, S. and Rögner, K.: Die glazifluvialen Sedimente im unteren Günztal (Bayerisch Schwaben/Deutschland) nach morpho- und pedostratigraphischen Befunden sowie TL-Daten, Eiszeitalter u. Gegenwart, 45, 32–47, 1996.

Molodkov, A.: ESR Dating of Quaternary Shells: recent advances, Quaternary Sci. Rev., 7, 477–484, 1988.

Molodkov, A.: ESR-Dating of Non-marine Mollusc Shells, Appl. Radiat. Isot., 44, 145–148, 1993.

Murray, A. S. and Wintle, A. G.: The single aliquot regenerative dose protocol: Potential for improvements in reliability, Radiat. Meas., 37, 377–381, 2003.

Nathan, H.: Ein interglazialer Schotter südlich Moosburg in Oberbayern mit *Fagotia acicularis* Fèrussac (Melanopsenkies), Geologica Bavarica, 19, 315–334, 1953.

Penck, A.: Ueber Periodicität der Thalbildung, Verh. Ges. f. Erdkunde, XI, 39–59, 1884.

Penck, A. and Brückner, E.: Die Alpen im Eiszeitalter, 3 Bde., Tauchnitz, Leipzig, 1199 pp., 1901–1909.

Pigati, J. S., Rech, J. A., and Nekola, J. C.: Radiocarbon dating of small terrestrial gastropod shells in North America, Quat. Geochronol., 5, 519–532, 2010.

Prescott, J. R. and Hutton, J. T.: Cosmic ray contributions to dose rates for luminescence and ESR dating: large depths and long-term time variations, Radiat. Meas., 23, 497–500, 1994.

Rades, E. F., Fiebig, M., and Lüthgens, C.: Luminescence dating of the Rissian type section in southern Germany as a base for correlation, Quaternary Int., 478, 38–50, 2018.

Reimer, P. J., Bard, E., Bayliss, A., and Beck, J. W.: IntCal13 and Marine13 Radiocarbon Age Calibration Curves 0–50 000 Years cal BP, Radiocarbon, 55, 1869–1887, 2013.

Rögner, K., Löscher, M., and Zöller, L.: Stratigraphie, Paläogeographie und erste Thermolumineszenzdatierungen in der westlichen Iller-Lech-Platte (Nördliches Alpenvorland), Z. Geomorph. N.F., 70, 51–73, 1988.

Rohdenburg, H.: Ein Beitrag zur Deutung des "Gefleckten Horizonts", Eiszeitalter u. Gegenwart, 15, 66–71, 1964.

Schaefer, I.: Die Würmeiszeit im Alpenvorland zwischen Riß und Günz, Abhandlungen des Naturkunde- und Tiergartenvereins für Schwaben, Geologisch-Paläontologische Reihe 1, Schwabenlandverlag, Augsburg, 1940.

Schaefer, I.: Zur Gliederung der Würmeiszeit im Illergebiet, Geologica Bavarica, 18, 13–64, 1953.

Schaefer, I.: Geologische Karte von Augsburg und Umgebung 1 : 50 000 mit Erläuterungen, Bayerisches Geologisches Landesamt, München, Germany, 92 pp., 1957.

Schaefer, I.: Der Talknoten von Donau und Lech, Mitteilungen Geographische Gesellschaft München, 51, 59–111, 1966.

Schellmann, G.: Jungquartäre Talgeschichte an der unteren Isar und der Donau unterhalb von Regensburg, Ph.D. thesis, University of Düsseldorf, Germany, 332 pp., 1988.

Schellmann, G.: Fluviale Geomorphodynamik im jüngeren Quartär des unteren Isar- und angrenzenden Donautales, Düsseldorfer Geogr. Schr., 29, 131 pp., 1990.

Schellmann, G.: Zur Talgeschichte der unteren Oberweser im jüngeren Quartär, Düsseldorfer Geographische Schriften, 34, 1–56, 1994.

Schellmann, G.: Neue Befunde zur Verbreitung, geologischen Lagerung und Altersstellung der würmzeitlichen (NT1 bis NT3) und holozänen (H1 bis H7) Terrassen im Donautal zwischen Regensburg und Bogen, Bamberger Geographische Schriften, 24, 1–77, 2010.

Schellmann, G. (Ed.): Bamberger physisch-geographische Studien 2008–2015, Teil III: Geomorphologisch-quartärgeologische Kartierungen im bayerischen Lech-, Wertach- und Schmuttertal, Bamberger Geographische Schriften, 12, 356 pp., 2016a.

Schellmann, G.: Quartärgeologische Karte von Bayern 1 : 25 000 des Schmuttertals auf Blatt Nr. 7530 Gablingen mit Erläuterungen, Bamberger Geographische Schriften, 12, 1–40, 2016b.

Schellmann, G. (Ed.): Bamberger physisch-geographische Studien 2012–2014, Teil IV: Geomorphologisch-quartärgeologische Kartierungen im bayerischen Donautal zwischen Sontheim und Dillingen, Bamberger Geographische Schriften, 13, 237 pp., 2017a.

Schellmann, G.: Quartärgeologische Karte 1 : 25 000 des Donautals auf Blatt 7428 Dillingen West mit Erläuterungen, Bamberger Geographische Schriften, 13, 69–187, 2017b.

Schellmann, G. (Ed.): Bamberger physisch-geographische Studien 2008–2017, Teil V: Geomorphologisch-quartärgeologische Kartierungen im bayerischen Isar- und Donautal sowie im Tal der Großen und der Kleinen Laber, Bamberger Geographische Schriften, 14, 252 pp., 2018a.

Schellmann, G.: Quartärgeologische Karte 1 : 25 000 des Isar- und Ampertals auf Blatt 7537 Moosburg mit Erläuterungen, Bamberger Geographische Schriften, 14, 1–104, 2018b.

Schellmann, G. and Kelletat, D.: Chronostratigraphische Untersuchungen litoraler und äolischer Formen und Ablagerungen an der Südküste von Zypern mittels ESR-Altersbestimmungen an Mollusken- und Landschneckenschalen, Essener Geographische Arbeiten, 32, 75–98, 2001.

Schellmann, G. and Radtke, U.: Problems encountered in the determination of dose and dose rate in ESR dating of mollusc shells, Quaternary Sci. Rev., 18, 1515–1527, 1999.

Schellmann, G. and Radtke, U.: Progress in ESR dating of Pleistocene corals – a new approach for $D_E$ determination, Quaternary Sci. Rev., 20, 1015–1020, 2001.

Schellmann, G., Beerten, K., and Radtke, U.: Electron sin resonance (ESR) dating of Quaternary materials, E&G Quaternary Sci. J., 57, 150–178, https://doi.org/10.3285/eg.57.1-2.6, 2008.

Schellmann, G., Irmler, R., and Sauer, D.: Zur Verbreitung, geologischen Lagerung und Alterstellung der Donauterrassen auf Blatt L7141 Straubing, Bamberger Geographische Schriften, 24, 89–178, 2010.

Schellmann, G., Brückner, H., and Brill, D.: Geochronology, in: Encyclopedia of Coastal Science, edited by: Finkl, C. W. and Makowski, C., Springer International Publishing AG, Cham, 1–11, 2018.

Scheuenpflug, L.: Die risszeitliche Hochterrasse des Lechs nördlich Augsburg und die Schutter (Bayerisch Schwaben), Heidelberger Geographische Arbeiten, 49, 194–209, 1979.

Scheuenpflug, L.: Die Schotterfazies des Augsburger Umlandes, Berichte des Naturwissenschaftlichen Vereins für Schwaben e.V., 85, 14–21, 1981.

Schielein, P.: Jungquartäre Flussgeschichte des Lechs unterhalb von Augsburg und der angrenzenden Donau, Bamberger Geographische Schriften, 9, 150 pp., 2012.

Schielein, P. and Schellmann, G.: Geologische Karte von Bayern 1 : 25 000, Blatt Nr. 7531 Gersthofen mit Erläuterungen, Bamberger Geographische Schriften, 12, 41–73, 2016a.

Schielein, P. and Schellmann, G.: Geologische Karte von Bayern 1 : 25 000, Blatt Nr. 7331 Rain mit Erläuterungen, Bamberger Geographische Schriften, 12, 141–166, 2016b.

Schielein, P., Schellmann, G., and Lomax, J.: Stratigraphy of Late Quaternary fluvial terraces at the confluence of the Lech and Danube valleys, E&G Quaternary Sci. J., 60, 27, https://doi.org/10.3285/eg.60.4.02, 2011.

Schielein, P., Schellmann, G., Lomax, J., Preusser, F., and Fiebig, M.: Chronostratigraphy of the Hochterrassen in the lower Lech valley (Northern Alpine Foreland), E&G Quaternary Sci. J., 64, 15–28, https://doi.org/10.3285/eg.64.1.02, 2015.

Semmel, A.: Studien über den Verlauf jungpleistozäner Formung in Hessen, Frankfurter Geographische Hefte, 45, 133 pp., 1968.

Srivastava, S. K., Balbudhe, A. Y., Vishwa Prasad, K., Paqdma Savithri, P., Tripathi, R. M., and Puranik, V. D.: Variation in the uranium isotopic ratios $^{234}U/^{238}U$, $^{238}U$/ total-U and $^{234}U$/ total-U in Indian soil samples: Application to environmental monitoring, Radioprotection, 2012, 1–12, 2012.

Stuiver, M. and Reimer, P. J.: Extended $^{14}C$ database and revised CALIB radiocarbon calibration program, Radiocarbon, 35, 215–230, 1993.

Tillmanns, W., Münzing, K., Brunnacker, K., and Löscher, M.: Die Rainer Hochterrasse zwischen Lech und Donau, Jahresberichte und Mitteilungen des oberrheinischen geologischen Vereins N.F., 64, 79–99, 1982.

Tillmanns, W., Brunnacker, K., and Löscher, M.: Erlauterungen zur Geologischen Übersichtskarte der Aindlinger Terrassentreppe zwischen Lech und Donau 1 : 50 000, Geologica Bavarica, 85, 83 pp., 1983.

Trauerstein, M., Lowick, S. E., Preusser, F., and Veit, H.: Testing the suitability of dim sedimentary quartz from Northern Switzerland for OSL burial dose estimation, Geochronometria, 44, 66–76, 2017.

Unger, H. J.: Zur Geologie im Donautal zwischen Straubing und Pleinting, Documenta Naturae, 128, 110 pp., 1999.

Vigier, N. and Bourdon, B.: Constraining Rates of Chemical and Physical Erosion using U-Series Radionuclides, in: edited by: Baskaran, M., Handbook of Environmental Isotope Geochemistry, 553–571, Springer Verlag, Berlin Heidelberg, 2012.

Weißhaar, R.: Isotopengeochemie des Heidelberger Neckarschwemmfächers, U/Th-Ungleichgewichte und Pb-Isotopie quartärer klastischer Sedimente, Diss. University of Heidelberg, Heidelberg, 2000.

Winsemann, J., Lang, J., Roskosch, J., Polom, U., Böhner, U., Brandes, Chr., Glotzbach, C., and Frechen, M.: Terrace styles and timing of terrace formation in the Weser and Leine valleys, northern Germany: Response of a fluvial system to climate change and glaciation, Quaternary Sci. Rev., 123, 31–57, 2015.

Xu, B., Gu, Z., Han, J., Hao, Q., Lu, Y., Wang, L., Wu, N., and Peng, Y.: Radiocarbon age anomalies of land snail shells in the Chinese Loess Plateau, Quat. Geochronol., 6, 383–389, 2011.

Zöller, L.: Würm- und Rißlöß-Stratigraphie und Thermolumineszenz-Datierung in Süddeutschland und angrenzenden Gebieten, habilitation thesis, University of Heidelberg, Germany, 224 pp., 1995.

E&G Quaternary Sci. J., 68, 165–176, 2019
https://doi.org/10.5194/egqsj-68-165-2019


Open Access E&G Quaternary Science Journal

Research article

# $^{10}$Be-based exploration of the timing of deglaciation in two selected areas of southern Norway

**Philipp Marr**[1], **Stefan Winkler**[2], **Steven A. Binnie**[3], **and Jörg Löffler**[1]

[1]Department of Geography, University of Bonn, Meckenheimer Allee 166, 53115 Bonn, Germany
[2]Department of Geography and Geology, University of Würzburg, Am Hubland, 97074 Würzburg, Germany
[3]Institute for Geology and Mineralogy, University of Cologne, Zülpicherstr., 49B, 50674 Cologne, Germany

**Correspondence:** Philipp Marr (marr@uni-bonn.de)

**Relevant dates:** Received: 18 January 2019 – Revised: 2 May 2019 – Accepted: 13 June 2019 – Published: 30 July 2019

**How to cite:** Marr, P., Winkler, S., Binnie, S. A., and Löffler, J.: $^{10}$Be-based exploration of the timing of deglaciation in two selected areas of southern Norway, E&G Quaternary Sci. J., 68, 165–176, https://doi.org/10.5194/egqsj-68-165-2019, 2019.

**Abstract:** We present new $^{10}$Be surface exposure ages from two selected locations in southern Norway. A total of five $^{10}$Be samples allow a first assessment of local deglaciation dynamics of the Scandinavian Ice Sheet at Dalsnibba (1476 m a.s.l.) in southwestern Norway. The bedrock ages from the summit of Dalsnibba range from $13.3 \pm 0.6$ to $12.7 \pm 0.5$ ka and probably indicate the onset of deglaciation as a glacially transported boulder age ($16.5 \pm 0.6$ ka) from the same elevation likely shows inheritance. These ages indicate initial deglaciation commencing at the end of the Bølling–Allerød interstadial ($\sim$ 14.7–12.9 kyr BP) and ice-free conditions at Dalsnibba's summit during the Younger Dryas. Bedrock samples at lower elevations imply vertical ice surface lowering down to 1334 m a.s.l. at $10.3 \pm 0.5$ ka and a longer overall period of downwasting than previously assumed. Two further $^{10}$Be samples add to the existing chronology at Blåhø (1617 m a.s.l.) in south-central Norway. The $^{10}$Be erratic boulder sample on the summit of Blåhø sample yields $20.9 \pm 0.8$ ka, whereas a $^{10}$Be age of $46.4 \pm 1.7$ ka for exposed summit bedrock predates the Late Weichselian Maximum. This anomalously old bedrock age infers inherited cosmogenic nuclide concentrations and suggests low erosive cold-based ice cover during the Last Glacial Maximum. However, due to possible effects of cryoturbation and frost heave processes affecting the erratic boulder age and insufficient numbers of $^{10}$Be samples, the glaciation history on Blåhø cannot conclusively be resolved. Comparing the different timing of deglaciation at both locations in a rather short west–east distance demonstrates the complex dynamics of deglaciation in relation to other areas in southern Norway.

**Kurzfassung:** Es werden neue $^{10}$Be Oberflächenexpositionsdatierungsalter zweier ausgewählter Lokalitäten in Südnorwegen vorgestellt. Insgesamt fünf $^{10}$Be Altersdatierungen erlauben eine erste Bewertung der lokalen Deglaziationsdynamiken des Skandinavischen Eisschildes auf Dalsnibba (1476 m ü.d.M., über dem Meeresspiegel) im westlichen Südnorwegen. Die Expositionsalter des anstehenden Grundgesteins zwischen $13.3 \pm 0.6$ und $12.7 \pm 0.5$ ka vom Gipfel der Dalsnibba indizieren den Beginn der Deglaziation, da das Alter des glazial transportierten Blocks ($16.5 \pm 0.6$ ka) von ähnlicher Höhenlage stammt und dieser wahrscheinlich eine ererbte kosmogene Nuklidkonzentration besitzt. Dies deutet auf eine beginnende initiale Deglaziation am Ende des Bølling–Allerød interstadial (∼ 14.7–12.9 kyr BP) und einen eisfreien Gipfel der Dalsnibba während der Jüngeren Dryas hin. Expositionsalter für Grundgestein in niedrigerer Höhenlage weisen auf ein anschließendes Absinken der vertikalen Eisausdehnung auf 1334 m ü.d.M. um $10.3 \pm 0.5$ ka sowie auf eine länger anhaltende Eisschmelzperiode als bisher angenommen hin. Es werden zwei zusätzliche Datierungen zur bereits bestehenden Deglaziationschronologie von Blåhø (1617 m ü.d.M.) im zentralen Südnorwegen präsentiert. Das $^{10}$Be Alter eines erratischen Blocks auf Blåhø ergibt $20.9 \pm 0.8$ ka und das erzielte Alter von $46.4 \pm 1.7$ ka eines Grundgesteinsaufschluss am Gipfel liegt zeitlich vor dem Spätweichsel-Maximum (LGM). Das ungewöhnlich hohe Grundgesteinsalter lässt sich auf eine ererbte kosmogene Nuklidkonzentration sowie eine Bedeckung mit wenig erosivem, kaltbasalen Eis auf Blåhø während des LGM schließen. Allerdings ist eine abschließende Bewertung der Vergletscherungsgeschichte Blåhø schwierig, da mögliche Effekte von Kryoturbation und Frosthebungsprozessen das Alter des Blocks beeinflusst haben könnten und die Anzahl der Expositionsdatierungen unzureichend ist. Der Vergleich des unterschiedlichen Beginns der Deglaziation in beiden Untersuchungsgebieten in geringer West–Ost Distanz deutet auf komplexe dynamische Deglaziationsprozesse in Relation zu anderen Gebieten in Südnorwegen hin.

## 1 Introduction

The growth and decay of Quaternary glaciers and ice sheets has had fundamental implications for environmental changes worldwide (Ehlers and Gibbard, 2007). Based on numerical terrestrial or marine radiocarbon and cosmogenic nuclide surface exposure ages in addition to pollen stratigraphy, the chronology of the last deglaciation of the Scandinavian Ice Sheet (SIS) following the Last Glacial Maximum (LGM, 26.5–20 kyr; Clark et al., 2009) and related ice marginal positions in Norway are generally perceived as well constrained (Hughes et al., 2016; Stroeven et al., 2016; Patton et al., 2017). The detailed vertical extent of the SIS in Norway for this period remains, however, uncertain over large areas. Scenarios ranging from maximum models with a central ice dome (Sollid and Reite, 1983; Mangerud, 2004) to minimum models implying a thin multi-domed ice sheet and larger ice-free areas (Dahl et al., 1997; Wohlfarth, 2010) are the topic of ongoing discussion. The knowledge of the vertical dimension of the LGM ice sheet could provide crucial information on palaeoenvironmental factors like sea-level changes, atmospheric and oceanic circulation, (de-)glaciation patterns, ice-sheet erosion rates, landscape evolution, and englacial thermal boundaries (Winguth et al., 2005; Rinterknecht et al., 2006; Goehring et al., 2008). The interpretation of bedrock with different degree of weathering in mountain areas affected by Quaternary glaciation can, therefore, be important for determining ice-sheet behaviour and thickness during the last glaciation periods (Brook et al., 1996; Briner et al., 2006; McCarroll, 2016). There are several concepts to explain the limit between differently weathered bedrock (trimline) separating highly weathered uplands comprising blockfields and tors from relatively unweathered lower exposures of freshly eroded glacial features (Rea et al., 1996; Briner et al., 2006). The two most discussed scenarios suggest on the one hand the preservation of highly weathered uplands by a cover of non-erosive cold-based ice; thus the trimline would reflect an englacial thermal boundary. The alternative explanation suggests that the trimline represents the true upper vertical ice surface and erosional limit of a former warm-based ice sheet with ice-free nunatak areas above that boundary (Stroeven et al., 2002).

The rise of terrestrial cosmogenic nuclides (TCNs) for surface exposure dating as a key tool to yield numerical ages of landforms and bedrock surfaces representing specific glacier and ice sheet dynamics has revolutionized deglaciation chronologies (Dunai, 2010), especially for settings where organic material is not available for dating. TCNs have been frequently used to reconstruct glacial chronologies worldwide, often utilizing ages derived from erratic boulders or bedrock surfaces (Dunai, 2010; Stroeven et al., 2016, and references therein). To successfully apply TCNs and to establish timing and rates of the last deglaciation, it is necessary that any cosmogenic nuclide produced prior to the last deglaciation has been removed by erosion (Briner et al., 2006; Dunai, 2010). Consequently, the erosive capacity of an ice sheet is mirrored in the concentration of cosmogenic nuclides, as the degree of erosion governs the level of inheritance (Harbor et al., 2006). Erosive capacity is largely causally connected to the basal temperature regime of the ice and its related ability to move by basal sliding. Therefore, cosmogenic nuclide concentrations may also serve as a tool to identify englacial thermal boundaries between warm-based and cold-based zones or estimate palaeo-ice thickness of entirely warm-based glaciers (Kleman, 1994).

The SIS constituted the largest unit of the Eurasian ice sheet (Hughes et al., 2016). Despite the progress with reconstructing volume, margins and timing, the information from terrestrial sources about the former ice cover is limited (Patton et al., 2016). Only a few deglaciation studies have been carried out in the Geiranger Fjord area in southwestern Norway, where our first selected site, Dalsnibba, is located (e.g. Fareth, 1987; Aarseth et al., 1997). These studies have mostly relied on $^{14}$C dates which have repeatedly been questioned (e.g. Donner, 1996). Hence, only limited numerical age data are available and there is a need for more reliable data for a better understanding of deglaciation dynamics in this area. Our second selected site at Blåhø was previously studied by several authors focussing on deglaciation following the LGM (e.g. Nesje et al., 1994; Goehring et al., 2008; Marr et al., 2018). We provide additional ages from an erratic boulder and from a bedrock outcrop to improve the image of the glaciation history.

In the wake of growing evidence for a more dynamic SIS through the last glacial cycle (Rinterknecht et al., 2006; Mangerud et al., 2010), it is essential to establish a robust deglaciation chronology, particularly for its inner mountainous region, to understand landform evolution and ice sheet dynamics. Given the importance of ice sheets with respect to the climate system, a better understanding of their evolution and the rate and timing of their ice retreat across the mountainous parts of southern Norway is necessary. Here, we report cosmogenic $^{10}$Be surface exposure ages from boulder and bedrock surfaces of two selected mountain sites in southwestern and south-central Norway to improve our knowledge on the (de)glaciation history (Fig. 1). Our main study objectives were as follows:

1. to apply terrestrial cosmogenic $^{10}$Be dating and to determine $^{10}$Be surface exposure ages from the collected boulder and bedrock samples
2. to present the first estimate for the timing of initial local deglaciation for Dalsnibba in Opplendskedalen based on $^{10}$Be
3. to assess and further improve the existing deglaciation chronology for Blåhø in the light of new $^{10}$Be ages presented in this study
4. to explore the ice sheet dynamics and characteristics during the deglaciation in the selected areas in southern Norway.

## 2 Study area

### 2.1 Dalsnibba

Dalsnibba (62°4′43 N, 7°17′35 E; 1476 m a.s.l.) is located in Opplendskedalen on the Geirangerfjellet in the western part of south-central Norway. The summit area is dominated by glacially eroded bedrock outcrops which are moderately weathered, but there is no blockfield on Dalsnibba. The general morphology was strongly influenced by Quaternary glaciations with well-developed glacial valleys and deep fjords constituting prevailing macro-landforms (Holtedahl, 1967; Klemsdal and Sjulsen, 1988). Four bedrock samples from glacially eroded bedrock surfaces and one glacially transported boulder sample taken at four elevations ranging from 1334 to 1476 m a.s.l. were analysed. We aimed for sampling along a vertical transect from Dalsnibba to the valley bottom of Opplendskedalen at ∼ 1050 m a.s.l. However, inaccessibility and/or inappropriate sampling sites prohibited us from doing so. Sub-oceanic climatic conditions prevail at the site with mean annual air temperature between 0 and 2 °C (1971–2000) and mean annual precipitation between 2000 and 3000 mm a$^{-1}$ (1971–2000) (http://www.senorge.no, last access: 18 April 2019). The gneiss bedrock is mainly quartz dioritic to granitic and partly migmatitic and is part of the so-called Western Gneiss Region (Tveten et al., 1998). The sampled boulder had the equivalent lithological composition.

The ice retreat following the LGM probably saw the ice margin approaching the inner parts of Storfjorden during the Bølling–Allerød interstadial (∼ 14.7–12.9 kyr BP; Patton et al., 2017) when the glacier probably experienced several short standstills in the Geiranger Fjord (Longva et al., 2009). Glaciers readvanced during the Younger Dryas (YD, 12.9–11.7 cal. kyr BP; Lohne et al., 2013) and created moraines at the fjord mouth (Longva et al., 2009). Little is known about the vertical ice limit during the YD; Andersen et al. (1995) suggest a thickness of 800–1200 m in fjords that became ice-free during the Bølling–Allerød interstadial. The final deglaciation following the YD in the fjords in western Norway generally falls between 11.2 ± 0.4 and 10.9 ± 0.2 cal. kyr BP (cf. Nesje and Dahl, 1993; calibration from Hughes et al., 2016, applied).

### 2.2 Blåhø

Blåhø (61°53′51 N, 9°16′58 E; 1617 m a.s.l.) is located in Ottadalen in the central part of southern Norway. Smooth undulating surfaces at summit level are present, with three lower peaks – Rundhø (1556 m a.s.l.), Veslrundhø (1514 m a.s.l.) and Storhøi (1455 m a.s.l.) – part of the mountain ridge. The Blåhø summit is covered by an autochthonous blockfield extending down to a trimline at ∼ 1500 m a.s.l. (Nesje et al., 1994). Two samples were collected at the summit: one from a bedrock slab at the eastern edge of the blockfield and one from an erratic boulder. Climatic conditions are continental, with a mean annual temperature of −2 to −1 °C and a mean annual precipitation of 750–1000 mm a$^{-1}$ at the summit and less than 500 mm a$^{-1}$ (1971–2000) in the valley (http://www.senorge.no); it is among the driest areas in Norway. The area is dominated by quartz-rich Precambrian bedrock. The summit itself is dominated by meta-conglomerate and meta-sandstone on higher and lower slopes, respectively (Tveten et al., 1998). The sampled erratic boulder from the summit is quartz pegmatite.

The (de)glaciation history of Blåhø has attracted researchers' attention for decades (e.g. Nesje et al., 1994; Goehring et al., 2008; Marr and Löffler, 2017). It has been debated whether the summit was covered by cold-based ice

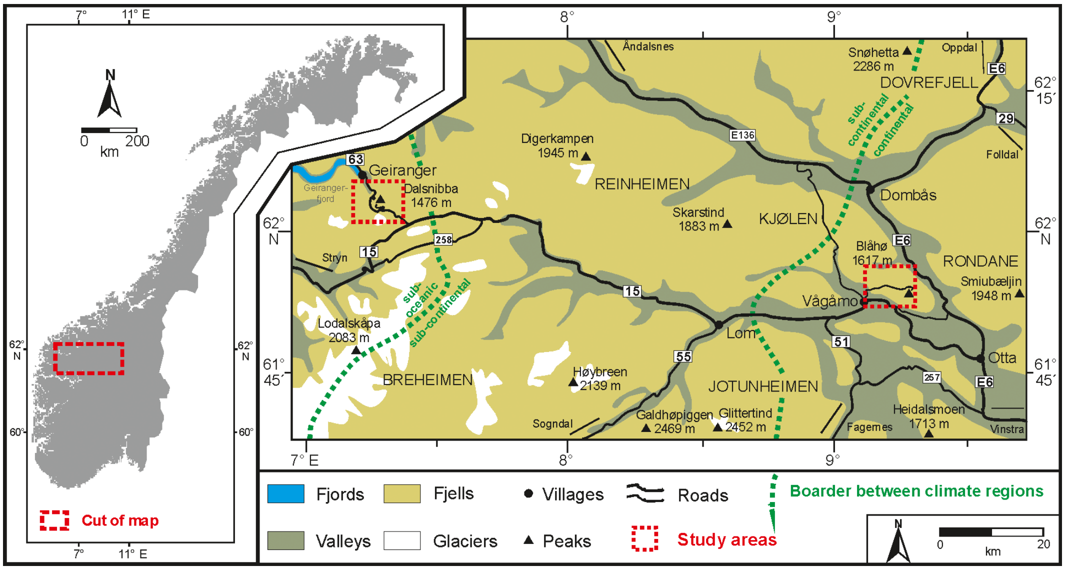


**Figure 1.** Study areas in southern Norway and the location of Dalsnibba in the west and Blåhø in the east (modified after Löffler and Pape, 2004).

(Goehring et al., 2008) or remained ice-free during the LGM (Nesje et al., 1994). Goehring et al. (2008) established a deglaciation chronology following the LGM, commencing at $25.1 \pm 1.8$ ka based on a $^{10}$Be age from an erratic boulder at the summit to $11.7 \pm 1.0$ ka at the lowermost sample (1086 m a.s.l.).

## 3 Methods

### 3.1 Material and measurement

Surface exposure dating utilizes the in situ build-up of cosmogenic nuclides like $^{10}$Be, $^{26}$Al or $^{36}$Cl by secondary cosmic rays to assess the duration of surface exposure at or near the earth's surface (Balco et al., 2008). The calculation of surface exposure ages using cosmogenic nuclide concentrations from glacial landforms is based on several assumptions. Exposure ages obtained using a single nuclide species are often considered minimum ages, as it is assumed that the samples were constantly exposed at the surface during one single period only, and that they neither contain an inherited nuclide concentration nor were they affected by significant snow shielding or erosion (Stroeven et al., 2002; Briner et al., 2006). In this study, we measured the $^{10}$Be concentration of five bedrock (-bed) and two boulder (-bo) samples (Fig. 2). We targeted bedrock outcrops to provide additional new data to existing datasets (Goehring et al., 2008) and to explore the potential thermal and erosional properties of the ice sheet (Harbor et al., 2006; Dunai, 2010) because erratics on top of (glacially modified) bedrock may (Fabel et al., 2002; Dunai, 2010), but not necessarily, provide deglaciation ages (cf. Heymann et al., 2011). It has to be acknowledged, however, that our limited $^{10}$Be ages ($n = 7$), especially in the eastern study area, allow us to improve and assess the existing deglaciation chronology rather than construct an independent one.

The samples were collected by hammer and chisel, and only boulders broader than 20 cm in diameter were selected for measurement to minimize the probability of post-depositional disturbance. All samples were obtained from flat surfaces (dip $< 5°$) with at least 25 cm distance from any edges for the large boulder and the longest distance possible from the edges of the smaller boulder. Both bedrock samples were obtained from locations with weathered surfaces and/or lichen cover to avoid surfaces so intensively weathered that slabs had potentially broken off the boulder surfaces (Fig. S5 in the Supplement). We sampled from local topographic highs to minimize the influence of snow cover. Geographical coordinates and elevations of sampling locations were recorded with a handheld GPS. Topographic shielding was derived from compass and clinometer measurements at each sample site.

After crushing and sieving, between ca. 10 to 44 g of purified quartz was extracted from the rock samples using the approach of Kohl and Nishiizumi (1992). Quartz samples were spiked with around 300 µg of a commercial beryllium solution (Scharlab, 1000 mg L$^{-1}$, density 1.02 g cm$^{-3}$) before being dissolved in a concentrated HF/HNO$_3$ mixture. Preparation of the purified quartz as AMS (accelerator mass spectrometry) targets was undertaken in tandem with a reagent blank. Target preparation chemistry was undertaken in the clean laboratory at the University of Cologne using the single-step column approach described by Binnie et al. (2015). Beryllium hydroxide was co-precipitated with Ag, according to Stone et al. (2004), for pressing

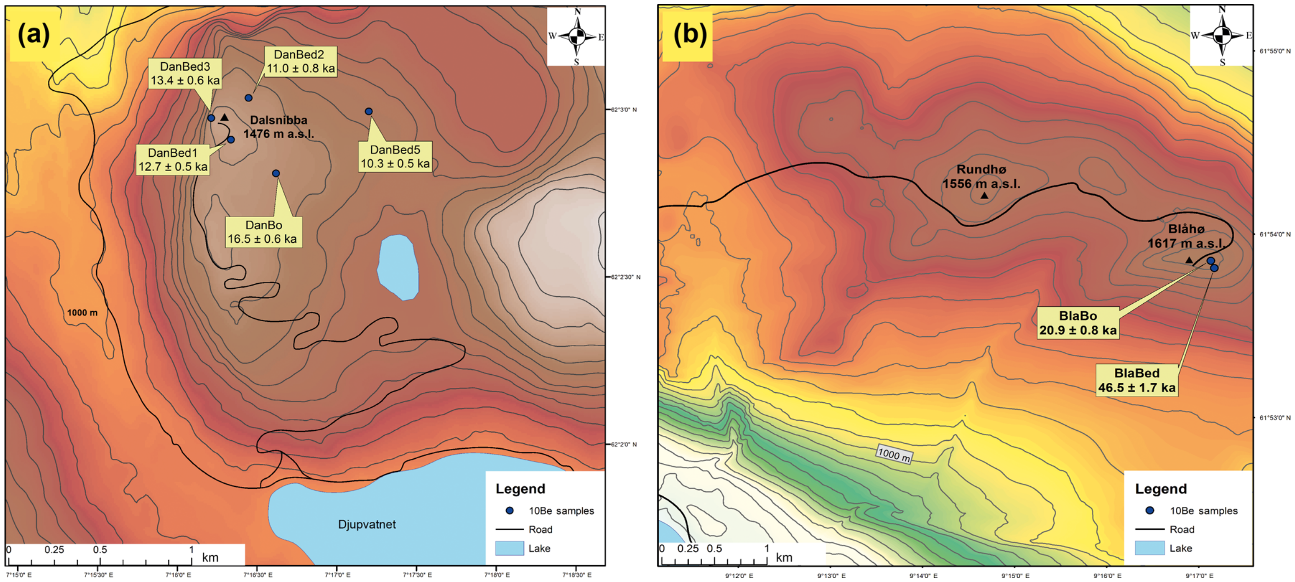


**Figure 2.** Detailed sampling locations at **(a)** Dalsnibba and **(b)** Blåhø. The bedrock samples in both study areas are labelled as -bed, the boulder samples as -bo. The calculated $^{10}$Be ages of every sample are reported with $1\sigma$ uncertainty in ka. The contour line intervals are a distance of 50 m (source: http://www.kartverket.no, last access: 14 January 2019).

into AMS targets. Measurements of $^{10}$Be/$^{9}$Be were undertaken at CologneAMS (Dewald et al., 2013), normalized to the revised standard values reported by Nishiizumi et al. (2007). Uncertainties in the blank-corrected $^{10}$Be concentrations were derived by propagating (summing in quadrature) the 1 SD uncertainties in the AMS measurements of the blanks and the samples along with an estimated 1 % uncertainty (1 SD) in the mass of $^{9}$Be added as a carrier.

## 3.2 Exposure age calculations

The $^{10}$Be surface exposure ages were calculated with the online exposure age calculator version 3, formerly known as the CRONUS-Earth online exposure age calculator (Balco et al., 2008; Balco, 2017; http://hess.ess.washington.edu/, last access: 30 April 2019). The spallation-induced regional production rate for western Norway (normalized to sea-level high latitude) was used, as surfaces of unknown age can be dated more precisely due to the proximity of the calibration site (Goehring et al., 2012a, b). We applied the time-dependent LSD scaling model of Lifton et al. (2014) and used the 07KNSTD flag in the online calculator. A rock density of 2.6 g cm$^{-3}$ was applied for all samples. We did not correct our ages for atmospheric pressure anomalies, temporal shielding by snow, sediment or vegetation. Erosion of 1 mm kyr$^{-1}$ was applied in the online calculator, a comparable erosive capacity in summit areas as presented by Andersen et al. (2018a) for Reinheimen, close to Blåhø.

One parameter required within the calibration process for calculating $^{10}$Be age is the elevation of the sampled bedrock or boulder surface. Any correction for the effect of postglacial glacio-isostatic uplift is, however, quite challenging. No detailed local uplift data for Dalsnibba are available, but an estimate of ca. 100 m total uplift based on reports of former shoreline displacement or modelling attempts seems reasonable (Svendsen and Mangerud, 1987; Fjeldskaar et al., 2000; Steffen and Wu, 2011). For Blåhø, the total postglacial uplift is estimated at around 300 m (Morén and Påsse, 2001). However, this postglacial uplift cannot be described as a linear function as data from other localities in western Norway highlight (e.g. Fjeldskaar, 1994; Helle et al., 2007). An initial strong uplift during Allerød halted during the Younger Dryas and resumed after its termination with high uplift rates in the Early Holocene that subsequently significantly decreased (Lohne et al., 2007). According to newest modelling by Fjeldskaar and Amatonov (2018) the calculated uplift between Allerød and Younger Dryas at around Dalsnibba would summarize to around 50 m, i.e. half of the suggested total postglacial glacio-isostatic uplift. Because postglacial uplift first becomes relevant for $^{10}$Be age calculation after exposure of the sampled surface, a circular reference emerges as surface exposure age (the unknown factor itself) needed to be known to precisely determine the amount of uplift that had already occurred according to established models (cf. Jones et al., 2019). To resolve this problem and simplify the correction for postglacial uplift, we assume initial fast uplift between 13 and 11.5 kyr totaling 50 m following Fjeldskaar and Amatonov (2018), followed by linear uplift during the Holocene that accounts for the remaining 50 m. The resulting reduction for sample elevation is ca. 30 m for Dalsnibba. Following similar considerations for Blåhø, a maximum reduction of 150 m in relation to modern elevation is considered. However, the alternative influence of ca. 100 m reduction and no uplift correction are also assessed because of a likely non-linear uplift function, with maximum uplift during or immediately following deglaciation. The results of different uplift scenarios on Blåhø ages are presented in Table S3 in the Supplement. A reduction of sample elevation of ca. 100 m averaged over the entire surface exposure time seems reasonable and needs to be treated as a maximum value as Early Holocene uplift rates may be underestimated. Finally, with respect to all potential uncertainties with the calculation and calibration of $^{10}$Be surface exposure age estimates (production rates, selected scaling schemes, etc.), our simplified postglacial uplift correction appears appropriate.

## 4 Results

AMS analysis gave $^{10}$Be/$^{9}$Be ratios ranging from $1.65 \times 10^{-12}$ to $8.69 \times 10^{-14}$. The reagent blank prepared alongside the samples gave a $^{10}$Be/$^{9}$Be value of $6.47 \times 10^{-15}$, and the blank subtractions were < 4 % of the total number of $^{10}$Be atoms measured in the samples, aside from sample DanBed2, which yielded less quartz, resulting in a blank subtraction that was 7.5 % of the total.

The cosmogenic exposure ages calculated for all samples from Dalsnibba and Blåhø are shown in Fig. 2 and Table 1. The boulder sample from the summit of Dalsnibba (DanBo) was the oldest from this site at $16.5 \pm 0.6$ ka. The $^{10}$Be ages from Blåhø are $46.4 \pm 1.7$ ka (BlaBed) for the bedrock from the blockfield, whereas the boulder resting on the blockfield gave $20.9 \pm 0.8$ ka (BlaBo). The recalculated ages for Goehring et al. (2008) are presented in Table S4. Results for the effect of different glacio-isostatic uplift rates for Dalsnibba and Blåhø are presented in Tables S2 and S3. The considered uplift of 30 m vs. no uplift for Dalsnibba results in a ∼ 3 % age increase. An uplift of 100 m at Blåhø leads to ∼ 9 % older ages if compared to no correction for no uplift. For the maximum scenario of 150 m uplift the corresponding value is a ∼ 14 % age increase.

## 5 Discussion

### 5.1 Methodological considerations and processes affecting $^{10}$Be concentrations

We collected our rock samples from three different settings: bedrock outcrops from weathered debris/blockfields, glacially eroded bedrock surfaces, and boulders. Erosion of the sampled surfaces or undetected shielding (e.g. snow or vegetation cover) would lower the nuclide concentrations and consequently lead to underestimated ages (Stroeven et al., 2002; Hughes et al., 2016). Further, samples collected above the weathering limit, where outcrops are prone to surface degradation by severe frost weathering, also result in an underestimation of the true surface exposure (Brook et al., 1996).

The uplift model used by Goehring et al. (2008) applied on Blåhø reveals ∼ 22 % older ages from high-elevation samples (> 1400 m a.s.l.). The recalculated data from Goehring et al. (2008) applying our uplift correction approach (with 100 m) give an estimated age difference of ∼ 9 %. A total uplift of 150 m results in ∼ 14 % older ages, which is closer to the value obtained by Goehring et al. (2008). For further discussion we rely on the most realistic option with a total uplift of 100 m for Blåhø.

The impact of snow cover on the $^{10}$Be ages was estimated on the basis of Gosse and Philipps (2001) with recent snow conditions (data from http://www.senorge.no, averaged 1958–2019). By assuming 150 cm during 9–10 months in the west and 40 cm for 7–8 months (snow density 0.3 g cm$^{-3}$) in the east are representative of this interglacial, the $^{10}$Be calculations could result in 18 %–20 % too young ages in the west and 4.2 %–4.8 % in the east. It needs, however, to be pointed out that it is impossible to assess whether modern snow conditions are representative of the conditions during the entire Holocene with its known climate variability (Nesje, 2009). We are aware that due to our limited dataset it is impossible to make conclusive statements about the glaciation history, especially for Blåhø, and to definitively identify geological bias and sample outliers (Stroeven et al., 2016). Furthermore, our restrictions to a single cosmogenic nuclide ($^{10}$Be) does not allow us to obtain information on any complex burial history that would require pairing $^{10}$Be with other nuclides like $^{26}$Al (Fabel et al., 2002). Nevertheless, we assume our results to have the capacity to contribute to the discussion of the timing of deglaciation in both areas because of their generally coherent ages in relation to previously published timings of deglaciation between $11.2 \pm 0.4$ and $10.9 \pm 0.2$ cal. kyr BP (cf. Nesje and Dahl, 1993; calibration from Hughes et al., 2016, applied) in the west and $21.8 \pm 1.6$ ka (Goehring et al., 2008, recalculated) in the east. Recent findings indicate the timing of the last deglaciation at $11 \pm 0.2$ ka in Reinheimen, located between our study areas (Andersen et al., 2018a).

### 5.2 Timing of deglaciation at Dalsnibba

The obtained $^{10}$Be surface exposure ages from Dalsnibba offer the possibility of presenting the first age constraints for local deglaciation based on cosmogenic nuclides. The internal consistency of our $^{10}$Be exposure ages from glacially eroded bedrock surfaces with their post-LGM age implies that glacial erosion was sufficient to remove any inherited nuclide concentration, and that the bedrock had been continuously exposed since. This supports the concept that glaciers in fjord landscapes were highly effective erosional agents and consequently warm-based (Aarseth et al., 1997; Matthews et al., 2017), especially in the valleys. This is in agreement with Landvik et al. (2005), who claim that frozen-bed conditions throughout the growth and decay of glaciers in coastal environments are unlikely. However, there are blockfield-covered summits between the fjords which are mostly located at a

**Table 1.** Sample and laboratory data and calculated $^{10}$Be surface exposure ages.

| Sample ID | Sample type | Latitude (°) | Longitude (°) | Altitude (m a.s.l.) | Sample thickness (cm) | Topographic shielding | Blank-corrected $^{10}$Be conc. ($10^5$ at g$^{-1}$) | Uncertainty (1$\sigma$) blank-corrected $^{10}$Be conc. ($10^3$ at g$^{-1}$) | External uncertainty (year) | Exposure age (year) |
|---|---|---|---|---|---|---|---|---|---|---|
| DanBed1 | Bedrock | 62.047639 | 7.274044 | 1476 | 4.8 | 0.999935 | 2.04 | 8 | 1100 | 12 700 ± 500 |
| DanBed2 | Bedrock | 62.049925 | 7.275275 | 1418 | 3.5 | 0.999997 | 1.70 | 13 | 1200 | 11 000 ± 800 |
| DanBed3 | Bedrock | 62.049314 | 7.270258 | 1464 | 5.9 | 0.999976 | 2.10 | 8 | 1200 | 13 300 ± 600 |
| DanBed5 | Bedrock | 62.048295 | 7.287856 | 1334 | 4.7 | 0.999544 | 1.48 | 6 | 900 | 10 300 ± 500 |
| DanBo | Boulder | 61.897524 | 9.282407 | 1438 | 6.5 | 1 | 2.60 | 10 | 1500 | 16 500 ± 600 |
| BlaBed | Bedrock | 61.897700 | 9.284238 | 1615 | 2.4 | 1 | 7.49 | 26 | 4200 | 46 400 ± 1700 |
| BlaBo | Boulder | 62.044505 | 7.274839 | 1617 | 2.8 | 1 | 3.59 | 14 | 1900 | 20 900 ± 800 |

All ages are calculated using version 3 of the calculator code found at https://hess.ess.washington.edu/ (last access: 30 April 2019) (Balco et al., 2008; Balco, 2017). The western Norway $^{10}$Be production rate (Goehring et al., 2012a, b) is applied with standard atmosphere and pressure "std" and a rock density of 2.6 g cm$^{-3}$. The time-dependent LSD scaling model of Lifton et al. (2014) was used. An uplift for 30 m for Dalsnibba and 100 m for Blåhø was assumed as well as an erosion of 1 mm kyr$^{-1}$.

higher altitude above the blockfield boundary, indicating that they were potentially protected by cold-based ice (Brook et al., 1996). The two uppermost bedrock ages and the glacial boulder are from comparable altitudinal settings, whereas the boulder is ∼ 3.8 to 3.2 ka older than the bedrock samples. This points to inherited cosmogenic nuclide inventory, and we therefore interpret the uppermost bedrock ages ranging from 13.3 ± 0.6 to 12.7 ± 0.5 ka as the timing of deglaciation on Dalsnibba. The bedrock ages mark the subsequent lowering of the ice surface; by plotting sample age with altitude (Fig. S4, $R^2 = 0.91$) the dynamics of ice surface lowering through time becomes clear. As the lowermost sample in this study is at 1334 m a.s.l. (which cannot cover the spectrum until the final downmelt of the ice), the exposure age of the valley bottom of Opplendskedalen (7.47 ± 0.73 ka at 1045 m a.s.l.; Marr et al., 2019) is used to determine the ice surface lowering rate. This gives an ice surface lowering of about 430 m within ∼ 5.8 ka. We calculate a thinning rate of ∼ 7.3 cm a$^{-1}$, which is comparable to the inland thinning rate determined by Linge et al. (2007) of 5 cm a$^{-1}$. We explain this with the persistence of a small ice cap on Dalsnibba and/or glacial readvances (with related fluctuations of the vertical ice limit) as the YD in the valleys probably led to a prolonged ice coverage. Our results from the western study site have three important implications in terms of the local glaciation history:

1. We suggest that the vertical ice limit must have exceeded 1476 m a.s.l. to be able to transport and deposit the boulder at its location. This contrasts to some extent with the view that ice thickness in coastal areas was supposed to be relatively thin due to effective ice drainage (Nesje et al., 1987), but it needs to be considered that Dalsnibba is located at the innermost fjord head of the Geiranger Fjord. Some authors anyway infer the possibility of nunataks on high coastal surfaces in western Norway (Mangerud, 2004; Winguth et al., 2005). In the light of our results, we have to reject the possibility that Dalsnibba was a nunatak during the LGM but suggest that the summit was covered by warm-based ice.

2. The timing of deglaciation between 13.3 ± 0.6 and 12.7±0.5 ka overlaps with the Bølling–Allerød interstadial, during which the summit of Dalsnibba was probably ice-free, and coincides with when the deglaciation reached Storfjord (Longva et al., 2009). Subsequently, Dalsnibba was not affected by the Younger Dryas readvance. Our results indicate that the deglaciation on Dalsnibba began at the end of the Bølling–Allerød or later, and Dalsnibba constituted a nunatak during the Younger Dryas.

3. There is only sparse information on the final deglaciation in the Scandinavian mountains; it is supposed to have commenced shortly after ∼ 10 ka (cf. Hughes et al., 2016). In Reinheimen, east of Dalsnibba, Andersen et al. (2018a) suggest 11 ± 0.2 ka as the timing of the last deglaciation. With our $^{10}$Be results it is difficult to constrain the final deglaciation as our lowermost sample was collected at 1334 m a.s.l. However, we can clearly state that the ice persisted at ∼ 1330 m a.s.l. until 10.3 ± 0.5 ka when the final local deglaciation was partly inferred for the region 11.2±0.4 and 10.9±0.2 cal. kyr BP (cf. Nesje and Dahl, 1993; calibration from Hughes et al., 2016, applied). Therefore, our results open up the possibility that the ice coverage at Dalsnibba lasted longer than previously anticipated and also longer than in the Reinheimen area, unless the last part of deglaciation was characterized by a sudden collapse of the remaining ice.

### 5.3 Implications of $^{10}$Be exposure ages from Blåhø

The $^{10}$Be ages from the blockfield support the overall interpretation that these relict features have survived glaciation with little or no erosion, which indicates long-term landform preservation (Rea et al., 1996; Linge et al., 2006). By acknowledging the widely accepted scenario that anomalously high $^{10}$Be concentrations of bedrock samples, such as BlaBed, are the consequence of cold-based ice cover, the blockfield boundary might represent the former englacial boundary between cold-based and warm-based ice (Fabel et al., 2002; Marquette et al., 2004). This implies that the bedrock sample is likely compromised by inherited $^{10}$Be from previous exposure followed by preservation beneath cold-based ice (Linge et al., 2006). This scenario appears realistic for the Blåhø bedrock sample, which, consequently, confirms the presence of non-erosive cold-based ice in line with several models suggesting thick ice coverage for this part of Norway (Stroeven et al., 2002; see Goehring et al., 2008). Notably, few of the weighted average bedrock ages from Reinheimen (Andersen et al., 2018a) show inheritance and provide ages of $\sim 11$ ka. This may point towards different thermal basal ice conditions within a short distance. Cosmogenic $^{10}$Be and $^{26}$Al nuclide concentration data indicate that some repeatedly glaciated sites have experienced negligible glacial erosion over the entire Quaternary (Briner et al., 2006; Harbor et al., 2006). Therefore, the inherited cosmogenic nuclides must have accumulated during multiple phases of exposure and have subsequently been preserved by cold-based ice (Hughes et al., 2016). Subtracting the exposure age since deglaciation ($\sim 21$ ka) the surface experienced $\sim 25$ kyr of prior exposure. By using the ice coverage modelled by Mangerud et al. (2010) and Hughes et al. (2016), we evaluate the $^{10}$Be concentration accumulation over time (Stroeven et al., 2002). With this approach it seems possible that the bedrock sample on Blåhø was first exposed at the surface during the Early Weichselian or the Eemian interglacial. Some authors suggest even older blockfield ages (e.g. Linge et al., 2006). In this scenario, boulder ages are often considered to reflect the timing of deglaciation (Marquette et al., 2004; Goehring et al., 2008). Following this, our boulder age of $20.9 \pm 0.8$ ka reflects the beginning of deglaciation, which agrees with the termination of the LGM (Fig. 3). This and the recalculated boulder age of $21.8 \pm 1.6$ ka (Goehring et al., 2008) supports their statement of the onset of deglaciation around this time. However, alternative interpretations of these boulder ages cannot be rejected, e.g. age overestimation due to post-depositional shielding by burial and subsequent exhumation by frost heave, deposition prior to LGM followed by long-term shielding, or deposition during a readvance following LGM (Briner et al., 2006; Heymann et al., 2011). But Marr et al. (2018) show evidence that the blockfield stabilized $\sim 18$ ka during severe periglacial conditions, which indicates the absence of ice cover close to the inferred time of boulder deposition.

The alternative interpretation of the bedrock $^{10}$Be nuclide concentration assumes continuous surface exposure since at least $46.4 \pm 1.7$ ka. Geomorphic evidence, such as periglacial activity of the summit blockfield until 18 ka, challenges the inferred presence of cold-based ice on Blåhø during the LGM (Marr et al., 2018). Recently, Andersen et al. (2018b) stated that high-elevation low-relief areas in south-central Norway

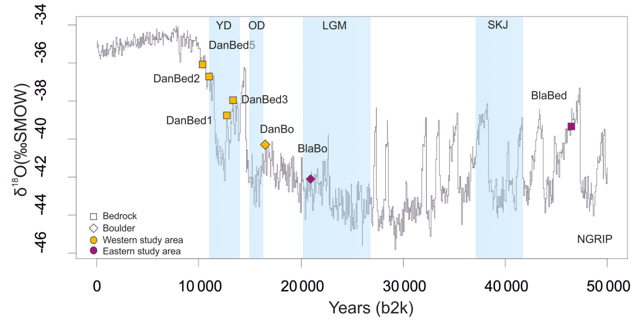


**Figure 3.** The ages are plotted against the North Greenland Ice Core Project (North Greenland Ice Core Project members, 2004) $\delta^{18}$O with $^{10}$Be ages. The key cold climate events are the Younger Dryas (YD), Older Dryas (OD), Last Glacial Maximum (LGM) and Skjonghelleren Stadial (SKJ); data are from Clark et al. (2009), Mangerud et al. (2010), Lohne et al. (2013) and Hughes et al. (2016).

were not covered by cold-based but warm-based ice as they calculated significant erosion rates. Therefore, whether the consistent trimline represents an englacial boundary remains ambiguous as englacial thermal boundaries may change frequently and may be unstable over long time periods (Nesje et al., 1987). However, decisive statements on glaciation history based on a single age are not possible; to resolve this issue on Blåhø, more numerical age data are necessary.

### 5.4 Implications for the regional glaciation history

The time difference of about 6–9 kyr for deglaciation between Dalsnibba and Blåhø is noteworthy. Taking into account the timing of deglaciation at $11 \pm 0.2$ ka in Reinheimen (Andersen et al., 2018a), located between our study areas, the deglaciation pattern in southern Norway was spatially and temporally variable. In relation to these ages the summit of Blåhø became apparently ice-free relatively early during deglaciation, whereas Dalsnibba at the inner fjord head of Geiranger Fjord became ice-free around 2 kyr later than the Reinheimen plateau. This means that during the YD readvance Reinheimen must have still been ice-covered, but the summit of Dalsnibba was already ice-free.

## 6 Conclusion

In this paper we present seven in situ cosmogenic $^{10}$Be surface exposure ages from two selected mountain locations in southern Norway. Despite uncertainties related to the uncertainties of our $^{10}$Be surface exposure ages and the limited dataset, we can delineate age constraints for the timing of deglaciation in the Geirangerfjellet in southwestern Norway. Further, we contribute new age estimates to the previously established deglaciation chronology for Blåhø in south-central Norway. The following conclusions can be drawn from this study:

1. According to the summit bedrock exposure ages ranging from $13.3 \pm 0.6$ to $12.7 \pm 0.5$ ka, deglaciation of the summit of Dalsnibba in Opplendskedalen commenced during the termination of the Bølling–Allerød interstadial. The summit successively remained ice-free during the Younger Dryas. However, the ice cover in the valley below the summit lasted longer (until $10.3 \pm 0.5$ ka) than previously assumed. In contrast to other studies, our results conclude that Dalsnibba was not a nunatak but covered by warm-based ice during the LGM.

2. The bedrock age from Blåhø ($46.4 \pm 1.7$ ka) indicates long-term weathering history and exposure predating the LGM. Most likely, inherited cosmogenic nuclides preserved through shielding by non-erosive cold-based ice are responsible for its old age. However, possible post-depositional disturbance of the boulder and the lack of larger suitable datasets restrict its interpretation.

3. The different timing of deglaciation in both selected sites and in nearby Reinheimen implies complex deglaciation patterns within a spatially limited area. The vertical extent of the Younger Dryas readvance seems to have been less pronounced in the inner fjord areas.

**Data availability.** All data sources are publicly accessible online; supporting ground imagery can be found in the Supplement.

**Supplement.** The supplement related to this article is available online at: https://doi.org/10.5194/egqsj-68-165-2019-supplement.

**Author contributions.** PM prepared the manuscript with contributions from all co-authors. SAB was responsible for the $^{10}$Be measurements at CologneAMS.

**Competing interests.** The authors declare that they have no conflict of interest.

**Special issue statement.** This article is part of the special issue "Connecting disciplines – Quaternary archives and geomorphological processes in a changing environment". It is a result of the First Central European Conference on Geomorphology and Quaternary Sciences, Gießen, Germany, 23–27 September 2018.

**Acknowledgements.** We thank Peter Wilson and one anonymous reviewer for very constructive and thoughtful comments that helped to improve the manuscript. We also thank Tibor Dunai for his expertise and his help. We further acknowledge permission to conduct field work in the Geiranger World Natural Heritage and Landscape Protection Area for over 20 years.

**Financial support.** This research has been supported by the Friedrich-Ebert-Stiftung (PhD scholarship grant).

## References

Aarseth, I., Austbo, P. K., and Risnes, H.: Seismic stratigraphy of Younger Dryas ice-marginal deposits in western Norwegian fjords, Norsk Geol. Tidsskr., 77, 65–85, 1997.

Andersen, B. G., Mangerud, J., Sørensen, R., Reite, A., Sveian, H., Thoresen, M., and Bergström, B.: Younger Dryas ice-marginal deposits in Norway, Quatern. Int., 28, 147–169, https://doi.org/10.1016/1040-6182(95)00037-J, 1995.

Andersen, J. L., Egholm, D. L., Knudsen, M. F., Linge, H., Jansen, J. D., Goodfellow, B. W., Pedersen, V. K., Tikhomirov, D., Olsen, J., and Fredin, O.: Pleistocene Evolution of a Scandinavian Plateau Landscape, J. Geophys. Res.-Earth, 123, 3370–3387, https://doi.org/10.1029/2018JF004670, 2018a.

Andersen, J. L., Egholm, D. L., Knudsen, M. F., Linge, H., Jansen, J. D., Pedersen, V. K., Nielsen, S. B., Tikhomirov, D., Olsen, J., Fabel, D., and Xu, S.: Widespread erosion on high plateaus during recent glaciations in Scandinavia, Nat. Commun., 9, 830, https://doi.org/10.1038/s41467-018-03280-2, 2018b.

Balco, G.: Production rate calculations for cosmic-ray-muon-produced $^{10}$Be and $^{26}$Al benchmarked against geological calibration data, Quat. Geochronol., 39, 150–173, https://doi.org/10.1016/j.quageo.2017.02.001, 2017.

Balco, G., Stone, J. O., Lifton, N. A., and Dunai, T. J.: A complete and easily accessible means of calculating surface exposure ages or erosion rates from $^{10}$Be and $^{26}$Al measurements, Quat. Geochronol., 3, 174–195, https://doi.org/10.1016/j.quageo.2007.12.001, 2008.

Binnie, S. A., Dunai, T. J., Voronina, E., Goral, T., Heinze, S., and Dewald, A.: Separation of Be and Al for AMS using single-step column chromatography, Nucl. Instrum. Methods Phys. Res. Sect. B Beam Interact. Mater. Atoms, 361, 397–401, https://doi.org/10.1016/j.nimb.2015.03.069, 2015.

Briner, J. P., Miller, G. H., Thompson Davis, P., and Finkel, R. C.: Cosmogenic radionuclides from fiord landscapes support differential erosion by overriding ice sheets, Geol. Soc. Am. B., 118, 406–420, https://doi.org/10.1130/B25716.1, 2006.

Brook, E. J., Nesje, A., Lehman, S. J., Raisbeck, R. M., and Yiou, F.: Cosmogenic nuclide exposure ages along a vertical transect in western Norway: Implications for the height of the Fennoscandian ice sheet, Geology, 24, 207–210, https://doi.org/10.1130/0091-7613(1996)024<0207:CNEAAA>2.3.CO;2, 1996.

Clark, P. U., Dyke, A. S., Shakun, J. D., Carlson, A. E., Clark, J., Wohlfarth, B., Mitrovica J. X., Hostetler, S. W., and McCabe, A. M.: The last glacial maximum, Science, 325, 710–714, https://doi.org/10.1126/science.1172873, 2009.

Dahl, S. O., Nesje, A., and Øvstedal, J.: Cirque glaciers as morphological evidence for a thin Younger Dryas ice sheet in east-central southern Norway, Boreas, 26, 161–180, https://doi.org/10.1111/j.1502-3885.1997.tb00850.x, 1997.

Dewald, A., Heinze, S., Jolie, J., Zilges, A., Dunai, T., Rethemeyer, J., Melles, M., Staubwasser, M., Kuczewski, B., Richter, J., Radtke, U., von Blanckenburg, F., and Klein, M.: CologneAMS, a dedicated center for accelerator mass spectrometry in Germany, Nucl. Instrum. Methods Phys. Res. Sect. B Beam Interact. Mater. Atoms, 294, 18–23, https://doi.org/10.1016/j.nimb.2012.04.030, 2013.

Donner, J.: The early and middle Weichselian Interstadials in the central area of the Scandinavian glaciations, Quaternary Sci. Rev., 15, 471–479, https://doi.org/10.1016/0277-3791(96)00002-9, 1996.

Dunai, T. J.: Cosmogenic Nuclides: Principles, Concepts and Applications in the Earth Surface Sciences, Cambridge University Press, Cambridge, https://doi.org/10.1017/CBO9780511804519, 2010.

Ehlers, J. and Gibbard, P. L.: The extent and chronology of Cenozoic Global Glaciation, Quatern. Int., 164–165, 6–20, https://doi.org/10.1016/j.quaint.2006.10.008, 2007.

Fabel, D., Stroeven, A. P., Harbor, J., Kleman, J., Elmore, D., and Fink, D.: Landscape preservation under Fennoscandian ice sheets determined from in situ produced $^{10}$Be and $^{26}$Al, Earth Planet. Sc. Lett., 201, 397–406, https://doi.org/10.1016/S0012-821X(02)00714-8, 2002.

Fareth, O. W.: Glacial geology of Middle and Inner Nordfjord, western Norway, Technical Report 408, Geological Survey of Norway, Trondheim, 1987.

Fjeldskaar, W.: Viscosity and thickness of the asthenosphere detected from the Fennoscandian uplift, Earth Planet. Sc. Lett., 126, 399–410, https://doi.org/10.1016/0012-821X(94)90120-1, 1994.

Fjeldskaar, W. and Amatonov, A.: Younger Dryas transgression in western Norway: a modelling approach, Norsk Geol. Tidsskr., 98, 127–139, https://doi.org/10.17850/njg98-1-08, 2018.

Fjeldskaar, W., Lindholm, C., Dehls, J. F., and Fjeldskaar, I.: Postglacial uplift, neotectonics and seismicity in Fennoscandia, Quaternary Sci. Rev., 19, 1413–1422, https://doi.org/10.1016/S0277-3791(00)00070-6, 2000.

Goehring, B. M., Brook, E. J., Linge, H., Raisbeck, G. M., and Yiou, F.: Beryllium-10 exposure ages of erratic boulders in Southern Norway and implications for the history of the Fennoscandian Ice Sheet, Quaternary Sci. Rev., 27, 320–336, https://doi.org/10.1016/j.quascirev.2007.11.004, 2008.

Goehring, B. M., Lohne, Ø. S., Mangerud, J., Svendsen, J. I., Gyllencreutz, R., Schaefer, J., and Finkel, R.: Late glacial and Holocene $^{10}$Be production rates for western Norway, J. Quaternary Sci., 27, 89–96, https://doi.org/10.1002/jqs.2548, 2012a.

Goehring, B. M., Lohne, Ø. S., Mangerud, J., Svendsen, J. I., Gyllencreutz, R., Schaefer, J., and Finkel, R.: Erratum. Late glacial and Holocene $^{10}$Be production rates for western Norway, J. Quaternary Sci., 27, 544, https://doi.org/10.1002/jqs.2548, 2012b.

Gosse, J. C. and Phillips, F. M.: Terrestrial in situ cosmogenic nuclides: theory and application, Quaternary Sci. Rev., 20, 1475–1560, https://doi.org/10.1016/S0277-3791(00)00171-2, 2001.

Harbor, J., Stroeven, A. P., Fabel, D., Clarhäll, A., Kleman, J., Li, Y., Elmore, D., and Fink, D.: Cosmogenic nuclide evidence for minimal erosion across two subglacial sliding boundaries of the late glacial Fennoscandian ice sheet, Geomorphology, 75, 90–99, https://doi.org/10.1016/j.geomorph.2004.09.036, 2006.

Helle, S. K., Rye, N., Stabell, B., Prösch-Danielsen, L., and Hoel, C.: Neotectonic faulting and the Late Weichselian shoreline gradients in SW Norway, J. Geodyn., 44, 96–128, https://doi.org/10.1016/j.jog.2007.01.001, 2007.

Heymann, J., Stroeven, A. P., Harbor J. M., and Caffee, M. W.: Too young or too old: Evaluating cosmogenic exposure dating based on an analysis of compiled boulder exposure ages, Earth Planet. Sc. Lett., 302, 71–80, https://doi.org/10.1016/j.epsl.2010.11.040, 2011.

Holtedahl, H.: Notes on the formation of fjord and fjord-valleys, Geogr. Ann. A., 49, 188–203, https://doi.org/10.1080/04353676.1967.11879749, 1967.

Hughes, A. L. C., Gyllencreutz, R., Lohne, Ø. S., Mangerud, J., and Svendsen, J. I.: The last Eurasian ice sheets – a chronological database and time-slice reconstruction, DATED-1, Boreas, 45, 1–45, https://doi.org/10.1111/bor.12142, 2016.

Jones, R. S., Whitehouse, P. L., Bentley, P. M., Small, S., and Dalton, A. S.: Impact of glacial isostatic adjustment on cosmogenic surface-exposure dating, Quaternary Sci. Rev., 212, 206–212 https://doi.org/10.1016/j.quascirev.2019.03.012, 2019.

Kleman, J.: Preservation of landforms under ice sheets and ice caps, Geomorphology, 9, 19–32, https://doi.org/10.1016/0169-555X(94)90028-0, 1994.

Klemsdal, T. and Sjulsen, E.: The Norwegian macrolandforms: Definition, distribution and system of evolution, Norsk Geogr. Tidsskr., 42, 133–147, https://doi.org/10.1080/00291958808552192, 1988.

Kohl, C. P. and Nishiizumi, K.: Chemical isolation of quartz for measurement of in-situ produced cosmogenic nuclides, Geochim. Cosmochim. Ac., 56, 3583–3587, 1992.

Landvik, J. Y., Ingólfsson, Ó., Mienert, J., Lehman, S. J., Solheim, A., Elverhøi, A., and Ottesen, D.: Rethinking Late Weichselian ice-sheet dynamics in coastal NW Svalbard, Boreas, 34, 7–24, https://doi.org/10.1111/j.1502-3885.2005.tb01001.x, 2005.

Lifton, N., Sato, T., and Dunai, T. J.: Scaling in situ cosmogenic nuclide production rates using analytical approximations to atmospheric cosmic-ray fluxes, Earth Planet. Sc. Lett., 386, 149–160, https://doi.org/10.1016/j.epsl.2013.10.052, 2014.

Linge, H., Brook, E. J., Nesje, A., Raisbeck, G., Yiou, F., and Clark, H.: In situ $^{10}$Be exposure ages from southeastern Norway: implications for the geometry of the Weichselian Scandinavian ice sheet, Quaternary Sci. Rev., 25, 1097–1109, https://doi.org/10.1016/j.quascirev.2005.10.007, 2006.

Linge, H., Olsen, L., Brook, E. J., Darter, J. R., Mickelson, D. M., Raisbeck, G. M., and Yiou, F.: Cosmogenic nuclide surface exposure ages from Nordland, northern Norway: implications for deglaciation in a coast to inland transect, Norsk Geol. Tidsskr., 87, 269–280, 2007.

Löffler, J. and Pape, R.: Across scale temperature modelling using a simple approach for the characterization of high mountain ecosystem complexity, Erdkunde, 58, 331–348, https://doi.org/10.3112/erdkunde.2004.04.04, 2004.

Lohne, Ø. S., Bondevik, S., Mangerud, J., and Svendsen, J. I.: Sea-level fluctuations imply that the Younger Dryas ice-sheet expansion in western Norway commenced during the Allerød, Quaternary Sci. Rev., 26, 2128–2151, https://doi.org/10.1016/j.quascirev.2007.04.008, 2007.

Lohne, Ø. S., Mangerud, J., and Birks, H. H.: Precise $^{14}$C ages of the Vedde and Saksunarvatn ashes and the Younger Dryas boundaries from western Norway and their comparison with the Greenland Ice Core (GICC05) chronology, J. Quaternary Sci., 28, 490–500, https://doi.org/10.1002/jqs.2640, 2013.

Longva, O., Blikra, L. H., and Dehls, J. F.: Rock avalanches: distribution and frequencies in the inner part of Storfjorden, Møre og

Romsdal County, Norway, Technical Report 2009.002, Geological Survey of Norway, Trondheim, 2009.

Mangerud, J.: Ice sheets limits in Norway and on the Norwegian continental shelf, in: Quaternary Glaciations Extent and Chronology, edited by: Ehlers, J. and Gibbard, P. L., Elsevier, Amsterdam, 271–294, 2004.

Mangerud, J., Gulliksen, S., and Larsen, E.: $^{14}$C-dated fluctuations of the western flank of the Scandinavian Ice Sheet 45–25 kyr BP compared with Bølling–Younger Dryas fluctuations and Dansgaard–Oeschger events in Greenland, Boreas, 39, 328–342, https://doi.org/10.1111/j.1502-3885.2009.00127.x, 2010.

Marquette, G. C., Gray, J. T., Gosse, J. C., Courchesne, F., Stockli, L., Macpherson, G., and Finkel, R.: Felsenmeer persistence under non-erosive ice in the Torngat and Kaumajet mountains, Quebec and Labrador, as determined by soil weathering and cosmogenic nuclide exposure dating, Can. J. Earth Sci., 41, 19–38, https://doi.org/10.1139/e03-072, 2004.

Marr, P. and Löffler, J.: Establishing a multi-proxy approach to alpine blockfield evolution in south-central Norway, AUC Geogr., 52, 219–236, https://doi.org/10.14712/23361980.2017.18, 2017.

Marr, P., Winkler, S., and Löffler, J.: Investigations on blockfields and related landforms at Blåhø (Southern Norway) using Schmidt-hammer exposure-age dating: palaeoclimatic and morphodynamic implications, Geogr. Ann. A., 100, 285–306, https://doi.org/10.1080/04353676.2018.1474350, 2018.

Marr, P., Winkler, S., and Löffler, J.: Schmidt-hammer exposure-age dating (SHD) performed on periglacial and related landforms in Opplendskedalen, Geirangerfjellet, Norway: Implications for mid- and late-Holocene climate variability, Holocene, 29, 97–109, https://doi.org/10.1177/0959683618804634, 2019.

Matthews, J. A., Shakesby, R. A., and Fabel, D.: Very low inheritance in cosmogenic surface exposure ages of glacial deposits: A field experiment from two Norwegian glacier forelands, Holocene, 27, 1406–1414, https://doi.org/10.1177/0959683616687387, 2017.

McCarroll, D.: Trimline trauma: the wider implications of a paradigm shift in recognising and interpreting glacial limits, Scottish Geogr. J., 132, 130–139, https://doi.org/10.1080/14702541.2016.1157203, 2016.

Morén, L. and Påsse, T.: Climate and shoreline in Sweden during Weichsel and the next 150,000 years, SKB Technical Report 01-19, Swedish Nuclear Fuel and Waste Management Co., Stockholm, 67, 2001.

Nesje, A.: Late Pleistocene and Holocene alpine glacier fluctuation in Scandinavia, Quaternary Sci. Rev., 28, 2119–2136, https://doi.org/10.1016/j.quascirev.2008.12.016, 2009.

Nesje, A. and Dahl, S. O.: Lateglacial and Holocene glacier fluctuations and climatic variations in western Norway: A review, Quaternary Sci. Rev., 12, 255–261, https://doi.org/10.1016/0277-3791(93)90081-V, 1993.

Nesje, A., Anda, E., Rye, N., Lien, R., Hole P. A., and Blikra, H.: The vertical extent of the Late Weichselian ice sheet in the Nordfjord-Møre area, western Norway, Norsk Geol. Tidsskr., 67, 125–141, 1987.

Nesje, A., McCarroll, D., and Dahl, S. O.: Degree of rock surface weathering as an indicator of ice-sheet thickness along an east–west transect across Southern Norway, J. Quaternary Sci., 9, 337–347, https://doi.org/10.1002/jqs.3390090404, 1994.

Nishiizumi, K., Imamura, M., Caffee, M. W., Southon, J. R., Finkel, R. C., and McAninch, J.: Absolute calibration of $^{10}$Be AMS standards, Nucl. Instrum. Methods Phys. Res. Sect. B Beam Interact. Mater. Atoms, 258, 403–413, https://doi.org/10.1016/j.nimb.2007.01.297, 2007.

North Greenland Ice Core Project members: High-resolution record of Northern Hemisphere climate extending into the last interglacial period, Nature, 431, 147–151, https://doi.org/10.1038/nature02805, 2004.

Patton, H., Hubbard, A., Andreassen, K., Winsborrow, M., and Stroeven, A. P.: The build-up, configuration, and dynamical sensitivity of the Eurasian ice-sheet complex to Late Weichselian climatic and oceanic forcing, Quaternary Sci. Rev., 154, 97–121, https://doi.org/10.1016/j.quascirev.2016.10.009, 2016.

Patton, H., Hubbard, A., Andreassen, K., Auriac, A., Whitehouse, P. L., Stroeven, A. P., Shackleton, C., Winsborrow, M., Heyman, J., and Hall, A. M.: Deglaciation of the Eurasian ice sheet complex, Quaternary Sci. Rev., 169, 148–172, https://doi.org/10.1016/j.quascirev.2017.05.019, 2017.

Rea, B. R., Whalley, W., Rainey, M. M., and Gordon, J. E.: Blockfields, old or new? Evidence and implications from some plateaus in northern Norway, Geomorphology, 15, 109–121, https://doi.org/10.1016/0169-555X(95)00118-O, 1996.

Rinterknecht, V. R., Clark, P. U., Raisbeck, G. M., Yiou, F., Brook, E. J., Marks, L., Zelčs, V., Lunkka, J.-P., Pavlovskaya, I. E., Piotrowski, J. A., and Raukas, A.: The last deglaciation of the southeastern sector of the Scandinavian Ice Sheet, Science, 311, 1449–1452, https://doi.org/10.1126/science.1120702, 2006.

Sollid, J. L. and Reite, J. A.: The last glaciation and deglaciation of Central Norway, in: Glacial deposits of North-West Europe, edited by: Ehlers, J., Balkema, Rotterdam, 41–59, 1983.

Steffen, H. and Wu, P.: Glacial isostatic adjustment in Fennoscandia – A review of data and modeling, J. Geodyn., 52, 169–204, https://doi.org/10.1016/j.jog.2011.03.002, 2011.

Stone, J. O., Fifield, L. K., Beer, J., Vonmoos, M., Obrist, C., Grajcar, M., Kubik, P., Muscheler, R., Finkel, R., and Caffee, M.: Co-precipitated silver metal oxide aggregates for accelerator mass spectrometry of Be-10 and Al-26, Nucl. Instrum. Meth. B, 223–224, 272–277, https://doi.org/10.1016/j.nimb.2004.04.055, 2004.

Stroeven, A. P., Fabel, D., Hättestrand, C., and Harbor, J.: A relict landscape in the centre of Fennoscandian glaciation: cosmogenic radionuclide evidence of tors preserved through multiple glacial cycles, Geomorphology, 44, 145–154, https://doi.org/10.1016/S0169-555X(01)00150-7, 2002.

Stroeven, A. P., Hättestrand, C., Kleman, J., Heyman, J., Fabel, D., Fredin, O., Goodfellow, B. W., Harbor, J. M., Jansen, J. D., Olsen, L., Caffee, M. W., Fink, D., Lundqvist, J., Rosqvist, G. C., Strömberg, B., and Jansson, K. N.: Deglaciation of Fennoscandia, Quaternary Sci. Rev., 147, 91–121, https://doi.org/10.1016/j.quascirev.2015.09.016, 2016.

Svendsen, J. I. and Mangerud, J.: Late Weichselian and Holocene sea-level history for a cross-section of western Norway, J. Quaternary Sci., 2, 113–132, https://doi.org/10.1002/jqs.3390020205, 1987.

Tveten, E., Lutro, O., and Thorsnes, T.: Geologisk kart over Norge 1 : 250 000, Norges Geologiske Undersøkelse, Ålesund, 1998.

Winguth, C., Mickelson, D. M., Larsen, E., Darter, J. R., Moeller, C. A., and Stalsburg, K.: Thickness evolution of the Scandinavian Ice Sheet during the Late Weichselian in Nordfjord, western Norway: evidence from ice-flow modeling, Boreas, 34, 176–185, https://doi.org/10.1111/j.1502-3885.2005.tb01013.x, 2005.

Wohlfarth, B.: Ice-free conditions in Sweden during Marine Oxygen Isotope Stage 3?, Boreas, 39, 377–398, https://doi.org/10.1111/j.1502-3885.2009.00137.x, 2010.

E&G Quaternary Sci. J., 68, 177–188, 2019
https://doi.org/10.5194/egqsj-68-177-2019


Open Access E&G Quaternary Science Journal

# Chemotaxonomic patterns of vegetation and soils along altitudinal transects of the Bale Mountains, Ethiopia, and implications for paleovegetation reconstructions – Part 1: stable isotopes and sugar biomarkers

**Betelhem Mekonnen[1,2], Wolfgang Zech[3], Bruno Glaser[1], Bruk Lemma[1,4], Tobias Bromm[1], Sileshi Nemomissa[5], Tamrat Bekele[5], and Michael Zech[1,6]**

[1]Institute of Agronomy and Natural Sciences, Soil Biogeochemistry, Martin-Luther University, Halle-Wittenberg, Von-Seckendorff-Platz 3, 06120, Halle, Germany
[2]Department of Urban Agriculture, Misrak Polytechnic College, P.O. Box 785, Addis Ababa, Ethiopia
[3]Institute of Soil Science and Soil Geography, University of Bayreuth, 95440 Bayreuth, Universitätsstrasse 30, Germany
[4]Forest and Rangeland Biodiversity Directorate, Ethiopian Biodiversity Institute, P.O. Box 30726, Addis Ababa, Ethiopia
[5]Department of Plant Biology and Biodiversity Management, Addis Ababa University, P.O. Box 3434, Addis Ababa, Ethiopia
[6]Institute of Geography, Technical University of Dresden, Helmholtzstrasse 10, 01062, Dresden, Germany

**Correspondence:** Betelhem Mekonnen (betymekonnen19@gmail.com)

**Relevant dates:** Received: 9 August 2018 – Revised: 6 March 2019 – Accepted: 25 July 2019 – Published: 4 September 2019

**How to cite:** Mekonnen, B., Zech, W., Glaser, B., Lemma, B., Bromm, T., Nemomissa, S., Bekele, T., and Zech, M.: Chemotaxonomic patterns of vegetation and soils along altitudinal transects of the Bale Mountains, Ethiopia, and implications for paleovegetation reconstructions – Part 1: stable isotopes and sugar biomarkers, E&G Quaternary Sci. J., 68, 177–188, https://doi.org/10.5194/egqsj-68-177-2019, 2019.

**Abstract:** Today, on the Sanetti Plateau in the Bale Mountains of Ethiopia, only fragmented patches of *Erica* species can be found at high altitudes (between 3900 and 4200 m a.s.l.). However, it is hypothesized that during the later part of the last glacial period and the early Holocene the plateau was extensively covered by *Erica* shrubs. Furthermore, it is assumed that the vegetation was later heavily destroyed by human-induced fire and/or climate change phenomena. The objective of this study is to contribute to paleovegetation reconstructions of the Sanetti Plateau by evaluating the potential of stable isotopes ($\delta^{13}C$ and $\delta^{15}N$) and sugar biomarkers for distinguishing the dominant plant species, including *Erica*, and the soils below the plants. In a companion paper (Lemma et al., 2019a) we address the same issue by evaluating lignin-derived phenols and leaf-wax-derived *n*-alkane biomarkers.

The stable carbon ($\delta^{13}C$) and nitrogen ($\delta^{15}N$) isotope values of the plant samples range from −27.5 ‰ to −23.9 ‰ and −4.8 ‰ to 5.1 ‰, respectively. We found no significant $\delta^{13}C$ and $\delta^{15}N$ differences between the dominant plant species. Mineral topsoils ($A_h$ horizons) yielded more positive values than plant samples and organic layers (O layers), which reflects mineralization processes. Moreover, the $\delta^{15}N$ values became generally more negative at higher altitudes. This likely indicates that the N cycle is more closed compared to lower altitudes. $\delta^{15}N$ maxima around 4000 m a.s.l. point to fire-induced opening of the N cycle at the chosen study sites. *Erica* species yielded the lowest overall total sugar concentration (ranging from 58 to 118 mg g$^{-1}$), dominated by galactose (G) and mannose

(M). By contrast, *Festuca* species revealed much higher total sugar concentrations ranging from 104 to 253 mg $g^{-1}$, dominated by the pentose sugars arabinose (A) and xylose (X). Although a differentiation between *Erica* versus *Festuca, Alchemilla* and *Helichrysum* is possible based on (G + M) / (A + X) ratios, *Erica* cannot be unambiguously distinguished from all other plant species occurring on the Sanetti Plateau. In addition, plant-characteristic (G + M) / (A + X) sugar patterns change during soil organic matter formation in the $A_h$ horizons. This can be likely attributed to degradation effects and soil microbial build-up of galactose and mannose. In conclusion, soil degradation processes seem to render sugar biomarker proxies unusable for the reconstruction of the past extent of *Erica* on the Sanetti Plateau, Bale Mountains, Ethiopia. This finding is of relevance beyond our case study.

**Kurzfassung:** Das Sanetti Plateau in den Bale Bergen Äthiopiens ist in seinen höheren Lagen (zwischen 3900 und 4200 m ü. NN) durch das fragmentarische Vorkommen von *Erica* geprägt. Möglicherweise kam *Erica* während des Spätglazials und dem Frühholozän dagegen flächendeckend auf dem Plateau vor und wurde erst im Laufe des Holozäns durch Klimaveränderungen und menschlich verursachte Feuer zurückgedrängt. Das Ziel unserer Studie war es herauszufinden, ob sich die im Untersuchungsgebiet dominant vorkommenden Pflanzenarten einschließlich *Erica* und die sich unter der jeweiligen Vegetation entwickelten Böden anhand ihrer Stabilkohlenstoff- und Stickstoffisotopien ($\delta^{13}$C und $\delta^{15}$N) sowie ihrer Zucker-Biomarkermuster chemotaxonomisch unterscheiden lassen. In einem Begleitartikel (Lemma et al., 2019a) verfolgen wir dasselbe Ziel anhand von Lignin-bürtigen Phenolen und Blattwachs-bürtigen *n*-Alkan-Biomarkern.

Die $\delta^{13}$C und $\delta^{15}$N-Werte für die untersuchten Pflanzen reichen von $-27,5$ ‰ bis $-23,9$ ‰ bzw. von $-4,8$ ‰ bis $+5,1$ ‰ und weisen keine signifikanten Unterschiede zwischen den dominanten Pflanzenarten auf. Positivere $\delta^{13}$C und $\delta^{15}$N-Werte in den $A_h$ Horizonten im Vergleich zu den Pflanzenproben und O-Lagen lassen sich mit der Mineralisations-bedingten Anreicherung von $^{13}$C und $^{15}$N in Böden erklären. Tendenziell negativere $\delta^{15}$N-Werte mit zunehmender Höhe spiegeln vermutlich wider, dass der N-Kreislauf klimatisch bedingt in größeren Höhen zunehmend geschlossen ist. Lokale $\delta^{15}$N Maxima in etwa 4000 m Höhe können sehr gut mit der hier feuerbedingten Öffnung des N-Kreislaufs erklärt werden. *Erica* weist mit 58 bis 118 mg $g^{-1}$ die niedrigsten Zucker-Konzentrationen auf; es dominieren die Zucker Galactose und Mannose (G und M). Im Gegensatz dazu variieren die Zucker-Konzentrationen im weit verbreitet vorkommenden Gras der Gattung *Festuca* zwischen 104 und 253 mg $g^{-1}$; hier dominieren die Zucker Arabinose und Xylose (A und X). Obwohl *Erica* anhand des (G + M) / (A + X) Verhältnisses von *Festuca*, *Alchemilla* und *Helichrysum* chemotaxonomisch unterschieden werden kann, gilt dies nicht für weitere untersuchte Pflanzenarten wie *Kniphofia* und *Lobelia*. Darüber hinaus offenbaren die Datenreihen Pflanze – O-Lage – $A_h$-Horizont, dass die zum Teil pflanzencharakteristischen (G + M) / (A + X) Verhältnisse systematischen Veränderungen unterliegen. Dies kann vermutlich auf Degradation und den bodenmikrobiellen Aufbau von Galaktose und Mannose zurückgeführt werden und legt nahe, dass weder anhand von $\delta^{13}$C und $\delta^{15}$N, noch anhand von Zuckerbiomarkern eine verlässliche Rekonstruktion der Vegetation auf dem Sanetti Plateau möglich ist.

## 1 Introduction

The Bale Mountains in the southeast of Ethiopia constitute the largest area with afroalpine and Ericaceous vegetation on the African continent (Hedberg, 1951; Miehe and Miehe, 1994). The area is best known for its large numbers of local endemic flora such as *Lobelia rhynchopetalum*, *Lobelia scebelii* and *Senecio* species (Hillman, 1986). Similar to other tropical high-altitude mountains in East Africa such as Mount Kenya, Mount Kilimanjaro and Mount Meru, the vegetation of the Bale Mountains is characterized by altitudinal zones (or belts) with an afromontane forest belt, an Ericaceous belt and an afroalpine belt (Hedberg, 1969; Miehe and Miehe, 1994).

Vegetation reconstructions in the Bale Mountains have been done using mainly pollen records from pit cores (Hamilton, 1982) and sediments (Bonnefille, 1983; Bonnefille and Hamilton, 1986; Umer et al., 2007). Bonnefille (1983) reported, for the Gadeb basin north of the Bale Mountains, on the abundant occurrence of *Erica* pollen in sediments of a Pliocene lake between 2.5 and 2.4 myr. Pollen records from Mount Badda (north-northwest of the Bale

Mountains) and the Danka valley (Bale Mountains) suggest that the upper limit of the Ericaceous belt (3830 to 4040 m a.s.l.) developed between 8000 and 3500 years BP (Bonnefille and Hamilton, 1986; Miehe and Miehe, 1994). A pollen study from Gerba Guracha in the Bale Mountains (Umer et al., 2007) showed that the vegetation after deglaciation at about 16 cal kyr BP mainly consisted of grasses. Only with the beginning of the Holocene at 11 cal kyr BP did the Ericaceous belt rise and extend across the Sanetti Plateau, according to Miehe and Miehe, 1994. From about 4.5 cal kyr BP *Erica* shrubs and forests decreased in area and altitude and the afroalpine ecosystem with *Alchemilla* and Poaceae species expanded on the Sanetti Plateau. According to Kidane et al. (2012), Miehe and Miehe (1994), Umer et al. (2007), and Wesche et al. (2000), the most likely explanation for the decrease in *Erica* is fire caused by human invasion. Increasing aridity during the mid to late Holocene (Tiercelin et al., 2008) may have contributed to the destruction of the *Erica* woodlands on the Sanetti Plateau as well. However, the reason for the contemporary occurrence of only fragmented patches of *Erica* is still not clear.

At present, human impact is steadily increasing (Belayneh et al., 2013), despite large areas having been protected within the Bale Mountains National Park since 1970 (Hillman, 1986). During fieldwork in February 2015 and 2017, we observed people in the Bale Mountains mainly subsisting on pastoralism and illegal logging, thus increasingly placing the natural resources and wildlife under immense pressure, leading to deforestation, overgrazing and frequent fire occurrence. Wildfires have likely been a common phenomenon in the Bale Mountains for a long time. However, they seem to have become more severe in recent years (Johansson, 2013).

During the past decades the analyses of stable carbon ($\delta^{13}$C) and nitrogen ($\delta^{15}$N) isotopes have significantly contributed to a better understanding of (paleo-)ecological processes (Tiunov, 2007). This technique has high potential for tracing biogeochemical processes and for reconstructing past and current interactions between humans, plants and the surrounding environment (Dawson et al., 2002; Zech, 2006; Zech et al., 2011a). Furthermore, $\delta^{13}$C analyses of soils and sediments are particularly used to reconstruct alpine vegetation changes in terms of $C_3$ versus $C_4$ photosynthetic pathway (Glaser and Zech, 2005; Zech et al., 2011b). Stable isotopes have been previously used in Ethiopia for reconstructing vegetation history (Gebru et al., 2009; Levin et al., 2011) and to infer land use and land cover change (Eshetu and Högberg, 2000; Liu et al., 2007; Solomon et al., 2002) as well as physiological processes (Krepkowski et al., 2013). Gebru et al. (2009) found that the vegetation has changed from $C_3$ to $C_4$ during the late Holocene (3300 years BP) in Tigray due to agricultural expansion. Eshetu and Högberg (2000) suggested that the vegetation shifted from grassland to forest in the Menagesha forest and Wendo Genet areas several hundred years ago.

Given that pollen preservation is often poor in soils due to oxidation (Brewer et al., 2013; Hevly, 1981; Li et al., 2007) there have been large efforts during the last decades toward developing proxies based on organic molecules that are specific to certain plant and vegetation types (chemotaxonomy) in order to contribute to the reconstruction of vegetation changes. This is mostly done with lipid biomarkers (Jansen et al., 2006a, b, 2008; see our companion paper, Lemma et al., 2019a, for further details). In addition, Kebede et al. (2007) have used amplified fragment length polymorphisms (AFLPs) to infer the phylogeographical history of the afromontane species (*Lobelia giberroa*) in the Bale Mountains. Sugar monomers build up polysaccharides such as cellulose and hemicellulose (Simoneit, 2002). While arabinose and xylose are very abundant in plants, fucose and rhamnose are important components of bacterial cell walls. Fucose and rhamnose are therefore often used as proxies for microbe-derived organic matter in soils (Sauheitl et al., 2005). Moreover, sugar biomarkers were proposed and applied as proxies for paleovegetation reconstructions (Glaser and Zech, 2005; Prietzel et al., 2013). For instance, Jia et al. (2008) could chemotaxonomically distinguish between lichens, *Sphagnum* and vascular plants based on the ratio (mannose + galactose) / (arabinose + xylose) and percentage of (rhamnose + fucose). Similarly, Hepp et al. (2016) suggested the sugar ratios fucose /(arabinose + xylose) and (fucose + xylose) / arabinose as proxies in paleolimnological studies for distinguishing between terrestrial versus aquatic sedimentary organic matter.

The objectives of this study were to evaluate (i) whether the dominant plant and vegetation types of the afroalpine region of the Bale Mountains can be distinguished chemotaxonomically based on their stable carbon and nitrogen isotopic composition and/or sugar biomarkers and (ii) whether the isotope and biomarker patterns of plants are reflected in the soils below correspond to contemporary plants. Note that in our companion paper (Lemma et al., 2019a) we address the same questions but instead focusing on other biomarkers, namely lignin-derived phenols and leaf-wax-derived *n*-alkanes. Overall the results of our two companion studies were meant to form a modern-day calibration for reconstructing the Late Quaternary vegetation history (mainly of *Erica*) on the Sanetti Plateau of the Bale Mountains.

## 2 Material and methods

### 2.1 Study site

The study was conducted in the Bale Mountains National Park, located in the Oromia Region of Ethiopia (Fig. 1) between 6°40′ and 7°10′ N and 39°30′ and 39°58′ E (Miehe and Miehe, 1994, Tiercelin et al., 2008; Umer et al., 2007). It covers an area of 2200 km$^2$ and an altitudinal range from 1400 to 4377 m a.s.l., including the second highest peak in the country (Tullu Dimtu). The intertropical convergence

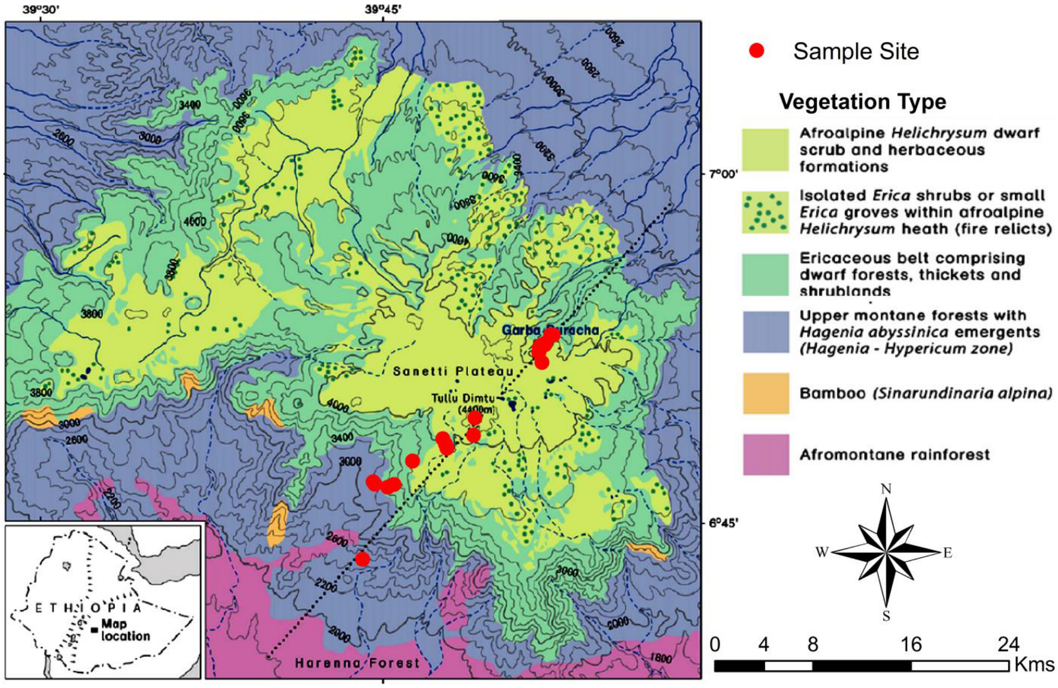


**Figure 1.** Map of the Bale Mountains showing the vegetation zones and study sites along the northeastern–southwestern transect (modified from Miehe and Miehe, 1994). Dominant vegetation types sampled comprise the Ericaceous and afroalpine belt.

zone (ITCZ), altitudinal and topographic features are the major factors influencing precipitation in the Bale Mountains (Miehe and Miehe, 1994; Bonnefille, 1983). Most of the year, the Bale Mountains are strongly influenced by southeasterlies originating from the Indian Ocean that provide monsoonal precipitation. A recent study done by Lemma et al. (2019b) suggested that the Bale Mountains receive precipitation from the Arabian Sea and southern Indian Ocean during the dry and wet season, respectively. The area experiences two rainy seasons: one lasting from March to June and a second heavy rainy season from July to October. In Dinsho (the Bale Mountains National Park headquarters at 3070 m a.s.l.), mean annual precipitation is 1069 mm and mean annual temperature is 11.8 °C. Monthly mean maximum and minimum temperatures are 19.9 and 3.4 °C, respectively (Ethiopian Metrological Services Agency, 2004–2015). Kidane et al. (2012) emphasized, however, that the mountains experience a highly variable climate from north to south as a result of altitudinal difference and the influence of lowland hot air masses. Extreme temperature variation between the wet and dry seasons is a common phenomenon on the Sanetti Plateau.

The afromontane forest of the Bale Mountains is divided into a southern declivity, or zonation of Harenna forest (1450 to 3200 m a.s.l. to the southwest), and northern declivity (drier montane forest 2200 to 3750 m a.s.l.). These vegetation zones are dominated by *Podocarpus falcatus, Warburgia ugandensis, Pouteria adolfi-friederici, Croton macrostachyus, Juniperus procera, Hagenia abyssinica* and *Hypericum revolutum* (Friis, 1986; Lisanework and Mesfin, 1989; Yineger et al., 2008). Regions above 3500 m.a.s.l., including the tree line ecotone in eastern Africa, which is comprised of a number of taxa with small sclerophyllous leaves, are characterized as Ericaceous vegetation (Miehe and Miehe, 1994). This vegetation is commonly found on most African mountains, especially in the Atlas Range in North Africa, the Tibesti Mountains of the central Sahara, the Ethiopian Highlands and in the mountains of eastern Africa that extend southwards to Malawi (Jacob et al., 2015; Messerli and Winiger, 1992). This vegetation zone stretches from 3500 to 3800 m a.s.l. and it becomes patchy on the Sanetti Plateau above 3800 m a.s.l.. It is continuously dominated by shrubs and shrubby trees such as *Erica arborea, Erica trimera, Hypericum revolutum* and perennial shrubs or herbs such as *Alchemilla haumannii, Anthemis tigreensis, Helichrysum citrispinum, H. splendidum, H. gofense, Senecio schultzii, Thymus schimperi* and *Kniphofia foliosa* (Friis et al., 2010). Some of these species are also found in the afroalpine belt, since the upper and lower boundaries of this belt are very difficult to define. The afroalpine vegetation, which extends from 3800 to 4377 m a.s.l., is more open and richer in grass. It is mainly characterized by a combination of giant *Lobelia* (*Lobelia rhynchopetalum*), species of *Helichrysum*, shrubby species of *Alchemilla*, grasses (*Festuca richardii, Agrostis quinqueseta* and *Pentaschistis pictigluma*) and the creeping dwarf shrub *Euryops prostata*.

The soils in the Bale Mountains National Park are often shallow, rich in stones and with organic layers (O layers), mineral topsoils ($A_h$ horizons), mineral subsoils (B horizons) and parent material (C horizons). Some soils are clearly stratified with bolder rich surface layers (O, A, B) above fine textured ash layers (2C). They are derived from volcanic materials such as lava of various kinds, basalt and agglomerates (Miehe and Miehe 1994) and can be classified as Andosols, Cambisols and Leptosols (Abbate et al., 2015; Billi, 2015; Yimer et al., 2006). In addition, Gleysols and Histosols occur frequently in depressions.

### 2.2 Sample collection

Leaf and soil samples were collected along a northeast (3870 to 4134 m a.s.l.) to southwest (2550 to 4377 m a.s.l.) transect (Fig. 1). Leaf samples were taken from dominant plants comprising: *Erica arborea* L. ($n = 5$), *Erica trimera* (Engl.) Beentje ($n = 5$), *Alchemilla haumannii* Rothm ($n = 5$), *Helichrysum splendidum* Thunb. L. ($n = 2$), *Lobelia rhynchopetalum* Hemsl. ($n = 1$), *Kniphofia foliosa* Hochst. ($n = 1$) and *Festuca abyssinica* Hochst. ex A. Rich. ($n = 6$) (Fig. 2). *Erica* leaves were collected from the upper part of the crown. Moreover, 23 mineral topsoils ($A_h$ horizons) from each sampling site were collected in order to test whether these horizons represent the typical biogeochemical features of the standing vegetation. Additionally, where available, humified organic layers (O layers) excluding litter were sampled ($n = 15$).

### 2.3 Sample analyses

Soil samples were air dried and sieved (< 2 mm). An aliquot of plant and soil samples was ground using a ball mill and weighted into separate tin capsules. Total organic carbon (TOC), total nitrogen (TN), and the natural abundance of $^{13}C$ and $^{15}N$ of the samples were measured using an elemental analyzer coupled to an isotope ratio mass spectrometer (EA-IRMS). Samples were converted into $CO_2$ and $NO_2$ by an oxidation reactor filled with tungsten trioxide and aluminum oxide and cobalt (II, III) oxide (silvered) (1020 °C). Subsequently, $NO_2$ was further reduced to $N_2$ by a reduction reactor filled with copper wires (650 °C). Water was removed by a magnesium perchlorate trap. Helium (purity 99.9997 %) was used as carrier gas at 100 mL min$^{-1}$. The precision of the stable isotope analyses as determined by replication measurements of standards was 0.3 ‰ and 0.2 ‰ for $\delta^{13}C$ and $\delta^{15}N$, respectively.

Sugar monomers in the plant and soil samples were extracted hydrolytically with 10 mL 4M trifluoroacetic acid (TFA) and 100 µg of myo-inositol (as internal standard) for 4 h at 105 °C, following the method described by Zech and Glaser (2009). This extraction procedure does not liberate considerable amounts of monosaccharides from cellulose (Amelung et al., 1996). Therefore, this fraction is sometimes called "non-cellulosic polysaccharides" (NCP) in the literature (e.g., Prietzel et al., 2013). The hydrolyzed samples were filtered through a vacuum suction system and the filtrates were collected in 100 mL conical flasks. The filtrates were then evaporated using rotary evaporators in order to remove the acid and the water that were added to the samples. In order to remove humic substances and cations, the redissolved samples were passed through XAD and Dowex resin columns, respectively, following Amelung et al. (1996), and the filtrates were collected in 50 mL conical flasks. The filtrates were dried using rotary evaporators and a freeze drier. The purified neutral sugars were transferred into Reacti-Vials. Derivatization of the freeze-dried sugars was done with N-methyl-2-pyrrolidone (NMP) at 75 °C for 30 min in a heating block. After cooling, 400 µL of BSTFA (N, O-Bis(trimethylsilyl)trifluoracetamide) were added to the vials and the samples were heated again to 75 °C for 5 min. The samples were transferred to auto-sampler vials after cooling and measured using gas chromatography (SHIMADZU GC-2010, Kyoto, Japan) equipped with a flame ionization detector (FID). Sugars were separated on a Supelco SPB-5 column (length, 30 m; inner diameter, 0.25 mm; film thickness, 0.25 µm) using helium as carrier gas. The temperature was ramped from 160 to 185 °C, held for 4 min, then ramped to 240 °C and held for 0 min, and finally ramped to 300 °C and held for 5 min. The temperature of the injector was set at 250 °C. Hierarchical cluster analysis and notch box plots for the sugar biomarkers data were done by using the R software (version 3.4.4, 15 March 2018).

## 3 Results and discussion

### 3.1 Elemental composition, $\delta^{13}C$ and $\delta^{15}N$ of dominant plants

Total organic carbon and nitrogen contents were used to calculate TOC / TN ratios in order to characterize and possibly distinguish the investigated plant types. The leaf samples yielded values covering a wide range from 14.5 (*Lobelia*) to 80.4 (*Erica*). The boxplot diagrams in Fig. 3a depict that plant leaves are characterized by significantly higher TOC / TN ratios compared to corresponding O layers and $A_h$ horizons. Mean TOC / TN values for all investigated dominant plants are > 40, thus confirming the finding of Zech (2006) and Zech et al. (2011b) from Mt. Kilimanjaro that subalpine and alpine vegetation has typically very high TOC / TN values.

The $\delta^{13}C$ values of *Erica* are not significantly different from the other plants (Fig. 3b). Note that *Kniphofia* has a more positive value, but a statistical comparison could not be applied because only one sample is available. No significant variation in stable isotopes among the rest of dominant plant species could be detected either. Overall, the $\delta^{13}C$ values of all investigated plants range from −27.5 (*Erica*) to −23.9 ‰ (*Kniphofia*); thus, they are well within the typical

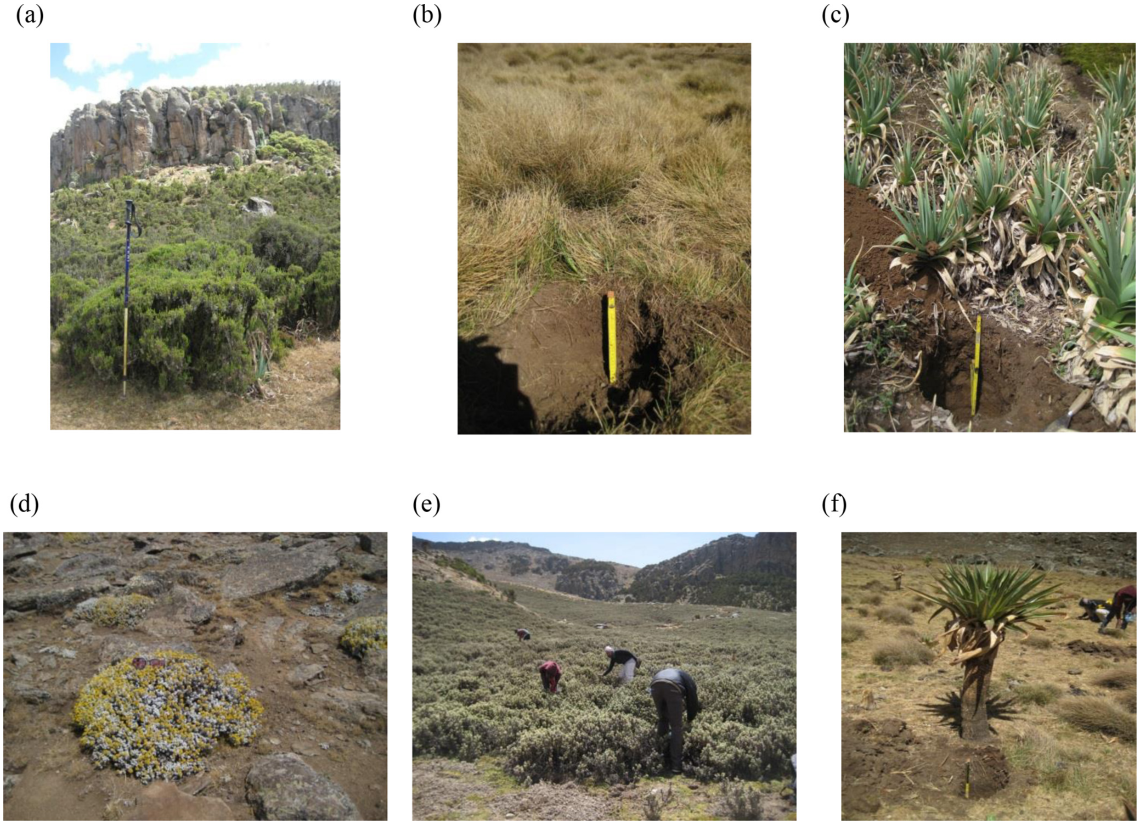


**Figure 2.** Photos showing plant species investigated in this study: **(a)** *Erica trimera* (3870 m a.s.l.), **(b)** *Festuca abyssinica* (3920 m a.s.l.), **(c)** *Alchemilla haumannii* (3947 m a.s.l.), **(d)** *Helichrysum splendidum* (4377 m a.s.l.), **(e)** *Kniphofia Foliosa* (3930 m a.s.l.) and **(f)** *Lobelia rhynchopetalum* (3922 m a.s.l.).

range for $C_3$ plants. The occurrence of (sub)alpine $C_4$ plants similar to those on Mt. Kenya (Street-Perrott et al., 2004; Young and Young, 1983) is hitherto not confirmed for the Bale Mountains based on the admittedly quite limited plant sample set presented here. However, the absence of $C_4$ would be in agreement with the findings of Zech et al. (2011b) from Mt. Kilimanjaro. Furthermore, our $\delta^{13}$C leaf data do not reveal a dependence on altitude, as reported by Körner et al. (1991) for a global dataset. This likely reflects that local climatic conditions and other factors exert a higher control in our study area. The $\delta^{15}$N values for leaf material range from −4.8 (*Erica*) to 5.1 ‰ (*Alchemilla*). Such a relatively large $\delta^{15}$N variability is well described for plants and can be explained by different nitrogen sources being taken up and by different mechanisms of N uptake including mycorrhizae being present. Similar to the $\delta^{13}$C results, $\delta^{15}$N values of *Erica* are not significantly different from other plants (Fig. 3c).

## 3.2 Elemental composition, $\delta^{13}$C and $\delta^{15}$N in O layers and $A_h$ horizons

Apart from revealing similarities and/or differences in TOC / TN, $\delta^{13}$C and $\delta^{15}$N between the dominant plants, Fig. 3a furthermore reveals that TOC / TN ratios generally strongly decrease from leaf material over O layers to the respective $A_h$ horizons. This reflects the preferential loss of carbon versus nitrogen during mineralization (Meyers, 1994). At the same time, this decrease implies that TOC / TN ratios of plants cannot be used as a straight-forward proxy for paleovegetation reconstructions in archives that are prone to organic matter degradation and mineralization.

According to Fig. 3b, the O layers tend to have slightly more negative $\delta^{13}$C values compared to leaf material. By contrast, $A_h$ horizons have generally more positive $\delta^{13}$C values. We explain the former finding with the preferential loss of an easily degradable $^{13}$C-enriched organic matter pool, like sugars during a very early stage of leaf litter degradation. The later finding is in agreement with numerous studies (Ehleringer et al., 2000; Garten et al., 2000; Natelhoffer and Fry, 1988) reporting on increasing $\delta^{13}$C values with increasing soil depths. This $^{13}$C enrichment in soils is usually explained by the preferential enzymatically controlled loss of $^{12}$C during soil organic matter degradation (Farquhar et al., 1982; Friedli et al., 1986; Zech et al., 2007). It may be noteworthy that two $A_h$ horizons of the northeastern part of the transect yielded very positive $\delta^{13}$C values of −21.2 ‰ and −19.1 ‰, respectively, which are higher than expected for

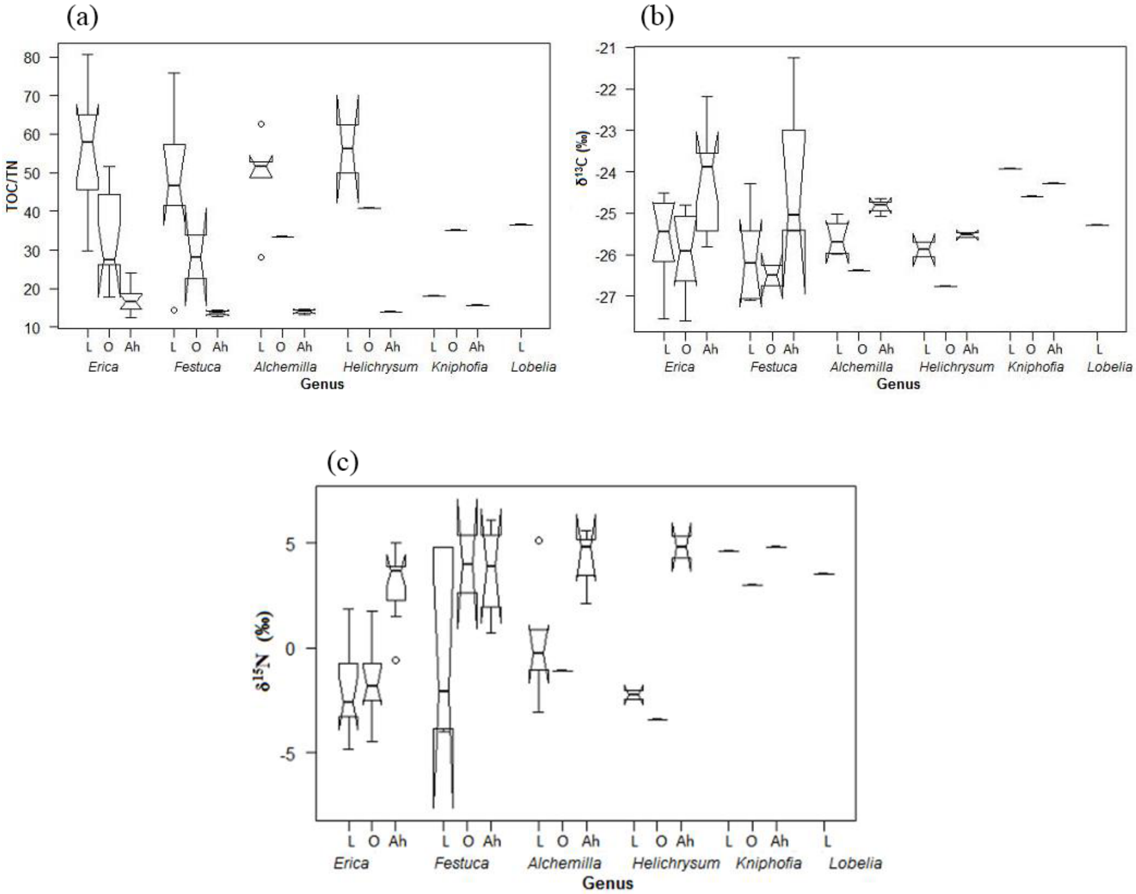


**Figure 3.** Boxplot diagrams showing **(a)** TOC / TN and **(b)** $\delta^{13}$C and **(c)** $\delta^{15}$N results for leaves (L), O layers and $A_h$ horizons of the investigated dominant vegetation types in the Bale Mountains. The upper and lower bold lines indicate the 75th and 25th quartiles, respectively, and the middle bold line shows the median. The lines extending outside the box (whiskers) show variability outside the quartiles and notches indicate the 95 % confidence interval. White circles represent outliers. Note that short horizontal single lines are due to small sample sizes.

soils that have developed under pure $C_3$ vegetation. Given that our plant sample set is rather small, it cannot be excluded that those soils received litter from $C_4$ grasses and we encourage further studies in order to clarify whether $C_4$ grasses occur in the Bale Mountains like on Mt. Kenya or not (see Sect. 3.1).

Like $\delta^{13}$C, $\delta^{15}$N of soils is also reported to be strongly affected by soil organic matter degradation and mineralization (Natelhoffer and Fry, 1988; Zech et al., 2007). It is hence not surprising that the investigated $A_h$ horizons are clearly $^{15}$N-enriched compared to the leaf samples (Fig. 3c). Furthermore, the O layers and the $A_h$ horizons across the altitudinal transects of the Bale Mountains reveal a general trend toward more negative values with increasing altitude (Fig. 4). Similar findings were reported for the southern and northern slopes of Mt. Kilimanjaro (Zech et al., 2011a, b) and reflect that the N cycle is open at lower altitudes as it is characterized by higher temperatures. By contrast, at higher altitudes N mineralization and N losses are reduced (closed N cycle) due to lower temperatures. As an exception from this overall trend, the O layers reveal a maximum between 3920 and 3950 m a.s.l. and the $A_h$ horizons reveal two maxima around 3950 as well as around 4130 m a.s.l. Given that O layers and $A_h$ horizons act as integrated recorders of the N cycle taken from periods of several years and hundreds of years, respectively, those maxima indicate that at the respective sampling sites the N cycle was open and significant N losses occurred during the past. Several studies emphasized already that the subalpine and alpine zones in the Bale Mountains are heavily affected by human-induced fires (Johansson, 2013; Kidane et al., 2012; Miehe and Miehe,1994; and Wesche et al., 2000). Therefore, we attribute this opening of the N cycle to the repeated burning (and thus loss) of the relatively $^{15}$N-depleted vegetation cover.

## 3.3 Sugar concentrations and patterns of dominant plants

As shown in Fig. 5, the overall non-cellulosic sugar concentrations in leaves range from 58 to 253 mg g$^{-1}$. We found high contents in *Festuca* and *Alchemilla*, whereas *Erica* is

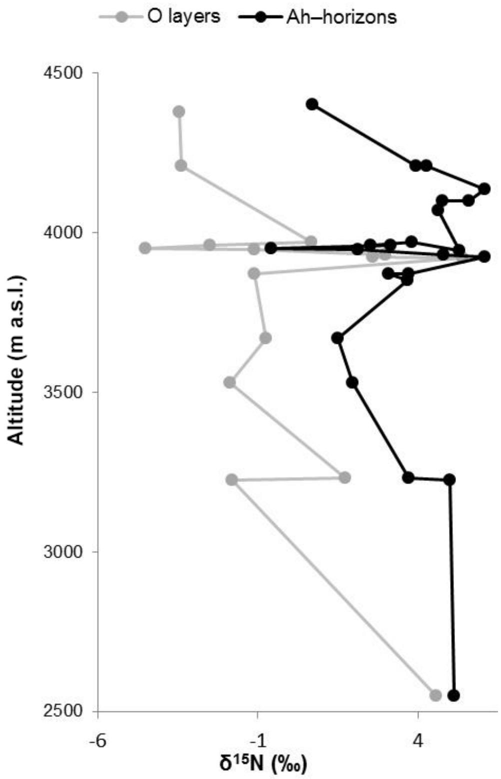


**Figure 4.** $\delta^{15}$N results of O layers and $A_h$ horizons along altitudinal transects of the Bale Mountains.

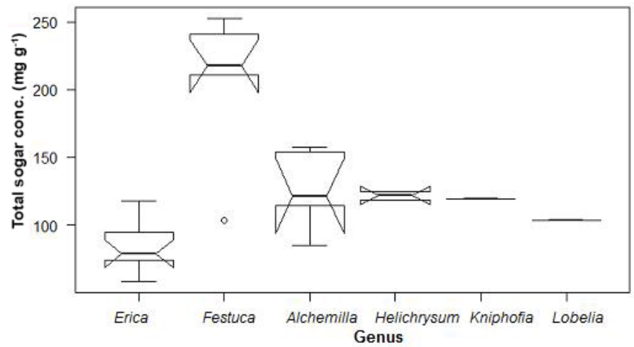


**Figure 5.** Total sugar concentrations of the investigated plant leaves along altitudinal transects of the Bale Mountains. The upper and lower bold lines indicate 75th and 25th quartiles, respectively, and the middle bold line shows the median. The lines extending outside the box (whiskers) show variability outside the quartiles and notches indicate the 95 % confidence interval. White circles represent outliers. Note that short horizontal single lines are due to small sample sizes.

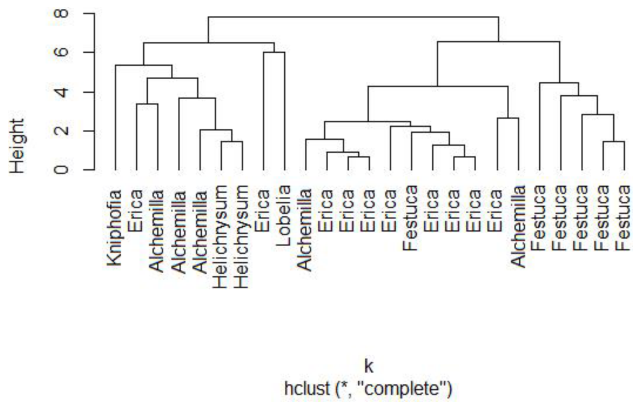


**Figure 6.** Cluster formation based on non-cellulosic sugar biomarker concentrations of leaf samples from the dominant vegetation types in the Bale Mountains.

characterized by relatively low non-cellulosic sugar concentrations. This has implications for paleovegetation reconstructions because plants producing lower amounts of sugars are less represented in soils and sedimentary archives. A comparable example for such an issue is leaf-wax-derived *n*-alkane biomarkers not being sensitive enough for coniferous trees due to the very low *n*-alkane concentrations of coniferous needles (Zech et al., 2012).

Nevertheless, a hierarchical cluster analysis performed for leaves on the basis of their individual sugar monomers arabinose, fucose, galactose, mannose, rhamnose, ribose, xylose, glucuronic acid and galacturonic acid resulted in three main groups, suggesting that a chemotaxonomic differentiation of the dominant vegetation types on the Bale Mountains may be possible (Fig. 6). The first group mainly represents *Kniphofia, Alchemilla* and *Helicrysum* species indicating close similarity between them. The second group predominantly contains *Erica* spp. and the third group is mainly composed of *Festuca* spp. This result allows the conclusion that the plant species under study vary in their foliar sugar composition. *Erica* and *Festuca* vary especially clearly in their sugar signatures.

Both Jia et al. (2008) and Prietzel et al. (2013) used the ratio of galactose and mannose versus arabinose and xylose ($(G+M)/(A+X)$) in particular, in order to distinguish between different vegetation types. In the Bale Mountains, *Erica* leaves yielded significantly higher $(G+M)/(A+X)$ ratios compared to *Alchemilla*, *Festuca* and *Helichrysum* (Fig. 7a). Hence, one might be tempted to recommend the $(G+M)/(A+X)$ ratio as a proxy in soils and sediments for reconstructing *Erica* distribution during the past. Note that the $(G+M)/(A+X)$ ratios around 1 for *Erica, Kniphofia* and *Lobelia* are clearly higher than the ratios reported to be typical for plants according to Oades (1984). By contrast, the fucose to arabinose and xylose ratios ($F/(A+X)$) are very low, as expected for plants (cf. Hepp et al., 2016), with a mean value of $0.05 \pm 0.05$ ($n = 25$). *Erica* is characterized by higher ratios than *Festuca* (Fig. 7b).

### 3.4 Sugar patterns of O layers and $A_h$ horizons

The characteristic $(G+M)/(A+X)$ and $F/(A+X)$ ratios for the dominant vegetation types are not well reflected in

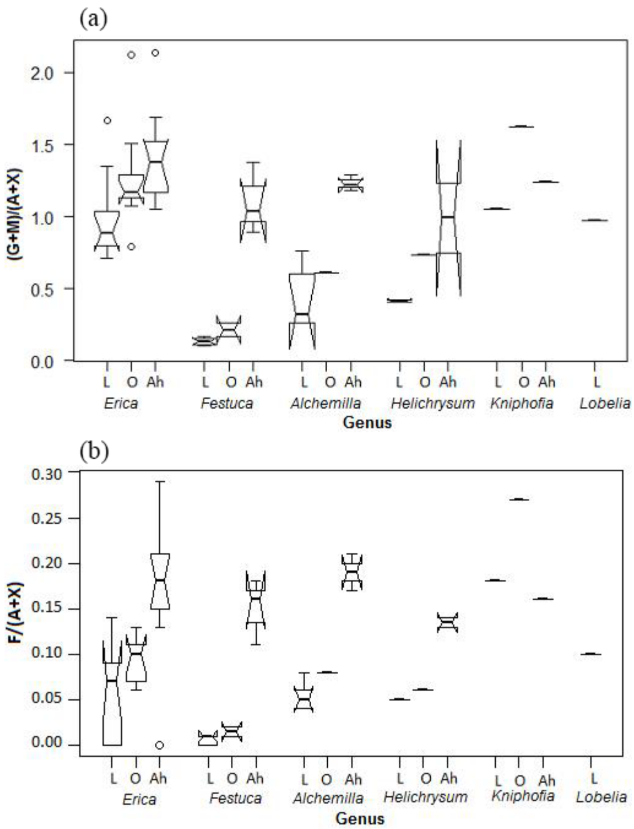


**Figure 7.** Boxplot diagram showing the **(a)** (G + M) / (A + X) and **(b)** F / (A + X) ratios of leaves (L), O layers and $A_h$ horizons, respectively, along the altitudinal transect across the Bale Mountains. The upper and lower bold lines indicate 75th and 25th quartiles, respectively, and the middle bold line shows the median. The lines extending outside the box (whiskers) show variability outside the quartiles and notches indicate the 95 % confidence interval. White circles represent outliers. Note that short horizontal single lines are due to small sample sizes.

the respective O layers and $A_h$ horizons (Fig. 7). Rather, the ratios generally increase, indicating that both arabinose and xylose are preferentially degraded or that galactose, mannose and fucose are built-up by soil microorganisms. This later interpretation is in agreement with Oades (1984), who reported that soil microorganisms are characterized by (G + M) / (A + X) ratios > 2. The F / (A + X) ratios of $0.18 \pm 0.07$ observed for $A_h$ horizons in this study are well within the range reported for terrestrial soils by Hepp et al. (2016). Apart from soil microorganisms, a considerable contribution of root-derived sugars, including root exudates, is very likely as well (Gunina and Kuzyakov, 2015). More systematic respective biomarker studies, similar to, for instance, the one carried out by Prietzel et al. (2013) are therefore encouraged in order to address this effect more quantitatively in the future.

As a result, soils under *Alchemilla* and *Festuca* yield (G + M) / (A + X) ratios similar to those of *Erica* leaves. This has severe implications for paleovegetation reconstructions based on sugar biomarkers and resembles degradation problems reported for lignin-derived phenol and leaf-wax-derived *n*-alkane biomarkers (Lemma et al., 2019a; Zech et al., 2012). In the case of the Bale Mountains, only fresh leaves or leaf material that has undergone little degradation (as it may hold true in anoxic lacustrine sediments) allow a chemotaxonomic differentiation between *Erica* and other dominant vegetation types, such as *Alchemilla, Festuca* and *Helichrysum*. Given that by contrast good preservation of sugar biomarkers is usually not the case in soils, we consider neutral sugar biomarkers unsuitable for reconstructing former *Erica* expansion from paleosols in our study area and instead encourage studies focusing on other biomarkers.

## 4 Conclusions

Having investigated plant material, O layers and $A_h$ horizons along altitudinal transects, we found no clear evidence for the modern-day occurrence of $C_4$ grasses in the Bale Mountains. Neither $\delta^{13}$C nor $\delta^{15}$N values allow a clear chemotaxonomic differentiation of *Erica* from other dominant vegetation types such as *Alchemilla, Festuca* and *Helichrysum*. TOC / TN ratios strongly decrease and both $^{13}$C and $^{15}$N become generally enriched from the leaves to the $A_h$ horizons due to degradation and mineralization. $\delta^{15}$N is furthermore generally more negative at higher altitudes, which reflects a low degree of mineralization and overall a relatively closed N cycle due to low temperatures. $\delta^{15}$N maxima around 4000 m a.s.l. indicate the likely fire-induced opening of the N cycle at the respective study sites. *Erica* leaves are characterized by relatively low total sugar concentrations and can be chemotaxonomically distinguished from the other dominant vegetation types mainly because of their higher relative amounts of galactose and mannose. However, these sugar monomers are produced by soil microorganisms as well. Therefore, soils under *Alchemilla* and *Festuca* yielded (G + M) / (A + X) ratios similar to those of *Erica* leaves, and even in soils under *Erica* this ratio significantly increased. This suggests that sugar biomarkers alone do not allow the establishment of a straight-forward proxy for reconstructing the former expansion of *Erica* on the Sanetti Plateau. Therefore, future work should emphasize alternative promising molecular markers, such as tannin-derived phenols and terpenoids. In addition, black carbon should be analyzed in order to reveal the impact of fire on the extent of the Ericaceous vegetation.

**Data availability.** The data are archived in the following Zenodo repository: https://doi.org/10.5281/zenodo.3371636, available at: https://zenodo.org/record/3371636\T1\textbackslash#.XVrf3N4zbIU.

**Author contributions.** WZ and BG designed the research. The fieldwork (sample collection) was done by WZ, BM and BL. BM and TB did the laboratory work and BM prepared the manuscript with the help of MZ. All co-authors contributed to, read and approved the manuscript.

**Competing interests.** The authors declare that they have no conflict of interest.

**Acknowledgements.** We are grateful to the Bale Mountains National Park, Ethiopian Biodiversity Institute and Ethiopian Wildlife Conservation Authority for permitting the scientific field work and facilitating the access to the plant and soil materials used in this study. We would like to express our gratitude to the Department of Plant Biology and Biodiversity Management at Addis Ababa University for their scientific collaboration. We also extend our sincere thanks to Marianne Benesch for analyzing the stable isotopes and Heike Maennicke for her great help with the sugar analysis. We acknowledge the financial support within the funding program Open Access Publishing by the German Research Foundation (DFG). Last, but not least, Betelhem Mekonnen acknowledges the support given by the Katholischer Akademischer Ausländer-Dienst (KAAD). We kindly thank three anonymous reviewers for their constructive comments and suggestions that greatly helped to improve our manuscript.

**Financial support.** This research has been supported by the DFG (grant nos. GL327/18-1, ZE844/10-1).

## References

Abbate, E., Bruni, P., and Sagri, M.: Geology of Ethiopia: A Review and Geomorphological Perspectives, in: Landscapes and Landforms of Ethiopia, edited by: Billi, P., Springer Netherlands, Dordrecht, 33–64, 2015.

Amelung, W., Cheshire, M. V., and Guggenberger, G.: Determination of neutral and acidic sugars in soil by capillary gas liquid chromatography after trifluoroacetic acid hydrolysis, Soil Biol. Biochem., 28, 1631–1639, https://doi.org/10.1016/S0038-0717(96)00248-9, 1996.

Belayneh, A., Yohannes, T., and Worku, A.: Recurrent and extensive forest fire incidence in the Bale Mountains National Park (BMNP), Ethiopia: Extent, Cause and Consequences, Int. J. Environ. Sci., 2, 29–39, 2013.

Billi, P.: Geomorphological Landscapes of Ethiopia, in Landscapes and Landforms of Ethiopia, edited by: Billi, P., 3–32, Springer Netherlands, Dordrecht, 2015.

Bonnefille, R.: Evidence for a Cooler and Drier Climate in Ethiopia 2.5 Mys, Nature, 303, 487–491, 1983.

Bonnefille, R. and Hamilton, C.: Quaternary and Late Tertiary history of Ethiopian vegetation, Acta Uni. Upps. Symb. Bot. Upps. 26, 48–63, 1986.

Brewer, S., Guiot, J., and Barboni, D.: Use of Pollen as Climate Proxies, Encycl. Quat. Sci. Second Ed., 805–815, https://doi.org/10.1016/B978-0-444-53643-3.00180-1, 2013.

Dawson, T. E., Mambelli, S., Plamboeck, A. H., Templer, P. H., and Tu, K. P.: Stable Isotopes in Plant Ecology, Annu. Rev. Ecol. Syst., 33, 507–559, https://doi.org/10.1146/annurev.ecolsys.33.020602.095451, 2002.

Ehleringer, J. R., Buchmann, N., and Flanagan, L. B.: Carbon isotope ratios in belowground carbon cycle processes, Ecol. Appl., 10, 412–422, 2000.

Eshetu, Z. and Högberg, P.: Reconstruction of Forest Site History in Ethiopian Highlands Based on $^{13}C$ Natural Abundance of Soils, AMBIO A J. Hum. Environ., 29, 83–89, https://doi.org/10.1579/0044-7447-29.2.83, 2000.

Farquhar, G., O'Leary, and Berry, J.: On the relationship between carbon isotope discrimination and the intercellular carbon dioxide concentration in leaves, Aust. J. Plant Physiol., 9, 121–137, 1982.

Friedli, H., Lötscher, H., Oeschger, H., Siegenthaler, U., and Stauffer, B.: Ice core record of the $^{13}C/^{12}C$ ratio of atmospheric $CO_2$ in the past two centuries, Nature, 324, 237–238, https://doi.org/10.1038/324237a0, 1986.

Friis, I.: Zonation of Forest Vegetation on the South Slope of Bale Mountains, South Ethiopia, Ethiop. J. Sci., 9, 29–44, 1986.

Friis, I., Sebsebe, D., and Breugel, P. V.: Atlas of the Potential Vegetation of Ethiopia, The Royal Danish Academy of Sciences and Letters, Addis Ababa University Press and Shama Books, Addis Ababa, Ethiopia, 307 pp., 2010.

Garten, C. T., Cooper, L. W., Post, W. M., and Hanson, P. J.: Climate Controls on Forest Soil C Isotope Ratios in the Southern Appalachian Mountains, Ecology, 81, 1108–1119, 2000.

Gebru, T., Eshetu, Z., Huang, Y., Woldemariam, T., Strong, N., Umer, M., DiBlasi, M., and Terwilliger, V. J.: Holocene palaeovegetation of the Tigray Plateau in northern Ethiopia from charcoal and stable organic carbon isotopic analyses of gully sediments, Palaeogeogr. Palaeocl., 282, 67–80, https://doi.org/10.1016/j.palaeo.2009.08.011, 2009.

Glaser, B. and Zech, W.: Reconstruction of climate and landscape changes in a high mountain lake catchment in the Gorkha Himal, Nepal during the Late Glacial and Holocene as deduced from radiocarbon and compound-specific stable isotope analysis of terrestrial, aquatic and microbial biomarkers, Org. Geochem., 36, 1086–1098, https://doi.org/10.1016/j.orggeochem.2005.01.015, 2005.

Gunina, A. and Kuzyakov, Y.: Soil Biology & Biochemistry Sugars in soil and sweets for microorganisms: Review of origin, content, composition and fate, Soil Biol. Biochem., 90, 87–100, 2015.

Hamilton, A. C.: Environmental history of East Africa, A study of the Quarternary, London, Academic Press, https://doi.org/10.2307/2259986, 328 pp., 1982.

Hedberg, O.: Vegetation belts of the east african mountains, Svenska botaniska fôreningens, Stockholm, 1951.

Hedberg, O.: Evolution and speciation in a tropical high mountain flora, Biol. J. Linn. Soc., 1, 135–148, https://doi.org/10.1111/j.1095-8312.1969.tb01816.x, 1969.

Hepp, J., Rabus, M., Anhäuser, T., Bromm, T., Laforsch, C., Sirocko, F., Glaser, B., and Zech, M.: A sugar biomarker proxy for assessing terrestrial versus aquatic sedimentary input, Org. Geochem., 98, 98–104, https://doi.org/10.1016/j.orggeochem.2016.05.012, 2016.

Hevly, R. H.: Pollen production, transport and preservation?, Potentials and limitations in archaeological palynology, 39–54, 1981.

Hillman, J. C.: Conservation in Bale Mountains National Park, Ethiopia, Oryx, 20, 89–94, https://doi.org/10.1017/S0030605300026314, 1986.

Jacob, M., Annys, S., Frankl, A., De Ridder, M., Beeckman, H., Guyassa, E. and Nyssen, J.: Tree line dynamics in the tropical African highlands – identifying drivers and dynamics, J. Veg. Sci., 26, 9–20, https://doi.org/10.1111/jvs.12215, 2015.

Jansen, B., Nierop, K. G. J., Kotte, M. C., de Voogt, P., and Verstraten, J. M.: The applicability of accelerated solvent extraction (ASE) to extract lipid biomarkers from soils, Appl. Geochem., 21, 1006–1015, https://doi.org/10.1016/j.apgeochem.2006.02.021, 2006a.

Jansen, B., Nierop, K. G. J., Hageman, J. A., Cleef, A. M., and Verstraten, J. M.: The straight-chain lipid biomarker composition of plant species responsible for the dominant biomass production along two altitudinal transects in the Ecuadorian Andes, Org. Geochem., 37, 1514–1536, https://doi.org/10.1016/j.orggeochem.2006.06.018, 2006b.

Jansen, B., Haussmann, N. S., Tonneijck, F. H., Verstraten, J. M., and de Voogt, P.: Characteristic straight-chain lipid ratios as a quick method to assess past forest-páramo transitions in the Ecuadorian Andes, Palaeogeogr. Palaeocl., 262, 129–139, https://doi.org/10.1016/j.palaeo.2008.02.007, 2008.

Jia, G., Dungait, J. A. J., Bingham, E. M., Valiranta, M., Korhola, A., and Evershed, R. P.: Neutral monosaccharides as biomarker proxies for bog-forming plants for application to palaeovegetation reconstruction in ombrotrophic peat deposits, Org. Geochem., 39, 1790–1799, https://doi.org/10.1016/j.orggeochem, 2008.

Johansson, M.: Fire and grazing in subalpine heathlands and forests of Bale Mountains, Ethiopia, Institutionen för skogens ekologi och skötsel, Sveriges lantbruksuniversitet, Umeå, 14, 1652–1668, 2013.

Kebede, M., Ehrich, D., Taberlet, P., Nemomissa, S., and Brochmann, C.: Phylogeography and conservation genetics of a giant lobelia (Lobelia giberroa) in Ethiopian and Tropical East African mountains, Mol. Ecol., 16, 1233–1243, https://doi.org/10.1111/j.1365-294X.2007.03232.x, 2007.

Kidane, Y., Stahlmann, R., and Beierkuhnlein, C.: Vegetation dynamics, and land use and land cover change in the Bale Mountains, Ethiopia, Environ. Monit. Assess., 184, 7473–7489, https://doi.org/10.1007/s10661-011-2514-8, 2012.

Körner, C., Farquhar, G. D., and Wong, S. C.: Carbon isotope discrimination by plants follows latitudinal and altitudinal trends, Oecologia, 88, 30–40, https://doi.org/10.1007/BF00328400, 1991.

Krepkowski, J., Gebrekirstos, A., Shibistova, O., and Br, A.: Stable carbon isotope labeling reveals different carry-over effects between functional types of tropical trees in an Ethiopian mountain forest, New Phytol., 199, 431–440, 2013.

Lemma, B., Mekonnen, B., Glaser, B., Zech, W., Nemomissa, S., Bekele, T., Bittner, L., and Zech, M.: Chemotaxonomic patterns of vegetation and soils along altitudinal transects of the Bale Mountains, Ethiopia, and implications for paleovegetation reconstructions – Part II: lignin-derived phenols and leaf-wax-derived $n$-alkanes, E&G Quaternary Sci. J., 69, 189–200, https://doi.org/10.5194/egqsj-69-189-2019, 2019a.

Lemma, B., Kebede, S., Nemomissa, S., Otte, I., Glaser, B., and Zech, M.: Spatial and temporal $^{2}$H and$^{18}$O isotope variation of contemporary precipitation in the Bale Mountains, Ethiopia, Isotopes in Environmental and Health Studies, submitted, 2019b.

Levin, N. E., Brown, F. H., Behrensmeyer, A. K., Bobe, R., and Cerling, T. E.: Paleosol carbonates from the omo group: Isotopic records of local and regional environmental change in East Africa, Palaeogeogr. Palaeocl., 307, 75–89, https://doi.org/10.1016/j.palaeo.2011.04.026, 2011.

Li, Y. C., Hai, Q., Corresp, X., Yang, X. L., Chen, H., Lu, X. M., Li, Y., Xu, Q., Yang, X., Chen, H. U. I., and Lu, X.: Pollen – vegetation relationship and pollen preservation on the Northeastern Qinghai – Tibetan Plateau, Grana, 44, 160–171, https://doi.org/10.1080/00173130500230608, 2005.

Lisanework, N. and Mesfin, T.: An ecological study of the vegetation of the Harenna forest, Bale, Ethiopia. Ethiop. J. Sci. 12, 63–93, 1989.

Liu, X. H., Zhao, L. J., Gasaw, M., Gao, D. Y., Qin, D. H., and Ren, J. W.: Foliar $\delta^{13}$C and $\delta^{15}$N values of $C_3$ plants in the Ethiopia Rift Valley and their environmental controls, Chinese Sci. Bull., 52, 1265–1273, https://doi.org/10.1007/s11434-007-0165-5, 2007.

Miehe, S. and Miehe, G.: Ericaceous forest and heath land in Bale Mountains of South Ethiopia, Ecology and Man's Impact, Hamburg, Stiftung Walderhaltung in Africa Hamburg, Germany, 1994.

Messerli, B. and and Winiger, M.: Climate, Environmental Change, and Resources of the African Mountains from the Mediterranean to the Equator, Mt. Res. Dev., 12, 315–336, https://doi.org/10.2307/3673683, 1992.

Meyers, P. A.: Preservation of elemental and isotopic source identification of sedimentary organic matter, Chem. Geol., 114, 289–302, https://doi.org/10.1016/0009-2541(94)90059-0, 1994.

Natelhoffer, K. J. and Fry, B.: Controls on Natural Nitrogen-15 and Carbon-13 Abundances in Forest Soil Organic Matter, Soil Sci. Soc. Am. J., 52, 1633–1640, https://doi.org/10.2136/sssaj1988.03615995005200060024x, 1988.

Oades, J. M.: Soil organic matter and structural stability: mechanisms and implications for management, Plant Soil, 76, 319–337, https://doi.org/10.1007/BF02205590, 1984.

Prietzel, J., Dechamps, N., and Spielvogel, S.: Analysis of non-cellulosic polysaccharides helps to reveal the history of thick organic surface layers on calcareous Alpine soils, Plant Soil, 365, 93–114, https://doi.org/10.1007/s11104-012-1340-2, 2013.

Sauheitl, L., Glaser, B., and Bol, R.: Short-term dynamics of slurry-derived plant and microbial sugars in a temperate grassland soil as assessed by compound-specific $\delta^{13}$C analyses, Rapid Commun. Mass Spec., 19, 1437–1446, https://doi.org/10.1002/rcm.1965, 2005.

Simoneit, B.: Molecular Indicators (Biomarkers) of past life, The Anatomical Record, 286, 186–195, https://doi.org/10.1002/ar.10153, 2002.

Solomon, D., Fritzsche, F., Lehmann, J., Tekalign, M., and Zech, W.: Soil organic matter dynamics in the sub-humid agroecosystems of the Ethiopian highlands: Evidence from natural $C_{13}$ abundance and particle-size fractionation, Soil Sci. Soc. Am. J., 66, 969–978, 2002.

Street-Perrott, F. A., Ficken, K. J., Huang, Y., and Eglinton, G.: Late Quaternary changes in carbon cycling on Mt. Kenya, East Africa: An overview of the $\delta^{13}$C record in lacustrine organic matter, Quat. Sci. Rev., 23, 861–879, https://doi.org/10.1016/j.quascirev.2003.06.007, 2004.

Tiercelin, J. J., Gibert, E., Umer, M., Bonnefille, R., Disnar, J. R., Lézine, A. M., Hureau-Mazaudier, D., Travi, Y., Keravis, D., and Lamb, H. F.: High-resolution sedimentary record of the last deglaciation from a high-altitude lake in Ethiopia, Quat. Sci. Rev., 27, 449–467, https://doi.org/10.1016/j.quascirev.2007.11.002, 2008.

Tiunov, A. V.: Stable isotopes of carbon and nitrogen in soil ecological studies, Biol. Bull., 34, 395–407, https://doi.org/10.1134/S1062359007040127, 2007.

Umer, M., Lamb, H. F., Bonnefille, R., Lézine, A. M., Tiercelin, J. J., Gibert, E., Cazet, J. P., and Watrin, J.: Late Pleistocene and Holocene vegetation history of the Bale Mountains, Ethiopia, Quat. Sci. Rev., 26, 2229–2246, https://doi.org/10.1016/j.quascirev.2007.05.004, 2007.

Wesche, K., Miehe, G., and Kaeppeli, M.: The Significance of Fire for Afroalpine Ericaceous Vegetation, Mt. Res. Dev., 20, 340–347, https://doi.org/10.1659/0276-4741(2000)020[0340:TSOFFA]2.0.CO;2, 2000.

Yimer, F., Ledin, S., and Abdelkadir, A.: Soil property variations in relation to topographic aspect and vegetation community in the south-eastern highlands of Ethiopia, For. Ecol. Manage., 232, 90–99, https://doi.org/10.1016/j.foreco.2006.05.055, 2006.

Yineger, H., Kelbessa, E., Bekele, T., and Lulekal, E.: Floristic Composition and Structure of the Dry Afromontane Forest At Bale Mountains National Park, Ethiopia, J. Sci., 31, 103–120, https://doi.org/10.4314/sinet.v31i2.66551, 2008.

Young, H. J. and Young, T. P.: Local distribution of C3 and C4 grasses in sites of overlap on Mount Kenya, Oecologia, 58, 373–377, https://doi.org/10.1007/BF00385238, 1983.

Zech, M.: Evidence for Late Pleistocene climate changes from buried soils on the southern slopes of Mt. Kilimanjaro, Tanzania, Palaeogeogr. Palaeocl., 242, 303–312, https://doi.org/10.1016/j.palaeo.2006.06.008., 2006.

Zech, M. and Glaser, B.: Compound-specific $\delta^{18}$O analyses of neutral sugars in soils using gas chromatography-pyrolysis-isotope ratio mass spectrometry: Problems, possible solutions and a first application, Rapid Commun. Mass Spec., 23, 3522–3532, https://doi.org/10.1002/rcm.4278, 2009.

Zech, M., Zech, R., and Glaser, B.: A 240,000-year stable carbon and nitrogen isotope record from a loess-like palaeosol sequence in the Tumara Valley, Northeast Siberia, Chem. Geol., 242, 307–318, https://doi.org/10.1016/j.chemgeo.2007.04.002, 2007.

Zech, M., Bimüller, C., Hemp, A., Samimi, C., Broesike, C., Hörold, C., and Zech, W.: Human and climate impact on $^{15}$N natural abundance of plants and soils in high-mountain ecosystems: A short review and two examples from the Eastern Pamirs and Mt. Kilimanjaro, Isotopes Environ. Health Stud., 47, 286–296, https://doi.org/10.1080/10256016.2011.596277, 2011a.

Zech, M., Leiber, K., Zech, W., Poetsch, T., and Hemp, A.: Late Quaternary soil genesis and vegetation history on the northern slopes of Mt. Kilimanjaro, East Africa, Quat. Int., 243, 327–336, https://doi.org/10.1016/j.quaint.2011.05.020, 2011b.

Zech, M., Rass, S., Buggle, B., Löscher, M., and Zöller, L.: Reconstruction of the late Quaternary paleoenvironments of the Nussloch loess paleosol sequence, Germany, using $n$-alkane biomarkers, Quat. Res., 78, 326–335, https://doi.org/10.1016/j.yqres.2012.05.006, 2012.

E&G Quaternary Sci. J., 68, 189–200, 2019
https://doi.org/10.5194/egqsj-68-189-2019


Open Access E&G Quaternary Science Journal

# Chemotaxonomic patterns of vegetation and soils along altitudinal transects of the Bale Mountains, Ethiopia, and implications for paleovegetation reconstructions – Part II: lignin-derived phenols and leaf-wax-derived *n*-alkanes

**Bruk Lemma**[1,2], **Betelhem Mekonnen**[1,3], **Bruno Glaser**[1], **Wolfgang Zech**[4], **Sileshi Nemomissa**[5], **Tamrat Bekele**[5], **Lucas Bittner**[1], **and Michael Zech**[1,6]

[1]Institute of Agronomy and Nutritional Sciences, Soil Biogeochemistry, Martin Luther University Halle-Wittenberg, Von-Seckendorff-Platz 3, 06120, Halle, Germany
[2]Forest and Rangeland Biodiversity Directorate, Ethiopian Biodiversity Institute, P.O. Box 30726, Addis Ababa, Ethiopia
[3]Department of Urban Agriculture, Misrak Polytechnic College, P.O. Box 785, Addis Ababa, Ethiopia
[4]Institute of Soil Science and Soil Geography, University of Bayreuth, Universitätsstrasse 30, 95440, Bayreuth, Germany
[5]Department of Plant Biology and Biodiversity Management, Addis Ababa University, P.O. Box 3434, Addis Ababa, Ethiopia
[6]Institute of Geography, Technical University of Dresden, Helmholtzstrasse 10, 01062, Dresden, Germany

**Correspondence:** Bruk Lemma (bruklemma@gmail.com)

**Relevant dates:** Received: 9 August 2018 – Revised: 6 March 2019 – Accepted: 25 July 2019 – Published: 4 September 2019

**How to cite:** Lemma, B., Mekonnen, B., Glaser, B., Zech, W., Nemomissa, S., Bekele, T., Bittner, L., and Zech, M.: Chemotaxonomic patterns of vegetation and soils along altitudinal transects of the Bale Mountains, Ethiopia, and implications for paleovegetation reconstructions – Part II: lignin-derived phenols and leaf-wax-derived *n*-alkanes, E&G Quaternary Sci. J., 68, 189–200, https://doi.org/10.5194/egqsj-68-189-2019, 2019.

**Abstract:** *Erica* is a dominant vegetation type in many sub-afroalpine ecosystems, such as the Bale Mountains in Ethiopia. However, the past extent of *Erica* is not well known and climate versus anthropogenic influence on altitudinal shifts are difficult to assign unambiguously, especially during the Holocene. The main objective of the present study is to chemotaxonomically characterize the dominant plant species occurring in the Bale Mountains using lignin phenols and *n*-alkane biomarkers and to examine the potential of those biomarkers for reconstructing vegetation history. Fresh plant material, organic layer and mineral topsoil samples were collected along a northeastern and a southwestern altitudinal transect (4134–3870 and 4377–2550 m a.s.l., respectively). Lignin-derived vanillyl, syringyl and cinnamyl phenols were analyzed using the cupric oxide oxidation method. Leaf-wax-derived *n*-alkanes were extracted and purified using Soxhlet and aminopropyl columns. Individual lignin phenols and *n*-alkanes were separated by gas-chromatography and detected by mass spectrometry and flame ionization detection, respectively.

We found that the relative contributions of vanillyl, syringyl and cinnamyl phenols allow us to chemotaxonomically distinguish contemporary plant species of the Bale Mountains. *Erica* in particular is characterized by relatively high cinnamyl contributions of $> 40\,\%$. However, litter degradation strongly decreases the lignin phenol concentrations and completely changes the lignin phenol patterns. Relative cinnamyl contributions in soils under *Erica* were < 40 %, while soils that developed under Poaceae (*Festuca abyssinica*) exhibited relative cinnamyl contributions of > 40 %.

Similarly, long-chain $n$-alkanes extracted from the leaf waxes allowed for differentiation between *Erica* versus *Festuca abyssinica* and *Alchemilla*, based on lower $C_{31}$ / $C_{29}$ ratios in *Erica*. However, this characteristic plant pattern was also lost due to degradation in the respective O layers and $A_h$ horizons. In conclusion, although in modern-day plant samples a chemotaxonomic differentiation is possible, soil degradation processes seem to render the proxies unusable for the reconstruction of the past extent of *Erica* on the Sanetti Plateau, Bale Mountains, Ethiopia. This finding is of high relevance beyond our case study.

**Kurzfassung:** *Erica* prägt als dominante Pflanzengattung viele Subafro-alpine Ökosysteme, so auch die Bale Berge in Äthiopien. Das Ausmaß der flächenhaften Ausdehnung von *Erica* in der Vergangenheit ist jedoch unklar, genauso wie die klimatische versus menschliche Verursachung solcher Vegetationsänderungen insbesondere im Holozän. Das Ziel dieser Studie war es herauszufinden (i) ob sich die dominante Vegetation in den Bale Bergen anhand von ligninbürtigen Phenolen und blattwachsbürtigen $n$-Alkanbiomarkern chemotaxonomisch unterscheiden lässt und (ii) ob diese Biomarker das Potential haben zur Vegetationsrekonstruktion im Untersuchungsgebiet beizutragen. In einem Begleitartikel (Mekonnen et al., 2019) verfolgen wir dasselbe Ziel, jedoch anhand von Stabilkohlenstoff- und Stickstoffisotopen sowie Zuckerbiomarkern. Untersucht wurden Pflanzenproben, O-Lagen und $A_h$ Horizonte entlang eines Nord- und eines Südwest-Höhentransektes (3870–4134 m bzw. 2550–4377 m ü. NN). Die ligninbürtigen Phenoleinheiten Vannilly, Syringyl und Cinnamyl wurden mittels der Kupferoxidationsmethode gewonnen; die $n$-Alkane wurden mittels Soxhlet extrahiert und über Aminopropylsäulen aufgereinigt. Die Quantifizierung der Ligninphenole und $n$-Alkane erfolgte mittels Gaschromatographie – Massenspektrometrie bzw. Gaschromatographie – Flammenionisationsdetektion.

Die Ergebnisse zeigen, dass sich die dominanten Pflanzenarten in den Bale Bergen anhand ihrer Vanillyl, Syringyl und Cinnamyl Einheiten chemotaxonomisch unterscheiden lassen. So weist insbesondere *Erica* charakteristischerweise relativ hohe Cinnamyl-Anteile von > 40 % auf. Vermutlich degradationsbedingt nimmt jedoch in der Reihe Pflanze – O-Lage – $A_h$ Horizont nicht nur die Ligninkonzentration stark ab, sondern auch die Ligninmuster ändern sich völlig. Dadurch weisen Böden unter *Erica* Cinnamyl-Anteile < 40 % auf, während Böden die sich unter der dominanten Grasart *Festuca abyssinica* entwickelt haben Cinnamyl-Anteile von > 40 % aufweisen. Auch anhand der Alkanbiomarker ist eine chemotaxonomische Unterscheidung zumindest zwischen *Erica* versus *Festuca abyssinica* und *Alchemilla* möglich. Als Proxy dient hier das Verhältnis von $C_{31}$ zu $C_{29}$. Allerdings führt auch hier Degradation in der Reihe Pflanze – O-Lage – $A_h$ Horizont zum Verlust des charakteristischen Alkanmusters. Obwohl sich rezentes Pflanzenmaterial chemotaxonomisch unterscheiden lässt, zwingt dies zur Schlussfolgerung, dass Degradationseffekte bei der Rekonstruktion von *Erica* im Untersuchungsgebiet der Bale Berge in Äthiopien anhand von ligninbürtigen Phenolen und blattwachsbürtigen Alkanbiomarkern nicht unberücksichtigt bleiben dürfen. Dieser Befund ist über unsere Fallstudie hinaus von hoher Relevanz.

## 1 Introduction

The Bale Mountains are an eastern afromontane biodiversity hotspot area with 27 endemic species of flowering plants (Hillman, 1988). Like in many other afromontane ecosystems, an altitudinal zonation of the vegetation is well established, with an Ericaceous belt forming a prominent feature. Ericaceous vegetation dominates above 3300 m a.s.l., shows different stages of post-fire succession and remains continuous up to 3800 m a.s.l. However, it becomes patchy on the Sanetti Plateau (Miehe and Miehe, 1994). The Bale Mountains National Park is increasingly under threat from climate change and anthropogenic impacts (Kidane et al., 2012). Ascertaining the past environmental and vegetation history of the area will support conservation efforts and may help to disentangle the influence of climate versus human impact on the present biodiversity.

Until now, the vegetation history of the Bale Mountains was studied using pollen records from lacustrine sediments and peat deposits (Bonnefille and Hamilton, 1986; Bonnefille and Mohammed, 1994; Hamilton, 1982; Umer et al., 2007). The results suggest the extension of the Ericaceous belt towards higher altitudes during the early and middle Holocene. As potential drawbacks, such pollen studies depend on pollen preservation and can be biased by variable pollination rates as well as middle- and long-distance pollen transport (Hicks, 2006; Jansen et al., 2010; Ortu et al., 2006). By contrast, stable isotopes and biomarkers can also be applied to more degraded sedimentary archives and soils and are assumed to reflect the standing vegetation more (Glaser and Zech, 2005). Thus, they offer the potential to complement pollen-based vegetation reconstructions and to reconstruct vegetation at a higher temporal and spatial resolution. For instance, the stable carbon isotopic composition ($\delta^{13}C$) of lacustrine sediments suggests an expansion of alpine $C_4$ grasses on Mount Kenya, especially during glacial times (Street-Perrott et al., 2004), whereas $\delta^{13}C$ results from (paleo-)soils provide no evidence for $C_4$ grass expansion close to Mount Kilimanjaro during late Pleistocene glacial period (Zech, 2006; Zech et al., 2011b). We focus here on lignin-derived phenols and leaf-wax-derived $n$-alkanes as biomarkers, while stable isotopes and sugar biomarkers and their chemotaxonomic potential for reconstructions of the Bale Mountains vegetation are addressed in a companion paper by Mekonnen et al. (2019).

Lignin has a polyphenolic biochemical structure produced by terrestrial vascular plants (Ertel and Hedges, 1984) providing strength and rigidity to the plants (Thevenot et al., 2010). The lignin-derived phenols vanillyl (V), syringyl (S) and cinnamyl (C) as products of cupric oxide (CuO) oxidation are used to differentiate sources of organic matter and provide information about the diagenetic state (degree of degradation) of vascular plant material in terrestrial and aquatic sediments (Castañeda et al., 2009; Hedges et al., 1988; Tareq et al., 2004, 2006; Ziegler et al., 1986). For instance, low ratios of $S/V \sim 0$ were suggested as a proxy for the relative contribution of gymnosperms, and elevated S / V ratios were found to be indicative for the presence of angiosperms (Tareq et al., 2004). Likewise, the C / V ratio was proposed to indicate the relative contribution of woody ($C/V < 0.1$) and non-woody ($C/V > 0.1$) plants to the soil and sediment organic matter (Tareq et al., 2011). Moreover, the ratios of acid to aldehyde forms of vanillyl and syringyl units $(Ac/Al)_{v,s}$ were suggested as proxies for quantifying the degree of lignin degradation (Amelung et al., 2002; Hedges and Ertel, 1982; Möller et al., 2002).

$n$-alkanes are important constituents of plant leaf waxes (Kolattukudy, 1970), where they serve to protect plants against water loss by evaporation as well as from fungal and insect attacks (Eglinton and Hamilton, 1967; Koch et al., 2009). Due to their recalcitrant nature, they are often well preserved in sedimentary archives and used as biomarkers (also called molecular fossils) in paleoclimate and environmental studies (Eglinton and Eglinton, 2008; Glaser and Zech, 2005; Zech et al., 2011c). The potential of $n$-alkanes for chemotaxonomic studies has been suggested based on the finding that the homologues $C_{27}$ and $C_{29}$ are sourced predominantly from trees and shrubs, whereas the homologues $C_{31}$ and $C_{33}$ are sourced predominantly from grasses and herbs (Maffei, 1996; Maffei et al., 2004; Rommerskirchen et al., 2006; Schäfer et al., 2016; Zech, 2009). Potential pitfalls when applying $n$-alkane proxies in paleovegetation studies should not be overlooked. For instance, (Bush and McInerney, 2013) caution against the chemotaxonomic application of $n$-alkanes because of high $n$-alkane pattern variability within graminoids and woody plants (Schäfer et al., 2016) emphasized the need for establishing regional calibration studies and Zech et al., (2011a, 2013) point to degradation affecting $n$-alkane proxies.

While the overall aim of our research is to contribute to the reconstruction of the paleoclimate and environmental history of the Bale Mountains, this study focuses more specifically on the following questions: (i) do lignin phenols and $n$-alkane biomarkers allow a chemotaxonomic differentiation of the dominant plant types of the Bale Mountains? (ii) Are the biomarker patterns of the plants reflected by and incorporated into the respective soils? (iii) Which implications have to be drawn from those results for planned paleovegetation reconstructions in the study area, e.g., concerning the reconstruction of the former extent of *Erica*? Finally, improved knowledge of the vegetation history of the Bale Mountains may help to support the biodiversity conservation program of the park in the face of future climate change and increasing human pressure.

## 2 Material and methods

### 2.1 Study area and sample description

The Bale Mountains are located 400 km southeast of Addis Ababa, the capital of Ethiopia (Hillman, 1986). Geographically, they belong to the Bale–Arsi massif, which forms the western section of the southeastern Ethiopian Highlands (Hillman, 1988; Miehe and Miehe, 1994; Tiercelin et al., 2008). The Bale Mountains National Park (BMNP) is situated at 39°28′ to 39°57′ E and 6°29′ to 7°10′ N, (Hillman, 1988; Miehe and Miehe, 1994; Umer et al., 2007) with elevations ranging from 1400 to 4377 m a.s.l. The highest part forms the Sanetti Plateau, on which the second highest peak of the country, Mount Tullu Dimtu at 4377 m a.s.l. is also located (Hillman, 1988). The plateau is limited by the steep Harenna escarpment in the south and the southeast. The northeastern part is encompassed by high ridges and broad valleys that gradually descend towards the extensive Arsi–Bale plateaus and further into the Central Rift Valley lowlands (Hillman, 1988; Tiercelin et al., 2008). The topography of the Bale Mountains results in climatic gradients with respect to spatial and temporal distribution of rainfall as well as temperature (Tiercelin et al., 2008). Mean maximum temperature (MMT) on the mountain peaks ranges between 6 and 12 °C. At Dinsho (headquarters, 3170 m a.s.l.) the MMT is 11.8 °C. Mean mini-

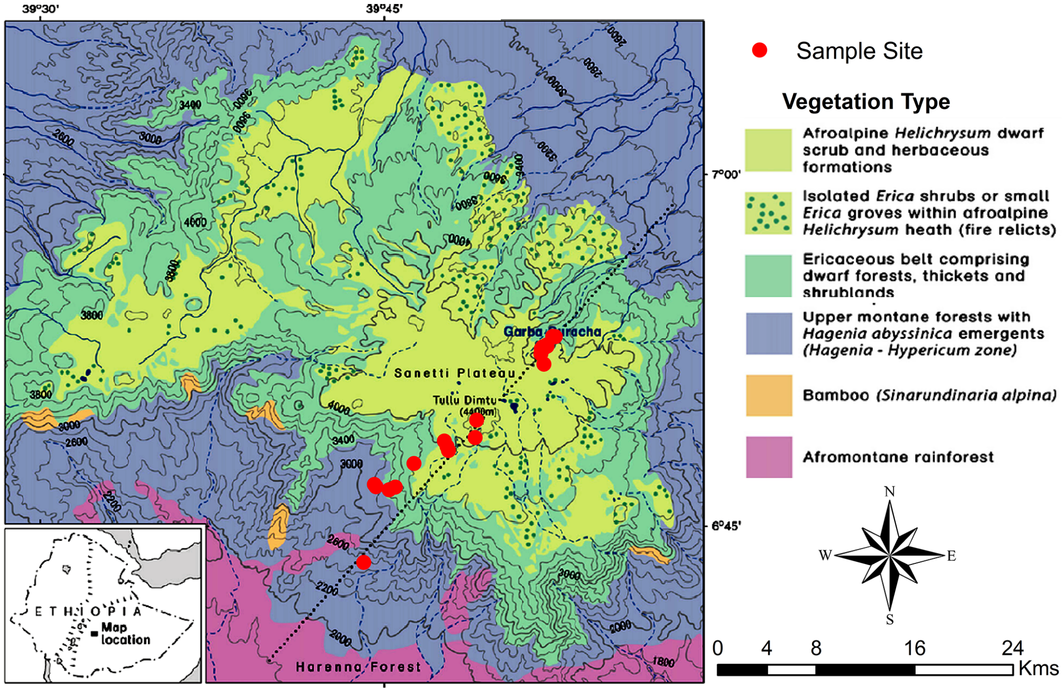


**Figure 1.** Map of the Bale Mountains for the vegetation zones and study sites along the northeastern and the southwestern transect (modified following Miehe and Miehe, 1994). Dominant vegetation types sampled that comprise the Ericaceous and afroalpine belt.

mum temperature ranges from 0.6 to 10 °C, with frequent frost occurring in the high peak areas during the winter season (Tiercelin et al., 2008). The highest annual rainfall and humidity occurs in the southwest part of the mountain with 1000–1500 mm $yr^{-1}$, and the northern part of the mountains exhibits annual rainfall ranging between 800 and 1000 mm $yr^{-1}$ (Woldu et al., 1989). The vegetation shows an altitudinal zonation comprised of the afromontane rainforest (1450–2000 m a.s.l.), the upper montane forests dominated by *Hagenia* and *Hypericum* species (2000–3200 m a.s.l.); the Ericaceous belt (3200–3800 m a.s.l.); and the afroalpine zone (3800–4377 m a.s.l.) dominated by dwarf shrubs such as *Helichrysum, Alchemilla*, herbs, and grasses (mostly *Festuca*; Fig. 1) (Friis, 1986; Miehe and Miehe, 1994). Geologically, the Bale Mountains consist of a highly elevated volcanic plateau dominated by alkali basalt, tuffs and rhyolite rocks. During the Last Glacial Maximum (LGM), it is understood that the regions of the high peak summits were glaciated and later flattened by repeated glaciations (Kidane et al., 2012; Osmaston et al., 2005; Umer et al., 2004). The soils having developed on the basaltic and trachyte rocks can be generally characterized as silt loam, having a reddish brown to black color (Woldu et al., 1989). They are usually shallow, gravelly and are assumed to have developed since the glacial retreat (Hedberg, 1964). Andosols are the most ubiquitous soil types. Nevertheless, Cambisols and Leptosols are also prevalent soil types in some parts of the Bale Mountains. In wetland and sedimentary basins, Gleysols and Histosols are also common (Billi, 2015; Yimer et al., 2006).

In February 2015, 25 leaf and twig samples of the dominant plant species were collected (Fig. 1) along a southwestern and a northeastern transect (ranging from 2550 to 4377 m a.s.l. and 3870 to 4134 m a.s.l., respectively). Samples comprised of *Erica trimera* (Engl.) Beentje ($n = 5$), *Erica arborea* L. ($n = 5$), *Alchemilla haumannii* Rothm. ($n = 5$), *Festuca abyssinica* Hochst. ex A. Rich. ($n = 6$), *Helichrysum splendidum* Thunb. L. ($n = 2$), *Kniphofia foliosa* Hochst. ($n = 1$) and *Lobelia rhynchopetalum* Hemsl. ($n = 1$). Additionally, 15 organic surface layers (= O layers, strongly humified plant residues) and 22 mineral topsoils (= $A_h$ horizons) that developed under the above listed dominant vegetation were collected from 27 sampling sites, resulting in 62 samples in total. For photos illustrating the investigated plant species and typical study sites, the reader is referred to Fig. 2 of our companion paper by Mekonnen et al. (2019). All samples were air-dried in the Soil Store Laboratory of the National Herbarium, Department of Plant Biology and Biodiversity Management, Addis Ababa University. In the laboratories of the Soil Biogeochemistry Group, Martin Luther University of Halle-Wittenberg, soil samples were sieved using a mesh size of 2 mm, finely ground, homogenized and subjected to further biogeochemical analysis.

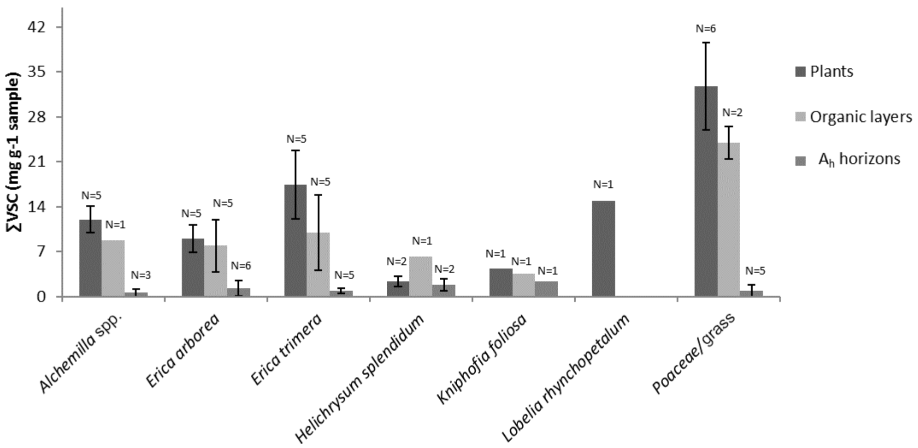


**Figure 2.** Sum of lignin phenol concentrations ($\sum$VSC) of contemporary plants, O layers and $A_h$ horizons. Error bars illustrate standard deviations.

## 2.2 Analysis of lignin-derived phenol and leaf-wax-derived $n$-alkane biomarkers

Lignin phenols were extracted from 35, 50 and 500 mg of plant, O-layer and $A_h$-horizon soil samples, respectively. The analytical procedure followed the cupric oxidation (CuO) method developed by Hedges and Ertel (1982) and modified later on by Goñi and Hedges (1992). Briefly, the samples were transferred into Teflon digestion tubes together with 100 mg of $(NH_4)_2Fe(SO_4)_2 \times 6H_2O$, 500 mg of CuO, 50 mg of $C_6H_{12}O_6$, 1 mL of ethylvanillin solution (100 ppm) as internal standard 1 (IS1) and 15 mL of 2M NaOH and digested at 170 °C for 2 h under pressure. Reaction products were cooled overnight and transferred into centrifuge tubes. Then the phenolic compounds were purified by adsorption on $C_{18}$ columns, desorbed by ethylacetate and concentrated under a stream of nitrogen gas for 30 min. Residue was dissolved in 1 mL phenylacetic acid (PAA), a working internal standard stock solution to determine the recovery of ethylvanillin before derivatization (Amelung et al., 2002; Möller et al., 2002). Finally, the samples were derivatized using 200 µL of N, O-bis(trimethylsilyl)trifluoroacetamide (BSTFA) and 100 µL of pyridine. Oxidation products of lignin phenols were quantified using a SHIMADZU QP 2010 gas chromatography (GC) instrument coupled with a mass spectrometer (MS), (GCMS–QP2010, Kyoto, Japan).

After recovery correction, the concentration of each lignin phenol (in mg $g^{-1}$) was calculated from two or three CuO oxidation products according to the Eqs. (1), (2) and (3), respectively.

$$\text{Vanillyl (V)} = \text{vanillin} + \text{acetovanillone} + \text{vanillic acid} \quad (1)$$

$$\text{Syringyl (S)} = \text{syringaldehyde} + \text{acetosyringone} + \text{syringic acid} \quad (2)$$

$$\text{Cinnamyl (C)} = p\text{-coumaric acid} + \text{ferulic acid} \quad (3)$$

For data evaluation, the sum of V, S, and C ($\sum$VSC); the ratios of S / V, and C / V; and the ratios of acids to aldehydes (Ac / Al) for the syringyl and vanillyl units were additionally calculated.

Leaf-wax-derived $n$-alkanes were extracted from 0.5 to 1 g of plant, O-layer and $A_h$-horizon soil samples using Soxhlet extraction by adding 150 mL of dichloromethane (DCM) and methanol (MeOH) as solvents (9 : 1 ratio) for 24 h following a method modified following Zech and Glaser (2008). In brief, 50 µL of 5$\alpha$-androstane were added to the total lipid extracts (TLEs) as internal standard. TLEs were concentrated using rotary evaporation and transferred to aminopropyl columns. Three lipid fractions containing the $n$-alkanes, alcohols and fatty acids, respectively, were eluted successively by using 3 mL of hexane, DCM / MeOH (1 : 1), and diethyl ether and acetic acid (95 : 5) as eluent. The $n$-alkanes were separated on a gas chromatograph (GC) and detected by a flame ionization detector (FID), whereas the other two lipid fractions (alcohols and fatty acids) were archived. The GC instrument (GC–2010 SHMADZU) was equipped with a SPB–5 column (28.8 m length, 0.25 mm inner diameter, 0.25 µm film thickness). The injector and detector temperature were 300 and 330 °C, respectively. The initial oven temperature was 90 °C. It is then raised in three ramps to 250 °C at 20 °C $min^{-1}$, further to 300 °C at 2 °C $min^{-1}$ and finally to 320 °C at 4 °C $min^{-1}$, resulting in a total oven runtime of 50 min. Helium (He) was used as carrier gas and $n$-alkane mixture ($C_8$–$C_{40}$) was used as external standard for peak identification and quantification.

The total $n$-alkane concentration (TAC), the average chain length (ACL, following Poynter et al., 1989) and the odd over even predominance (OEP, following Hoefs et al. (2002), the latter being very similar to the carbon preference index (CPI), were calculated according to the Eqs. (4), (5) and (6), respectively.

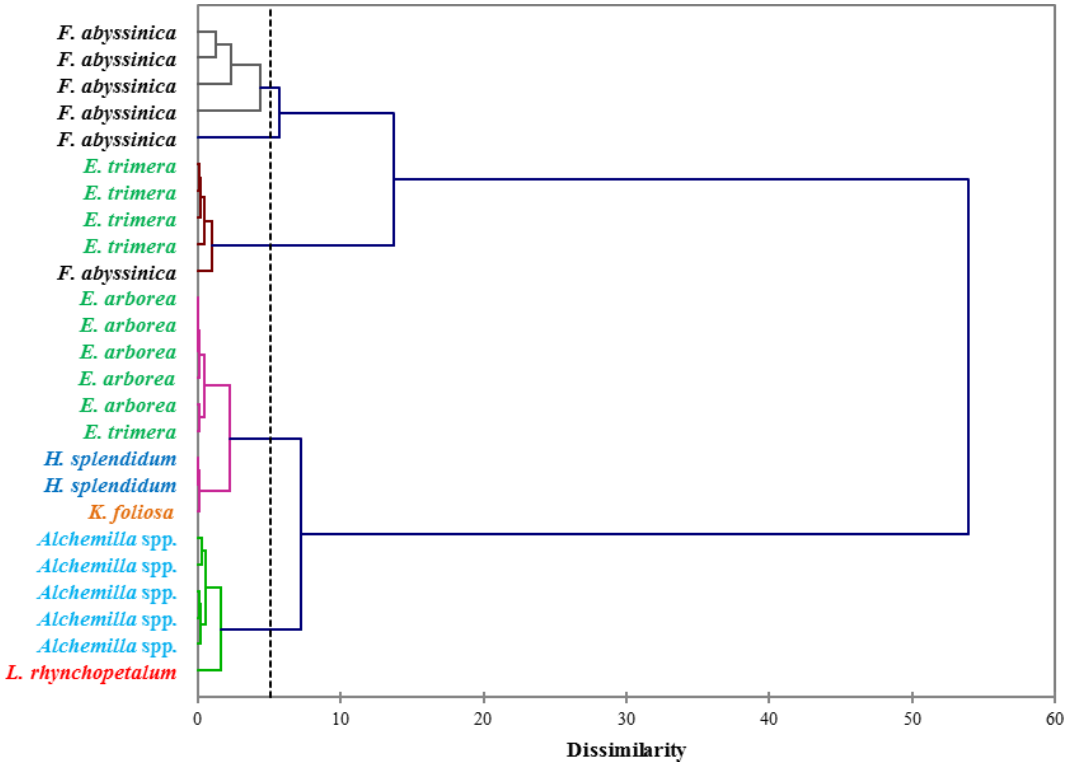


**Figure 3.** Dendrogram differentiating the dominant plant species of the Bale Mountains based on the concentrations of vanillyl, syringyl and cinnamyl lignin phenols (mg g$^{-1}$ sample). The dotted vertical line represents the distance or dissimilarity between clusters.

$$\mathrm{TAC} = \Sigma \mathrm{C}_n, \text{ with } n \text{ ranging from 25 to 35,} \tag{4}$$

$$\mathrm{ACL} = \Sigma(\mathrm{C}_n \times n)/\Sigma \mathrm{C}_n, \tag{5}$$

where $n$ refers to the odd numbered $n$-alkanes ranging from 27 to 33

$$\mathrm{OEP} = (\mathrm{C}_{27}+\mathrm{C}_{29}+\mathrm{C}_{31}+\mathrm{C}_{33})/(\mathrm{C}_{26}+\mathrm{C}_{28}+\mathrm{C}_{30}+\mathrm{C}_{32}). \tag{6}$$

All calibrated datasets of the analytical results were subjected to simple correlation test and agglomerative hierarchical clustering (AHC) using XLSTAT (2014) statistical software. R software version 3.4.2 was also used to demonstrate taxonomic differences and the effect of biodegradation on the sample materials via ternary diagrams and notched box plots.

## 3 Results and discussion

### 3.1 Lignin phenol concentration and patterns of contemporary vegetation

The $\sum$VSC of modern plants investigated from the two transects of the Bale Mountains ranges from 1.8 to 41.8 mg g$^{-1}$, the sample with *Festuca* yielding the highest average contribution to TOC with up to 33 mg g$^{-1}$ sample (Fig. 2). This is within the range reported in the literature (Belanger et al., 2015; Hedges et al., 1986). Note that lignin phenol concentrations of grasses are higher compared to other vegetation of the Bale Mountains, although it is known that grasses contain only low amounts of lignin when compared to trees.

The concentrations of individual lignin phenols (vanillyl, syringyl and cinnamyl) allow us to chemotaxonomically differentiate the contemporary dominant plant species of the Bale Mountains. This is illustrated in Fig. 3, based on an agglomerative hierarchical cluster analysis (AHC). The abundance of individual lignin phenols (V, S and C) was specific to individual or restricted groups of plant and/or tissues applied to cluster different taxa (Belanger et al., 2015; Castañeda et al., 2009; Goñi and Hedges, 1992; Hedges and Mann, 1979; Tareq et al., 2004, 2006).

While Fig. 3 highlights the potential for chemotaxonomic differentiation of the investigated plants, it does not yet become clear from this hierarchical cluster analyses result which lignin phenols are characteristic for which plants and which lignin proxy might have potential for paleovegetation reconstructions. Therefore, Fig. 4 shows the relative abundance of V, S and C for all investigated plant species in a ternary diagram. Accordingly, *Erica arborea* and *Erica trimera* are characterized by cinnamyl percentages of $> 40\,\%$, whereas, except for two *Festuca* samples, all other plants are characterized by cinnamyl percentages of $< 40\,\%$. Our results from fresh plant material are hence not in agree-

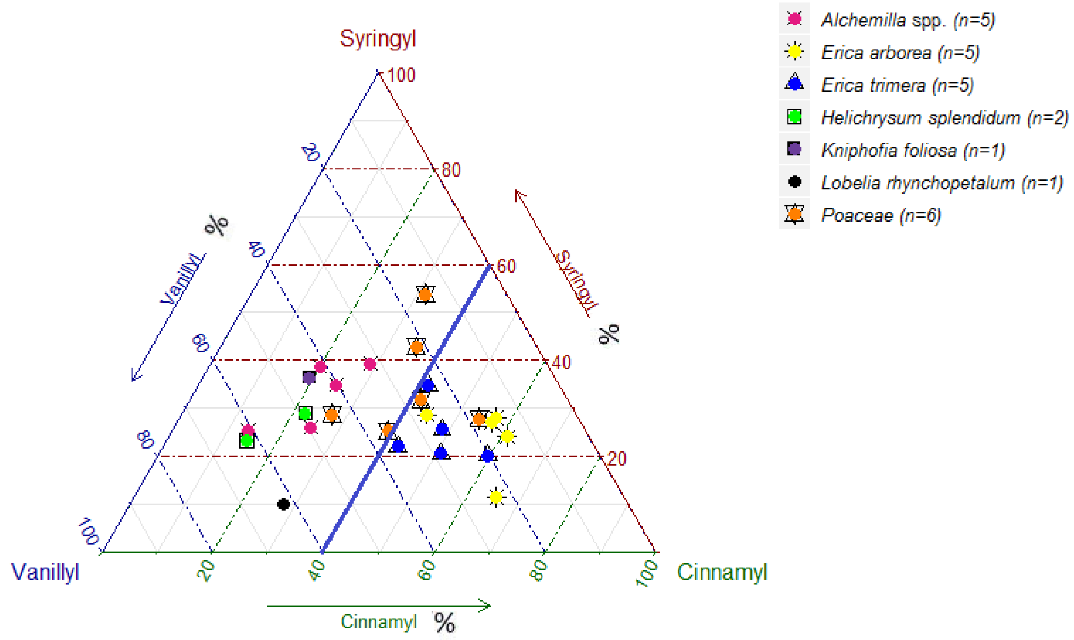


**Figure 4.** Ternary diagram for the relative abundances (%) of vanillyl, syringyl and cinnamyl lignin phenols of the dominant vegetation. The blue line separates samples with more (right) versus less (left) than 40 % cinnamyl.

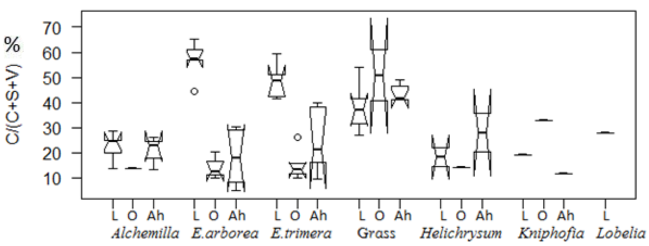


**Figure 5.** Box plot for the relative abundance of cinnamyl phenols (expressed as C / (V + S + C) in %) in plants, O layers and $A_h$ horizons. The box plots indicate the median (solid line between the boxes) and interquartile range (IQR), with upper (75 %) and lower (25 %) quartiles and possible outliers (white circles). The notches display the confidence interval around the median within $\pm 1.57 \times$ IQR/sqrt. Note that small sample sizes result in unidentifiable boxes (particularly *Kniphofia* and *Lobelia*).

ment with the finding of Hedges and Mann (1979) and Hedges et al. (1988) that high contributions of cinnamyl phenols are characteristic of non-woody grass and fern. Despite a relatively large scattering and a partial overlapping, our results suggest that the ratio C / (V + S + C) might be used as a proxy for distinguishing *Erica* spp. from other vegetation types of the Bale Mountains, with values > 0.40 being generally characteristic for *Erica* spp.

## 3.2 Lignin phenol patterns of O layers and $A_h$ horizons

$\sum$VSC strongly decreases from plants over O layers to $A_h$ horizons, except for *Helichrysium*, which yielded the lowest $\sum$VSC values of all plants (Fig. 2). This descending trend is in agreement with the literature (Amelung et al., 1997; Belanger et al., 2015) and reflects the preferential degradation of the plant-derived lignin phenols compared to other soil organic matter constituents. At the same time, the input of root-derived lignin is very likely. As a result of both processes, i.e., degradation and lignin input by roots and the large and chemotaxonomically characteristic contribution of C in *Erica* plant material ($\geq$ 41.5 %) is lost in the O layers (C < 27 %), whereas the two investigated O layers under *Festuca* yielded relative C contributions > 40 %. Similarly, $A_h$ horizons under *Festuca* are characterized by C contributions > 40 %, while all $A_h$ horizons that developed under other vegetation types are characterized by C contributions < 40 %. This finding does not ad hoc preclude the above proposed lignin phenol proxy C / (V + S + C) for reconstructing vegetation history, but it definitely challenges its application. Degradation and lignin input by roots need to be considered when interpreting phenol proxies. This is relevant beyond our case study concerning *Erica* versus *Festuca* and *Helichrysum* (Fig. 5) and is likely more relevant in paleosols than in sedimentary archives.

In our study, we found no consistent increase and systematic relationship between Ac / Al ratios of V and S, which are used as degradation proxies in some studies (Amelung et al., 2002; Hedges and Ertel, 1982; Möller et al., 2002; Tareq

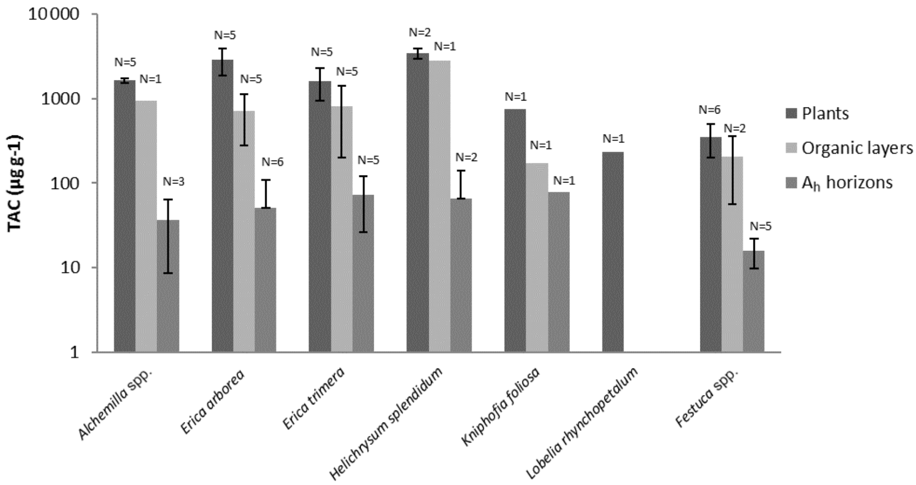


**Figure 6.** Total long-chain $n$-alkane concentrations (TACs) of plants, O layers and $A_h$ horizons. Error bars illustrate standard deviations.

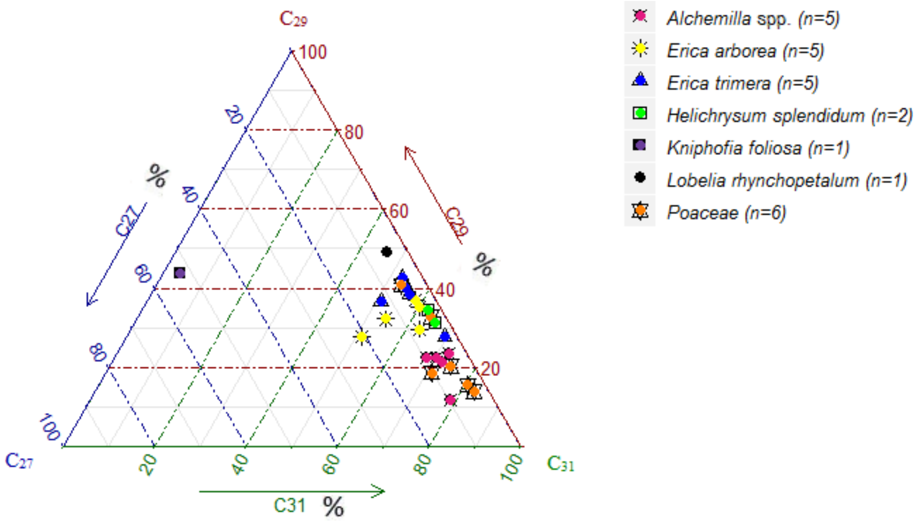


**Figure 7.** Ternary diagram illustrating the relative abundance (%) of the $n$-alkanes $C_{27}$, $C_{29}$ and $C_{31}$ in the investigated plant samples.

et al., 2011), and source proxy (S / V). This is in agreement with other studies (Belanger et al., 2015), and we therefore suggest that caution needs to be taken when using Ac / Al ratios as degradation proxies.

### 3.3 *n*-alkane concentrations and patterns of contemporary plants

To characterize the dominant plant species chemotaxonomically, $n$-alkanes with a chain length of 21–37 C atoms were considered as characteristic for epicuticular leaf waxes, typical for higher plants (Eglinton and Hamilton, 1967; Hoffmann et al., 2013). Most of the investigated plant species showed total $n$-alkane concentrations (TAC, $C_{25}$–$C_{35}$) above 800 $\mu g\,g^{-1}$. Only *Lobelia* and *Festuca* exhibited total $n$-alkane concentrations below 800 $\mu g\,g^{-1}$ (Fig. 6). The TAC values of the O layers were only slightly lower when compared to contemporary plants. By contrast, the TAC values of the $A_h$ horizons were significantly lower compared to contemporary plants (Fig. 6). The $n$-alkane concentrations in this study are in agreement with research findings for fresh plant materials (Bush and McInerney, 2013; Feakins et al., 2016) and soils (Schäfer et al., 2016).

Contrary to lignin phenols, hierarchical cluster analysis of individual $n$-alkanes did not allow for unambiguous differentiation between *Erica* and non-*Erica* species. Therefore, the $n$-alkane patterns do not allow for developing a proxy for identifying *Erica*, at least in the Bale Mountains. Average chain length values (ACLs) of plant and soil $n$-alkanes range between 28 to 32 and 29 to 31, respectively. The ACLs of *Erica arborea* (30.5) and *Erica trimera* (30.5) are identical, which could be explained by the monophyletic origin of the species (Guo et al., 2014). Grass sam-

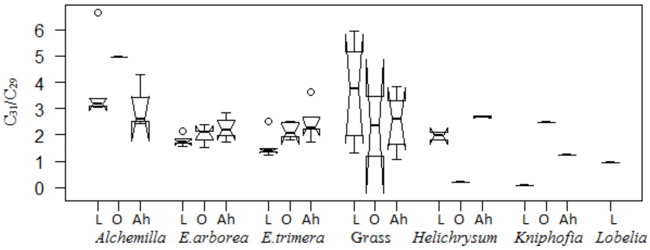


**Figure 8.** Box plot for the ratio $C_{31}$ / $C_{29}$ in plant samples, organic layers and $A_h$ horizons. The box plots indicate the median (solid line between the boxes) and interquartile range (IQR), with upper (75 %) and lower (25 %) quartiles and possible outliers (white circles). The notches display the confidence interval around the median within $\pm 1.57 \times$ IQR/sqrt. Note that small sample sizes result in unidentifiable boxes (particularly *Kniphofia* and *Lobelia*).

ples (*Festuca abyssinica*) exhibited a clear predominance of $C_{31}$ (Fig. 7), which was reported before by different authors (Schäfer et al., 2016; Zech, 2009). Most other investigated plant species revealed a predominance of either $C_{29}$ or $C_{31}$. Only *Kniphofia foliosa* is characterized by high relative abundance of $C_{27}$ and $C_{29}$, while $C_{31}$ is almost absent (Fig. 7).

Apart from individual *n*-alkanes, the ratio of $C_{31}$ / $C_{29}$ depicts *Erica* litter as significantly distinguishable from the other species, except for *Helichrysum splendidum* (Fig. 8).

### 3.4 *n*-alkane concentration and pattern of O layers and $A_h$ horizons

The TAC values decrease in the following order: plants > O layers > $A_h$ horizon (Fig. 6). The odd over even predominance values (OEPs) of the plants, O layers and $A_h$ horizons range from 5 to 90 ($\bar{x} = 21$), 4 to 42 ($\bar{x} = 15$) and 2 to 37 ($\bar{x} = 16$), respectively. The OEP values of the plants (which are almost identical to the CPI values) are therefore well within the range reported (Diefendorf et al., 2011) for angiosperms. Decreasing OEP values towards O layers and $A_h$ horizons are often observed and can be explained with organic matter degradation (Schäfer et al., 2016; Zech et al., 2011b). The still relatively high OEP values ($\bar{x} = 16$) obtained for the topsoils of our study area indicate that the *n*-alkanes are not strongly degraded. Importantly, *n*-alkane degradation affects not only the OEP values but also the *n*-alkane ratios, such as the above presented ratio $C_{31}$ / $C_{29}$ that allows distinguishing *Erica* from non-*Erica* vegetation. As a result, this ratio in particular no longer allows for chemotaxonomically distinguishing between soils that have developed under *Erica* versus *Alchemilla* and grass (Fig. 8). Unlike with lignin phenols, a noteworthy influence from root-derived *n*-alkanes on O layers and $A_h$ horizons can be excluded. This is based on the notion that roots contain lower *n*-alkane concentrations by several magnitudes than above-ground plant material and results from studies using $^{14}C$ dating of *n*-alkanes in loess–paleosol sequences (Häggi et al., 2014; Zech et al., 2017).

## 4 Conclusions and implications for paleovegetation reconstructions in the Bale Mountains

One of the premises within the Mountain Exile Hypothesis project (DFG-FOR 2358) is to reconstruct the dynamics of *Erica* vegetation on the Sanetti Plateau in the Bale Mountains National Park, Ethiopia. While our companion paper by Mekonnen et al. (2019) focused on stable carbon and nitrogen isotopes and hemicellulose-derived sugar biomarkers, we tested in this regional calibration study the potential of cupric oxide lignin phenols and leaf-wax-derived *n*-alkanes to serve as unambiguous proxies for differentiating between *Erica* versus non-*Erica* vegetation.

A hierarchical cluster analysis of individual lignin phenols was promising and allowed the chemotaxonomic differentiation of *Erica* from non-*Erica* vegetation based on relatively high relative contribution of cinnamyl (≥ 40 %) phenols. However, this characteristic pattern is not reflected in the O layers and $A_h$ horizons. In all likelihood, the loss of the cinnamyl dominance is caused by preferential degradation. Unlike expected, we found no overall evidence for increasing $(Ac / Al)_{V+S}$ ratios as a proxy for degradation from plant material over O layers to $A_h$ horizons.

*Erica* could not be differentiated chemotaxonomically from all other investigated plant species using *n*-alkanes in a hierarchical cluster analysis. Nevertheless, *Erica* was still characterized in our dataset by significantly lower $C_{31}$ / $C_{29}$ ratios compared to *Alchemilla* and grasses. However, like lignin-derived phenol proxies, the *n*-alkane patterns are changing due to degradation from plant material over O layers to $A_h$ horizons, thus inhibiting their application for an unambiguous chemotaxonomic identification of *Erica* in soils and sediments. Therefore, future work is planned focusing on alternative molecular markers such as tannin-derived phenols and terpenoids.

**Data availability.** The underlying datasets used in this study are accessible via https://doi.org/10.5281/zenodo.3372104.

**Author contributions.** BG, WZ and MZ developed the project idea in collaboration with SN and TB. WZ, BL and BM designed and handled field research work. BL and LB performed the laboratory work. The manuscript was prepared by BL with the support of MZ and the other co-authors.

**Competing interests.** The authors declare that they have no conflict of interest.

**Acknowledgements.** We are grateful to the Ethiopian Biodiversity Institute, Ethiopian Wildlife Conservation Authority, Bale Mountains National Park and Addis Ababa University for providing us with access to the plant genetic resources, access to the Bale Mountains National Park and for their scientific collaboration, respectively. We acknowledge the financial support within the funding program Open Access Publishing by the German Research Foundation (DFG). Bruk Lemma expresses his gratitude to the Catholic Academic Exchange Services (KAAD, Germany) for the PhD scholarship and his sincere thanks to Heike Maennicke for kind assistance during the laboratory work. We kindly thank three anonymous reviewers for their constructive comments and suggestions that helped us to improve the quality of this paper.

**Financial support.** This research has been supported by the DFG within Research Unit "The Mountain Exile Hypothesis" (grant nos. GL 327/18-1, ZE 844/10-1 and ZE 154/70-1).

## References

Amelung, W., Zech, W., and Flach, K. W.: Climatic effects on soil organic matter composition in the Great Plains, Soil Sci. Soc. Am. J., 61, 115–123, 1997.

Amelung, W., Martius, C., Bandeira, A. G., Garcia, M. V., and Zech, W.: Lignin characteristics and density fractions of termite nests in an Amazonian rain forest–indicators of termite feeding guilds, Soil Biol. Biochem., 34, 367–372, 2002.

Belanger, E., Lucotte, M., Gregoire, B., Moingt, M., Paquet, S., Davidson, R., Mertens, F., Passos, C. J. S., and Romana, C.: Lignin signatures of vegetation and soils in tropical environments, Adv. Enviro. Res., 4, 247–262, 2015.

Billi, P.: Geomorphological landscapes of Ethiopia, in: Landscapes and landforms of Ethiopia, edited by: Billi, P., Springer, Dordrecht, Netherlands, 3–32, 2015.

Bonnefille, R. and Hamilton, A.: Quaternary and late Tertiary history of Ethiopian vegetation, Symb. Bot. Ups, 26, 48–63, 1986.

Bonnefille, R. and Mohammed, U.: Pollen-inferred climatic fluctuations in Ethiopia during the last 3000 years, Palaeogeogr. Palaeocl., 109, 331–343, 1994.

Bush, R. T. and McInerney, F. A.: Leaf wax n-alkane distributions in and across modern plants: implications for paleoecology and chemotaxonomy, Geochim. Cosmochim. Ac., 117, 161–179, 2013.

Castañeda, I. S., Werne, J. P., Johnson, T. C., and Filley, T. R.: Late Quaternary vegetation history of southeast Africa: the molecular isotopic record from Lake Malawi, Palaeogeogr. Palaeocl., 275, 100–112, 2009.

Diefendorf, A. F., Freeman, K. H., Wing, S. L., and Graham, H. V.: Production of $n$-alkyl lipids in living plants and implications for the geologic past, Geochim. Cosmochim. Ac., 75, 7472–7485, 2011.

Eglinton, G. and Hamilton, R. J.: Leaf epicuticular waxes, Science, 156, 1322–1335, 1967.

Eglinton, T. I. and Eglinton, G.: Molecular proxies for paleoclimatology, Earth Planet. Sc. Lett., 275, 1–16, 2008.

Ertel, J. R. and Hedges, J. I.: The lignin component of humic substances: distribution among soil and sedimentary humic, fulvic, and base-insoluble fractions, Geochim. Cosmochim. Ac., 48, 2065–2074, 1984.

Feakins, S. J., Peters, T., Wu, M. S., Shenkin, A., Salinas, N., Girardin, C. A., Bentley, L. P., Blonder, B., Enquist, B. J., and Martin, R. E.: Production of leaf wax $n$-alkanes across a tropical forest elevation transect, Org. Geochem., 100, 89–100, 2016.

Friis, I.: Zonation of Forest Vegetation on the South Slope of Bale Mountains, South Ethiopia, Sinet-an Ethiopian Journal of Science, 29–44, 1986.

Glaser, B. and Zech, W.: Reconstruction of climate and landscape changes in a high mountain lake catchment in the Gorkha Himal, Nepal during the Late Glacial and Holocene as deduced from radiocarbon and compound-specific stable isotope analysis of terrestrial, aquatic and microbial biomarkers, Org. Geochem., 36, 1086–1098, 2005.

Goñi, M. A. and Hedges, J. I.: Lignin dimers: Structures, distribution, and potential geochemical applications, Geochim. Cosmochim. Ac., 56, 4025–4043, 1992.

Guo, N., Gao, J., He, Y., Zhang, Z. and Guo, Y.: Variations in leaf epicuticular $n$-alkanes in some Broussonetia, Ficus and Humulus species, Biochem. Syst. Ecol., 54, 150–156, 2014.

Häggi, C., Zech, R., McIntyre, C., Zech, M., and Eglinton, T. I.: On the stratigraphic integrity of leaf-wax biomarkers in loess paleosols, Biogeosciences, 11, 2455–2463, https://doi.org/10.5194/bg-11-2455-2014, 2014.

Hamilton, A. C.: Environmental history of East Africa: a study of the Quaternary, Academic Press, London, UK, 328 pp., 1982.

Hedberg, O.: Features of afroalpine plant ecology, Swedish Science Press, Uppsala, Sweden, 148 pp., 1964.

Hedges, J. I. and Ertel, J. R.: Characterization of lignin by gas capillary chromatography of cupric oxide oxidation products, Anal. Chem., 54, 174–178, 1982.

Hedges, J. I. and Mann, D. C.: The characterization of plant tissues by their lignin oxidation products, Geochim. Cosmochim. Ac., 43, 1803–1807, 1979.

Hedges, J. I., Clark, W. A., Quay, P. D., Richey, J. E., Devol, A. H., and Santos, M.: Compositions and fluxes of particulate organic material in the Amazon River1, Limnol. Oceanogr., 31, 717–738, 1986.

Hedges, J. I., Blanchette, R. A., Weliky, K., and Devol, A. H.: Effects of fungal degradation on the CuO oxidation products of lignin: a controlled laboratory study, Geochim. Cosmochim. Ac., 52, 2717–2726, 1988.

Hicks, S.: When no pollen does not mean no trees, Veg. Hist. Archaeobot., 15, 253–261, 2006.

Hillman, J. C.: Conservation in Bale mountains national park, Ethiopia, Oryx, 20, 89–94, 1986.

Hillman, J. C.: The Bale Mountains National Park area, southeast Ethiopia, and its management, Mountain Research and Development, 253–258, 1988.

Hoefs, M. J., Rijpstra, W. I. C., and Damsté, J. S. S.: The influence of oxic degradation on the sedimentary biomarker record I: Evidence from Madeira Abyssal Plain turbidites, Geochim. Cosmochim. Ac., 66, 2719–2735, 2002.

Hoffmann, B., Kahmen, A., Cernusak, L. A., Arndt, S. K., and Sachse, D.: Abundance and distribution of leaf wax $n$-alkanes in leaves of Acacia and Eucalyptus trees along a strong humidity gradient in northern Australia, Org. Geochem., 62, 62–67, 2013.

Jansen, B., van Loon, E. E., Hooghiemstra, H., and Verstraten, J. M.: Improved reconstruction of palaeo-environments through unravelling of preserved vegetation biomarker patterns, Palaeogeogr. Palaeocl., 285, 119–130, 2010.

Kidane, Y., Stahlmann, R., and Beierkuhnlein, C.: Vegetation dynamics, and land use and land cover change in the Bale Mountains, Ethiopia, Environ. Monit. Assess., 184, 7473–7489, 2012.

Koch, K., Bhushan, B., and Barthlott, W.: Multifunctional surface structures of plants: an inspiration for biomimetics, Prog. Mater. Sci., 54, 137–178, 2009.

Kolattukudy, P. E.: Plant waxes, Lipids, 5, 259–275, 1970.

Maffei, M.: Chemotaxonomic significance of leaf wax alkanes in the Gramineae, Biochem. Syst. Ecol., 24, 53–64, 1996.

Maffei, M., Badino, S., and Bossi, S.: Chemotaxonomic significance of leaf wax $n$-alkanes in the Pinales (Coniferales), J. Biol. Res., 1, 3–19, 2004.

Mekonnen, B., Zech, W., Glaser, B., Lemma, B., Bromm, T., Nemomissa, S., Bekele, T., and Zech, M.: Chemotaxonomic patterns of vegetation and soils along altitudinal transects of the Bale Mountains, Ethiopia, and implications for paleovegetation reconstructions – Part 1: stable isotopes and sugar biomarkers, E&G Quaternary Sci. J., 69, 177–188, https://doi.org/10.5194/egqsj-69-177-2019, 2019.

Miehe, S. and Miehe, G.: Ericaceous forest and heath land in Bale Mountains of South Ethiopia, Ecology and Man's Impact, Hamburg, Stiftung Walderhaltung in Africa Hamburg, Germany, 1994.

Möller, A., Kaiser, K., and Zech, W.: Lignin, carbohydrate, and amino sugar distribution and transformation in the tropical highland soils of northern Thailand under cabbage cultivation, Pinus reforestation, secondary forest, and primary forest, Soil Res., 40, 977–998, 2002.

Ortu, E., Brewer, S., and Peyron, O.: Pollen-inferred palaeoclimate reconstructions in mountain areas: problems and perspectives, J. Quaternary Sci., 21, 615–627, 2006.

Osmaston, H. A., Mitchell, W. A., and Osmaston, J. N.: Quaternary glaciation of the Bale Mountains, Ethiopia, J. Quaternary Sci., 20, 593–606, 2005.

Poynter, J. G., Farrimond, P., Robinson, N., and Eglinton, G.: Aeolian-derived higher plant lipids in the marine sedimentary record: Links with palaeoclimate, in Paleoclimatology and paleometeorology: modern and past patterns of global atmospheric transport, Springer, 435–462, 1989.

Rommerskirchen, F., Plader, A., Eglinton, G., Chikaraishi, Y., and Rullkötter, J.: Chemotaxonomic significance of distribution and stable carbon isotopic composition of long-chain alkanes and alkan-1-ols in $C_4$ grass waxes, Org. Geochem., 37, 1303–1332, 2006.

Schäfer, I. K., Lanny, V., Franke, J., Eglinton, T. I., Zech, M., Vysloužilová, B., and Zech, R.: Leaf waxes in litter and topsoils along a European transect, Soil, 2, 551–564, 2016.

Street-Perrott, F. A., Ficken, K. J., Huang, Y. and Eglinton, G.: Late Quaternary changes in carbon cycling on Mt. Kenya, East Africa: an overview of the $\delta$13C record in lacustrine organic matter, Quaternary Sci. Rev., 23, 861–879, 2004.

Tareq, S. M., Tanaka, N., and Ohta, K.: Biomarker signature in tropical wetland: lignin phenol vegetation index (LPVI) and its implications for reconstructing the paleoenvironment, Sci. Tot. Environ., 324, 91–103, 2004.

Tareq, S. M., Handa, N., and Tanoue, E.: A lignin phenol proxy record of mid Holocene paleovegetation changes at Lake DaBuSu, northeast China, J. Geochem. Explor., 88, 445–449, 2006.

Tareq, S. M., Kitagawa, H., and Ohta, K.: Lignin biomarker and isotopic records of paleovegetation and climate changes from Lake Erhai, southwest China, since 18.5 ka BP, Quatern. Int., 229, 47–56, 2011.

Thevenot, M., Dignac, M.-F., and Rumpel, C.: Fate of lignins in soils: a review, Soil Biol. Biochem., 42, 1200–1211, 2010.

Tiercelin, J.-J., Gibert, E., Umer, M., Bonnefille, R., Disnar, J.-R., Lézine, A.-M., Hureau-Mazaudier, D., Travi, Y., Kéravis, D., and Lamb, H. F.: High-resolution sedimentary record of the last deglaciation from a high-altitude lake in Ethiopia, Quaternary Sci. Rev., 27, 449–467, 2008.

Umer, M., Kebede, S., and Osmaston, H.: Quaternary glacial activity on the Ethiopian Mountains, Developments in Quaternary Sciences, 2, 171–174, 2004.

Umer, M., Lamb, H. F., Bonnefille, R., Lézine, A.-M., Tiercelin, J.-J., Gibert, E., Cazet, J.-P., and Watrin, J.: Late pleistocene and holocene vegetation history of the bale mountains, Ethiopia, Quaternary Sci. Rev., 26, 2229–2246, 2007.

Woldu, Z., Feoli, E., and Nigatu, L.: Partitioning an elevation gradient of vegetation from Southeastern Ethiopia by probabilistic methods, Plateau, 81, 189–198, 1989.

Yimer, F., Ledin, S., and Abdelkadir, A.: Soil organic carbon and total nitrogen stocks as affected by topographic aspect and vegetation in the Bale Mountains, Ethiopia, Geoderma, 135, 335–344, 2006.

Zech, M.: Evidence for Late Pleistocene climate changes from buried soils on the southern slopes of Mt. Kilimanjaro, Tanzania, Palaeogeogr. Palaeocl., 242, 303–312, 2006.

Zech, M.: Reconstructing Quaternary vegetation history in the Carpathian Basin, SE Europe, using $n$-alkane biomarkers as molecular fossils: problems and possible solutions, potential and limitations, E&G Quaternary Sci. J., 58, 148–155, 2009.

Zech, M. and Glaser, B.: Improved compound-specific $\delta$13C analysis of $n$-alkanes for application in palaeoenvironmental studies, Rapid Commun. Mass Sp., 22, 135–142, 2008.

Zech, M., Pedentchouk, N., Buggle, B., Leiber, K., Kalbitz, K., Marković, S. B., and Glaser, B.: Effect of leaf litter degradation and seasonality on D/H isotope ratios of n-alkane biomarkers, Geochim. Cosmochim. Ac., 75, 4917–4928, 2011a.

Zech, M., Leiber, K., Zech, W., Poetsch, T., and Hemp, A.: Late Quaternary soil genesis and vegetation history on the northern slopes of Mt. Kilimanjaro, East Africa, Quaternary Int., 243, 327–336, 2011b.

Zech, M., Zech, R., Buggle, B., and Zöller, L.: Novel methodological approaches in loess research – interrogating biomarkers and compound-specific stable isotopes, E&G Quaternary Sci. J., 60, 13, https://doi.org/10.3285/eg.60.1.12, 2011c.

Zech, M., Krause, T., Meszner, S., and Faust, D.: Incorrect when uncorrected: reconstructing vegetation history using $n$-alkane biomarkers in loess-paleosol sequences – a case study from the Saxonian loess region, Germany, Quaternary Int., 296, 108–116, 2013.

Zech, M., Kreutzer, S., Zech, R., Goslar, T., Meszner, S., McIntyre, C., Häggi, C., Eglinton, T., Faust, D., and Fuchs, M.: Comparative $^{14}C$ and OSL dating of loess-paleosol sequences to evaluate post-depositional contamination of $n$-alkane biomarkers, Quaternary Res., 87, 180–189, 2017.

Ziegler, F., Kögel, I. and Zech, W.: Alteration of gymnosperm and angiosperm lignin during decomposition in forest humus layers, Z. Planz. Bodenkunde, 149, 323–331, 1986.

E&G Quaternary Sci. J., 68, 201–213, 2019
https://doi.org/10.5194/egqsj-68-201-2019


Open Access E&G Quaternary Science Journal

Research article

# Combining geomorphological–hydrological analyses and the location of settlement and raw material sites – a case study on understanding prehistoric human settlement activity in the southwestern Ethiopian Highlands

**Elena A. Hensel**[1], **Oliver Bödeker**[2], **Olaf Bubenzer**[3], **and Ralf Vogelsang**[4]

[1]Institute of Geography, University of Cologne, Cologne, 50923, Germany
[2]Department of Geoscience, University of Cologne, Cologne, 50923, Germany
[3]Institute of Geography & Heidelberg Center for the Environment (HCE), Heidelberg University, Heidelberg, 69120, Germany
[4]Institute of Prehistoric Archaeology, University of Cologne, Cologne, 50923, Germany

**Correspondence:** Elena A. Hensel (elena.hensel@uni-koeln.de)

**Relevant dates:** Received: 8 January 2019 – Revised: 26 August 2019 – Accepted: 29 August 2019 – Published: 17 October 2019

**How to cite:** Hensel, E. A., Bödeker, O., Bubenzer, O., and Vogelsang, R.: Combining geomorphological–hydrological analyses and the location of settlement and raw material sites – a case study on understanding prehistoric human settlement activity in the southwestern Ethiopian Highlands, E&G Quaternary Sci. J., 68, 201–213, https://doi.org/10.5194/egqsj-68-201-2019, 2019.

**Abstract:** During this study, the recent relations between the hydrological systems and the distribution of archaeological sites and obsidian raw material outcrops within the catchment of the Bisare River, around Mt Damota, and around Mt Sodicho in the southwestern Ethiopian Highlands were investigated. To do so, we combined geomorphological–hydrological analyses with field surveys and GIS mapping. The aim was to try to transfer these recent interrelations into the past to better understand the factors that influenced prehistoric human settlement activity. The natural geomorphodynamics in landscapes such as the southwestern Ethiopian Highlands were and still are characterized by the interplay between endogenous processes (tectonics, volcanism) and climatic fluctuations and, during the recent past, also by human activity. In the considered region, protective and potentially habitable rock shelters are found at the volcanic slopes of Mt Damota and Mt Sodicho at high elevations. In addition, in some areas recent morphodynamic processes make obsidian raw material available near the surface. However, archaeological and terrestrial paleoenvironmental archives that allow an understanding of the interplay between prehistoric settlement activity and paleoenvironmental conditions are still rare. Therefore, the surroundings of formerly occupied rock shelters were investigated to illustrate the effect of the recent fluvial morphodynamics (erosion and accumulation) on surface visibility and preservation of archaeological obsidian raw material. This recent information can be used to make assumptions about the former hydrological system and to thereby get answers to research questions such as those about the past accessibility of obsidian raw material for prehistoric humans. The results suggest that the study area is currently affected by a highly dynamic hydrological system, which is indicated by phenomena such as the formation of swamps due to sedimentation in natural depressions. In addition, wide areas of the Bisare River catchment are affected by gully erosion, which leads to land degradation but also to the exposure of the above-mentioned lithic raw material outcrops. Human influence strongly increased during the Holocene until today, especially on the mountain flanks. This in turn increased soil loss and erosion of archaeological sites, which complicates the transfer of the current morphodynamics into the past. Although it cannot be finally confirmed that prehistoric hunters and gatherers systematically used fluvially exposed raw material, based on our results it can be assumed that humans frequented this area, due to the local availability of such kind of material.

**Kurzfassung:** Im Rahmen dieser Studie wurden die aktuellen Zusammenhänge zwischen hydrologischen Systemen, sowie der Verbreitung archäologischer Fundplätze und von Obsidian-Rohmateriallagerstätten im Einzugsgebiet des Bisareflusses, um Mount Damota sowie um Mount Sodicho im südwestlichen äthiopischen Hochland untersucht. Hierfür wurden geomorphologisch-hydrologische Analysen mit Geländesurveys und Gis-Kartierungen kombiniert. Das Ziel war der Versuch, die aktuelle Situation in die Vergangenheit zu übertragen, um die prähistorische menschliche Siedlungsaktivität besser zu verstehen. Das natürliche geomorphologische Prozessgeschehen in Landschaften wie dem südwestlichen äthiopischen Hochland wurde und wird durch das Zusammenspiel von endogenen Prozessen (Tektonik, Vulkanismus) sowie Klimaschwankungen und in jüngster Zeit auch durch menschliche Aktivitäten geprägt. In der betrachteten Region finden sich höher gelegene, schützende und potentiell bewohnbare Felsüberhänge (Rockshelter) an den Vulkanhängen des Mt. Damota und des Mt. Sodicho. Außerdem wird durch aktuelle morphodynamische Prozesse in einigen Bereichen Obsidian als Rohmaterial oberflächennah verfügbar. Archäologische und terrestrische Paläoumweltarchive, die es ermöglichen, das Zusammenspiel zwischen prähistorischer Besiedlung und Umweltbedingungen zu verdeutlichen, sind jedoch noch selten. Daher wurde die Umgebung der ehemals bewohnten Rockshelter untersucht, um die Auswirkungen der rezenten fluvialen Morphodynamik (Abtragung und Akkumulation) auf die oberflächennahe Sichtbarkeit und Erhaltung archäologischer Rohmaterial-Fundstellen zu verdeutlichen. Die gewonnen Informationen können dafür verwendet werden, Annahmen über das ehemalige hydrologische System zu treffen und somit Antworten auf Forschungsfragen wie jener nach der ehemaligen Zugänglichkeit von Obsidian-Lagerstätten für den prähistorischen Menschen zu erhalten. Die Ergebnisse legen nahe, dass das Untersuchungsgebiet derzeit von einem hochdynamischen hydrologischen System geprägt wird, was sich beispielsweise durch Phänomene wie der Ausbildung von Sümpfen aufgrund von Sedimentation in natürlichen Depressionen zeigt. Darüber hinaus stehen weite Bereiche des Einzugsgebiets des Bisareflusses unter dem Einfluss von Gullyerosion (Grabenerosion), welche zu Bodendegradierung und zur Freilegung der oben genannten lithischen Rohmaterialien führt. Insbesondere an den Bergflanken nahm der anthropogene Einfluss während des Holozäns stark zu. Dies wiederum verstärkte den Bodenabtrag und die Erosion archäologischer Fundstellen, was den Transfer der aktuellen Morphodynamik auf die Vergangenheit erschwert. Obwohl nicht eindeutig nachgewiesen werden kann, dass prähistorische Jäger und Sammler fluvial freigelegtes Rohmaterial gezielt nutzten, kann basierend auf unseren Ergebnissen davon ausgegangen werden, dass die lokale Rohmaterialverfügbarkeit zu einer verstärkten Frequentierung der Region durch prähistorische Menschen führte.

## 1 Introduction

The landscape of the southwestern Ethiopian Highlands was created by tectonic stresses and Late Pleistocene–Holocene eruptive activity, as well as by the increasing influence of human activity in recent times. The development of topographic barriers and natural basins that were induced by tectonic uplift or faulting created a complex relief with ridges and ravines (De La Torre et al., 2007; Benito-Calvo et al., 2007). Large areas of today's surface are influenced by erosional processes, for example, by widespread gully erosion and badlands formation that are common causes of morphological transformations in Ethiopia today (Billi and Dramis, 2003). In many cases, this development is linked to human influence and the intensification of agriculture (Castillo and Gómez, 2016). Up to now, there are only a few terrestrial geoarchives in East Africa with reconstructions of Pleistocene and Holocene precipitation or temperature changes (Tierney et al., 2008; Tierney et al., 2011; Foerster et al., 2012, 2015). Due to the rare paleoclimatic data but also due to the lack of valuable archaeological information, there is still an ongoing discussion on how short- and long-term climatic events and trends affected prehistoric humans living on the Horn of Africa. Available paleoclimatic records from lake sediments from Ethiopia and Kenya document wet–dry transitions that likely affected prehistoric humans and their adaption to the changing environment. In this context, one proposed hypothesis is the retreat of human groups into highland regions with higher precipitation rates during dry periods (Basell, 2008; Foerster et al., 2015; Junginger and Trauth, 2013).

Our study discusses the following research questions. (1) How does the actual hydrological system of the study area look like? (2) What role does this system play in present accessibility of obsidian raw material sources and the visibility and preservation of archaeological sites? (3) Which geomorphological features related to erosion are present? (4) Can we make assumptions about the ancient hydrological system and landscape dynamics and, on their influence, on the accessibility of past obsidian raw material sources? For our studies we selected three research areas in the southwestern Ethiopian Highlands, ca. 250 km southwest of Addis Ababa, that are located within a radius of 40 km of one another (Fig. 2). (1) Mt Damota is a volcanic mountain that became of archaeological interest because of its key site, the Mochena Borago Rockshelter, which is one of the most important Late Pleistocene and Holocene sites in eastern Africa (Brandt et al., 2012). (2) Mt Sodicho is located ca. 40 km to the northwest of Mt Damota and marks the second research area. The archaeological site Sodicho Rockshelter is located on the southern flanks of this volcanic mountain. (3) The banks of the Bisare River, a tributary of the Bilate River, are located southeast of Mt Damota (Fig. 2a).

Archaeological records within the rock shelter sediments of, e.g. Mt Damota or Mt Sodicho, provide information about ancient human–environment interactions. Additionally, numerous open-air sites at the slopes of Mt Damota provide a complementary record of former human settlement (Brandt et al., 2012; Vogelsang and Wendt, 2018). The main trench at Mochena Borago yielded three major lithostratigraphic units with archaeological material classified as Middle Stone Age (MSA), dating to ages between 36 and $>50$ ka (Brandt et al., 2017). However, a sedimentological hiatus in the stratigraphy from $\sim 36$ to $\sim 8$ ka leaves unanswered questions about deposition processes and the occupation at that site until the Holocene (Brandt et al., 2012, 2017). Vogelsang and Wendt (2018) examined multiple archaeological surface localities classified as MSA and Late Stone Age (LSA) sites on the western flank of Mt Damota to reconstruct prehistoric settlement patterns. They recognized intensification of settlement activities from the MSA to the LSA, as well as a different organization of the site clusters along the mountain slopes. Whereas the reconstructed MSA settlement areas show a linear, vertical orientation and include different altitudinal belts, the LSA sites form one large cluster with interconnected smaller sub-groups. The former is interpreted as a land use model that offered short access to various eco-zones in different elevations, a strategy that might have been advantageous during times of environmental stress. Following our first results for the Sodicho Rockshelter, archaeological settlement layers with preserved and recently dated lithic material fill the Late Pleistocene and Holocene occupational gap ($\sim 36$ to $\sim 8$ ka) from Mochena Borago. Generally, the volcanic rocks of Mt Damota and Mt Sodicho do not contain any naturally occurring obsidian, although this is the most common raw material used for the production of stone artefacts at all archaeological sites in the region (Brandt et al., 2012, 2017). The third study area at the permanent Bisare River site shows a high potential for geoarchaeological investigation (Benito-Calvo et al., 2007), since obsidian raw material was exposed by gully erosion and archaeological artefacts from all stone age periods are scattered within the catchment area. The main causes of gully formation and further development are still not clear, although several factors are potentially relevant for the development of this incision. These often include, e.g. higher precipitation after arid phases, loose topsoil material, and sparse vegetation due to intense land use (Billi and Dramis, 2003; Fryirs and Brierley, 2013; Mukai, 2017). By studying swamp formation in the upper Bisare catchment, the influence of alternating wet and dry phases on the regional landscape dynamics could exemplarily be investigated for the last several years (for long-term climatic fluctuations, please compare Trauth et al., 2019). These alternations lead to changes in erosion and deposition. Generally, our analysis of the landscape archive at the Bisare River sheds light on site preservation and raw material availability.

In order to understand ancient human–environment interactions, understanding the past morphodynamics is crucial. We followed a diachronous approach and tried to transfer today's knowledge about the local fluvial dynamics that affect archaeological assemblages and raw material outcrops by degradation into the past. In the framework of this study we applied geomorphological and hydrological analyses via remote sensing and field surveys. In doing so, we mapped the current flow directions and stream networks and compared these with signs of former human occupation.

## 2 General settings of the study area

### 2.1 Geological and geomorphological setting

The study area is located in the southwestern Ethiopian Highlands north of Lake Abaya, between the north–south-running Omo River in the west and the Bilate River in the east, at the border of the western central and southern Main Ethiopian Rift and the southern Ethiopian Plateau (Fig. 1b). On average, the mountain ranges rise to 2000–3000 m above sea level (a.s.l.). Plio–Pleistocene volcanic activity and Late Pleistocene to Holocene tectonic stress formed characteristic natural basins, steep slopes, and gorges. Silicic volcanic material, including the trachytic solid rocks of Mt Damota and

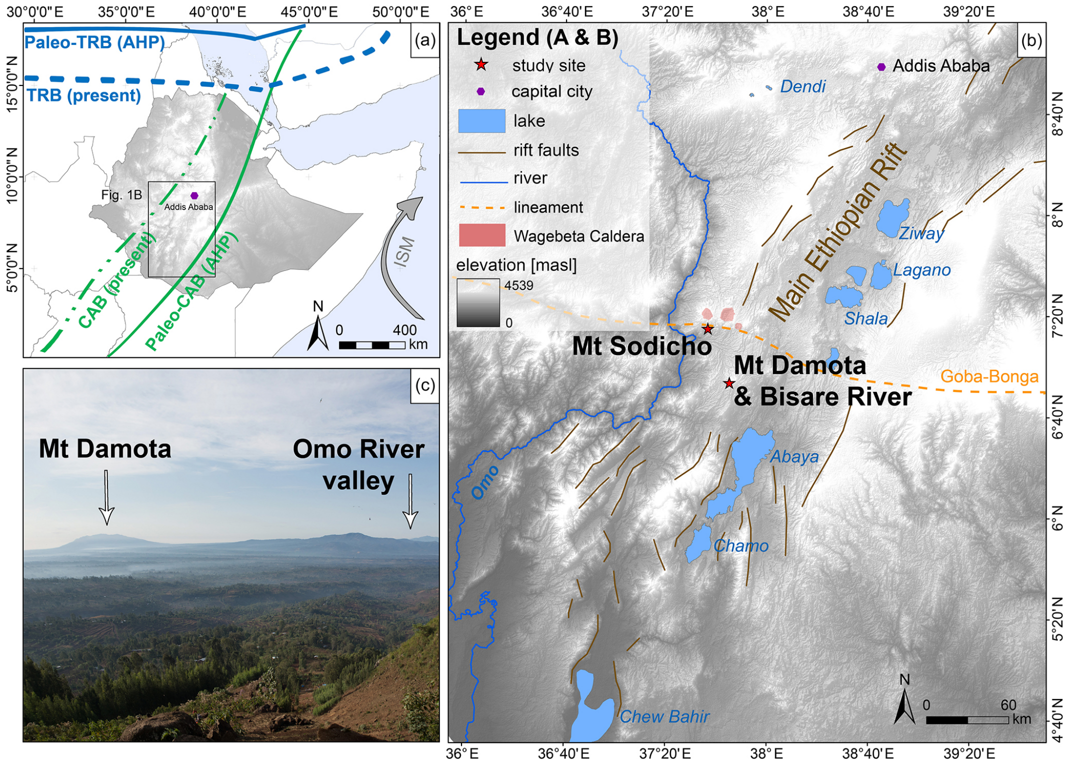


**Figure 1.** **(a)** Map showing the flow of the Indian Summer Monsoon (ISM) and the current northernmost position of the tropical rain belt (TRB) during August (TRB, present) and its shifted northernmost position for August during the African humid period (Paleo-TRB, AHP, ~ 15 ka BP to ~ 5 ka BP). The map also refers to the present position of the Congo Air Boundary (CAB) and its shift during the AHP (modified from Junginger and Trauth 2013). **(b)** Research area at the rift margins in the southwestern Ethiopian Highlands, showing the major geological fault system of the Main Ethiopian Rift, the big lake systems, the Wagebeta Caldera Complex, and the Goba-Bonga lineament. The study sites are marked by red stars (DEM data by ASTER GDEM; illustration by Elena Hensel). **(c)** Photo taken from the southern flank of Mt Sodicho, showing the silhouette of Mt Damota and the Omo River valley (viewing direction south-southwest) (Photo by Christian Schepers, illustration by Elena Hensel).

Mt Sodicho, is part of the rift shoulder trachytic volcanism, which developed in the Pliocene during the late stages of the formation of the Ethiopian Rift (Chernet, 2011; Corti et al., 2013; Abbate et al., 2015).

Mt Damota is a dormant igneous volcanic mountain with a height of 2908 m a.s.l., which is primarily composed of greenish grey trachyte (Brandt et al., 2012). It is part of a larger silicic complex and overlies a pyroclastic rock formation of rhyolitic to trachytic lava and ignimbrites that are associated with the Nazret Group (Chernet, 2011; Corti et al., 2013). Woldegabriel et al. (1990) assumed a formation of the trachytic flows of the volcano during the Late Pliocene (~ 2.9 Ma). Mt Sodicho, with an elevation of about 2100 m a.s.l., belongs to the Wagebeta Caldera Complex (Fig. 1b). The mountain lies directly on the Goba-Bonga lineament, a transversal east–west depression with transversal structures that crosses the Main Ethiopian Rift (Bonini et al., 2005; Corti, 2009; Corti et al., 2013). The Bisare River catchment is situated southwest of Mt Damota within the Hobitcha Caldera structure (Fig. 2c). The river is a western tributary of the Bilate River that flows into the northern part of Lake Abaya. This lake is located in a quasi-endorheic basin (Schütt et al., 2005). The Bisare River is associated with glacis and valley fills including interbedded volcanic rocks. The latter are not older than 200 ka and developed from the Middle to Upper Pleistocene up to the Holocene (De La Torre et al., 2007). Archaeological finds in the area of the Bisare River catchment comprise open-air artefact scatters and widespread raw material locations, which are currently exposed as a result of river incision (Benito-Calvo et al., 2007; De La Torre et al., 2007; Abbate et al., 2015; Vogelsang, unpublished observation, 2011, 2012).

## 2.2 Climatic setting

The Ethiopian Highlands receive more than 2000 mm of annual rainfall, which is the highest average amount at the Horn of Africa (Griffith, 1972; Viste and Sorteberg, 2013). Annual climatic variations in Ethiopia are related to moisture brought by the summer monsoon that interacts with the dry northeastern "Harmattan" wind system and to changes in the north–south directed pressure gradient (Viste and Sorteberg, 2013; Nicholson, 2018). A further influence is changes in sea surface temperatures of the adjacent Indian Ocean (Griffith, 1972; Tierney et al., 2008; Segele et al., 2009; Viste et al., 2013). Inter-annual changes in precipitation are linked to the shifting of the tropical rain belt (TRB), low-level convergences, and the role of the accentuated topography (Nicholson, 2018) (Fig. 1a). The Congo Air Boundary (CAB) is an additional but less relevant source for moisture variability in Ethiopia (Junginger and Trauth, 2013). Most of the annual precipitation (50 %–90 %) falls during boreal summer from June to September, called "Kirmet" in this area. Regions with the highest precipitation receive up to 350 mm of rainfall per month (Berhanu et al., 2013). The vegetation of the study area around Mt Damota and Mt Sodicho encompasses two classification types according to Friis et al. (2010): grasslands and mountainous woodland between 1600 and 3300 m a.s.l. belong to the "dry evergreen montane forest and grassland complex" classification and evergreen trees between 1500 and 2600 m a.s.l. to the "moist evergreen montane forest" classification. The mountain flanks of Mt Damota and Mt Sodicho were reshaped by human deforestation, intensive subsistence farming, and subsequent partly severe soil erosion during the last few decades (Fig. 1c). The paleoclimate of southwestern Ethiopia of the last 45 ka was characterized by fluctuations of moister and drier conditions (Foerster et al., 2012; Trauth et al., 2019). According to the paleoclimate record of the Chew Bahir drill cores, arid conditions during the Last Glacial Maximum (LGM, ∼ 24–18 ka) led to a desiccation of the former paleolake (Foerster et al., 2012, 2015; Trauth et al., 2019) (Fig. 1b). Subsequently, an abrupt change is visible after ∼ 15 ka with a transition from extreme arid to humid conditions, marking the starting point of the African humid period (AHP, ∼ 15 to 5 ka). This was a period with a generally higher and stable availability of moisture but was, however, interrupted by several dry spells. Exemplary arid phases were the Older Dryas stadial (OD, ∼ 14 ka) and the Younger Dryas event (YD, 12.8–11.6 ka), followed by shorter dry events (∼ 10.5, ∼ 9.5, 8.15–7.8 and ∼ 7 ka). The end of the AHP was marked by an increase in aridity that persists to this day. Exceptions were short humid events at ∼ 3, ∼ 2.2, and 1.3 ka (Foerster et al., 2012, 2015).

## 3 Material and methods

### 3.1 Mapping and survey

The research areas around Mt Damota and Mt Sodicho were mapped during field surveys from 2015 to 2018 that were supported by high-resolution satellite imagery. Geomorphological mapping in the field included the description of rock outcrops, surface exposures, geomorphological features, and signs of the influence of extensive modern human occupation in the area. Afterwards, topographical features such as reliefs and slopes, as well as drainage ways and further geomorphological properties, were extracted from a high-resolution digital elevation model (DEM) (Sect. 3.2). Archaeological surveys in the surrounding area of Mt Damota were conducted from 2010 to 2014, resulting in the discovery of 63 open-air sites. The surveys included different landforms of the tropical highlands in various altitudes, following "stratified random sampling" (Shafer, 2016; Vogelsang and Wendt, 2018). Systematic archaeological and geomorphological surveys of the western Bisare River and Bilate River were undertaken in 2006 by the research group around De la Torre et al. (2007) and in 2011, 2012, and 2014 by the research team of the Collaborative Research Centre 806 (CRC806) "Our way to Europe". The excavations at Sodicho Rockshelter on Mt Sodicho started in 2015.

### 3.2 GIS-based analyses

The image analysis software ENVI (5.3 by Harris Geospatial Solutions) was used to extract high-resolution digital elevation models (DEM) using panchromatic images of Pléiades 1A (by Astrium Services/Spot Image, Airbus Defence and Space) satellites, with a 2 m resolution, and ASTER GDEM data (by METI and NASA), with a resolution of 30 m. For this, identical tie points on both satellite images were manually fitted together to create panchromatic images. The high-resolution DEMs generated from the Pléiades satellite scenes cover areas spanning Mt Sodicho, Mt Damota, and the Bisare River catchment, and singular ASTER scenes were used to fill gaps.

Surface and hydrological data were determined by a Geographical Information System (ArcGIS 10.6 by ESRI) using the beforehand-created DEMs functioning as base "maps". The modelling tools of Arc Hydro (ESRI) were used for the extraction of the hydrological features, such as flow direction and accumulation, surface runoff, and catchment areas. The calculated GIS data sets can be requested from the CRC 806 Database via https://doi.org/10.5880/SFB806.49. These parameters allowed a quantitative raster- and vector-based calculation of the actual drainage systems (Bolten et al., 2006). Freely available satellite images of the Google Earth Timelapse NASA Landsat programme from 2009 to 2017 were used to identify annual landscape transformations, i.e. swamp formation and reduction (Fig. 3). In addition, viewshed analyses from both mountaintops (Mt Damota and Mt Sodicho) were conducted with ArcGIS 10.6 (ESRI) to test the significance of the archaeological rock shelters at high evaluations and their importance for prehistoric hunter-gatherers. To do so, a body height of 1.60 m was defined.

### 3.3 Radiocarbon dating

Several percussion drilling cores were obtained from 11 drilling locations in the basin of the Bisare River swamps in 2014 and 2015. The drilling locations were placed over the entire swamp area. Drilling locations in the surrounding area were not considered, since the surroundings are dominated

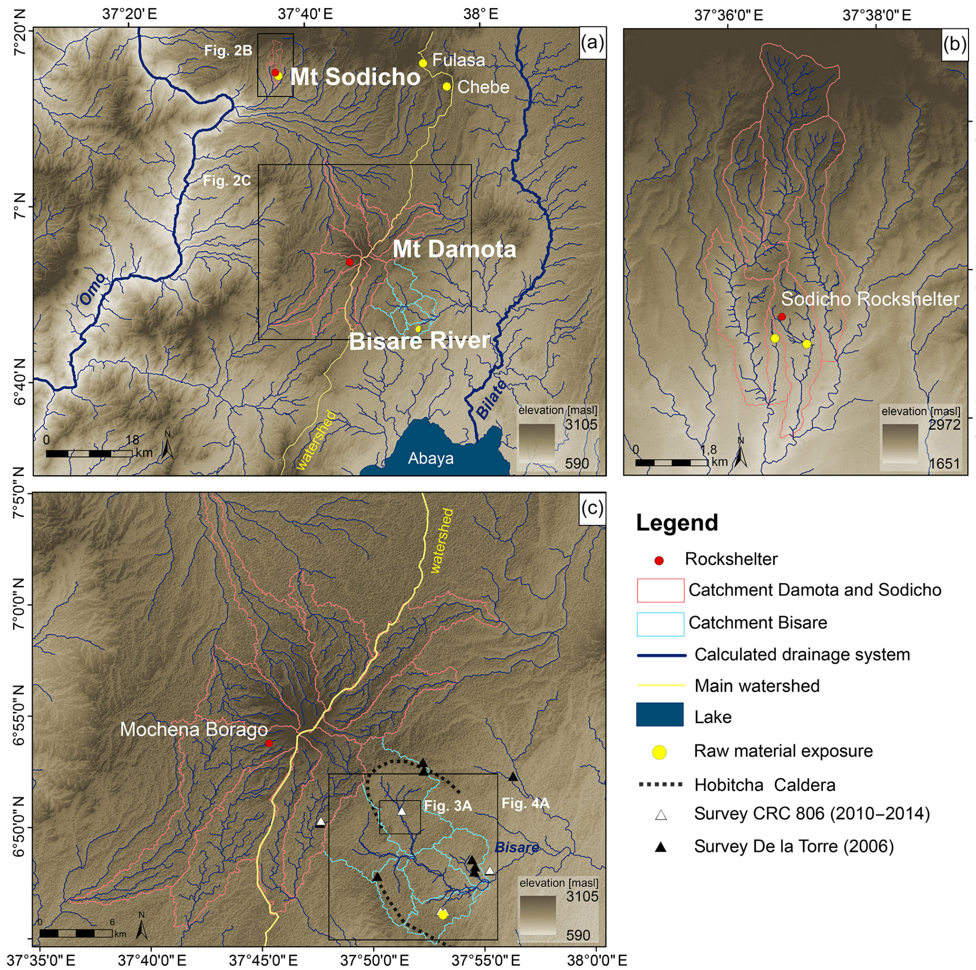


**Figure 2.** **(a)** Map showing the calculated drainage networks in the study area for the three study sites: Mt Damota, the Bisare River catchment, and Mt Sodicho. Primary drainage systems mainly support the two major south running rivers: Omo and Bilate. **(b)** Drainage network at the southern flank of Mt Sodicho. **(c)** Drainage network of Mt Damota and the Bisare River. The triangles illustrate archaeological evidence mapped by De la Torre (2006) and by the CRC 806 (2010–2014) (DEM data from Mochena and Bisare by ASTER GDEM; DEM data from Sodicho by Astrium's Pléiades; illustration by Elena Hensel).

**Table 1.** Radiocarbon ages for the samples from the BIS03 and BIS07 drilling cores.

| Sample label | Sample ID | Material | Depth b.s.l. (cm) | Age (years BP) | ± | Age (years CE) | $\delta^{13}C$ (‰) |
|---|---|---|---|---|---|---|---|
| COL2819.1.1 | BIS03-RC1 | plant | 118 | −325 | 34 | n/a | −28.6 |
| COL3300.1.1 | BIS07-C1_W | plant | 280 | > modern | – | 1957–1998 | −11.2 |
| COL3301.1.1 | BIS07-C1_S | sediment | 280 | 25 | 35 | 1694–1919 | −21.2 |

n/a: not applicable.

by modern agriculture and therefore excessively influenced by human activity. In this study, we present three samples from cores BIS03 and BIS07 of the uppermost part of swamp 1, which were tested for radiocarbon dating (Table 1). Both cores were drilled in fluvial sequences located on the edges of the swamp (Fig. 3a). The three radiocarbon samples, from either plant (BIS03-PC1 and BIS07_W) or sediment material (BIS07-C1_S), were extracted from silty to sandy sediments in the upper 3 m of the drilling cores. The radiocarbon AMS lab of the University of Cologne analysed the samples with acid and alkali (AAA) pre-treatment to remove inorganic carbon and humid acids. The conventional radiocarbon ages were calibrated with OxCal v. 4.2.3, applying the calibration curve IntCal13 (Ramsey et al., 2013; Reimer et al., 2013).

## 4 Results

### 4.1 GIS-based analyses

The geomorphological and hydrological analyses of the two mountains and the Bisare River catchments were based on high-resolution DEMs that were calculated based on remote sensing data. With the help of the catchment analysis, recent large-scale drainage lines of the study area around Mt Damota and Mt Sodicho were defined (Fig. 2a). In combination with a geomorphological field survey, small-scale and large-scale gully erosion could be identified.

1. Mt Damota has a typical radial drainage system, which is crossed by a main watershed (Fig. 2c). This watershed is running north–south through the entire study area, separating the runoff into a western and an eastern direction. The western streams drain into the Omo River basin, whereas the eastern streams drain towards Lake Abaya but without an inflow into the Bisare River catchment. This is caused by the horseshoe-shaped Hobitcha Caldera that functions as a barrier between the eastern streams and the Bisare River catchment.

2. Mt Sodicho's stream network and drainage lines mainly flow into the Omo River basin. According to the hydrological analyses and the field observations from 2017, Mt Sodicho has a radial drainage network, which gave the mountain its characteristic irregular form (Fig. 2b). Permanent streams and seasonal creeks (only flowing during the rainy season) flow down the mountain flanks into a larger south-running dendritic drainage network that belongs to the drainage network of the Wagebeta Caldera Complex. Nowadays, the surface morphology on Mt Sodicho is influenced by intensive agriculture. Small-scale surface erosion (10–20 m in width) was mapped on the upper slopes (Fig. 1c). In the past, the vegetation was probably removed to create cultivation areas, which are now jeopardized by increasing erosion. These active gullies are currently used as pathways for the local population and their cattle, which further enhances degradation and runoff. Raw material provenance of lithic artefacts that were found at Mt Sodicho is still not proven. So far, obsidian raw material with distinct signs of transport could be observed as fluvially transported boulders or debris along the surrounding drainage systems and river banks. In Fig. 2b, these raw material findings are illustrated as yellow dots. Additionally, two obsidian outcrops were discovered to the east of Mt Sodicho during the latest survey in November 2018. Within a distance of 30–36 km from Sodicho Rockshelter, the two outcrops named Chebe and Fulasa were still in the range of movement of the Late Pleistocene hunter-gatherers (Fig. 2a).

3. The Bisare River flows into the Bilate River. The latter is the main tributary of the 15 000 km$^2$ large catchment of Lake Abaya (Chernet, 2011). Based on the hydrological and geomorphological analyses, different geomorphic features could be observed (Fig. 2c): the research area lies within a dynamic hydrological system, showing a high to moderate runoff of surface water (Berhaun et al., 2013). With the help of a longitudinal profile, starting at the Bisare River catchment and following the Bilate River into Lake Abaya, a sudden change in the slope (knickpoint) could be identified. This knickpoint is situated $\sim$ 15 km along the profile, where the river flows out from the Hobitcha Caldera (Fig. 5). The study of knickpoints can be used to identify potential areas for sedimentation. Three connected swamps of different sizes and altitudes formed in low-energy parts of the river valley in the upper part of the catchment (Fig. 3). They were documented during geomorphological field mapping in 2014. A highly exaggerated longitudinal profile, running transversely through the lakes, illustrates the local stair-like morphology. Unlike swamp 3, the two upper basins of swamps 1 and 2 are situated in an area with highly dynamic permanent and episodic streams. Via satellite imagery (Google Earth Timelapse NASA Landsat programme), we observed that the two upper swamps are supplied by episodic tributaries during wet seasons (Fig. 3b–d). Gully erosion and sheetwash erosion are widespread phenomena particularly in the lower part of the Bisare catchment (Fig. 4a). Here, surface runoff and erosion-outcropped artefact assemblages are predominantly from the Middle Stone Age (De La Torre et al., 2007). These assemblages were preserved in Pleistocene alluvial soils at the flanks of the river basin. Also, outcrops of in situ obsidian raw material and scattered lithic surface finds were found by De La Torre et al. (2007) and our research team in the southern degraded areas. Formerly buried material was exposed to the surface, and the lithics had been partly transported due to constant erosion and extensive badlands formation, mainly at the lower part of the river catchment. Erosion and badlands formation initiated from the edge of the rift valley and spread upstream of the Bisare (Fig. 4c–e). Figure 4d and e visualize subsurface material cropping out in this degraded area, which varies between reddish-brown regolith and greyish ignimbrite.

According to the viewshed analyses from the mountaintops of Mt Damota and Mt Sodicho, all-round views over the landscape are possible. The views reach from the lakes of the central Main Ethiopian Rift Valley in the distant north, over the Bilate River in the east, Lake Abaya to the south, the Gibe and Omo river valleys to the southwest, and up the Wolayta–

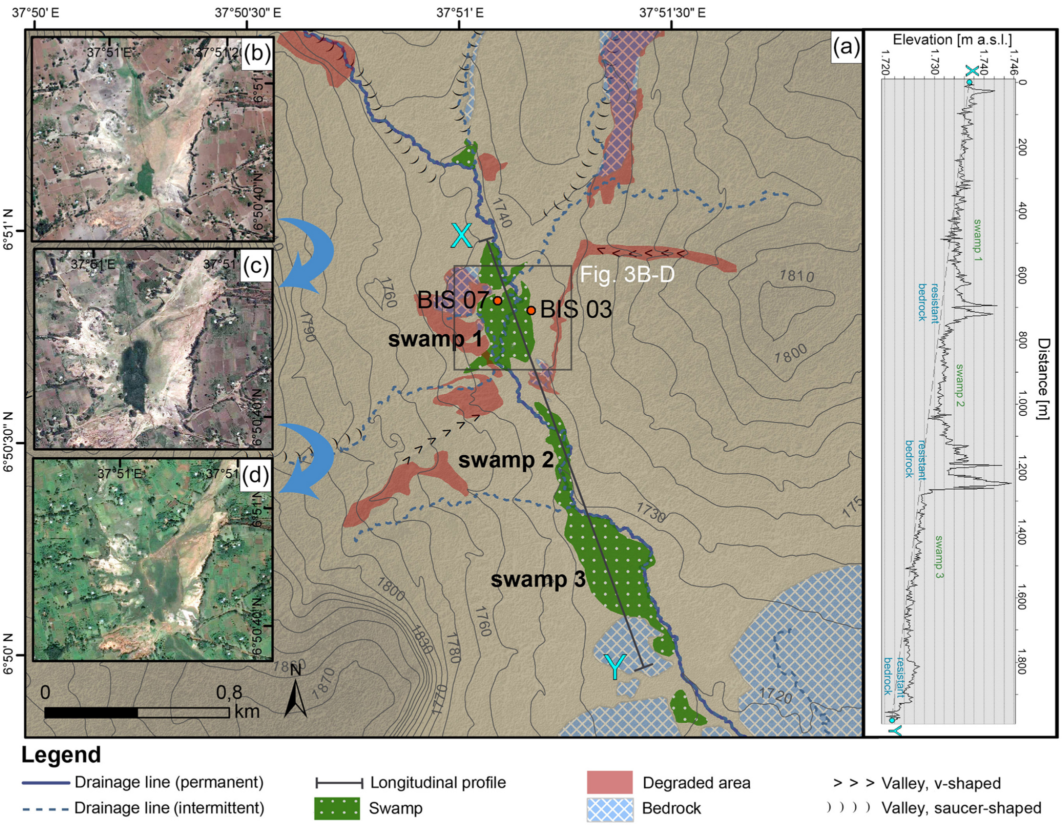


**Figure 3.** **(a)** Map showing the dimension of the three swamps on the Bisare River. The positions of the two drillings in swamp 1 are marked with red dots (DEM data by ASTER GDEM). The sequence of images **(b)–(d)** illustrates the changes of swamp 1 during different wet and dry phases: **(b)** following a dry season (21 March 2009), **(c)** following a wet season (15 November 2009), and **(d)** during a wet season (17 October 2014) (swamp data set by Svenja Meyer; Satellite images by ©Google Earth Timelapse NASA Landsat programme). The super-elevated longitudinal profile X–Y illustrates the geomorphological position of the swamps in the Bisare River basin, leading to a step-like topography, extracted from the DEM based on Pléiades 1A satellite imagery (DEM data by ASTER GDEM; illustration by Elena Hensel).

Hadiya Highlands to the west. During clear weather conditions, the opening area of the Sodicho Rockshelter offers a complete view to Mt Damota and the Omo River basin in the west (Fig. 1c). The view directly from Mochena Borago is limited to the southeast and east, and therefore Mt Sodicho is out of sight. These results verify a locational advantage of both rock shelters, i.e. Mochena Borago on Mt Damota and Sodicho Rockshelter on Mt Sodicho, for watching game in the surrounding lowlands.

### 4.2 Radiocarbon dating

The modern radiocarbon ages of two botanical samples (BIS03-PC1 and BIS07_W) and one sediment sample (BIS07-C1_S), originating from two drilling cores taken in a depth of up to 2 m below the surface level in the uppermost part of swamp 1, revealed that the upper 3 m of the sedimentary basin fill are of modern age (Table 1). This demonstrates a high sedimentation rate at least in this swamp.

## 5 Discussion

Several processes of degradation, such as gully or river erosion, led to the exposure of obsidian raw material localities and open-air sites with scatters of stone artefacts (Fig. 4a–d). This is particularly true in the Bisare River basin with its areas of different stream energy where the swamps form sediment traps for the eroded material today. One main question was why these step-like swamps formed and if their formation process can be used to obtain paleoenvironmental information. We propose that during wetter phases stronger gully erosion is activated, and resulting sediment slugs are able to hold up further sediment flux. This can be described as a cut-and-fill process with sediment accumulation in times with relatively intensive erosion and active gullying, and channel incision in periods of less active gullying, e.g. less intensive erosion (Nanson and Croke, 1992; Brierley and Fryirs, 1999; Fryirs and Brierley, 2013; Orti et al., 2019). The consequence is swamp development due to damming of the stream and sediment trapping. Therefore, this area can be assumed to

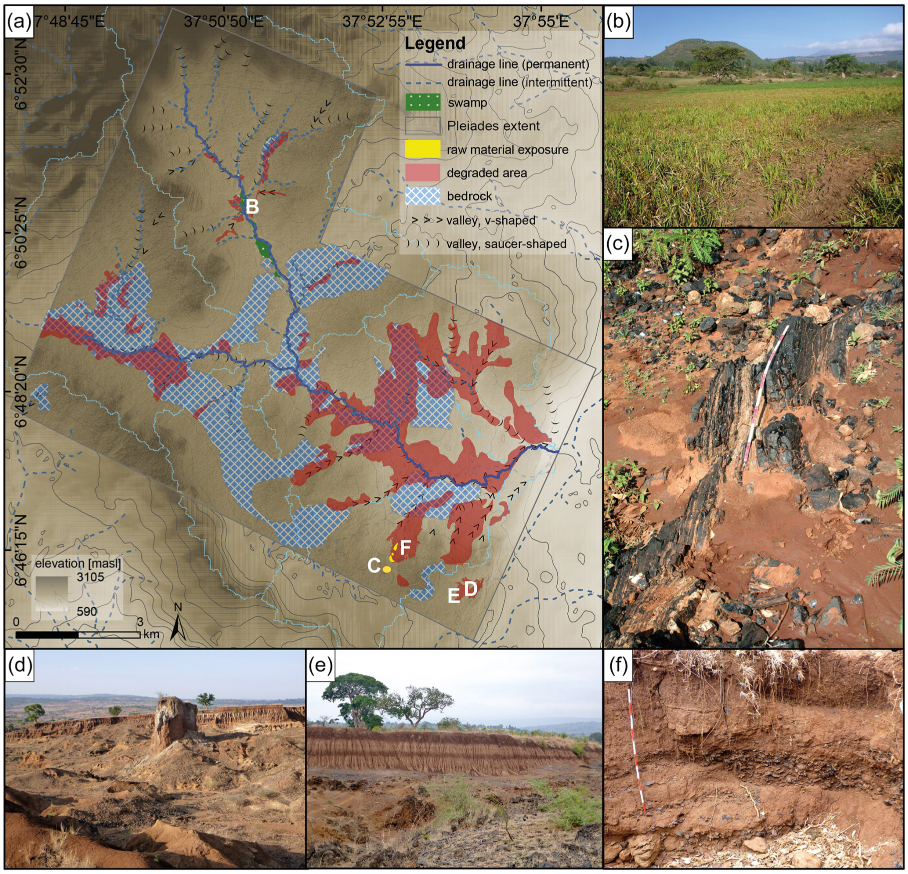


**Figure 4.** **(a)** Map showing the Bisare River catchment. Degraded areas are mainly characterized by gully erosion. **(b)** Image of the wet, swampy area in the upper part of the catchment (swamp 1). **(c)** Obsidian raw material outcrop. **(d)** Badlands formation and gully erosion is a common phenomenon in the depressions of the catchment. **(e)** Gully-erosion-exposed paleosols alternating with volcanic ash. **(f)** Relocated obsidian flakes exposed in a gully of a degraded area (swamp data set by Svenja Meyer; photography by Olaf Bubenzer; illustration by Elena Hensel).

be very sensitive towards external changes and disturbances, e.g. a change in sediment flux rate. The southernmost part of swamp 3 has the widest dimension, which is most probably the result of a change of bedrock (Fig. 3). A more resistant rock type must have created a natural "bottleneck", which caused natural damming that was intensified by additional damming by sediment slugs during certain periods. As a consequence, the slow-moving water got dammed up, leading to sedimentation and preventing erosion of these accumulated sediments (Machado, 2015). Generally, changes of sediment supply from tributaries into the Bisare and then into the Bilate River must have had a significant geomorphological effect on the main hydrological system in the form of the incision and subsequent aggradation of transported material. In summary, we view this as a geogenic sediment cascade system, where relatively young sediments should have been transported into the lower basin only after the higher basins were filled up (Fig. 3a) (Fryirs and Brierley, 2013; Fryirs, 2016). However, the radiocarbon samples (BIS07-C1) of the sediment in the uppermost basin yielded modern ages, although they are assumed to contain the oldest sediments (Table 1). With a possible sediment cascade and our radiocarbon dates in mind, we state that the development of the swamps must be a relatively recent phenomenon that is linked with the current high erosion and accumulation rates in the area of the Bisare River. Therefore, we suggest that the surficial Pleistocene deposits that are currently largely being exposed by badlands formation in the region must have been completely removed by fluvial erosion, leading to formation of the basins. Afterwards, the basins were refilled by the recent fine-grained sediment that we dated with radiocarbon (Table 1).

With respect to the present-day lithic raw material accessibility and preservation, our geomorphological field observations from 2014 and 2015 coincide with the published observations by Vogelsang and Wendt (2018) on obsidian outcrops in the Humbo area of the Bisare River catchment (Fig. 2c). These authors state that the predominance of obsidian for the production of stone artefacts is not surprising, considering the proximity of the rich sources in the Humbo area to known archaeological sites (Vogelsang and Wendt, 2018). Furthermore, the glassy structure of the obsidian allows a very precise production of lithic tools (Rapp, 2009). Together, this could explain the extreme dominance of obsidian in all lithic assemblages. However, the question arises whether the activity of the hydrological system and erosion processes at Bisare had a comparable intensity during Late Pleistocene and early Holocene to mid-Holocene, leading to the exposure of a similar amount of raw material. If this was not the case, hunter-gatherers were not able to focus only on the local obsidian deposit in the Humbo area but had to select alternative sources. In this context, also the effects of today's vegetation have to be considered. Today's intensive farming and deforestation, e.g. at the flanks of Mt Sodicho, strongly changed the actual surface runoff but might also directly destroy archaeological deposits. The current destruction and relocation of raw material is visible in the form of scattered obsidian debris and large boulders found along the streams at Mt Sodicho (Fig. 2b). At the moment, we cannot verify if prehistoric hunter-gatherers were able to use such kinds of displaced raw material, but this would be an interesting question for future research. Generally, we think that understanding the hydrological system is fundamental for the evaluation of obsidian raw material availability in this area. However, we still do not know the rate and the start of gully erosion and badlands formation in our study area that are known as inhomogeneous processes – in intensity as well as in duration (Castillo and Gómez, 2016). If the Late Pleistocene hydrological system was as highly dynamic as it is today, gully erosion might have already been initiated by natural processes during that period. We only expect this for certain climatic phases in which the paleoenvironmental conditions promoted such a dynamic system due to higher precipitation. Accordingly, several studies demonstrated variable climatic conditions at the Horn of Africa during the Late Pleistocene and Holocene. Transitions from humid to arid conditions and vice versa led to rise and shrinkage of lake levels and also affected the connecting drainage networks (Sagri et al., 2008; Carnicelli et al., 2009; Foerster et al., 2012; Junginger and Trauth, 2013; Foerster et al., 2015; Trauth et al., 2019). We propose that the connected drainage systems in our research area, such as the Bisare River, might have reacted to these transitions with changes in their depositional and erosional behaviour. Furthermore, considering the location of our research areas within a region that have been tectonically active since the Plio–Pleistocene, we can assume that the aforementioned extensive surface processes most likely started already during the Late Pleistocene (Fig. 5). However, we propose that due to today's intensified human impact in the form of clearance of the vegetation cover and cropland expansion, leading to higher runoff, obsidian raw material comes more frequently and in higher amounts up to the surface than during prehistoric times.

Archaeological evidence from Mt Damota and Sodicho Rockshelter shows that groups of prehistoric humans seem

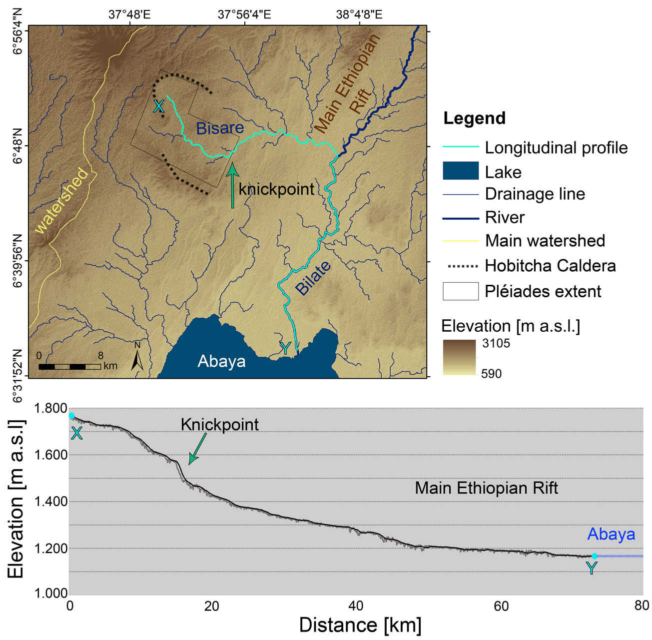


**Figure 5.** Map showing the calculated drainage networks southeast of the Bisare River catchment that flow into Lake Abaya. Following the longitudinal profile of the Bisare River (green line and graph), a sudden change in slope (knickpoint) at the outflow from the Hobitcha Caldera stands out (DEM data by ASTER GDEM; illustration by Elena Hensel).

to have adapted to former climatic and hydrological changes, leading to different environmental conditions, with repeated occupation of the rock shelters at higher elevations under different environmental conditions (Brandt et al., 2012, 2017; Vogelsang and Wendt, 2018). During such periods these groups were probably exploiting these higher elevated areas with the awareness of their sufficient water and food resources, shelter, and the access to obsidian raw material (cf. Vogelsang et al., 2018). Although it is not yet clear which specific obsidian outcrops were used by the prehistoric humans, first results of obsidian microprobe analysis point to the exploitation of raw material from outcrops in the Bisare area by the inhabitants of both rock shelters (Vogelsang, unpublished information, 2019).

## 6 Conclusions

This study gives an insight into to the potential of a combination of hydrological and geomorphological analyses by applying field surveys, remote sensing, geographical information systems, and radiocarbon dating, as well as investigations of the archaeological site distribution, to reconstruct the interplay between past hydrological conditions and Paleolithic settlement activity in a mountainous area of the southwestern Ethiopian Highlands. With our results, we were able to describe the current landscape dynamics and the actual state of known rock shelters and open-air sites, as well as raw material preservation in the study areas. The preserved evidence for repeated human occupation during the Late Pleistocene and Holocene at Sodicho Rockshelter (Vogelsang, unpublished information, 2015 to 2018) hints that the highlands could have provided a refugium during arid phases such as the Last Glacial Maximum (LGM, $\sim 21 \pm 2$ ka) (Mark and Osmaton, 2008). At Mochena Borago, settlement activities reach back $>50$ ka. During such periods, the exploitation of different, elevation-bound ecosystems allowed access to a heterogeneous spectrum of faunal and lithic resources for prehistoric humans (Vogelsang and Wendt, 2018). Humid–arid transitions in the past must have led to pronounced erosion and badlands formation. We suggest that there is a relationship between widespread gully erosion, badlands formation, and raw material availability. Currently, the study area is a region with strong recent sediment erosion and simultaneous accumulation in a cascading system. Looking into the future, given strongly increased human impact during the last few decades acting together with the currently very active hydrological system, intensified soil loss will lead to further degradation of the archaeological material. However, the transfer of today's circumstances into prehistoric times is complicated, as we cannot prove that currently active processes, e.g. swamp formation, were also active during the Pleistocene. Furthermore, the research sites are situated in an area close to the Main Ethiopian Rift, i.e. a region with pronounced tectonic activity that also has a significant impact on the regional geomorphodynamics. Therefore, at this stage the results do not allow any distinct statement about the transfer of the modern morphodynamics to ancient times, as we have identified only recent phenomena. This means that the calculated drainage lines show the current state in a very active hydrological system that is influenced by both natural effects and intensive human activity. Nevertheless, in the context of further interdisciplinary research that combines well-resolved archaeological and alluvial chronostratigraphies it will be possible to obtain a better general understanding of the interplay between former settlement activity and paleoenvironmental conditions in the Ethiopian Highlands during the Pleistocene.

**Data availability.** GIS data sets can be requested from the CRC 806 Database via https://doi.org/10.5880/SFB806.49 (Hensel et al., 2019).

**Author contributions.** The geomorphological field mapping and drilling were carried out by OBu and OBo. Archaeological survey was conducted by RV. EAH performed GIS-based mapping, geomorphological–hydrological analyses, and preparation of the paper. All co-authors contributed to, read, and approved the paper.

**Competing interests.** The authors declare that they have no conflict of interest.

**Special issue statement.** This article is part of the special issue "Geoarchaeology and past human–environment interactions". It is not associated with a conference.

**Acknowledgements.** We kindly thank the Authority for Research and Conservation of Cultural Heritage (ARCCH) of Ethiopia for their permission and general support, and the Ministry of Mines and Energy for the approval of our export permits. This study was conducted as a part of project A1 "Out of Africa – Late Pleistocene Rock Shelter Stratigraphies and Palaeoenvironments in Northeast Africa" in the framework of the Collaborative Research Centre 806 (CRC 806) "Our way to Europe". We thank Janet Rethemeyer and colleagues from the radiocarbon AMS lab of the University of Cologne for radiocarbon dating the Bisare samples. We are very grateful to Svenja Meyer for her great effort for project A1 and for her participation during various field seasons in Ethiopia especially. Special thanks also go to Taylor Otto for the English proofreading, as well as to Minassie Tekelemariam and Bahru Zinaye for their support in the field. We thank Andrea Zerboni, an anonymous referee, and the editors for constructive and insightful comments, which significantly helped to improve this paper.

**Financial support.** This research has been supported by the Deutsche Forschungsgemeinschaft (DFG, German Research Foundation) (grant no. 57444011 – SFB 806).

## References

Abbate, E., Bruni, P., and Sagri, M.: Geology of Ethiopia: a review and geomorphological perspectives, in: Landscapes and Landforms of Ethiopia, edited by: Billi, P., Springer, Dordrecht, the Netherlands, 33–64, https://doi.org/10.1007/978-94-017-8026-1_2, 2015.

Basell, L. S.: Middle Stone Age (MSA) site distributions in eastern Africa and their relationship to Quaternary environmental change, refugia and the evolution of Homo sapiens, Quaternary Sci. Rev., 27, 2484–2498, https://doi.org/10.1016/j.quascirev.2008.09.010, 2008.

Benito-Calvo, A., De la Torre, I., Mora, R., Tibebu, D., Morán, N., and Martínez-Moreno, J.: Geoarchaeological potential of the western bank of the Bilate River (Ethiopia), Analele Universităţii din Oradea, Seria Geographie, XVII, 99–104, 2007.

Berhanu, B., Melesse, A. M., and Seleshi, Y.: GIS-based hydrological zones and soil geo-database of Ethiopia, CATENA, 104, 21–31, https://doi.org/10.1016/j.catena.2012.12.007, 2013.

Billi, P. and Dramis, F.: Geomorphological investigations on gully erosion in the Rift Valley and the northern highlands of Ethiopia, CATENA, 50, 353–368, https://doi.org/10.1016/S0341-8162(02)00131-5, 2003.

Bolten, A., Bubenzer, O., and Darius, F.: A digital elevation model as a base for the reconstruction of Holocene land-use potential in arid regions, Geoarchaeology, 21, 751–762, https://doi.org/10.1002/gea.20137, 2006.

Bonini, M., Corti, G., Innocenti, F., Manetti, P., Mazzarini, F., Abebe, T., and Pecskay, Z.: Evolution of the Main Ethiopian Rift in the frame of Afar and Kenya rifts propagation, Tectonics, 24, 1–21, https://doi.org/10.1029/2004TC001680, 2005.

Brandt, S., Hildebrand, E., Vogelsang, R., Wolfhagen, J., and Wang, H.: A new MIS 3 radiocarbon chronology for Mochena Borago Rockshelter, SW Ethiopia: Implications for the interpretation of Late Pleistocene chronostratigraphy and human behavior, J. Archaeol. Sci. Reports, 11, 352–369, https://doi.org/10.1016/j.jasrep.2016.09.013, 2017.

Brandt, S. A., Fisher, E. C., Hildebrand, E. A., Vogelsang, R., Ambrose, S. H., Lesur, J., and Wang, H.: Early MIS 3 occupation of Mochena Borago Rockshelter, Southwest Ethiopian Highlands: implications for Late Pleistocene archaeology, paleoenvironments and modern human dispersals, Quatern. Int., 274, 38–54, https://doi.org/10.1016/j.quaint.2012.03.047, 2012.

Brierley, G. J. and Fryirs, K.: Tributary–trunk stream relations in a cut-and-fill landscape: a case study from Wolumla catchment, New South Wales, Australia, Geomorphology, 28, 61–73, https://doi.org/10.1016/S0169-555X(98)00103-2, 1999.

Carnicelli, S., Benvenuti, M., Ferrari, G., and Sagri, M.: Dynamics and driving factors of late Holocene gullying in the Main Ethiopian Rift (MER), Geomorphology, 103, 541–554, https://doi.org/10.1016/j.geomorph.2008.07.019, 2009.

Castillo, C. and Gómez, J. A.: A century of gully erosion research: Urgency, complexity and study approaches, Earth Sci. Rev. 160, 300–319, https://doi.org/10.1016/j.earscirev.2016.07.009, 2016.

Chernet, T.: Geology and hydrothermal resources in the northern Lake Abaya area (Ethiopia), J. Afr. Earth. Sci., 61, 129–141, https://doi.org/10.1016/j.jafrearsci.2011.05.006, 2011.

Corti, G.: Continental rift evolution: from rift initiation to incipient break-up in the Main Ethiopian Rift, East Africa, Earth. Sci. Rev., 96, 1–53, https://doi.org/10.1016/j.earscirev.2009.06.005, 2009.

Corti, G., Sani, F., Philippon, M., Sokoutis, D., Willingshofer, E., and Molin, P.: Quaternary volcano-tectonic activity in the Soddo region, western margin of the Southern Main Ethiopian Rift, Tectonics, 32, 861–879, https://doi.org/10.1002/tect.20052, 2013.

De La Torre, I., Benito-Calvo, A., Mora, R., Martínez-Moreno, J., Morán, N., and Tibebu, D.: Stone Age occurrences in the western bank of the Bilate River (Southern Ethiopia) – Some preliminary results, Nyame Akuma, 67, 14–25, 2007.

Foerster, V., Junginger, A., Langkamp, O., Gebru, T., Asrat, A., Umer, M., Lamb, H.F., Wennrich, V., Rethemeyer, J., Nowaczyk, N., Trauth, M. H., and Schaebitz, F.: Climatic change recorded in the sediments of the Chew Bahir basin, southern Ethiopia, during the last 45,000 years, Quaternary Int., 274, 25–37, https://doi.org/10.1016/j.quaint.2012.06.028, 2012.

Foerster, V., Vogelsang, R., Junginger, A., Asrat, A., Lamb, H. F., Schaebitz, F., and Trauth, M. H.: Environmental change and human occupation of southern Ethiopia and northern Kenya during the last 20,000 years, Quaternary Sci. Rev., 129, 333–340, https://doi.org/10.1016/j.quascirev.2015.10.026, 2015.

Friis, I., Sebsebe, D., and Breugel, P.: Atlas of the potential vegetation of Ethiopia, Det Kongelige Danske Videnskabernes Selskab, Copenhagen, 2010.

Fryirs, K. A.: River sensitivity: a lost foundation concept in fluvial geomorphology, Earth Surf. Proc. Land., 42, 55–70, https://doi.org/10.1002/esp.3940, 2016.

Fryirs, K. A. and Brierley, G. J.: Geomorphic analysis of river systems: an approach to reading the landscape, John Wiley & Sons, Chichester, West Sussex, England, 2013.

Griffiths, J.: Ethiopian highlands, World survey of climatology, 10, 369–381, 1972.

Hensel, E. A., Bödeker, O., Bubenzer, O., and Vogelsang, R.: Combining geomorphological–hydrological analyses and the location of settlement and raw material sites – a case study on understanding prehistoric human settlement activity in the southwestern Ethiopian Highlands, E&G Quaternary Sci. J., 69, 1–14, https://doi.org/10.5194/egqsj-69-1-2019, 2019.

Junginger, A. and Trauth, M. H.: Hydrological constraints of paleo-Lake Suguta in the Northern Kenya Rift during the African humid period (15–5 ka BP), Global Planet. Change, 111, 174–188, https://doi.org/10.1016/j.gloplacha.2013.09.005, 2013.

Junginger, A., Vonhof, H., and Foerster, V. E.: AGU Fall Meeting Abstracts, How wet is wet? Strontium isotopes as paleo-lake level indicators in the Chew Bahir basin (S-Ethiopia), American Geophysical Union, Fall Meeting 2016, (abstract no. PP23A-2310), 2016.

Machado, M. J.: Geomorphology of the Adwa District, in: Landscapes and Landforms of Ethiopia, edited by: Billi, P., Springer, Dordrecht, Netherlands, 163–178, https://doi.org/10.1007/978-94-017-8026-1, 2015.

Mark, B. G. and Osmaton, H. A.: Quaternary glaciation in Africa: Key chronologies and climatic implications, J. Quaternary Sci., 23, 589–608, https://doi.org/10.1002/jqs.1222, 2008.

Mukai, S.: Gully erosion rates and the analysis of determining factors: A case study from the semi-arid Main Ethiopian Rift Valley, Land Degrad. Dev., 28, 607–615, https://doi.org/10.1002/ldr.2532, 2017.

Nanson, G. C. and Croke, J. C.: A genetic classification of floodplains, Geomorphology, 4, 459–486, https://doi.org/10.1016/0169-555X(92)90039-Q, 1992.

Nicholson, S. E.: The ITCZ and the seasonal cycle over equatorial Africa, B. Am. Meteorol. Soc., 99, 337-348, https://doi.org/10.1175/BAMS-D-16-0287.1, 2018.

Orti, M. V., Negussie, K., Corral-Pazos-De-Provens, E., Höfle, B., and Bubenzer, O.: Comparison of Three Algorithms for the Evaluation of TanDEM-X Data for Gully Detection in Krumhuk Farm (Namibia), Remote Sensing, 11, 1327, https://doi.org/10.3390/rs11111327, 2019.

Ramsey, C., Scott, E., and Van der Plicht, J.: Calibration for Archaeological and Environmental Terrestrial Samples in the Time Range 26–50 ka cal BP, Radiocarbon, 55, 2021–2027, https://doi.org/10.2458/azu_js_rc.55.16935, 2013.

Rapp, G.: Lithic Materials, in: Archaeomineralogy, Natural Science in Archaeology, edited by: Rapp, G., Springer, Berlin, Heidelberg, Germany, 60–90, https://doi.org/10.1007/978-3-540-78594-1_4, 2009.

Reimer, P. J., Bard, E., Bayliss, A., Beck, J. W., Blackwell, P. G., Ramsey, C. B., Buck, C. E., Cheng, H., Edwards, R. L., Friedrich, M., Grootes, P. M., Guilderson, T. P., Haflidason, H., Hajdas, I., Hatté, C., Heaton, T. J., Hoffmann, D. L., Hogg, A. G., Hughen, K. A., Kaiser, K. F., Kromer, B., Manning, S. W., Niu, M., Reimer, R. W., Richards, D. A., Scott, E. M., Southon, J. R., Staff, R. A., Turney, C. S. M., and van der Plicht, J.: IntCal13 and Marine13 Radiocarbon Age Calibration Curves 0–50,000 Years cal BP, Radiocarbon, 55, 1869–1887, https://doi.org/10.2458/azu_js_ rc.55.16947, 2013.

Sagri, M., Bartolini, C., Billi, P., Ferrari, G., Benvenuti, M., Carnicelli, S., and Barbano, F.: Latest Pleistocene and Holocene river network evolution in the Ethiopian Lakes Region, Geomorphology, 94, 79–97, https://doi.org/10.1016/j.geomorph.2007.05.010, 2008.

Schütt, B.: Deposition of modern fluvio-lacustrine sediments in Lake Abaya, South Ethiopia – A case study from the delta areas of Bilate River and Gidabo River, northern basin, Z. Geomorph. N. F., 138, 131–151, 2005.

Segele, Z. T., Lamb, P. J., and Leslie, L. M.: Large-scale atmospheric circulation and global sea surface temperature associations with Horn of Africa June–September rainfall, Int. J. Climatol., 29, 1075–1100, https://doi.org/10.1002/joc.1751, 2009.

Shafer, H. J.: Research design and sampling techniques, in: Field Methods in Archaeology, edited by: Hester, T. R., Shafer, H. J., and Feder, K. I., Routledge, Oxford, England, 2016.

Tierney, J. E., Russell, J. M., Huang, Y., Damsté, J. S. S., Hopmans, E. C., and Cohen, A. S.: Northern Hemisphere Controls on Tropical Southeast African Climate During the Past 60,000 Years, Science, 322, 252–255, https://doi.org/10.1126/science.1160485, 2008.

Tierney, J. E., Lewis, S. C., Cook, B. I., LeGrande, A. N., and Schmidt, G., A.: Model, proxy and isotopic perspectives on the East African Humid Period, Earth Planet. Sc. Lett., 307, 103–112, https://doi.org/10.1016/j.epsl.2011.04.038, 2011.

Trauth, M. H., Asrat, A., Duesing, W., Foerster, V., Kraemer, K. H., Marwan, N., Maslin, M. A., and Schaebitz, F.: Classifying past climate change in the Chew Bahir basin, southern Ethiopia, using recurrence quantification analysis, Clim. Dynam., 53, 1–16, https://doi.org/10.1007/s00382-019-04641-3, 2019.

Viste, E. and Sorteberg A.: Moisture transport into the Ethiopian highlands, Int. J. Climatol., 33, 249–263, https://doi.org/10.1002/joc.3409, 2013.

Vogelsang, R. and Wendt, K. P.: Reconstructing prehistoric settlement models and land use patterns on Mt. Damota/SW Ethiopia, Quatern. Int., 485, 140–149, https://doi.org/10.1016/j.quaint.2017.06.061, 2018.

Vogelsang, R., Bubenzer, O., Kehl, M., Meyer, S., Richter, J., and Zinaye, B.: When Hominins Conquered Highlands – an Acheulean Site at 3000 m a.s.l. on Mount Dendi/Ethiopia, Journal of Paleolithic Archaeology, 1, 302-3013, https://doi.org/10.1007/s41982-018-0015-9, 2018.

Woldegabriel, G., James, L. A., and Robert, C. W.: Geology, geochronology, and rift basin development in the central sector of the Main Ethiopian Rift, Geol. Soc. Am. B., 102, 439–485, https://doi.org/10.1130/0016-7606(1990)102<0439:GGARBD>2.3.CO;2, 1990.

E&G Quaternary Sci. J., 68, 215–236, 2020
https://doi.org/10.5194/egqsj-68-215-2020


Open Access E&G Quaternary Science Journal

Research article

# Sediment-filled karst depressions and *riyad* – key archaeological environments of south Qatar

**Max Engel**[1,2], **Stefanie Rückmann**[1], **Philipp Drechsler**[3], **Dominik Brill**[1], **Stephan Opitz**[1], **Jörg W. Fassbinder**[4,5], **Anna Pint**[1], **Kim Peis**[1], **Dennis Wolf**[1], **Christoph Gerber**[6], **Kristina Pfeiffer**[7], **Ricardo Eichmann**[7], and **Helmut Brückner**[1]

[1]Institute of Geography, University of Cologne, 50674 Cologne, Germany
[2]Geological Survey of Belgium, OD Earth and History of Life, Royal Belgian Institute of Natural Sciences, 1000 Brussels, Belgium
[3]Section for Early Prehistory and Quaternary Ecology, University of Tübingen, 72070 Tübingen, Germany
[4]Geophysics Section, Department of Earth and Environmental Sciences, Ludwig Maximilian University of Munich, 80333 Munich, Germany
[5]Archaeological Prospection Section, Bavarian State Department for Monuments and Sites, 80539 Munich, Germany
[6]Institute of Prehistory, Protohistory and Near-Eastern Archaeology, University of Heidelberg, 69117 Heidelberg, Germany
[7]Orient Department, German Archaeological Institute (DAI), 14195 Berlin, Germany

**Correspondence:** Max Engel (max.engel@uni-koeln.de)

**Relevant dates:** Received: 1 April 2019 – Revised: 5 November 2019 – Accepted: 29 November 2019 – Published: 9 January 2020

**How to cite:** Engel, M., Rückmann, S., Drechsler, P., Brill, D., Opitz, S., Fassbinder, J. W., Pint, A., Peis, K., Wolf, D., Gerber, C., Pfeiffer, K., Eichmann, R., and Brückner, H.: Sediment-filled karst depressions and *riyad* – key archaeological environments of south Qatar, E&G Quaternary Sci. J., 68, 215–236, https://doi.org/10.5194/egqsj-68-215-2020, 2020.

**Abstract:** Systematic archaeological exploration of southern Qatar started in the 1950s. However, detailed local and regional data on climatic fluctuations and landscape changes during the Holocene, pivotal for understanding and reconstructing human–environment interactions, are still lacking. This contribution provides an overview on the variability of geomorphic environments of southern Qatar with a focus on depression landforms, which reveal a rich archaeological heritage ranging from Palaeolithic(?) and Early Neolithic times to the Modern era. Based on a detailed geomorphic mapping campaign, sediment cores and optically stimulated luminescence data, the dynamics of *riyad* (singular *rawdha*; shallow, small-scale, sediment-filled karst depressions clustering in the central southern peninsula) and the larger-scale Asaila depression near the western coast are studied in order to put archaeological discoveries into a wider environmental context. Geomorphic mapping of the Asaila basin shows a much greater geomorphic variability than documented in literature so far with relict signs of surface runoff. An 8 m long sediment core taken in the sabkha-type sand flats of the western basin reveals a continuous dominance of aeolian morphodynamics during the early to mid-Holocene. Mounds preserved by evaporite horizons representing capillarites originally grown in the vadose zone are a clear sign of groundwater-level drop after the sea-level highstand ca. 6000–4500 years ago. Deflation followed the lowering of the Stokes surface, leaving mounds where the relict capillarites were able to fixate and preserve the palaeo-surface. Abundant archaeological evidence of Early and Middle Neolithic occupation – the latter with a clear focus inside the central Asaila basin – indicate more favourable living conditions than today. In contrast, the sediment record of the investigated *riyad* in the south is very shallow, younger and controlled by surface discharge, deflation and the constantly diminishing barchan dune cover in Qatar over the Middle and Late Holocene. The young age of the infill (ca. 1500 to 2000 years) explains the absence of findings older than the Late Islamic period. Indicators of current net deflation may relate to a decrease in surface runoff and sediment supply only in recent decades to centuries. In the future, geophysical prospection of the *riyad* may help to locate thicker sedimentary archives and the analysis of grain size distribution, micromorphology, phytoliths or even pollen spectra may enhance our understanding of the interplay of regional environmental changes and cultural history.

**Kurzfassung:** Die systematische archäologische Erkundung des Südens der katarischen Halbinsel begann in den 1950er Jahren. Lokale und regionale Daten zu den die regionale Kulturentwicklung begleitenden klimatischen Schwankungen und Landschaftsveränderungen im Holozän fehlen allerdings weitgehend. Dieser Beitrag liefert einen Überblick über die geomorphologische Variabilität des südlichen Teils von Katar mit einem Schwerpunkt auf karstbürtigen Hohlformen, deren verhältnismäßig reiches archäologisches Erbe bis in das Paläolithikum(?)/Frühe Neolithikum zurückreicht. Basierend auf einer detaillierten geomorphologischen Kartierkampagne, Sedimentkernen und Altersdatierung mit Hilfe optisch stimulierter Lumineszenz erfolgt eine Rekonstruktion der Sedimentationsgeschichte der räumlich bedeutenden *Riyad* (Singular: *Rawdha*; flache, kleinskalige, sedimentgefüllte Karsthohlformen) und des größeren Beckens von Asaila in der Nähe der Westküste, um die während der vergangenen Dekaden getätigten archäologischen Funde und Erkenntnisse in einen erweiterten Umweltkontext einzuordnen. Die geomorphologische Kartierung des Asaila-Beckens zeigt eine weit größere Variabilität an Oberflächenformen als bisher in der Literatur dokumentiert, darunter auch deutliche Indikatoren für reliktischen Oberflächenabfluss. Während der 8 m lange Sedimentkern aus dem sabkhaähnlichen Bereich des westlichen Beckens eine kontinuierliche Dominanz der äolischen Morphodynamik über das frühe bis mittlere Holozän andeutet, sind die von kleinen hügelartigen Formen dominierten Bereiche durch reliktische, einst in der vadosen Zone gewachsene kapillare Evaporithorizonte fixiert worden. Dies ist ein deutliches Zeichen für vorherrschende Deflation seit dem Hochstand des Meeresspiegels (und des Grundwasserspiegels) vor ca. 6000–4500 Jahren. Zahlreiche früh- und mittelneolithische Streufunde – letztere mit einem klaren Schwerpunkt im zentralen Asaila-Becken – weisen auf günstigere Lebensbedingungen zu dieser Phase hin. Die sedimentäre Füllung der untersuchten *Riyad* ist deutlich flacher und jünger und wird durch Oberflächenabfluss, Deflation und die sukzessiv abnehmende Barchan-Dünenbedeckung in Katar während des Mittel- und Spätholozäns determiniert. Das junge Alter der Füllung (ca. 1500–2000 Jahre) erklärt das Fehlen archäologischer Funde, die älter als spätislamisch datieren. Indikatoren aktuell dominierender Deflation (lineare Korrasionsrillen, Mikro-Yardangs) sind mögliche Hinweise auf einen Rückgang von Oberflächenabfluss und Sedimenteintrag innerhalb der letzten Jahrzehnte bis wenigen Jahrhunderte. Eine geophysikalische Prospektion der *Riyad*, die die Lokalisierung möglichst mächtiger Sedimentpakete erlauben würde, in Kombination mit der Analyse von Korngrößenverteilung, Mikromorphologie, Phytolithen oder gar Pollenspektren, könnte in Zukunft Teil einer Strategie sein, hier detailliertere Daten zur Paläo-Umweltdynamik der zentralen Bereiche Katars zu generieren.

## 1 Introduction

Pioneering archaeological surveys and excavations in Qatar started more than 60 years ago (e.g. Glob, 1958; Kapel, 1967; de Cardi, 1978; Tixier, 1980; Inizan, 1988). During the last decade, these were supplemented by intensified interdisciplinary research on all phases of the peninsula's cultural heritage (e.g. Al-Naimi et al., 2011; Rees et al., 2011; Cuttler and Al-Naimi, 2013; Eichmann et al., 2014; Gerber et al., 2014; Drechsler, 2014; Drechsler et al., 2013, 2016; Izquierdo Zamora et al., 2015; McPhillips et al., 2015). While evidence for the Palaeolithic remains under debate (Glob, 1958; Kapel, 1967; Al-Naimi et al., 2010; Cuttler and Al-Naimi, 2013; Scott-Jackson et al., 2015; Drechsler, 2014; Drechsler et al., 2016), Early and Middle Neolithic flint scatters along with burial cairns at a number of locations testify the occurrence of mobile to semi-stationary groups at that time (Drechsler et al., 2016). The Early Neolithic mainly comprises Qatar-B sites sensu Kapel (1967) and Inizan (1988), tentatively dated to the 7th millennium BCE. The Middle Neolithic is often represented by surface finds of tile knives, scrapers, bifacial arrowheads and, in some cases, Ubaid-style pottery (Tixier, 1980; Inizan, 1988; Drechsler, 2014), which implies links with other Ubaid-related sites of the southern Arabian Gulf coast dated to the 6th–5th millennium BCE (Oates, 1978; Uerpmann and Uerpmann, 1996; Kainert and Drechsler, 2014). The earliest known settlement of Qatar was identified in Wadi Debayān at the northwest coast, dating back 7500 years (Al-Naimi et al., 2011; Tetlow et al., 2013). Of similar age are the fishermen's huts near Shagra at the east coast, which were associated with the Ubaid period by Inizan (1988). The decline of the Ubaid culture marked the onset of a period represented by very few cultural remains in Qatar, coinciding with the "Dark Millennium" as defined for the southeastern gulf shores (Uerpmann, 2003; Preston et al., 2012; Muhesen and Al-Naimi, 2014). The Bronze Age is only sparsely represented in Qatar, most prominently in the form of pottery and a purple-dye industry at Al-Khor north of Doha (Edens, 1999; Carter and Killick, 2010). Such finds are nearly absent in the southern part of the country (Gerber et al., 2014). Burial cairns are distributed over the entire peninsula and mostly from the Iron Age (ca. 300 BCE–300 CE) (Bibby, 1965; Buckley, 1973; Konishi et al., 1988), even though some of them have recently been dated to as old as the Ubaid period (Cuttler et al., 2013; Izquierdo Zamora et al., 2015). No evidence exists for Iron Age settlements, but a coexistence of nomadic pastoralism and sedentary lifestyles has been postulated (Muhasen and Al-Naimi, 2014). Permanent settlements emerged around the 8th century CE (Abbasid period), in particular along the northwestern coast (Guérin and Al-Naimi, 2009; Macumber, 2015). The nomadic and semi-nomadic Bedouin culture, however, coexisted and persisted well into the 20th century CE, focussing on the shallow karst depressions of the Qatar peninsula as campsites (McPhillips et al., 2015).

Underpinning research on the concomitant environmental changes is clearly in its infancy, consisting mainly of the outcome of the QNHER (Qatar National Historic Environment Record) project covering the northern part of the peninsula (e.g. Cuttler et al., 2011; Cuttler and Al-Naimi, 2013; Macumber, 2011, 2015; Tetlow et al., 2013). Isolated contributions to the framework of earlier archaeological missions mainly focus on Late Quaternary coastal changes and are rather preliminary (Vita-Finzi, 1978; Perthuisot, 1980). Thus, when the South Qatar Survey Project (SQSP) started in late 2012 as a joint operation between Qatar Museums and the Orient Department of the German Archaeological Institute, little well-established information existed regarding dynamics of vegetation, water availability and landforms. In the course of the archaeological survey, shallow, sediment-filled karst depressions referred to as *riyad* (singular *rawdha* or *rawdah*) (Batanouny, 1981; Babikir, 1986; Sadiq and Nasir, 2002; Al-Yousef, 2003; Macumber, 2011, 2015) turned out to be focal points of historic occupation, in contrast with the barren surrounding hamada (Eichmann et al., 2014; Gerber et al., 2014; Pfeiffer, 2015). A second priority of the SQSP was assigned to the large depression of Asaila in central-western Qatar (locally referred to as Jaow Al Bahath), which, compared to the rest of Qatar, preserves a high concentration of Early and Middle Neolithic single flint artefacts and flint artefact scatters, along with numerous findings of the pre-Islamic, Islamic and Modern periods (Kapel, 1967; Inizan, 1988; Pelegrin and Inizan, 2013; Drechsler, 2014; Drechsler et al., 2016).

This paper provides a general overview of the variability of geomorphic environments of southern Qatar (defined here as the part of the peninsula south of the Dukhan road; Fig. 1) over Holocene timescales. Based on a detailed geomorphic mapping campaign, sediment cores and optically stimulated luminescence (OSL) data, the dynamics of *riyad* and the basins of Asaila and adjacent Jaow Aqeeq (Fig. 1) are evaluated in order to put the Early Neolithic to Islamic archaeological discoveries of the SQSP (Drechsler, 2014; Drechsler et al., 2016; Eichmann et al., 2014; Gerber et al., 2014; Pfeiffer, 2015) into a wider environmental context.

## 2 The physical setting of southern Qatar

### 2.1 Geology and tectonic setting

The Qatar peninsula protrudes from the Arabian Peninsula into the Arabian Gulf. It represents an anticlinal structure of uplifted Palaeocene to Middle Eocene limestones, dolomites, marls, chalks and shales, intercalated with evaporites (Fig. 1). Lower and Middle Eocene carbonates comprise 80 % (Rus Formation $\sim 10$ %; Dammam Formation $\sim 70$ %) of Qatar's surface (Al-Yousef, 2003; Al-Saad, 2005). Miocene units are mainly found in southern Qatar, represented by the Dam and Hofuf formations. The Dam Formation consists of a sequence of shallow marine limestone, gypsum, dolomite and mud, whereas the Hofuf Formation also contains continental conglomerates with a matrix of aeolian sand and gypsum (Cavelier, 1970; Al-Yousef, 2003).

The topography is dominated by the central N–S-trending Qatar Anticline, which has been driven by tectonic uplift since the Palaeogene and created smaller anticlinal and dome structures. The Dukhan Anticline (NNW–SSE) in the west is another major structural feature, bearing the largest oil reservoirs of the area, creating a steeper surface relief than the Qatar Anticline and causing slight tilting of the entire limestone sequence (Al-Yousef, 2003).

### 2.2 Terrestrial geomorphic environments

#### 2.2.1 Hamadas

Notable topographic elevations occur only in the south, reaching 103 m a.s.l. (above mean sea level) at the highest point. The majority of the peninsula is flat and the most widespread landform is hamadas (Fig. S8 in the Supple-

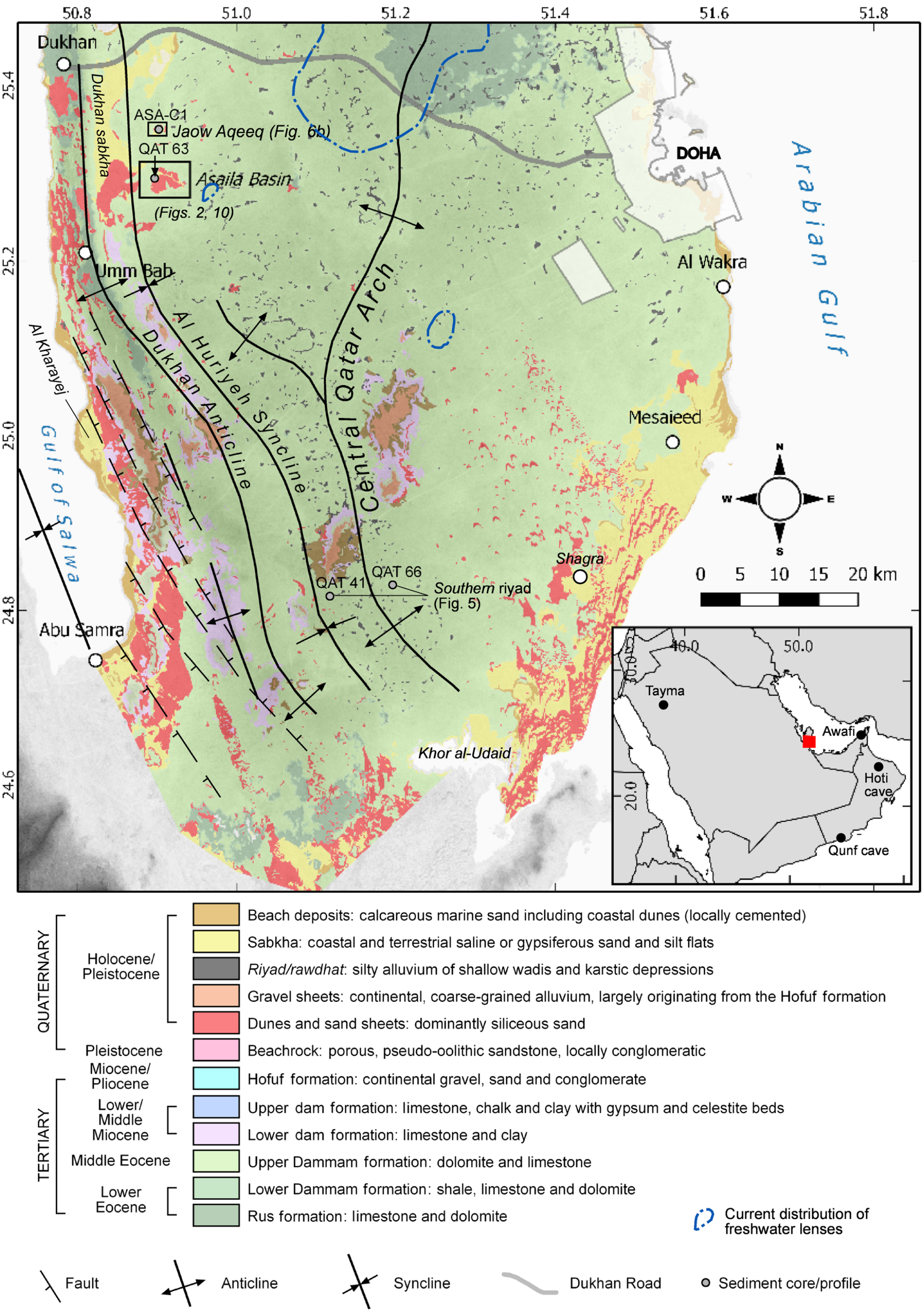


**Figure 1.** Geological map of southern Qatar based on the national geological map of 1980 (State of Qatar, 1980), overlying an ASTER global digital elevation model, which is a product of the US Ministry of Trade and Economy (METI) and the National Aeronautics and Space Administration (NASA). The main study area of the Asaila basin as well as coring sites in the Jaow Aqeeq basin further north (ASA-C1) and the southern *riyad* are depicted (QAT 41, QAT 66). Tectonic features are adapted from Al-Yousef (2003). The distribution of freshwater conditions in groundwater, which, depending on different sources, may have an upper limit of total dissolved solids of 3000 ppm (e.g. Heberger and Donnelly, 2015), are based on data of the Qatar Department of Environment, cited in Macumber (2012). The overview map indicates the location of the main map and palaeoclimate records referred to in the text.

ment), locally referred to as *hazm* (very gently sloping) or *mistah* (entirely flat), i.e. stone pavements covering most of the Dammam limestone province (Fig. 1) (Perthuisot, 1980; Batanouny, 1981). These plains are covered by mostly angular, in situ limestone gravel (see Benazzouz, 2004; Goudie, 2004b). Vegetation cover of the hamadas is very scarce; only isolated xerophile shrubs and trees such as *Tetraena qatarense*, *Acacia tortilis* or *Lycium shawii* are found between the surface stones (Batanouny, 1981).

### 2.2.2 Rocky ridges

Rocky ridges of southern Qatar relate to the N–S-trending anticlines, in particular to the Miocene Dam Formation along the southwest coast between Dukhan and south of Umm Bab (Fig. 1). They form mesas and buttes, controlled by varying resistivity of carbonate strata and reg surfaces, i.e. pavements of smaller, par-autochthonous clasts (see Benazzouz, 2004). Patchy sand accumulations in depressions of the rocky ridges are the only sites where sparse vegetation is found today, consisting mainly of *Panicum turgidum* and *Zygophyllum qatarense* (Fig. S14) (Batanouny, 1981).

### 2.2.3 Karst depressions

The term *rawdha* (Arabic "garden") refers to the fine-grained infill of shallow, round, slightly elongated or more irregular (e.g. when coalesced) inland depressions of 100 m up to a few kilometres in diameter. *Riyad* result from solution and collapse of the Eocene Rus and Dammam gypsum and limestone and are most abundant in the central part of the peninsula (Fig. 1). Their formation is related to the presence and orientation of anticlinal joints and fractures and, as hypothesized by Sadiq and Nasir (2002), to intensified karstification during the wetter Middle Pleistocene. *Riyad* sediments usually consist of light brown silty fine sand provided by sheet floods; carbonate and salt contents are low (Babikir, 1986). Usually they are topped by thin drapes of coarse aeolian sand or even nebkhas – mounds of aeolian sediment trapped and fixated by shrubs (Goudie, 2004a) – of up to 2 m height (Perthuisot, 1980; Macumber, 2011; Engel and Brückner, 2014). Most *riyad* are currently subject to deflation as indicated by micro-yardangs and linear corrasion features at the surface (Engel et al., 2018; Figs. S32, S33). The *riyad* of Qatar's interior provide evidence for occupation indicated by a considerable amount of pottery of different wares mostly dating into the (Late) Islamic and Modern periods. Stone structures of temporary character reflecting the presence of Bedouins are abundant (Eichmann et al., 2014; Gerber et al., 2014). The widest and deepest depressions of southern Qatar, significantly exceeding the dimensions of *riyad*, are the Asaila basin ("Acila depression" in Inizan, 1988; Macumber, 2012; Pelegrin and Inizan, 2013; local name is Jaow al Bahath), separated from the Dukhan continental sabkha by a massive limestone ridge, and the Jaow Aqeeq basin (Fig. 1). Both depressions result from collapse and solution over major faults and joint-flow drainage estimated to be active at least since the Miocene. Sadiq and Nasir (2002) suggest a genetic sequence reaching from deepening and widening cylindrical karst pits, which coalesce subterraneously (compound karst pits) and develop larger bottle- and bowl-shape karst pits through collapse processes. These pits gradually fill up with predominantly aeolian deposits to form such mature depressions or basins.

### 2.2.4 Wadis

Wadis are most prominent in the southwest of Qatar, where they accumulate some silt and clay and are intercalated by gravel sheets, which result from episodic rainfall events. The wadis show a relatively dense vegetation cover characterized by *Pennisetum divisum*, *Acacia ehrenbergiana*, *L. shawii* and, where aeolian dynamics increase, *Leptadenia pyrotechnica* (Batanouny, 1981).

### 2.2.5 Coastal sabkhas

The low-lying coastlines of Qatar support the formation of coastal sabkhas, i.e. saline flats in intertidal position. Coastal sabkhas are extensive in the southeast, around Khor al-Udaid, and are characterized by temporary flooding, a water table close to the surface and the precipitation of evaporites within the sediment column and on the surface. A large continental sabkha without surface connection to the sea is formed in the synclinal depression east of the Dukhan Ridge. Its lowest point is 6 m below sea level (Al-Yousef, 2003). The coastal sabkhas are Holocene features mostly resulting from coastal progradation along the entire Qatari coast following the mid-Holocene sea-level highstand (e.g. Billeaud et al., 2014; Strohmenger and Jameson, 2018). Coastal sabkhas with fine-grained soil may host halophile vegetation such as *Arthrocnemum glaucum*, *Juncus rigidus* or *Aeluropus lagopoides*. Where they merge into tidal flats not bordered by beach ridges, mangroves of *Avicennia* may establish (Batanouny, 1981).

### 2.2.6 Barchan dunes

In addition to the sand deposits found along the rocky ridges of southwestern Qatar, aeolian processes formed barchan dune fields in the southeast. The availability of quartz sand as source material and the regional Shamal wind system approaching from NW to NNW are the defining factors (Embabi and Ashour, 1993; Rao et al., 2001; Al Senafi and Anis, 2015). Once having crossed and covered the peninsula from NNW to SSE, the sediment source area towards the inner gulf became cut off due to the Holocene marine transgression into the Arabian Gulf, just before the mid-Holocene sea-level highstand. The southeastern dune population migrating with a speed of several metres per year represents a relict landform constantly diminishing in size as the dunes "calve" into the Arabian Gulf (Engel et al., 2018). While the barchan dunes themselves are free of vegetation, *Cyperus conglomeratus* may establish along their margins (Batanouny, 1981).

### 2.3 Present and former climate

The present climate of Qatar is arid, though the relative humidity may rise up to 90 %. Annual rainfall amounts to 50–80 mm and mainly occurs during winter and spring. However, the spatio-temporal pattern of rainfall is highly irregular (Embabi and Ashour, 1993). The NW-to-NNW Shamal winds are active mostly during early June to mid-July and November to March (Rao et al., 2001; Al-Yousef, 2003; Al Senafi and Anis, 2015), and they drive aeolian morphodynamics throughout the peninsula (Embabi and Ashour, 1993; Engel et al., 2018).

Climate as the dominant factor shaping the physical landscape, controlling water availability and influencing occupation patterns of Qatar, has varied in the past. During glacial–interglacial cycles, and even on millennial timescales over the Holocene, geological records from different parts of the Arabian Peninsula indicate considerable fluctuations (e.g. Fleitmann et al., 2007; Engel et al., 2012, 2017; Preston et al., 2012; Dinies et al., 2015, 2016; Guagnin et al., 2016; Parker et al., 2016, Breeze et al., 2017; Parton et al., 2018). The closest palaeoclimate record on the Arabian Peninsula is located at Ras al-Khaimah, UAE (Preston et al., 2012; Parker et al., 2016), where lake deposits reflecting a rainfall surplus date between 9.0–8.3 and 3.0 ka cal BP. The only reference presenting local Late Quaternary rainfall variability of Qatar describes humid conditions during the Last Glacial Maximum 20 kyr ago and increasing aridity towards the present with a short humid deviation during the mid-Holocene. However, this curve has to be considered with caution since no specific data source is provided (Perthuisot, 1980).

As recharge rates are low, permanent freshwater bodies are absent. Easily accessible, potable groundwater aquifers representing the main limiting factor of ancient settlement activity are rare. Most freshwater aquifers occur in the north, while in the south they are very local and isolated (Fig. 1). Groundwater tables at the coast tend to incline towards the sea level. According to Macumber (2011, 2015), the Asaila depression is one of the few sites with relatively easy access to shallow fresh to slightly brackish groundwater in the south of Qatar.

## 3 Methods

This study is based on work carried out at the Asaila basin, the basin of Jaow Aqeeq and two specific *riyad* in the southern part of the peninsula (Fig. 1). At Asaila, we conducted a detailed geomorphic mapping campaign, carried out a magnetometer prospection and took an 8 m long sediment core (QAT 63). At Jaow Aqeeq, a 3 m long sediment core (ASA-C1) was taken in order to compare sedimentation patterns inside both basins with different hydrological conditions. The sediment infill of two *riyad* was investigated based on a trench (QAT 41) and a short sediment core (QAT 66).

### 3.1 Geomorphic mapping

To develop our understanding of past and present geomorphic processes shaping the Asaila depression, a detailed geomorphic mapping campaign was initiated to identify environmental controls of landscape dynamics and explain the spatial distribution of archaeological surface findings. Pre-existing mapping resources included a multispectral IKONOS mosaic from 2004 (resolution $\sim$ 1 m pixel$^{-1}$), the geological map of Qatar (State of Qatar, 1980), the topographic map of Qatar (State of Qatar, 1971), a predecessor geomorphic map of Inizan (1988) and local geological maps of Al-Yousef (2003), which were used for an initial classification of landforms as polygons in ArcMap v10.3.1. A total of 2 weeks of field mapping in March 2016 included photographic documentation, verification and refinement of the existing documentation. Site location and topographic profiles were realized using a TOPCON Hiper Pro differential global navigation satellite system (DGNSS) with a lateral and vertical error of $\pm$2 cm, a manual GPS and a laser rangefinder (TruPulse 200, Laser Technology Inc.). The resulting map describes (i) geomorphic surface units based on the rock type and type of sediment deposit, (ii) morphodynamics and morphogenesis (aeolian, fluvial, etc.), and (iii) morphometry (slopes, microrelief). Vegetation within the depression was recorded and determined using Batanouny (1981) and Norton et al. (2009).

### 3.2 Magnetometer prospection

To verify the existence of former surface runoff patterns into the Asaila basin (see geomorphic map in Inizan, 1988) and to localize relict fluvial landforms, a magnetometer prospection was carried out in the area of the Acila 36 excavation (Inizan, 1988; Pelegrin and Inizan, 2013) in the northern part of the basin (Fig. 2). In order to reach the highest possible sensitivity, to realize a time-efficient prospection and to receive additional information on the enrichment of magnetic minerals in lateral sediment layers, we used the Cs total field magnetometer (Scintrex SM4G-Special) using the "duo-sensor" configuration (see examples in Fassbinder, 2015, 2017). Five adjacent grids of 40 m $\times$ 40 m were prospected. All details regarding the prospection and data analysis are presented in Supplement Sect. S1.

### 3.3 Sampling and survey of sediment archives

To study potential changes in depositional environments, which would have had essential implications for the interpretation of the survey findings, a vibracore (QAT 63) was taken in the western part of the Asaila basin using an Atlas Copco Cobra mk1 coring device and open steel probes of 6 and 5 cm

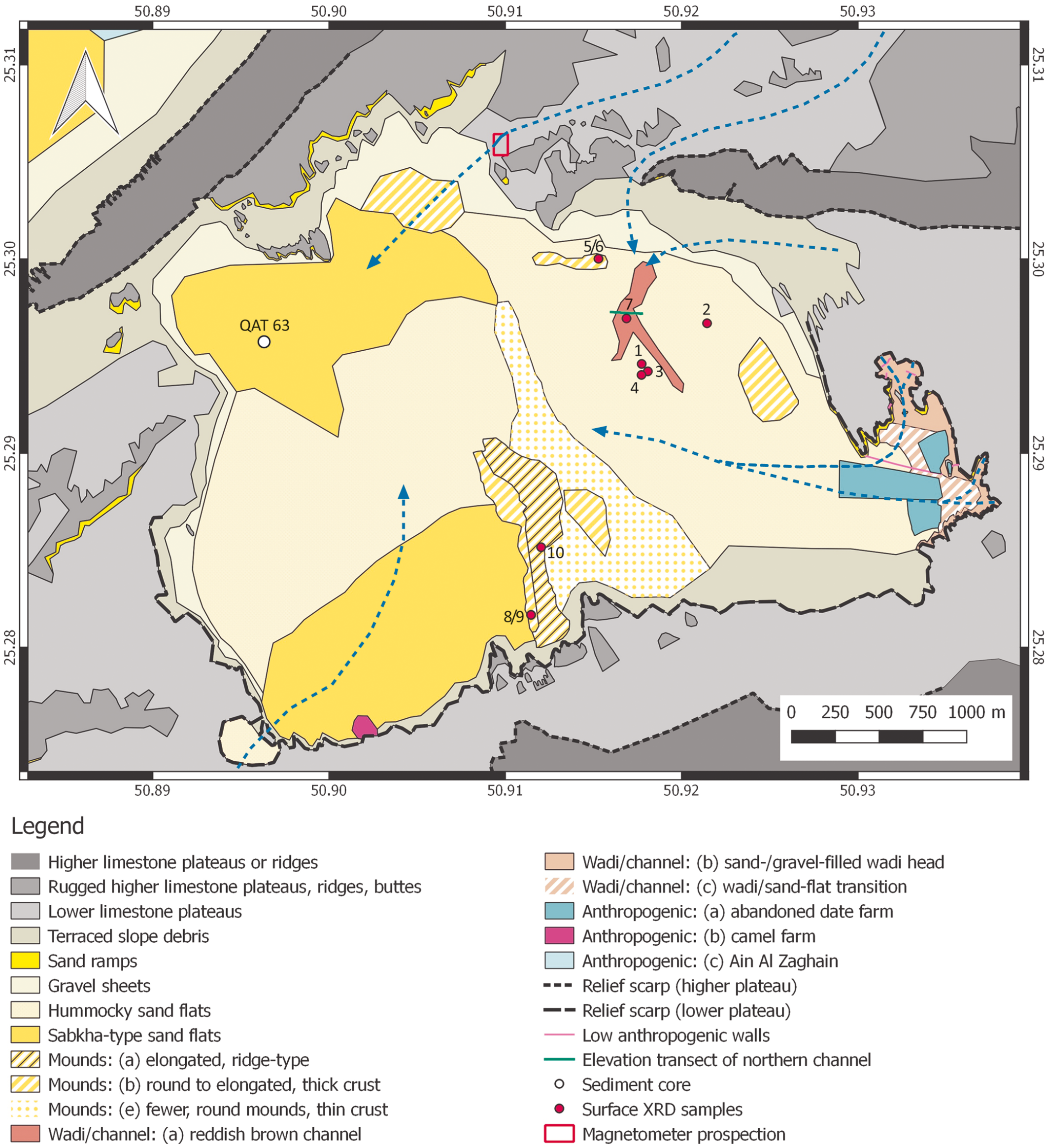


**Figure 2.** Geomorphic map of the Asaila basin indicating main pathways of surface water inflow (blue arrows; based on Inizan, 1988, and own landform interpretation) as well as the location of the elevation transect across the northern channel (Fig. 5), core QAT 63 (Fig. 6), surface XRD samples (Figs. S5–S7, Table S2) and the magnetogram (Fig. 4).

in diameter. A second shorter core (QAT 63 OSL) was taken at the same site using closed, opaque PVC liners in order to retrieve sample material for optically stimulated luminescence (OSL) dating (Drechsler et al., 2016). For comparison, we extended the analysis of sedimentary archives to the adjacent basin of Jaow Aqeeq, located seaward of the rocky ridge separating the Asaila depression from the Dukhan sabkha. Sediment core (ASA-C1) was taken in the northeastern part of the basin of Jaow Aqeeq (Fig. 1). In order to investigate the formation and dynamics of the key archaeological environments of the *riyad*, many were visited and described during the field surveys between 2012 and 2016, while two of them were studied in more detail using a sediment core (QAT 66) and a trench (QAT 41).

## 3.4 Sedimentary analyses and dating

### 3.4.1 Grain size analysis

Due to their overall coarse texture, samples of QAT 63 were analysed for grain size and grain shape by applying dynamic image analysis (Retsch Camsizer P4, particle size range of 30–30 000 µm). Samples from Jaow Aqeeq (ASA-C1) and the *riyad* (QAT 41, QAT 66) were measured using a laser particle analyser (Beckman Coulter LS 13320; particle size range of 0.04–2000 µm) because these had a significant silt component. For analysis of the latter, the pre-treatment procedure includes air-drying of sample material, careful hand pestling and dry-sieving < 1 mm. $H_2O_2$ (15 %) was added to a < 1 mm aliquot of 0.2–1.0 g in order to remove organic carbon. The sample was washed using a centrifuge until a pH value of 6–8 was reached to avoid neutralization after the addition of 0.5N $Na_4P_2O_7$ (55.7 g $L^{-1}$) for aggregate dispersion. Calculation of statistical parameters was performed using the GRADISTAT statistic package (Blott and Pye, 2001).

### 3.4.2 X-ray diffraction analysis

Selected surface samples from the Asaila depression were subjected to X-ray diffraction (XRD) analysis using a Siemens D5000 powder diffractometer (Cu tube) to determine if the landforms are actively formed or of relict nature (active formation may be indicated by the presence of easily soluble evaporites). Samples were measured over a range of 5–75° ($2\theta$) with a step size of 0.05° and a time of 4 s per step (aperture slit = 0.5). The diffractograms were analysed by employing the EVA software package and the ICDD (International Centre for Diffraction Data) database.

### 3.4.3 OSL dating

Due to a lack of material suitable for radiocarbon dating, age estimates for selected units in the Asaila depression and the *riyad* are derived from OSL dating of sand-sized quartz grains (see Sect. S2 and Figs. S1–S4 for details).

## 4 Results

### 4.1 Landforms of the Asaila basin

The Asaila basin has an extent of ca. 12 $km^2$. It is mostly closed, apart from its western margin, where it is connected with the southwestern extension of the Dukhan sabkha through a series of ridges and small depressions. Detailed field mapping revealed a surprisingly wide range of landform units (Fig. 2; see Sect. S4 for detailed explanations), some of which clearly relate to the former presence of surface water and were probably formed by surface processes during the Holocene.

The basin is framed by the flint-bearing limestone plateaus of the Dammam Formation, consisting of two clear plateau levels, i.e. the higher limestone plateau (ca. 13–18 m Qatar National Datum, QVD), including the rugged higher limestone plateau along its basinward transition (ca. 8–15 m QVD) and the lower limestone plateau (ca. 2–8 m QVD). The higher limestone plateau forms a massive NE–SW-trending structural landform and separates the Asaila basin from the adjacent Dukhan sabkha. Another unit of the higher limestone plateau bounds the basin in the northeast. The transition from the lower limestone plateau to the floor of the Asaila basin occurs quite abruptly in the southwest, south and east, in the form of a vertical step (Fig. 3a). In the north and northwest, the transition is relatively smooth with broad units of terraced slope debris and sand-and-gravel sheets (Figs. 2, 3a). In the northernmost part of the basin, where the lower limestone plateau merges into the gravel sheet, the excavation Acila 36 of Inizan (1988) and Pelegrin and Inizan (2013) is located. At this type site for the Middle Neolithic Qatar-B industries, a new magnetometer prospection was carried out (Fig. S13). Despite poor magnetic susceptibility of the loose sediment cover due to low heavy mineral and iron oxide contents and internal magnetization contrasts of only ±0.8 nT, an unequivocal 10–15 m wide channel structure covered by sand and gravel and running towards the basin can be inferred (Fig. 4). The finding corroborates the assumption of Inizan (1988) of a major inactive surface water trajectory into the basin in this area (Fig. 2). Other geomorphic features reflecting more recent fluvial activity include the following:

i. The first feature is a broad, vegetation-free, linear surface depression of 10–20 cm depth (Fig. 5) with a weak, reddish-brown surface crust of gypsum, quartz sand and calcite (Fig. S6, Table S2) as well as high amounts of clay and silt (Fig. S31). It extends from the central northern margin and bifurcates towards the centre of the basin (Fig. 2).

ii. The second feature is a wadi channel at the eastern end of the Asaila basin, characterized by retrogressive erosion (Figs. S29, S30). The wadi is filled with slope debris and experiences aeolian overprinting in the form of sand ramps (Figs. S12, S29a). However, horizontally bedded platy clasts in a poorly sorted, consolidated sandy matrix and an outwash channel exposing barren bedrock point to at least episodic surface water flows in recent times (Figs. S29a, S30a).

The most extensive landform unit inside the Asaila basin is the hummocky sand flats (Fig. 2), which mostly comprise nebkha fields originating from *Zygophyllum qatarense* shrubs. Some of the nebkhas seem inactive and are protected by thin evaporitic crusts made of gypsum, calcite and minor amounts of sylvine, mixed with quartz sand (samples ASA 1 and 2; Fig. S5, Table S2). In some areas, even halite was present (ASA 3; Fig. S5, Table S2).

Some areas in the central southern, northern and eastern parts are densely covered by characteristic mounds significantly higher than the nebkhas. They are fixated and protected by evaporitic horizons of massive to porous gypsum and minor amounts of calcite and sylvine (samples ASA 5, 6, 8–10; Figs. 3b, S6, S7, Table S2). These mounds vary from perfectly round, up to 1 m high, to narrow, cross-cutting ridges, several tens of metres long (Fig. 3b). Furthermore, large parts inside the basin are covered by vegetation-free sabkha-type sand flats (Fig. 3a, b) with gypsum- and halite-containing surface crusts, in some parts even polygonal structures (Figs. S19, S20).

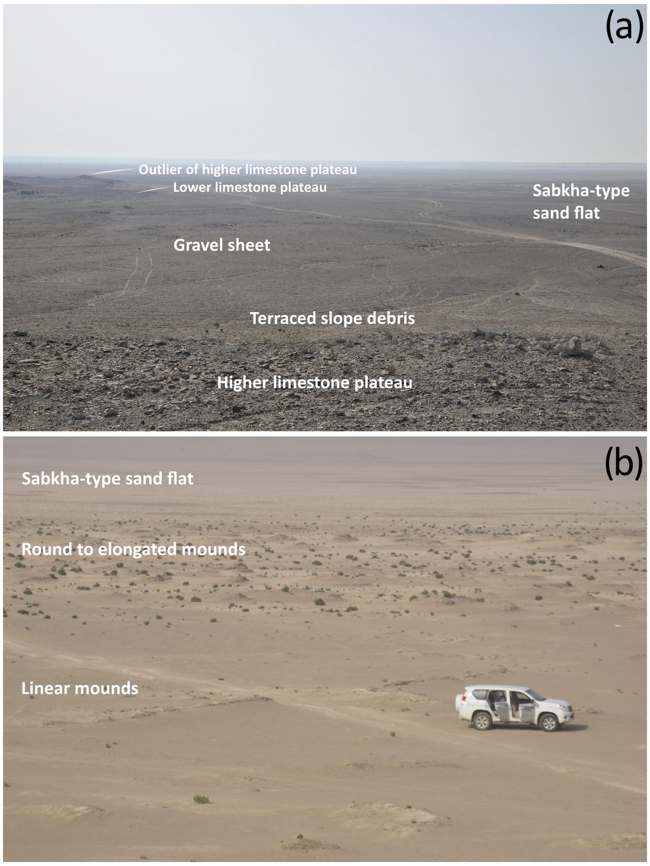


**Figure 3.** **(a)** View into the Asaila basin from the higher limestone plateau of the NE edge directed towards the east. It shows the terraced slope debris and the gravel sheet merging into the sabkha-type sand flat. In the background, the innermost outlier of the higher limestone plateau is visible, resting on top of the lower limestone plateau. **(b)** View into the basin from an outlier of the rugged higher limestone plateau of the central southern rim directed towards the west. It shows the linear, almost vegetation-free mounds in the foreground, followed by the elongated to round mounds with denser vegetation and the vegetation-less sabkha-type sand flat of the western basin.

## 4.2 Sedimentary infill of the Asaila depression

Sediment core QAT 63 was taken in the low-lying sabkha-type sand flats of the northwestern Asaila basin (Figs. 2, S21). It reached a depth of 8 m and consists of moderately sorted to moderately well-sorted fine to very fine gravelly medium sand (sensu Blott and Pye, 2001) (Fig. 6). Despite the slight variation in fine, medium and coarse sand, no facies changes occur. Grain size distributions are generally symmetrical to slightly coarsely skewed, apart from samples at 0.58–0.50 m below surface (b.s.) and ca. 1.55–1.40 m b.s., which are very coarsely skewed and poorly sorted. These samples, along with the surface sample, also have the lowest value for grain sphericity and width to length ratio of the entire sequence. A trench next to QAT 63 revealed a massive subsurface gypsum crust at 0.60–0.50 m b.s., while the overlying sands are clearly cross-bedded (Fig. 6b).

Three samples were taken for OSL dating at 0.40 (small trench), 1.90–1.60 and 2.90–2.60 m b.s. (both from core QAT 63 OSL). They reveal coarse-grain (150–200 µm) quartz ages of $5800 \pm 300$, $6400 \pm 300 - -7300 \pm 300$, and $7500 \pm 300$ years, respectively (Fig. 6, Table S1). While for the uppermost sample right above the gypsum crust the measured water content of 7 % was used for age calculation, two ages were generated for the sample 1.90–160 m b.s., which is probably located in the vertical fluctuation range of the local groundwater table. The younger age implies a water content of 10 % as measured in the laboratory, the older one assumes water saturation. While fluctuating water contents over time introduce dating uncertainties, the overdispersion of the rather symmetric equivalent dose distributions of 8 %–15 % suggests that incomplete signal resetting is not an issue (Fig. S4).

## 4.3 The depression of Jaow Aqeeq

Jaow Aqeeq is another larger-scale topographic depression north of Asaila, located close to the coastal sabkha of Dukhan and seaward of the SW–NE-trending limestone ridge separating Asaila from the Dukhan sabkha (Figs. 1, S32). Both depressions share strong geomorphic similarities, even though traces of surface runoff are more prevalent in Jaow Aqeeq compared to Asaila. Outside the depression along its eastern margin, a wide range of archaeological surface finds include fireplaces, clusters of pottery sherds and lithic artefacts (flakes, blade tools, arrowheads), cairns, shells, coins, metal pieces, bulbs of flint, remains of a provisional mosque, and several modern structures. Some of the lithic artefacts may correspond to the Early Neolithic Qatar-B industry, but the context is largely undated. Multiphase utilization of the site is evident. Distinct areas of domestic use and associated lithic workshops (later overprinted by cairns) as well as mosques and modern structures have been mapped (Fig. 7b). The record inside the basin is very poor so far, only consisting of modern garbage (Schönicke et al., 2016). The surface of the inner depression reveals higher moisture and higher abundance of halite- and gypsum-dominated crusts as compared with the Asaila basin.

In order to improve our understanding of the differences between Asaila and nearby Jaow Aqeeq and to evaluate sediment infill, hydrological conditions and palaeoenvironmental changes, sediment core ASA-C1 was taken inside the Jaow Aqeeq depression close to a temporary shallow standing waterbody (Figs. 7, S32). At the surface, the buckled gypsum crust, several centimetres thick and in some places thinly covered by white halite crystals, appeared very similar to sabkhas along the coast of southwest Qatar (e.g. Dukhan sabkha; Al-Yousef, 2003). The groundwater table was located at 35 cm b.s.

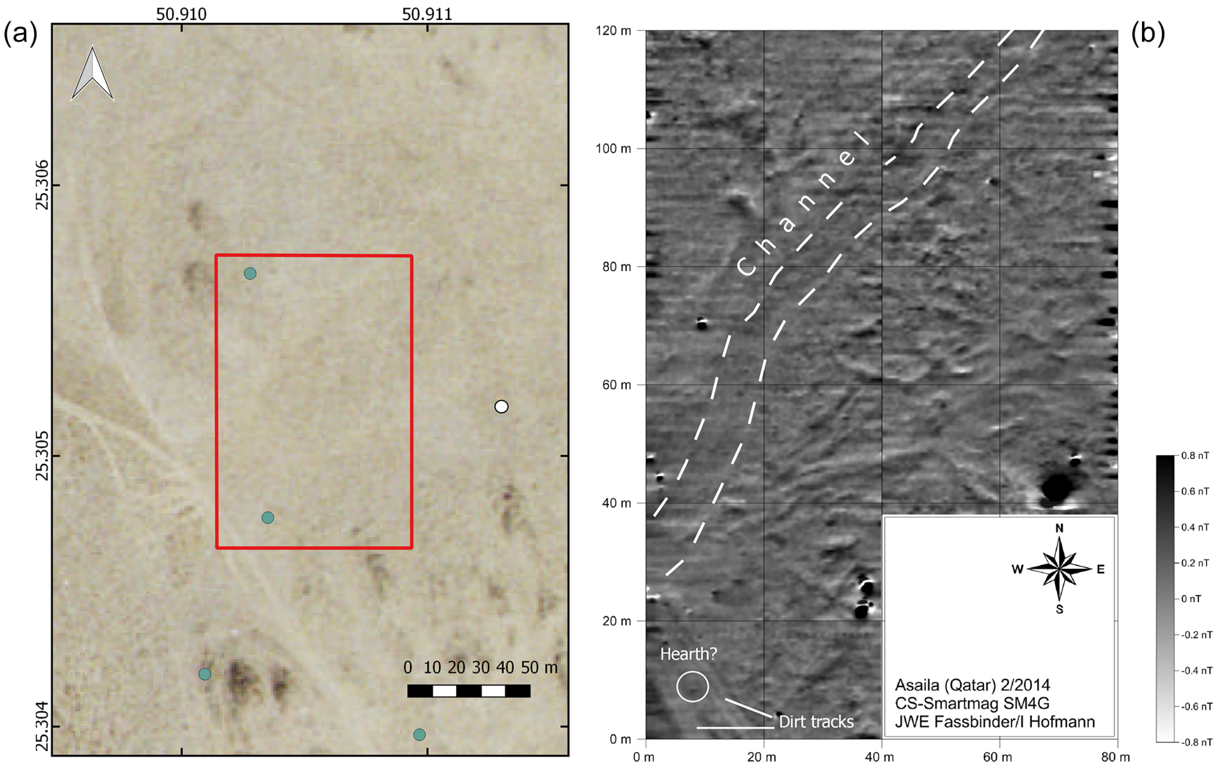


**Figure 4.** Magnetometer prospection (**b** and red frame in **a**) in the area of the Acila 36 excavation by Inizan (1988), located at the basinward end of the lower limestone plateau (see Fig. 1 for overview). The area, where several scatters of both worked and unworked flint (green dots on **a**) were found during the survey of Drechsler et al. (2016), some also associated with ceramics (white dot), slopes towards the southwest and merges into the sand and gravel sheets and the sabkha-type sand flats of the basin. The magnetogram shows an inactive, subsurface channel structure running towards the basin (white lines).

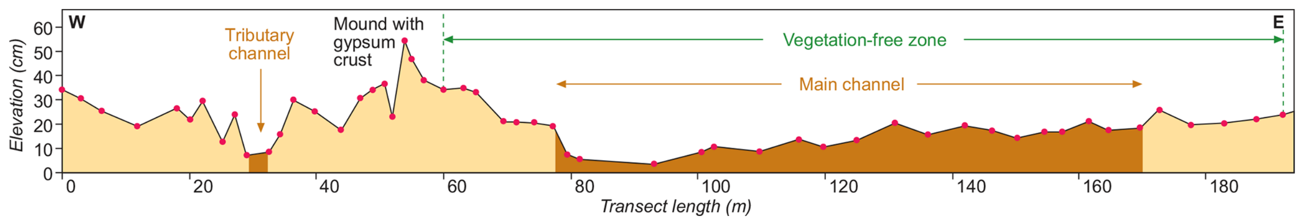


**Figure 5.** Elevation transect crossing the shallow and wide northern channel (green line in Fig. 2).

The amount of sand varies, while some sections (2.87–2.78, 1.53–1.33, 0.82–0.73 m b.s., uppermost 0.34 m) show a significant clay and silt component of up to 25 % (Fig. 7). The sand mostly consists of well-rounded quartz grains and minor appearances of feldspar, gypsum, reworked Dammam limestone and some dark heavy minerals. The sections with the highest amounts of silt and clay were checked for microfossil indicators for lacustrine environments, but only very isolated, highly abraded skeletal fragments were found. In most cases, the occasional gravel component coincides with large gypsum crystals, which occur in large numbers at several horizons, as either hardgrounds or gypsum mush (ca. 2.30, ca. 1.55, 1.00–0.90 m b.s., upper 20 cm). The sections 1.80–1.53 and 0.73–0.49 m b.s. appear well-stratified with alternating coarser and finer textures. Most sections are moderately sorted to moderately well-sorted, except those containing a more significant silt/clay or gypsum component.

## 4.4 The southern *riyad*

Two *riyad* were investigated (Fig. 8). At QAT 41 (site HAR 5183/QNHER 5183 in Gerber et al., 2013), a considerable surface relief has formed through wind sculpturing. The loose coarse sand on top is distributed in patches, partly developing wind ripples (Fig. 9b). While smaller limestone pebbles at the surface may result from sheet flood input into the endorheic depression of ca. 0.065 km$^2$, the small boulders, mostly found along the *rawdha* margins, were brought

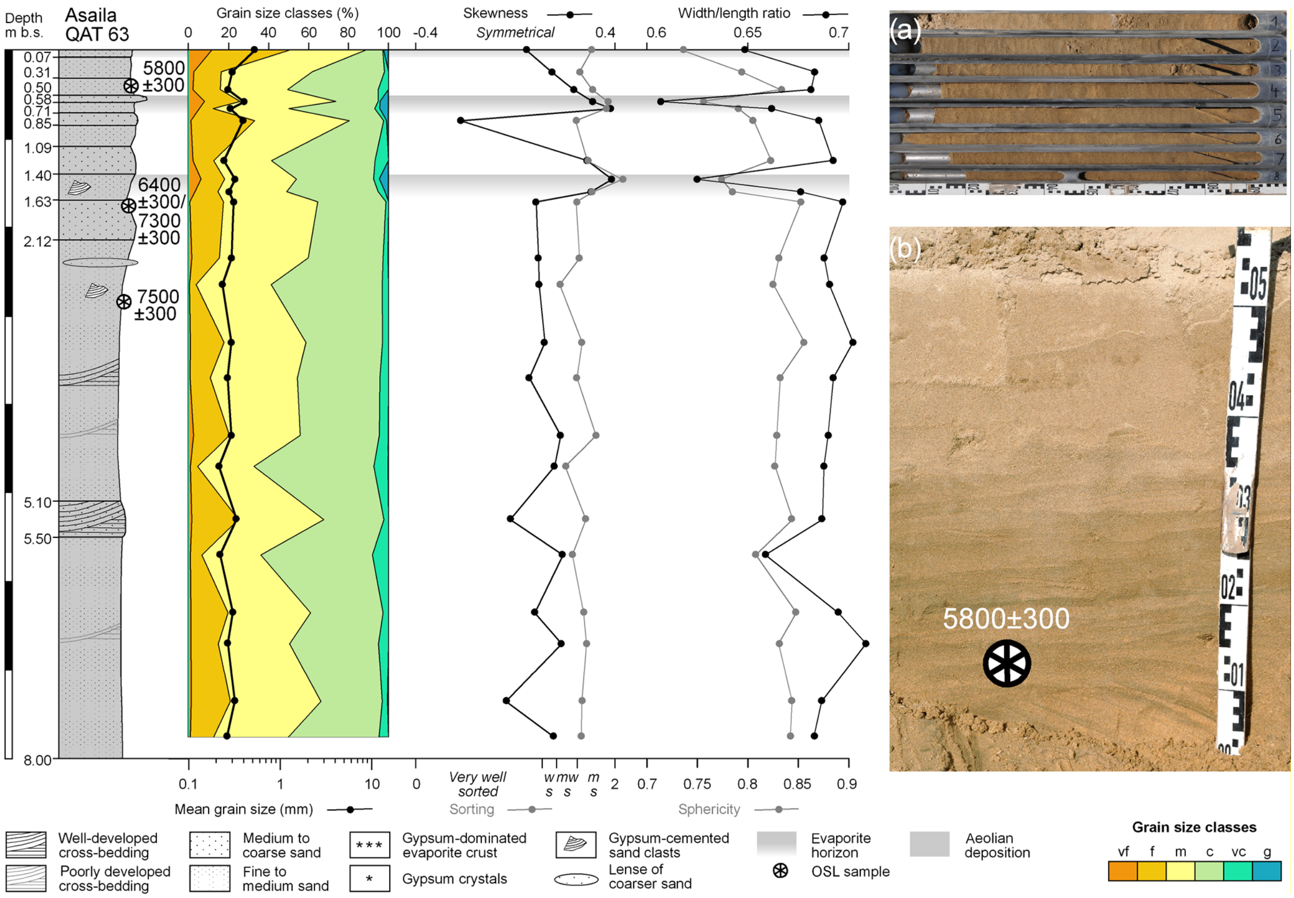


**Figure 6.** Vibracore QAT 63 from the lowest-lying sabkha-type sand flats of the western Asaila depression (see Fig. 1), showing core log, mean grain size, grain size classes (vf: very fine sand; f: fine sand; m: medium sand; c: coarse sand; vc: very coarse sand; g: gravel), sorting (ws: well-sorted; mws: moderately well-sorted; ms: moderately sorted), skewness, and the width to length ratio and sphericity of the grains (b.s.: below surface). **(a)** The entire core down to a depth of 8 m; **(b)** a close-up of the upper 50 cm of the stratigraphy with the position of the uppermost OSL sample and typical aeolian cross-bedding features (modified after Drechsler et al., 2016).

in by humans to stabilize their tents. Further archaeological findings comprise food remains (shells) (Gerber et al., 2014). A pit dug in the central part revealed only 80 cm of sedimentary infill. Overlying the Dammam limestone is a thin unconsolidated layer of limestone pebbles, up to 3 cm in diameter, in a fine sandy matrix. The section 0.75–0.48 m b.s. shows consolidated, greyish brown medium sand with a minor silt fraction as well as fine to coarse sand (Fig. 10). Furthermore, $CaCO_3$ concretions as pseudomorphs along former root channels were documented. The following layer (0.48–0.42 m b.s.) has a similar sand matrix but contains a greater amount of precipitated $CaCO_3$. The upper unit (0.42–0.00 m b.s.) consists of weakly consolidated silty fine sand with some carbonate concretions and root remains (Fig. 9b).

The two thicker units below and above the $CaCO_3$ horizon reveal OSL dates of $1200 \pm 100$ (0.60 m b.s.) and $710 \pm 30$ (0.30 m b.s.) years, respectively (Table S1). Since scatter and shape of equivalent dose distributions suggest relatively complete signal resetting prior to deposition (Fig. S4) and both samples are situated clearly above the groundwater level, the OSL ages provide robust estimates of the time of sediment deposition. Vertical sediment mixing through haloturbation potentially biasing the equivalent dose distributions can be excluded due to negligible salt contents (Babikir, 1986).

Sediment core QAT 66 was taken at the centre of a second, much larger *rawdha* (ca. 0.74 $km^2$) with a complex system of wadis entering from all sides (Fig. 8). QAT 66 hit bedrock at 0.79 m b.s., exposing an overlying sequence of consolidated, well-sorted, greyish light brown silt with a very small fine-sand component. Downcore changes are negligible. The deposit is compact and entirely dry. It forms an even surface with very sparse and low herbaceous vegetation grazed by goats and sheep. Shrubs trap aeolian sand and form nebkha mounds of > 1 m in elevation (Fig. 9a).

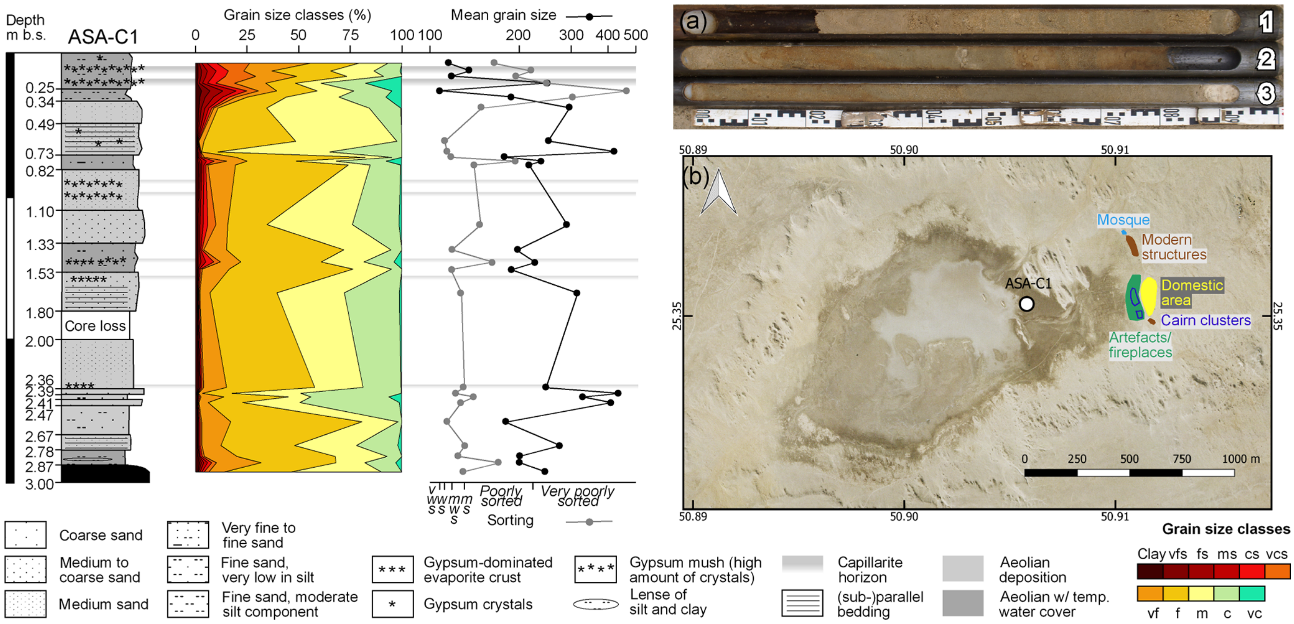


**Figure 7.** Vibracore ASA-C1 from the large-scale topographical depression of Jaow Aqeeq (Fig. 1), where limestone bedrock was encountered at 2.87 cm b.s. (below surface). Core log, mean grain size, grain size classes (vfs: very fine silt; fs: fine silt; mes: medium silt; cs: coarse silt; vcs: very coarse silt; vf: very fine sand; f: fine sand; m: medium sand; c: coarse sand; vc: very coarse sand) and sorting (vws: very well-sorted; ws: well-sorted; mws: moderately well-sorted; ms: moderately sorted) are shown. **(a)** The entire core down to a depth of 3 m. **(b)** Overview map of Jaow Aqeeq with coring site (basemap is IKONOS image of 2004) and archaeological surface findings according to Schönicke et al. (2016).

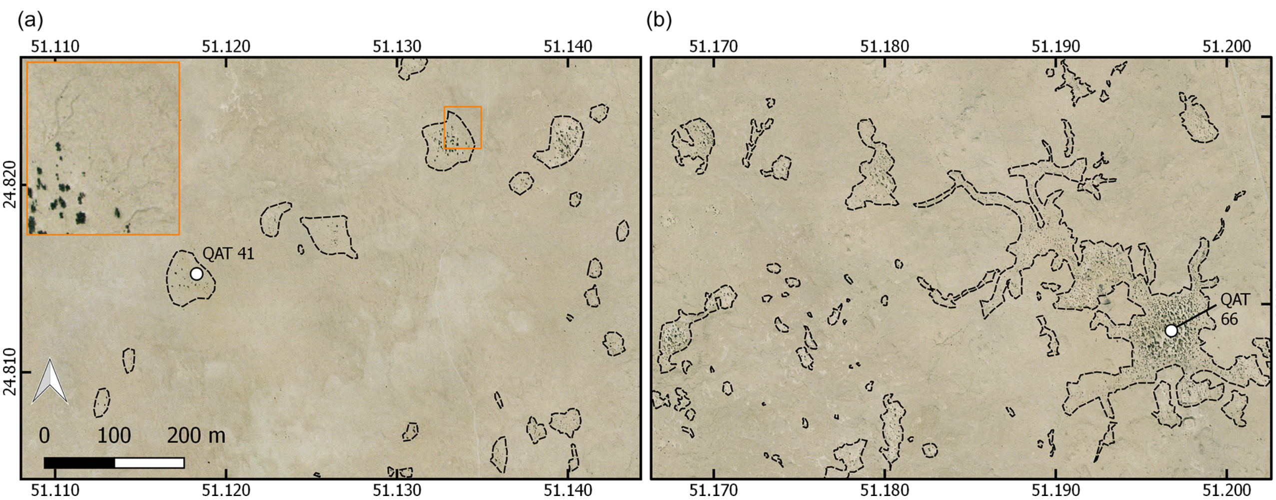


**Figure 8.** Map of *riyad* in south Qatar (see location in Fig. 1), which were investigated for their sediment infill during the SQSP (based on an IKONOS satellite image of 2004). The outlines of the *riyad* are mostly reflected by vegetation and, where they are more mature as in **(b)**, may develop extended networks of micro-wadis. Note the example of traces of surface discharge into the *riyad* in **(a)** (orange rectangle). QAT 41 represents a trench in *rawdha* HAR 5183 (Gerber et al., 2013) and QAT 66 a sediment core in a *rawdha*, which was not part of the archaeological survey (Fig. 9).

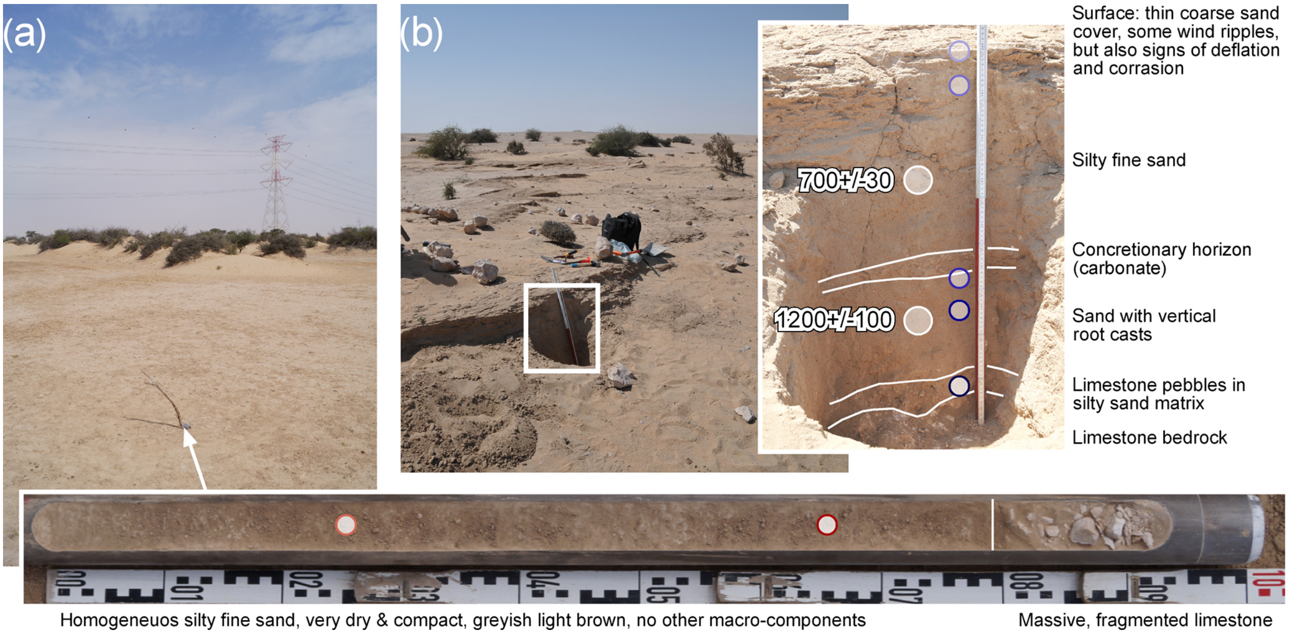


**Figure 9.** **(a)** Sediment core QAT 66 inside a larger *rawdha* with multiple wadis entering from all sides (Figs. 1, 8); the location of grain size samples is indicated on the core (Fig. 10). **(b)** Profile QAT 41 exposing the sediment infill of a smaller, more elliptic *rawdha* (HAR 5183), with brief stratigraphic log, OSL ages (Table S1) and grain size samples (Fig. 10).

## 5 Discussion

### 5.1 Holocene landscape dynamics of the Asaila basin

#### 5.1.1 The geomorphic system

Geomorphic mapping based on field surveys and satellite imagery reveals the polygenetic nature of landforms in the Asaila basin, driven by tectonic, aeolian and fluvial processes as well as subsurface hydrology. The macroscale relief is determined by the roughly N–S-trending anticline or syncline structures, in particular the Al Huriyeh syncline (Fig. 1). The basin's origin may be controlled by a NNE–SSW-striking fault (Inizan, 1988) initiating long-term, subsurface limestone dissolution and collapse since the Miocene (Sadiq and Nasir, 2002) and eventually creating a large-scale morphological depression at the surface. Definite field evidence for such a fault, however, is missing, and other sources emphasize the lack of surface expressions of major faulting on the Qatar peninsula (e.g. Cavalier, 1970; Sadiq and Nasir, 2002).

Surface water exists but is very short-lived and only occurs episodically during strong rainfall. Geomorphic evidence was mapped in the eastern part, in the form of fluvial bedforms in a narrow, shallow channel and a collapsed (sub)surface drainage system, i.e. a potential karst spring. The wadi channel mapped in the central northern part of the basin with its reddish-brown surface appears inactive; halite as a potential sign of recent flooding is absent (sample ASA 7). However, it unequivocally represents a significant pathway of surface runoff into the basin. Another major pathway of surface inflow exists in the northernmost part of the basin, where the higher limestone plateau is dissected in an ENE–WSW orientation (Fig. 2). The small valley entering at the northernmost extension of the basin hosts a subsurface channel morphology (Fig. 4), testifying to the relict nature of more significant surface runoff. There is, however, no evidence for the timing of this increased runoff.

#### 5.1.2 Prevalence of aeolian processes

Grain size measures of sediment core QAT 63 reflect a persisting aeolian environment. OSL data indicate that the sequence captures at least the entire Holocene. Both datasets in combination with present-day sabkha-type surfaces, nebkha formation, sand ripples, streamlined gypsum mounds showing clear signs of corrasion and sand ramps reflecting the main Shamal corridor show that aeolian processes have dominated the Asaila landscape at least since the arrival of humans in the Neolithic. QAT 63 rejects any type of lacustrine environment inside the Asaila basin during that time, which has been speculated by Macumber (2012).

#### 5.1.3 Fluctuations of the groundwater table and capillary evaporite formation

The three horizons of poorly sorted sediments, as well as a lower width to length ratio and sphericity of grains in the uppermost 1.5 m of QAT 63 are related to the ongoing precipitation of mostly gypsum crystals from ascending groundwater in the vadose zone. These processes are similar to

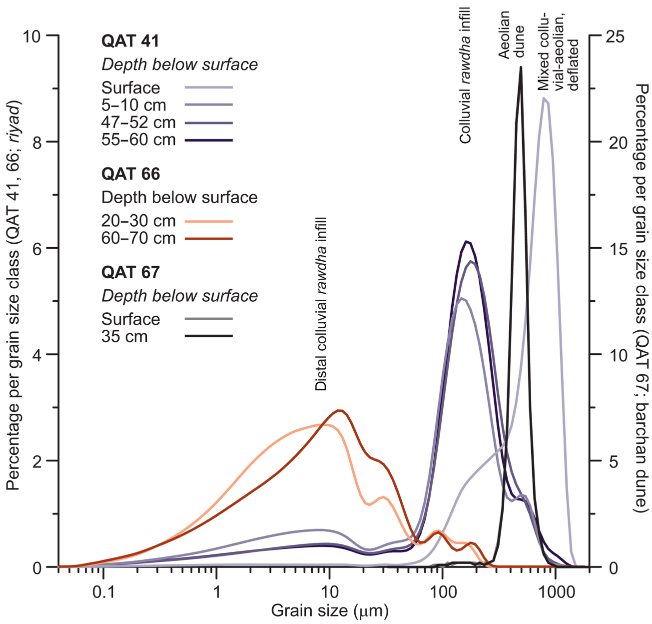


**Figure 10.** Grain size distribution of samples from the *riyad* (Fig. 9) and, for comparison, a typical barchan dune of south Qatar (QAT 67; curves almost entirely overlap).

those in continental sabkhas, where brines are significantly more highly concentrated (Sonnenfeld and Perthuisot, 1989; Yechieli and Wood, 2002; Ginau et al., 2012). Upward capillary movement from a shallow groundwater table (ca. 1.5 m deep in the Asaila basin today) leads to a halite-dominated and carbonate-containing crust at the surface, underlain by one or several layers of gypsum, also referred to as capillarites (Sonnenfeld and Perthuisot, 1989). This is also reflected by surface XRD samples from the hummocky sand flats, which, similar to the sabkha-type sand flats, represent active equilibrium surfaces of deflation and aeolian deposition. Crust formation is to a large extent driven by capillary rise and the position of the groundwater table. Sample ASA 3 still contains halite, whereas samples ASA 1 and 2 do not contain halite and show how easily salts are deflated and dissolved at the surface (Sonnenfeld and Perthuisot, 1989).

Even though Asaila is located at the southwestern fringe of the freshwater lens of Qatar (Fig. 1), subsurface gypsum dissolution in the Rus and underlying Umm er Radhuma Formations results in elevated levels of salinity and brackish to saline groundwater in the southern peninsula (Lloyd et al., 1987; Macumber, 2011, 2015). Asaila has relatively moderate salinity levels of around 3000 ppm (Macumber, 2012), which is still sufficient to precipitate capillary evaporites in the vadose zone and, in the eastern sabkha-type sand flats, thin buckled gypsum crusts at the surface. However, comparison with the sediment infill and the thick, halite-dominated surface crust at Jaow Aqeeq (ASA-C1) shows how a higher groundwater table and significantly higher groundwater salinity of about 8000 ppm (Macumber, 2012) may lead to more intense precipitation of evaporites in interstitial pore waters and the establishment of inland sabkha conditions. While Jaow Aqeeq seems to directly correspond with the Dukhan coastal sabkha in terms of hydrogeological exchange, the higher limestone plateau separating the Asaila depression from the southeasternmost extension of the Dukhan sabkha is also reflected by the strong SE–NW gradient on the groundwater salinity map in Macumber (2012).

### 5.1.4 The role of relative sea-level changes in landscape formation

The rate of aeolian sand sedimentation of 1–2 mm yr$^{-1}$ in the upper 3 m of QAT 63 averaged over the time between ca. 7500 and 5800 years ago as inferred from OSL data is driven by two factors: (i) greater sand availability further north (upwind), as large parts of the Qatar peninsula were then still covered by dune fields (Engel et al., 2018), and, (ii) at that time, relative sea level, which is coupled with groundwater levels in low-lying areas near the Qatari coast (Macumber, 2011), rose by several metres (Lambeck, 1996), reaching a highstand around 6000 years ago (Perthuisot, 1977; Engel and Brückner, 2014; Parker et al., 2018; Strohmenger and Jameson, 2018; Rivers et al., 2020). A rising groundwater table and capillary fringe stabilize newly deposited sand in dry climates and lead to net accumulation. Such a raised equilibrium surface close to the shallow groundwater table is referred to as the Stokes surface, below which deflation does not occur due to cohesion of the sediment provided by capillary moisture and initial cementation (Fryberger et al., 1988). It seems that after the sea-level highstand phase (+2–3 m, ca. 6000–4500 years ago; Vita-Finzi, 1978; Cuttler and Al-Naimi, 2013; Engel and Brückner, 2014; Parker et al., 2018; Strohmenger and Jameson, 2018; Rivers et al., 2020), deflation began due to the lowering of the groundwater and the capillary fringe along with sea level, thereby affecting the lowering Stokes surface.

The characteristic mounds covering specific areas of the Asaila basin (Figs. 2, 3a) are mainly preserved by porous, platy or needle-shaped gypsum (surface samples ASA 5, 6, 8–10). We assume that these gypcretes are relict horizons of interstitial gypsum in the vadose zone at the time of the sea-level and groundwater-level highstand. Predominant deflation afterwards in the era of sinking groundwater levels led to the removal of the halite–carbonate surface crust (see Sonnenfeld and Perthuisot, 1989), the aeolian sand below and parts of the more massive gypsum crusts. Where the gypsum withstood erosion, the crust protected the underlying deposits from denudation resulting in the formation of mounds.

### 5.1.5 Origin of the linear mounds

The origin of the linear mounds (Figs. 2, 3b) in the central southern part of the basin, some of which form irregular grids, remains enigmatic. In some parts, they resemble inverted canals as known from other arid environments, e.g. historical Lower Mesopotamia (Brückner, 2013; Engel and Brückner, 2018) or southern Peru (Beresford-Jones et al., 2009), but no other indication of an anthropogenic origin was found. Alternatively, the network of linear mounds could follow the pattern of subsurface small-scale joints, which provide better conditions for the capillary rise of water to form stable gypsum crusts. Further in-depth investigations are necessary to shed light on the origin of the linear shapes.

### 5.2 Landscape dynamics and the archaeological record

The limited availability of potable water has always determined ancient settlement patterns in Qatar, explaining why most archaeological sites are located on the northern peninsula. The generally poor groundwater quality in the southern part (Cuttler and Al-Naimi, 2013; Macumber, 2015) meant that Neolithic occupation concentrated mostly around the Asaila basin, where access is fairly easy and the salinity is moderate (Drechsler et al., 2016). Only in recent times have further potentially Palaeolithic and Neolithic sites been discovered closer to the coast (Drechsler, 2014). Several Early Neolithic flint knapping workshops were identified along the margins of the Asaila basin based on the spectrum of single diagnostic Qatar-B artefacts or artefact scatters (dated to ca. 7500–6500 BCE). They existed mostly in direct proximity to outcrops of flint raw material (Pfeiffer, 2015; Drechsler et al., 2016), comprising regular blades from bidirectional naviform cores (Inizan, 1988; Pelegrin and Inizan, 2013). In contrast, Middle Neolithic artefacts, i.e. unifacial and bifacial points, scrapers, and bifacially chipped winged and tanged arrowheads following the "Arabian bifacial lithic tradition" sensu Edens (1982, 1988) (ca. 6500–4500 BCE), show the greatest concentrations inside the basin (Fig. 11). They occur either as scatters of cores, flakes and flint tools in combination with burnt limestone and ashy sediment in the centre of the basin, indicating both in situ flint knapping and domestic activities, or as single tool findings at the lower western margins, where they point to incidental tool usage and discard (Drechsler et al., 2016). Successful refitting of single pieces of the same flint artefacts within a radius of only a few metres inside one of the survey units inside the basin shows that relocation of artefacts is negligible (Schönicke et al., 2016). There appears to have been quite a substantial occupation in the Middle Neolithic with a focus in the centre of the basin, which, at that time, might have provided a higher potential for grazing of both domesticated and wild animals (Drechsler et al., 2016).

Even though no local proxy record of Holocene climatic changes exists in Qatar, the high-resolution $\delta^{18}$O curve from a speleothem at Hoti Cave, Oman (Fleitmann et al., 2007; Fig. 12b), and the palaeo-lacustrine record from Awafi near Ras al-Khaimah, UAE (Parker et al., 2016; Fig. 12d), may provide important references. Both sites received a moisture surplus during Early Holocene to mid-Holocene summer seasons from the Indian Summer Monsoon (Fleitmann et al., 2007) and even more so from the intensified East African Summer Monsoon (EASM) penetrating into the Arabian Peninsula. The role of the mid-level westerlies for the Early Holocene Humid Period (EHHP) in the southeastern Arabian Peninsula, however, remains unclear (Parker et al., 2016). Recent climate model simulations by Jennings et al. (2015) and Guagnin et al. (2016) suggest that Qatar might have had an increase in rainfall following an intensification of the African–Asian monsoonal systems, although far less than the sites of Awafi, Hoti Cave, or another site in south Oman, i.e. Qunf Cave (Fig. 12c). The onset of lacustrine conditions as reflected by the Ti and magnetic susceptibility records from Awafi (Parker et al., 2016; Fig. 12d) overlaps well with the intensification of Middle Neolithic occupation at Asaila (Drechsler et al., 2016; Fig. 12g), which at its later stage also benefitted from the high groundwater table connected to the sea-level highstand (Lambeck, 1996; Parker et al., 2018; Strohmenger and Jameson, 2018; Fig. 12e). The Hoti Cave record indicates an even earlier onset of the EHHP, which may reflect more favourable environmental conditions and incipient human occupation at Asaila already in the Early Neolithic (Fig. 12b, g). The same applies to the northern Arabian palaeolake record from Tayma (Saudi Arabia), which reflects only a very short EHHP and appears offset, probably due to a complex interplay of a range of global and regional atmospheric moisture sources, e.g. the EASM, Mediterranean winter rains and winter–spring tropical plumes (Engel et al., 2012; Enzel et al., 2015; Neugebauer et al., 2018; Parton et al., 2018).

Macumber (2018) associates the phase of a wetter climate around the 6th and 5th millennia BCE with the formation of a massive subterraneous freshwater lens over large parts of Qatar. The subsequent absence of archaeological traces at Asaila – and a reduction of sites in the entire country (Muhesen and Al-Naimi, 2014) as well as across the wider gulf region (Uerpmann, 2003) – is associated with aridification on the eastern and southeastern Arabian Peninsula, sea-level drop and associated groundwater level fall (at least after the highstand plateau ended around 2500 BCE), and the onset of a predominant deflation regime inside the basin. After a hiatus, Islamic (610–1972 CE) to Modern (post 1972 CE) pottery and remains of campsites were found (Figs. 11, 12g), along with cairns on the higher plateau (Gerber et al., 2014; Drechsler et al., 2016), which are difficult to date (Cuttler et al., 2013; Izquierdo Zamora et al., 2015).

### 5.3 *Rawdha* formation

The uniform sedimentary infill of south Qatar's shallow karst depressions (*riyad*) appears rather young. The one which was dated in this study (QAT 41) has accumulated its silts and sands over the last 2000–1500 years as determined by OSL data. The low ages of the sediment infill explain the absence of older archaeological findings, which, in the *riyad* surveyed

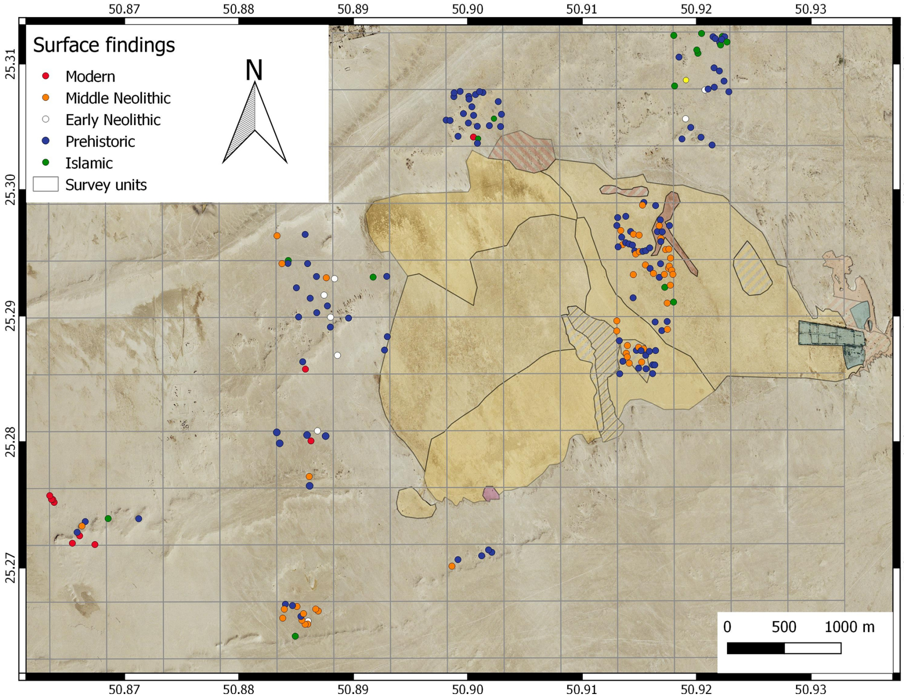


**Figure 11.** Spatial distribution of archaeological surface findings (basemap from IKONOS 2004) inside and around the Asaila basin. Selected squares (indicated by mapped surface findings) of 500 m × 500 m were surveyed by systematic back-and-forth walking in order to guarantee a 100 % coverage (Drechsler et al., 2016). Geomorphic units of the innermost Asaila basin are shown for orientation (see details in Fig. 2). "Prehistoric" refers to flint artefacts with unspecific character, which, in theory, may date from any period between the Palaeolithic and historical times (Drechsler et al., 2016).

by the SQSP, mainly consist of Late Islamic to Modern period pottery wares, modern trash, Chinese porcelain, coins or temporary mosque structures, all dating to the 18th century CE or younger (Eichmann et al., 2014; Schönicke et al., 2016).

Sedimentation inside the *riyad* is induced by surface runoff events as indicated by small wadi channels and runnels directed towards some of the larger landforms (Macumber, 2015; Fig. 8). The broad grain size distribution, in particular from the distal record inside the large *rawdha* (QAT 66), relates to colluvial processes, even though a contribution of aeolian dust as indicated by geochemical data from *riyad* surfaces of Qatar's interior presented by Yigiterhan et al. (2018) cannot be excluded. As small, endorheic basins, the *riyad* represent pivotal sites of meteoric groundwater recharge (Macumber, 2011, 2015; Cuttler and Naimi, 2013) and groundwater access through wells. They become flooded during rainfall events, which explains the distribution of remains of temporary camps only along their margins (Gerber et al., 2014; Schönicke et al., 2016). Accordingly, the silt component of their infill (Figs. 9, 10) settled out of suspension. Increased soil moisture, strong evaporation and significant sediment contributions of the local limestone-dominated hamada lead to carbonate crust formation in the vadose zone, as observed in QAT 41, and to incipient cementation. The finer grain size spectrum of QAT 66 (Fig. 10) compared to QAT 41 corresponds with its distal location in the centre of a very large *rawdha*.

Thus, net accumulation inside the *riyad* may represent a proxy for surface runoff, which is controlled by rainfall events and, as in our case, by land cover. In the Early Holocene and mid-Holocene, much of Qatar – most probably including the southern *riyad* – was covered and filled by mobile sands. Only after the southeastward migrating barchan dunes, which lost their source due to the transgression of the gulf (Embabi and Ashour, 1993; Engel et al., 2018), had left the *riyad* zone, could fine-grained colluvial deposits accumulate during surface runoff events. The *rawdha* HAR 5183 (QAT 41) is located ca. 21 km upwind of the migrating end of the barchan dunes west of Qatar's inland sea (Khor al-Udaid) (Fig. 1) according to the mean Shamal azimuth of 332° deviation from the north (Embabi and Ashour, 1993). This azimuth seems to have remained stable during the Holocene based on the similar orientation of drowned barchanoid dunes inside the Gulf of Salwa (Al-Hinai et al., 1987). Considering a migration rate of ca. 8–10 m $yr^{-1}$ measured for medium-sized barchan dunes in Qatar over the time span of several decades (Engel et al., 2018), the karst depression became dune-free around ca. 2600–2100 years ago, or even later, if higher migration rates of smaller-sized barchan

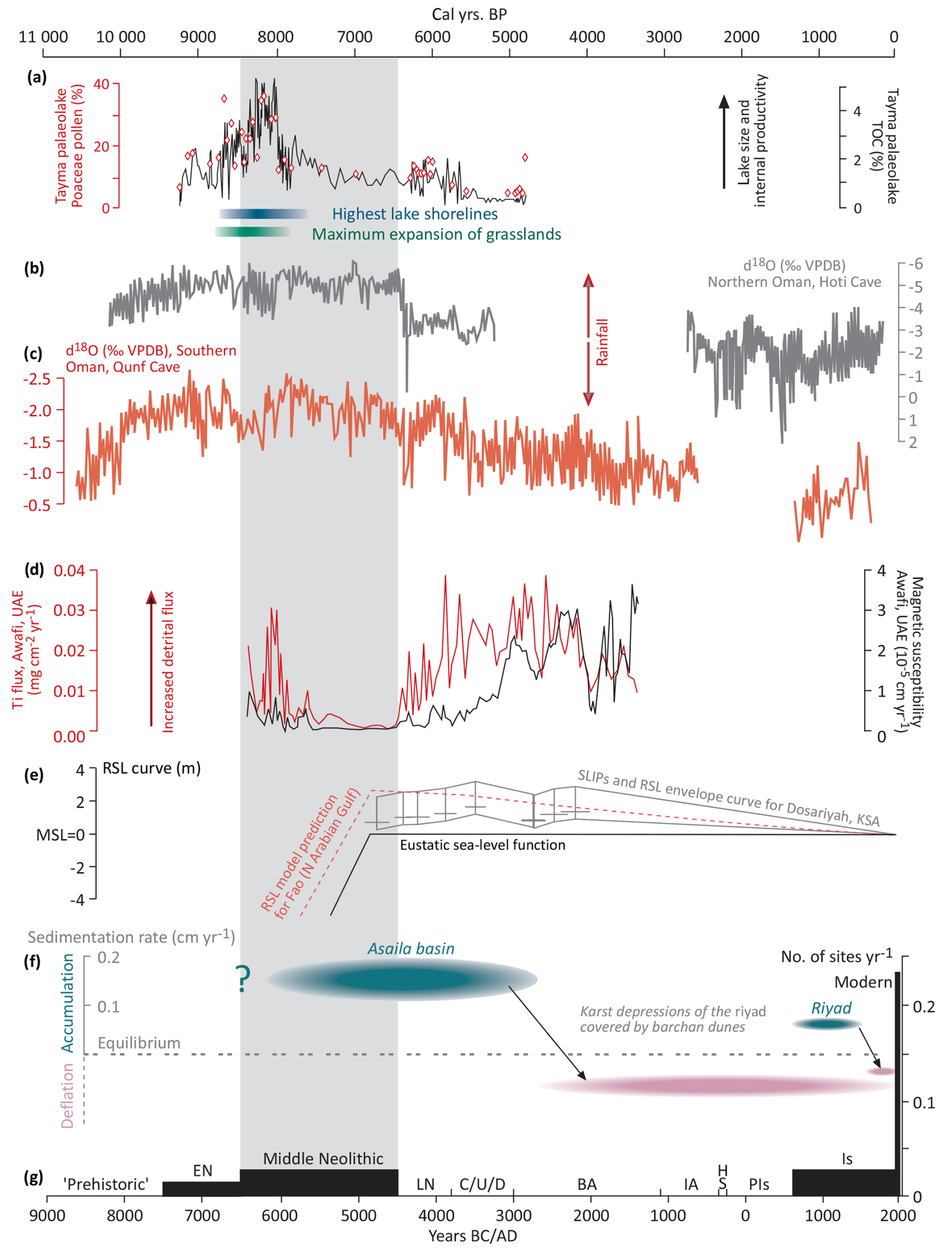


**Figure 12.** Synopsis of regional palaeoclimate and sea-level data in combination with accumulation–deflation phases in Asaila and the southern *riyad* as well as the chronological density of surface archaeological findings in Asaila. **(a)** TOC (total organic carbon) record and relative abundance of Poaceae pollen (grasses) (Dinies et al., 2016) combined with phases of the highest lake shorelines (Engel et al., 2012, considering revised chronology in Dinies et al., 2015) and maximum grassland expansion (Dinies et al., 2015) from the palaeo-lake and wetlands in the sabkha of Tayma, northern Arabia. Oxygen isotope records of stalagmites from **(b)** Hoti Cave, northern Oman, and **(c)** Qunf Cave, southern Oman (Fleitmann et al., 2007) (VPDB is relative to the Vienna Pee Dee Belemnite standard). **(d)** Ti flux and magnetic susceptibility from the lacustrine record of Awafi, UAE, where low values indicate landscape (dune) stability and higher moisture availability (Parker et al., 2016). **(e)** Envelope curve of relative sea-level stands from Dosariyah, Saudi Arabia, based on $^{14}$C-dated sea-level index points considering vertical and lateral error margins (Parker et al., 2018). It is shown in combination with the global eustatic sea-level function and a regional modelled sea-level prediction for the northern head of the Arabian Gulf (Lambeck, 1996), the peak of which is tentatively shifted to account for $^{14}$C calibration (MSL is mean sea level). **(f)** Sedimentation rates at Asaila and the southern *riyad* as inferred from OSL data of this study (Figs. 6, 9b, Table S1), and the inferred shift to a deflation regime. Barchan dune cover at *rawdha* QAT 41 was estimated based on migration rates inferred by Engel et al. (2018). Furthermore, the number of sites identified in and around the Asaila basin per year of the time span of each period is shown for the different historical and prehistoric periods (EN: Early Neolithic; MN; Middle Neolithic; LN: Late Neolithic; C: Chalcolithic; U: Uruk; D: Dilmun; BA: Bronze Age; IA: Iron Age; H: Hellenistic; S: Seleucid; PIs: pre-Islamic; Is: Islamic) as a proxy of the intensity of human occupation (Drechsler et al., 2016). The grey vertical bar crossing all proxy data curves emphasizes the Middle Neolithic, which is prominently represented by artefacts inside the Asaila basin (Fig. 11).

dunes are taken into account. This coincides with the start of the runoff-related silt and sand accumulation of the *rawdha* at some point before 1500 years ago, as inferred from OSL data. The archaeological record indicates significant human usage of the *riyad* during the last 300 years, when their infill already resembled today's situation. The only potential climate signal deduced from the surveyed *riyad* so far may be a shift to more pronounced aridity in very recent times indicated by ubiquitous surface deflation patterns and small, decimetre-scale yardangs (Figs. S33, S34). This process may have supported a concentration of young archaeological findings at the surface. Taking these observations into account, it can be concluded that the further north a *rawdha* is located, the longer it has been dune-free, and more time may be represented by its silty sediment record.

## 6 Conclusions

Among the diverse arid landform units of south Qatar, the Asaila basin as well as the numerous *riyad* of the central peninsula reveal the richest archaeological record. The former has a density of 108 surface findings per square kilometre extrapolated from the three surveyed squares inside the basin (Fig. 11). In contrast to previous maps of the Asaila basin, which only differentiate between "sabkha" and "aeolian deposits" (Al-Yousef, 2003), we demonstrate greater geomorphic variability and additional signs of (relict) surface runoff. The areas of mounds of different shapes – for the first time systematically investigated in this study – are important indicators for groundwater (and, thus, sea level) control of accumulation and deflation inside the basin. While the 8 m long sediment core reveals a continuous dominance of aeolian sedimentation over the Early Holocene to mid-Holocene, the mounds, cemented by capillary evaporites originally grown in the vadose zone, are a clear sign of deflation after the mid-Holocene sea-level (and groundwater-level) highstand. Abundant archaeological evidence of Early and Middle Neolithic occupation – the latter with a clear focus inside the Asaila basin – indicate more favourable living conditions. Whether these imply denser vegetation and better access to groundwater and are linked to the EHHP inferred from other records on the southeastern Arabian Peninsula (e.g. Fleitmann et al., 2007; Preston et al., 2012; Parker et al., 2016) still awaits verification. The existence of more favourable conditions inside the Asaila basin is particularly evident when compared with the adjacent basin of Jaow Aqeeq, which shows how a higher groundwater table and higher groundwater salinity are reflected by higher amounts of capillary gypsum and thicker surface evaporite crusts.

In contrast, the sediment records of the *riyad* in southern Qatar are very shallow, younger (only ca. 1500 years in the case of QAT 41) and apparently controlled by surface runoff, deflation and the constantly diminishing barchan dune cover over the Middle and Late Holocene (see Engel et al., 2018). The young age of the infill explains the exclusive presence of young artefacts, mainly covering the Late Islamic to Modern periods. In combination with the indicators of current deflation, it may relate to a decrease in rainfall and surface runoff in recent decades to centuries. Whether this shift is related to inactivity and burying of runoff channels identified at the northern margin of the Asaila (Figs. 4, 5) is a matter of future investigations. It remains to be stated that the Late Quaternary environmental changes on the peninsula of Qatar are still largely unknown due to a lack of suitable geological archives. This report adds to the scarce information available, e.g. from Wadi Debayān (e.g. Tetlow et al., 2013), northeast Qatar, or the Ras Abrouq peninsula north of Dukhan, where archaeological layers were encountered down to a depth of 2.6 m (Smith, 1978; Vita-Finzi, 1978), even though chronological resolution and climatic significance still need to be improved. In the future, geophysical prospection of the *riyad* further north, e.g. using the combined approach of electrical resistivity tomography and seismic refraction tomography as applied for dolines on Crete by Siart et al. (2010), may help to locate thicker *rawdha* infill with more detailed palaeoenvironmental information through a higher-resolution age model in combination with the analysis of grain size distribution, micromorphology, phytoliths or even pollen spectra.

**Data availability.** OSL and XRD data are provided in the Supplement file. All grain-size-related data will be provided by the corresponding author upon request.

**Supplement.** The supplement related to this article is available online at: https://doi.org/10.5194/egqsj-68-215-2020-supplement.

**Author contributions.** The study was conceived by ME and HB. The archaeological survey was led by CG, PD, KP and RE. PD provided data on the spatial distribution of archaeological findings in Asaila. Geomorphic mapping was performed by SR, ME, and AP. ME, HB, KP, AP, DW and SR took sediment cores. ME, HB and KP logged and sampled the *rawdha* trenches. JWB conducted the magnetometer prospection and data processing. DB measured luminescence signals and calculated ages. SO conducted XRD measurements and interpreted XRD spectra. ME and DW carried out sedimentological analyses. ME wrote the paper. All authors read, commented on and approved the paper.

**Competing interests.** The authors declare that they have no conflict of interest.

**Special issue statement.** This article is part of the special issue "Geoarchaeology and past human–environment interactions". It is not associated with a conference.

**Acknowledgements.** We thank H.E. Shaykha al-Mayassa bint Hama bin Khalifah Al-Thani and H.E. Shaykh Hassan bin Muhammad Al-Thani without whose interest and support the joint South Qatar Survey Project of Qatar Museums (QM), represented by Faisal Abdulla Al-Naimi, Thomas Leisten, Alice Bianchi and Ferhan Sakal, and the German Archaeological Institute (DAI) (https://www.dainst.org/en/projekt/-/project-display/612902; last access 4 November 2019), would not have been realized. Nina Szemkus is acknowledged for supporting the laboratory work. Comments by the three anonymous reviewers and the handling editor Hans von Suchodoletz helped to significantly improve the paper.

**Financial support.** This research has been supported by Qatar Museums.

## References

Al-Hinai, K. G., McMahon Moore, J., and Bush, P. R.: LANDSAT image enhancement study of possible submerged sand-dunes in the Arabian Gulf, Int. J. Remote Sens., 8, 251–258, https://doi.org/10.1080/01431168708948639, 1987.

Al-Naimi, F. A., Cuttler, R., Arrock, H., and Roberts, H.: A possible Upper Palaeolithic and Early Holocene flint scatter at Ra's 'Ushayriq, western Qatar, Proc. Sem. Arab. Stud., 40, 35–39, 2010.

Al-Naimi, F., Price, K. M., Cuttler, R., and Arrock, H.: Reassessing Wādī Debayan (Wādī al-abay'ān): an important Early Holocene Neolithic multi-occupational site in western Qatar, Proc. Sem. Arab. Stud., 41, 239–244, 2011.

Al-Saad, H.: Lithostratigraphy of the Middle Eocene Dammam Formation in Qatar, Arabian Gulf: Effects of sea-level fluctuations along a tidal environment, J. Asian Earth Sci., 25, 781–789, https://doi.org/10.1016/j.jseaes.2004.07.009, 2005.

Al Senafi, F. and Anis, A.: Shamals and climate variability in the Northern Arabian/Persian Gulf from 1973 to 2012, Int. J. Climatol., 35, 4509–4528, https://doi.org/10.1002/joc.4302, 2015.

Al-Yousef, M.: Mineralogy, Geochemistry and the origin of Quaternary sabkhas in the Qatar Peninsula, Arabian Gulf, PhD thesis, Faculty of Earth Sciences, University of Southampton, UK, 438 pp., 2003.

Babikir, A. A. A.: The vegetation of natural depressions in Qatar in relation to climate and soil, J. Arid Environ., 10, 165–173, https://doi.org/10.1016/S0140-1963(18)31236-9, 1986.

Batanouny, K. H.: Ecology and flora of Qatar, Alden Press, Oxford, 1981.

Benazzouz, M. T.: Hamada, in: Encyclopedia of Geomorphology, edited by: Goudie, A., Routledge, London, 512–513, 2004.

Beresford-Jones, D., Lewis, H., and Boreham, S.: Linking cultural and environmental change in Peruvian prehistory: Geomorphological survey of the Samaca Basin, Lower Ica Valley, Peru, Catena, 78, 234–249, https://doi.org/10.1016/j.catena.2008.12.010, 2009.

Bibby, G.: Arabian Archaeology, Kuml, 15, 133–152, 1965.

Billeaud, I., Caline, B., Livas, B., Tessier, B., Davaud, E., Frébourg, G., Hasler, C.-A., Laurier, D., and Pabian-Goyheneche, C.: The carbonate-evaporite lagoon of Al Dakhirah (Qatar): an example of a modern depositional model controlled by longshore transport, Geol. Soc. London Spec. Pub., 388, 561–588, https://doi.org/10.1144/SP388.7, 2014.

Blott, S. J. and Pye, K.: GRADISTAT: a grain size distribution and statistics package for the analysis of unconsolidated sediments, Earth Surf. Proc. Land., 26, 1237–1248, https://doi.org/10.1002/esp.261, 2001.

Breeze, P. S., Groucutt, H. S., Drake, N. A., Louys, J., Scerri, E. M. L., Armitage, S. J., Zalmout, I. S. A., Memesh, A. M., Haptari, M. A., Soubhi, S. A., Matari, A.H., Zahir, M., Al-Omari, A., Alsharekh, A. M., and Petraglia, M. D.: Prehistory and palaeoenvironments of the western Nefud Desert, Saudi Arabia, Archaeol. Asia, 10, 1–16, https://doi.org/10.1016/j.ara.2017.02.002, 2017.

Brückner, H.: Wasserstraßen im Wüstensand, Antike Welt, 44, 18–24, 2013.

Buckley, D. G.: The excavation of seven cairns on the Ras Aburuk peninsula, in: Qatar Archaeological Report – Excavations 1973, edited by: De Cardi, B., Oxford University Press, Oxford, UK, 120–135, 1978.

Carter Jr., R. and Killick, R. (Eds.): Al-Khor Island: Investigating Coastal Exploitation in Bronze Age Qatar, Moonrise Press, Ludlow, UK, 2010.

Cavalier, C.: Geological description of the Qatar Peninsula (Arabian Gulf), Government of Qatar, Department of Petroleum Affaires, Doha, 1970.

Cuttler, R., Tetlow, E., and Al-Naimi, F.: Assessing the value of palaeoenvironmental data and geomorphological processes for understanding Late Quaternary population dynamics in Qatar, Proc. Sem. Arab. Stud., 41, 47–60, 2011.

Cuttler, R., Al-Naimi, F., and Tetlow, E.: Typological and chronological variation of burial in Qatar: 'Ubaid to late pre-Islamic, Proc. Sem. Arab. Stud., 43, 99–109, 2013.

Cuttler, R. T. and Al Naimi, F. A.: From land-locked desert to maritime nation: Landscape evolution and taphonomic Pathways in Qatar from 14 ka, Adumatu, 28, 7–22, 2013.

De Cardi, B. (Ed.): Qatar Archaeological Report, Excavations 1973, Oxford University Press, Oxford, UK, 1978.

Dinies, M., Plessen, B., Neef, R., and Kürschner, H.: When the desert was green: Grassland expansion during the early Holocene in northwestern Arabia, Quatern. Int., 382, 293–302, https://doi.org/10.1016/j.quaint.2015.03.007, 2015.

Dinies, M., Neef, R., Plessen, B., and Kürschner, H.: Holocene vegetation in northwestern Arabia – changing natural resources, in: Actualités des recherches archéologiques en Arabie, edited by: Goy, J., Bessenay-Prolonge, J., Betouche, A., Decaix, A., Havé, A., Hiblot, S., Perriot, C., and Pichon, F., Routes de l'Orient, Hors-Séries, 2, 1–19, 2016.

Drechsler, P.: The Palaeolithic and Neolithic in South Qatar, Insights from Two Seasons in the Field, Z. Orient Archäol., 7, 276–289, 2014.

Drechsler, P., Berthold, C., Al-Naimi, F. A., and Eichmann, R.: Ceremonial objects or household items? Non-destructive $\mu$-XRD 2 and $\mu$-XRF studies on three Neolithic hematite axes from Qatar, Arab. Archaeol. Epigr., 24, 119–124, https://doi.org/10.1111/aae.12029, 2013.

Drechsler, P., Engel, M., Brill, D., and Gerber, C.: The Asaila depression, an archaeological landscape in Qatar, Proc. Sem. Arab. Stud., 46, 98–106, 2016.

Edens, C.: Towards a definition of the western Rub al-Khali "Neolithic", Atlal, 6, 109–124, 1982.

Edens, C.: The Rub al-Khali “Neolithic” revisited: the view from Nadqan, in: Araby the Blest, edited by: Potts, D. T., CNI Publications, Copenhagen, 5–43, 1988.

Edens, C.: Khor Ile-Sud, Qatar: The archaeology of Late Bronze Age purple-dye production in the Arabian Gulf, Iraq, 61, 71–88, https://doi.org/10.2307/4200468, 1999.

Eichmann, R., Gerlach, I., Drechsler, P., Pfeiffer, K., and Gerber, C.: Joint Qatari-German project – Exploration and visualization of cultural heritage in south Qatar, World Herit., 72, 78–87, 2014.

Embabi, N. S. and Ashour, M. M.: Barchan dunes in Qatar, J. Arid Environ., 25, 49–69, https://doi.org/10.1006/jare.1993.1042, 1993.

Engel, M. and Brückner, H.: The South Qatar Survey Project (SQSP): Preliminary findings on Holocene coastal changes and geoarchaeological archives, Z. Orient Archäol., 7, 290–301, 2014.

Engel, M. and Brückner, H.: Holocene climate variability of Mesopotamia and its impact on the history of civilization, EarthArXiv, https://doi.org/10.31223/osf.io/s2aqt, 2018.

Engel, M., Brückner, H., Pint, A., Wellbrock, K., Ginau, A., Voss, P., Grottker, M., Klasen, N., and Frenzel, P.: The early Holocene humid period in NW Saudi Arabia – evidence from sediments, microfossils and palaeo-hydrological modelling, Quatern. Int., 266, 131–141, https://doi.org/10.1016/j.quaint.2011.04.028, 2012.

Engel, M., Matter, A., Parker, A. G., Parton, A., Petraglia, M. D., Preston, G. W., and Preusser, F.: Lakes or wetlands? A comment on “The middle Holocene climatic records from Arabia: Reassessing lacustrine environments, shift of ITCZ in Arabian Sea, and impacts of the southwest Indian and African monsoons” by Enzel et al., Global Planet. Change, 148, 258–267, https://doi.org/10.1016/j.gloplacha.2016.11.001, 2017.

Engel, M., Boesl, F., and Brückner, H.: Migration of barchan dunes in Qatar–controls of the Shamal, teleconnections, sea-level changes and human impact, Geosciences, 8, 240, https://doi.org/10.3390/geosciences8070240, 2018.

Enzel, Y., Kushnir, Y., and Quade, J.: The middle Holocene climatic records from Arabia: reassessing lacustrine environments, shift of ITCZ in Arabian Sea, and impacts of the southwest Indian and African monsoons, Global Planet. Change, 129, 69–91, https://doi.org/10.1016/j.gloplacha.2015.03.004, 2015.

Fassbinder, J. W. E.: Seeing beneath the farmland, steppe and desert soil: Magnetic prospecting and soil magnetism, J. Archaeol. Sci., 56, 85–95, https://doi.org/10.1016/j.jas.2015.02.023, 2015.

Fassbinder, J. W. E.: Magnetometry for Archaeology, in: Encyclopedia of Geoarchaeology, edited by: Gilbert, A. S., Springer, Dordrecht, 499–514, https://doi.org/10.1007/978-1-4020-4409-0_169, 2017.

Fleitmann, D., Burns, S. J., Mangini, A., Mudelsee, M., Kramers, J., Villa, I., Neff, U., Al-Subbary, A. A., Buettner, A., Hippler, D., and Matter, A.: Holocene ITCZ and Indian monsoon dynamics recorded in stalagmites from Oman and Yemen (Socotra), Quaternary Sci. Rev., 26, 170–188, https://doi.org/10.1016/j.quascirev.2006.04.012, 2007.

Fryberger, S. G., Schenk, C. J., and Krystinik, L. F.: Stokes surfaces and the effects of near-surface groundwater-table on aeolian deposition, Sedimentology, 35, 21–41, https://doi.org/10.1111/j.1365-3091.1988.tb00903.x, 1988.

Gerber, C., Drechsler, P., Yaşin-Meier, D., Brückner, H., Engel, M., Tiltmann, S., Atas, N., Bley, J., Daitche, J., Hörwarthner, D., Lienig, A., Reising, R., and Riesenberg, M.: The South Qatar Survey Project (SQSP) – Final Report of the 2013 Spring Season. Qatar Museums (Doha) & German Archaeological Institute (Berlin), 141 pp., 2013.

Gerber, C., Drechsler, P., Yasin-Meier, D., Brückner, H., Engel, M., Meier, D. M. P., Götzelt, T., Daitche, J., Hörwarthner, D., Lienig, A., Reising, R., and Tiltmann, S.: The German-Qatari South Qatar Survey Project: The 2012–2013 Season, Z. Orient Archäol., 7, 248–275, 2014.

Ginau, A., Engel, M., and Brückner, H.: Holocene chemical precipitates in the continental sabkha of Tayma (NW Saudi Arabia), J. Arid Environ., 84, 26–37, https://doi.org/10.1016/j.jaridenv.2012.03.020, 2012.

Glob, P. V.: Oldtidsfund i Qatar, Kuml, 7, 167–178, 1958.

Goudie, A. (Ed.): Nebkha, in: Encyclopedia of Geomorphology, Routledge, London, 708, 2004a.

Goudie, A. (Ed.): Stone pavement, in: Encyclopedia of Geomorphology, Routledge, London, 998–999, 2004b.

Guagnin, M., Jennings, R., Eager, H., Parton, A., Stimpson, C., Groucutt, H. S., Drake, N. A., Pfeiffer, M., Stepanek, C., Alsharekh, A., and Petraglia, M. D.: Rock art imagery as a proxy for Holocene environmental change: a view from Shuwaymis, NW Saudi Arabia, Holocene, 26, 1822–1834, https://doi.org/10.1177/0959683616645949, 2016.

Guérin, A. and Al-Naimi, F.: Territory and settlement patterns during the Abbasid period (ninth century AD): the village of Murwab (Qatar), Proc. Sem. Arab. Stud., 39, 181–196, 2009.

Heberger, M. and Donnelly, K.: Oil, Food, and Water: Challenges and Opportunities for California Agriculture, Technical Report, Pacific Institute, Oakland, 2015.

Inizan, M.-L. (Ed.): Préhistoire à Qatar. Mission archéologique française à Qatar (2), Éditions Recherche sur les Civilisations, Paris, France, 1988.

Izquierdo Zamora, Á., Cuttler, R. T. H., and Al-Naimi, F. A.: Prehistoric and pre-Islamic burial archaeology in Qatar: new results and perspectives, Proc. Sem. Arab. Stud., 45, 159–173, 2015.

Jennings, R. P., Singarayer, J., Stone, E. J., Krebs-Kanzow, U., Khon, V., Nisancioglu, K. H., Pfeiffer, M., Zhang, X., Parker, A., Parton, A., Groucutt, H. S., White, T. S., Drake, N. A., and Petraglia, M. D.: The greening of Arabia: multiple opportunities for human occupation of the Arabian Peninsula during the late Pleistocene inferred from an ensemble of climate model simulations, Quatern. Int., 382, 181–199, https://doi.org/10.1016/j.quaint.2015.01.006, 2015.

Kainert, C. and Drechsler, P.: An interplay of imports and local traditions? The pottery assemblage from Dosariyah, Saudi Arabia, Proc. Sem. Arab. Stud., 44, 213–226, 2014.

Kapel H.: Atlas of the Stone-Age Cultures of Qatar. Reports of the Danish Archaeological Expedition to the Arabian Gulf, Jutland Archaeol. Soc. Pub., 6, 5–43, 1967.

Konishi, M., Gotoh, T., and Akashi, Y.: Archaeological researches in the Gulf – A Preliminary Report of the Excavations in Bahrain and Qatar, 1987/8 Season, Orient, 24, 18–46, https://doi.org/10.5356/orient1960.24.18, 1988.

Lambeck, K.: Shoreline reconstructions for the Persian Gulf since the last glacial maximum, Earth Planet. Sc. Lett., 142, 43–57, https://doi.org/10.1016/0012-821X(96)00069-6, 1996.

Lloyd, J. W., Pike, J. G., Eccleston, B. L., and Chidley, T. R. E.: The hydrogeology of complex lens conditions in Qatar, J. Hydrol., 89, 239–258, https://doi.org/10.1016/0022-1694(87)90181-8, 1987.

Macumber, P. G.: A geomorphological and hydrological underpinning for archaeological research in northern Qatar, Proc. Sem. Arab. Stud., 41, 187–200, 2011.

Macumber, P. G.: An examination of the impact of environmental disparity on the occupation of Qatar – Season 4, Copenhagen University Study of the Archaeology of Qatar, unpublished report, 96 pp., 2012.

Macumber, P. G.: Water heritage in Qatar, in: Cultural Heritages of Water: Thematic Study on The Cultural Heritages of Water in the Middle East and Maghreb, edited by: UNESCO World Heritage Convention, UNESCO, 223–239, 2015.

Macumber, P. G.: Sea level and climatic influences on the occupation of Qatar and the Gulf during the Holocene period, Proc. Sem. Arab. Stud., 48, 201–217, 2018.

McPhillips, S., Rosendahl, S., and Morgan, V.: Abbasid rural settlement in northern Qatar: seasonal tribal exploitation of an arid environment?, Proc. Sem. Arab. Stud., 45, 185–197, 2015.

Muhesen, S. and Al-Naimi, F.: Archaeological heritage of pre-Islamic Qatar, World Herit., 72, 46–53, 2014.

Neugebauer, I., Dinies, M., Plessen, B., Dräger, N., Brauer, A., Frenzel, P., Gleixner, G., Hoelzmann, P., Krahn, K., Pint, A, Schwab, V.F., Schwarz, A., Tjallingii, R., and Engel, M.: The Early Holocene Humid Period in N Arabia – proxy evidence from a unique varved lake record, Geophys. Res. Abstr., 20, EGU2018-15815, 2018.

Norton, J., Abdul Majid, S., Allan, D., Al Safran, M., Böer, B, and Richer, R.: An Illustrated Checklist of the Flora of Qatar, Ashford Colour Press Ltd, Gosport, 2009.

Oates, J.: 'Ubaid Mesopotamia and its relation to Gulf countries, in: Qatar Archaeological Report – Excavations 1973, edited by: De Cardi, B., Oxford University Press, Oxford, 39–52, 1978.

Parker, A. G., Preston, G. W., Parton, A., Walkington, H., Jardine, P. E., Leng, M. J., and Hodson, M. J.: Low latitude Holocene hydroclimate derived from lake sediment flux and geochemistry, J. Quaternary Sci., 31, 296 –299, https://doi.org/10.1002/jqs.2859, 2016.

Parker, A. G., Armitage, S. J., Engel, M., Morley, M. W., Parton, A., Preston, G. W., and Russ, H.: Geomorphology, geoarchaeology and palaeoenvironments, in: Dosariyah – An Arabian Neolithic Coastal Community in the Central Gulf, edited by: Drechsler, P., Archaeopress, Oxford, UK, 21–55, 2018.

Parton, A., Clark-Balzan, L., Parker, A. G., Preston, G.W., Sung, W. W., Breeze, P. S., Leng, M. J., Groucutt, H. S., White, T. S., Alsharekh, A., and Petraglia, M. D.: Middle-late Quaternary palaeoclimate variability from lake and wetland deposits in the Nefud Desert, Northern Arabia, Quaternary Sci. Rev., 202, 78–97, https://doi.org/10.1016/j.quascirev.2018.10.010, 2018.

Pelegrin, J. and Inizan, M.-L.: Soft hammerstone percussion use in bidirectional blade-tool production at Acila 36 and in bifacial knapping at Shagra (Qatar), Arab. Archaeol. Epigr., 24, 79–86, https://doi.org/10.1111/aae.12016, 2013.

Perthuisot, J.-P.: Contribution à l'étude du Quaternaire marine de la péninsule de Qatar, Bull. Soc. Géol. France, S7-XIX, 1167–1170, https://doi.org/10.2113/gssgfbull.S7-XIX.5.1167, 1977.

Perthuisot, J.-P.: Le Quaternaire de la péninsule, données liminaires et hypothèses, in: Mission archéologique à Qatar, tome 1, edited by: Tixier, J., Doha, 11–31, 1980.

Pfeiffer, K.: South Qatar Survey Project, Katar: Archäologische Surveys in der südlichen Landeshälfte Katars, e-Forschungsber. DAI, 3, 79–82, 2015.

Preston, G. W., Parker, A. G., Walkington, H., Leng, M. J., and Hodson, M. J.: From nomadic herder-hunters to sedentary farmers: the relationship between climate change and ancient subsistence strategies in south-eastern Arabia, J. Arid Environ., 86, 122–130, https://doi.org/10.1016/j.jaridenv.2011.11.030, 2012.

Rao, P. G., Al-Sulaiti, M., and Al-Mulla, A. H.: Winter shamals in Qatar, Arabian Gulf, Weather, 56, 444–451, https://doi.org/10.1002/j.1477-8696.2001.tb06528.x, 2001.

Rees, G., Richter, T., and Walmsley, A.: Investigations in al-Zubārah hinterland at Murayr and al-Furayah, north-west Qatar, Proc. Sem. Arab. Stud., 41, 309–316, 2011.

Rivers, J., Engel, M., Dalrymple, R., Yousif, R., Strohmenger, C. J., and Al-Shaikh, I.: Are carbonate barrier islands mobile? Insights from a mid to late-Holocene system, Al Ruwais, northern Qatar, Sedimentology, 67, 534–558, https://doi.org/10.1111/sed.12653, 2020.

Sadiq, A. M. and Nasir, S. J.: Middle Pleistocene karst evolution in the State of Qatar, Arabian Gulf, J. Cave Karst Stud., 64, 132–139, 2002.

Schönicke, J., Tiltmann, S., Drechsler, P., Engel, M., and Pfeiffer, K.: South Qatar Survey Project (SQSP) Qatari-German Joint Archaeological Fieldwork by QM (Doha) and DAI (Berlin) – Final Report of the 2016 Spring Season, Qatar Museums (Doha) & German Archaeological Institute (Berlin), 103 pp., 2016.

Scott-Jackson, J. E., Rose, J. I., Scott-Jackson, W., and Al-Naimi, F.: Found: the Palaeolithic of Qatar, Proc. Sem. Arab. Stud., 45, 329–336, 2015.

Siart, C., Hecht, S., Holzhauer, I., Altherr, R., Meyer, H. P., Schukraft, G., Eitel, B., Bubenzer, O., and Panagiotopoulos, D.: Karst depressions as geoarchaeological archives: The palaeoenvironmental reconstruction of Zominthos (Central Crete), based on geophysical prospection, sedimentological investigations and GIS, Quatern. Int., 216, 75–92, https://doi.org/10.1016/j.quaint.2009.06.020, 2010.

Smith, G. H.: Test excavations in the oasis of Bir Abaruk, site 3, in: Qatar Archaeological Report – Excavations 1973, edited by: De Cardi, B., Oxford University Press, Oxford, UK, 26–34, 1978.

Sonnenfeld, P. and Perthuisot, J.-P.: Brines and Evaporites – Short Course Presented at the 28th International Geological Congress Washington, D.C. AGU, Washington, 126 pp., 1989.

State of Qatar (Ed.): Topographic map, 1 : 50 000, sheets 150/375 & 150/400, State of Qatar, Ministry of Public Works, 1971.

State of Qatar (Ed.): Geological map, 1 : 100 000, sheets 2–4, State of Qatar, Industrial Development Technical Centre, 1980.

Strohmenger, C. J. and Jameson, J.: Gypsum stromatolites from Sawda Nathil: relicts from a southern coastline of Qatar, Carbonate. Evaporite., 33, 169–186, https://doi.org/10.1007/s13146-017-0365-2, 2018.

Tetlow, E., Cuttler, R., Al-Naimi, F., Sheharyer, A., Bouhali, O., Delaney, L., and Adcock, J.: Landscape visualization, sea-level change, and human occupation in Wādī Debayān, north-western Qatar, Proc. Sem. Arab. Stud., 43, 337–348, 2013.

Tixier, J. (Ed.): Mission archéologique française à Qatar i, Ministry of Information, Doha, Qatar, 1980.

Uerpmann, M.: The Dark Millennium – Remarks on the Final Stone Age in the Emirates and Oman, in: Archaeology of the United Arab Emirates. Proceedings of the 1st International Conference on the Archaeology of the U.A.E., edited by: Potts, D. T., Al Naboodah, H., and Hellyer, P., Trident Press, London, UK, 73–84, 2003.

Uerpmann, M. and Uerpmann, H.-P.: Ubaid pottery in the eastern Gulf – new evidence from Umm al-Qaiwain (U.A.E.), Arab. Archaeol. Epigr., 7, 125–139, https://doi.org/10.1111/j.1600-0471.1996.tb00096.x, 1996.

Vita-Finzi, C.: Environmental History, in: Qatar Archaeological Report – Excavations 1973, edited by: De Cardi, B., Oxford University Press, Oxford, UK, 11–25, 1978.

Yechieli, Y. and Wood, W.: Hydrogeologic processes in saline systems: playas, sabkhas, and saline lakes, Earth Sci. Rev., 58, 343–365, https://doi.org/10.1016/S0012-8252(02)00067-3, 2002.

Yigiterhan, O., Alfoldy, B. Z., Giamberini, M., Turner, J. C., Al-Ansari, E. S., Abdel-Moati, M. A., Al-Maslamani, I. A., Kotb, M. M., Elobaid, E. A., Hassan, H. M., and Obbard, J. P.: Geochemical composition of Aeolian dust and surface deposits from the Qatar Peninsula, Chem. Geol., 476, 24–45, https://doi.org/10.1016/j.chemgeo.2017.10.030, 2018.

**continued from back cover**



https://www.eg-quaternary-science-journal.net/

ISSN 0424-7116

## CONTENTS




**continued on the inside cover**



https://www.eg-quaternary-science-journal.net/ ISSN 0424-7116